Title
A Modular Approach to the Synthesis of Electron-Deficient Organic Semiconducting Materials

Author
Kolaczkowski, Matthew A

Publication Date
2019

Peer reviewed|Thesis/dissertation

A Modular Approach to the Synthesis of Electron-Deficient Organic Semiconducting Materials

By

Matthew A. Kolaczkowski

A dissertation submitted in partial satisfaction of the
requirements for the degree of

Doctor of Philosophy
in
Chemistry
in the
Graduate Division
of the
University of California, Berkeley

Committee in charge:

Dr. Yi Liu, Co-Chair
Professor Thomas Maimone, Co-Chair
Professor Matthew Francis
Professor Jie Yao

Fall 2019

A Modular Approach to the Synthesis of Electron-Deficient Organic Semiconducting Materials

By: Matthew A. Kolaczkowski

Abstract

A Modular Approach to the Synthesis of Electron-Deficient Organic Semiconducting Materials

By

Matthew A. Kolaczkowski

Doctor of Philosophy in Chemistry
University of California, Berkeley
Dr. Yi Liu, Co-chair
Professor Thomas Maimone, Co-chair

Utilizing extended π conjugated structures, organic semiconducting materials can effectively transport charges and are imbued with properties unique from inorganic systems. The field of organic electronics has achieved preliminary success in applying these semiconducting small molecules and polymers to intriguing new applications, such as thin-film technology, biologically compatible electronics, flexible devices, and many other areas.

Further advances in organic electronics require the discovery of new materials. For over two decades, fullerene based acceptors have been considered essential for high performance, slowing development of alternative electron deficient materials. Work undertaken in this dissertation focuses on advancing the next generation of non-fullerene acceptor materials. Robust and modular chemistry aids in the successful development of novel, high performance, electron acceptor materials with controllable physical and optoelectronic properties.

This modular and robust synthesis is exemplified by the development of bay-annulated indigo (BAI). Using indigo as a precursor, this stable amide-based withdrawing unit has outstanding charge transport properties, showing one of the highest recorded ambipolar conductivities. In order to better control intermolecular interactions, a method to desymmetrize the BAI core has been developed. Using this new methodology, a donor-acceptor BAI adduct is synthesized which self-assembles into nanowires that are capable of transporting charge. The use of this self-assembling material as an additive for photovoltaic applications gives an improvement in solar cell efficiency of ~11% over the control P3HT/PC[60]BM device.

To enhance the withdrawing character of existing conjugated systems, the 2-(1,3-dithiol-2-ylidene)malononitrile (DTM) group is proposed. Condensation of activated methylene compounds, such as malononitrile, with carbon disulfide produces a nucleophilic dithiolate salt that can participate in S_NAr reactions. Incorporation of this withdrawing group is found to significantly alter the optoelectronic properties of 1,2,5-benzothiadiazole (BTD) acceptors. When monomers functionalized with the DTM group are polymerized, the resulting polymers have broadened light absorption, strong thermochromic and solvatochromic behavior, and improved crystallinity compared to a control fluorinated polymer analogue. When used as the active

component in organic field effect transistors (OFETs) the DTM modified polymer is imbued with the ability to transport both electrons and holes, whereas the fluorinated polymer is a unipolar hole transport material.

Finally, a wide band gap acceptor is developed with the goal of improving the open circuit voltage (V_{OC}) in solar cells. Utilizing the flagship non-fullerene acceptor ITIC as a template, a new family of molecules are synthesized using weakly withdrawing thiobarbituric acid (TBTA) groups to raise the lowest unoccupied molecular orbital (LUMO) energy. Not only does this result in an increased V_{OC}, but the material outperforms the parent ITIC acceptor. To understand the solid state properties of the TBTA based acceptor, a morphological study is undertaken. The withdrawing TBTA groups are functionalized with a range of solubilizing hydrocarbon chains to provide a meaningful comparison. When applied to solar cells the effect on performance is drastic. Grazing incidence wide angle x-ray scattering (GIWAXS) experiments are performed to examine the crystallinity and intermolecular interactions in this system. Using this information, clear relationships are drawn between molecular functionality and device performance. This underlies the importance of morphological studies and demonstrates a need to understand these complex relationships.

To my parents, Dr. Larry and Lisa Kolaczkowski.

Table of Contents

Acknowledgements

First and foremost, I would like to thank my parents, Dr. Larry and Ms. Lisa Kolaczkowski. None of this would have been possible without you. Dad, you were the first chemist in my life. Your love of science inspired me to study chemistry, but more importantly, your character continually inspires me to be a good person. Mom, your love, encouragement, and patience have made me who I am today. I try my best to live up to your example.

I am also lucky to have such wonderful siblings. My sister Lauren, who has a big heart and can always make me laugh. And Steven, who is me, but better. I look forward to you getting your Ph.D. so we can have a trio of Drs. Kolaczkowski.

Endless gratitude goes out to my companion, Lauren Nowak, who gave me a reason to leave lab and explore the beauty of the Bay Area. You bring so much richness and color to my life. It was an adventure moving out to Berkeley together, and I am excited to continue our journey together.

I could never have survived grad school alone, and I am incredibly lucky to have met and worked with such amazing scientists and educators. I'd like to thank Team BLAGS; Lauren Nowak, Erin and Andy Creel, Iris Young, and Alex Aaring for the weekly game nights, Action Tuesdays (held on Thursdays), protests, and adventures. Meeting up was sometimes the only thing that kept me going during difficult weeks. I am also indebted to my fellow lab mate Chris Anderson for the countless discussions, synthesis lunches, late nights in lab, bouldering, and especially the tomfoolery. Working away from campus, you kept me from feeling completely isolated, and I will always be grateful for your companionship. You are all my family now, whether you like it or not.

I was also strongly supported by friends from undergrad and back home. I will always appreciate Joe Hagedorn, who has been one of my dearest friends since the second grade. Undergrad chemistry was made not just survivable, but enjoyable in no small part because of you and rest of the Chem Majors at the "University of Urbana"; Matt Frost, Bryan Kandelman, Robert Garcia, John Koenig, and Erika Bongen. I'd also like to thank Pathum Karunaratne, Spencer Carver, Kathy Chen, and Elizabeth Deutsch for encouraging and helping me discover who I am in some of my most formative years. Finally, thank you to Sara Thomas for the countless hours of commiseration and conversation that bolstered my sanity throughout grad school.

My Ph.D. would not be possible without the mentorship of Dr. Yi Liu. I will forever be indebted to you for taking me into your group when my future was uncertain, giving me the room to explore new ideas, and helping me develop as a chemist. The Liu group members and visiting students have provided a fantastic, collaborative research environment to work in. Your experiences from around the world have enriched my understanding and appreciation of diversity in science. Particularly, the guidance I received from Matt Jurow, Xinle Li, and David Hanifi has been incredibly valuable. I would especially like to recognize Akash Patel, a stellar undergraduate researcher whom I mentored in lab. Your brilliance and friendly nature will take you far. The Molecular Foundry 6th floor staff, especially Liana Klivansky, Teresa Chen, and Eric Dailing were instrumental in showing me the ropes and the importance of being a responsible scientist. Thank you to Prof. Matt Francis for words of wisdom and guidance over the years, especially during your role as interim organic facility director. Cheers to all the Molecular Foundry

6th Floor Users who I've crossed paths with over the years, including Pete Frischmann, Kira Gardner, Jessica Golden, Max Lyons, Daniel Sun, Justin Lim, and Zoey Herm.

I would also like to express my appreciation to Tom and the entire Maimone group for helping me transition into grad school and giving me a firm foundation of organic chemistry to build upon. I would like to express my deep gratitude to Xirui Hu, Kevin Hung, and Zach Brill, not only for their helpful discussions, but for their kindness and comradery when I needed it most.

I would not have even had the opportunity to study at Berkeley were it not for Prof. M. Christina White at UIUC, who gave me my first experience of academic organic chemistry research. It was working in your group that showed me that I wanted to pursue a career in chemistry research. I commend all the work that Grant Rice and Stephen Ammann did to mentor me when I was still learning how to be a chemist and constantly making mistakes. You were far more patient than I could recognize at the time. I would also like to acknowledge Prof. Martin Gruebele and the Gruebele group for teaching me things I never thought I would need and now use constantly. I would also be remiss to omit Prof. Martin Burke, whose lectures in introductory organic chemistry showed me the beauty in mechanism and chemical understanding.

I am extremely grateful for the opportunity to intern at Abbvie Inc. and for the outstanding researchers who were my guides to the world of industrial chemistry. You all took me from being a student to a researcher and were an incredible influence on my life. I would like to express my deep appreciation for Dr. Cynthia Burnell, Dr. Rajarathnam Reddy, Dr. Sanjay Chemburkar, Dr. Michael Hillier, Dr. Sarah Co, Dr. Li Sun, and Dr. Jose Restituyo for your invaluable mentorship. I would also like to remember Jay Paterson, who not only showed me how to think on my feet but taught me how humor can bridge ideological divides.

Finally, I would like to recognize my high school and grade school teachers, who gave me the attention and encouragement I needed to develop into who I am today. I was strongly influenced by high school physical science teachers Pieter Kreunen, Lindsay Consdorf, and John Cerauli and the Demo Show crew, who showed me that science has the ability to change in the world, and my English teacher Jason Baker who showed me the dangers of using that power irresponsibly.

Thanks everyone. I could not have done it without you.

Chapter 1. Design Principles for Organic Semiconducting Acceptor Materials

1.1 Motivation

Evolution in material synthesis and design has brought the field of organic electronics ever closer to the goal of inexpensive, printable electronics. If fully realized, organic materials could provide lightweight solar cells, flexible electronics,[1] biologically compatible devices,[2] neuromorphic computing,[3] and a host of applications unique to organic materials.

Organic semiconductors incorporated into thin flexible substrates are already opening up a new era of non-rigid electronics.[1] Thin film devices using organic field effect transistors (OFETs) are prime candidates for lightweight applications, such as use in clothing, personal devices, and aerospace applications. Flexible organic light emitting diode (OLED) displays[4] are already commercially available (**Figure 1a**), while "electronic skin"[5] and smart prosthetics with sensor arrays[2, 6] are being actively researched (**Figure 1b**).

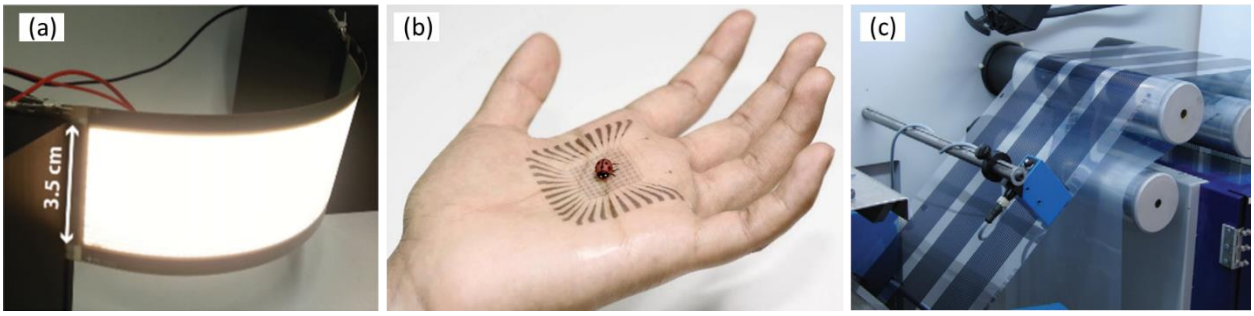

Figure 1: Emerging and established applications in organic electronics, such as (a) flexible OLEDs, (b) electronic skin, and (c) roll-to-roll printed solar cells. Reproduced with permission from reference [4d], Copyright © 2015, Wiley. Reproduced with permission from reference [7], Copyright © 2018, Springer Nature. Reproduced with permission from reference [8], Copyright © 2012, Elsevier

One of the Holy Grails of organic electronics is the realization of inexpensive, printed solar cells (**Figure 1c**).[9] Although the field is in its infancy, many outstanding improvements in efficiencies have already been demonstrated. Initial devices were less than 1% efficient, but the advent of new non-fullerene acceptors (NFAs) has boosted efficiencies of single junction organic photovoltaics (OPVs) to over 17.4%,[10] rivaling that of polycrystalline silicon (**Figure 2**). This brings within reach the commercialization target of devices 10% efficiency that are stable for 10 years.[8]

While many of these devices can be made from inorganic materials, the strength of organic electronics lies with the sheer vastness of design possibilities. Unlike inorganic materials, the properties of organic molecules can be altered on the atomic level, leading to fine control over the electronic structure and physical properties. This allows organic systems to be optimized in a way that is impossible for silicon and other inorganic species.

Despite the advances, access to new high-performance materials remains the largest barrier between those dreams and reality. The huge design-space provides nearly limitless potential, but also poses unique challenges in terms of controlling material properties. Ideal organic semiconducting materials must have good stability, proper energy level alignment, high carrier mobilities, strong light absorption, a conjugated structure, high solubility, a proper mix of

crystalline and mixed domains in the solid state, amongst a host of other properties. The work outlined in this dissertation is focused on the discovery of new semiconducting motifs and developing new strategies with the aim of pushing the limits in the design of organic semiconductors.

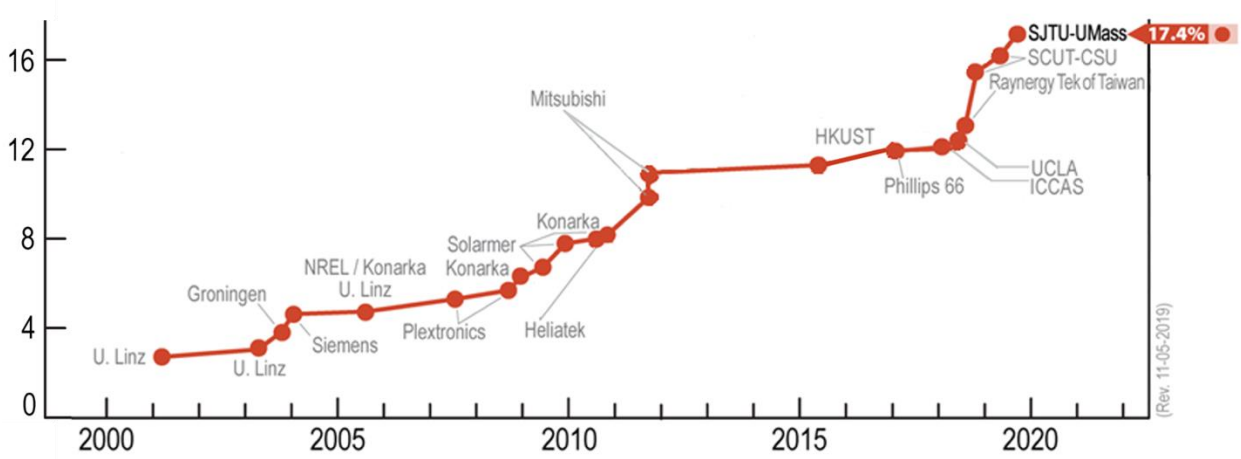

Figure 2: Research cell efficiencies, with organic thin film solar identified by red circles. This plot is courtesy of the National Renewable Energy Laboratory, Golden, CO.

1.2 Physical Origins of Organic Semiconductivity

Organic semiconductors allow the flow of electrons through a planar system of alternating single and double bonds. In order for carbon to participate in this flow of electrons, three of its four electrons are normally involved in covalent σ-bonds (or single bonds) formed directly between carbon and neighboring atoms, and one electron remains in a p orbital (**Figure 3a**). This p orbital has electron density above and below the plane formed by the other three bonds and has a node of zero density at the carbon center.

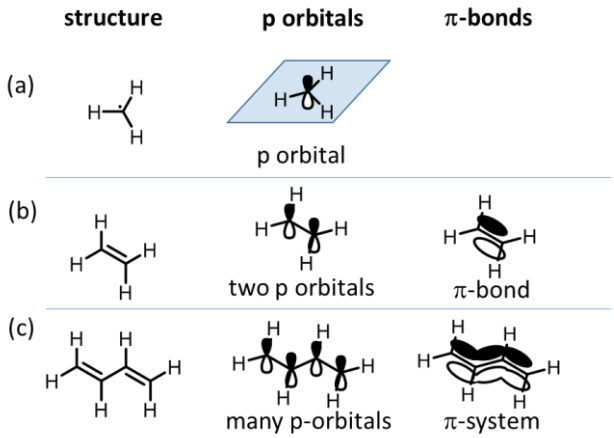

Figure 3: Diagram of (a) sp^2 carbon with a p orbital and a visualization of how neighboring p-orbitals create (b) π-bonds and (c) extended π-systems

If there are two p orbitals on neighboring atoms, they can come together to form a π-bond as seen with the double bond in ethylene (**Figure 3b**). While the electrons in a σ-bond are very tightly held and stable, electrons in a π-bond are higher in energy and mobile. As additional neighboring π orbitals are added, an extended π-system composed of multiple π-bonds can be formed (**Figure 3c**). The electrons in the π-system are not considered to be bound to a single atom but instead delocalized, free to move across the entire structure.

As the π system is extended the number of participating orbitals increases, pushing the highest occupied molecular orbital (HOMO) energy up and decreasing the lowest unoccupied molecular orbital (LUMO) energy, shrinking the energy gap between them (**Figure 4a**).[11] With a sufficient number of orbitals, the orbital diagram begins to approximate a traditional inorganic band structure, with a valence band (visualized in blue) filled with electrons and an empty conduction band (visualized in green). It is important to note that these are not truly continuous bands as seen in inorganic semiconducting systems. The calculated density of states (DOS) of polyacetylene clearly shows many gaps within the valence and conduction "bands" (**Figure 4b**).[12] However, it is a useful approximation and the origin of the term "band gap" used frequently in the organic semiconducting literature.

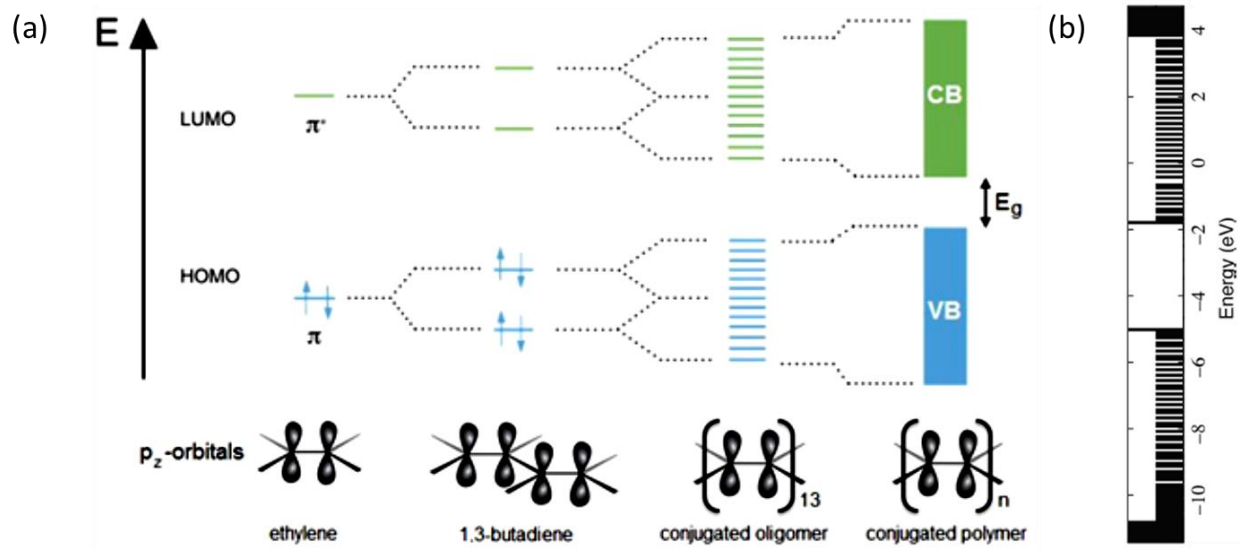

Figure 4: Composition of a polyacetylene (a) valence and conduction band by increasing ethylene units and (b) Density of States (DOS) for a 160 unit *trans*-polyacetylene calculated using hybrid DFT BH and HLYP3-21G method. Reproduced with permission from reference [11], Copyright © 2013, Wiley and [12], Copyright © 2006, National Academy of Sciences.

Although the concept of electrons flowing in resonance and in reactions has been well established, the idea of organic molecules as electrical conductors is rather new. This realization came with the refined synthesis of polyacetylene by Shirakawa in 1977, which established that polymers could be electronically conductive (**Figure 5a**).[13]

This system of alternating double and single bonds is inherently a semiconductor, but when doped, the conductivity increases over 7 orders of magnitude![14] When exposed to an oxidant such as iodine, the polymer can donate an electron leaving a radical cation (sometimes referred to as a polaron) present in the chain (**Figure 5b**).[15] The cation is kept close to the

triiodide (I_3^-) counter ion through electrostatic attraction, but the radical is free to travel up and down the polymer chain or "hop" to other polymer chains. An analogous process can occur with a reductant, such as lithium metal, where an electron can be injected into the system rather than removed (**Figure 5c**).[16] The resulting radical anion can also freely delocalize.

It is helpful to visualize these electronic effects within a band structure (**Figure 5d**). An undoped polymer of this nature is semiconducting and has low conductivity unless perturbed. The valence band or HOMO is filled with electrons that cannot move past each other. Above it in energy lies the conduction band, or LUMO, which has no electrons. The material becomes more conductive when more charge carriers are generated by adding or removing electrons from the system. When oxidized (p-doped) an electron is removed from the valence band (**Figure 5e**). This electron gap can move as electrons shift to fill the vacant position. In terms of moving charges, it is useful to think of this vacant position as a positively charged particle called a "hole" rather than a shifting gap. If the polymer is reduced (n-doped) an electron is placed into the conduction band where there are no electrons to impede its movement (**Figure 5f**). Many of these charge carriers (electrons or holes) moving at once in the same direction, causes an electrical current. This charge delocalization is the basis for organic electronics.

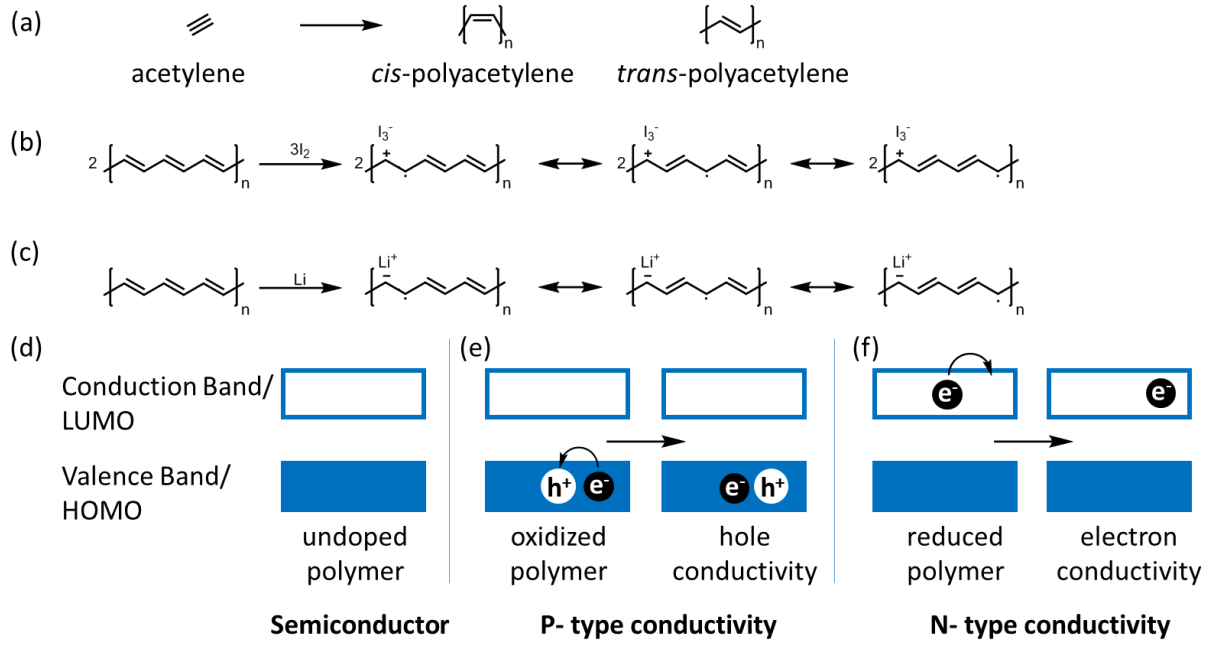

Figure 5: The formation of (a) *cis* and *trans*-polyacetylene as well as proposed resonance structures of (b) p-doped and (c) n-doped polyacetylene. A simplified depiction of the band structure of (d) an undoped polymer, (e) a p-doped polymer with a mobile hole in the valence band, and a (f) n-doped polymer with a mobile electron in the conduction band.

Although polyacetylene itself has not found application due to poor stability, it changed the paradigm of polymers being thought of solely as insulators and sparked a whole new field of research. For this, the work of discovery and characterization was recognized with a Nobel Prize in 2000.[17] The initial interest with the doped polyacetylene as a conductor faded with the discovery of semiconducting properties in undoped organic systems. Organic semiconductors

allow for entirely new applications, such as organic light emitting diodes (OLEDs),[4a, 4b] organic sensors,[18] organic electrochemical transistors (OECTs).[19] However, some of the largest efforts as a field and the focus of this dissertation will be on organic photovoltaic (OPV) and organic field effect transistor (OFET) applications.

1.3 Demand for New Acceptor Materials

For two decades, fullerene based acceptors have dominated the field of organic electronics due to their low LUMO and high carrier mobilities.[20] As one of the first high performance acceptor materials, fullerenes were a critical component in the development of organic electronics, earning The Nobel prize in chemistry in 1996 for its discovery.[21] Fullerene based solar cells have reached efficiencies up to 10.1%.[22] However, fullerenes are also burdened with a number of inherent limitations. The low LUMO energy is useful, but manipulating it is synthetically challenging. This means that the V_{OC} of solar cells using fullerenes is pinned to an unacceptably low level and, therefore, limits the number of compatible donor polymers. In addition, fullerenes have low absorption in the visible region of the spectrum, meaning they only weakly contribute to photocurrent generation.[23] But because they have been a staple for such an extended period, discovery of new acceptors has been slow compared to the development of donor polymers.

This limitation has long been recognized and an increased focus on acceptor research has given rise to a renaissance in acceptor design. The discovery of many high performing non-fullerene acceptor (NFA) molecules has recently surpassed the performance of fullerenes.[24] The work presented in this dissertation is aligned with this movement and focuses on the design and testing of new electron deficient molecules, polymers, and monomeric units.

There are a myriad of factors to consider when designing new semiconducting molecules and polymers. Not only do they need to be stable and semiconducting themselves, but also have appropriate orbital energy levels to interact with other device components. They also must strongly absorb light, transport charge over long distances, be soluble enough for processing into devices, and have good film properties. The following section will outline common design strategies used to make molecules which address these unique challenges.

1.4 Controlling the HOMO-LUMO Gap

One of the most important properties of organic semiconductors is the HOMO-LUMO gap or band gap. The presence of a small band gap is by definition what makes a material a semiconductor. This energy difference between the valence and conduction band corresponds to the minimum energy a photon must have to be absorbed. Any light that is absorbed with more energy than the band gap excites an electron into higher excited states and then quickly relaxes back to the LUMO energy level, with the excess energy lost as heat, vibration, or other non-radiative decay pathways. This means that a lower bandgap material can absorb more (lower energy) photons, but in return wastes the energy of lower wavelength photons.

As described previously with polyacetylene, extending the conjugated pathway leads to a lower band gap through increased electron delocalization (**Figure 4a**). The extended conjugation approach can be supplemented to decrease band gap even further. Both increasing quinoidal character and incorporating donor-acceptor pairs within a polymeric backbone have proven to be successful strategies for bandgap modification.

The relationship between the quinoidal character and band gap of a polymer was elucidated by Jean-Luc Brédas in 1985 (**Figure 6a**).[25] The amount of quinoidal character in a polymer can be estimated by the bond length alternation (BLA), the difference in the lengths of bonds connecting the rings vs. the neighboring bond within the ring (Δr). As the BLA decreases, the band gap also decreases to the point of being vanishingly small in some cases.

The term quinoidal comes from 1,4 and 1,2-benzoquinone which are well known for their stability and reversible reduction to the aromatic hydroquinones (**Figure 6b**). The quinoidal contribution to the electronic structure of polythiophene (PT) is relatively minor as it involves losing substantial aromatic stabilization energy (**Figure 6c**). This lack of quinoidal influence leaves the band gap at a relatively high 2.2 eV. However, by fusing an aromatic and quinoidal unit like in polyisothianaphthene (PTN), the quinoidal resonance form can be greatly stabilized, decreasing the band gap to 1.0 eV (**Figure 6d**). When doped, PTN also becomes conductive and transparent.[25b, 26]

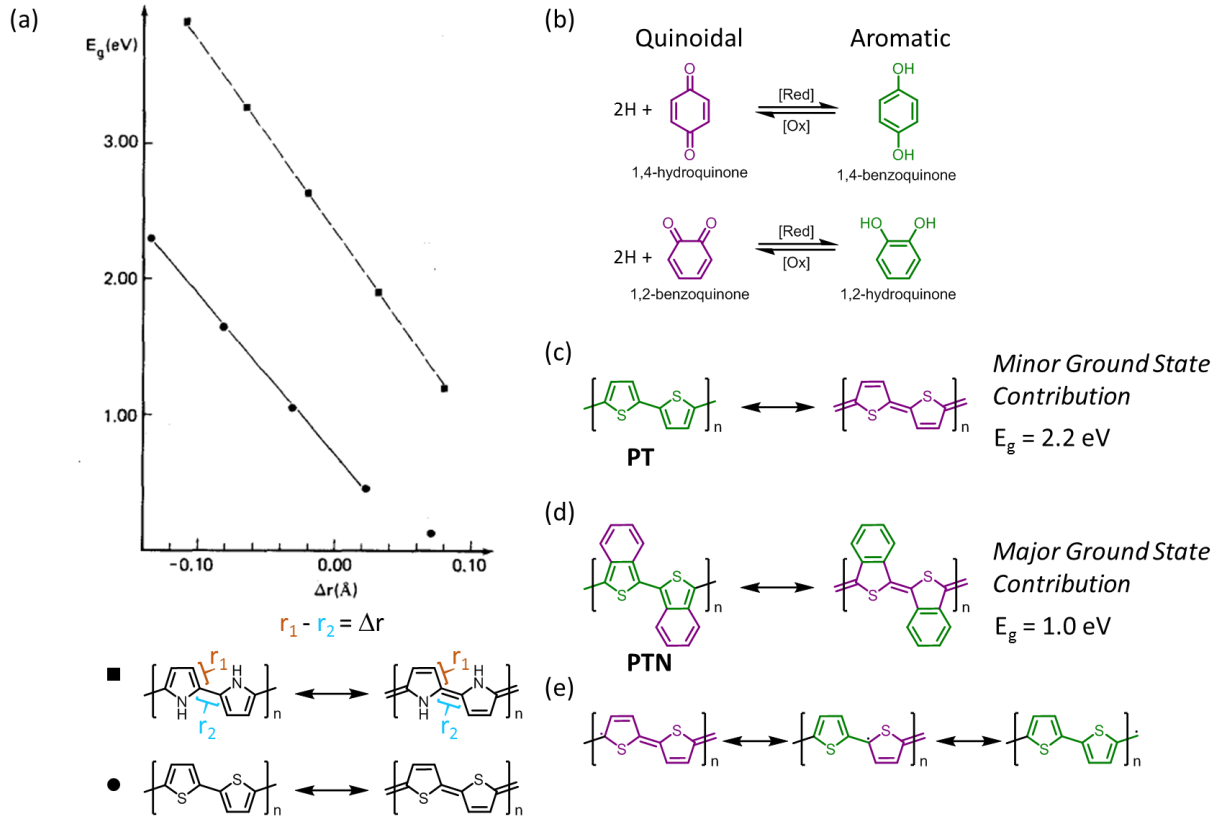

Figure 6: (a) The evolution of band gap as a function of bond length alternation BLA) and a comparison of (b) aromatic and quinoidal oxidation states in 1,2 and 1,4-quinones. The quinoidal contribution to (c) polythiophene (PT) and (d) polyisothianaphthene (PTN) are outlined, and (e) visualization of charge transport in such a system is visualized. Reproduced with permission from reference [25a], Copyright © 1985, American Institute of Physics.

Quinoidal systems are excellent at delocalizing charges since they are not bound within aromatic structures. The increased double bond character in the bridging bond between rings also helps prevent bond rotation, keeping the rings in a planar configuration. Charge injection

into such systems is also favorable since the quinoidal rings gain aromatic stabilization energy in the process (**Figure 6e**).

A more recent strategy to lower band gap has been to incorporate donor-acceptor pairs into semiconductors.[27] By pairing an electron-rich unit with an electron-poor one, charge transfer between the two is favorable and only takes a small amount of energy to induce (**Figure 7a**). By choosing which donor or acceptor subunit are used, the band gap and energy of the HOMO and LUMO can be controlled. A simplified frontier molecular orbital diagram depicts how orbital mixing of the donor and acceptor HOMO leads to a net increase in energy, while overlap of the LUMO provides a net decrease (**Figure 7b**). The result is a donor-acceptor adduct with a band gap smaller than either the donor or acceptor individually.

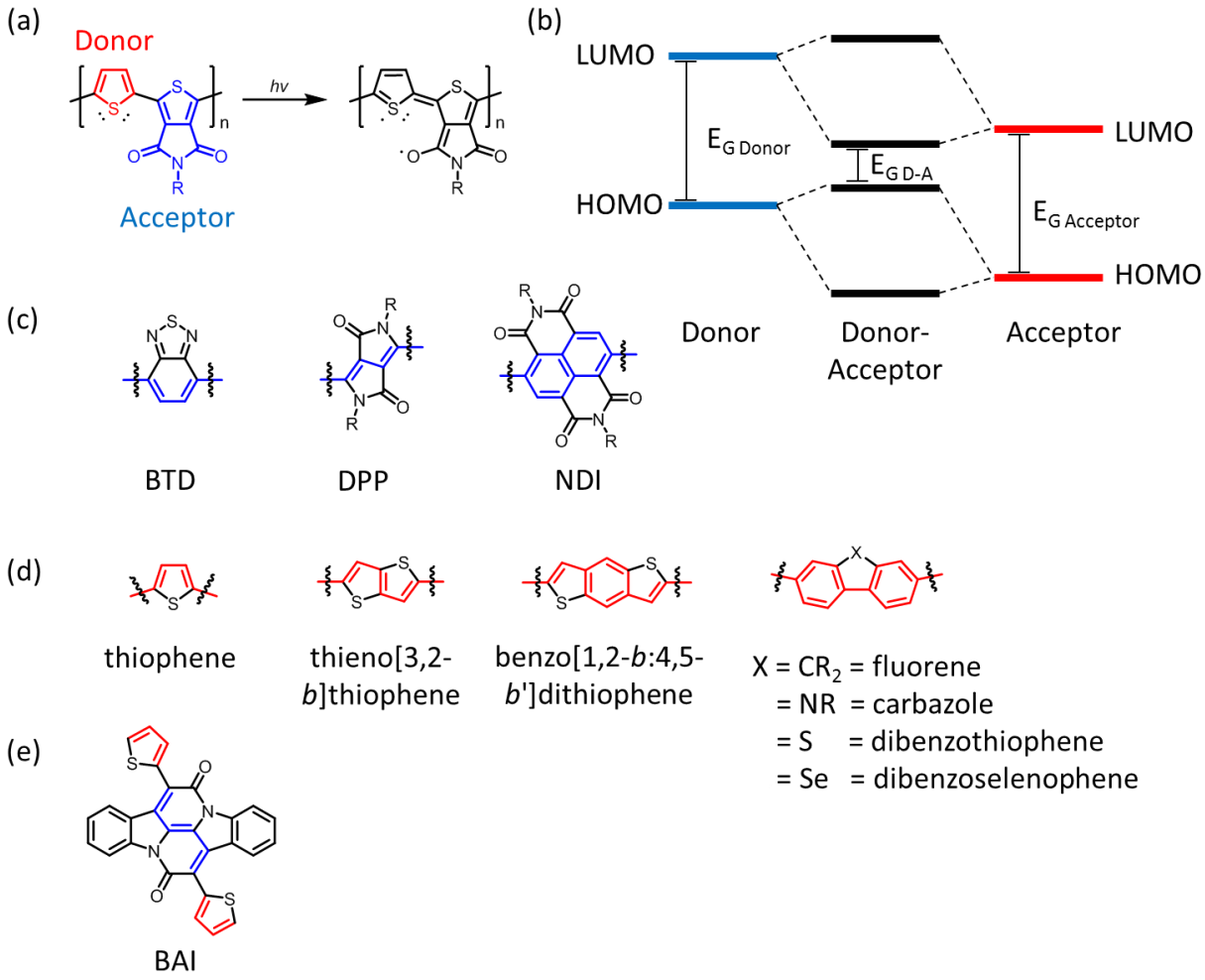

Figure 7: Construction of (a) an alternating donor-acceptor polymer and (b) the effect of orbital overlap between the components. Common (c) electron poor acceptor monomers (blue) and (d) electron rich donor monomers (red), and a new monomer explored in this work (e) Bay Annulated Indigo (BAI)

In order to allow electrons to flow within a molecule or polymer, there must be a continuous conjugation pathway. A common approach to make the system electron deficient is to attach withdrawing groups tangential to the flow of electrons. Popular monomers such as 1,2,5-benzothiadiazole (BTD), diketopyrrolopyrrole (DPP) and naphthalene diimide (NDI) are prime examples utilizing this strategy (**Figure 7c**).

The same principle applies to donor materials, but instead of adding a withdrawing group, an electron rich atom is used. Sulfur is the most common substituent due to high electron density, good orbital overlap with carbon, and low electronegativity.[28] As such, thiophene based polycyclic structures are the workhorse of organic donor monomers/subunits (**Figure 7d**). Although less common, selenium,[29] nitrogen,[30] and oxygen[31] have been used effectively in donors as well.

This donor-acceptor approach is used extensively in Chapter 2 of this dissertation which focuses on the development of a new electron acceptor called Bay Annulated Indigo (BAI) (**Figure 7e**).[32] The core of BAI uses highly stable amide electron withdrawing groups tangential to the conjugation pathway (blue). The withdrawing core can be easily coupled to a variety of donor groups, such as thiophene, to benefit from donor-acceptor interactions.

Any disruption in the continuous delocalization pathway will hinder charges as they move through a molecule or polymer. A mild example of this is when the conjugation pathway passes through benzene. Delocalization through strongly aromatic systems is impeded since the aromatic stabilization energy must be overcome in order for charge transfer to occur. The result is electrons are more localized to these units, decreasing the overall conjugation length.[33] This is the primary reason why fluorene, carbazole, dibenzothiophene, dibenzoselenophene are weaker donors than thienothiophene.

An extreme example of disrupting the delocalization pathway is cross conjugation. This occurs when a branching double bond intersects a linear conjugated pathway (**Figure 8a**). In this case, even though there is a continuous set of p-orbitals, there is no resonance form that can connect the end groups, leaving them only weakly coupled in the ground state.[34] A similar effect can occur with a heteroatom bridge, which similarly breaks electronic communication between sides (**Figure 8b**).

A relevant example of this can be seen in the dye, indigo. This molecule is used as a precursor to BAI and is cross conjugated in both ways described above (**Figure 8c**). Because of this cross conjugation, the two phenyl groups on each side cannot electronically communicate, despite there being a complete pathway of p-orbitals.

Despite the limitation that cross conjugation imposes to linear systems, it can still be used highly effectively under specific circumstances. Since the central alkene is still coupled to all connected functional groups, it can convey a strong resonance effect even if the ends cannot directly communicate. This effect is utilized multiple times throughout this dissertation. In Chapter 3, the 2-(1,3-dithiol-2-ylidene)malononitrile (DTM) group employs cross conjugation to enhance a push-pull resonance form to strengthen the resonance withdrawing effect of the BTD group (**Figure 8d**). By placing the cross conjugated group tangential to the flow of electrons, rather than in an end group position, this group is able to have a strong withdrawing effect without disrupting conjugation. In Chapter 4, the thiobarbituric acid (TBTA) group is used as an end group to accomplish a similar push-pull resonance form to purposefully induce a mild withdrawing effect to provide a high V_{OC} acceptor (**Figure 8e**).[35]

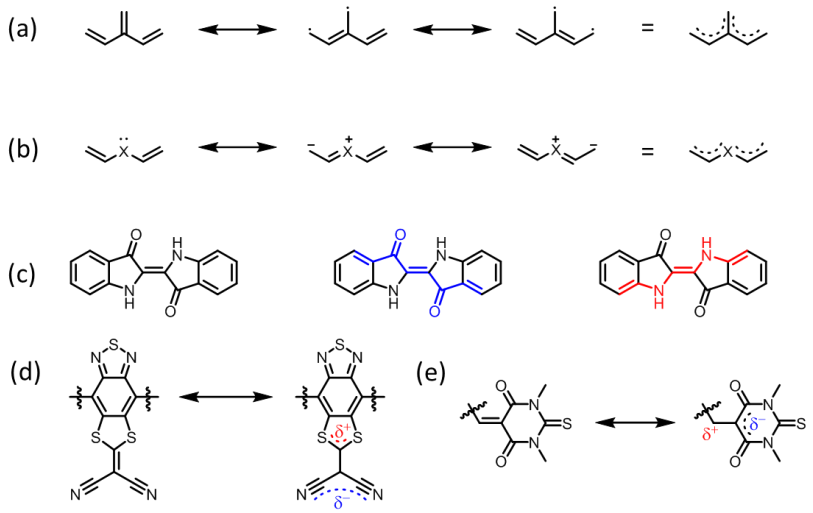

Figure 8: Cross conjugation induced by a (a) central double bond or (b) heteroatom and (c) visualization of both types in indigo. Examples of cross conjugation used in this dissertation, including (d) the 2-(1,3-dithiol-2-ylidene)malononitrile (DTM) group used to induce an electron withdrawing effect tangential to the conjugation pathway, and (e) thiobarbituric acid (TBTA) as a cross conjugated end group.

These principles can be seen at work in the most recent record OPV active layer.[36] Donor polymer PBDB-TF has a large amount of electron rich character gained from the benzodithiophene and thiophene groups highlighted in red (**Figure 9a**). It also contains a withdrawing benzodithiophene-4,8-dione (blue), however, which can lead to some confusion in naming.

The organic semiconductor community has used the terms donor and acceptor to describe electron rich and poor small molecules and polymers used in devices, such as the donor PBDB-TF. Unfortunately, the terms donor and acceptor are also used to describe the electron rich and poor monomers or subunits that make up those structures. This means that the acceptor molecule BTP-4Cl is made up of both donor units (highlighted in red) and acceptor units (highlighted in blue) (**Figure 9b**). To clarify this within the dissertation, the terms "donor" and "acceptor" will be used to describe entire molecules and polymers, whereas "withdrawing group/electron withdrawing group/acceptor subunit" and "donor group/electron rich group/donor subunit" will be used to describe fragments of a larger structure.

These materials can be used as an example to understand the makeup of donor and acceptor materials. It is clear from the structures that even though both contain donating and withdrawing groups, the donor material (PBDB-TF) has stronger electron rich subunits, and the acceptor (BTP-4Cl) has stronger accepting subunits. The ratio and strength of the donor vs. acceptor groups which make up of these materials is reflected in their overall energetics (**Figure 9c**). The electronegative and withdrawing groups in BTP-4Cl lower the HOMO and LUMO energies, whereas the electron rich groups in PBDB-TF raise FMO energy. Control over these energy levels has an enormous impact on whether a material will be electron and/or hole conductors, in addition to determining a number of critical OPV properties.

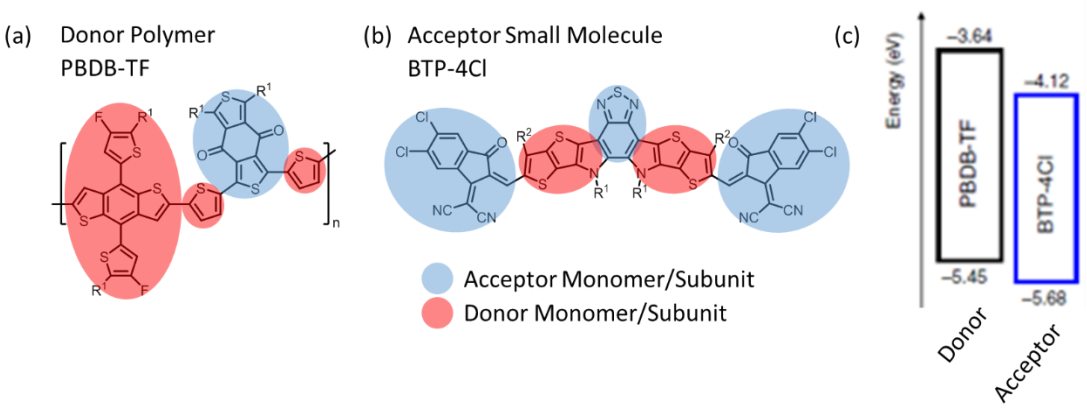

Figure 9: The (a) donor and (b) acceptor materials used in the highest performing single junction OPV active layer, with the electron rich subunits highlighted in red and poor subunits highlighted in blue. The (c) energy levels of the materials are also provided. Reproduced with permission from reference [36], Copyright © 2019, Springer Nature

It is also interesting to note that many of the acceptor units within the donor and acceptor materials have quinoidal subunits, such as the benzothiadiazole in BTP-4Cl and the 1,4-quinone in PBDB-TF. The quinoidal and donor-acceptor approaches to lower band gap are often cooperative and it is common to see both used within semiconducting materials.

1.5 Enforcing Planarity

In order to maximize the above effects and increase charge delocalization, the π surface must be planar enough to allow conjugation over long length scales. Perfect planarity is often unnecessary, but significant deviation can inhibit charge transport. While energetically favorable for neighboring p-orbitals to be planar, the single bonds between aromatic units can rotate out of plane due to steric and kinetic effects (**Figure 10a**).

One of the most effective ways to maintain planarity is to covalently lock it into place, creating a ladder polymer. Because the backbone is linked via a fused ring there are no rotatable single bonds present that can break conjugation.[37] While this is highly effective, it severely decreases the solubility of most species, even when compensated with alkyl chains. Despite the challenges, the benefits can still be realized in an oligomeric form. The ladderized core of IDTT has been used in some of the most effective acceptors, and is utilized extensively as a building block in the work revealed in Chapter 4 (**Figure 10b**).[38]

A creative approach to overcome some of the problems with covalent ladderization is to instead use intramolecular interactions such as hydrogen bonding (**Figure 10c**)[39], boron coordination (**Figure 10d**)[40] or other "conformational locks"[41] to moderate these interactions. Under certain conditions, these intramolecular interactions can be inhibited, thus improving their solubility over covalent ladder polymers. Upon removal of these inhibitory conditions, usually from evaporation of solvent or deprotection, an enforced planar structure is revealed.

The final approach is to design a system where the bond rotation highly favors a single desired orientation. This is found to be the case in the BAI system studied in this work.[42] BAI has a narrow energy well that only slightly skews from planarity while still maintaining conjugation. A reference molecule, thiophene arylated NDI, has a broad distribution of possible rotations that

have similar energies (**Figure 10e**). This leads to a high probability of the thiophene in BAI residing between 0 and 45 degrees, whereas NDI-T has a wide distribution of favorable rotational orientations (**Figure 10f**).

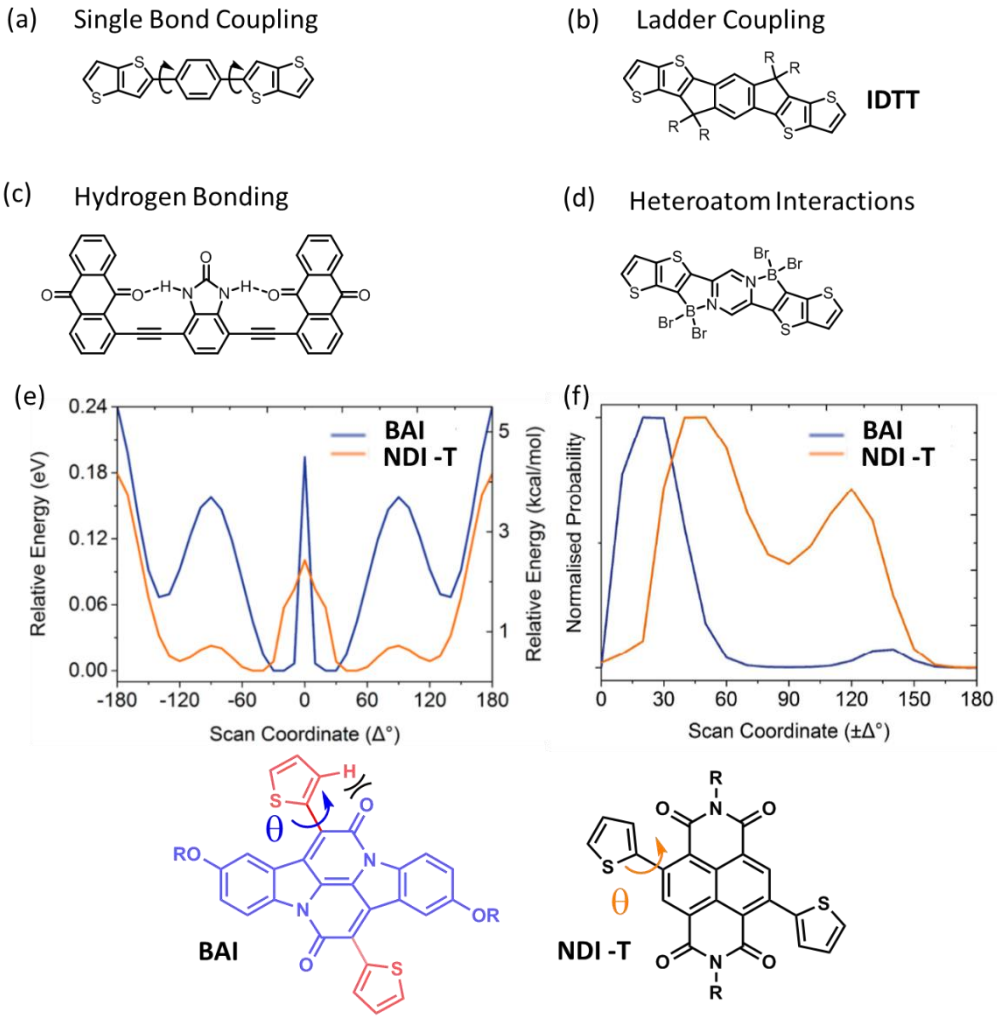

Figure 10: In order to prevent bond rotation (a) strategies have been developed to maintain planarity, such as (b) covalent ladderization, intramolecular (c) hydrogen bonding or (d) boron-ion pair interactions. Effective conjugation can also be obtained through (e) restriction of the bond angle, as visualized for the narrow potential well for **BAI-T** as opposed to the wide potential well for **NDI-T**, leading to (f) a highly favored rotational orientation. Reproduced with permission from reference [42], Copyright © 2016, American Chemical Society

1.6 Morphological and Solubility Considerations

Having a planar structure itself is often not enough to guarantee high performance. In polymeric systems, high molecular weights (long polymer length) are also crucial for good charge mobilities. Small molecules and oligomers are prone to forming crystallites of different orientations (**Figure 11a**).[43] Grain boundaries between these crystallites are a major impediment to charge transfer. Since the π systems of neighboring crystallites are rarely aligned, charge

hopping can be greatly inhibited at these interfaces. High molecular weight polymers not only increase the exciton diffusion length, but crucially act as bridges between separate crystalline domains (**Figure 11b**). These softened boundaries between crystallites vastly improve charge mobility.[44]

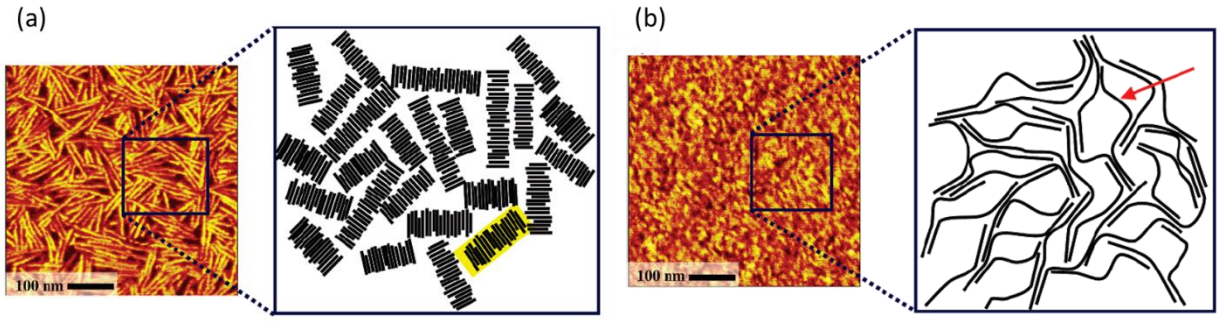

Figure 11: AFM and accompanying sketches depicting the effect of low molecular weight (a) and high molecular weight (b) on crystallites. Reproduced with permission from reference [43], Copyright © 2005, American Chemical Society

All of the described methods that are used to increase charge delocalization, such as planar and ladderized backbones, and high molecular weight polymers, increase the π surface area available for π–π stacking between molecules or polymers. These properties increase the crystallinity, which often has positive effects on charge mobility. However, it also has the unintended consequence of severely decreasing solubility. An electronically perfect semiconductor is useless if it cannot be processed into a device.

To improve solubility in organic solvents, alkyl chains are often appended to the semiconducting materials. Alkyl chains sterically interfere with π–π stacking which inhibits aggregation in solution. Branched sidechains, such as the very common 2-ethylhexyl group, are more sterically demanding than the linear n-octyl group. Accordingly, 2-ethylhexyl groups do a better job at improving solubility than octyl groups and are utilized more regularly.

However, alkyl chains that are placed inappropriately or are too bulky can negate the benefits of planarity. Alkyl chains are inherently insulating and excessive steric hindrance can prevent efficient π–π stacking which is essential for good device performance. Additionally, if alkyl chains are placed improperly, the planarity can be disrupted by steric effects. This can be readily observed when comparing the properties of poly-3-hexylthiophene (P3HT) with varying degrees of head-to-tail regioregularity (**Figure 12a**). In a regioregular head-to-tail configuration, steric interactions between monomer units is minimized (**Figure 12b**). In a regiorandom polymer, unfavorable steric interactions twist the backbone out of plane, disrupting conjugation and long range order in the solid state (**Figure 12c**).[45] The extent of head-to-tail regioregularity has a direct correlation with higher hole mobility in OFET devices (**Figure 12d**). Among other properties, highly regioregular P3HT has also been shown to have significantly better light absorption and crystallinity.[45-46]

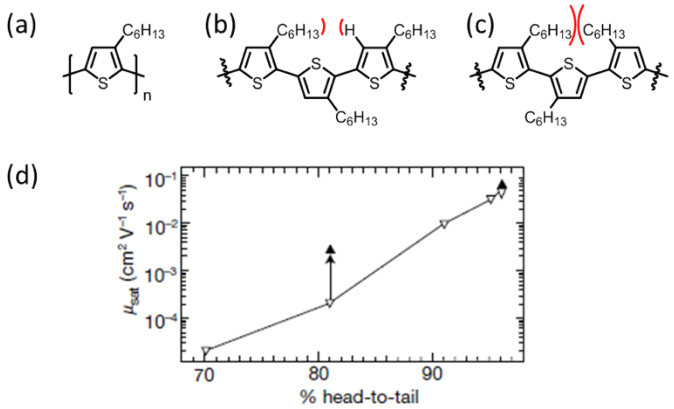

Figure 12: Visualization of the minimal steric interactions in (a) regioregular P3HT and (b) severe interactions when there are deviations from the head-to-tail configuration. The effect of (c) increasing the steric interactions in P3HT on the hole mobility in OFET devices, where solid triangles represent spuncast and inverted empty triangles represent solution-cast films. Reproduced with permission from reference [46b], Copyright © 1999, Springer Nature

A balance must be found between having sufficient alkyl chains to solubilize molecules, while preventing interactions that inhibit charge transport. The focus of Chapter 4 is the study of these alkylation effects on a new non-fullerene acceptor (**Figure 13**). Simply modifying the alkyl chains of the thiobarbituric acid endgroups have a large impact on device performance. The ethyl and benzyl groups provide good efficiencies of 8.77 and 7.41%, but both shorter and longer chains drastically decrease solar cell performance.

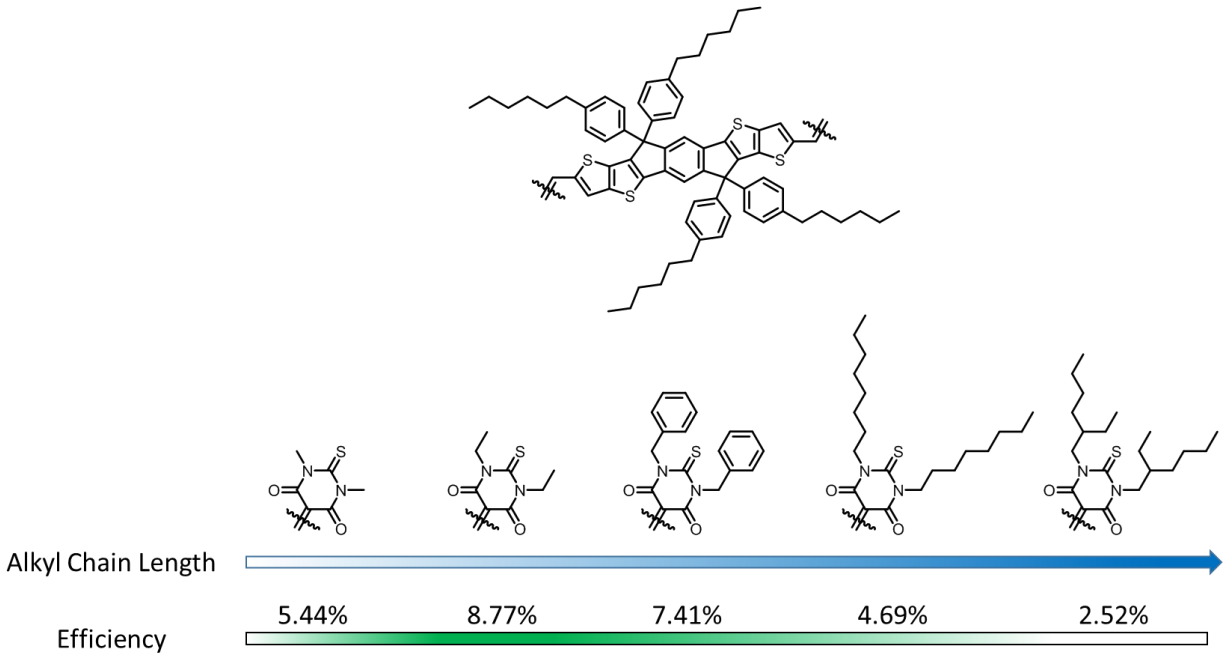

Figure 13: Increasing alkyl chain length and its effect on OPV performance.

1.7 Implementation of Design Principles

The strategies and tools outlined in this chapter are used throughout the dissertation work to develop and synthesize new organic semiconductors to push the boundaries of the field.

Bay Annulated Indigo (**Figure 7e**) was developed using donor-acceptor interactions to provide a high stability acceptor.[47] Due to the effect of restricted bond angle, it was found to have one of the highest reported ambipolar mobilities (**Figure 10e,f**).[42]

Cross conjugation was used in the design of the 2-(1,3-dithiol-2-ylidene)malononitrile (DTM) group. By inducing a withdrawing effect tangential to the conjugation pathway, the benzothiadiazole unit was made significantly more electron deficient (**Figure 8d**). This proves to have a number of advantages, such as introducing electron conductivity into a normally hole conductive material and improving crystallinity.

The final chapter takes a more in-depth look at morphological effects of in the active layer of semiconductor films. Using cross conjugated thiobarbituric acid groups, a model acceptor IDTT-TBTA was synthesized with different alkyl groups to moderate intermolecular interactions (**Figure 8e**).[35] The electronic effects are unaltered by changing alkyl groups, allowing for a focused study of the effect of alkylation on morphology. Characterizing the intermolecular interactions and correlating them to the efficiencies of solar cells allow for the development of useful structure-property relationships (**Figure 13**).

The ultimate goal of developing new molecules and polymers is to apply them to organic electronic devices. To acquaint the reader with application specific factors, and to clarify results later in the dissertation, a summary of the chemistry and physics behind the operation of organic photovoltaic (OPV) and organic field effect transistor (OFETS) devices is provided in the appendix.

Appendix I Device Background

Introduction to Organic Photovoltaics (OPVs)

Unlike in doped polyacetylene, a photovoltaic system generates charge carriers directly through photoexcitation of electrons within a molecule or polymer. Organic molecules absorb light in the visible region of the spectrum through interaction with the π bonding system. For a photon to be absorbed it must have equal or higher energy than the HOMO-LUMO gap or band gap. In organic systems this most often corresponds to a π to π * transition. When light absorption occurs, an electron is excited directly from the HOMO to the LUMO, leaving a hole behind (**Figure A-1a**).

What happens to these charge carriers varies depending on the dielectric constant of the material. This is a measure of how much a material can decrease the electric field between charges. In a high dielectric system, such as silicon (ε_r = 11.7), these charges are highly shielded from each other and can, therefore, be immediately separated, to be collected at the electrodes.[48] However, because organic materials have a lower dielectric constant, normally around ε_r 2-4, the electron and hole remain attracted to each other, bound in a pseudo-particle called an exciton.[49] The theoretical reasoning for the existence of excitons can be found by setting the Coulomb binding energy equal to the available thermal energy (k_BT) (**Equation 1**).[50]

$$k_B T = \frac{e^2}{4\pi\varepsilon_0\varepsilon_r r} \quad (1)$$

In this equation, k_B is Boltzmann's constant, e is the elementary charge, e_0 is the permittivity of free space, e_r is the dielectric constant, and r is the interaction distance. Solving for r provides an equation for the Coulomb capture radius (**Equation 2**).

$$r_c = \frac{e^2}{4\pi\varepsilon_0\varepsilon_r k_B T} \quad (2)$$

Low dielectric constants in organic materials directly cause a large interaction radius keeping a photoexcited electron and hole in close proximity, forming an exciton. This large interaction radius also explains the high recombination rate in photovoltaic cells. Free electrons and holes must keep further than r_c or they will be attracted and potentially recombine, meaning the active layer can support fewer carriers than a material with higher dielectric constant.

The exciton can move freely along a polymer chain or move via a 'hopping' mechanism to new molecules or polymers either via a Forster or Dexter energy transfer.[51] However, the exciton is unstable and has a limited lifetime before it recombines back to the ground state. The distance an average exciton can move within that time is the exciton diffusion length L_D. Although this varies by material, it is usually between 5-20 nm, though it can be much higher in polycrystalline films.[51] The low exciton diffusion length and high recombination rate that result are a very significant challenge for organic photovoltaics.

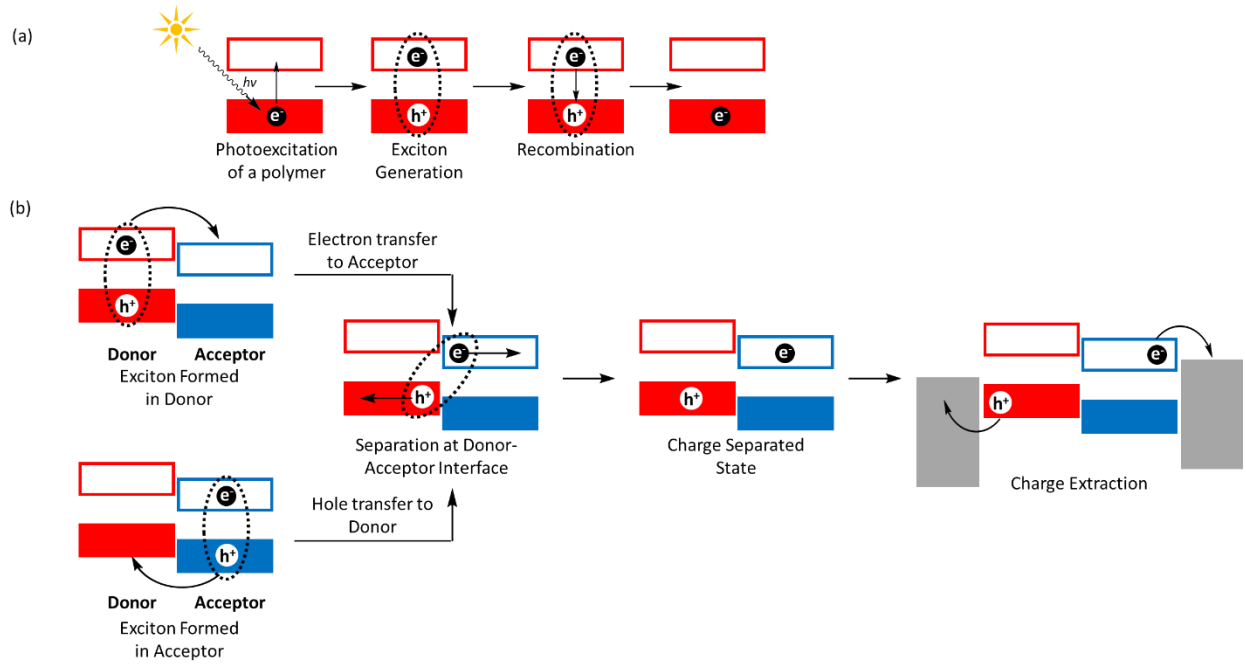

Figure A-1: Exciton generation in (a) a single polymer chain, leading to excitation and recombination. Exciton generation in (b) a mixture of donor and acceptor polymers, allows for charge separation and extraction.

A breakthrough came with the discovery that mixing both an electron rich material (donor) and electron poor material (acceptor) vastly improves OPV performance.[52] If an exciton is

formed in the donor material, it can migrate to an interface with an acceptor (**Figure A-1b**). When the donor and acceptor are close enough, the electron can transfer from the Donor LUMO to the lower energy acceptor LUMO, overcoming the exciton binding energy (0.3-0.5 eV).[51] In this charge transfer (CT) state the electron and hole are still attracted, but can easily escape to form a charge separated state. The entropy increase from charge separation makes the energetic barrier significantly smaller than for the exciton, and separation can readily occur if the charges are separated by ~4nm.[50]

After the charges are separated, they are free to delocalize throughout the respective donor and acceptor domains to reach the electrodes for collection. If an exciton is formed in the acceptor domain, it can do an analogous transfer of a hole to the donor material and participate in the same pathway.

The efficiency of this process is measured in a J-V curve, which relates the current produced by the device to the voltage applied across it under irradiation (**Figure A-2a**). The figure of merit for solar cells is the Power Conversion Efficiency (PCE), which is a measure of how efficient a solar cell is at absorbing photons to generate an electrical current (**Equation 3**).

$$PCE = \frac{P_{max}}{P_{in}} = \frac{(J_{SC})(V_{OC})(FF)}{P_{in}} \quad (3)$$

In this equation, J_{SC} is the current generated when there is no voltage applied, V_{OC} is the potential at which no more current is produced, FF is an ideality ratio that compares the maximum power output to the theoretical power output based on J_{SC} and V_{OC}, and P_{in} is the power of the light source.

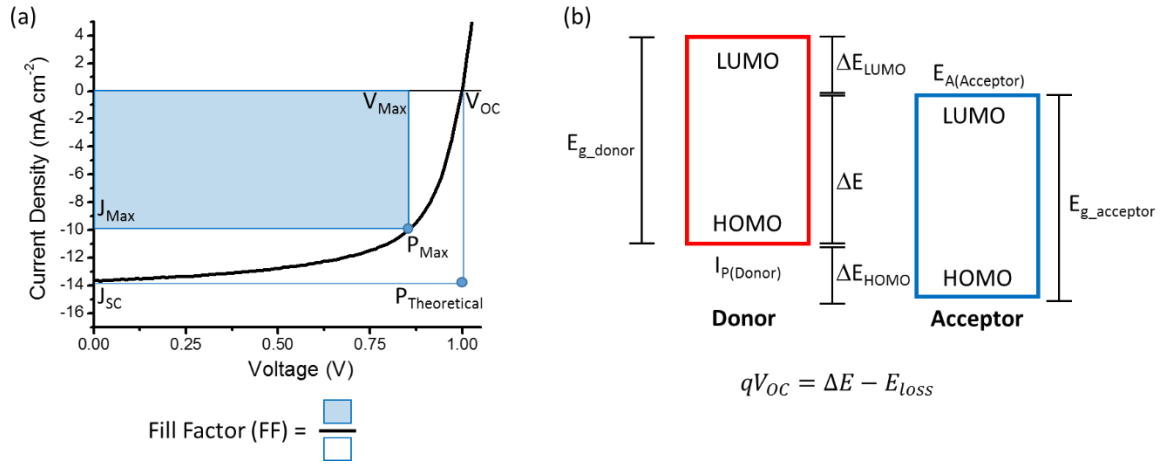

Figure A-2: OPV performance is characterize by an (a) J-V curve, with the fill factor defined as the ratio of the shaded and unshaded areas. The (b) V_{OC} is roughly equivalent to energy difference (DE) between the ionization potential of the donor and the electron affinity of the acceptor.

The efficiency of an OPV is determined by the donor and acceptor properties. It is important that the HOMO and LUMO of the donor and acceptor are aligned properly, as these energy offsets determine many critical values (**Figure A-2b**). A large ΔE increases the V_{OC}, but if the ΔE_{HOMO} or ΔE_{LUMO} levels are too close in energy, charge separation may be inhibited.[53]

Improved J_{SC} is associated with decreased E_{G_donor} and $E_{G\_acceptor}$. This leads to potential conflict where increasing the acceptor LUMO or decreasing the donor HOMO independently will increase V_{OC}, but decrease J_{sc} and vice versa.[54] Therefore, these factors must be taken into account when choosing donor acceptor pairs for devices.

How the donor and acceptor form a film also plays a critical role. The short circuit current (J_{SC}) is an indirect measure of the carrier mobility, and increases if the electron or hole can travel further before recombining.[55] Active layers with poor morphology are riddled with traps, lowering the mobility leading to low J_{SC} and low efficiency. Likewise, the fill factor (FF) is a direct measure of resistance in the cell, a largely morphological factor.[56]

Making a donor-acceptor active layer capable of forming and collecting charges places significant morphological constraints on material design. The first organic photovoltaic devices were made in a bilayer with the donor and acceptor sandwiched between the electrodes (**Figure A-3a**). However, the low surface area and large separation between electrodes lead to very low currents.[57] The ideal structure would have interdigitated donor and acceptor domains, which are within the exciton diffusion length (**Figure A-3b**). This process offers the best opportunity for excitons to diffuse to an interface before recombining and, therefore provides a direct path to the electrode for collection. While these systems have been made, they require levels of processing that are prohibitively complex and expensive.[58]

The current approach is to form a so called Bulk Heterojunction (BHJ) active layer (**Figure A-3c**).[52] By mixing the donor and acceptor materials, intermolecular interactions and crystallization effects often form an interconnected network which is much more efficient than a bilayer and much simpler to make than an interdigitated system. This means that a material must be crystalline enough to form a percolation pathway through the material to the electrode in order to collect the charges. However, it cannot be so crystalline that it does not form mixed domains where charge separation can occur. Since the active layers are made through solution processing techniques such as spin coating, dip coating, and doctor blade coating, the materials must be fully soluble in organic solvents.

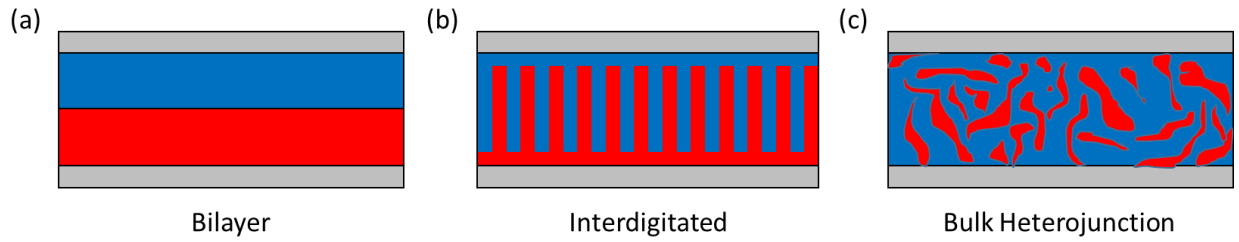

Figure A-3: The evolution of active layer architecture over time, with (a) a bilayer, (b) interdigitated, and (c) bulk heterojunction structures.

The long list of electronic constraints needs to be paired with a delicate balance of crystallinity and solubility. This make the discovery of new, high-performance materials quite challenging. Morphological control is one of the most critical aspects of materials design and one of the hardest to predict. As such, it is a large focus of the dissertation to design molecules and polymers where the intermolecular interactions can be finely tuned and studied.

Introduction to Organic Field Effect Transistors (OFETs)

Organic thin film transistors have gained increasing attention as an alternative to amorphous silicon. The low processing temperature means that they are compatible with flexible plastic substrates, which significantly reduce processing and cost. It additionally opens up new applications in wearable, flexible, and lightweight applications. High performing p-type (hole conductive) transistors are well established, with pentacene being the most studied material with a single crystal mobility of μ_{hole} = 35 $cm^2\ V^{-1}\ s^{-1}$.[59] However, progress in producing the corresponding n-type transistor has been lagging.[60]

N-type transistors are necessary in order to employ complimentary circuit design, in which both positive and negative gate voltages are used to lower power consumption.[61] This type of circuit is particularly attractive for low-power applications such as radio frequency identification (RFID) tags.

However, n-type materials have their own challenges, particularly with low stability. The anions formed as charge carriers are strong reductants, making these polymers prone to reactivity with ambient oxygen and water, which that takes place at -3.6 eV (**Equations 4 and 5**).[62]

$$2H_2O + 2e^- \leftrightarrow\ \ H_2 + 2OH^- \tag{4}$$

$$2H_2O \leftrightarrow \mathrm{O_2} + 4\mathrm{H^+} + 4\mathrm{e^-} \tag{5}$$

If the LUMO of the n-type semiconductor is not below this value, oxygen and water can act as traps, reacting with excited state electrons before they can be collected. Materials with a LUMO below 3.0 eV can still be high performing, but extra care must be taken to protect them from ambient conditions.[61]

Another frequently overlooked issue is the choice of electrode material. In OFETs, gold electrodes are commonly used due to high oxidative stability. But with a work function of 5.1 eV, it is much better used for hole injection in p-type systems than for electron injection in n-type systems. Large contact resistance between gold and the n-type active layer can significantly lower measured electron mobilities in these systems. Metals such as aluminum, calcium, and barium have lower work functions that are more compatible with electron injection, but they are easily oxidized and must also be protected.

An OFET is a three electrode device. A source and drain electrode are separated by a semiconducting organic material. Underneath these is the gate electrode which is separated from the source and drain by an insulator (dielectric), which is responsible for turning the device on and off. When a voltage is applied to the gate the dielectric blocks current but allows charge buildup. The capacitor-like charge buildup on the gate electrode induces production of the opposing charges within the organic active layer. When the drain and gate voltages are set to an operating level, current can flow between the source and drain.

In an example n-type transistor with no potential applied, the HOMO and LUMO rest between the Fermi levels of the electrodes (**Figure A-4a**).[61] Because the organic layer is a semiconductor, there are effectively no charge carriers present under these conditions. Applying a drain voltage (V_D) pulls electron density towards the drain, but because the carrier density is so low it does not produce a current (**Figure A-4b**). When a positive gate voltage (V_G) is applied, the capacitative effect of the dielectric layer induces a build-up of electrons in the active layer. The gate voltage necessary to induce mobile electrons is termed the threshold voltage (V_T). Without a drain voltage, the charge carriers have no directionality to their movement, and thus do not create a current (**Figure A-4c**). When both a gate and drain current are applied, there are ample electrons in the active layer and the positive drain potential allows them to freely flow into the drain electrode (**Figure A-4d**). If the drain potential is increased further, electrons flow into the drain at the same rate they are generated and increasing the V_D further does not increase the current (**Figure A-4e**). At this point the transistor is said to be saturated.

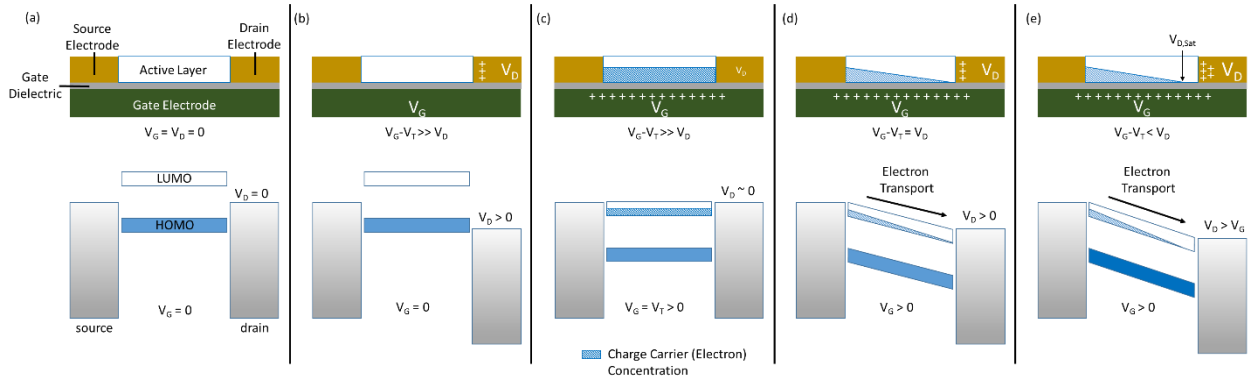

Figure A-4: Schematic of an OFET, with corresponding energy levels at different phases of operation. There is no current flow when (a) no potential is being applied, (b) when only a drain potential is applied, (c) when only a gate potential is applied. When (d) a gate and drain potential are applied, a current can flow, but increasing the V_D beyond saturation (e) produces no additional current.

OFETs are characterized by testing the current across the transistor at a range of gate and drain voltages. An output curve is produced when drain voltage is swept at constant V_G and recording the resulting current across the semiconductor (**Figure A-5a**). Whereas a transfer curve is a plot of V_G at constant V_D vs. the output current (**Figure A-5b**).

The figures of merit for OFETs are the charge carrier mobility ($\mu_{electron}$ or μ_{hole}), the threshold voltage (V_T) and the I_{on}/I_{off} ratio. The carrier mobility is an intrinsic measurement of how freely a carrier can move in a material and is measured in $cm^2\ V^{-1}\ s^{-1}$. The threshold voltage is the gate potential that needs to be applied in order to produce mobile carriers. If the material has traps, the V_T will increase, and if the material is doped (possibly through impurities), the V_T will decrease. The on-off ratio (I_{on}/I_{off}) is a measure of the current difference between when a transistor is in the on vs. off state. This is usually reported in terms of 10^X.

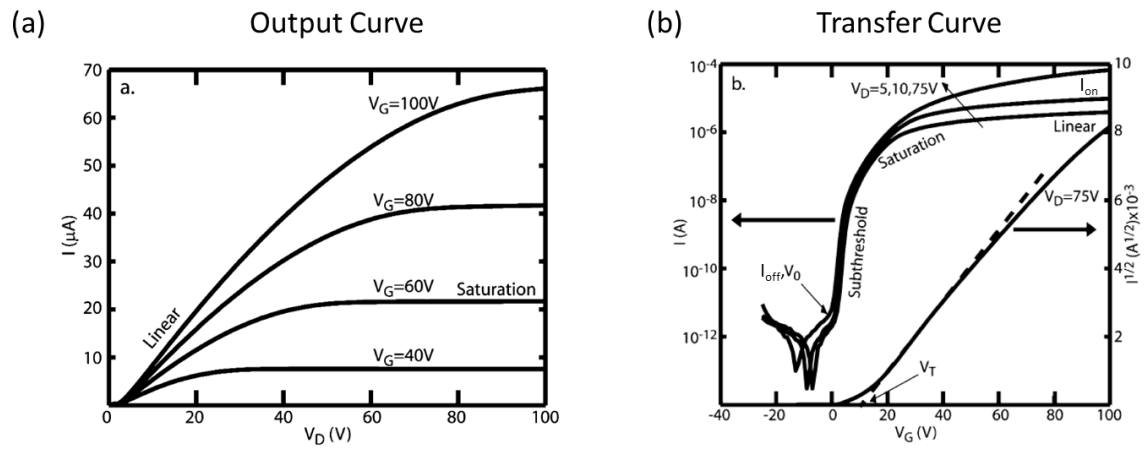

Figure A-5: OFET performance is characterized by an (a) output curve and (b) transfer curve. Plotting the transfer curve on a semilog scale ($I^{1/2}$ vs. V_G) is used to calculate important metrics such as threshold voltage (V_T) and m using equation 6. Reproduced with permission from reference [61], Copyright © 2004, American Chemical Society

These metrics are most easily determined through the transfer curve by fitting it to the equation for a transistor in saturation (**Equation 6**).[61]

$$I_{D,sat} = \frac{W}{2L} C_{ox} \mu_{sat} (V_G - V_T)^2 \quad (6)$$

In this case W and L are the channel dimensions, C_{ox} is the capacitance of the dielectric layer in nF/cm^2, μ_{sat} is the carrier mobility, and V_G and V_T are the gate and threshold voltage. The mobility and threshold voltage can be easily determined by plotting a semilog curve of V_G vs. $I_{D,sat}^{1/2}$. The mobility can be determined from the slope of the linear region, and V_T is the x-intercept.

References

[1] a) H. Ling, S. Liu, Z. Zheng, F. Yan, *Small Methods* **2018**, *2*, 1800070; b) Y. Wang, L. Sun, C. Wang, F. Yang, X. Ren, X. Zhang, H. Dong, W. Hu, *Chem. Soc. Rev.* **2019**, *48*, 1492-1530.

[2] T. Someya, Z. Bao, G. G. Malliaras, *Nature* **2016**, *540*, 379.

[3] J. Rivnay, S. Inal, A. Salleo, R. M. Owens, M. Berggren, G. G. Malliaras, *Nat. Rev. Mater.* **2018**, *3*, 17086.

[4] a) J.-J. Kim, M.-K. Han, Y.-Y. Noh, *Semicond. Sci. Technol.* **2011**, *26*, 030301; b) Y.-F. Liu, J. Feng, Y.-G. Bi, D. Yin, H.-B. Sun, *Adv. Mater. Technol.* **2019**, *4*, 1800371; c) C. I. Park, M. Seong, M. A. Kim, D. Kim, H. Jung, M. Cho, S. H. Lee, H. Lee, S. Min, J. Kim, M. Kim, J.-H. Park, S. Kwon, B. Kim, S. J. Kim, W. Park, J.-Y. Yang, S. Yoon, I. Kang, *J. Soc. Inf. Disp.* **2018**, *26*, 287-295; d) M. Morales-Masis, F. Dauzou, Q. Jeangros, A. Dabirian, H. Lifka, R. Gierth, M. Ruske, D. Moet, A. Hessler-Wyser, C. Ballif, *Adv. Funct. Mater.* **2016**, *26*, 384-392.

[5] a) A. Chortos, J. Liu, Z. Bao, *Nat. Mater.* **2016**, *15*, 937; b) Y. Qiao, Y. Wang, H. Tian, M. Li, J. Jian, Y. Wei, Y. Tian, D.-Y. Wang, Y. Pang, X. Geng, X. Wang, Y. Zhao, H. Wang, N. Deng, M. Jian, Y. Zhang, R. Liang, Y. Yang, T.-L. Ren, *ACS Nano* **2018**, *12*, 8839-8846; c) S. Wang, J. Xu, W. Wang, G.-J. N. Wang, R. Rastak, F. Molina-Lopez, J. W. Chung, S. Niu, V. R. Feig, J. Lopez, T. Lei, S.-K. Kwon, Y. Kim, A. M. Foudeh, A. Ehrlich, A. Gasperini, Y. Yun, B. Murmann, J. B. H. Tok, Z. Bao, *Nature* **2018**, *555*, 83.

[6] T. R. Ray, J. Choi, A. J. Bandodkar, S. Krishnan, P. Gutruf, L. Tian, R. Ghaffari, J. A. Rogers, *Chem. Rev.* **2019**, *119*, 5461-5533.

[7] S. Wang, J. Xu, W. Wang, G.-J. N. Wang, R. Rastak, F. Molina-Lopez, J. W. Chung, S. Niu, V. R. Feig, J. Lopez, T. Lei, S.-K. Kwon, Y. Kim, A. M. Foudeh, A. Ehrlich, A. Gasperini, Y. Yun, B. Murmann, J. B. H. Tok, Z. Bao, *Nature* **2018**, *555*, 83-88.

[8] R. Søndergaard, M. Hösel, D. Angmo, T. T. Larsen-Olsen, F. C. Krebs, *Mater. Today* **2012**, *15*, 36-49.

[9] X. Gu, Y. Zhou, K. Gu, T. Kurosawa, Y. Guo, Y. Li, H. Lin, B. C. Schroeder, H. Yan, F. Molina-Lopez, C. J. Tassone, C. Wang, S. C. B. Mannsfeld, H. Yan, D. Zhao, M. F. Toney, Z. Bao, *Adv. Energy Mater.* **2017**, *7*, 1602742.

[10] National Renewable Energy Lab, https://www.nrel.gov/pv/cell-efficiency.html, **2019**.

[11] A. Banerji, M. W. Tausch, U. Scherf, *Educación Química* **2013**, *24*, 17-22.

[12] X. Lin, J. Li, C. J. Först, S. Yip, *PNAS* **2006**, *103*, 8943-8946.

[13] a) H. Shirakawa, T. Ito, S. Ikeda, *Die Makromolekulare Chemie* **1978**, *179*, 1565-1573; b) H. Shirakawa, S. Ikeda, *Polym. J.* **1971**, *2*, 231-244.

[14] a) N. Basescu, Z. X. Liu, D. Moses, A. J. Heeger, H. Naarmann, N. Theophilou, *Nature* **1987**, *327*, 403-405; b) C. K. Chiang, S. C. Gau, C. R. F. Jr., Y. W. Park, A. G. MacDiarmid, A. J. Heeger, *Appl. Phys. Lett.* **1978**, *33*, 18-20.

[15] J. P. Louboutin, F. Beniere, *J. Phys. Chem. Solids* **1982**, *43*, 233-241.

[16] F. Rachdi, P. Bernier, E. Faulques, S. Lefrant, F. Schué, *Polymer* **1982**, *23*, 173-175.

[17] a) H. Shirakawa, *Angew. Chem. Int. Ed.* **2001**, *40*, 2574-2580; b) S. Rasmussen, *Bull. Hist. Chem.* **2014**, *39*, 64-72.

[18] S. Ruth, S. Joseph, *Organic Electronics in Sensors and Biotechnology*, McGraw-Hill Education, New York, **2009**.

[19] J. Rivnay, S. Inal, A. Salleo, R. M. Owens, M. Berggren, G. G. Malliaras, *Nat. Rev. Mater.* **2018**, *3*, 17086.

[20] S. F. A. Acquah, A. V. Penkova, D. A. Markelov, A. S. Semisalova, B. E. Leonhardt, J. M. Magi, *ECS J. Solid State Sci. Technol.* **2017**, *6*, M3155-M3162.

[21] a) H. W. Kroto, *Angew. Chem.* **1992**, *31*, 111-129; b) R. F. Curl, *Angew. Chem.* **1997**, *36*, 1566-1576; c) R. E. Smalley, *Angew. Chem.* **1997**, *36*, 1594-1601.

[22] Z. Li, D. Yang, X. Zhao, T. Zhang, J. Zhang, X. Yang, *Adv. Funct. Mater.* **2018**, *28*, 1705257.

[23] L. Krückemeier, P. Kaienburg, J. Flohre, K. Bittkau, I. Zonno, B. Krogmeier, T. Kirchartz, *Commun. Phys.* **2018**, *1*, 27.

[24] a) C. Yan, S. Barlow, Z. Wang, H. Yan, A. K. Y. Jen, S. R. Marder, X. Zhan, *Nat. Rev. Mater.* **2018**, *3*, 18003; b) A. Wadsworth, M. Moser, A. Marks, M. S. Little, N. Gasparini, C. J. Brabec, D. Baran, I. McCulloch, *Chem. Soc. Rev.* **2019**, *48*, 1596-1625.

[25] a) J. L. Brédas, *J. Chem. Phys* **1985**, *82*, 3808-3811; b) J. L. Brédas, A. J. Heeger, F. Wudl, *J. Chem. Phys* **1986**, *85*, 4673-4678.

[26] F. Wudl, M. Kobayashi, A. J. Heeger, *J. Org. Chem.* **1984**, *49*, 3382-3384.

[27] a) H. T. Turan, O. Kucur, B. Kahraman, S. Salman, V. Aviyente, *Phys. Chem. Chem. Phys.* **2018**, *20*, 3581-3591; b) Z. G. Zhang, J. Wang, *J. Mater. Chem.* **2012**, *22*, 4178-4187.

[28] F. A. Larik, M. Faisal, A. Saeed, Q. Abbas, M. A. Kazi, N. Abbas, A. A. Thebo, D. M. Khan, P. A. Channar, *J. Mater. Sci.: Mater. Electron.* **2018**, *29*, 17975-18010.
[29] H. Sugino, K. Takimiya, *Chem. Lett.* **2017**, *46*, 345-347.
[30] a) P.-L. T. Boudreault, S. Wakim, N. Blouin, M. Simard, C. Tessier, Y. Tao, M. Leclerc, *J. Am. Chem. Soc.* **2007**, *129*, 9125-9136; b) Y. Li, Y. Wu, B. S. Ong, *Macromolecules* **2006**, *39*, 6521-6527.
[31] a) P. Huang, J. Du, M. C. Biewer, M. C. Stefan, *J. Mater. Chem. A* **2015**, *3*, 6244-6257; b) Z. Zhao, H. Nie, C. Ge, Y. Cai, Y. Xiong, J. Qi, W. Wu, R. T. K. Kwok, X. Gao, A. Qin, J. W. Y. Lam, B. Z. Tang, *Adv. Sci.* **2017**, *4*, 1700005.
[32] M. A. Kolaczkowski, Y. Liu, *Chem Rec.* **2019**, *19*, 1062-1077.
[33] J. Roncali, *Chem. Rev.* **1997**, *97*, 173-206.
[34] a) P. A. Limacher, H. P. Lüthi, *Wiley Interdiscip. Rev. Comput. Mol. Sci.* **2011**, *1*, 477-486; b) N. F. Phelan, M. Orchin, *J. Chem. Educ.* **1968**, *45*, 633.
[35] a) B. He, B. Yang, M. A. Kolaczkowski, C. A. Anderson, L. M. Klivansky, T. L. Chen, M. A. Brady, Y. Liu, *ACS Energy Lett.* **2018**, *3*, 1028-1035; b) L. Xiao, B. He, Q. Hu, L. Maserati, Y. Zhao, B. Yang, M. A. Kolaczkowski, C. L. Anderson, N. J. Borys, L. M. Klivansky, T. L. Chen, A. M. Schwartzberg, T. P. Russell, Y. Cao, X. Peng, Y. Liu, *Joule* **2018**, *2*, 2154-2166.
[36] Y. Cui, H. Yao, J. Zhang, T. Zhang, Y. Wang, L. Hong, K. Xian, B. Xu, S. Zhang, J. Peng, Z. Wei, F. Gao, J. Hou, *Nat. Commun.* **2019**, *10*, 2515.
[37] J. Lee, A. J. Kalin, T. Yuan, M. Al-Hashimi, L. Fang, *Chemical Science* **2017**, *8*, 2503-2521.
[38] K.-T. Wong, T.-C. Chao, L.-C. Chi, Y.-Y. Chu, A. Balaiah, S.-F. Chiu, Y.-H. Liu, Y. Wang, *Org. Lett.* **2006**, *8*, 5033-5036.
[39] C. Zhu, Z.-H. Guo, A. U. Mu, Y. Liu, S. E. Wheeler, L. Fang, *J. Org. Chem.* **2016**, *81*, 4347-4352.
[40] C. Zhu, X. Ji, D. You, T. L. Chen, A. U. Mu, K. P. Barker, L. M. Klivansky, Y. Liu, L. Fang, *J. Am. Chem. Soc.* **2018**, *140*, 18173-18182.
[41] H. Huang, L. Yang, A. Facchetti, T. J. Marks, *Chem. Rev.* **2017**, *117*, 10291-10318.
[42] K. J. Fallon, N. Wijeyasinghe, E. F. Manley, S. D. Dimitrov, S. A. Yousaf, R. S. Ashraf, W. Duffy, A. A. Y. Guilbert, D. M. E. Freeman, M. Al-Hashimi, J. Nelson, J. R. Durrant, L. X. Chen, I. McCulloch, T. J. Marks, T. M. Clarke, T. D. Anthopoulos, H. Bronstein, *Chem. Mater.* **2016**, *28*, 8366-8378.
[43] R. J. Kline, M. D. McGehee, E. N. Kadnikova, J. Liu, J. M. J. Fréchet, M. F. Toney, *Macromolecules* **2005**, *38*, 3312-3319.
[44] H. Kang, M. A. Uddin, C. Lee, K.-H. Kim, T. L. Nguyen, W. Lee, Y. Li, C. Wang, H. Y. Woo, B. J. Kim, *J. Am. Chem. Soc.* **2015**, *137*, 2359-2365.
[45] Y. Kim, S. Cook, S. M. Tuladhar, S. A. Choulis, J. Nelson, J. R. Durrant, D. D. C. Bradley, M. Giles, I. McCulloch, C.-S. Ha, M. Ree, *Nat. Mater.* **2006**, *5*, 197-203.
[46] a) R. Mauer, M. Kastler, F. Laquai, *Adv. Funct. Mater.* **2010**, *20*, 2085-2092; b) H. Sirringhaus, P. J. Brown, R. H. Friend, M. M. Nielsen, K. Bechgaard, B. M. W. Langeveld-Voss, A. J. H. Spiering, R. A. J. Janssen, E. W. Meijer, P. Herwig, D. M. de Leeuw, *Nature* **1999**, *401*, 685-688.
[47] a) M. A. Kolaczkowski, B. He, Y. Liu, *Org. Lett.* **2016**, *18*, 5224-5227; b) B. He, A. B. Pun, D. Zherebetskyy, Y. Liu, F. Liu, L. M. Klivansky, A. M. McGough, B. A. Zhang, K. Lo, T. P. Russell, L. Wang, Y. Liu, *J. Am. Chem. Soc.* **2014**, *136*, 15093-15101.
[48] W. C. Dunlap, R. L. Watters, *Phys. Rev.* **1953**, *92*, 1396-1397.
[49] a) M. P. Hughes, K. D. Rosenthal, N. A. Ran, M. Seifrid, G. C. Bazan, T.-Q. Nguyen, *Adv. Funct. Mater.* **2018**, *28*, 1801542; b) A. Armin, D. M. Stoltzfus, J. E. Donaghey, A. J. Clulow, R. C. R. Nagiri, P. L. Burn, I. R. Gentle, P. Meredith, *J. Mater. Chem. C* **2017**, *5*, 3736-3747.
[50] S. N. Hood, I. Kassal, *J. Phys. Chem. Lett.* **2016**, *7*, 4495-4500.
[51] O. V. Mikhnenko, P. W. M. Blom, T.-Q. Nguyen, *Energy Environ. Sci.* **2015**, *8*, 1867-1888.
[52] G. Yu, J. Gao, J. C. Hummelen, F. Wudl, A. J. Heeger, *Science* **1995**, *270*, 1789-1791.

[53] a) N. Li, I. McCulloch, C. J. Brabec, *Energy Environ. Sci.* **2018**, *11*, 1355-1361; b) N. K. Elumalai, A. Uddin, *Energy Environ. Sci.* **2016**, *9*, 391-410; c) M. T. Greiner, Z.-H. Lu, *NPG Asia Mater.* **2013**, *5*, e55-e55.
[54] Z.-Q. Jiang, T.-T. Wang, F.-P. Wu, J.-D. Lin, L.-S. Liao, *J. Mater. Chem. A* **2018**, *6*, 17256-17287.
[55] U. Würfel, D. Neher, A. Spies, S. Albrecht, *Nat. Commun.* **2015**, *6*, 6951.
[56] a) M. Dadu, A. Kapoor, K. N. Tripathi, *Sol. Energy Mater. Sol. Cells* **2002**, *71*, 213-218; b) N. Wu, Y. Wu, D. Walter, H. Shen, T. Duong, D. Grant, C. Barugkin, X. Fu, J. Peng, T. White, K. Catchpole, K. Weber, *Energy Technol.* **2017**, *5*, 1827-1835.
[57] P. Heremans, D. Cheyns, B. P. Rand, *Acc. Chem. Res.* **2009**, *42*, 1740-1747.
[58] H. Youn, H. J. Park, L. J. Guo, *Energy Technol.* **2015**, *3*, 340-350.
[59] O. D. Jurchescu, J. Baas, T. T. M. Palstra, *Appl. Phys. Lett.* **2004**, *84*, 3061-3063.
[60] a) J. T. E. Quinn, J. Zhu, X. Li, J. Wang, Y. Li, *J. Mater. Chem. C* **2017**, *5*, 8654-8681; b) A. F. Paterson, S. Singh, K. J. Fallon, T. Hodsden, Y. Han, B. C. Schroeder, H. Bronstein, M. Heeney, I. McCulloch, T. D. Anthopoulos, *Adv. Mater.* **2018**, *30*, 1801079.
[61] C. R. Newman, C. D. Frisbie, D. A. da Silva Filho, J.-L. Brédas, P. C. Ewbank, K. R. Mann, *Chem. Mater.* **2004**, *16*, 4436-4451.
[62] a) Y. Lu, J.-Y. Wang, J. Pei, *Chem. Mater.* **2019**, *31*, 6412-6423; b) H. T. Nicolai, M. Kuik, G. A. H. Wetzelaer, B. de Boer, C. Campbell, C. Risko, J. L. Brédas, P. W. M. Blom, *Nat. Mater.* **2012**, *11*, 882-887; c) M. L. Tietze, B. D. Rose, M. Schwarze, A. Fischer, S. Runge, J. Blochwitz-Nimoth, B. Lüssem, K. Leo, J.-L. Brédas, *Adv. Funct. Mater.* **2016**, *26*, 3730-3737; d) D. M. de Leeuw, M. M. J. Simenon, A. R. Brown, R. E. F. Einerhand, *Synth. Met.* **1997**, *87*, 53-59.

Chapter 2. Development of Desymmetrized Bay-Annulated Indigo and its Application as a Light-Absorbing, Solid Additive for Morphological Tuning of Organic Photovoltaic Active Layers

Abstract

The advancement of organic electronics has been continually pushed by the need for stable and high performance acceptor materials. By utilizing inexpensive and stable indigo dye as a starting material, Bay-Annulated Indigo (BAI) provides a new motif for the development of semiconducting materials. Modular and straightforward synthesis makes BAI an outstanding platform for molecular design, while excellent stability, strong absorption, and high ambipolar mobility render BAI-based materials excellent candidates for organic electronics. BAI-based polymers and small molecules have taken advantage of these properties to show promising results in a variety of applications. With a goal to explore self-assembled BAI constructs, a new synthetic strategy to desymmetrized BAI was developed. In doing so, a more efficient route to BAI formation was discovered. The morphological and optoelectronic studies provided understanding of the material characteristics necessary to incorporate them into organic electronic devices. Through addition of a self-assembling triphenylamine based BAI material, P3HT:PC60BM organic photovoltaic devices showed an ~11% improvement in efficiency.

Portions of the work presented in this chapter have been reported in the following publications:

Kolaczkowski, M. A.; He, B.; Liu, Y. Stepwise Bay Annulation of Indigo for the Synthesis of Desymmetrized Electron Acceptors and Donor-Acceptor Constructs, *Org. Lett.*, **2016**, *18*, 5224-5227.

Yang, B.; Kolaczkowski, M. A.; Brady, M. A.; Keum, J. K.; Browning, J. F.; Chen, T. L.; Liu, Y. Enhancing the Efficiency of Organic Photovoltaics by a Photoactive Molecular Mediator, *Solar RRL*, **2018**, *2*, 1700208.

Kolaczkowski, M. A.; Liu, Y. Functional Organic Semiconductors Based on Bay-Annulated Indigo, *Chem. Rec.*, **2019**, *19*, 1-17.

Rhoders, M.; Kolaczkowski, M. A.; Hollingsworth, W. R.; Seban, R.; Liu, Y.; Ayzner, A. L. Charge-Transport Networks via Small-Molecule Self-Assembly in Conjugated Polymer Bulk Heterojunctions, *J. Phys. Chem. C*, **2019**, *123*, 27305-27316.

2.1 Bay-Annulated Indigo Conceptualization

Evolution in material synthesis and device structure has brought the field of organic electronics ever closer to the goal of inexpensive, printable electronics. A fully realized organic electronics field holds the temptation of biologically compatible devices, light-weight solar cells that could be inexpensively printed onto flexible substrates, smart windows, and a myriad of other applications.[1] Despite these advances, the availability of high-performance materials still remains one of the largest barriers between those dreams and reality.

Ideal organic semiconducting materials would be stable, conjugated to allow for the flow of charges and high carrier mobilities, good light absorbers, planar to encourage favorable arrangement with other components, and easy to process into devices. There are a number of strategies in order to fulfill these requirements, but the most utilized and consistent are "push-pull" systems.[2] By alternating electron-rich and electron-poor building blocks, these molecules and polymers are able to absorb a greater range of wavelengths in the visible spectrum and the energetics of the system can be controlled, making it possible to improve the semiconducting properties.

While there are a wide variety of high performing electron donating building blocks available, electron deficient units are comparatively underdeveloped. Amide groups, perhaps best known for making up the backbone of proteins, are great candidates for building robust acceptor materials. A number of established amide-based acceptors such as isoindigo, diketopyrrolopyrrole (DPP)[3], and benzodipyrrolidone (BDPD), have already pushed the boundaries of the field (**Figure 1**).[4] In addition to the coplanarity, these systems also feature the attachment of two strongly withdrawing amide groups immediately next to the conjugation pathway (visualized through bolded bonds).

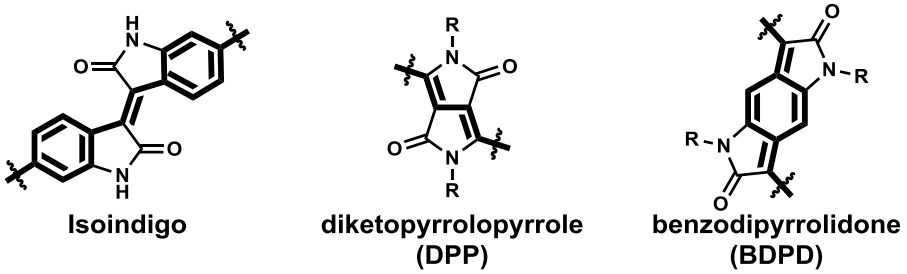

Figure 1: Examples of common amide-based acceptor monomers with conjugation pathway accentuated with bolded bonds. Reproduced with permission from reference [5], Copyright © 2019 Wiley

We were particularly taken by indigo **1** with its outstanding stability, rich history, and global presence (**Figure 2a**). Widely known as the molecule responsible for the color of blue jeans, this dye has been utilized for over 6000 years and is produced at over 50 kilotons per year.[6] The functional-group rich molecule contains a C=C double bond, two amine groups and two carbonyl groups, which at the same time maintain high planarity due to intramolecular hydrogen bonding interactions. This H-chromophore produces astounding absorption properties and stability for a molecule of such small size (**Figure 2b** - highlighted in red).[7] Upon photoexcitation, an Excited State Intramolecular Proton Transfer (ESIPT) occurs, maintaining the planar configuration and preventing C=C bond isomerization, which would break planarity. Alkene isomerization is

common in derivatives lacking the same hydrogen bonding motif, such as thioindigo, which prevent them from being suitable molecules for organic semiconductor applications (**Figure 2c**).

Indigo itself has been utilized in limited organic electronics applications, showing good stability and the ability to conduct both electrons and holes efficiently. However, one of the properties that makes indigo a fantastic dye, namely its low solubility, renders it highly impractical to process into devices. Vacuum deposition and protection-deprotection routes have been utilized, but have also encountered issues with scalability and morphological defects.[8]

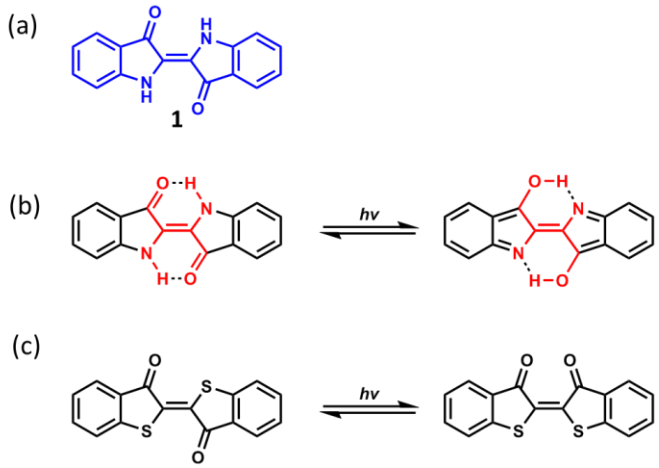

Figure 2: Unique properties of indigo **1** (a) are described. The H-chromophore (in red) allows for ESIPT (b) preventing central alkene isomerization, as is shown for thioindigo (c)

In order to make indigo into a higher performing and processable material there are a number of functional handles available for modification. Unfortunately, individual alteration to the amine, ketone, and phenyl groups do not allow for uninterrupted conjugation through the molecule, a necessity for polymeric systems (**Figure 3a**). Cibalackrot, an indigo-derived dye first produced by The Swiss Society of Chemical Industry of Basle (CIBA) in 1914, provided a creative solution to these problems (**Figure 3b**).[9] By combining *N*-alkylation and carbonyl condensation at the "bay positions" of indigo, the coplanarity of the parent indigo is reinforced after replacing the intramolecular H-bonding groups with two annulated rings, thus removing the hydrogen bonding while still preventing central C=C bond isomerization.

Furthermore, this annulation opens up an uninterrupted conjugation pathway that is orthogonal to the long molecular axis of the parent indigo molecule, concurrent with two amide groups installed adjacent to the conjugation pathway. These features endowed excellent electron accepting characteristics for Cibalackrot, yet its use in organic semiconductors had not been explored until our work in 2014. By altering the phenyl groups with the more electron-donating thiophene groups, the parent Bay-Annulated Indigo (BAI) **2** was first conceived and has been subsequently shown to behave as a versatile electron accepting unit for a wide variety of molecules and polymers with a diverse set of properties.[10]

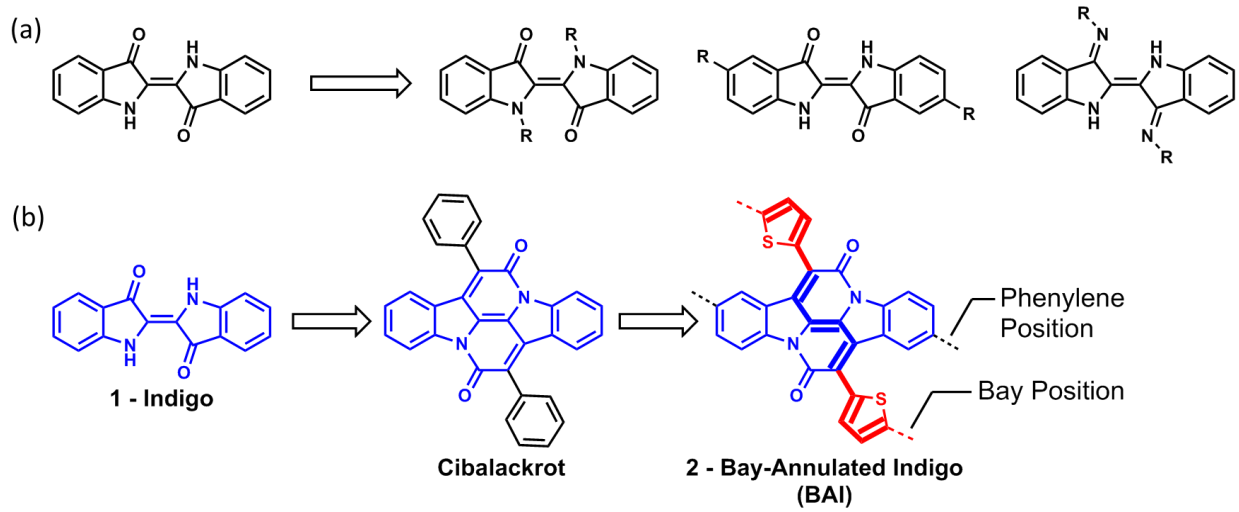

Figure 3: (a) Several conventional modification motifs of indigo lead to molecules with no direct conjugation pathway, and (b) the introduction of a conjugated pathway (bold) in BAI through annulation of the parent indigo using Cibalackrot as a starting point. Reproduced with permission from reference [5], Copyright © 2019 Wiley

With the successful synthesis of linear polymers, we were interested in the incorporation of BAI into supramolecular structures. By utilizing self-assembly, a wide variety of functional systems could be designed from the molecular level. In order to achieve this, some form of asymmetry must first be introduced to the system. To this end we designed desymmetrized BAI, where a stepwise bay annulation would allow for different aromatic groups to be added to each annulation site. Such desymmetrization not only offers great synthetic flexibility toward more complex donor−acceptor constructs, but also provides fine control over the energy levels through modular synthesis.

Desymmetrized functionalization has been explored in electron acceptors such as arene diimide.[11] The commonly adapted stepwise imidation procedure has little influence on the electronic properties of these imide-based acceptors as the substituents are electronically isolated from the core. Promisingly, recent indigo chelation chemistry has hinted at different reactivity of the functional group clusters on each bay position of indigo. The reported diketoimine indigo derivative, Ninidigo, forms distinct mono- and bis-BF_2 adducts, as well as metal complexes.[12] In desymmetrized BAIs, the different aromatic units attached to the bay positions were expected to have a significant impact on the electronic structures and thus the optoelectronic output.

2.2 Improvement of Bay-Annulation Reaction Through Pre-Acylation

Because of the abundance of indigo, the starting material for synthesizing BAI can be obtained inexpensively (several US dollars per kilogram). Simple treatment of indigo with commercially available 2-thiopheneacetyl chloride (4 equivalents) under refluxing xylene conditions provides good yields of doubly annulated BAI product which can be purified in gram scales by precipitation (**Scheme 1**).[10] A proposed mechanism involves initial acylation of the indigo amine with thiopheneacetyl chloride followed by quick condensation of the activated methylene position onto the carbonyl (attempts at isolating the pre-ring closed product were unsuccessful).

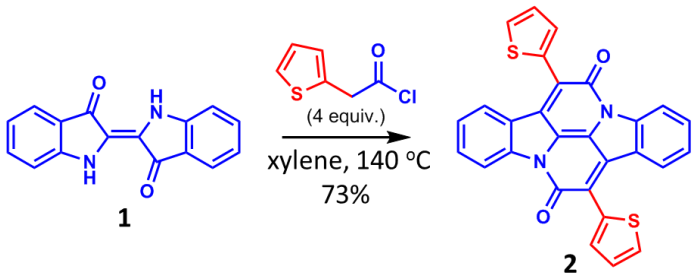

Scheme 1: Bay Annulation reaction of indigo

Experience with the symmetric bay-annulation reaction suggested that selective monoannulation should be possible. When the standard reaction was monitored by TLC, a highly colored intermediate was observed, which was confirmed to be the monoannulation product **4a** after purification by preparative TLC. This product could be formed preferentially by introducing 1.1 equivalents of thiophene-2-acetyl chloride to indigo in 1,4-dioxane at 140 °C. The resulting reaction conditions produced the product in 54% yield, and the doubly annulated product in 6% yield, along with residual indigo (**Scheme 5a**). The poor solubility of these species due to extensive hydrogen bonding and large π surfaces increases aggregation, making purification especially difficult. Attempts to improve yield through modification of solvent, temperature, base, Lewis acid, and amide coupling reagents provided little improvement over 50% yield. It is proposed that because an equivalent of water is formed during the condensation step, an equivalent amount of thiophene-2-acetyl chloride is made inactive due to hydrolysis to thiophene-2-acetic acid, severely limiting the yield.

With this monoannulated product in hand, an attempt was made to make a desymmetrized product with hydrogen substitution at the bay position through condensation with acetic anhydride. Surprisingly, only the *N*-acylation product **4a-Ac** was isolated which had not yet been observed in other BAI reactions. This species was highly soluble in organic solvents and was easily purified. When attempting to ring close the acyl group to form the annulated product under acidic or basic conditions, it quantitatively returned to the monoannulation product **4**.

This facile deacylation prompted us to reason that a preacylated indigo compound, such as *N*,*N*'-diacetylindigo would be a superior starting material which would ensure high solubility while retaining good reactivity toward annulation through *in situ* deprotection.[13] To test this reaction route, *N,N'*-diacetylindigo **5** was synthesized in high yield and purity following a modified acetylation protocol that involves treating indigo **1** with acetyl chloride and acetic anhydride at

140 °C (**Scheme 2b**).[14] As predicted, *N,N'*-diacetylindigo was significantly more soluble than indigo in common organic solvents.

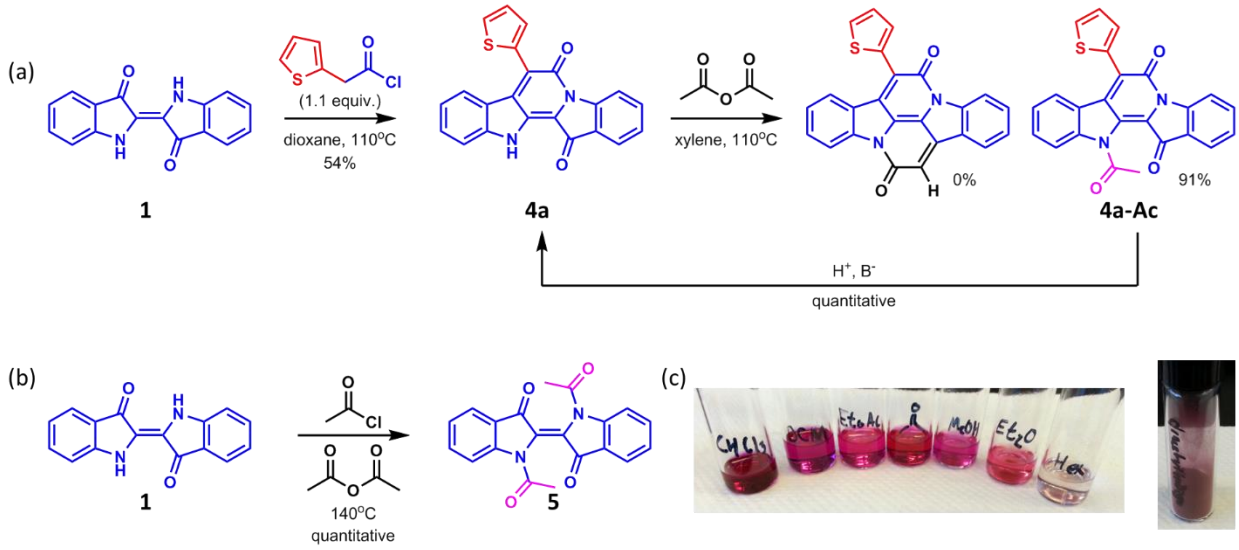

Scheme 2: (a) Reversible acylation of **4a**, (b) synthesis of *N,N'*-diacetylindigo **5**, and (c) improved solubility of **5**

When **5** was subjected to reaction with 2-thiopheneacetyl chloride (**3a**) in dioxane, **4a** was obtained in 87% isolated yield (**Scheme 3a**). The reaction proceeded much more cleanly compared to that of indigo **1**, with high conversion rate and <5% of bis-annulated product **2**. The increased solubility of precursors contributed to a significantly higher isolated yield of the desired monoannulated product, with the added benefit of easier tracking and purification due to fewer side products. No acylated **4a-Ac** was isolated from the reaction, suggesting a facile deacylation step following monoannulation. Solvent also plays a role. Changing the solvent to toluene resulted in additional side products with depressed yields. Utilizing acetic anhydride as solvent also provided good yield but with product isolated in its acylated form **4a-Ac** (**Scheme 3b**). Reaction of indigo under these conditions with 2.5 equiv. acetyl chloride showed an improvement in yield (70%), compared to 58% yield without the acetyl chloride additive (**Scheme 3c**). This enhancement presumably arises through *in situ* formation of acylated indigo intermediates. Running the annulation reaction with 1.5 equivalents of thiopheneacetyl chloride produces 65% **4a**, and 29% **2**, suggesting that reaction with diacetylindigo could be a more effective way to produce symmetrical products as well.

To gain a deeper understanding of the BAI formation from *N,N'*-diacetylindigo, NMR experiments were conducted in d^8-dioxane (**Figure 4**). As the reaction progressed the acetyl groups on indigo were slowly converted into acetic acid and acetic anhydride. Thiopheneacetyl chloride was nearly completely consumed after 7 hours, with the appearance of thiopheneacetic acid. Interestingly, the amount of thiophene acetic acid also decreased over time, implying that even though it is formed in the reaction, it is also being consumed. The appearance of these reaction byproducts suggests transformations that are commensurate with the improvement in yield (**Figure 5**).

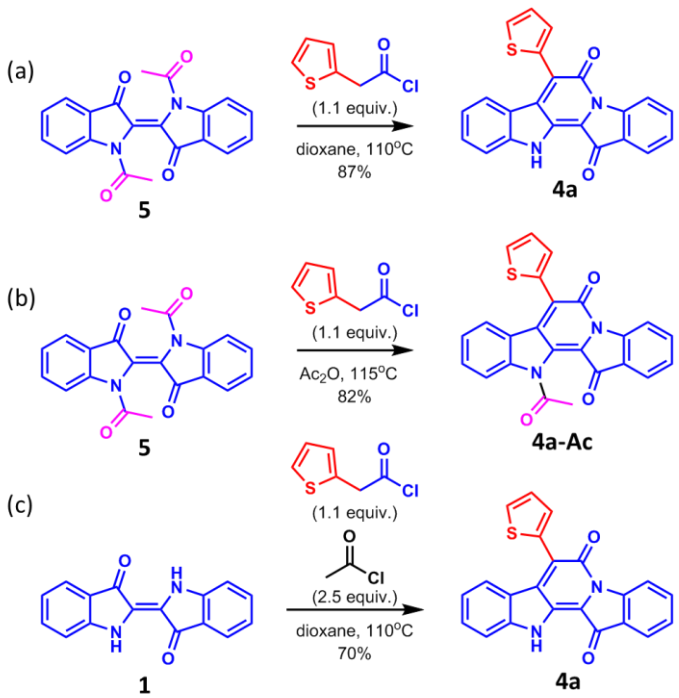

Scheme 3: Monoannulation of *N,N'*-diacetylindigo **5** in (a) dioxane, and (b) acetic anhydride, and monoannulation of indigo with acetyl chloride additive.

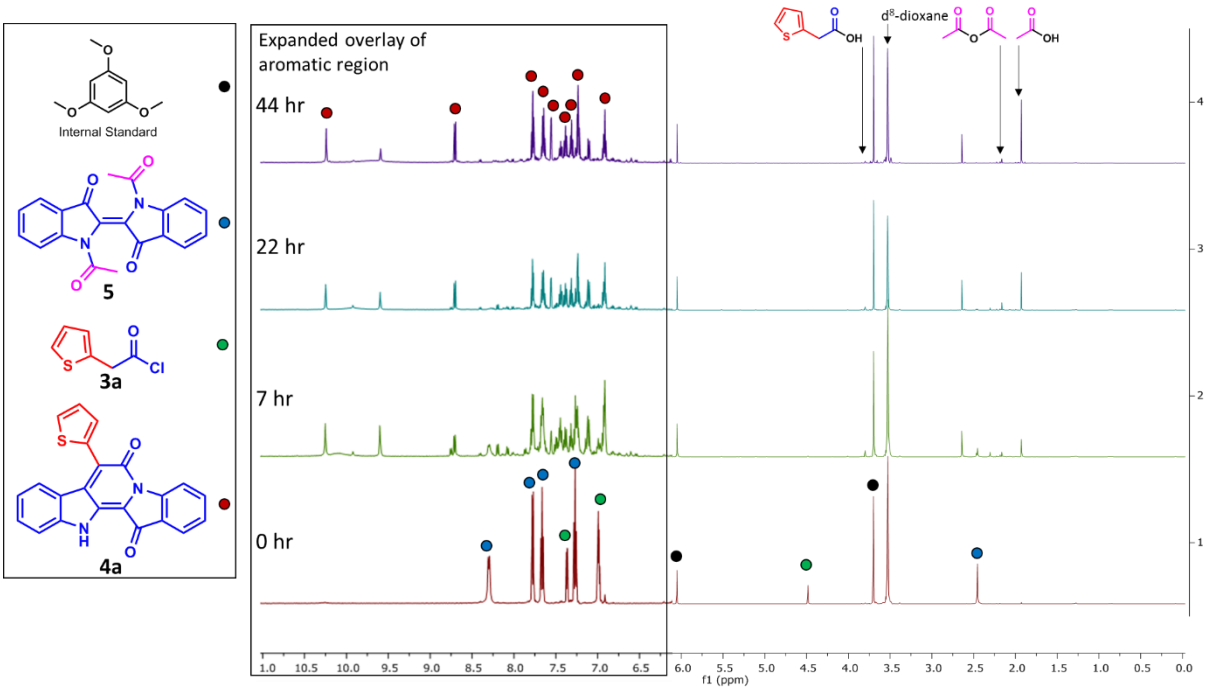

Figure 4: Selected NMR timepoints and identified compounds for a monoannulation of **5.** Reproduced with permission from reference [15], Copyright © 2016 American Chemical Society

Water, which is a byproduct of the cyclodehydration reaction, can form deleterious byproducts through hydrolysis of the thiopheneacetyl chloride starting material. The water that is formed during the condensation can react with **5** to yield acetic acid. Because it is significantly less nucleophilic than water, it can slow the rate of degradation of the thiopheneacetyl chloride reagent. If reaction between acetic acid and the thiopheneacetyl chloride does occur, it would form a mixed anhydride which is still a competent intermediate, allowing it to reenter the reaction cycle (**Figure 6**). Initial deacylation of **1a** is proposed to come from a catalytic amount of water.

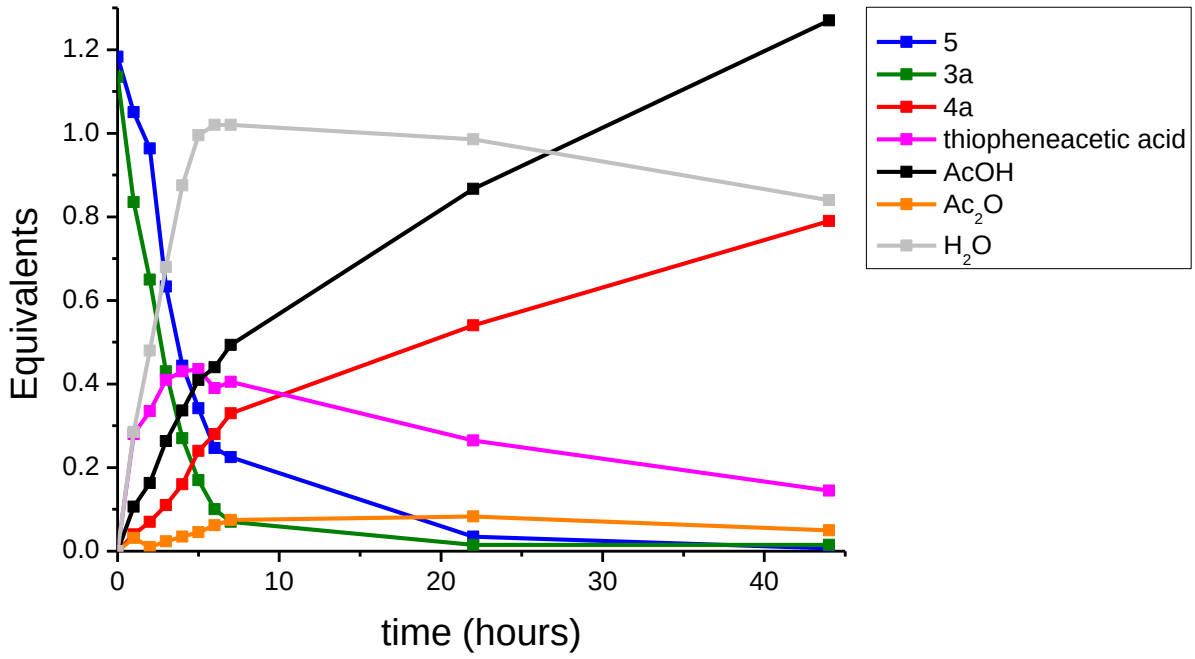

Figure 5: Tracked equivalents of identified intermediates and side products over time

N-acetylation transforms the parent indigo into a highly soluble species that permits simple monitoring of the reaction progress while also increasing yield by remediating the effects of water formation. The result is an annulation reaction that allows for clean conversion to a single addition product **4** with only 1 equivalent of acetyl chloride.

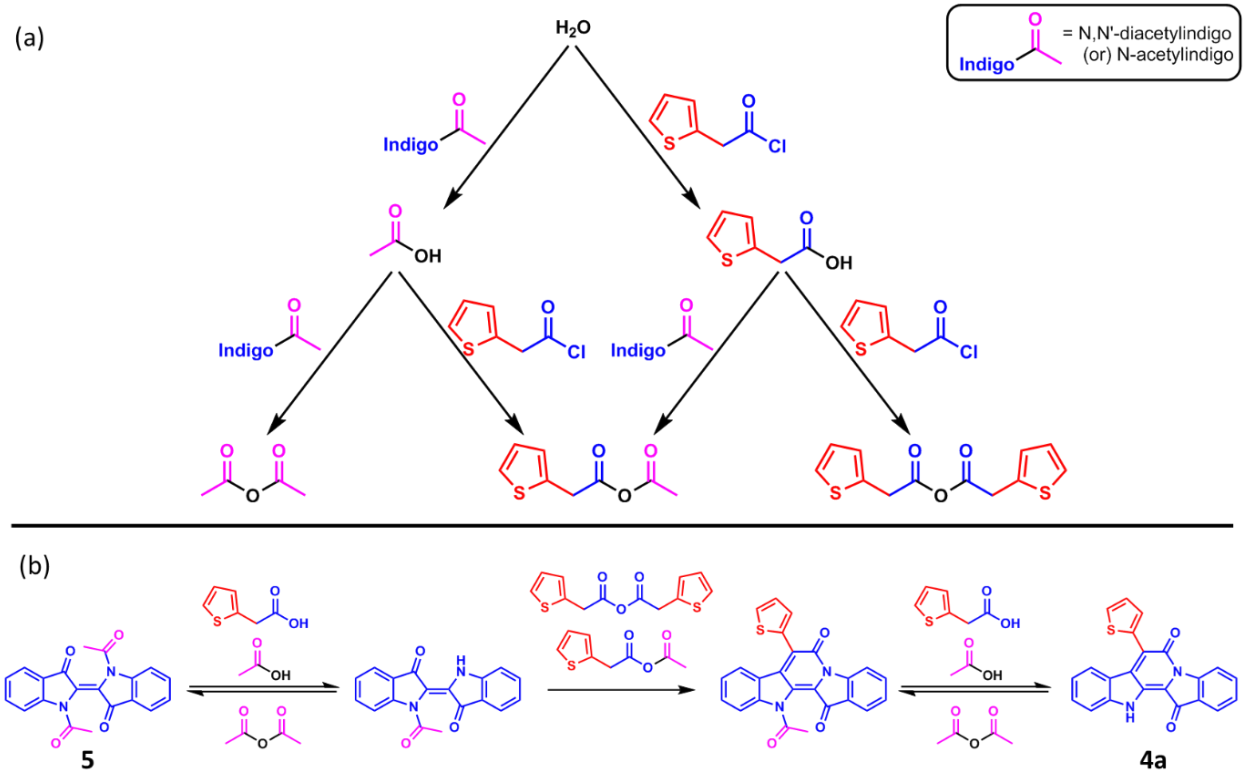

Figure 6: Proposed mechanism of the bay annulation reaction with precursor **5**

2.3 Asymmetric Bay-Annulation Reaction

Exploring the scope of this methodology revealed that several aromatic acetyl chlorides were competent reactants for a selective monoannulation (**Scheme 4**). In addition to phenyl **4b**, a 4-bromophenyl adduct **4c** was obtained in decent yield following the same reaction conditions. Monoadducts **4d**– **4f** bearing alkyl or glycol chains can also be obtained from the corresponding substituted 2-arylacetyl chlorides in good to excellent yields.

The synthesis of desymmetrized BAIs was attempted by reacting monoannulated products with a second equivalent of 2-arylacetyl chloride in xylene at 145 °C, which proceeded smoothly to give a range of desymmetrized BAIs (**Scheme 5a**). This stepwise annulation allows the introduction of amphiphilicity onto the opposite bay positions of BAI, such as **6a**, or selective tuning of conjugation via the incorporation of a thiophene unit, such as **6b** and **6c**. The amphiphilic **6a** was synthesized as a good candidate for the formation of self-assembled monolayers through a Langmuir–Blodgett process.[16] Compounds **6b** and **6c** could be easily functionalized for incorporation into more complex donor–acceptor systems. As shown in **Scheme 5b**, selective bromination on thiophene units proceeds in high yield under mild conditions to produce bromides **7b** and **7c**, respectively.

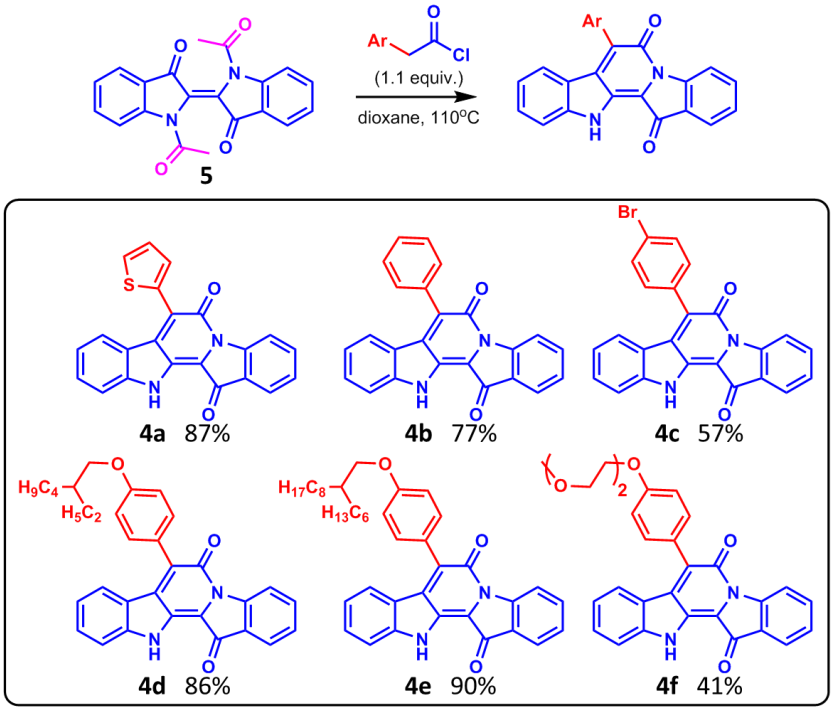

Scheme 4: Scope of monoannulation reaction

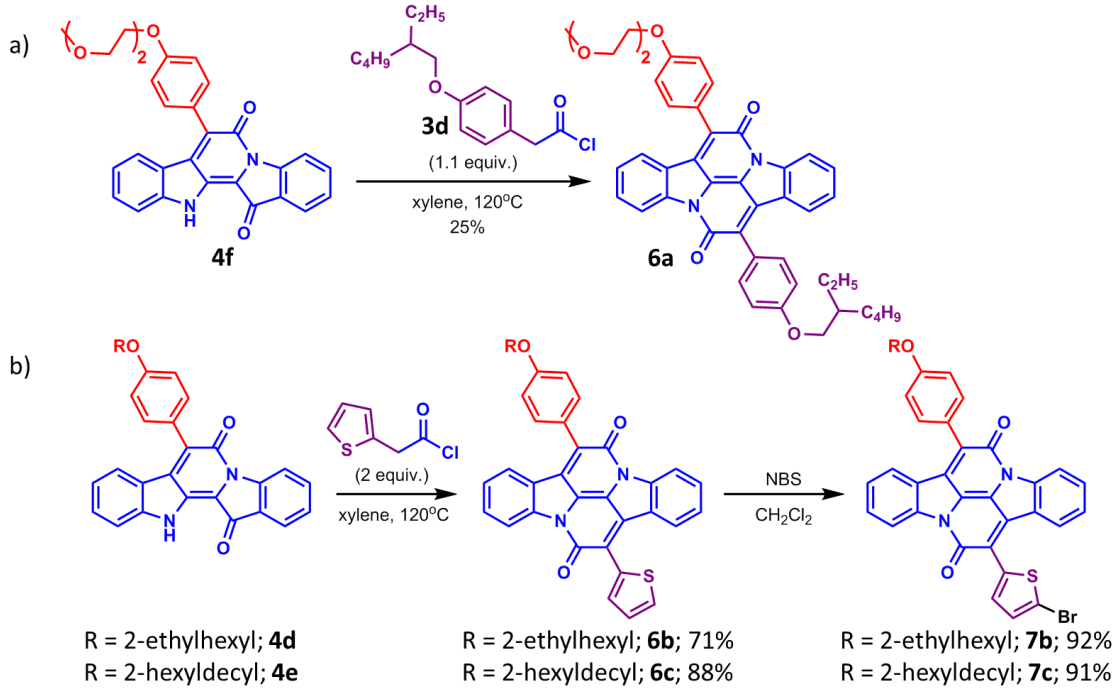

Scheme 5: Synthesis of desymmetrized BAI compounds

Further reaction of these compounds with a number of donor units via Suzuki or Stille coupling conditions gave rise to linear or C_3-symmetric donor–acceptor systems including BAI adducts of fluorene (F) **10**, benzodithiophene (BDT) **11**, and triphenylamine (TPA) **12** (**Scheme 6**). Molecules with similar donor–acceptor architecture have shown great promise in engineering

long-range energy transport, an unusual property dominated by ordered molecular self-assembly in the aggregated state.[17]

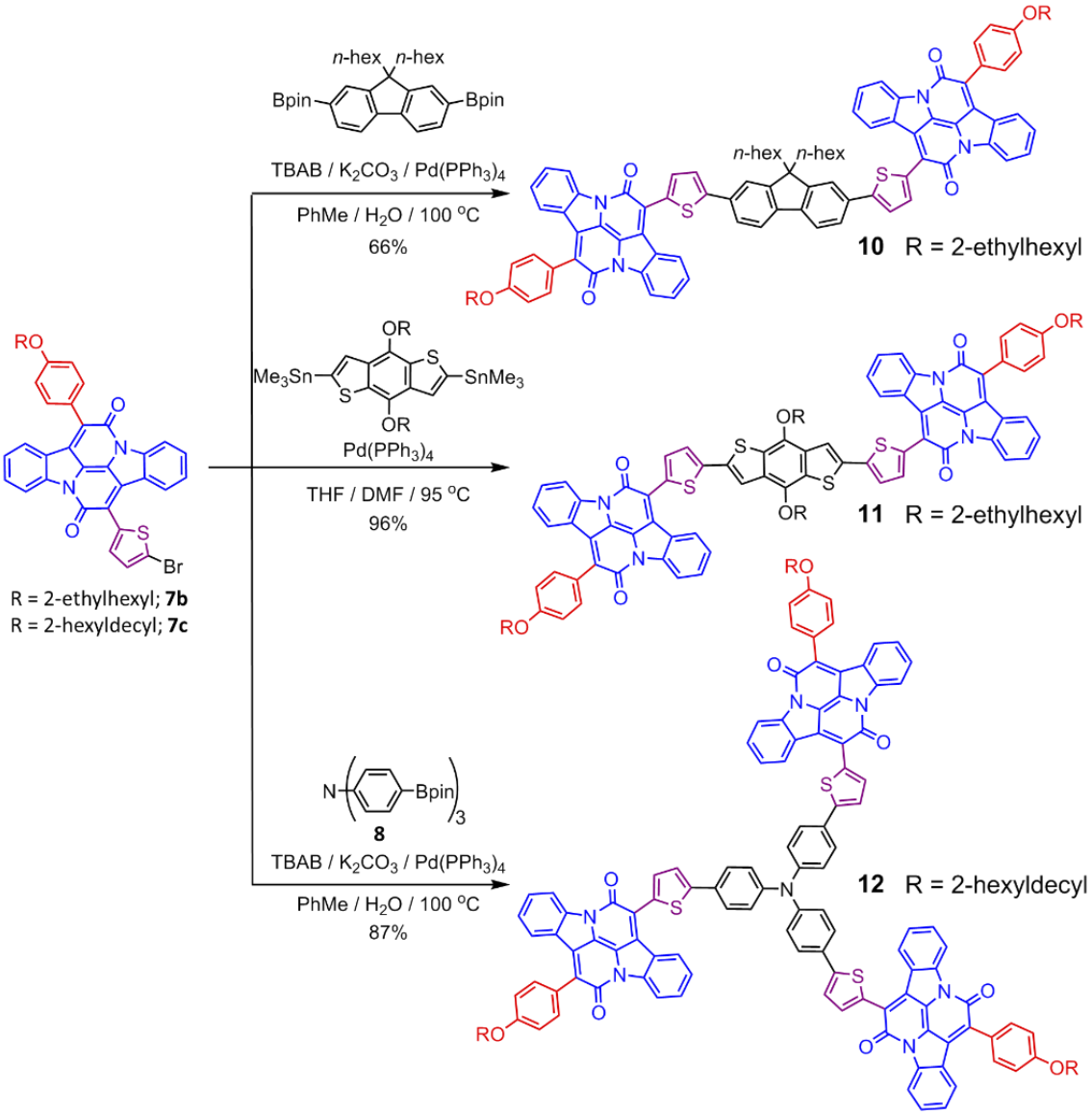

Scheme 6: Synthesis of donor-acceptor BAI adducts

2.4 Optoelectronic Properties of Dissymmetric Bay-Annulated Indigo

Due to the extended conjugation and donor-acceptor nature of BAI **2**, these molecules absorb light into the visible spectrum and near-IR. The desymmetrized functionalization provides a convenient method to tune the energy levels through the incorporation of different aromatic units on each of the bay positions. Compared to the parent indigo, the monoannulation products displayed a blue shift of 40–60 nm for its lowest energy absorption peak due to partial loss of the "H-chromophore" characteristics, as revealed by UV–vis spectroscopy.[18] A red shift, corresponding to a decrease of 0.04 eV in optical bandgap, is observed when the flanking aromatic substituent is changed from phenyl groups to a more donating thiophene (**Figure 7a**). The characteristic donor-acceptor peaks corresponding to electronic π–π^* and intramolecular

charge transfer processes occur at the longest wavelengths. This often appears as an initial broad $\pi-\pi^*$ peak with a shoulder attributed to charge transfer processes.

The electronic effect of the flanking aromatic units on the optical properties was consistently observed in the doubly annulated BAIs. The stacked absorption spectra of BAIs **6a**, **6c**, and **2** in **Figure 7b** indicate well-resolved and progressive red shifts of the absorption maximum in the order of 0.05 eV, when the aromatic substituents were changed successively from phenyl to thienyl. This is in full agreement with the different electron donating ability between phenyl and thiophene groups, which confirms good electronic coupling between BAI acceptors and the attached aromatic substituents. The high sensitivity of the optoelectronic properties in response to slight structural modifications further manifests the powerful nature of desymmetrization chemistry. Coupling to stronger donors, such as in the donor–acceptor conjugates **10**, **12**, and **11**, led to more drastic red shifts in the absorption spectra (**Figure 7c**), corresponding to optical bandgaps of 1.8, 1.7, and 1.6 eV.

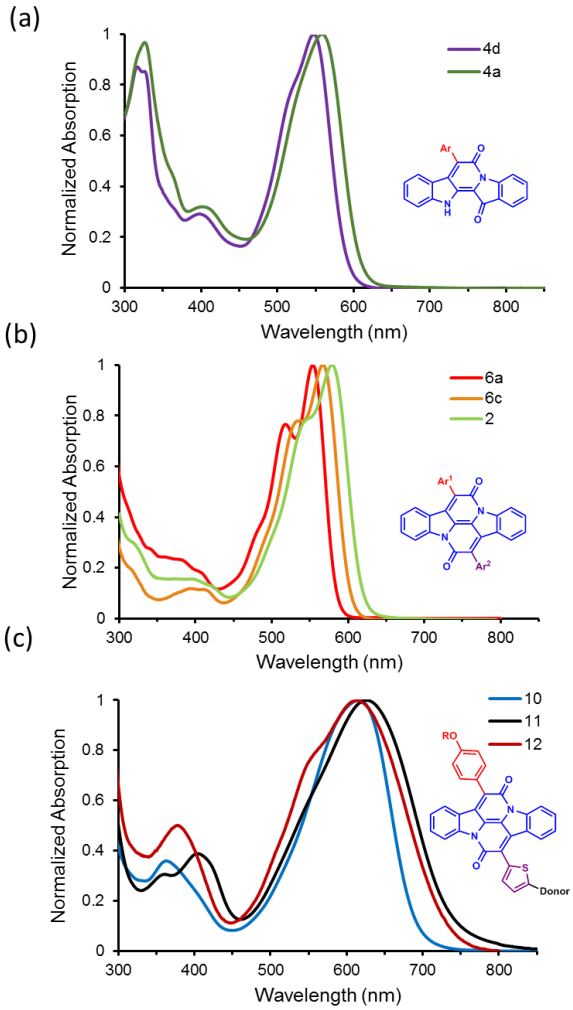

Figure 7: UV-Vis spectra for (a) monoannulated indigo, (b) doubly annulated indigo, and (c) larger donor-acceptor adducts

This sensitivity of the BAI scaffold to electronic effects is exemplified through later studies which compared extension of conjugation in the bay and phenylene positions (**Figure 8a**). As was observed with the dissymmetric BAI, as conjugation is extended along the bay position the absorption peak is red-shifted due to both larger conjugation area and stronger donor character paired with the BAI acceptor (**Figure 8b**). Absorption to 1000 nm or above is facilitated by more electron rich donor monomers. The extinction coefficients of polymers regularly reach $\varepsilon=10^5$ M^{-1} cm^{-1} whereas small molecules generally exhibit coefficients in the $\varepsilon=10^4$ M^{-1} cm^{-1} range. While extended conjugation in the bay direction pushes the absorption to longer wavelengths, it leaves a large void space in the blue region of the visible spectrum.[19] However, by extending conjugation off of the phenylene position it was discovered that the corresponding absorbance occurs in the blue region of the spectrum, providing complementary absorption (**Figure 8c**). Because the phenylene rings are not linked together through an uninterrupted conjugation pathway, pendant groups have a smaller overall delocalized π surface, resulting in a peak absorption in the blue region of the spectrum. This complementarity allows for panchromatic absorption, where extended conjugation on the bay axis red-shifts the absorption, while extension of the phenylene region fills in absorption in the smaller wavelengths. By doing so, these compounds can absorb light across the majority of the visible spectrum (**Figure 8d**).

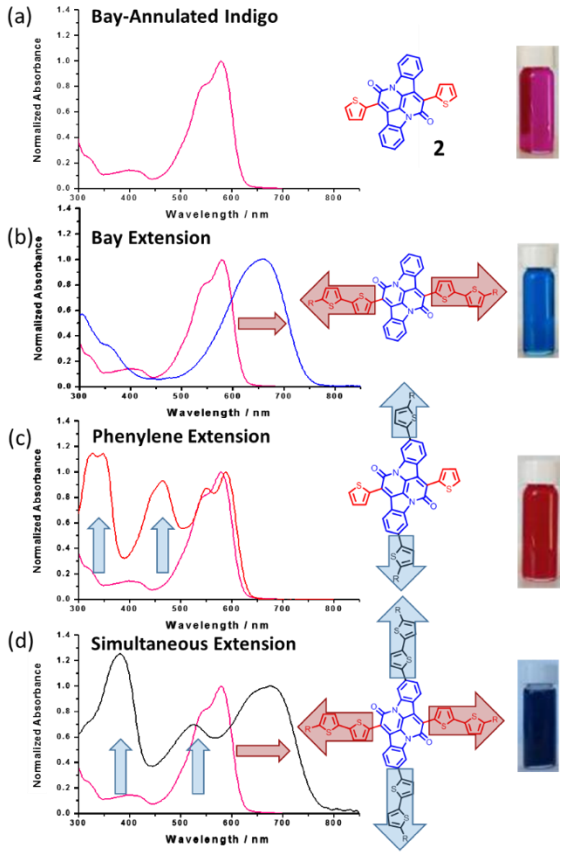

Figure 8: UV-Vis spectrum of (a) **2** and the effect of aromatic extension in the (b) bay direction, (c) aromatic direction, and (d) both directions simultaneously to provide panchromatic absorption. Reproduced with permission from reference [5], Copyright © 2019 Wiley

Cyclic voltammetry allows for an approximation of the energy levels for the frontier molecular orbitals of the BAI system. At reducing potentials, two quasireversible one-electron reduction processes were observed for all the compounds, with similar lowest unoccupied molecular orbital (LUMO) energy levels situated within the range of −3.5 to −3.6 eV (**Figure 9a**). These likely correspond to the reduction of the conjugated bis-amide in the BAI core. The corresponding oxidations were mostly irreversible or pseudoreversible with energy levels varying widely between -4.9 and -5.5 eV depending on the pendant donor groups. The determined electrochemical bandgaps could be estimated from the onset of redox peaks (except for compound **11**), all of which match well with the optical bandgaps. The overall trend shows consistent LUMO energies, suggesting the localization of LUMO on the central core, while the HOMO is strongly dependent on the coupled electron donors. FMO energy levels determined from cyclic voltammetry were found to be consistent across multiple techniques used by other groups including ultraviolet photoelectron spectroscopy (UPS) + UV/Vis[20] and photoelectron spectroscopy (PESA) + UV/Vis.[21] This trend is corroborated by a comparison of frontier molecular orbital (FMO) energies across a wide variety of BAI structures (**Figure 9b**).

An energy level diagram is given to compare the FMO energies of BAI systems with some benchmark organic semiconductors (**Figure 9c**). In comparison with donor systems such as poly-3-hexylthiophene (P3HT), BAI has sufficiently lower HOMO and LUMO to make it energetically compatible for charge transfer. When compared to acceptors, BAI have a higher HOMO and LUMO than fullerene based acceptor phenyl-C60-butyric acid methyl ester (PC60BM), but approximately equivalent HOMO levels as the common non-fullerene acceptor (3,9-bis(2-methylene-(3(1,1-dicyanomethylene)indanone))-5,5,11,11-tetrakis(4-hexylphenyl)dithieno [2,3*d*: 2′,3′*d*′]indaceno[1,2*b*:5,6*b*′] dithiophene) ITIC.[22]

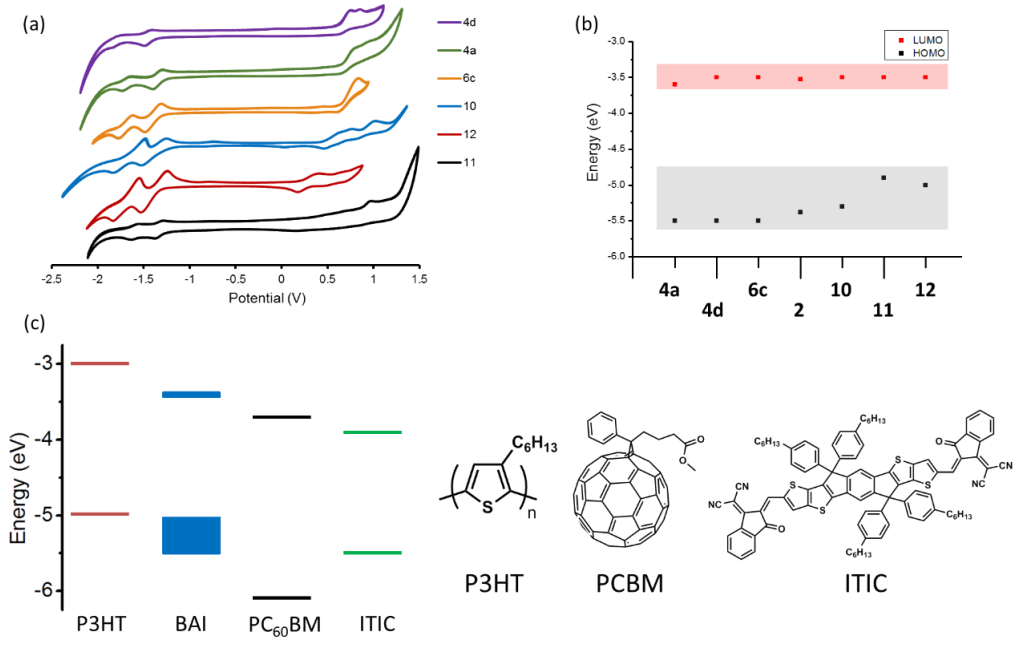

Figure 9: Analysis of the frontier molecular orbital energy of BAI compounds by (a) cyclic voltammetry and using band diagrams to compare (b) measured BAI materials, and (c) common organic semiconductors

DFT calculations were carried out to model the molecular orbitals and frontier orbital energies, utilizing a B3LYP functional with the 6-31G* basis set.[23] The relative order of the calculated HOMO−LUMO energy gap is consistent with the experimental results (**Figure 15**). The theoretical LUMO frontier orbitals of both monoannulation (**4a, 4d**) and double annulation (**6c**) indicated significant delocalization over the BAI core with a small contribution from the attached donors. On the other hand, the HOMO orbitals spread over the central diketopiperidopiperidine unit and extend into the conjugated donor units but with varying degrees of delocalization onto the two benzene rings from the parent indigo. The calculations on the dimeric and trimeric donor−acceptor conjugates further illustrated that the HOMOs have better delocalization along the conjugation backbone, while the LUMOs are mainly localized on BAI units, which is consistent with the experimental observation that they all have very similar LUMO energies.

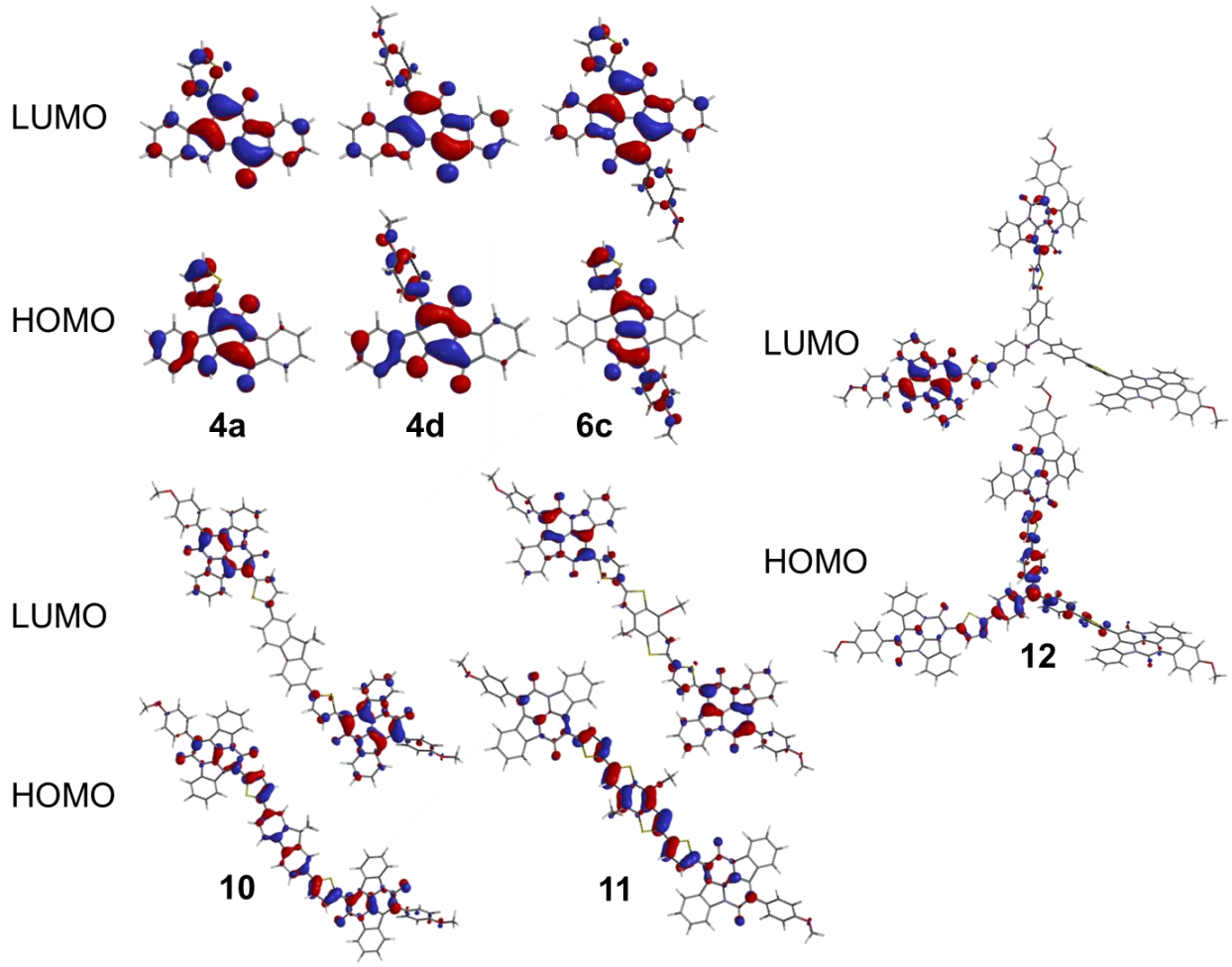

Figure 10: Orbital diagrams of BAI compounds. Reproduced with permission from reference [15], Copyright © 2016 American Chemical Society

Table 1: Summary of optical, electrochemical, and calculated data

Compd	UV-Vis				Cyclic Voltammetry			Computation		
	λ_{max} (cm)	ε_{max} (M^{-1} cm^{-1})	λ_{onset} (cm)	E_g^{opt} (eV)	E_{HOMO} (eV)	E_{LUMO} (eV)	E_g^{Elec} (eV)	E_{HOMO} (eV)	E_{LUMO} (eV)	E_g^{Calc} (eV)
4d	548	14 600	590	2.1	-5.5	-3.5	2.0	-5.2	-2.6	2.6
4a	560	14 500	602	2.1	-5.5	-3.6	1.9	-5.3	-2.8	2.5
5c	567	22 300	606	2.1	-5.5	-3.5	2.0	-5.1	-2.8	2.5
7	616	90 300	690	1.8	-5.3	-3.5	1.7	-4.9	-2.8	2.1
8	617	70 800	730	1.7	-5.0	-3.5	1.5	-4.7	-2.8	1.9
9	628	58 100	760	1.6	-	-3.5	-	-4.8	-3.0	1.8

2.5 Self-Assembly Properties of Desymmetrized BAI

Self-assembly provides a unique opportunity to make complex structures from simple precursors. This is perhaps most well known in cell membranes, in which phospholipids self-assemble into mono- and bilayers to enclose a cell. With a goal of designing materials for optoelectronic applications, triphenylamines were chosen as a self-assembly scaffold. Triphenylamines (TPAs) are known to form nanowires through direct face-to-face stacking of the amine moiety.[24] Strong π stacking with a cup-like geometry provides a strong thermodynamic driving force and a preferred orientation for this organization, as is seen in bowlic liquid crystalline systems.[25] Both photo and chemical oxidation of TPA to the radical cation have been shown to facilitate this interaction, where charge can be stabilized through delocalization throughout the wire stack.[26] The outer alkyl chains are thought to reinforce tight packing within individual nanowires.

Triphenylamine based semiconductors have been used as hole conducting materials[27] in a variety of applications, such as sensing [28], OFET[29], OLED[30], OPV[31] and as plasmonic interconnects between nanoparticles,[32] among others. These systems also display some unique properties such as multiphoton absorption[33] and stable electrochromic behavior.[34] With the produced compound **12** in hand, deliberate attempts to form nanowires were undertaken and characterized by optical microscopy and Scanning Electron Microscopy (SEM). It was determined that despite propensity to form nanowires, **12** was capable of forming a wide range of morphologies depending on the deposition conditions. Solvent had a drastic effect on nanowire formation. Seemingly similar solvents such as chloroform and dichloromethane (DCM) could provide very different outcomes (**Figure 11a,b**). Chloroform produced fairly uniform wires, while DCM provided strips of material with large variability in thickness. This difference could be due to the high volatility of DCM, potentially kinetically trapping the **12** in a non-equilibrated state. Benzene solutions of **12** produced films, while THF provided clean networks of nanowires, similarly to chloroform (**Figure 11c,d**).

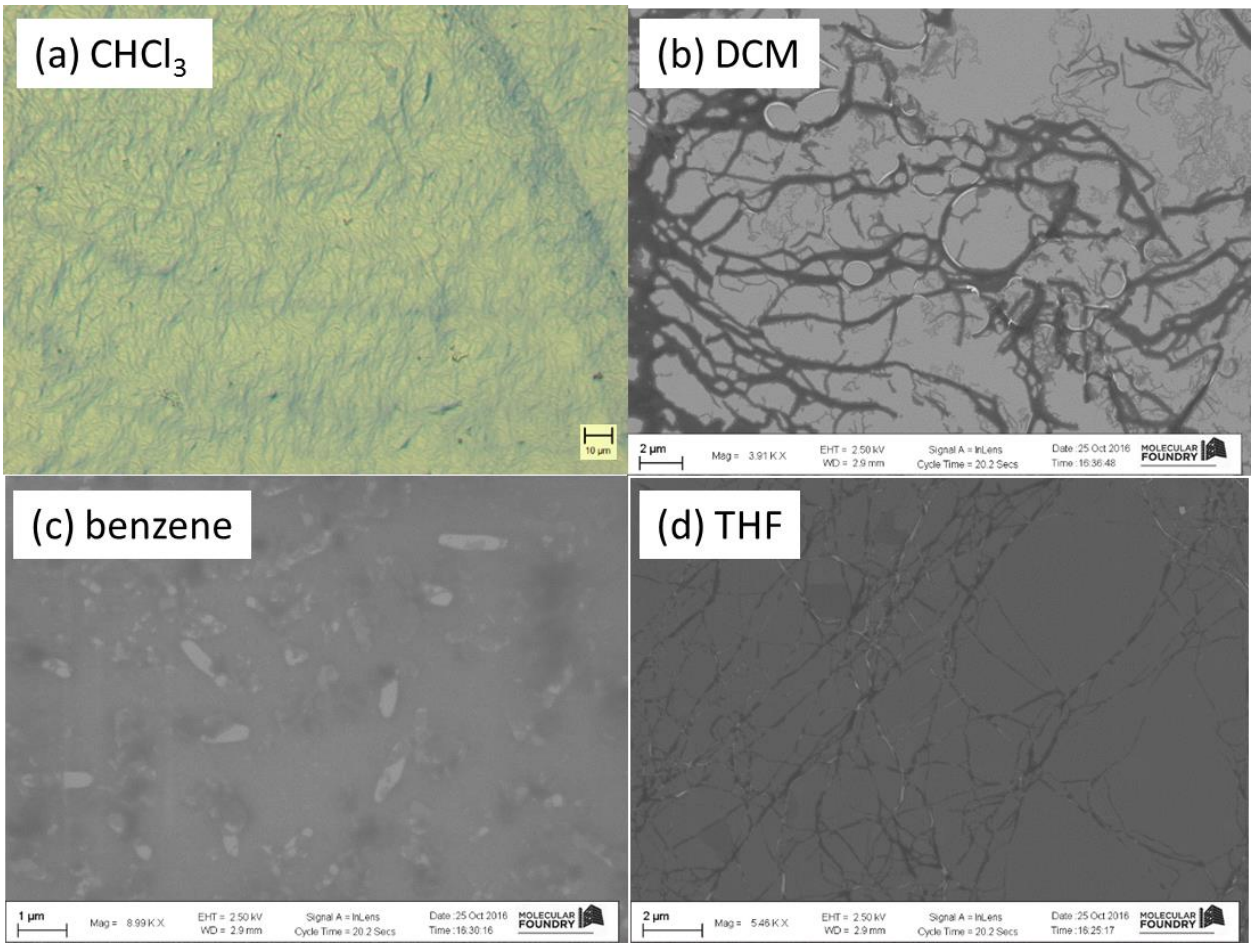

Figure 11: The effect of solvent on nanostructure with **12** dropcast from solutions of (a) chloroform, (b) DCM, (c) benzene, and (d) THF

Studies using toluene as the solvent also determined that both deposition method and concentration are significant factors in determining morphology. Spincoating is a technique often used for depositing uniform films. In a typical spincoating process, a concentrated solution is dropped onto a rapidly spinning substrate which both sheds excess solution and rapidly evaporates the solvent due to high surface area exposure (**Figure 12a**). This process is in contrast to another dropcasting process for film formation, in which the sample solution is added to a non-spinning substrate and slow evaporation plays a larger role. Because of the longer timeframe for evaporation, the molecules can reorganize into thermodynamically favorable orientations. Additionally, because no material is lost (unlike spin coating) the effective concentration of the solution increases over time as the solvent evaporates. These factors together often lead dropcast films to have higher roughness, but more crystalline films **(Figure 12d)**.

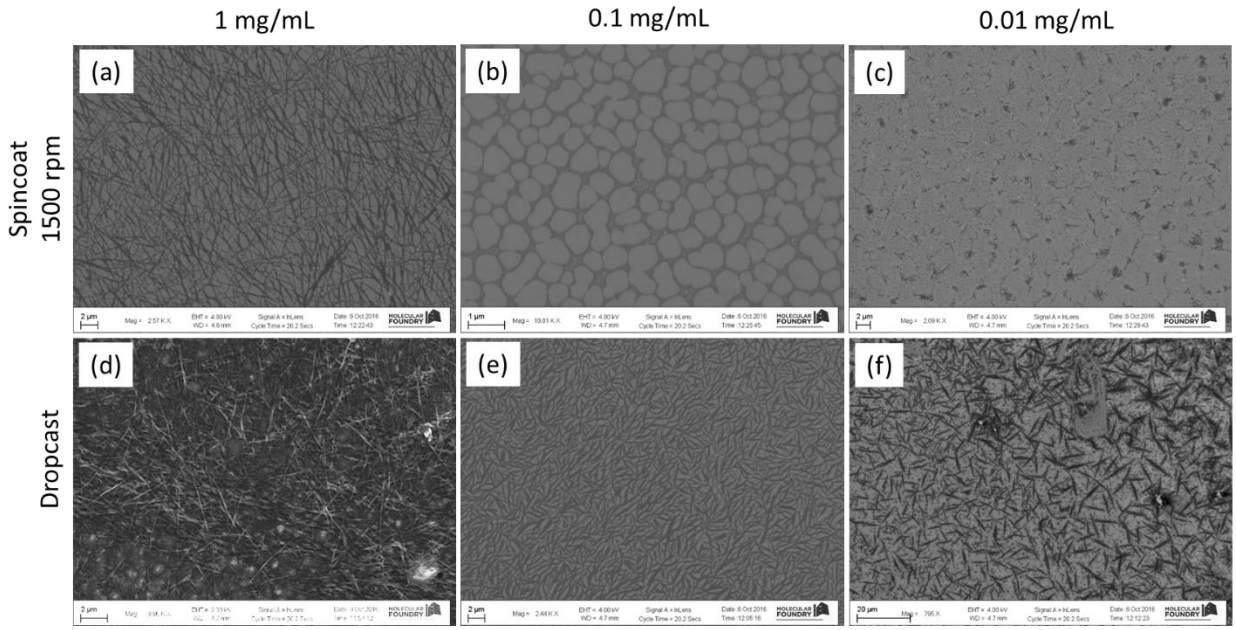

Figure 12: The effect of deposition method and solution concentration of **12** in toluene on nanostructure, with films spuncast at 1500 rpm from (a) 1 mg/mL, (b) 0.1 mg/mL, and (c) 0.01 mg/mL solutions of **12** in toluene, and dropcast from (d) 1 mg/mL, (e) 0.1 mg/mL, and (f) 0.01 mg/mL solutions of **12** in toluene

As the concentration of these solutions are decreased, the aggregate size also decreases (**Figure 12b,e**). However, given the right conditions, **12** is still capable of forming interconnected networks of material even at extremely low concentrations. Even at 0.01 mg/mL concentrations, both dropcast and spincoated films are still interconnected (**Figure 12c,f**). Conversely, when concentrations increased, vast networks of hair-like wires are observed (**Figure 13a**). Utilizing scanning electron microscopy (SEM), it was determined that each of the wires observed at a low magnification are made up of bundles of smaller nanowires (**Figure 13b,c**). A 3.7E5 times magnification scan of an individual wire showed that it is comprised of individual strands with a width of ~4 nm (**Figure 13d**). This matches very closely with the theoretical thickness of an individual molecule (circumference 3.97 nm). This gives strong evidence that each of the individual nanowires is molecularly wide, comprised of single molecules arranged in a stacked bowl fashion (**Figure 14a)**. These wires are proposed to align parallel with other wires to form larger supramolecular bundles, possibly driven by intermolecular forces between alkyl chains (**Figure 14b**).

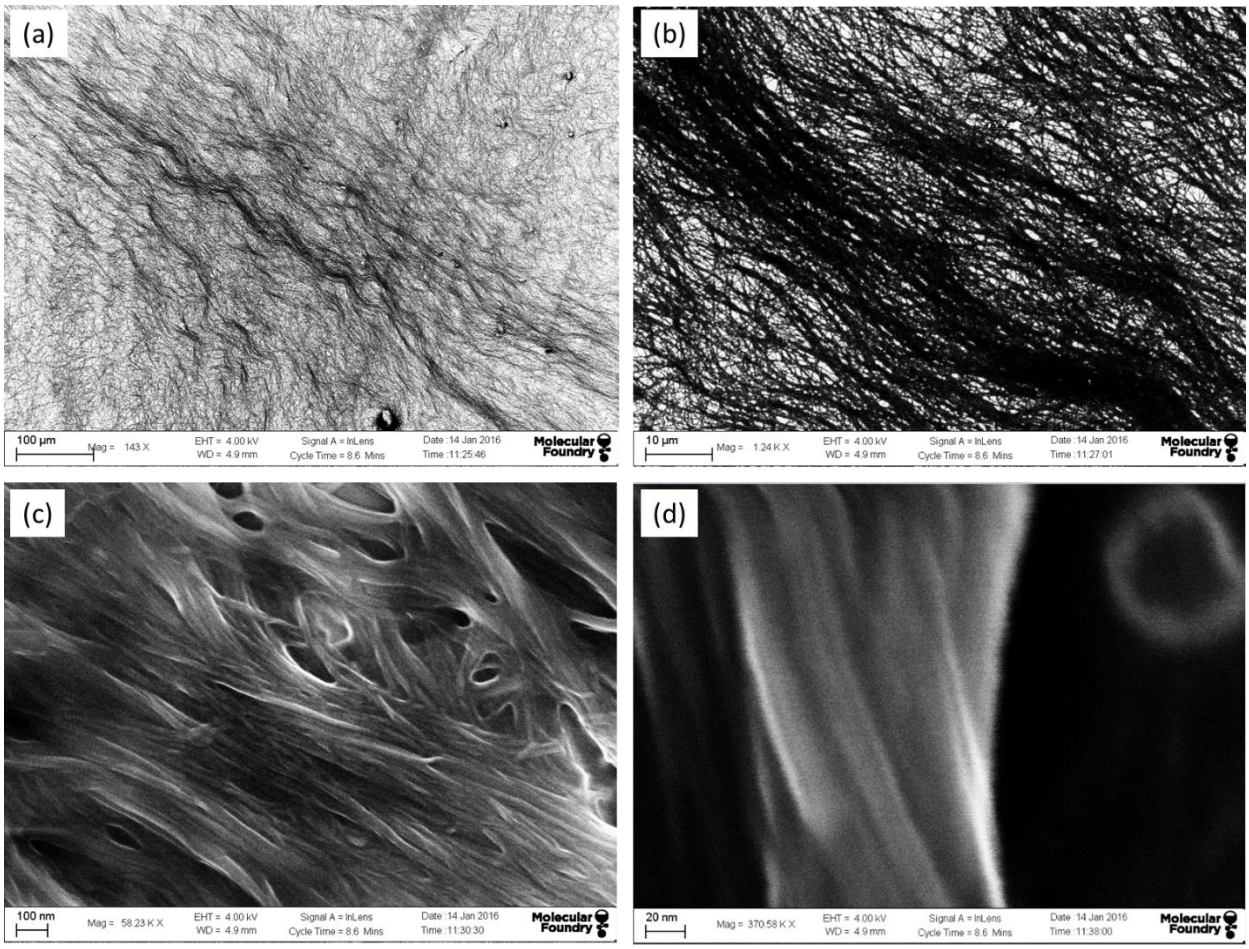

Figure 13: Scanning electron microscopy images of **12** at increasing levels of magnification

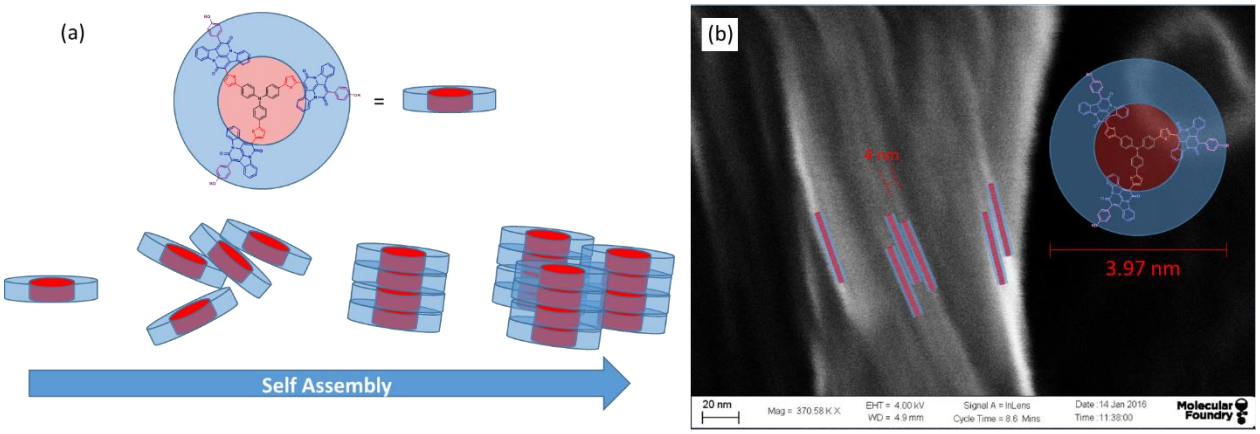

Figure 14: Schematic representation of (a) self-assembly process of **12**, and (b) superposition of the model nanowires on the SEM image presented in **Figure 13d**

This model is further supported through Grazing Incidence Small Angle X-ray Scattering (GISAXS) (**Figure 15a**). This data, provided by a collaborator Michael Roders in the Ayzner group, showed periodicity within the film with a size of 4 nm on the q_{xy} plane (**Figure 15b**). Our own experiments with Grazing Incidence Wide Angle X-ray Scattering (GIWAXS), demonstrated that

supramolecular structure has a preferred edge-on orientation with the substrate, consistent with wires lying on the substrate surface (**Figure 15c**).

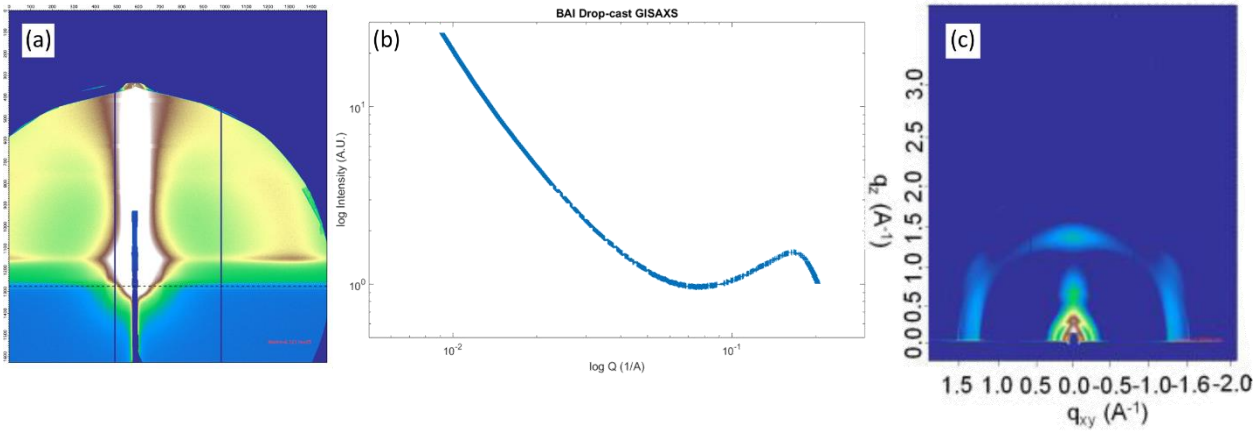

Figure 15: X-ray scattering of nanowires of **12.** (a) GISAXS plot and (b) line cut as well as (c) GIWAXS plot

With such a strong driving force for aggregation, we became curious as to whether the molecules were preaggregated when dissolved in solution. This was initially suspected after ^{1}H NMR spectrum of **12** showed unusually broad peaks, suggesting that the chemical environment around each molecule in solution was highly variable, possibly due to aggregation. To test this hypothesis, variable temperature UV-Vis spectroscopy was undertaken (**Figure 16**). It was observed that when increasing the temperature, all peaks progressively decreased in size and blue-shifted. This is proposed to be due to disaggregation at elevated temperatures. As the temperature is increased, entropy plays more of a role in molecular ordering, slowly overcoming the thermodynamic preference for aggregation. The disaggregation of heating was fully reversed by recooling of the solution. Unfortunately, heating temperature was limited by the boiling point of the solvent ($BP_{chloroform}$ = 61 ^oC), so a UV-Vis of the completely disaggregated species was not possible in this case. Future attempts in a higher boiling solvent such as toluene or xylene could provide further details about the temperature-dependent aggregation behavior.

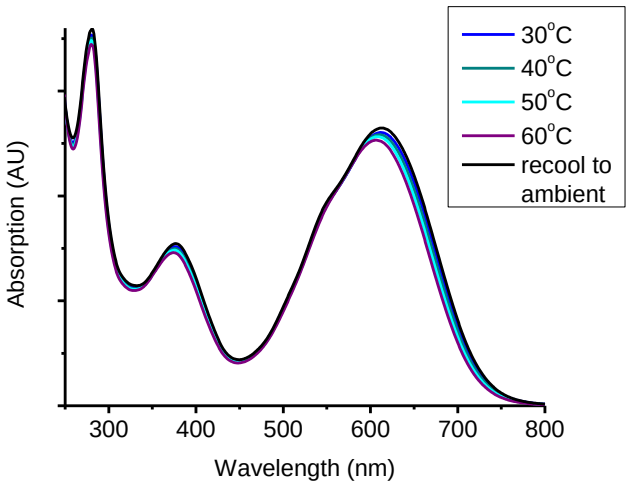

Figure 16: Variable temperature UV-Vis spectroscopy of **12** in chloroform

2.6 Conductivity of Self-Assembled Structures

Work undertaken in collaboration with Michael Roders in the Ayzner group gave further insight into the aggregation properties of these molecules and how they relate to their electronic properties. To understand the relation between structure, self-assembly, and conductivity, both (triphenylamine) NBAI (**12**) and (fluorene) FBAI (**10**) were processed into polymer matrices for testing. A conductive PPDI-2T matrix was utilized for charge transfer analysis,[35] while a non-conductive poly(hexylmethacrylate) (PHM)[36] matrix was used to obtain information about the electronic properties of BAI supramolecular networks independent of matrix (**Figure 17a**). Interestingly, in these two polymers as well as with polystyrene (PS)[37], a strikingly similar self-assembly motif was observed for each molecule. Compound **12** showed mesoscopic nanowires that percolate through the polymer matrix, leading to charge-transport networks characterized by a larger effective charge mobility and somewhat fewer deep electronic traps compared to fractal FBAI networks (**Figure 17b**). The FBAI on the other hand consistently formed a disorganized fractal like pattern, similar to those observed for diffusion-limited aggregation (DLA)[38] (**Figure 17c**). Just as DLA is a nonequilibrium phenomenon, so is formation of kinetically trapped small-molecule networks inside the polymer matrix upon solvent evaporation and solid film formation. This implies that the ordering preference is determined on the molecular level, and can overcome organizational preferences of the host polymer matrix.

Measuring space-charge limited currents (SCLC) is a sensitive way to assess the trap states in a crystalline system.[39] By passing a current through a crystal, the presence of traps will decrease the current and also distort the current-voltage curve. The deviations in the shape from an ideal square curve can be used to determine the energy distribution of traps. To this end, networks of **12** and **10** in insulating PHM polymer host were studied in a diode configuration.[40] The current was measured at constant voltage (14V) as a function of BAI mole fraction (**Figure 17d**). At the lowest ratio of BAI/monomer the current is low for both derivatives, implying that the network is near the percolation threshold. Increases in concentration show a huge increase in current flow through the NBAI **12**, while in FBAI **10** current only increases gradually. At the highest ratio, the NBAI **12** shows three times higher current than FBAI **10**, indicating much greater charge mobility.

In order to quantify the charge transport differences between these molecules, current density vs. voltage was plotted on a double log scale for the highest PHM:BAI molar ratio blends (**Figure 17e**). The power-law slopes were fitted at high bias to provide the power law scaling exponent, which provided the thermodynamic temperature (T_c). A low thermodynamic temperature implies trap distribution varies rapidly with changes in energy, while a high Tc implies a gradual change in trap distribution.[39b]

The magnitude of the power-law scaling exponent of the current-voltage curve is inversely proportional to the characteristic temperature of the trap distribution, T_c, such that

$$J \propto V^{T_c/T+1} \tag{1}$$

where T is the thermodynamic temperature. T_c is related to the energetic 1/e *width* of the trap distribution via

$$P(E) \propto e^{-|E_{VB}-E|/k_B T_c} \tag{2}$$

E_{VB} is the valence-band (HOMO) level, and k_B is the Boltzmann constant. We find a slightly larger scaling exponent of the PHM:FBAI blend (4.55) relative to PHM:NBAI (4.39). Within the exponential-trap model, this implies a broader distribution with a larger density of relatively deep traps, changing T_c from 1058 K for FBAI **10** to 1010 K for NBAI **12**. Though the difference is small, it is consistent with the physical network structure.

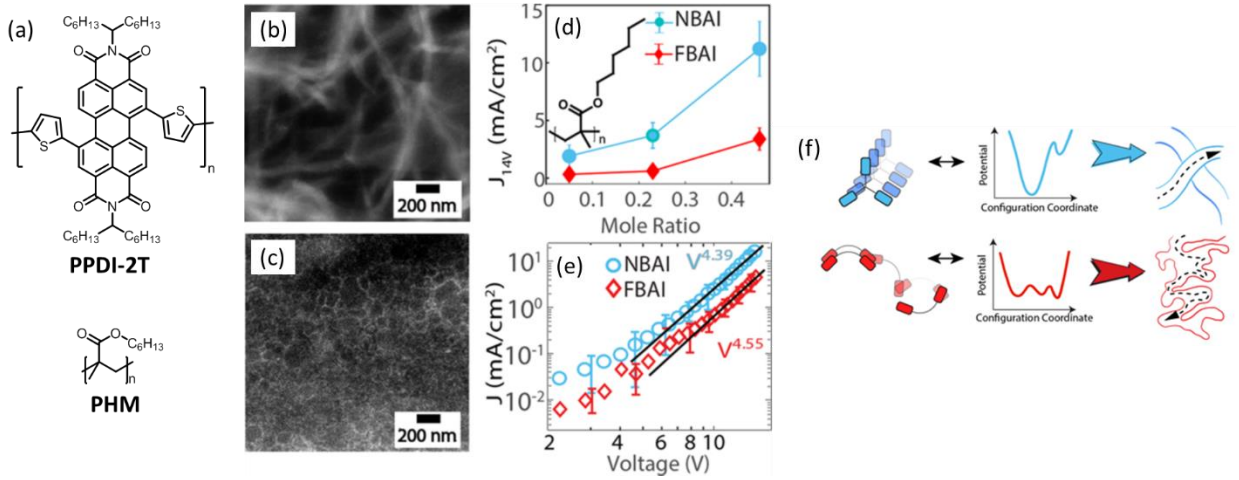

Figure 17: (**a**) Structure of polymer matrices and HAADF-STEM images of (**b**) PHM:NBAI (**12**) and (**c**) PHM:FBAI (**10**) at 14kX magnification; (**d**) injected current density at 14 V as a function of PHM:BAI mole ratio; (**e**) double-logarithmic plot of current density vs. voltage for the highest PHM:BAI mole ratio blends with power-law slopes fitted at high bias; (**f**) cartoon highlighting the connection between small-molecule packing in the polymer blend and the complex energetic landscape (as a function of a collective configuration coordinate), which determines the practical accessible states of the mesoscale network. Reproduced with permission from reference [40], Copyright © 2019 American Chemical Society

It is through these studies that a relationship between structure and function is elucidated (**Figure 17f**). In the angstrom scale, triphenylamine based **12** has strong and directed intramolecular interactions that drive it to self-assemble into columnar stacks. This robust stacking corresponds to a thermodynamic minimum in the energetic landscape which favors a percolated network of nanowires. These nanowires form a more continuous and interconnected pathway which provides high conductivity. Alternatively, fluorene based **10** has similar intramolecular π–π interactions available, but with no favored orientation. This allows for a large number of relatively shallow minima in the energy landscape, leading to a disordered mesoscale network connected in "tortuous pathway" and low carrier mobilities. It may be prevented in participating in liquid crystalline behavior seen in other bent systems[41] due to steric interference from alkyl chains branching from the fluorene spirocenter.

2.7 Basis for Incorporating 12 into Organic Photovoltaic (OPV) Devices

With an understanding of the aggregation properties of BAI, we set out to incorporate them into devices. Solution-processed organic photovoltaics (OPVs) have drawn increasing attention in the past few decades[42] for their potential use as building-integrated photovoltaics, which is attractive not only for providing a viable renewable energy solution, but also for meeting

the artistic needs of building design using organic materials with tunable optical properties.[43] Such applications, however, are still limited by the inferior device stability and low power conversion efficiency (PCE) of OPVs. Recently, the PCE in single junction OPVs has been raised to over 17.4% through design and synthesis of new photoactive organic materials (e.g., low bandgap non-fullerene acceptors).[44] Further improvement in both device stability and PCE requires the tuning of supramolecular organization (e.g., molecular packing, molecular orientation) and nanoscale phase morphology (e.g., domain size, donor/acceptor phase separation).[45]

Ideally, the domain size of the donors and acceptors should be smaller than the exciton diffusion length, typically less than 20 nm,[43e] to ensure successful exciton dissociation. At the same time, the donor and acceptor domains should form inter-domain percolation pathways to ensure efficient charge transport and collection. The deposition solvent is a major determinant of how the domains form through differing solvation of the donor and acceptor species, as well as by the rate of evaporation (**Figure 18a**). Adding supplementary solvents to the deposition solvent has been found to alter the morphology even further (**Figure 18b,c**). Previous studies have shown that the bulk heterojunction morphology can be tailored by a trace amount of high boiling-point solvent processing additives, such as 1,8-diiodooctane (DIO)[46] and chloronaphthalene (CN),[47] to improve the nanoscale phase separation and intercalation between polymer donors and fullerene acceptors for enhanced PCEs.[48] However, solvent additives[49] remain in the active films for extended times, leading to unstable device performance.[49b] It was found that the devices with DIO degraded faster than those without DIO due to the faster evolution of nanophase morphology during the slow evaporation or migration of solvent additive residues in the bulk heterojunction films.[48d] An alternative approach is to introduce solid state molecular mediators which will remain in the thin film while tuning the phase morphology (**Figure 18d**). This approach has been demonstrated in both organic field effect transistors[50] and OPVs,[51] in which a small amount of "impurities" were blended with the matrix of organic semiconductors to impose supramolecular ordering on the matrix molecules by noncovalent intermolecular interactions.[50] In addition to morphology tuning, molecular mediators for OPVs can further enhance device performances by more effective absorption of sunlight. This aspect, however, has remained rarely explored in OPVs.

The triphenylamine BAI system has extended π conjugation surface, good solution processability, strong electron accepting ability, low optical bandgap (~1.5 eV), excellent charge transport, and photoresponse properties that are critical for high performance organic thin film transistors (OTFTs) and other optoelectronic devices.[10] It is proposed that the intriguing structural features of **12** would impact the nanophase separation in the active layer of OPVs, however, such effect has never been demonstrated before. As a proof of concept, an established OPV system was chosen that aligned with the HOMO and LUMO of **12**. We hypothesized that **12** could not only be used as a solid state molecular mediator to effectively tune the packing of active materials in poly(3-hexylthiophene-2,5-diyl) (P3HT):PC60BM based bulk heterojunction OPV devices, but also contribute to additional absorption to the active layer of photovoltaic devices. This solid-state photoactive molecular mediator could be employed as an alternative to the commonly used solvent additives for improved film morphology and optical absorption and device performance.[52]

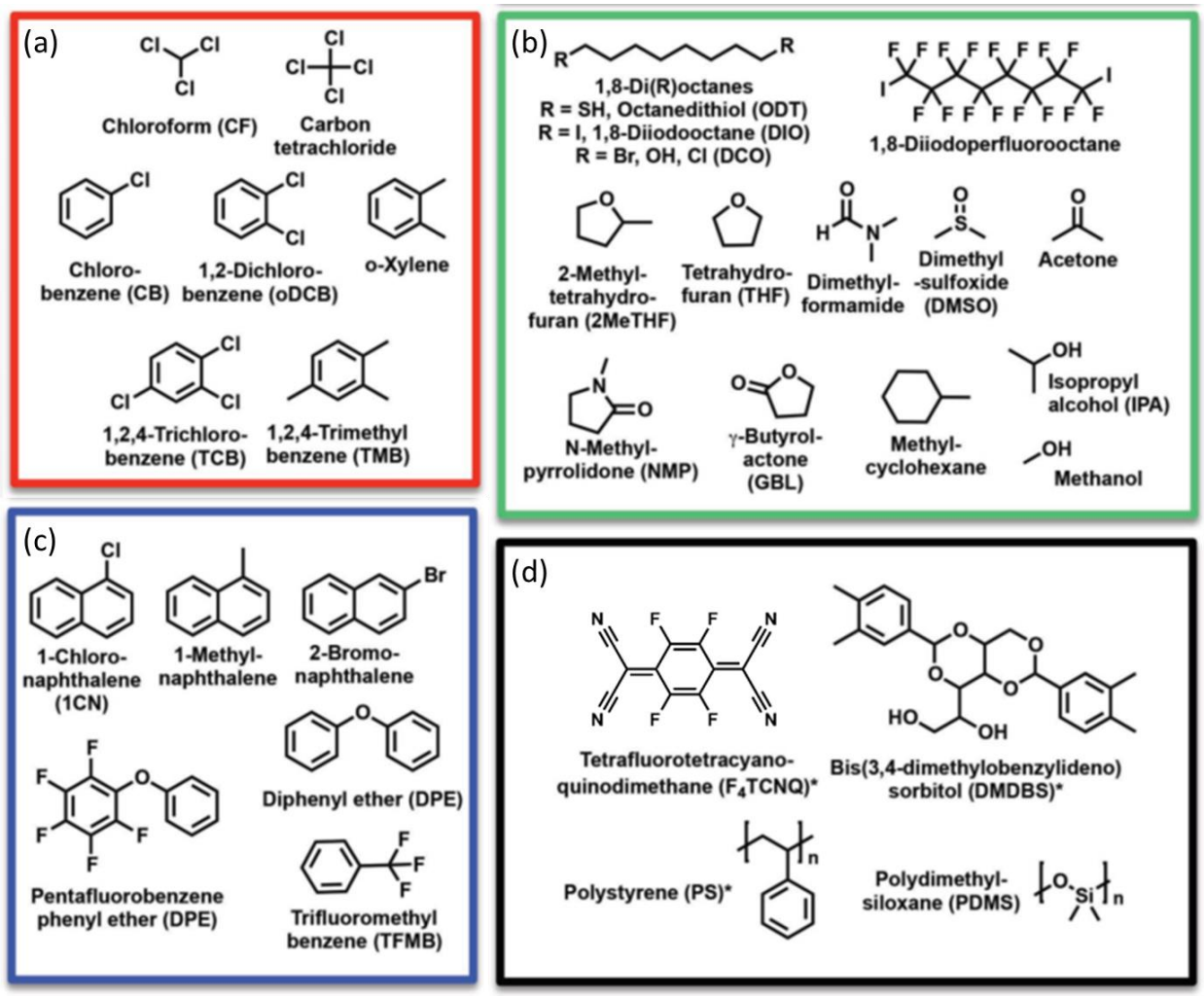

Figure 18: Structure of common additives grouped as (a) deposition solvents, (b) non-aromatic solvents, (c) aromatic solvents, and (d) solid additives. Reproduced with permission from reference [52a], Copyright © 2018 Wiley

2.8 OPV Device Performance

To assess how **12** tunes the molecular packing and nanoscale morphology as well as photovoltaic performance, a P3HT:PC60BM model system was selected, to which **12** was added. **Figure 19a** shows the typical device structure (ITO/PEDOT:PSS/P3HT:PC60BM:**12**/Ca/Al) and molecular structures of the three components in the active layer. The energy diagram of the ternary devices (**Figure 19b**) shows that the energy levels of **12** align well with these of P3HT and PC60BM. Such an energy level cascade allows for efficient photoinduced charge separation within the three-component bulk active layer.

We firstly characterized the variation of photovoltaic performance when tuning the composition ratio of **12** in the P3HT:PC60BM mixture films. The P3HT:PC60BM control device containing no **12** exhibited an open-circuit voltage (V_{OC}) of 0.595 V, a short-circuit-current-density (J_{SC}) of 9.2mA/ cm^2, a fill-factor (FF) of 67%, and a PCE of 3.7% (**Figure 19c**), which are consistent with the performance of typical P3HT:PC60BM devices.[42c, 53] A 11% enhancement of PCE was realized by adding only 1wt% of mediator into the P3HT:PC60BM blend film, together with the following device characteristics: V_{OC} 0.585 V, J_{SC} 10.0 mA/cm^2, FF 70%, and PCE 4.1%. Adding more **12**, for example 5 and 10 wt%, however, resulted in a dramatic decrease in the PCE to 2.5 and 0.5%, respectively. The decrease of PCEs is mainly correlated to the variation in J_{SC} upon increasing the percentage of mediator.

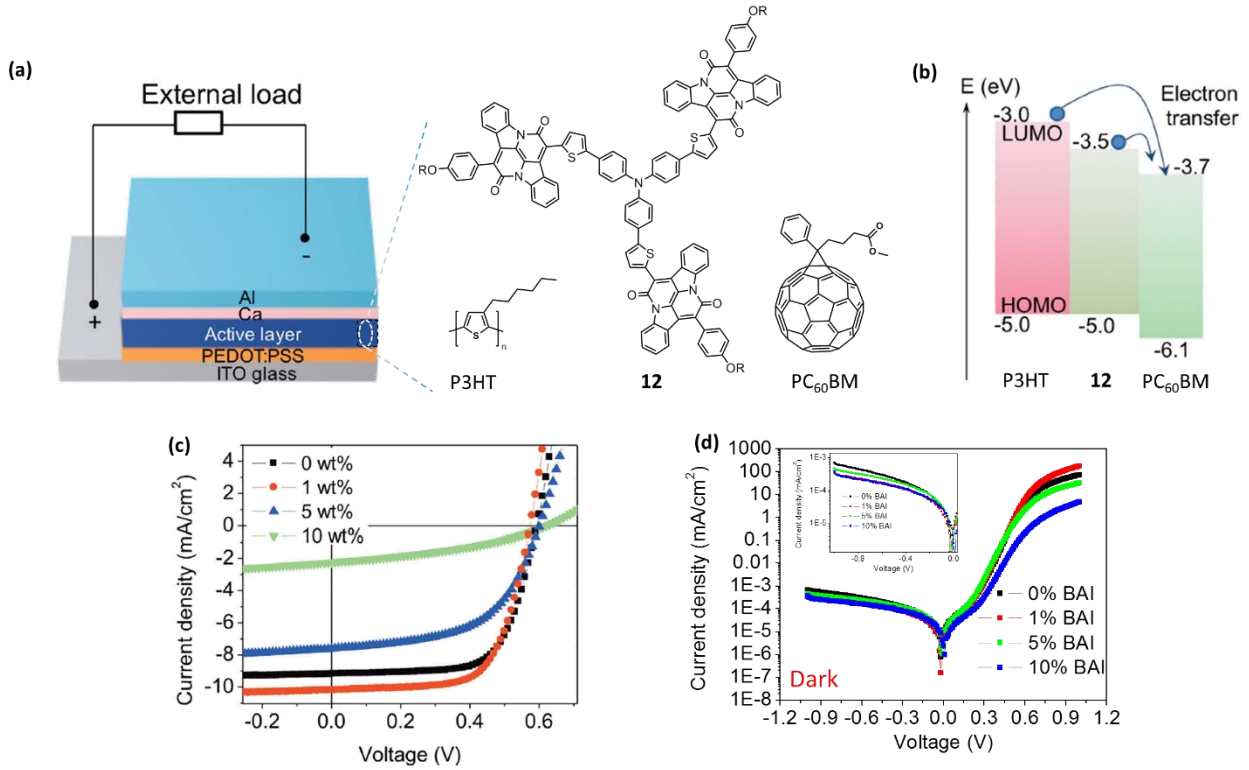

Figure 19: The (a) OPV schematic and (b) band diagram for the devices tested, along with the output J-V curves in (c) light and (d) dark conditions. Reproduced with permission from reference [54], Copyright © 2018 Wiley

Table 2: OPV Device Output

					Light		Dark	
Percent **12** (Wt %)	J_{SC} (mA/cm^2)	V_{OC} (V)	FF (%)	PCE (%)	R_{series} (Ω)	R_{shunt} (Ω)	R_{series} (Ω)	R_{shunt} (Ω)
0	9.18	0.595	67	3.68	4.5	1.4E3	4.5	2.3E6
1	10.5	0.585	70	4.08	1.6	1.7E3	1.6	3.3E6
5	7.61	0.605	55	2.52	8.6	6.5E2	10.8	2.4E6
10	2.24	0.625	37	0.512	36.8	6.0E2	55.0	3.6E6

To verify the **12** induced variation in J_{SC}, the external quantum efficiencies (EQEs) of the devices were measured (**Figure 20**). Compared to the mediator-free devices, the EQEs in the spectral range 450–680 nm increased when adding 1 wt% **12** into the P3HT:PC60BM blend film, whereas the introduction of more mediator led to the decrease in EQE in this region, which was consistent with the variation trend in J_{SC}. Concomitantly, the EQE between 680 and 870 nm was enhanced for thin films employing **12** up to 5 wt%, suggesting the small but positive contribution to J_{SC} from the lower energy optical absorption of **12**. This low energy contribution from **12** is supported by 1) negligible EQEs in the spectral range 680–870 nm were observed for the **12**-free devices, and 2) the increase in the compositional ratio of **12** led to EQE enhancement in the same spectral range. Normalization of the EQE curves revealed that the EQEs from 680 to 870 nm increased monotonically with rising percentage of **12** (**inset in Figure 20a**), further confirming the mediator's contribution to the photocurrent generation.

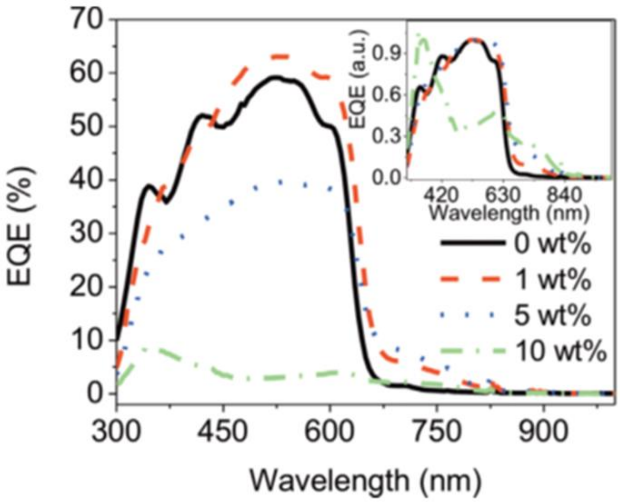

Figure 20: The EQE curve for the active layer mixtures. Reproduced with permission from reference [54], Copyright © 2018 Wiley

The use of **12** as a solid state molecular mediator within P3HT:PC60BM active films, resulted in ~11% enhancement of device efficiency. This proof of concept establishes **12** as a photoactive mediator, capable of improving both the electronic and physical components of OPV devices.

By analyzing the dark currents of the relative devices (**Figure 19d**), adding only 1 wt% **12** resulted in the decrease in series resistance and increase in shunt resistance, beneficial to device performance. Further introduction of $N(BAI)_3$ led to the increase in series resistance (R_s) and decrease in shunt resistance (R_{sh}) (**Table 2**). Large shunt resistances in solar cells are advantageous because they prevent current loss through parasitic pathways.[55] While large series resistances are problematic, as they point to poor electrical contact between the components of the solar cell. Poor resistive properties of devices have a strongly negative effect on the fill factor (FF). The lowest R_s and highest R_{sh} are observed with 1% additive, in line with the high FF and superior device performance. The pattern of parasitic electrical characteristics suggests that the variation of device performance is likely due to morphological changes in the active layer induced by the introduction of BAI based mediators.

2.9 Study of the Optical Properties of 12 as an Additive in P3HT:PC60BM OPV Active Layers

To help probe the optical effects of P3HT-**12** interactions, UV-vis spectroscopic studies were carried out on the P3HT only film and P3HT films blended with different mediator ratios. As shown in **Figure 20b**, three characteristic peaks (510, 550, and 600 nm) are assigned to 0-2, 0-1, and 0-0 vibronic transitions from the ground state to excited states of P3HT (**Figure 21a**).[56] By comparing the ratio of peak intensity among 0-2, 0-1, and 0-0 transitions, we found that the intensity of 0-0 transition was slightly enhanced by adding only 1 wt% **12**, indicating that **12** can enhance inter-chain π–π stacking of P3HT, while adding more **12** decreased the π–π stacking of P3HT (**Figure 21b, Table 3**)[56c] The variation of photoluminescence (PL) spectra of these films was also studied. As shown in **Figure 21c**, the (0-0) vibronic transition at 670 nm was enhanced upon adding 1 wt% mediator, as a result of the enhanced π–π stacking of P3HT molecules, whereas adding more **12** (10 wt%) decreased the (0-0) transition peak, which was consistent with the observation from the absorption spectra study.

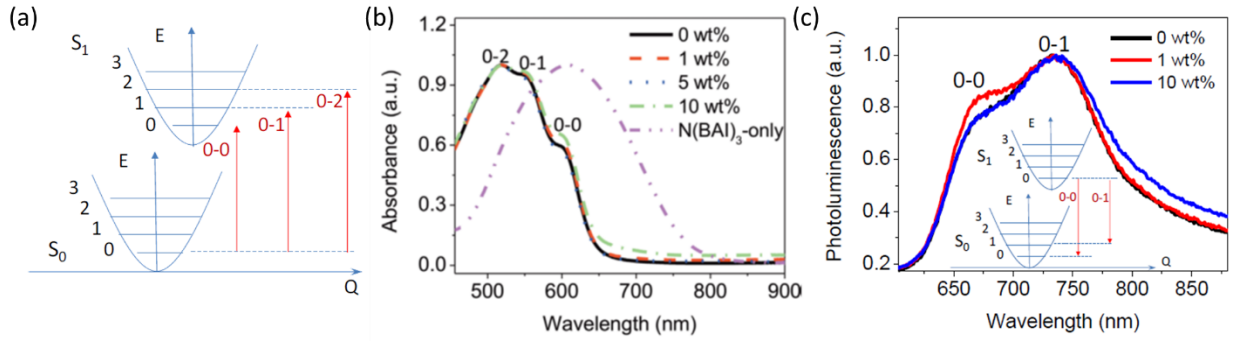

Figure 21: The (a) vibronic transitions assigned to the (b) onset UV-Vis absorption peak, and corresponding (c) photoluminescence peak with inset fluorescence transitions. Reproduced with permission from reference [54], Copyright © 2018 Wiley

Table 3: The Ratio of Peak Intensity for the 0-0/0-1 and 0-0/0-2 Absorption Transitions Shown in Figure 21b

Percent **12** (Wt %)	Peak(0/0) /Peak(0/1)	Peak(0/0) /Peak(0/2)
0	0.9592	0.9084
1	0.9648	0.9235
5	0.9538	0.8890

2.10 Study of the Phase Morphology of 12 as an Additive in P3HT:PC60BM OPV Active Layers

Atomic force microscopy (AFM) was further utilized to gain insight into the phase segregation behavior. The contrast in the AFM phase image of P3HT and PC60BM-rich domains arises due to differences in elasticity and phase angle change response of the cantilever.[53, 57] Compared to the pristine P3HT:PC60BM blend film without **12** (0 wt% in **Figure 22a**), the addition of 1 wt% **12** resulted in clear nanoscale phase separation (**Figure 22b**). While the phase separation is clearly discernible in the 5 wt% blended film (**Figure 22c**), using a high percentage of **12** (10 wt%, **Figure 22d**) led to a smeared phase morphology. The improved phase separation may be attributed to the enhanced π–π stacking of P3HT molecules induced by the mediator (**12)**

that possesses large π conjugation surface and good coplanarity. However, excess **12** may interfere with P3HT aggregation and is thus detrimental to the formation of nanoscale donor-acceptor interfaces.

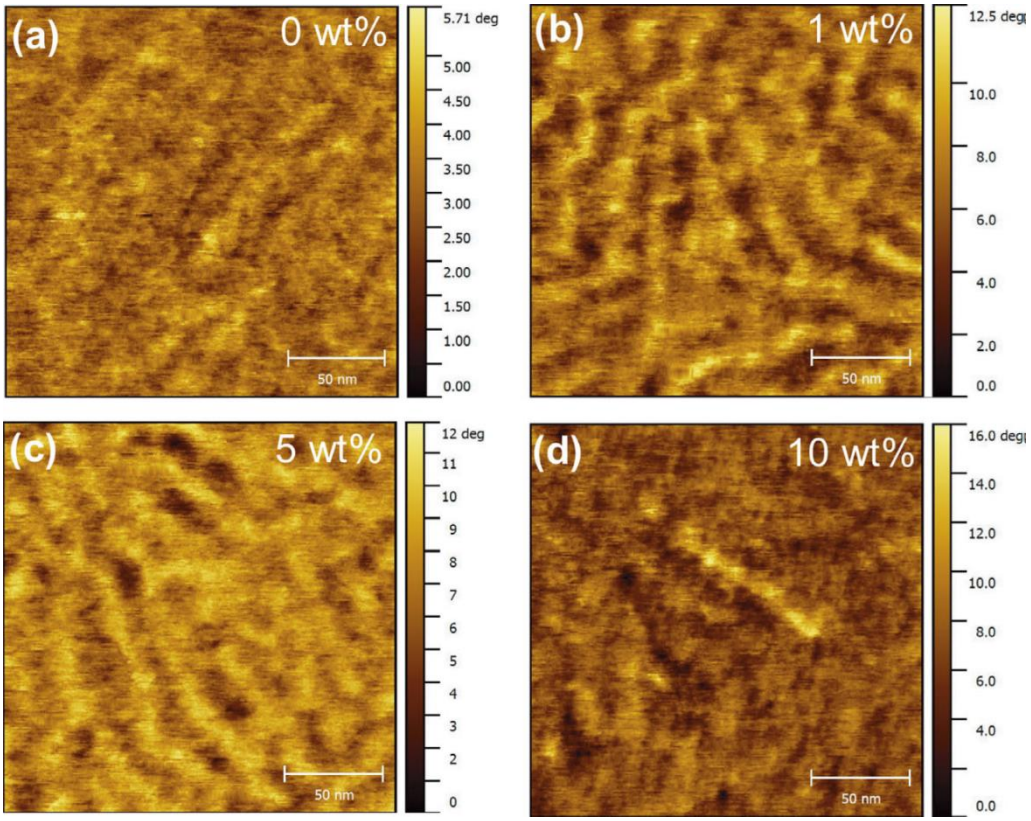

Figure 22: AFM phase images of P3HT:PC60BM:**12** mixtures with (a) 0%, (b) 1%, (c) 5%, and (d) 10% of **12** added. Reproduced with permission from reference [54], Copyright © 2018 Wiley

To probe the morphological changes caused by the mediator, the P3HT:PC60BM:**12** three-component thin films were characterized by GIWAXS to reveal lateral crystalline domain information within the films (**Figure 23a-d**). In the P3HT:PC60BM blend film without **12**, the (100), (200), (300) peaks in the q_z direction are indicative of lamellar stacking of P3HT chains, while the (010) peak in the q_x direction represents the aromatic π–π stacking of chains. PC60BM shows an isotropic orientation with a broad distribution of intensity in all directions, indicative of randomly oriented aggregates of the fullerene derivative. The vertical and lateral line profiles are shown in **Figure 23e and f**, respectively. Introduction of 1 wt% **12** resulted in narrower lamellar stacking (100) peak and π– π stacking (010) peak, which means that the crystallites of P3HT are largest and perhaps more ordered when 1 wt% mediator is introduced, with lamellar and π-π stacking Scherrer sizes of 65.9 and 16.8 nm, respectively. The azimuthal spread of the (100) and (010) peaks are also the narrowest for 1 wt% blended film, suggesting the formation of more oriented polymer lamella. Crystallite sizes, and perhaps degree of order, decrease for all other weight ratios of **12** (including the neat blend), which agrees well with the observations from both absorption/PL spectra and AFM characterizations (**Table 4**). It is hypothesized that at low blending ratio such as 1 wt%, **12** molecules are more evenly distributed in the active layer, and its interaction with active materials is conducive to nanoscale crystallization. As the percentage

of **12** increases over 1 wt%, self-aggregation becomes more dominant, making it less desirable for nanoscale crystallization and phase separation.

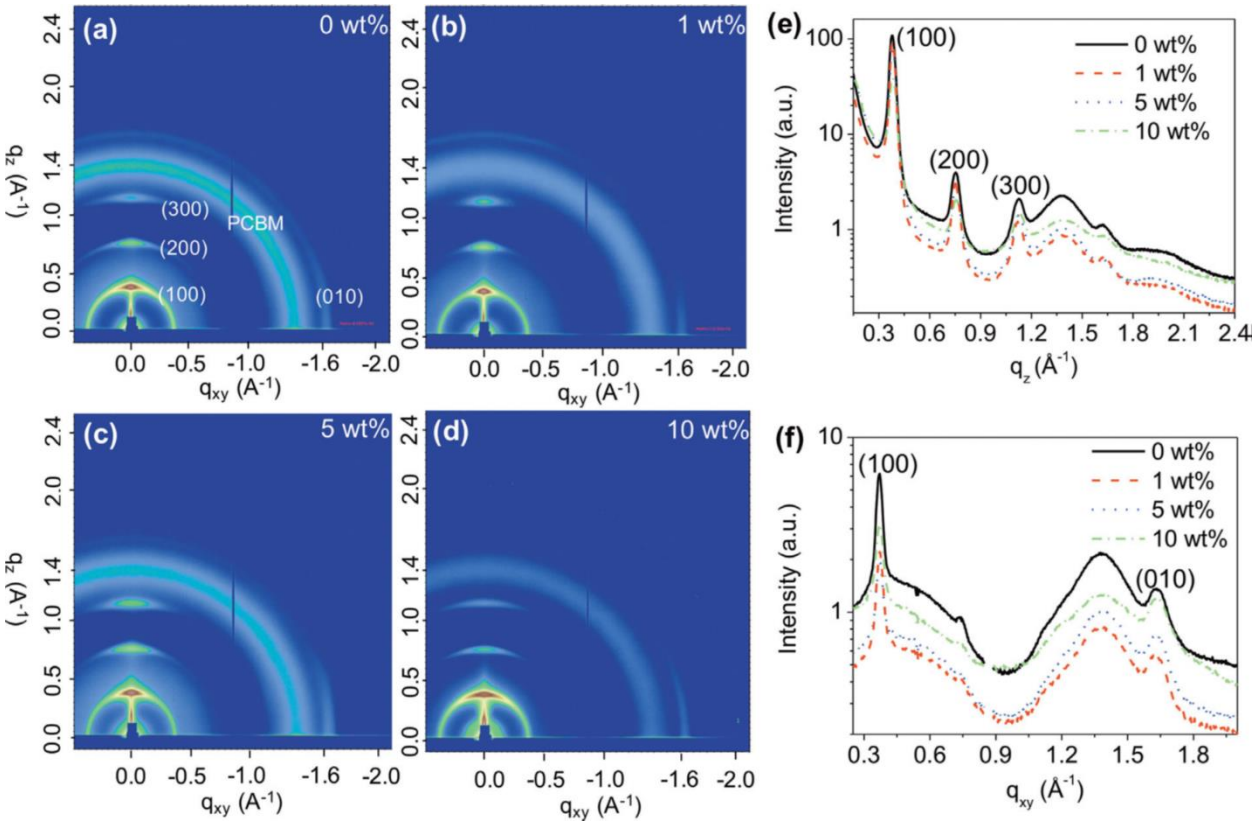

Figure 23: GIWAXS plots for P3HT:PC60BM films with (a) 0%, (b) 1%, (c) 5%, and (d) 10% of **12** additive, along with overlaid linecuts in the (e) out-of-plane q_z and (f) in-plane q_{xy} directions. Reproduced with permission from reference [54], Copyright © 2018 Wiley

Table 4: Scherrer Analysis of the 100 Lamellar and 010 π–π Stacking Peaks

	Lamellar Scherrer Analysis			π–π stacking Scherrer Analysis		
Percent **12** (Wt %)	FWHM (nm^{-1})	Bragg (nm^{-1})	Tau (nm)	FWHM (nm^{-1})	Bragg (nm^{-1})	Tau (nm)
0	0.19924	3.7952	56.77	0.82855	16.106	13.69
1	0.17156	3.8120	65.93	0.67709	16.219	16.76
5	0.19720	3.8197	57.36	1.06270	16.161	10.68
10	0.22174	3.8237	51.01	3.51520	16.153	3.23

In order to understand the impact of **12** as a mediator on the vertical phase morphology of the blended films, neutron reflectometry was employed as a complementary technique to GIWAXS. The neutron reflectivity curves for the P3HT: PC60BM films blended with different amount of **12** mediator are shown in **Figure 24a**, from which the volume fraction profiles of PC60BM were obtained (**Figure 24b**) by fitting the neutron reflectivity profiles in with a previously established model.[58] The scattering length density model used to fit the neutron reflectivity

profiles was shown in **Figure 24c**. The comparison indicates that while the PC60BM fraction was rather evenly distributed across the depth of the thin films from the bottom substrate, clear contrasts were observed near the top interface of these films. The curve of the 1 wt% **12** blended thin film indicated the formation of a very thin PC60BM enriched layer residing at the interface between the active layer and the cathode (**Figure 24b**). The 5 wt% **12** blended thin film showed similar vertical morphology as the 1 wt% **12** film. The 0 and 10 wt% **12** films have similar vertical morphologies, suggesting that adding a larger amount of **12** does not improve the phase morphology.

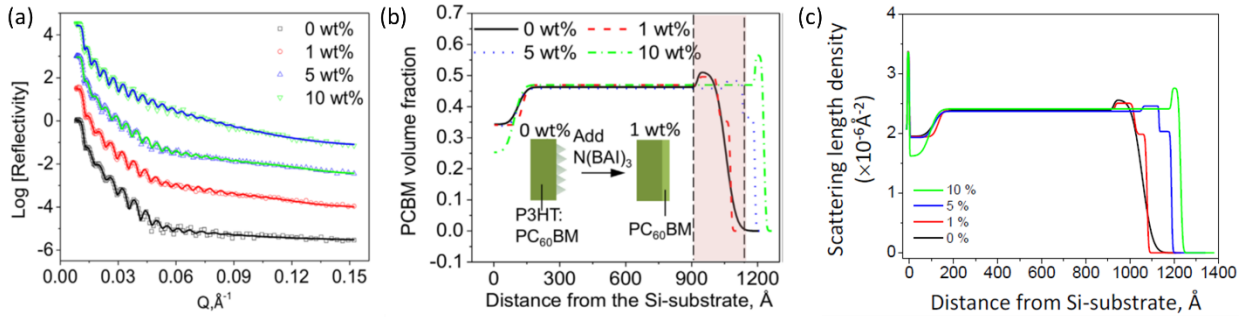

Figure 24: (a) Neutron reflectivity curves for P3HT:PC60BM films with varying ratios of **12** and the (b) volume fraction profiles for the films based on the following (c) scattering length density model.[59] Reproduced with permission from reference [54], Copyright © 2018 Wiley

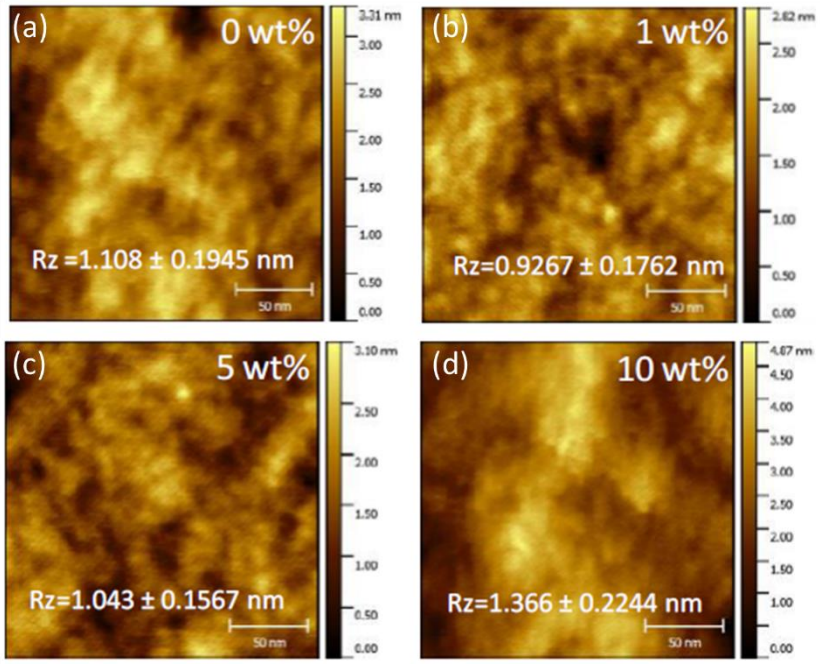

Figure 25: AFM height images of P3HT:PCBM:BAI mixtures with provided RMS roughness for (a) 0%, (b) 1%, (c) 5%, and (d) 10% BAI additive

Furthermore, the surface roughness of P3HT: PC60BM films was reduced by adding 1 wt% **12**, but increased when adding additional mediator, which is consistent with the observation from AFM height images (**Figure 25c,d**). The reduction of surface roughness is attributed to the

formation of a PC60BM thin layer on the surface of the blend films, an observation that is similar to solvent additive mediated extrusion of PC60BM molecules to the surface. It suggests that, when only a small amount (i.e., 1wt%) of **12** is present, the interaction between the three components is balanced such that different vertical domains of PC60BM are formed to give a very thin interfacial layer at the surface of the blend film (**Figure 25b**). Such a layer at the cathode/active layer interface in an OPV device can act as a hole-blocking layer and effectively reduce the charge recombination.

2.11 Conclusions

The ability to synthesize diverse materials from simple and inexpensive starting materials through straightforward transformations makes BAI a great building block for semiconductor development. Development of desymmetrized BAI has both provided a more convenient synthesis and given access to materials capable of self-assembly. The triphenylamine based BAI **12** in particular has been studied intently and has shown a strong propensity for nanowire formation. BAI **6a** remains a good candidate for self-assembled monolayer formation via the Langmuir-Blodgett method. Overall BAI-based materials show promising performance in a number of organic semiconductor applications due to stability, high absorbance ($\varepsilon = 10^5$ M^{-1} cm^{-1}) into the near IR region, and fine control over both electronics and physical properties through choice of bay-annulation and monomer.

There are still many applications to explore in this area of research. When **12** is used as an additive in prototypical P3HT:PC60BM solar cells, a ~11% enhancement was observed by adding only 1 wt% **12** into the active layer. The PCE enhancement is ascribed to two factors: one is the improvement of phase morphology of the active layer by the BAI mediator, which not only tunes molecular packing behavior for more ordered lamellar stacking (100) and aromatic (π–π) stacking (010), but also promotes the formation of thin layer of PC60BM at the cathode/active layer interface to reduce the charge recombination; the other is the additional optical absorption by the **12** which also contributes to the photocurrent generation for higher PCEs. The use of **12** as a solid-state photoactive additive serves as a proof-of-principle that blending is a promising alternative to the commonly used solvent additives to improve the performance of OPVs or other optoelectronic devices. It is envisioned that the solid-state photoactive molecular mediator **12** may yield more stable device performance compared to the commonly used liquid-state processing additives due to the absence of slow evaporation or migration of solvent additive residues in the bulk heterojunction films. In addition, it has been shown that multiarmed molecules can facilitate the formation of a locked 3D mesh of donor polymer matrix through strong charge transfer interactions, resulting in enhanced thermal stability of devices by impeding the diffusion and aggregation of embedded PC60BM molecules.[59]

Looking forward, non-fullerene acceptors (NFA) have emerged as an alternative to traditional fullerene based electron acceptors. Many NFAs such as ITIC possess HOMO levels very similar to the BAI polymers, and may be too energetically similar to effect charge separation. However, as more NFA species are becoming available with deeper HOMOs, polymeric BAI materials may be effective donors for OPV. Additionally, the high LUMO levels of BAI molecules and polymers make them particularly well suited for high V_{OC} applications. Although BAI OPVs have shown promising results, there is much room for improvement, particularly in synthesizing novel polymers with improved active layer phase morphology.

Due to the relatively high HOMO and LUMO levels of the BAI system, it has been exclusively used as an additive or donor material in OPV. In order to enable its use as an acceptor material a number of strategies can be utilized. A fluorination approach has been successfully applied in many cases to lower the frontier molecular orbitals but often comes with additional benefits such as improved charge transport, and improved intermolecular interactions.[60] Alternatively, the addition of secondary acceptor groups on the bay position could lower the LUMO to make the overall molecule or polymer electron accepting. By taking advantage of the complementary absorption in molecules with aryl substitution at the phenylene position, EQE and J_{SC} could be greatly increased. This strategy for increasing adsorption has been wholly underutilized and could have a large impact on device performance.

Finally, desymmetrized BAI units have untapped potential, for the synthesis of new semiconductors and electroactive supramolecular structures. DSSC could potentially benefit from a desymmetrized BAI molecule with additional sidechain engineering to increase loadings. Molecular wires have shown promising results, but there is still further room for exploration.

2.12 Materials and Methods

Reagents were purchased from Aldrich or synthesized as described. Dry solvents were collected from an activated alumina column purification system. Volatile solvents were removed under reduced pressure using a rotary evaporator. Thin-layer chromatography (TLC) was carried out using glass sheets, precoated with silica gel 60F (Merck 5554). The plates were visualized by UV-light or $KMnO_4$ stain. Proton and carbon nuclear magnetic resonance spectra (^{1}H-NMR and ^{13}C-NMR) spectra were recorded on a Bruker Avance500 II, using locking to the deuterated solvent and using tetramethylsilane as an internal standard. All chemical shifts are quoted using the δ scale, and all coupling constants (J) are expressed in Hertz (Hz). Matrix-assisted laser desorption ionization (MALDI) mass spectra were measured on 4800 MALDI TOF/TOF analyzer from Applied Biosystems. Cyclic voltammetry was performed using a 273A potentiostat (Princeton Applied Research), wherein glassy carbon, platinum and a silver wire act as the working electrode, the counter electrode and the pseudo-reference electrode, respectively. Samples were prepared in $CHCl_3$ solution with tetrabutylammonium hexafluorophosphate (0.1 M) as the electrolyte at a scan rate of 100 mV s^{-1}, using ferrocene/ferrocenium (Fc/Fc^+) redox couple as an internal standard. The HOMO and LUMO levels of compounds are calculated from the difference between the onset of first oxidation potential (E_{OX}) or reduction potential (E_{red}) of the compounds and the oxidation potential of ferrocene (E_{HOMO} = -(4.8+E_{OX}) eV, E_{LUMO} = -(4.8+E_{RED}) eV).[61] UV-Vis-NIR spectra were recorded using a Cary 5000 UV-Vis-NIR spectrometer. For DFT calculations, the ground state geometries of the molecules in the solvent were first optimized using B3LYP/6-31+G* basis set. The optimized geometries were then used for evaluating the low-lying excited states by time-dependent DFT (TD-DFT) calculations using 6-31G* basis set.

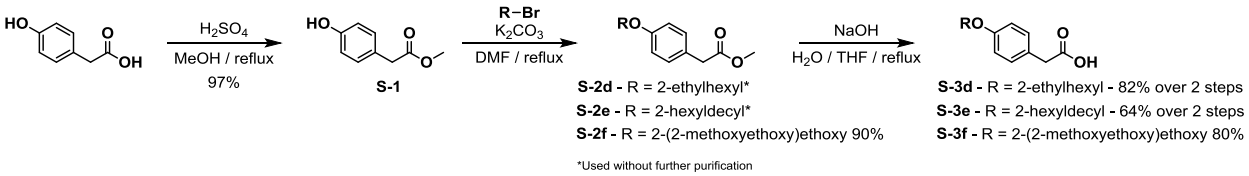

S-1 methyl 2-(4-hydroxyphenyl)acetate[62]

Solid 4-hydroxyphenylacetic acid (5.00 g, 32.9 mmol, 1 equiv.) was added to a round bottom flask equipped with a reflux condenser and dissolved in methanol (130 mL, 0.25 M). Sulfuric acid (0.35 mL, 6.6 mmol, 0.2 equiv.) was added and the solution was heated to reflux overnight. Upon reaction completion as monitored by TLC, the solution was concentrated and diluted with ethyl acetate. The organic layer was washed three times with water and brine and dried with $MgSO_4$. The organic layer was concentrated under reduced pressure to produce **1** as a yellow tinged oil (5.28 g, 31.8 mmol, 97%) ^{1}H NMR (500 MHz, $CDCl_3$): δ = 7.06 (d, J = 8.5 Hz, 2H), 6.73 (d, J = 8.5 Hz, 2H), 3.66 (s, 3H), 3.53 (s, 2H). ^{13}C NMR (125 MHz, $CDCl_3$) δ = 173.7, 155.1, 130.3, 125.2, 115.6, 52.3, 40.2. HRMS (ESI-TOF) $[M+Na]^+$ calculated: 189.0528, found: 189.0954.

S-2d methyl 2-(4-((2-ethylhexyl)oxy)phenyl)acetate

To an oven dried flask equipped with a reflux condenser was placed potassium carbonate (8.29 g, 60 mmol, 4 equiv.) and backfilled with N_2. A solution of **1** (2.50 g, 15 mmol) in dry DMF (23 mL, 0.66 M) was added and allowed to stir for 5 minutes before the addition of 2-ethylhexyl bromide (5.33 mL, 30 mmol, 2 equiv.). The mixture was heated to 140 ^{o}C overnight. Upon reaction completion as monitored by TLC, the solution was neutralized with 2 M HCl and extracted three times with ethyl acetate. The organic layer was washed with brine, dried with $MgSO_4$, and concentrated under reduced pressure to yield **2a** as a mixture of product and residual bromide that was use without further purification.

S-2e methyl 2-(4-((2-hexyldecyl)oxy)phenyl)acetate

The synthesis of **S-2e** followed the same procedure as that of **S-2d.**

S-2f methyl 2-(4-(2-(2-methoxyethoxy)ethoxy)phenyl)acetate[63]

To an oven dried flask equipped with a reflux condenser was added potassium carbonate (332 mg, 2.4 mmol, 4 equiv.) and backfilled with N_2. A solution of **S-1** (100 mg, 0.6 mmol) in dry acetonitrile (2.5 mL, 0.24 M) was added and allowed to stir for 5 minutes before the addition of 1-bromo-2-(2-methoxyethoxy)ethane (220 mg, 1.2 mmol, 2 equiv.). The mixture was heated to 80 ^{o}C overnight. Upon reaction completion as monitored by TLC, the solution was neutralized with 2 M HCl and extracted three times with ethyl acetate. The organic layer was washed with brine, dried with $MgSO_4$, and concentrated under reduced pressure. The resulting clear oil was purified by column chromatography (gradient elution using 0 to 50% ethyl acetate in hexanes) to yield **S-2f** (145 mg, 0.54 mmol, 90%) as a clear oil. ^{1}H NMR (500 MHz, $CDCl_3$): δ = 7.15 (d, J = 8.7 Hz, 2H), 6.84 (d, J = 8.7 Hz, 2H), 4.09 (t, J = 4.4 Hz, 2H), 3.82 (t, J = 5.1, 4.7 Hz, 2H), 3.70 – 3.67 (m, 2H), 3.65 (s, 3H), 3.57 – 3.49 (m, 2H), 3.53 (s, 2H), 3.36 (s, 3H). ^{13}C NMR (125 MHz, $CDCl_3$): δ = 172.3, 157.9, 130.2, 126.2, 114.7, 71.9, 70.7, 69.7, 67.4, 59.0, 51.9, 40.2. HRMS (ESI-TOF) $[M+Na]^+$ calculated: 291.1208, found: 291.1554.

S-3d 2-(4-((2-ethylhexyl)oxy)phenyl)acetic acid

To a solution of potassium hydroxide (4.94 g, 88 mmol, 14 equiv.) in water (10 mL, 0.65 M) was add the mixture of **2a** (1.75 g, 6.29 mmol) and residual 2-ethylhexyl bromide in THF (10 mL, 0.65 M). The solution was heated to reflux overnight. Upon reaction completion as monitored by TLC, the solution was concentrated under reduced pressure, neutralized with 2 M HCl and extracted

with ethyl acetate. The organic layer was washed with brine and dried with $MgSO_4$ before concentrating under vacuum. The resulting oil was purified by column chromatography with gradient elution (0 to 30% ethyl acetate in hexanes) to provide the title compound as a colorless oil (1.36 g, 5.13 mmol, 82% over two steps). ^{1}H NMR (500 MHz, $CDCl_3$): δ = 7.18 (d, *J* = 8.5 Hz, 2H), 6.86 (d, *J* = 8.6 Hz, 2H), 3.82 (dd, *J* = 5.8, 2.0 Hz, 2H), 3.59 (s, 2H), 1.71 (hept, *J* = 6.2 Hz, 1H), 1.54 – 1.27 (m, 8H), 0.95 – 0.85 (m, 4H). ^{13}C NMR (125 MHz, $CDCl_3$): δ = 178.3, 158.7, 130.4, 125.4, 114.7, 70.5, 40.5, 39.4, 30.6, 29.2, 23.9, 23.2, 14.2, 11.2. HRMS (ESI-TOF) $[M+H]^+$ calculated: 255.1227, found: 255.1597.

S-3e 2-(4-((2-hexyldecyl)oxy)phenyl)acetic acid

To a solution of potassium hydroxide (7.36 g, 131 mmol, 8 equiv.) in water (25 mL, 0.65 M) was add the mixture of **2a** (15 mmol) and residual 2-ethylhexyl bromide in THF (25 mL, 0.65 M). The solution was heated to reflux overnight. Upon reaction completion as monitored by TLC, the solution was concentrated under reduced pressure, neutralized with 2 M HCl and extracted with ethyl acetate. The organic layer was washed with brine and dried with $MgSO_4$ before concentrating under vacuum. The resulting oil was purified by column chromatography with gradient elution (0 to 30% ethyl acetate in hexanes) to provide the title compound as a colorless oil (3.97 g, 10.6 mmol, 64% over two steps). ^{1}H NMR (500 MHz, $CDCl_3$): δ = 10.77 (s, 1H), 7.18 (d, *J* = 8.7 Hz, 2H), 6.86 (d, *J* = 8.9 Hz, 2H), 3.80 (d, *J* = 5.7 Hz, 2H), 3.58 (s, 2H), 1.75 (h, *J* = 5.6 Hz, 1H), 1.47 – 1.34 (m, 2H), 1.36 – 1.24 (m, 24H), 0.91 – 0.84 (m, 6H). ^{13}C NMR (125 MHz, $CDCl_3$): δ = 177.2, 158.9, 130.5, 125.1, 114.8, 71.0, 40.1, 38.1, 32.1, 32.0, 31.5, 31.5, 30.2, 29.8, 29.7, 29.5, 27.0, 27.0, 22.8, 14.3. HRMS (ESI-TOF) $[M+Na]^+$ calculated: 287.1623, found: 287.1952.

S-3f 2-(4-(2-(2-methoxyethoxy)ethoxy)phenyl)acetic acid

To a solution of potassium hydroxide (3.24 g, 57.8 mmol, 17 equiv.) in water (6.3 mL, 0.65 M) was add the mixture of **2c** (1.11 g, 4.1 mmol) and residual bromide in THF (6.3 mL, 0.65 M). The solution was heated to reflux overnight. Upon reaction completion as monitored by TLC, the solution was concentrated under reduced pressure, neutralized with 2 M HCl and extracted with ethyl acetate. The organic layer was washed with brine and dried with $MgSO_4$ before concentrating under vacuum. The resulting oil was purified by column chromatography with gradient elution (0 to 50% ethyl acetate in hexanes) to provide the title compound as needle-shaped crystals (819 mg, 3.2 mmol, 80%). ^{1}H NMR (500 MHz, $CDCl_3$): δ = 7.17 (d, *J* = 8.7 Hz, 2H), 6.87 (d, *J* = 8.8 Hz, 2H), 4.12 (t, *J* = 5.0 Hz, 2H), 3.88 – 3.82 (m, 2H), 3.72 (ddd, *J* = 11.8, 3.3, 1.8 Hz, 2H), 3.62 – 3.53 (m, 4H), 3.39 (s, 3H). ^{13}C NMR (125 MHz, $CDCl_3$): δ = 177.3, 158.2, 130.5, 125.7, 114.9, 72.1, 70.9, 69.9, 67.6, 59.2, 40.2. HRMS (ESI-TOF) $[M+Na]^+$ calculated: 399.2875, found: 399.3095.

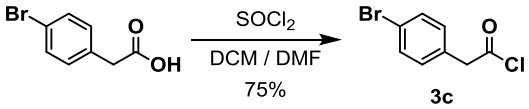

3c

3c 2-(4-bromophenyl)acetyl chloride [64]

To an oven dried vial with a septa cap was added 4-bromophenylacetic acid (2.0 g, 9.3 mmol). The vial was backfilled three times with N_2 followed by addition of dry CH_2Cl_2 (3 mL) and DMF (1 drop). Thionyl chloride (0.75 mL, 10 mmol, 1.1 equiv.) was added and stirred for 3 hours. Upon

reaction completion as verified by a MeOH quench test (see page S23 for details of the procedure), the solution was concentrated to give an orange oil, which was subjected to short-path reduced pressure distillation (100 mtorr, 105-110 °C) to give the title compound as a pink oil (1.62 g, 6.93 mmol, 75%). ^{1}H NMR (500 MHz, $CDCl_3$): δ = 7.51 (d, *J* = 8.4 Hz, 2H), 7.15 (d, *J* = 8.4 Hz, 2H), 4.10 (s, 2H). ^{13}C NMR (125 MHz, $CDCl_3$): δ = 171.6, 132.3, 131.3, 130.3, 122.5, 52.5.

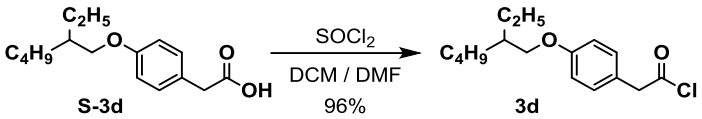

3d 2-(4-((2-ethylhexyl)oxy)phenyl)acetyl chloride

To an oven dried vial with a septa cap was added **3a** (265 mg, 1 mmol). The vial was backfilled three times with N_2 followed by addition of dry CH_2Cl_2 (1 mL, 1 M) and DMF (1 drop). Thionyl chloride (0.11 mL, 1.5 mmol, 1.5 equiv.) was added and stirred for 1 hour. Upon reaction completion as verified by a MeOH quench test (see page S23 for details of the procedure), the volatiles were removed under reduced pressure to give the title compound as a yellow oil (271 mg, 0.96 mmol, 96%). ^{1}H NMR (500 MHz, $CDCl_3$): δ = 7.17 (d, *J* = 8.6 Hz, 2H), 6.90 (d, *J* = 8.7 Hz, 2H), 4.08 (s, 2H), 3.84 (dd, *J* = 5.7, 1.8 Hz, 2H), 1.73 (hept, *J* = 6.2 Hz, 1H), 1.56 – 1.36 (m, 4H), 1.32 (dq, *J* = 7.2, 3.3 Hz, 4H), 0.92 (m, 6H). ^{13}C NMR (125 MHz, $CDCl_3$): δ = 172.5, 159.4, 130.7, 123.0, 115.0, 70.6, 52.5, 39.5, 30.6, 29.2, 24.0, 23.2, 14.2, 11.2.

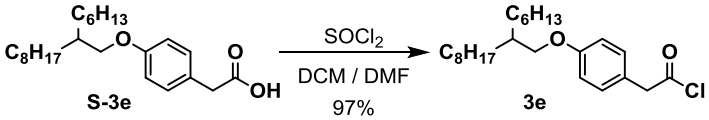

3e 2-(4-((2-hexyldecyl)oxy)phenyl)acetyl chloride

To an oven dried vial with a septa cap was added **3b** (100 mg, 0.27 mmol). The vial was backfilled three times with N_2 followed by addition of dry CH_2Cl_2 (1 mL) and DMF (1 drop). Thionyl chloride (29 μL, 0.4 mmol, 1.5 equiv.) was added and stirred for 1 hour. Upon reaction completion as verified by a MeOH quench test (see page S23 for details of the procedure), the volatiles were removed under reduced pressure to give the title compound as a yellow oil (103 mg, 0.26 mmol, 97%). ^{1}H NMR (500 MHz, $CDCl_3$): δ = 7.17 (d, *J* = 8.2 Hz, 2H), 6.89 (d, *J* = 8.5 Hz, 2H), 4.07 (s, 2H), 3.82 (d, *J* = 5.7 Hz, 2H), 1.76 (p, *J* = 6.0 Hz, 1H), 1.49 – 1.39 (m, 2H), 1.42 – 1.27 (m, 22H), 0.91 – 0.84 (m, 6H). ^{13}C NMR (125 MHz, $CDCl_3$): δ = 172.5, 159.4, 130.7, 123.0, 115.1, 71.1, 52.5, 38.1, 32.1, 32.0, 31.5, 31.5, 30.2, 29.8, 29.7, 29.5, 27.0, 27.0, 22.8, 14.3.

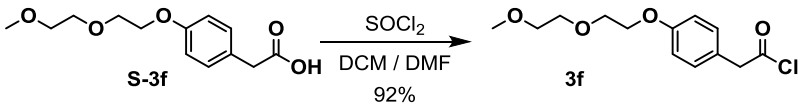

3f 2-(4-(2-(2-methoxyethoxy)ethoxy)phenyl)acetyl chloride

To an oven dried vial with a septa cap was added **3c** (68 mg, 0.27 mmol). The vial was backfilled three times with N_2 followed by addition of dry CH_2Cl_2 (1 mL) and DMF (1 drop). Thionyl chloride (29 μL, 0.4 mmol, 1.5 equiv.) was added and stirred for 1 hour. Upon reaction completion as verified by a MeOH quench test (see page S23 for details of the procedure), the volatiles were removed under reduced pressure to give the title compound as a yellow oil (68 mg, 0.25 mmol,

92%). ^{1}H NMR (500 MHz, $CDCl_3$): δ = 7.16 (d, J = 8.8 Hz, 2H), 6.90 (d, J = 8.8 Hz, 2H), 4.17 – 4.11 (m, 2H), 4.07 (s, 2H), 3.89 – 3.83 (m, 2H), 3.75 – 3.69 (m, 2H), 3.61 – 3.53 (m, 2H), 3.39 (s, 3H). ^{13}C NMR (125 MHz, $CDCl_3$): δ = 172.4, 158.8, 130.8, 123.6, 115.2, 72.1, 70.9, 69.8, 67.58, 59.2, 52.4.

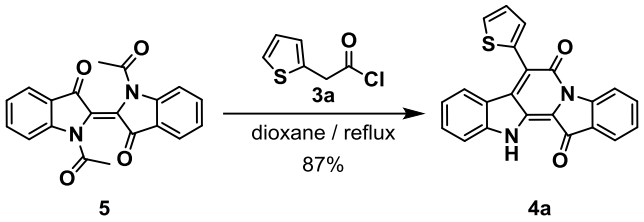

5 4a

4a 7-(thiophen-2-yl)-BAI

To an oven dried microwave vial with a stir bar was added **5** (15 mg, 0.043 mmol). The reaction vial was sealed with a septa cap and backfilled three times with N_2. Dry dioxane (2 mL) was added followed by 2-thiopheneacetyl chloride **3a** (5.9 μL, 0.048 mmol, 1.1 equiv.) and the vial was placed in a 115 °C bath overnight. Upon reaction completion as confirmed by TLC, the volatiles was concentrated under reduced pressure, and the residue was subjected to chromatography (eluent: $CHCl_3$) to give the title compound as a purple solid (13.9 mg, 0.038 mmol, 87%). ^{1}H NMR (500 MHz, DMSO-d_6): δ = 11.68 (s, 1H), 8.61 (dt, J = 8.1, 0.8 Hz, 1H), 7.92 (dd, J = 5.1, 1.2 Hz, 1H), 7.83 (dt, J = 7.3, 1.1 Hz, 1H), 7.73 (ddd, J = 8.5, 7.5, 1.4 Hz, 1H), 7.51 (dd, J = 3.6, 1.2 Hz, 1H), 7.47 (ddd, J = 8.2, 7.0, 1.1 Hz, 1H), 7.41 (dddd, J = 10.7, 7.4, 1.9, 0.9 Hz, 3H), 7.31 (dd, J = 5.1, 3.5 Hz, 1H), 6.96 (ddd, J = 8.1, 7.0, 1.2 Hz, 1H). ^{13}C NMR (125 MHz, DMSO-d_6): δ = 179.7, 155.9, 147.5, 145.8, 137.9, 135.3, 133.5, 131.8, 129.6, 129.5, 128.9, 126.8, 126.7, 126.1, 124.8, 123.5, 123.4, 120.6, 119.3, 117.4, 114.6, 112.4. HRMS (ESI-TOF) $[M+H]^+$ calculated: 369.0692, found: 369.0886.

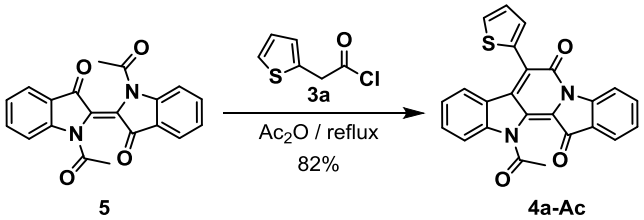

5 4a-Ac

4a-Ac

To an oven dried microwave vial with a stir bar was added **5** (15 mg, 0.043 mmol). The reaction vial was sealed with a septa cap and backfilled three times with N_2. Acetic anhydride (2 mL) was added, followed by 2-thiopheneacetyl chloride **3a** (5.9 μL, 0.048 mmol, 1.1 equiv.) and the vial was placed in a 115 °C bath overnight. Upon reaction completion as confirmed by TLC, the volatiles was concentrated under reduced pressure, and the residue was subjected to chromatography (eluent: $CHCl_3$) to give the title compound as a red solid (14.5 mg, 0.035 mmol, 82%). ^{1}H NMR (500 MHz, $CDCl_3$): δ = 8.77 (d, J = 8.2 Hz, 1H), 8.04 (d, J = 8.4 Hz, 1H), 7.86 (dd, J = 7.3, 1.2 Hz, 1H), 7.74 – 7.65 (m, 2H), 7.51 (ddd, J = 8.5, 7.3, 1.3 Hz, 1H), 7.50 – 7.41 (m, 2H), 7.37 (td, J = 7.5, 0.9 Hz, 1H), 7.30 – 7.25 (m, 1H), 7.12 (ddd, J = 8.1, 7.3, 1.0 Hz, 1H), 2.59 (s, 3H). ^{13}C NMR (125 MHz, $CDCl_3$): δ = 180.7, 170.7, 157.9, 147.1, 145.4, 139.3, 136.8, 133.1, 132.6, 129.9, 127.6, 127.4, 127.3, 126.9, 124.7, 124.5, 124.5, 122.1, 120.7, 118.8, 115.2, 25.4. HRMS (MALDI-TOF) $[M+H]^+$ calculated: 411.0798, found: 411.0000.

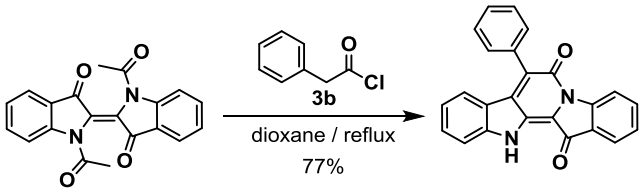

5 4b

4b 7-phenyl-BAI

To an oven dried microwave vial with a stirbar was added **5** (50 mg, 0.144 mmol). The reaction vial was sealed with a septa cap and backfilled three times with N_2. Dry dioxane (5 mL, 0.03 M) was added, followed by phenylacetyl chloride (21 μL, 0.159 mmol, 1.1 equiv.) and the vial was placed in a 115 °C bath overnight. Upon reaction completion as confirmed by TLC, the volatiles was concentrated under reduced pressure, and the residue was subjected to chromatography (eluent: $CHCl_3$) to give the title compound as a purple solid (40 mg, 0.11 mmol, 77%). ^{1}H NMR (500 MHz, 50 °C, DMSO-d_6): δ = 11.65 (s, 1H), 8.59 (d, J = 8.1 Hz, 1H), 7.82 (d, J = 7.5 Hz, 1H), 7.72 (t, J = 7.8 Hz, 1H), 7.63 – 7.51 (m, 5H), 7.44 – 7.37 (m, 3H), 6.89 – 6.80 (m, 2H). ^{13}C NMR (125 MHz, 50 °C, DMSO-d_6): δ = 179.6, 156.3, 147.4, 145.9, 137.8, 135.3, 134.0, 133.7, 131.4, 129.3, 129.0, 128.6, 128.3, 125.9, 124.7, 123.7, 123.3, 120.5, 119.4, 117.3, 114.5, 112.3. HRMS (ESI-TOF) $[M+H]^+$ calculated: 363.1128, found: 363.1325.

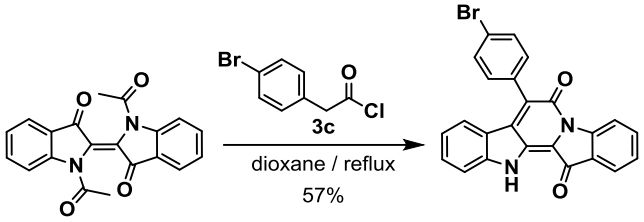

5 4c

4c 7-(4-bromophenyl)-BAI

To an oven dried microwave vial with a stirbar was added **5** (50 mg, 0.144 mmol). The reaction vial was sealed with a septa cap and backfilled three times with N_2. Compound **3c** (37 mg, 0.159 mmol, 1.1 equiv.) was added as a solution in dry dioxane (5 mL, 0.03 M) and the vial was placed in a 115 °C bath overnight. Upon reaction completion as confirmed by TLC, the volatiles was concentrated under reduced pressure, and the residue was subjected to chromatography (eluent: $CHCl_3$) to give the title compound as a purple solid (36 mg, 0.082 mmol, 57%). ^{1}H NMR (500 MHz, $C_2D_2Cl_4$, 398 K): δ = 8.88 (s, 1H), 8.64 (d, J = 8.1 Hz, 1H), 7.86 (d, J = 6.9 Hz, 1H), 7.75 (dt, J = 4.7, 2.3, 2.2 Hz, 2H), 7.69 – 7.65 (m, 1H), 7.53 – 7.44 (m, 3H), 7.37 (td, J = 7.5, 0.9 Hz, 1H), 7.27 (d, J = 8.0 Hz, 1H), 7.15 (d, J = 7.9 Hz, 1H), 6.98 (dd, J = 26.2, 7.5 Hz, 1H). ^{13}C NMR (125 MHz, $C_2D_2Cl_4$, 398 K): δ = 181.5, 156.9, 146.6, 146.0, 137.7, 135.9, 133.3, 132.1, 132.0, 131.4, 129.4, 126.4, 124.9, 124.0, 123.4, 121.7, 120.2, 119.8, 118.1, 115.1, 111.5, 99.4. HRMS (ESI-TOF) $[M+H]^+$ calculated: 441.0233, found: 441.0351.

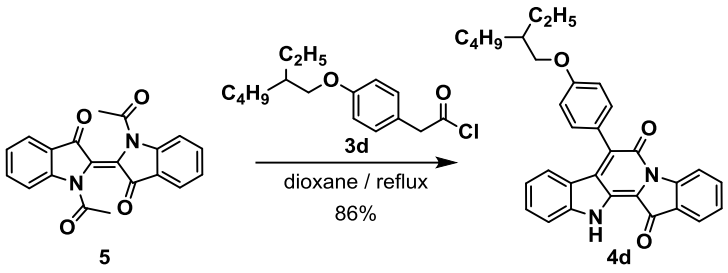

4d 7-(4-((2-ethylhexyl)oxy)phenyl)-BAI

To an oven dried microwave vial with a stir bar was added **5** (145 mg, 0.41 mmol). The reaction vial was sealed with a septa cap and backfilled three times with N_2. To the vial was added **3d** (142 mg, 0.502 mmol, 1.2 equiv.) as a solution in dry dioxane (15 mL) and the vial was placed in a 115 ^{o}C bath overnight. Upon reaction completion as confirmed by TLC, the volatiles was concentrated under reduced pressure, and the residue was subjected to chromatography (eluent: $CHCl_3$) to give the title compound as a purple solid (173 mg, 0.35 mmol, 86%). ^{1}H NMR (500 MHz, $CDCl_3$): δ = 8.95 (s, 1H), 8.69 (d, *J* = 8.1 Hz, 1H), 7.83 (dd, *J* = 7.3, 1.0 Hz, 1H), 7.62 (ddd, *J* = 8.3, 7.4, 1.3 Hz, 1H), 7.53 (d, *J* = 8.8 Hz, 2H), 7.42 (ddd, *J* = 8.4, 7.4, 1.2 Hz, 1H), 7.32 (ddd, *J* = 7.4, 6.0, 1.1 Hz, 2H), 7.24 (t, *J* = 7.6 Hz, 1H), 7.09 (d, *J* = 8.7 Hz, 2H), 6.96 – 6.90 (m, 1H), 3.96 (dd, *J* = 5.7, 2.0 Hz, 2H), 1.79 (p, *J* = 6.2 Hz, 1H), 1.58 – 1.34 (m, 3H), 1.25 (m, 5H), 1.01 – 0.82 (m, 6H). ^{13}C NMR (125 MHz, $CDCl_3$): δ = 181.7, 160.5, 157.9, 147.1, 146.1, 137.2, 135.9, 135.6, 131.7, 131.3, 130.2, 126.3, 125.5, 125.3, 125.2, 124.0, 121.7, 120.8, 118.6, 114.9, 111.4, 100.1, 70.8, 39.6, 30.7, 29.86, 29.3, 24.0, 23.2, 14.3, 11.3. HRMS (ESI-TOF) $[M+H]^+$ calculated: 491.2329, found: 491.2405.

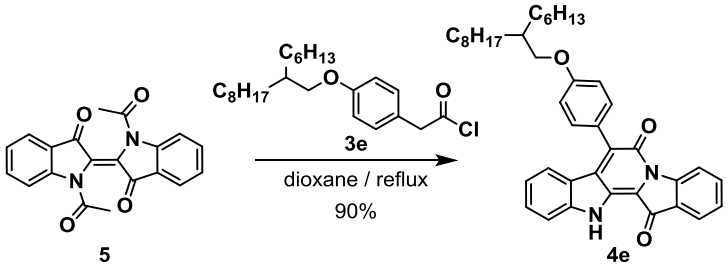

4e 7-(4-((2-hexyldecyl)oxy)phenyl)-BAI

To an oven dried microwave vial with a stir bar was added **5** (100 mg, 0.289 mmol). The reaction vial was sealed with a septa cap and backfilled three times with N_2. To the vial was added **3e** (132 mg, 0.334 mmol, 1.15 equiv.) as a solution in dry dioxane (15 mL, 0.02M), and the vial was placed in a 115 ^{o}C bath overnight. Upon reaction completion as confirmed by TLC, the volatiles was concentrated under reduced pressure, and the residue was subjected to chromatography (eluent: $CHCl_3$) to give the title compound as a purple solid (156 mg, 0.259 mmol, 90%) ^{1}H NMR (500 MHz, $CDCl_3$): δ = 8.84 (s, 1H), 8.69 (dt, *J* = 8.1, 0.8 Hz, 1H), 7.84 (dt, *J* = 7.2, 1.1 Hz, 1H), 7.63 (ddd, *J* = 8.5, 7.4, 1.4 Hz, 1H), 7.57 – 7.50 (m, 2H), 7.42 (ddd, *J* = 8.3, 7.3, 1.2 Hz, 1H), 7.36 – 7.23 (m, 2H), 7.27 – 7.19 (m, 1H), 7.09 (d, *J* = 8.8 Hz, 2H), 6.93 (td, *J* = 7.6, 1.0 Hz, 1H), 3.94 (d, *J* = 5.6 Hz, 2H), 1.87 – 1.81 (m, 1H), 1.49 (t, *J* = 7.2 Hz, 2H), 1.42 (t, *J* = 6.8 Hz, 1H), 1.40 – 1.24 (m, 21H), 0.94 – 0.85 (m, 6H). ^{13}C NMR (125 MHz, $CDCl_3$): δ = 181.7, 160.5, 157.9, 147.1, 146.1, 137.2, 135.9, 135.6, 131.7, 131.3, 130.2, 126.3, 125.5, 125.3, 125.2, 124.0, 121.7, 120.8, 118.6, 114.9, 111.4, 71.2, 38.1, 32.1, 32.0, 31.6, 30.2, 29.9, 29.8, 29.5, 27.1, 27.0, 22.9, 14.3. HRMS (ESI-TOF) $[M+H]^+$ calculated: 603.3581, found: 603.3591.

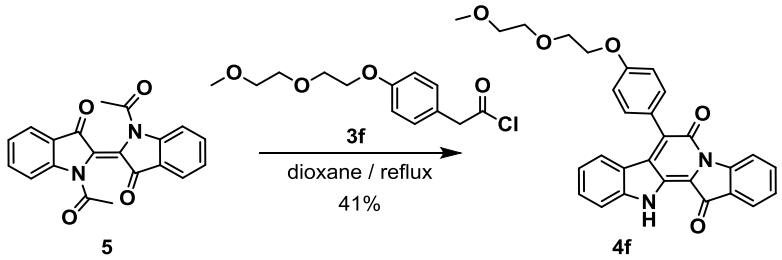

5 4f

4f 7-(4-(2-(2-methoxyethoxy)ethoxy)phenyl)-BAI

To an oven dried microwave vial with a stir bar was added **5** (79 mg, 0.22 mmol). The reaction vial was sealed with a septa cap and backfilled three times with N_2. To the vial was added **4f** (65 mg, 0.24 mmol, 1.05 equiv.) as a solution in dry dioxane (2 mL), and the vial was placed in a 115 ^{o}C bath overnight. Upon reaction completion as confirmed by TLC, the volatiles was concentrated under reduced pressure, and the residue was subjected to chromatography (eluent: $CHCl_3$) to give the title compound as a purple solid (44 mg, 0.092 mmol, 41%). ^{1}H NMR (500 MHz, $CDCl_3$): δ = 8.85 (s, 1H), 8.69 (dt, *J* = 8.2, 0.9 Hz, 1H), 7.84 (ddd, *J* = 7.6, 1.4, 0.6 Hz, 1H), 7.62 (ddd, *J* = 8.2, 7.4, 1.4 Hz, 1H), 7.57 – 7.50 (m, 2H), 7.42 (ddd, *J* = 8.3, 7.4, 1.3 Hz, 1H), 7.32 (td, *J* = 7.5, 0.9 Hz, 1H), 7.22 (dd, *J* = 33.2, 8.4 Hz, 1H), 7.12 (dt, *J* = 4.6, 2.9, 2.7 Hz, 2H), 6.93 (ddd, *J* = 8.1, 7.3, 1.0 Hz, 1H), 4.27 (dd, *J* = 42.3, 4.8 Hz, 2H), 3.94 (dd, *J* = 45.1, 5.0 Hz, 2H), 3.78 (ddd, *J* = 23.6, 3.4, 1.8 Hz, 2H), 3.62 (ddd, *J* = 34.4, 2.9, 1.3 Hz, 2H), 3.43 (s, 3H). ^{13}C NMR (125 MHz, $CDCl_3$): δ = 181.7, 159.8, 157.8, 147.1, 146.2, 137.4, 135.9, 135.4, 131.7, 131.3, 130.2, 126.3, 125.8, 125.5, 125.2, 124.0, 121.7, 120.7, 118.6, 115.0, 111.5, 72.1, 70.0, 69.9, 67.7, 59.3. HRMS (ESI-TOF) $[M+H]^+$ calculated: 481.1758, found: 481.1855.

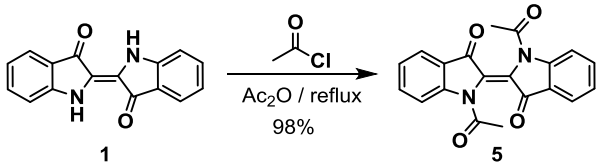

1 5

5 N,N'-diacetylindigo [65]

Indigo **1** (1.311 g, 5 mmol) was added to a flask equipped with a stir bar and a reflux condenser. Acetic anhydride (20 mL) and acetyl chloride (0.89 mL, 12.5 mmol, 2.5 equiv.) were added and the solution was heated to reflux overnight. The reaction was concentrated and used without further purification (1.695 g, 4.9 mmol, 98%) as a dark-red powder. Trace (<5%) mono-acetyl indigo could be removed by precipitation into Et_2O/hexanes (3:1) and collecting by filtration, to provide **5** (1.404 g, 4.05 mmol, 81%) as a brick-red powder. ^{1}H NMR (500 MHz, $CDCl_3$): δ = 8.27 (s, 2H), 7.77 (ddd, *J* = 7.6, 1.5, 0.6 Hz, 2H), 7.66 (ddd, *J* = 8.5, 7.3, 1.4 Hz, 2H), 7.29 – 7.26 (m, 2H), 2.56 (s, 6H). ^{13}C NMR (125 MHz, $CDCl_3$): δ = 184.3, 170.2, 149.3, 137.0, 126.4, 125.4, 124.5, 122.0, 117.4, 77.4, 77.2, 76.9, 24.1. HRMS (ESI-TOF) $[M+H]^+$ calculated: 347.1026, found: 347.1316.

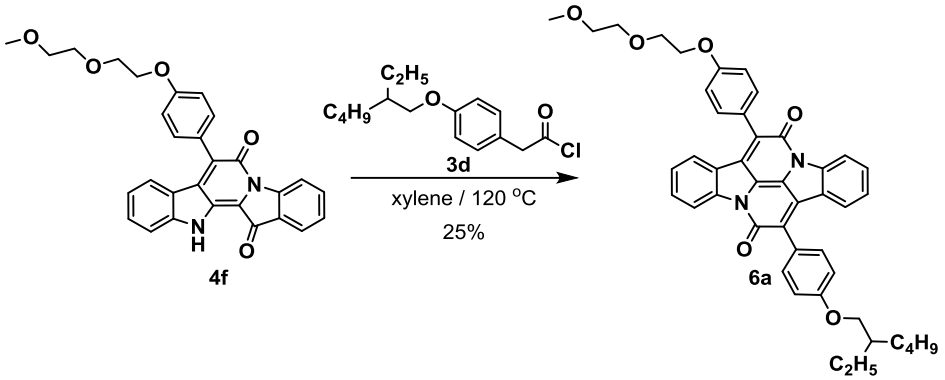

6a 7-(4-(2-(2-methoxyethoxy)ethoxy)phenyl)-14-(4-((2-ethylhexyl)oxy)phenyl)-BAI

To an oven dried microwave vial with a stir bar was added **4f** (44 mg, 0.092 mmol). The vial was sealed with a septa cap and backfilled three times with N_2. Dry xylene (6.0 mL, 0.015 M) was added, followed by thiopheneacetyl chloride (65 mg, 0.23 mmol, 2.5 equiv.), and the vial was placed in a 145 °C bath overnight. Upon reaction completion as confirmed by TLC, the volatiles was concentrated under reduced pressure, and the residue was subjected to chromatography (gradient elution 0 to 25% ethyl acetate in chloroform) to give the title compound as a bright red solid (16 mg, 0.023 mmol, 25%). ^{1}H NMR (500 MHz, $CDCl_3$): δ = 8.49 (d, J = 8.1 Hz, 2H), 7.67 (td, J = 12.6, 7.9 Hz, 6H), 7.53 (dd, J = 75.4, 7.4 Hz, 2H), 7.25 – 7.17 (m, 2H), 7.13 – 7.07 (m, 4H), 4.32 – 4.25 (m, 2H), 4.01 – 3.92 (m, 4H), 3.86 – 3.75 (m, 2H), 3.66 – 3.60 (m, 2H), 3.43 (s, 3H), 1.80 (hept, J = 6.3 Hz, 1H), 1.62 – 1.24 (m, 8H), 1.01 – 0.90 (m, 6H). ^{13}C NMR (125 MHz, $CDCl_3$): δ = 160.4, 159.8, 159.8, 159.7, 144.7, 144.6, 132.0, 132.0, 131.8, 131.7, 131.6, 131.4, 131.1, 130.7, 129.8, 126.1, 126.1, 126.0, 125.5, 125.5, 125.5, 122.1, 122.0, 117.7, 114.8, 114.7, 72.1, 71.0, 70.7, 69.9, 67.7, 59.3, 39.5, 30.7, 29.3, 24.0, 23.2, 23.2, 14.3, 11.3. HRMS (ESI-TOF) $[M+H]^+$ calculated: 709.3272, found: 709.3395.

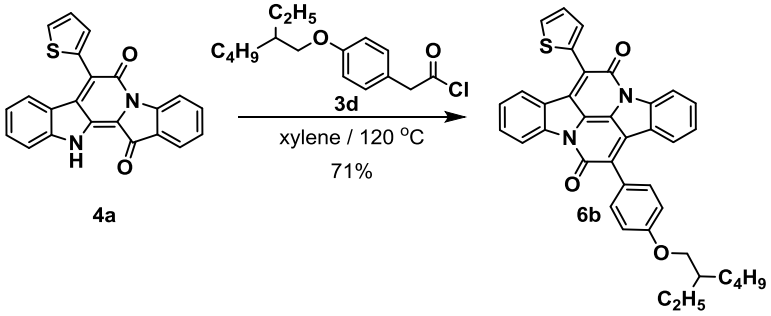

6b 7-(4-((2-ethylhexyl)oxy)phenyl)-14-(thiophen-2-yl)-BAI

To an oven dried microwave vial with a stir bar was added **4d** (95 mg, 0.193 mmol). The vial was sealed with a septa cap and backfilled three times with N_2. Dry xylene (10 mL) was added, followed by thiopheneacetyl chloride (54 μL, 0.437 mmol, 2.25 equiv.) and the vial was placed in a 145 °C bath overnight. Upon reaction completion as confirmed by TLC, the volatiles was concentrated under reduced pressure, and the residue was subjected to chromatography (eluent: $CHCl_3$) to give the title compound as a purple solid (83 mg, 0.14 mmol, 71%). ^{1}H NMR (500 MHz, $CDCl_3$): δ = 8.54 (dq, J = 8.1, 1.0 Hz, 2H), 8.17 (dd, J = 8.1, 0.9 Hz, 1H), 7.73 (dd, J = 3.6, 1.2 Hz, 1H), 7.71 – 7.66 (m, 4H), 7.56 (dddd, J = 10.9, 8.6, 7.8, 1.2 Hz, 2H), 7.35 – 7.16 (m, 3H), 7.13 – 7.06 (m, 2H), 4.02 – 3.92 (m, 2H), 1.80 (hept, J = 6.3 Hz, 1H), 1.60 – 1.19 (m, 8H), 1.01 – 0.90 (m, 6H). ^{13}C NMR (125 MHz, $CDCl_3$): δ = 160.5, 159.8, 159.0, 144.6, 144.4, 135.0, 132.4, 132.0, 131.8, 131.6,

131.3, 130.9, 130.0, 130.0, 126.5, 126.3, 126.1, 126.1, 125.9, 125.5, 125.4, 125.3, 124.1, 122.1, 122.1, 117.9, 117.8, 114.7, 70.8, 39.6, 30.7, 29.3, 24.1, 23.2, 14.3, 11.3. HRMS (MALDI-TOF) $[M+H]^+$ calculated: 597.2206, found: 597.1504.

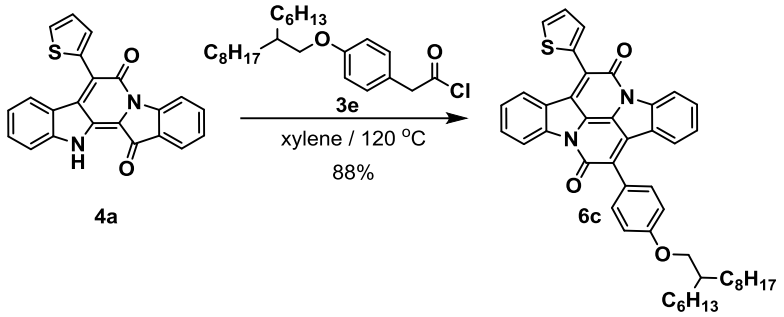

6c 7-(4-((2-hexyldecyl)oxy)phenyl)-14-(thiophen-2-yl)-BAI

To three separate oven dried microwave vials with stir bars were each placed **4e** (1.109 g, 1.84 mmol). Each vial was sealed with a septa cap and backfilled three times with N_2. Dry xylene (15 mL, 0.12 M) was added followed by thiopheneacetyl chloride (0.57 mL, 4.6 mmol, 2.5 equiv.) and the vials were placed in a 145 °C bath overnight. Upon reaction completion as confirmed by TLC, the vials were combined, and the volatiles were concentrated under reduced pressure. The residue was redissolved in chloroform. The chloroform solution was added dropwise into hexane and the precipitate was collected by filtration (2.849 g). This process was repeated a second time with the filtrate (0.306 g). The final filtrate was concentrated and purified by column chromatography ($CHCl_3$ eluent). The precipitates and columned portions were combined to provide **6c** (3.278 g, 4.62 mmol, 88%) as a purple solid. ^{1}H NMR (500 MHz, $CDCl_3$): δ = 8.54 (dd, J = 8.1, 0.9 Hz, 2H), 8.17 (dt, J = 7.8, 1.0 Hz, 1H), 7.74 (dd, J = 3.6, 1.2 Hz, 1H), 7.72 – 7.65 (m, 4H), 7.62 – 7.52 (m, 2H), 7.34 – 7.19 (m, 3H), 7.12 – 7.07 (m, 2H), 3.95 (d, J = 5.6 Hz, 2H), (hept, J = 6.3 Hz, 1H), 1.53 – 1.23 (m, 24H), 0.94 – 0.86 (m, 6H). ^{13}C NMR (125 MHz, $CDCl_3$): δ = 160.5, 159.8, 159.0, 144.6, 144.4, 135.0, 132.4, 132.0, 131.8, 131.6, 131.3, 130.9, 130.0, 130.0, 126.5, 126.3, 126.1, 126.1, 125.9, 125.5, 125.4, 125.3, 124.4, 122.1, 122.1, 117.9, 117.8, 114.7, 71.2, 38.1, 32.1, 32.0, 31.6, 30.2, 29.9, 29.8, 29.5, 27.1, 27.0, 22.9, 14.3. HRMS (MALDI-TOF) $[M+H]^+$ calculated: 709.3458, found: 709.3570.

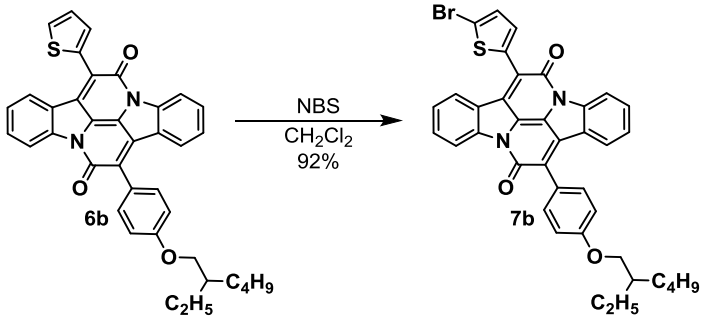

7b 7-(5-bromothiophen-2-yl)-14-(4-((2-ethylhexyl)oxy)phenyl)-BAI

To an oven dried vial with a stir bar was added **6b** (44 mg, 0.074 mmol) and N-bromosuccinimide (14.5 mg, 0.081 mmol, 1.1 equiv). The vial was sealed with a septa cap and backfilled three times with N_2. Dry chloroform (1.5 mL) was added and a noticeable red to purple color change was observed. The mixture was stirred until completion as monitored by TLC (1 hour), at which point

it was diluted with chloroform, washed two times with NaOH (2 M). The organic layer was washed with brine and dried with $MgSO_4$ before concentrating under reduced pressure. The crude material was purified by column chromatography ($CHCl_3$ eluent) to yield the title compound (46 mg, 0.068 mmol, 92%) ^{1}H NMR (500 MHz, $CDCl_3$): δ = 8.52 (dd, *J* = 14.1, 8.1 Hz, 2H), 8.21 (d, *J* = 8.0 Hz, 1H), 7.68 (dd, *J* = 17.9, 8.2 Hz, 3H), 7.62 – 7.51 (m, 4H), 7.32 (t, *J* = 7.8 Hz, 1H), 7.28 – 7.20 (m, 1H), 7.10 (d, *J* = 8.7 Hz, 2H), 3.97 (dd, *J* = 5.7, 2.0 Hz, 2H), 1.80 (hept, *J* = 6.3 Hz, 1H), 1.61 – 1.20 (m, 8H), 0.98 (t, *J* = 7.5 Hz, 3H), 0.94 (dd, *J* = 33.7, 7.0 Hz, 1H). ^{13}C NMR (125 MHz, $CDCl_3$): δ = 160.5, 159.6, 158.5, 144.4, 144.0, 136.7, 132.4, 132.0, 131.8, 131.0, 129.9, 129.8, 129.1, 126.5, 126.1, 125.9, 125.5, 125.4, 125.2, 125.1, 123.4, 122.0, 121.9, 118.1, 117.8, 117.7, 114.6, 70.8, 39.6, 30.7, 29.3, 24.1, 23.3, 14.3, 11.3. HRMS (MALDI-TOF) $[M+H]^+$ calculated: 675.1312, found: 675.0342.

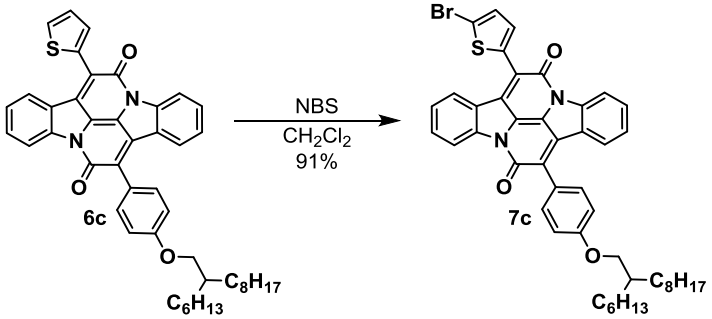

7c 7-(5-bromothiophen-2-yl)-14-(4-((2-hexyldecyl)oxy)phenyl)-BAI

To an oven dried vial with a stir bar was added **6c** (118 mg, 0.166 mmol) and N-bromosuccinimide (32.6 mg, 0.183 mmol, 1.1 equiv). The vial was sealed with a septa cap and backfilled three times with N_2. Dry chloroform (5 mL) was added and a noticeable red to purple color change was observed. The mixture was stirred until completion as monitored by TLC (1 hour), at which point it was diluted with chloroform, washed two times with NaOH (2 M). The organic layer was washed with brine and dried with $MgSO_4$ before concentrating under reduced pressure. The crude material was purified by column chromatography ($CHCl_3$ eluent) to yield the title compound (119 mg, 0.151 mmol, 91%) ^{1}H NMR (500 MHz, CDCl3): δ = 8.41 (dd, *J* = 17.7, 8.0 Hz, 2H), 8.16 (d, *J* = 7.9 Hz, 1H), 7.65 (dd, *J* = 20.8, 8.3 Hz, 3H), 7.52 – 7.44 (m, 3H), 7.30 – 7.16 (m, 3H), 7.07 (d, *J* = 8.8 Hz, 2H), 3.96 (d, *J* = 5.6 Hz, 2H), 1.85 (h, *J* = 6.1 Hz, 1H), 1.55 – 1.22 (m, 24H), 0.96 – 0.84 (m, 6H). ^{13}C NMR (125 MHz, $CDCl_3$): δ = 160.6, 159.6, 158.4, 144.4, 144.0, 136.7, 132.3, 132.0, 131.8, 130.9, 129.8, 129.8, 129.1, 126.4, 126.1, 125.9, 125.5, 125.4, 125.2, 125.1, 123.3, 122.1, 121.9, 118.1, 117.8, 117.7, 114.6, 71.2, 38.2, 32.1, 32.1, 31.6, 30.2, 29.9, 29.8, 29.5, 27.1, 27.0, 22.9, 14.3. HRMS (MALDI-TOF) $[M^+]$ calculated: 786.2491, found: 786.2236.

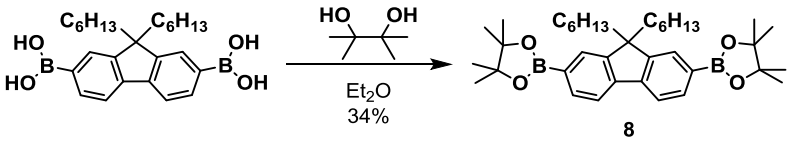

8 2,2'-(9,9-dihexyl-9H-fluorene-2,7-diyl)bis(4,4,5,5-tetramethyl-1,3,2-dioxaborolane)

Pinacol (140 mg, 1.18 mmol, 1 equiv.) and (9,9-dihexyl-9H-fluorene-2,7-diyl)diboronic acid (500 mg, 1.18 mmol, 1 equiv.) were added to a vial with septa cap and backfilled three times with N_2. Dry ether (5 mL) was added, forming a cloudy solution which was stirred overnight. The mixture was filtered and concentrated under reduced pressure. The crude material was purified by

column chromatography (gradient elution 0 to 50% ethyl acetate in hexanes) to produce compound **8** (117 mg, 0.2 mmol, 34%) as a white powder. ^{1}H NMR (500 MHz, $CDCl_3$): δ = 7.80 (dd, *J* = 7.6, 1.0 Hz, 2H), 7.76 – 7.69 (m, 4H), 2.03 – 1.96 (m, 4H), 1.39 (s, 24H), 1.17 – 0.93 (m, 12H), 0.74 (t, *J* = 7.2 Hz, 6H), 0.54 (m, 4H). ^{13}C NMR (125 MHz, $CDCl_3$): *δ* = 150.6, 144.1, 139.3, 133.8, 129.1, 119.5, 83.9, 55.3, 40.3, 31.6, 29.8, 25.1, 23.7, 22.7, 14.2. HRMS (MALDI-TOF) [M^+] calculated: 586.4365, found: 586.3967.

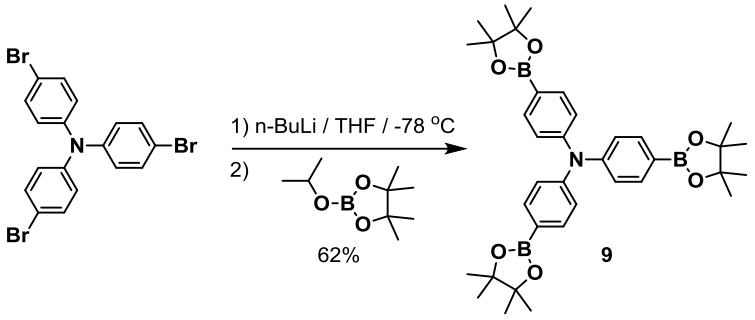

9 tris(4-(4,4,5,5-tetramethyl-1,3,2-dioxaborolan-2-yl)phenyl)amine[31b]

Tris(4-bromophenyl)amine (1 g, 2.34 mmol) was added to a flask with stirbar and backfilled three times with N_2. Dry THF (15 mL) was added and the solution cooled to -78 °C in a dry ice/acetone bath. To this mixture, a 1.6 M solution of *n*-BuLi in hexanes (4.8 mL, 7.7 mmol, 3.3 equiv.) was added dropwise to give a cloudy solution. After two hours, 2-isopropoxy-4,4,5,5-tetramethyl-1,3,2-dioxaborolane (1.67 mL, 8.19 mmol, 3.5 equiv.) was added, forming a clear solution, which was warmed to ambient temperature overnight. The reaction mixture was concentrated under reduced pressure, diluted in CH_2Cl_2, washed with water until the aqueous layer was clear. The organic layer was washed with brine and dried over $MgSO_4$. The crude mixture was purified by column chromatography (gradient elution 0 to 100% ethyl acetate in hexanes) to provide **9** (910 mg, 1.46 mmol, 62%) as a white powder. ^{1}H NMR (500 MHz, $CDCl_3$): *δ* = 7.68 (d, *J* = 8.7 Hz, 6H), 7.07 (d, *J* = 7.8 Hz, 6H), 1.34 (s, 36H). ^{13}C NMR (125 MHz, $CDCl_3$): *δ* = 149.9, 136.1, 133.6, 123.6, 83.8, 77.4, 77.2, 76.9, 25.0. HRMS (ESI-TOF) [M^+] calculated: 623.3761, found: 623.3910.

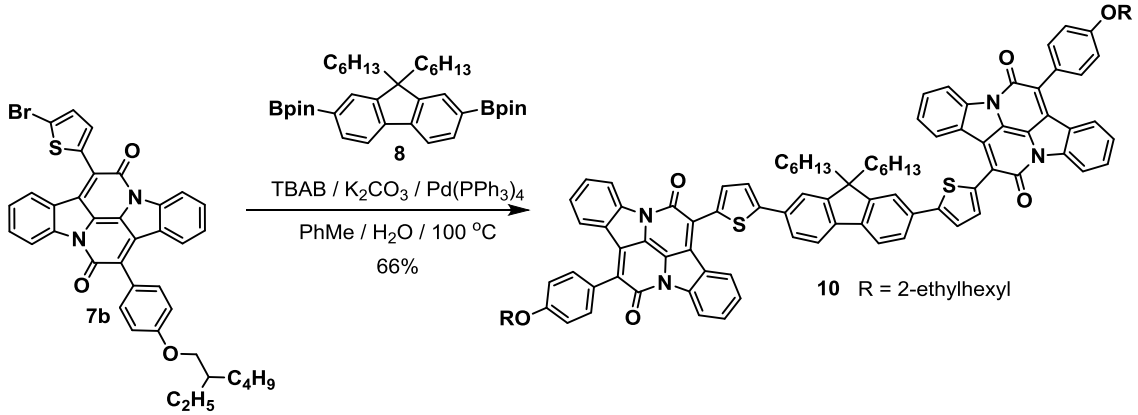

10 14,14'-((9,9-dihexyl-9H-fluorene-2,7-diyl)bis(thiophene-5,2-diyl))bis(7-(4-((2-ethylhexyl)oxy)phenyl)-BAI

Bromide **7b** (19 mg, 0.028 mmol, 2.2 equiv), boronic ester **8** (7.5 mg, 0.013 mmol, 1 equiv), and tetrabutylammonium bromide (8.6 mg, 0.026 mmol, 2 equiv.), and toluene (2.5 mL) were added to a vial with a stir bar. To this vial was added an aqueous solution of K_2CO_3 (2 M, 60 μL) and the

solution was degassed by bubbling nitrogen while stirring for 10 minutes. Palladium tetrakistriphenylphosophine (2.25 mg, 0.002 mmol, 0.15 equiv) was dissolved in toluene and transferred to the vial which was degassed for an additional 10 minutes. A septa cap was added, the N_2 line was removed, and the vial was placed in a 100 °C bath overnight. Upon completion by TLC, the mixture was diluted in $CHCl_3$, washed three times with water, and dried with brine and $MgSO_4$. The product was purified through column chromatography ($CHCl_3$ eluent) to provide a blue solid (13 mg, 0.0085 mmol, 66%) ^{1}H NMR (500 MHz, $CDCl_3$): δ = 8.56 (t, *J* = 7.8 Hz, 4H), 8.36 (d, *J* = 8.0 Hz, 2H), 7.81 (dd, *J* = 19.1, 2.7 Hz, 2H), 7.77 (s, 4H), 7.72 (t, *J* = 6.9 Hz, 4H), 7.68 (d, *J* = 8.2 Hz, 4H), 7.59 (d, *J* = 3.7 Hz, 2H), 7.55 (q, *J* = 8.4 Hz, 4H), 7.33 (t, *J* = 7.9 Hz, 2H), 7.23 (t, *J* = 7.8 Hz, 2H), 7.10 (d, *J* = 9.3 Hz, 4H), 3.98 (d, *J* = 4.7 Hz, 4H), 2.10 (t, *J* = 8.1 Hz, 4H), 1.81 (p, *J* = 6.2 Hz, 2H), 1.63 – 1.43 (m, 8H), 1.43 – 1.20 (m, 8H), 1.19 – 1.04 (m, 16H), 0.97 (dt, *J* = 20.3, 7.1 Hz, 12H), 0.77 (t, *J* = 7.1 Hz, 6H). ^{13}C NMR (125 MHz, $CDCl_3$): δ = 160.5, 159.8, 158.9, 152.2, 150.1, 144.4, 144.2, 141.0, 134.4, 133.3, 132.1, 131.9, 131.9, 131.4, 131.2, 131.1, 129.6, 126.4, 126.2, 126.1, 126.0, 125.5, 125.1, 124.7, 122.6, 122.4, 121.8, 120.5, 120.4, 117.9, 117.8, 114.7, 70.8, 55.7, 40.8, 39.6, 31.7, 30.7, 29.9, 29.3, 24.1, 23.3, 22.8, 14.3, 14.2, 11.3. HRMS (MALDI-TOF) $[M+H]^+$ calculated: 1523.6693, found: 1523.6423.

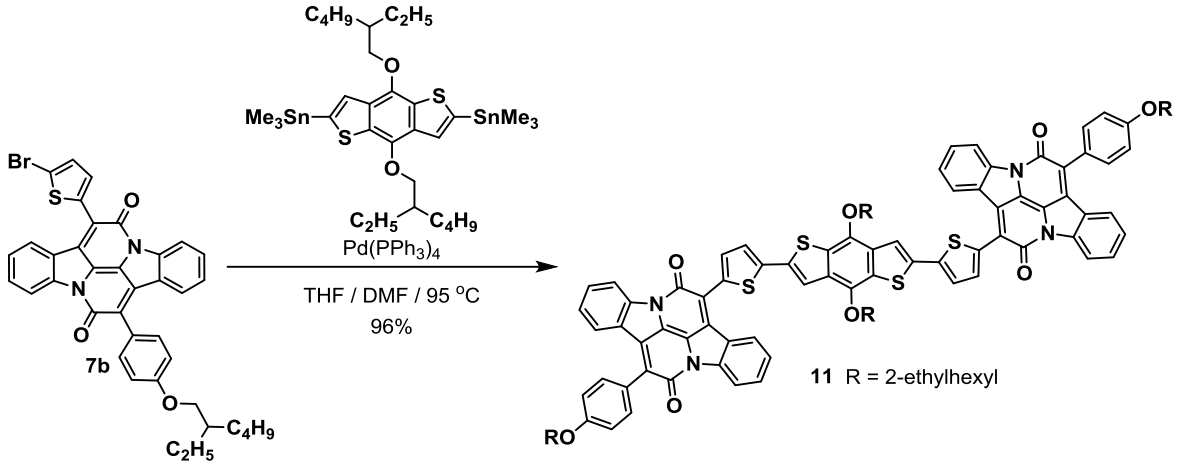

11 14,14'-((4,8-bis((2-ethylhexyl)oxy)benzo[1,2-b:4,5-b']dithiophene-2,6-diyl)bis(thiophene-5,2-diyl))bis(7-(4-((2-ethylhexyl)oxy)phenyl)-BAI

Bromide **7b** (25 mg, 0.037 mmol, 2 equiv), (4,8-bis((2-ethylhexyl)oxy)benzodithiophene-2,6-diyl)bis(trimethylstannane) (14.3 mg, 0.0185 mmol, 1 equiv), and tetrakistriphenylphosphine palladium (4.3 mg, 0.0037 mmol, 0.1 equiv) were added to a vial with a stir bar and septa cap. After the vial was backfilled three times with N_2, dry tetrahydrofuran (0.5 mL) and *N,N*-dimethylformamide (0.5 mL) were added and the vial placed in a 95 °C bath. After the reaction was complete as monitored by TLC, the reaction mixture was concentrated under reduced pressure, diluted in hot $CHCl_3$ and precipitated into hexanes three times, producing the title compound as a blue solid (29 mg, 0.0177 mmol, 96%). ^{1}H NMR (500 MHz, $CDCl_3$): δ = 8.46 (d, *J* = 8.0 Hz, 2H), 8.33 (dd, *J* = 24.0, 6.9 Hz, 4H), 7.75 – 7.65 (m, 8H), 7.54 (s, 2H), 7.46 (q, *J* = 6.1, 4.1 Hz, 4H), 7.21 – 7.15 (m, 6H), 7.10 (d, *J* = 8.2 Hz, 4H), 4.22 (d, *J* = 5.5 Hz, 4H), 4.00 (d, *J* = 5.9 Hz, 4H), 2.35 (t, *J* = 7.5 Hz, 2H), 1.95 – 1.91 (m, 2H), 1.89 – 1.21 (m, 32H), 1.15 (t, *J* = 7.5 Hz, 6H), 1.01 (tt, *J* = 21.7, 6.4 Hz, 12H), 0.89 (t, *J* = 6.8 Hz, 6H). The acquisition of a ^{13}C NMR spectrum with good

signal-to-noise ratio was unsatisfactory due to limited solubility. HRMS (MALDI-TOF) $[M]^+$ calculated: 1634.6267, found: 1634.6865.

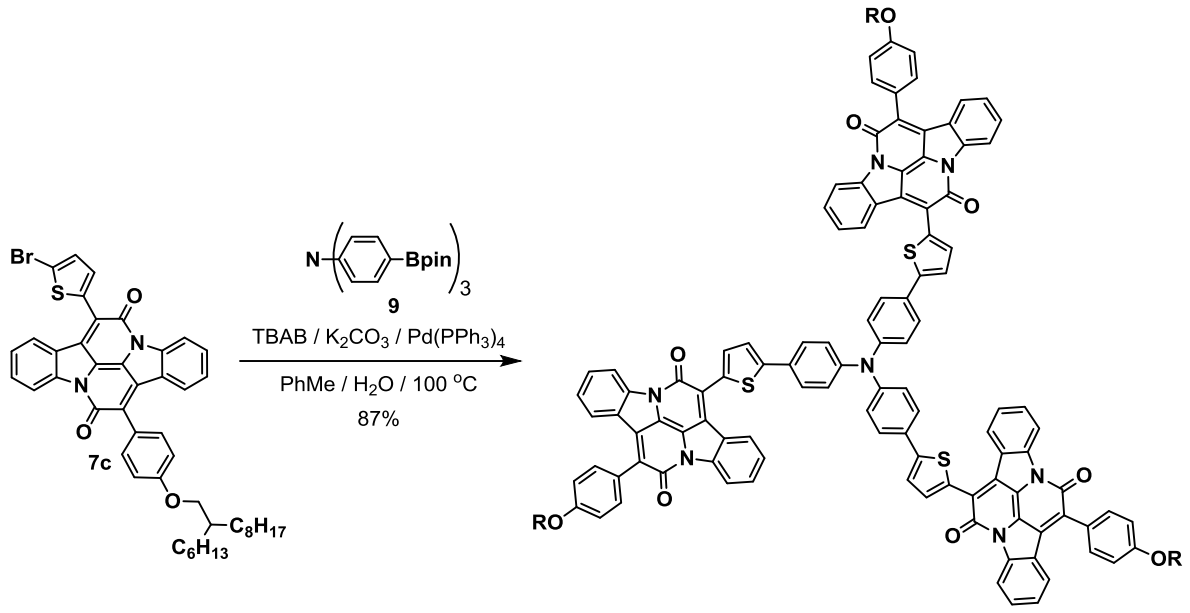

12 R = 2-hexyldecyl

12 14,14',14''-((nitrilotris(benzene-4,1-diyl))tris(thiophene-5,2-diyl))tris(7-(4-((2-hexyldecyl)oxy)phenyl)-BAI[30]

Bromide **7c** (87 mg, 0.11 mmol, 3.5 equiv), **9** (20 mg, 0.031 mmol, 1 equiv), tetrabutylammonium bromide (735 mg, 0.11 mmol, 3.3 equiv.), and potassium carbonate (40 mg, 0.29 mmol, 9 equiv) were added to a vial with a stir bar and diluted with toluene (2.5 mL) and water (0.145 mL). To this vial was degassed by bubbling nitrogen while stirring for 10 minutes. Palladium tetrakistriphenylphosophine (5.5 mg, 0.005 mmol, 0.15 equiv) was dissolved in toluene and transferred to the vial which was degassed for an additional 10 minutes. A septa cap was added, the N_2 line was removed, and the vial was placed in a 100 ^oC bath overnight. Upon completion as monitored by TLC, the mixture was diluted in $CHCl_3$, washed with water and brine, and dried with $MgSO_4$. The product was purified through column chromatography ($CHCl_3$ eluent) to provide a blue solid (64 mg, 0.027 mmol, 87%). Debrominated starting material **7b** was also isolated (8 mg, 0.011 mmol, 10% of the starting material). ^1H NMR (500 MHz, $CDCl_3$): δ = 8.25 (d, J = 7.9 Hz, 1H), 8.07 (t, J = 8.0 Hz, 2H), 7.63 (dd, J = 8.3, 4.1 Hz, 4H), 7.57 (dd, J = 13.9, 5.7 Hz, 2H), 7.30 (d, J = 3.7 Hz, 1H), 7.24 (t, J = 7.7 Hz, 1H), 7.19 (d, J = 8.2 Hz, 2H), 7.07 – 7.00 (m, 3H), 6.94 (q, J = 7.6, 7.1 Hz, 2H), 3.99 (d, J = 5.6 Hz, 2H), 1.89 (h, J = 6.1 Hz, 1H), 1.60 – 1.25 (m, 24H), 0.98 – 0.87 (m, 6H). ^{13}C NMR (125 MHz, $CDCl_3$): δ = 160.5, 159.1, 158.1, 148.9, 146.6, 143.8, 143.7, 134.4, 132.3, 131.7, 131.6, 131.4, 130.2, 129.7, 128.3, 127.3, 126.0, 125.9, 125.6, 125.6, 125.2, 124.9, 124.7, 124.5, 122.4, 121.7, 121.1, 117.6, 117.4, 116.9, 116.9, 116.8, 115.3, 114.6, 71.6, 38.4, 32.1, 32.1, 31.8, 30.3, 30.0, 29.9, 29.6, 27.2, 27.2, 22.9, 22.9, 14.3, 14.2. HRMS (MALDI-TOF) $[M+H]^+$ calculated: 2365.0965, found: 2365.1228.

Methanol Quench Test

To determine completion of acid chloride reactions to form products **3c**, **3d**, **3e**, **3f** the following procedure was utilized. A small aliquot of the reaction mixture was removed via syringe and injected directly into a vial containing methanol, quantitatively reforming the methyl ester. The resulting solution was spotted against the starting acid (**S-3c**, **S-3d**, **S-3e**, **S-3f**) and the methyl ester precursors (**S-2d**, **S-2e**, **S-2f**) respectively to determine reaction completion. Upon complete conversion from the acid to the methyl ester the reactions were carried forward.

2.13 References

[1] a) A. Facchetti, *Nat. Mater.* **2013**, *12*, 598; b) T. W. Kelley, P. F. Baude, C. Gerlach, D. E. Ender, D. Muyres, M. A. Haase, D. E. Vogel, S. D. Theiss, *Chem. Mater.* **2004**, *16*, 4413-4422.

[2] a) K. Takimiya, I. Osaka, M. Nakano, *Chem. Mater.* **2014**, *26*, 587-593; b) Z. G. Zhang, J. Wang, *J. Mater. Chem.* **2012**, *22*, 4178-4187; c) P. M. Beaujuge, J. M. J. Fréchet, *J. Am. Chem. Soc.* **2011**, *133*, 20009-20029; d) Y. Lin, X. Zhan, *Acc. Chem. Res.* **2016**, *49*, 175-183.

[3] a) L. Dou, J. Gao, E. Richard, J. You, C.-C. Chen, K. C. Cha, Y. He, G. Li, Y. Yang, *J. Am. Chem. Soc.* **2012**, *134*, 10071-10079; b) J. C. Bijleveld, A. P. Zoombelt, S. G. J. Mathijssen, M. M. Wienk, M. Turbiez, D. M. de Leeuw, R. A. J. Janssen, *J. Am. Chem. Soc.* **2009**, *131*, 16616-16617.

[4] a) W. Cui, J. Yuen, F. Wudl, *Macromolecules* **2011**, *44*, 7869-7873; b) S. M. McAfee, J. M. Topple, J.-P. Sun, I. G. Hill, G. C. Welch, *RSC Adv.* **2015**, *5*, 80098-80109.

[5] M. A. Kolaczkowski, Y. Liu, *Chem Rec.* **2019**, *19*, 1062-1077.

[6] E. Steingruber, in *Ullmann's Encyclopedia of Industrial Chemistry*, Wiley-VCH Verlag GmbH & Co. KGaA, **2000**.

[7] S. Yamazaki, A. L. Sobolewski, W. Domcke, *Phys. Chem. Chem. Phys.* **2011**, *13*, 1618-1628.

[8] a) M. Irimia-Vladu, E. D. Głowacki, P. A. Troshin, G. Schwabegger, L. Leonat, D. K. Susarova, O. Krystal, M. Ullah, Y. Kanbur, M. A. Bodea, V. F. Razumov, H. Sitter, S. Bauer, N. S. Sariciftci, *Adv. Mater.* **2012**, *24*, 375-380; b) C. Guo, J. Quinn, B. Sun, Y. Li, *J. Mater. Chem. C,* **2015**, *3*, 5226-5232.

[9] a) G. Engi, *Angewandte Chemie* **1914**, *27*, 144-148; b) T. Posner, E. Wallis, *Berichte der deutschen chemischen Gesellschaft (A and B Series)* **1924**, *57*, 1673-1681; c) C. Simon, in *The Chemical Industry in Europe, 1850–1914: Industrial Growth, Pollution, and Professionalization* (Eds.: E. Homburg, A. S. Travis, H. G. Schröter), Springer Netherlands, Dordrecht, **1998**, pp. 9-27; d) J. Seixas de Melo, R. Rondão, H. D. Burrows, M. J. Melo, S. Navaratnam, R. Edge, G. Voss, *J. Phys. Chem. A,* **2006**, *110*, 13653-13661.

[10] B. He, A. B. Pun, D. Zherebetskyy, Y. Liu, F. Liu, L. M. Klivansky, A. M. McGough, B. A. Zhang, K. Lo, T. P. Russell, L. Wang, Y. Liu, *J. Am. Chem. Soc.* **2014**, *136*, 15093-15101.

[11] a) W. Chen, J. Zhang, G. Long, Y. Liu, Q. Zhang, *J. Mater. Chem. C* **2015**, *3*, 8219-8224; b) K. Tambara, N. Ponnuswamy, G. Hennrich, G. D. Pantoş, *J. Org. Chem.* **2011**, *76*, 3338-3347; c) Y. Che, A. Datar, K. Balakrishnan, L. Zang, *J. Am. Chem. Soc.* **2007**, *129*, 7234-7235.

[12] a) S. R. Oakley, G. Nawn, K. M. Waldie, T. D. MacInnis, B. O. Patrick, R. G. Hicks, *Chem. Commun.* **2010**, *46*, 6753-6755; b) G. Nawn, S. R. Oakley, M. B. Majewski, R. McDonald, B. O. Patrick, R. G. Hicks, *Chemical Science* **2013**, *4*, 612-621; c) G. Nawn, K. M. Waldie, S. R. Oakley, B. D. Peters, D. Mandel, B. O. Patrick, R. McDonald, R. G. Hicks, *Inorganic Chemistry* **2011**, *50*, 9826-9837; d) P. Mondal, A. Das, G. K. Lahiri, *Inorganic Chemistry* **2016**, *55*, 1208-1218.

[13] M. Sytnyk, E. D. Głowacki, S. Yakunin, G. Voss, W. Schöfberger, D. Kriegner, J. Stangl, R. Trotta, C. Gollner, S. Tollabimazraehno, G. Romanazzi, Z. Bozkurt, M. Havlicek, N. S. Sariciftci, W. Heiss, *J. Am. Chem. Soc.* **2014**, *136*, 16522-16532.

[14] J. H. Porada, J.-M. Neudörfl, D. Blunk, *New Journal of Chemistry* **2015**, *39*, 8291-8301.

[15] M. A. Kolaczkowski, B. He, Y. Liu, *Org. Lett.* **2016**, *18*, 5224-5227.
[16] D. R. Talham, T. Yamamoto, M. W. Meisel, *J. Phys. Condens. Matter* **2008**, *20*, 184006.
[17] A. T. Haedler, K. Kreger, A. Issac, B. Wittmann, M. Kivala, N. Hammer, J. Köhler, H.-W. Schmidt, R. Hildner, *Nature* **2015**, *523*, 196.
[18] C. Guo, B. Sun, J. Quinn, Z. Yan, Y. Li, *J. Mater. Chem. C* **2014**, *2*, 4289-4296.
[19] B. He, D. Zherebetskyy, H. Wang, M. A. Kolaczkowski, L. M. Klivansky, T. Tan, L. Wang, Y. Liu, *Chemical Science* **2016**, *7*, 3857-3861.
[20] K. J. Fallon, N. Wijeyasinghe, E. F. Manley, S. D. Dimitrov, S. A. Yousaf, R. S. Ashraf, W. Duffy, A. A. Y. Guilbert, D. M. E. Freeman, M. Al-Hashimi, J. Nelson, J. R. Durrant, L. X. Chen, I. McCulloch, T. J. Marks, T. M. Clarke, T. D. Anthopoulos, H. Bronstein, *Chem. Mater.* **2016**, *28*, 8366-8378.
[21] K. J. Fallon, A. Santala, N. Wijeyasinghe, E. F. Manley, N. Goodeal, A. Leventis, D. M. E. Freeman, M. Al-Hashimi, L. X. Chen, T. J. Marks, T. D. Anthopoulos, H. Bronstein, *Adv. Funct. Mater.* **2017**, *27*, 1704069.
[22] Y. Lin, J. Wang, Z.-G. Zhang, H. Bai, Y. Li, D. Zhu, X. Zhan, *Adv. Mater.* **2015**, *27*, 1170-1174.
[23] J. S. Binkley, J. A. Pople, W. J. Hehre, *J. Am. Chem. Soc.* **1980**, *102*, 939-947.
[24] J. Kim, J. Lee, W. Y. Kim, H. Kim, S. Lee, H. C. Lee, Y. S. Lee, M. Seo, S. Y. Kim, *Nat. Commun.* **2015**, *6*, 6959.
[25] a) L. Lei, *Molecular Crystals and Liquid Crystals* **1987**, *146*, 41-54; b) L. Wang, D. Huang, L. Lam, Z. Cheng, *Liquid Crystals Today* **2017**, *26*, 85-111; c) B. Xu, T. M. Swager, *J. Am. Chem. Soc.* **1993**, *115*, 1159-1160.
[26] I. Nyrkova, E. Moulin, J. J. Armao, M. Maaloum, B. Heinrich, M. Rawiso, F. Niess, J.-J. Cid, N. Jouault, E. Buhler, A. N. Semenov, N. Giuseppone, *ACS Nano* **2014**, *8*, 10111-10124.
[27] P. Agarwala, D. Kabra, *J. Mater. Chem. A* **2017**, *5*, 1348-1373.
[28] L. Wenfeng, M. Hengchang, L. Ziqiang, *RSC Adv.* **2014**, *4*, 39351-39358.
[29] M. Sonntag, K. Kreger, D. Hanft, P. Strohriegl, S. Setayesh, D. de Leeuw, *Chem. Mater.* **2005**, *17*, 3031-3039.
[30] Y. Yang, Y. Zhou, Q. He, C. He, C. Yang, F. Bai, Y. Li, *J. Phys. Chem. B* **2009**, *113*, 7745-7752.
[31] a) Y. Lin, Y. Wang, J. Wang, J. Hou, Y. Li, D. Zhu, X. Zhan, *Adv. Mater.* **2014**, *26*, 5137-5142; b) D. Sahu, C.-H. Tsai, H.-Y. Wei, K.-C. Ho, F.-C. Chang, C.-W. Chu, *J. Mater. Chem.* **2012**, *22*, 7945-7953.
[32] J. J. Armao, Y. Domoto, T. Umehara, M. Maaloum, C. Contal, G. Fuks, E. Moulin, G. Decher, N. Javahiraly, N. Giuseppone, *ACS Nano* **2016**, *10*, 2082-2090.
[33] L. Guo, K. F. Li, M. S. Wong, K. W. Cheah, *Chem. Commun.* **2013**, *49*, 3597-3599.
[34] F. Chen, X. Fu, J. Zhang, X. Wan, *Electrochimica Acta* **2013**, *99*, 211-218.
[35] E. Kozma, D. Kotowski, F. Bertini, S. Luzzati, M. Catellani, *Polymer* **2010**, *51*, 2264-2270.
[36] H.-K. Jeong, H. Kikuchi, T. Kajiyama, *Polym. J.* **1999**, *31*, 974-978.
[37] L. Qiu, X. Wang, W. H. Lee, J. A. Lim, J. S. Kim, D. Kwak, K. Cho, *Chem. Mater.* **2009**, *21*, 4380-4386.
[38] T. A. Witten, L. M. Sander, *Physical Review Letters* **1981**, *47*, 1400-1403.
[39] a) Z. M. Beiley, E. T. Hoke, R. Noriega, J. Dacuña, G. F. Burkhard, J. A. Bartelt, A. Salleo, M. F. Toney, M. D. McGehee, *Adv. Energy Mater.* **2011**, *1*, 954-962; b) A. Rose, *Phys. Rev.* **1955**, *97*, 1538-1544.
[40] M. Roders, M. A. Kolaczkowski, W. R. Hollingsworth, R. Seban, Y. Liu, A. L. Ayzner, *J. Phys. Chem. C* **2019**, *123*, 27305-27316.
[41] a) Y. Yang, H. Pei, G. Chen, K. T. Webb, L. J. Martinez-Miranda, I. K. Lloyd, Z. Lu, K. Liu, Z. Nie, *Science Advances* **2018**, *4*, eaas8829; b) R. Achten, A. Koudijs, Z. Karczmarzyk, A. T. M. Marcelis, E. J. R. SudhÖLter, *Liquid Crystals* **2004**, *31*, 215-227; c) E. Gorecka, D. Pociecha, J. Mieczkowski, J. Matraszek, D. Guillon, B. Donnio, *J. Am. Chem. Soc.* **2004**, *126*, 15946-15947; d) J. Szydlowska, J. Mieczkowski, J. Matraszek, D. W. Bruce, E. Gorecka, D. Pociecha, D. Guillon, *Phys. Rev. E* **2003**, *67*, 031702.

[42] a) A. J. Heeger, *Adv. Mater.* **2014**, *26*, 10-28; b) F. C. Krebs, N. Espinosa, M. Hösel, R. R. Søndergaard, M. Jørgensen, *Adv. Mater.* **2014**, *26*, 29-39; c) G. Li, V. Shrotriya, J. Huang, Y. Yao, T. Moriarty, K. Emery, Y. Yang, *Nat. Mater.* **2005**, *4*, 864-868.

[43] a) S.-H. Bae, H. Zhao, Y.-T. Hsieh, L. Zuo, N. De Marco, You S. Rim, G. Li, Y. Yang, *Chem* **2016**, *1*, 197-219; b) S. Berny, N. Blouin, A. Distler, H.-J. Egelhaaf, M. Krompiec, A. Lohr, O. R. Lozman, G. E. Morse, L. Nanson, A. Pron, T. Sauermann, N. Seidler, S. Tierney, P. Tiwana, M. Wagner, H. Wilson, *Adv. Sci.* **2016**, *3*, 1500342; c) Z. Ding, V. Stoichkov, M. Horie, E. Brousseau, J. Kettle, *Sol. Energy Mater. Sol. Cells* **2016**, *157*, 305-311; d) V. Shrotriya, *Nat. Photonics* **2009**, *3*, 447; e) M. S. B. Yang, J. Keum, D. Geohegan, K. Xiao,, *Semiconductor Materials for Solar Photovoltaic Cells*, Springer, Switzerland, **2016**.

[44] a) J. Yuan, Y. Zhang, L. Zhou, G. Zhang, H.-L. Yip, T.-K. Lau, X. Lu, C. Zhu, H. Peng, P. A. Johnson, M. Leclerc, Y. Cao, J. Ulanski, Y. Li, Y. Zou, *Joule* **2019**, *3*, 1140-1151; b) Y. Cui, H. Yao, J. Zhang, T. Zhang, Y. Wang, L. Hong, K. Xian, B. Xu, S. Zhang, J. Peng, Z. Wei, F. Gao, J. Hou, *Nat. Commun.* **2019**, *10*, 2515; c) National Renewable Energy Lab, https://www.nrel.gov/pv/cell-efficiency.html, **2019**.

[45] a) P. W. M. Blom, V. D. Mihailetchi, L. J. A. Koster, D. E. Markov, *Adv. Mater.* **2007**, *19*, 1551-1566; b) K.-H. Kim, H. Kang, H. J. Kim, P. S. Kim, S. C. Yoon, B. J. Kim, *Chem. Mater.* **2012**, *24*, 2373-2381.

[46] a) S. J. Lou, J. M. Szarko, T. Xu, L. Yu, T. J. Marks, L. X. Chen, *J. Am. Chem. Soc.* **2011**, *133*, 20661-20663; b) M. Shao, J. K. Keum, R. Kumar, J. Chen, J. F. Browning, S. Das, W. Chen, J. Hou, C. Do, K. C. Littrell, A. Rondinone, D. B. Geohegan, B. G. Sumpter, K. Xiao, *Adv. Funct. Mater.* **2014**, *24*, 6647-6657.

[47] a) Q. V. Hoang, S. Rasool, S. Oh, D. Van Vu, D. H. Kim, H. K. Lee, C. E. Song, S. K. Lee, J.-C. Lee, S.-J. Moon, W. S. Shin, *J. Mater. Chem. C* **2017**, *5*, 7837-7844; b) A. M. Poe, A. M. Della Pelle, A. V. Subrahmanyam, W. White, G. Wantz, S. Thayumanavan, *Chem. Commun.* **2014**, *50*, 2913-2915; c) N. Shin, L. J. Richter, A. A. Herzing, R. J. Kline, D. M. DeLongchamp, *Adv. Energy Mater.* **2013**, *3*, 938-948.

[48] a) C. H. Y. Ho, Q. Dong, H. Yin, W. W. K. Leung, Q. Yang, H. K. H. Lee, S. W. Tsang, S. K. So, *Adv. Mater. Interfaces* **2015**, *2*, 1500166; b) J. Kniepert, I. Lange, J. Heidbrink, J. Kurpiers, T. J. K. Brenner, L. J. A. Koster, D. Neher, *J. Phys. Chem. C* **2015**, *119*, 8310-8320; c) L. A. Perez, J. T. Rogers, M. A. Brady, Y. Sun, G. C. Welch, K. Schmidt, M. F. Toney, H. Jinnai, A. J. Heeger, M. L. Chabinyc, G. C. Bazan, E. J. Kramer, *Chem. Mater.* **2014**, *26*, 6531-6541; d) Z. Xiao, Y. Yuan, B. Yang, J. VanDerslice, J. Chen, O. Dyck, G. Duscher, J. Huang, *Adv. Mater.* **2014**, *26*, 3068-3075.

[49] a) P. Cheng, X. Zhan, *Chem. Soc. Rev.* **2016**, *45*, 2544-2582; b) C. J. Schaffer, C. M. Palumbiny, M. A. Niedermeier, C. Burger, G. Santoro, S. V. Roth, P. Müller-Buschbaum, *Adv. Energy Mater.* **2016**, *6*, 1600712; c) B. J. Tremolet de Villers, K. A. O'Hara, D. P. Ostrowski, P. H. Biddle, S. E. Shaheen, M. L. Chabinyc, D. C. Olson, N. Kopidakis, *Chem. Mater.* **2016**, *28*, 876-884.

[50] a) Y. S. Chung, N. Shin, J. Kang, Y. Jo, V. M. Prabhu, S. K. Satija, R. J. Kline, D. M. DeLongchamp, M. F. Toney, M. A. Loth, B. Purushothaman, J. E. Anthony, D. Y. Yoon, *J. Am. Chem. Soc.* **2011**, *133*, 412-415; b) J. Smith, W. Zhang, R. Sougrat, K. Zhao, R. Li, D. Cha, A. Amassian, M. Heeney, I. McCulloch, T. D. Anthopoulos, *Adv. Mater.* **2012**, *24*, 2441-2446; c) Z. Wei, H. Xi, H. Dong, L. Wang, W. Xu, W. Hu, D. Zhu, *J. Mater. Chem.* **2010**, *20*, 1203-1207; d) Y. Zhang, D. Hanifi, E. Lim, S. Chourou, S. Alvarez, A. Pun, A. Hexemer, B. Ma, Y. Liu, *Adv. Mater.* **2014**, *26*, 1223-1228.

[51] a) K. R. Graham, J. Mei, R. Stalder, J. W. Shim, H. Cheun, F. Steffy, F. So, B. Kippelen, J. R. Reynolds, *ACS Appl. Mater. Interfaces* **2011**, *3*, 1210-1215; b) K. H. Park, Y. An, S. Jung, H. Park, C. Yang, *Energy Environ. Sci.* **2016**, *9*, 3464-3471.

[52] a) C. McDowell, M. Abdelsamie, M. F. Toney, G. C. Bazan, *Adv. Mater.* **2018**, *30*, 1707114; b) S. Holliday, C. K. Luscombe, *Advanced Electronic Materials* **2018**, *4*, 1700416.

[53] B. Yang, Y. Yuan, P. Sharma, S. Poddar, R. Korlacki, S. Ducharme, A. Gruverman, R. Saraf, J. Huang, *Adv. Mater.* **2012**, *24*, 1455-1460.
[54] B. Yang, M. A. Kolaczkowski, M. A. Brady, J. K. Keum, J. F. Browning, T. L. Chen, Y. Liu, *Solar RRL* **2018**, *2*, 1700208.
[55] C. B. H. S.G.Bowden, www.pveducation.org, **2019**.
[56] a) G. Nagarjuna, M. Baghgar, J. A. Labastide, D. D. Algaier, M. D. Barnes, D. Venkataraman, *ACS Nano* **2012**, *6*, 10750-10758; b) H. Yamagata, F. C. Spano, *J. Chem. Phys* **2012**, *136*, 184901; c) K. Yuan, L. Chen, Y. Chen, *J. Mater. Chem. C* **2014**, *2*, 3835-3845.
[57] Z. YE, X. ZHAO, *Journal of Microscopy* **2010**, *238*, 27-35.
[58] a) J. K. Keum, J. F. Browning, K. Xiao, M. Shao, C. E. Halbert, K. Hong, *Appl. Phys. Lett.* **2013**, *103*, 223301; b) M. Shao, J. Keum, J. Chen, Y. He, W. Chen, J. F. Browning, J. Jakowski, B. G. Sumpter, I. N. Ivanov, Y.-Z. Ma, C. M. Rouleau, S. C. Smith, D. B. Geohegan, K. Hong, K. Xiao, *Nat. Commun.* **2014**, *5*, 3180.
[59] C. H. Yi Ho, H. Cao, Y. Lu, T.-K. Lau, S. H. Cheung, H.-W. Li, H. Yin, K. L. Chiu, L.-K. Ma, Y. Cheng, S.-W. Tsang, X. Lu, S. K. So, B. S. Ong, *J. Mater. Chem. A* **2017**, *5*, 23662-23670.
[60] a) K. Kranthiraja, D. X. Long, V. G. Sree, W. Cho, Y.-R. Cho, A. Zaheer, J.-C. Lee, Y.-Y. Noh, S.-H. Jin, *Macromolecules* **2018**, *51*, 5530-5536; b) Q. Zhang, M. A. Kelly, N. Bauer, W. You, *Acc. Chem. Res.* **2017**, *50*, 2401-2409.
[61] J. Pommerehne, H. Vestweber, W. Guss, R. F. Mahrt, H. Bässler, M. Porsch, J. Daub, *Adv. Mater.* **1995**, *7*, 551-554.
[62] A. Kajetanowicz, J. Czaban, G. R. Krishnan, M. Malińska, K. Woźniak, H. Siddique, L. G. Peeva, A. G. Livingston, K. Grela, *ChemSusChem* **2013**, *6*, 182-192.
[63] V. G. H. Lafitte, A. E. Aliev, H. C. Hailes, K. Bala, P. Golding, *J. Org. Chem.* **2005**, *70*, 2701-2707.
[64] F. Zhang, S. Das, A. J. Walkinshaw, A. Casitas, M. Taylor, M. G. Suero, M. J. Gaunt, *J. Am. Chem. Soc.* **2014**, *136*, 8851-8854.
[65] J. H. Porada, J.-M. Neudorfl, D. Blunk, *New J. Chem.* **2015**, *39*, 8291-8301.

Appendix II. NMR Spectra for Compounds Discussed in Chapter 2

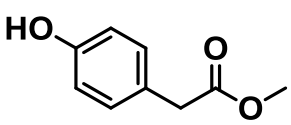

S-1

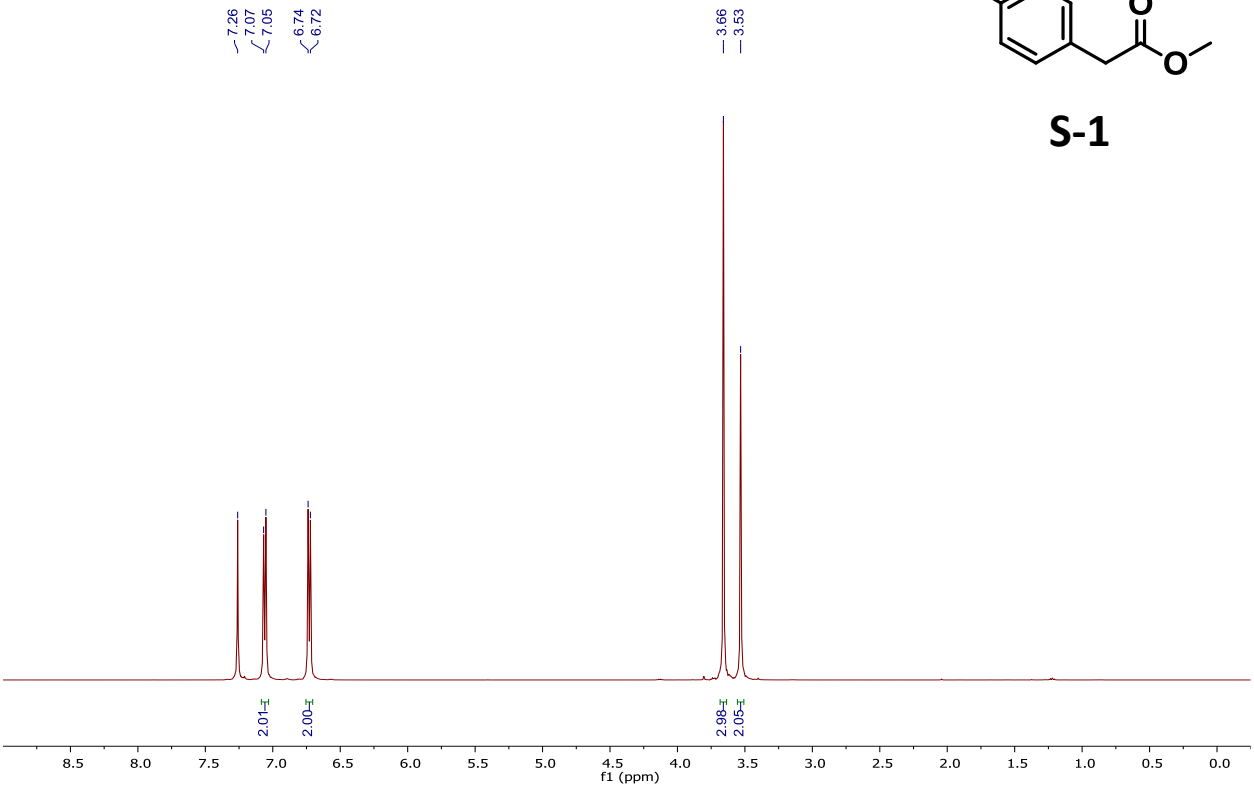

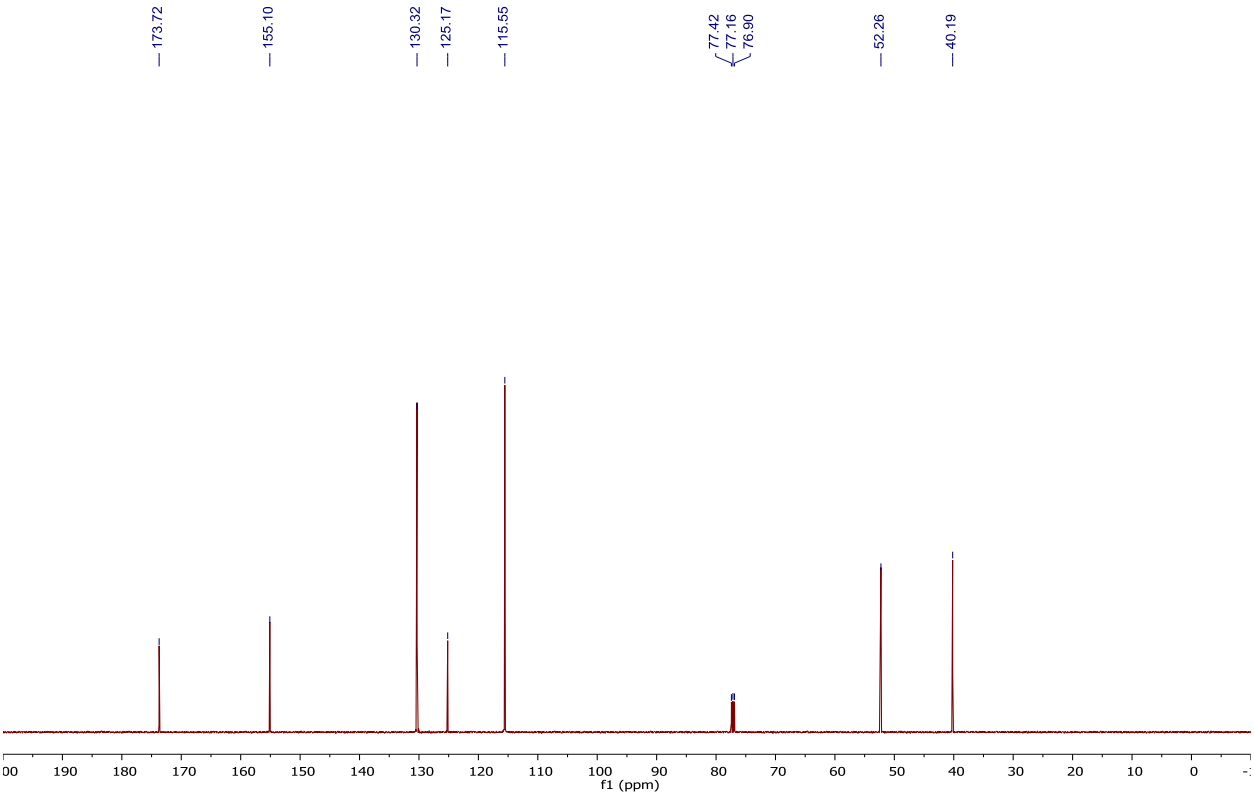


7.16
7.16
7.15
7.14
7.14
6.85
6.85
6.85
6.84
6.84
6.84
6.83
4.11
4.10
4.10
4.09
4.09
4.09
4.08
3.83
3.83
3.82
3.82
3.82
3.81
3.81
3.70
3.69
3.69
3.69
3.69
3.68
3.68
3.68
3.68
3.65
3.65
3.55
3.55
3.55
3.54
3.54
3.54
3.54
3.53
3.36
3.35

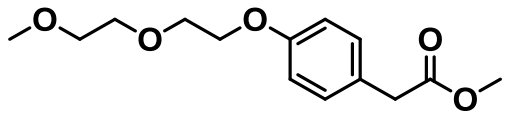

S-2f

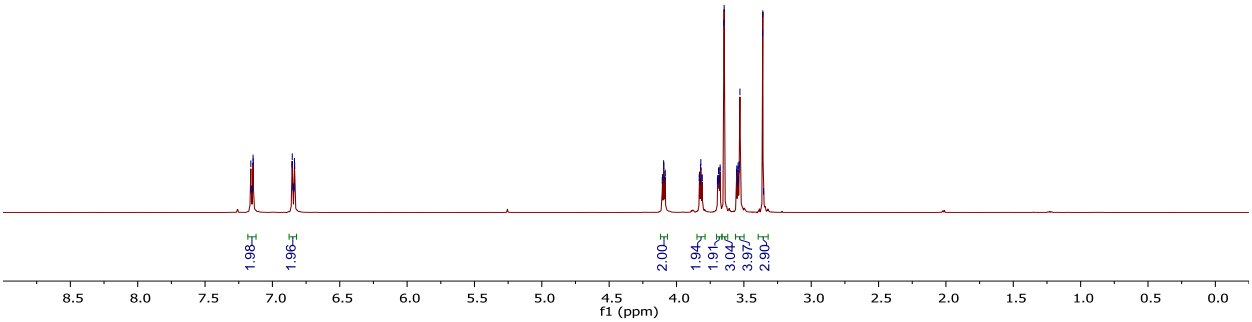
1.98
1.96
2.00
1.94
1.91
3.04
3.97
2.90
8.5
8.0
7.5
7.0
6.5
6.0
5.5
5.0
4.5
4.0
3.5
3.0
2.5
2.0
1.5
1.0
0.5
0.0
f1 (ppm)

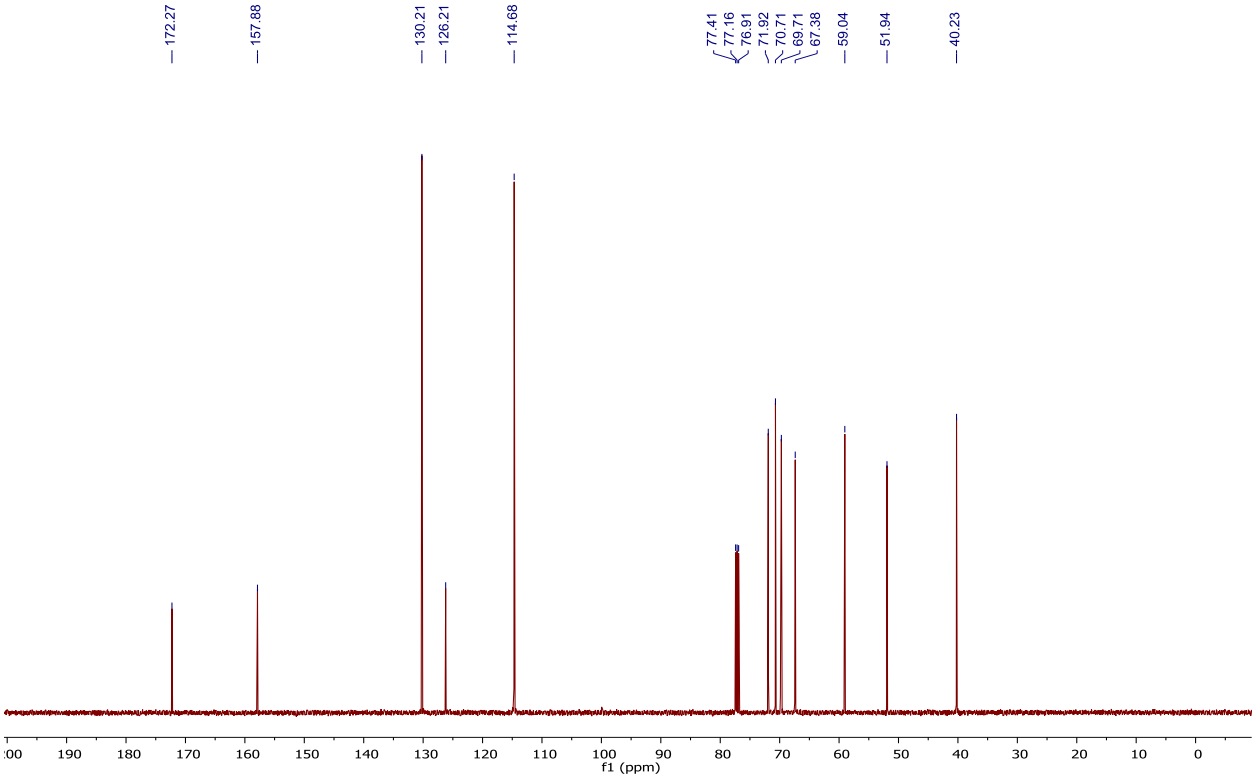
172.27
157.88
130.21
126.21
114.68
77.41
77.16
76.91
71.92
70.71
69.71
67.38
59.04
51.94
40.23
190
180
170
160
150
140
130
120
110
100
90
80
70
60
50
40
30
20
10
0
f1 (ppm)

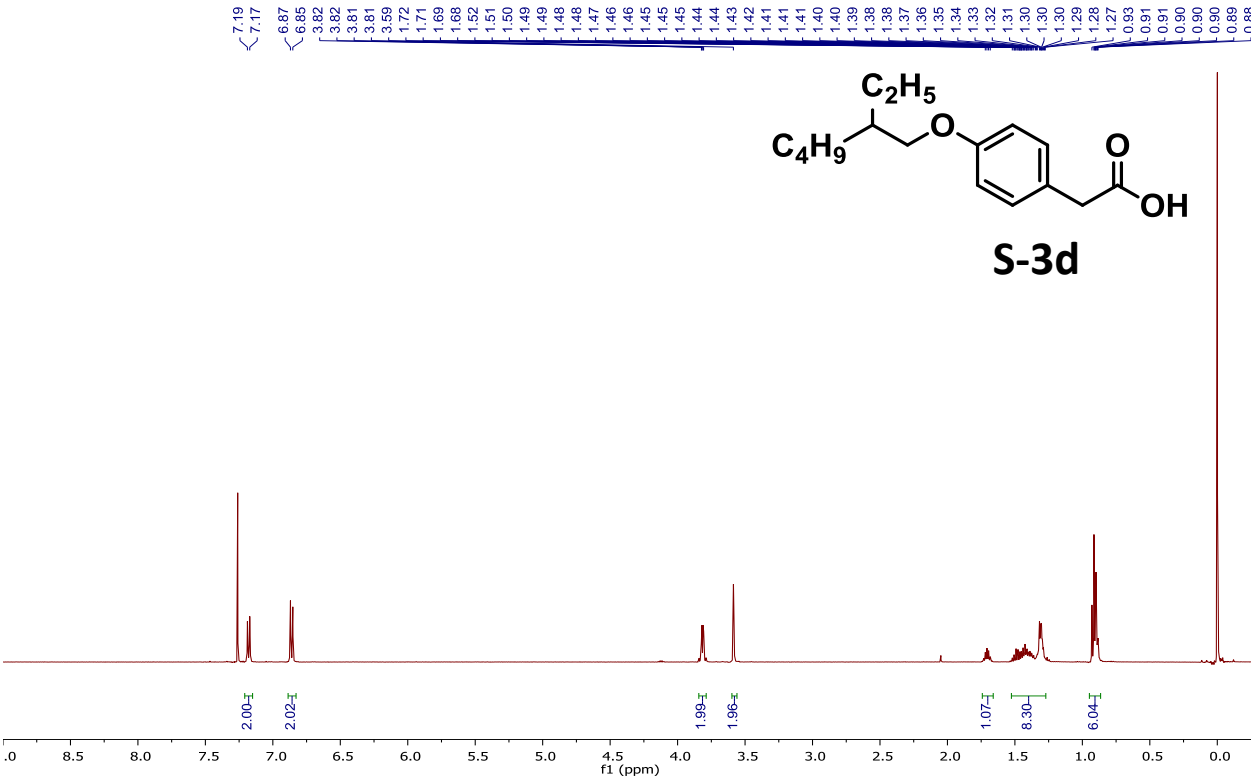
7.19
7.17
6.87
6.85
3.82
3.82
3.81
3.81
3.59
1.72
1.71
1.69
1.68
1.52
1.51
1.50
1.49
1.49
1.48
1.48
1.47
1.46
1.46
1.45
1.45
1.45
1.44
1.44
1.43
1.42
1.41
1.41
1.41
1.40
1.40
1.39
1.38
1.38
1.37
1.36
1.35
1.34
1.33
1.32
1.31
1.30
1.30
1.30
1.29
1.28
1.27
0.93
0.91
0.91
0.90
0.90
0.90
0.89
C2H5
C4H9
O
O
OH
S-3d
2.00
2.02
1.99
1.96
1.07
8.30
6.04
f1 (ppm)

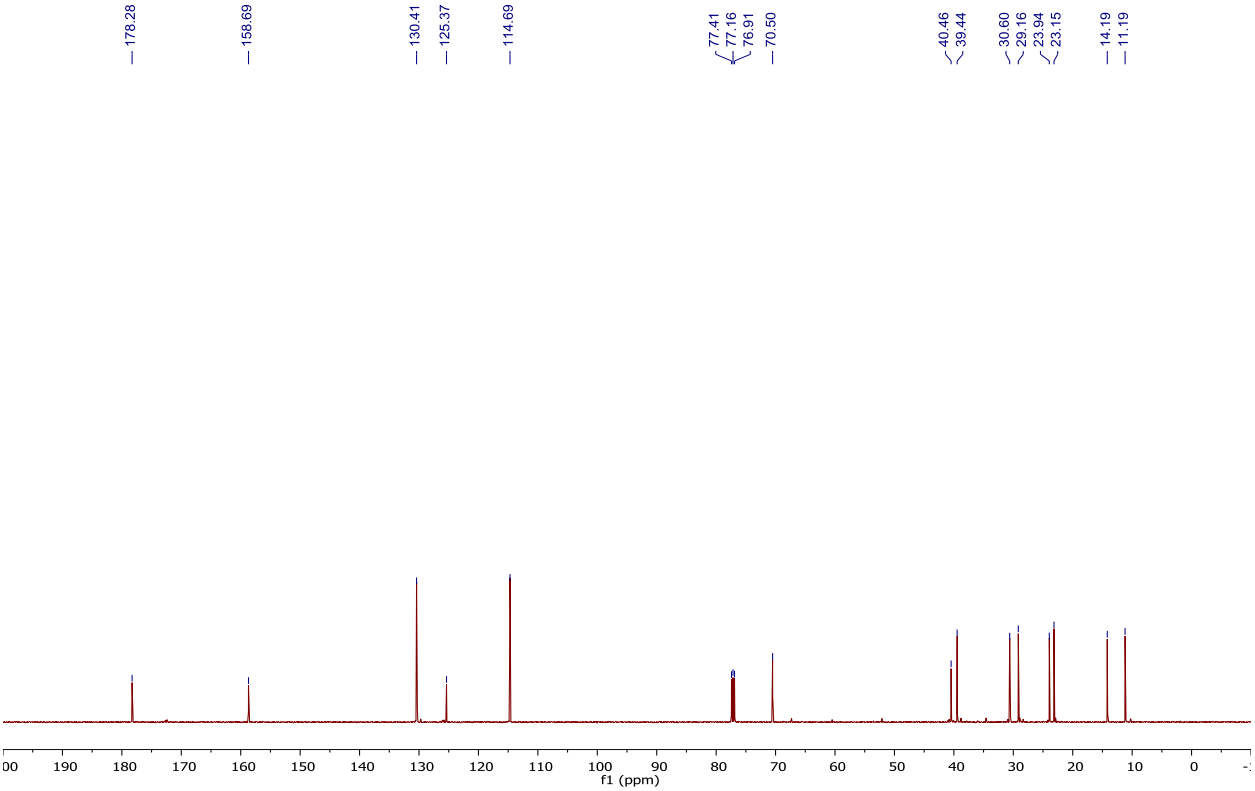
178.28
158.69
130.41
125.37
114.69
77.41
77.16
76.91
70.50
40.46
39.44
30.60
29.16
23.94
23.15
14.19
11.19
f1 (ppm)

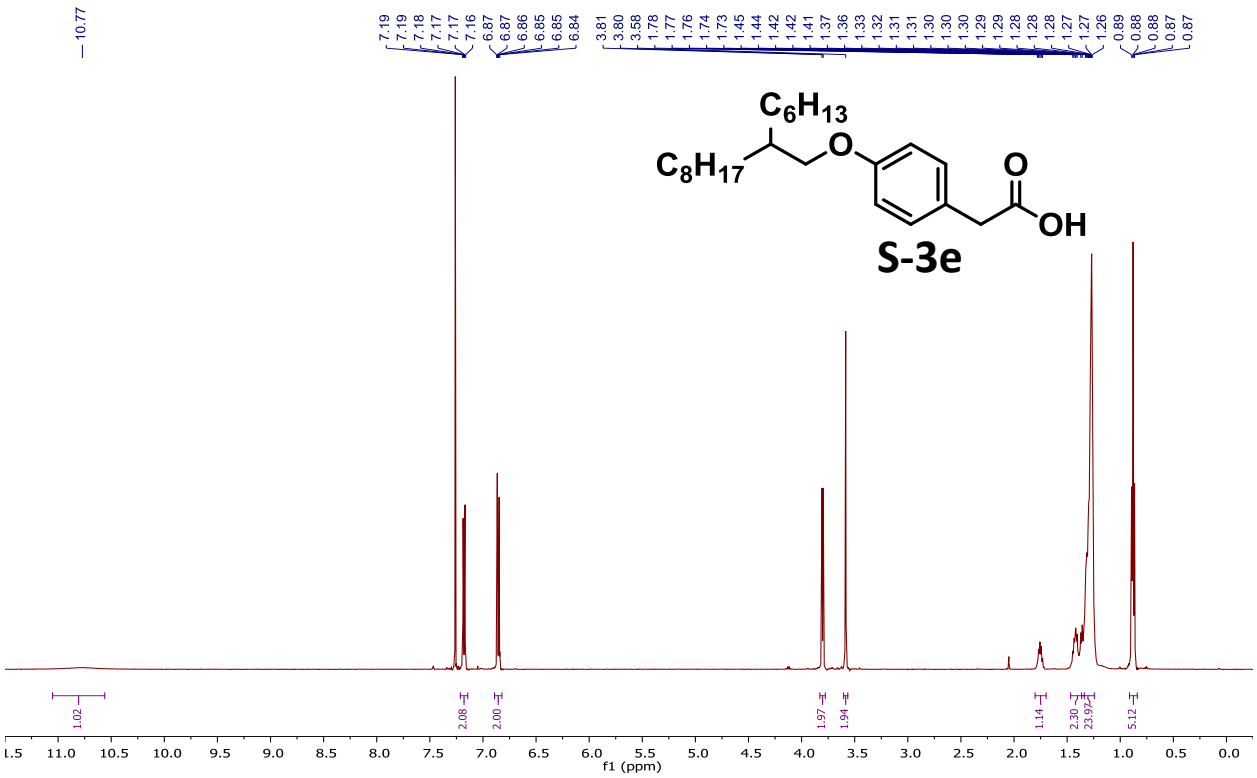
10.77
7.19
7.19
7.18
7.17
7.17
7.16
6.87
6.87
6.86
6.85
6.85
6.84
3.81
3.80
3.58
1.78
1.77
1.76
1.74
1.73
1.45
1.44
1.42
1.42
1.41
1.37
1.36
1.33
1.32
1.31
1.31
1.30
1.30
1.29
1.29
1.28
1.28
1.28
1.27
1.27
1.26
0.89
0.88
0.88
0.87
0.87
C6H13
C8H17
O
O
OH
S-3e
1.02
2.08
2.00
1.97
1.94
1.14
2.30
23.97
5.12
f1 (ppm)

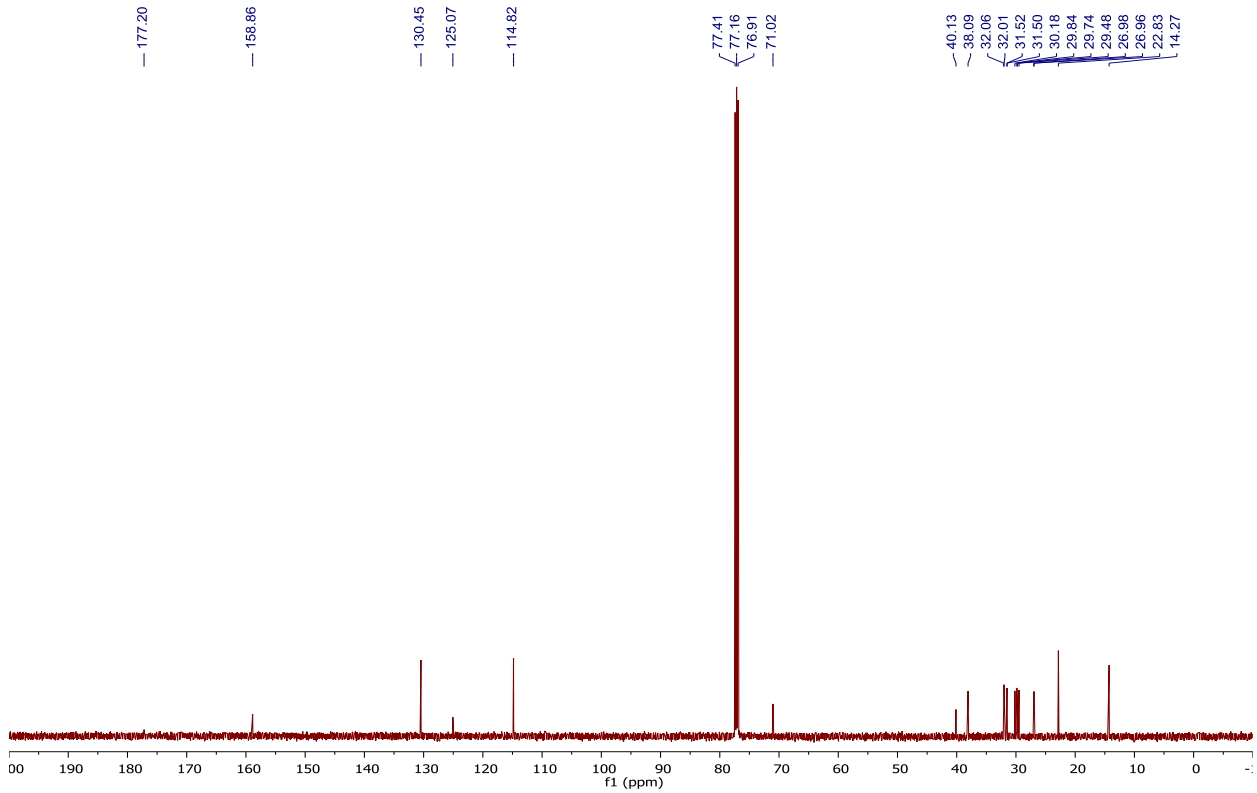
177.20
158.86
130.45
125.07
114.82
77.41
77.16
76.91
71.02
40.13
38.09
32.06
32.01
31.52
31.50
30.18
29.84
29.74
29.48
26.98
26.96
22.83
14.27
f1 (ppm)

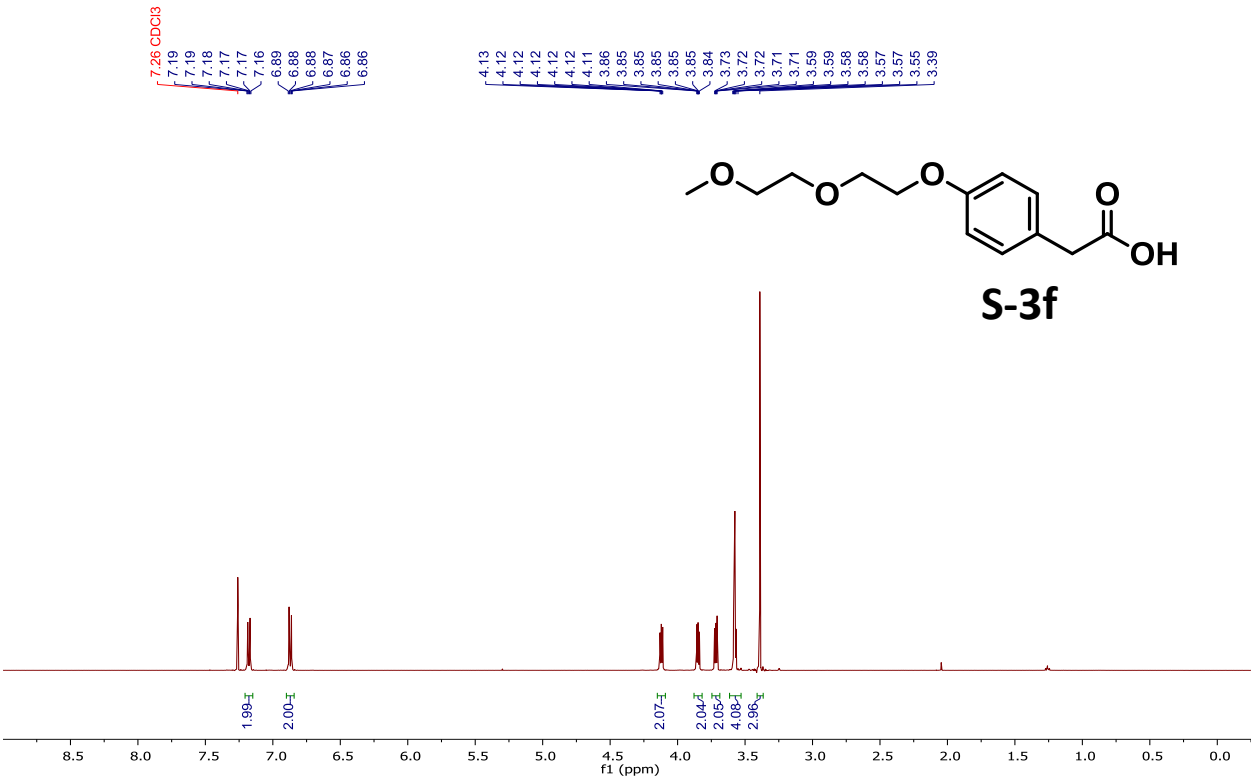
7.26 CDCl3
7.19
7.19
7.18
7.17
7.17
7.16
6.89
6.88
6.88
6.87
6.86
6.86
4.13
4.12
4.12
4.12
4.12
4.12
4.11
3.86
3.85
3.85
3.85
3.85
3.85
3.84
3.73
3.72
3.72
3.71
3.71
3.59
3.59
3.58
3.58
3.57
3.57
3.55
3.39
O
O
O
O
OH
1.99
2.00
2.07
2.04
2.05
4.08
2.96
8.5
8.0
7.5
7.0
6.5
6.0
5.5
5.0
4.5
4.0
3.5
3.0
2.5
2.0
1.5
1.0
0.5
0.0
f1 (ppm)

S-3f

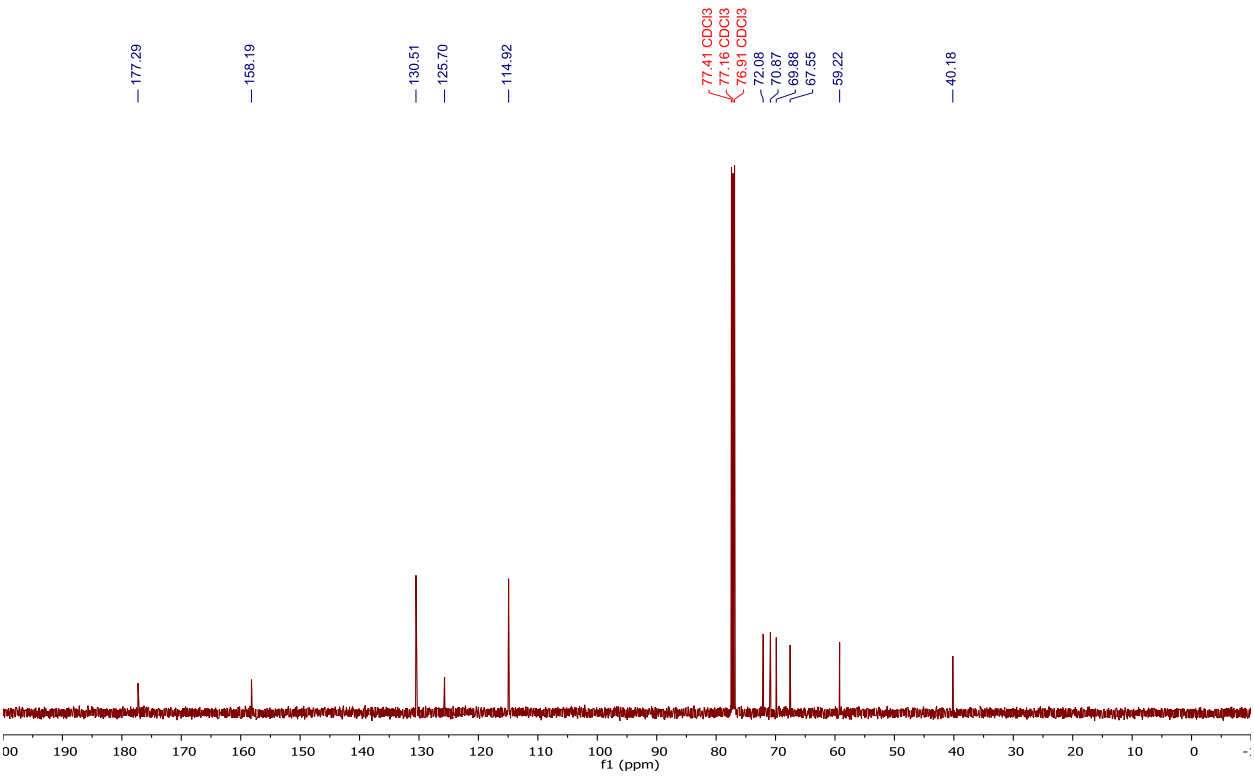
177.29
158.19
130.51
125.70
114.92
77.41 CDCl3
77.16 CDCl3
76.91 CDCl3
72.08
70.87
69.88
67.55
59.22
40.18
190
180
170
160
150
140
130
120
110
100
90
80
70
60
50
40
30
20
10
0
f1 (ppm)

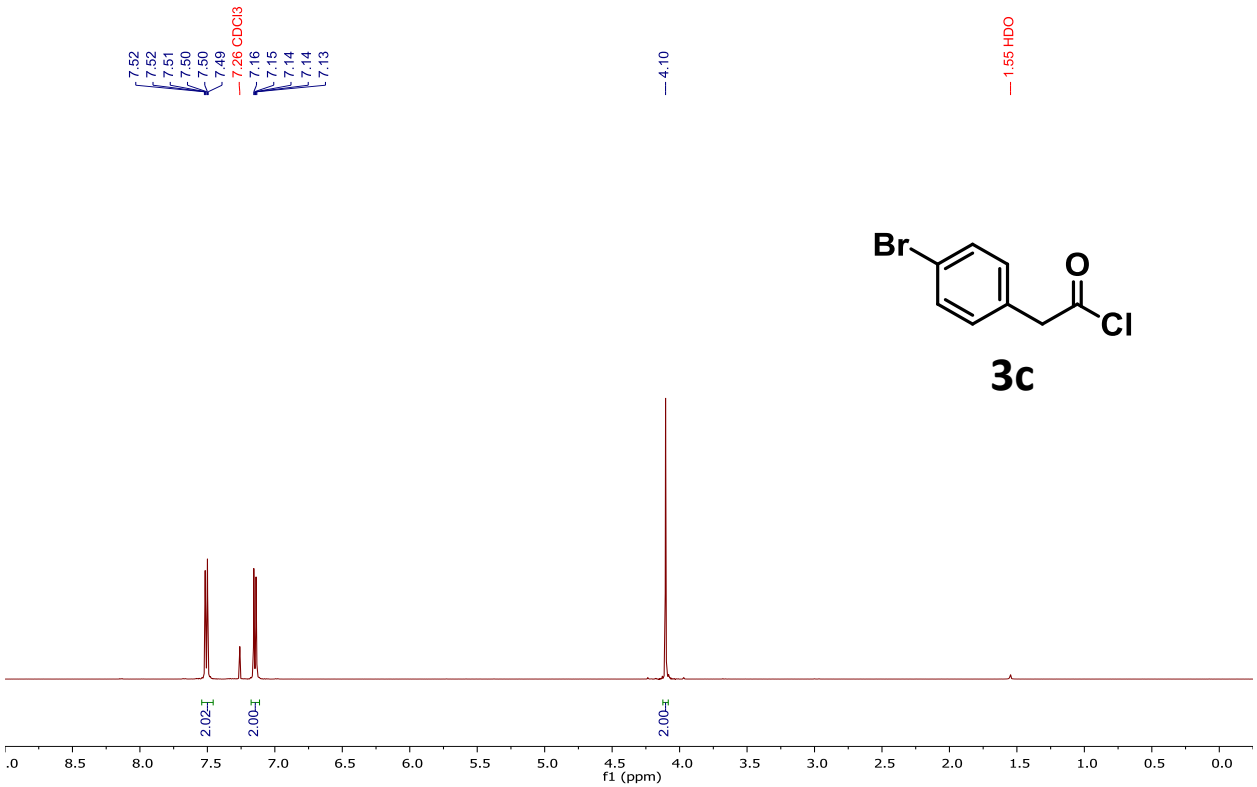
7.52
7.52
7.51
7.50
7.50
7.49
7.26 CDCl3
7.16
7.15
7.14
7.14
7.13
4.10
1.55 HDO
Br
O
Cl
3c
2.02
2.00
2.00
f1 (ppm)

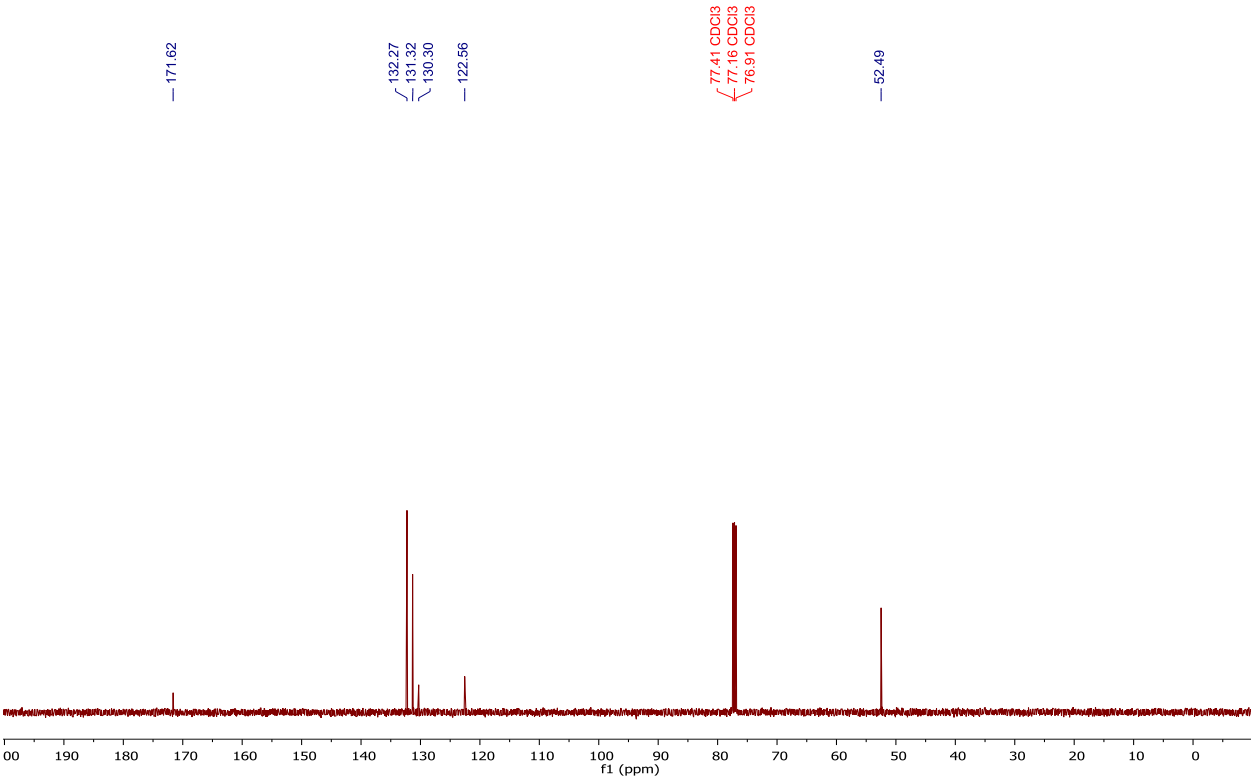
171.62
132.27
131.32
130.30
122.56
77.41 CDCl3
77.16 CDCl3
76.91 CDCl3
52.49
f1 (ppm)

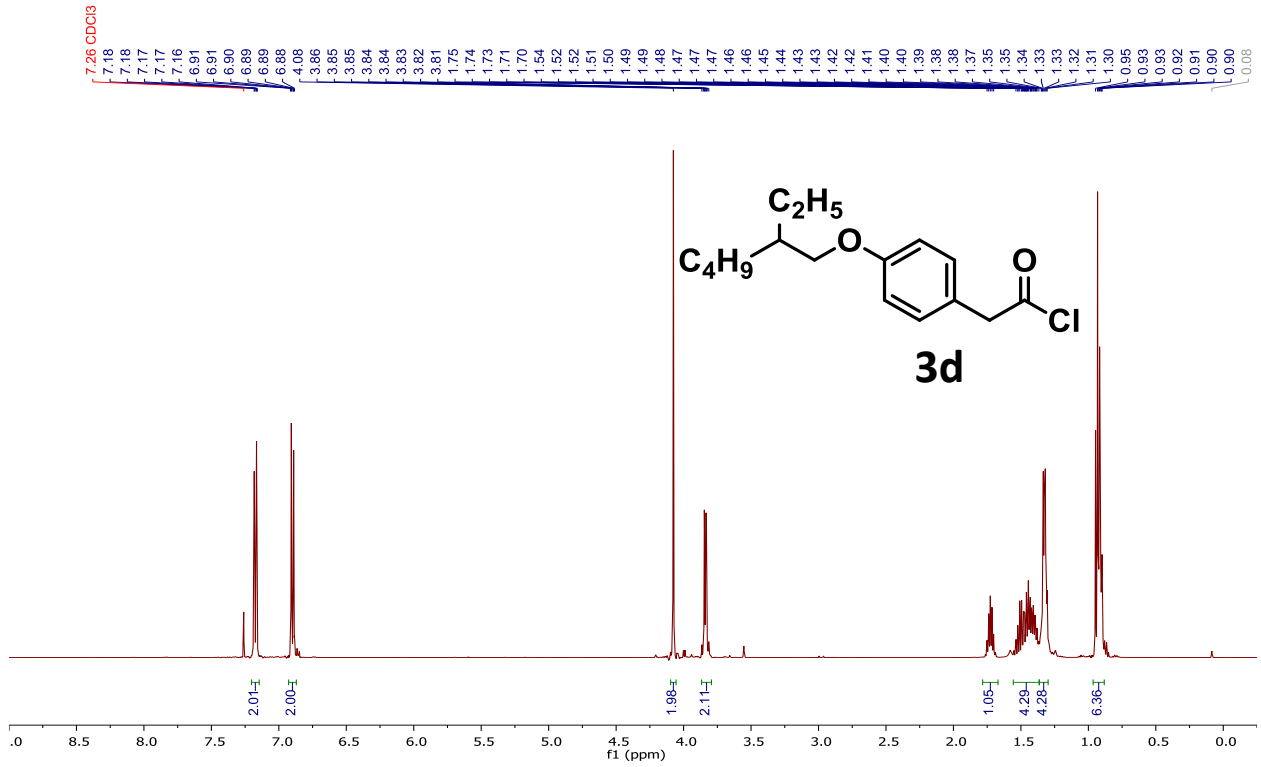
7.26 CDCl3
7.18
7.18
7.17
7.17
7.16
6.91
6.91
6.90
6.89
6.89
6.88
4.08
3.86
3.85
3.85
3.84
3.84
3.83
3.82
3.81
1.75
1.74
1.73
1.71
1.70
1.54
1.52
1.52
1.51
1.50
1.49
1.49
1.48
1.47
1.47
1.47
1.46
1.46
1.45
1.44
1.43
1.43
1.42
1.42
1.41
1.40
1.40
1.39
1.38
1.38
1.37
1.35
1.35
1.34
1.33
1.33
1.32
1.31
1.30
0.95
0.93
0.93
0.92
0.91
0.90
0.90
0.08
C2H5
C4H9
O
O
Cl
3d
2.01
2.00
1.98
2.11
1.05
4.29
4.28
6.36
f1 (ppm)

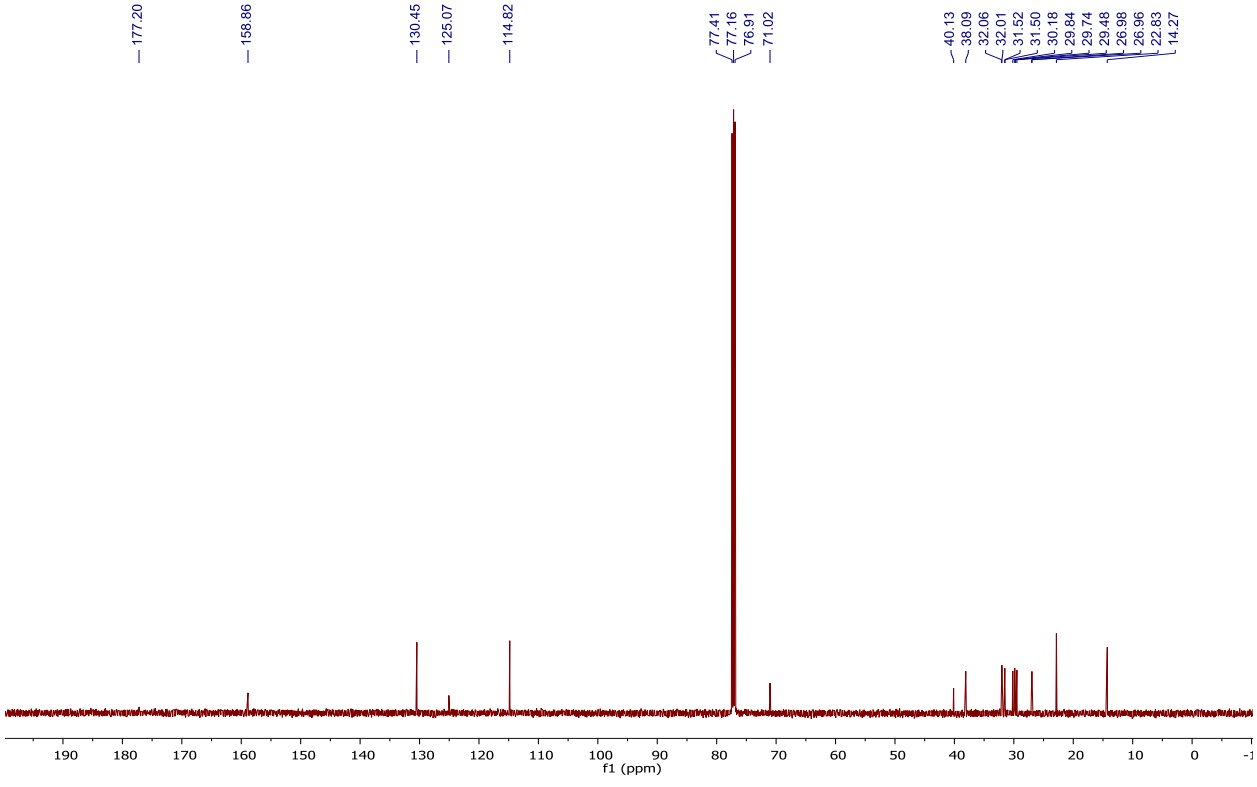
177.20
158.86
130.45
125.07
114.82
77.41
77.16
76.91
71.02
40.13
38.09
32.06
32.01
31.52
31.50
30.18
29.84
29.74
29.48
26.98
26.96
22.83
14.27
f1 (ppm)

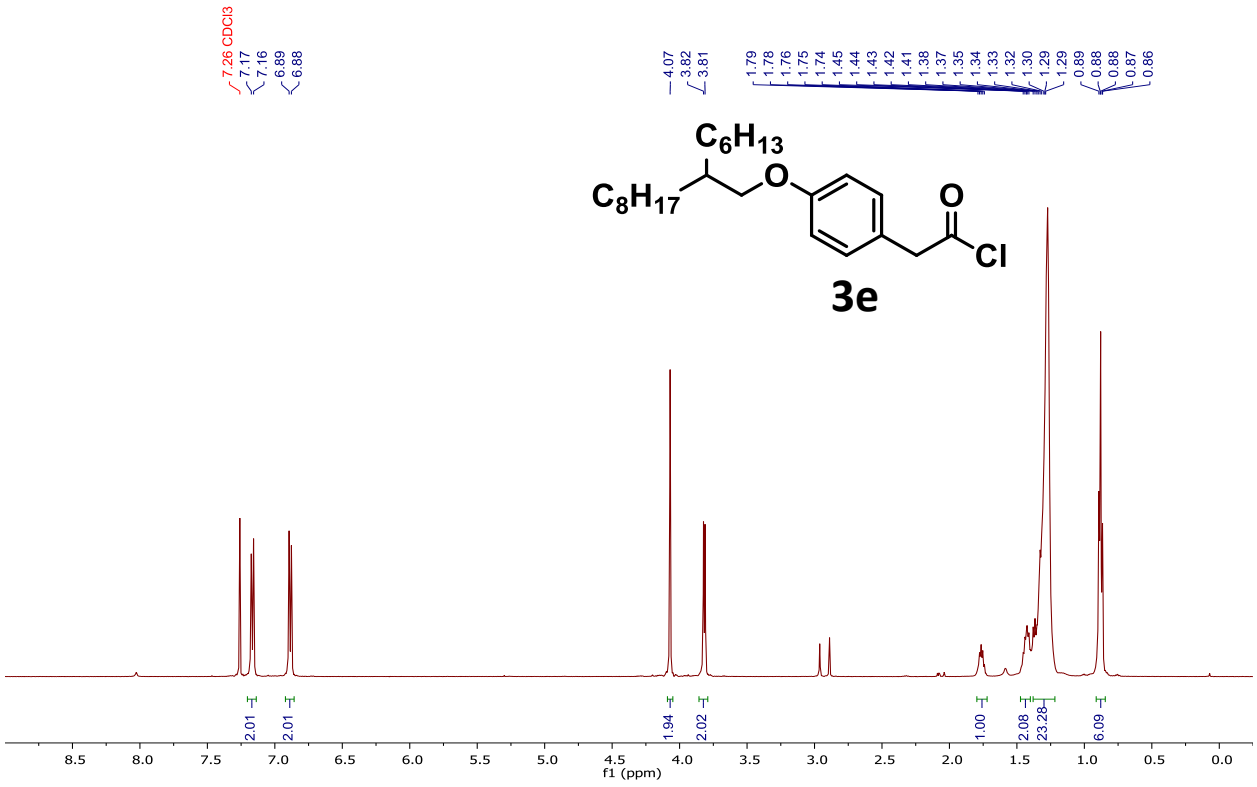
7.26 CDCl3
7.17
7.16
6.89
6.88
4.07
3.82
3.81
1.79
1.78
1.76
1.75
1.74
1.45
1.44
1.43
1.42
1.41
1.38
1.37
1.35
1.34
1.33
1.32
1.30
1.29
1.29
0.89
0.88
0.88
0.87
0.86
C6H13
C8H17
O
O
Cl
3e
2.01
2.01
1.94
2.02
1.00
2.08
23.28
6.09
f1 (ppm)

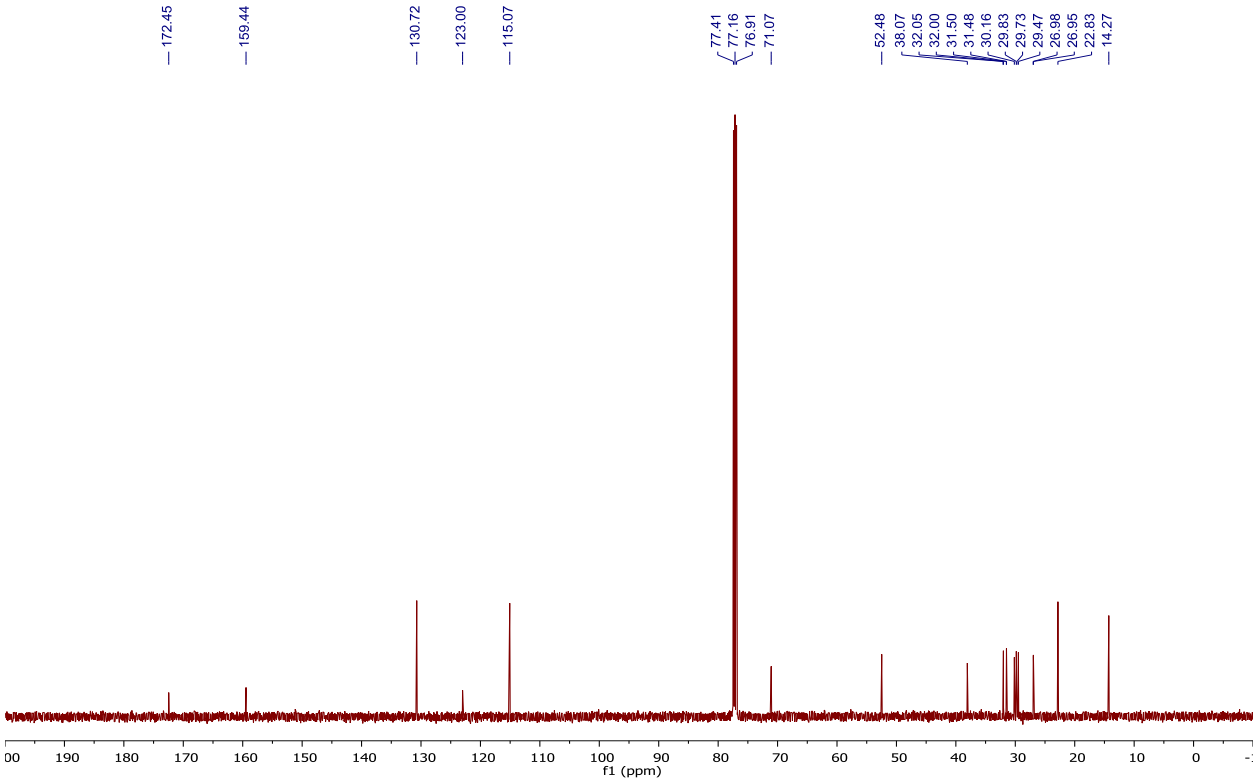
172.45
159.44
130.72
123.00
115.07
77.41
77.16
76.91
71.07
52.48
38.07
32.05
32.00
31.50
31.48
30.16
29.83
29.73
29.47
26.98
26.95
22.83
14.27
f1 (ppm)

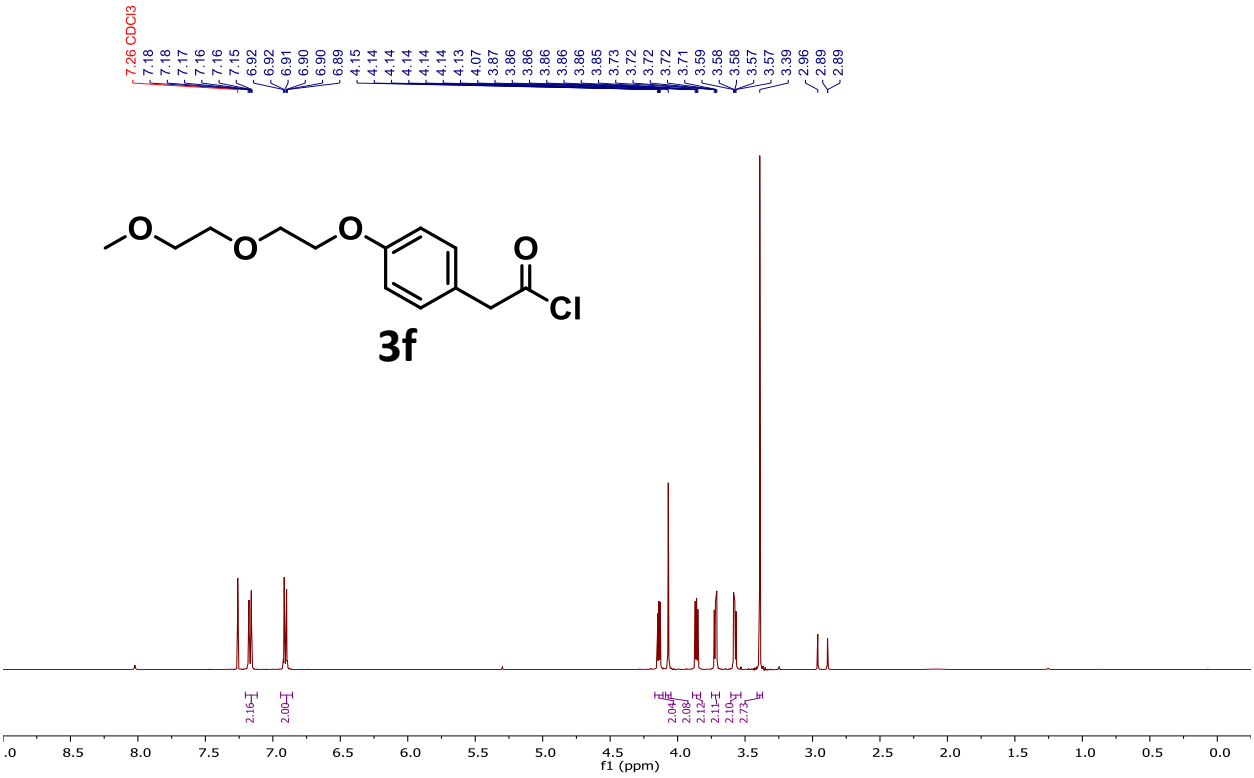
7.26 CDCl3
7.18
7.18
7.17
7.16
7.16
7.15
6.92
6.92
6.91
6.90
6.90
6.89
4.15
4.14
4.14
4.14
4.14
4.14
4.13
4.07
3.87
3.86
3.86
3.86
3.86
3.85
3.73
3.72
3.72
3.72
3.71
3.59
3.58
3.58
3.57
3.57
3.39
2.96
2.89
2.89
O
O
O
O
Cl
3f
2.16
2.00
2.04
2.08
2.12
2.11
2.10
2.73
f1 (ppm)

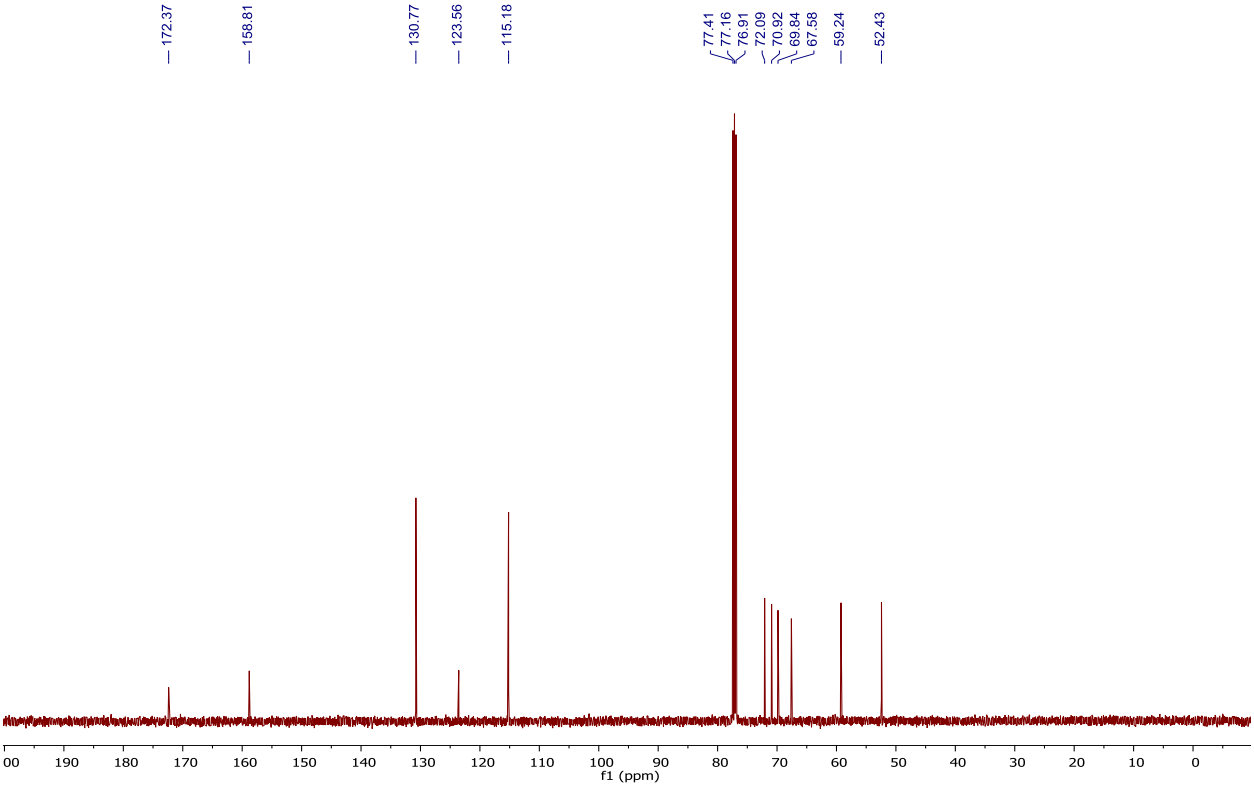
172.37
158.81
130.77
123.56
115.18
77.41
77.16
76.91
72.09
70.92
69.84
67.58
59.24
52.43
f1 (ppm)

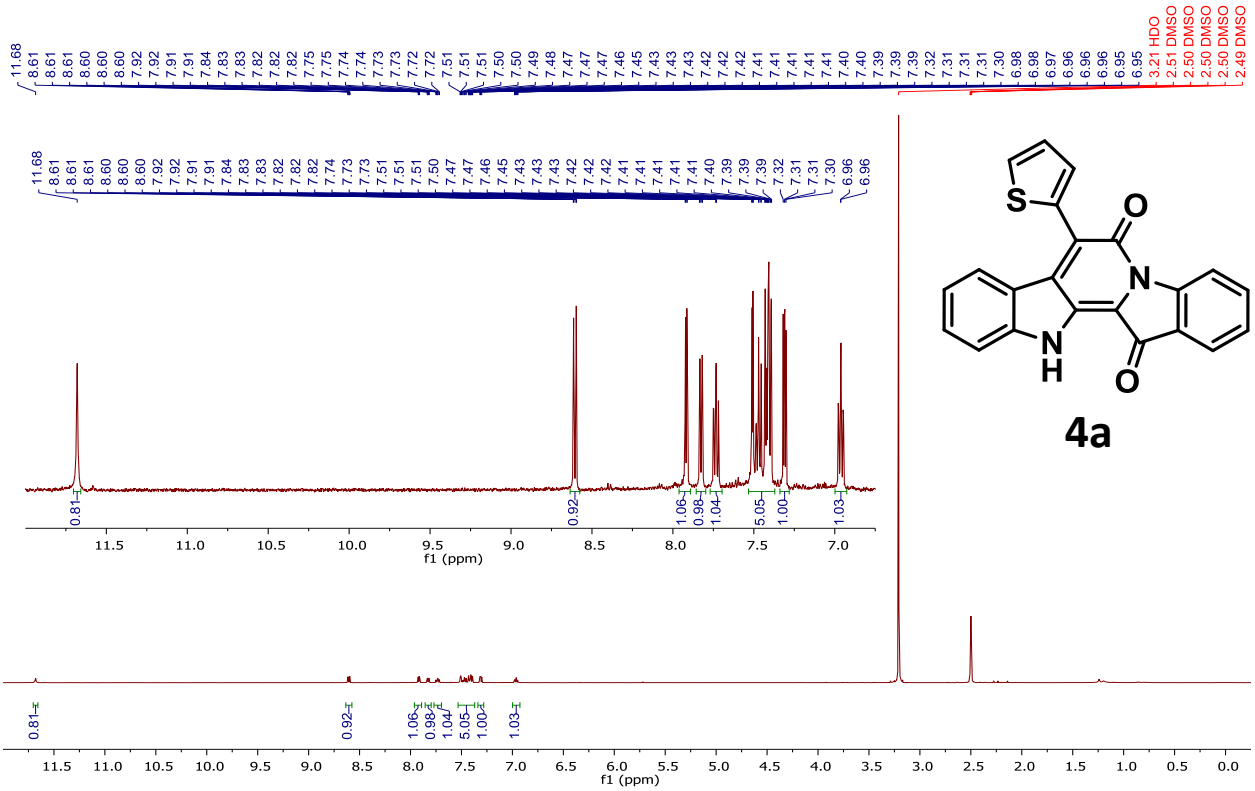
11.68 8.61 8.61 8.61 8.60 8.60 8.60 7.92 7.92 7.91 7.91 7.84 7.83 7.83 7.82 7.82 7.75 7.75 7.74 7.74 7.73 7.73 7.72 7.72 7.51 7.51 7.51 7.50 7.50 7.49 7.48 7.47 7.47 7.47 7.46 7.45 7.43 7.43 7.43 7.42 7.42 7.42 7.41 7.41 7.41 7.41 7.41 7.40 7.40 7.39 7.39 7.39 7.32 7.31 7.31 7.30 6.98 6.98 6.97 6.96 6.96 6.96 6.96 6.95 6.95 3.21 HDO 2.51 DMSO 2.50 DMSO 2.50 DMSO 2.50 DMSO 2.49 DMSO
0.81 0.92 1.06 0.98 1.04 5.05 1.00 1.03
f1 (ppm)
S O N N H O
4a

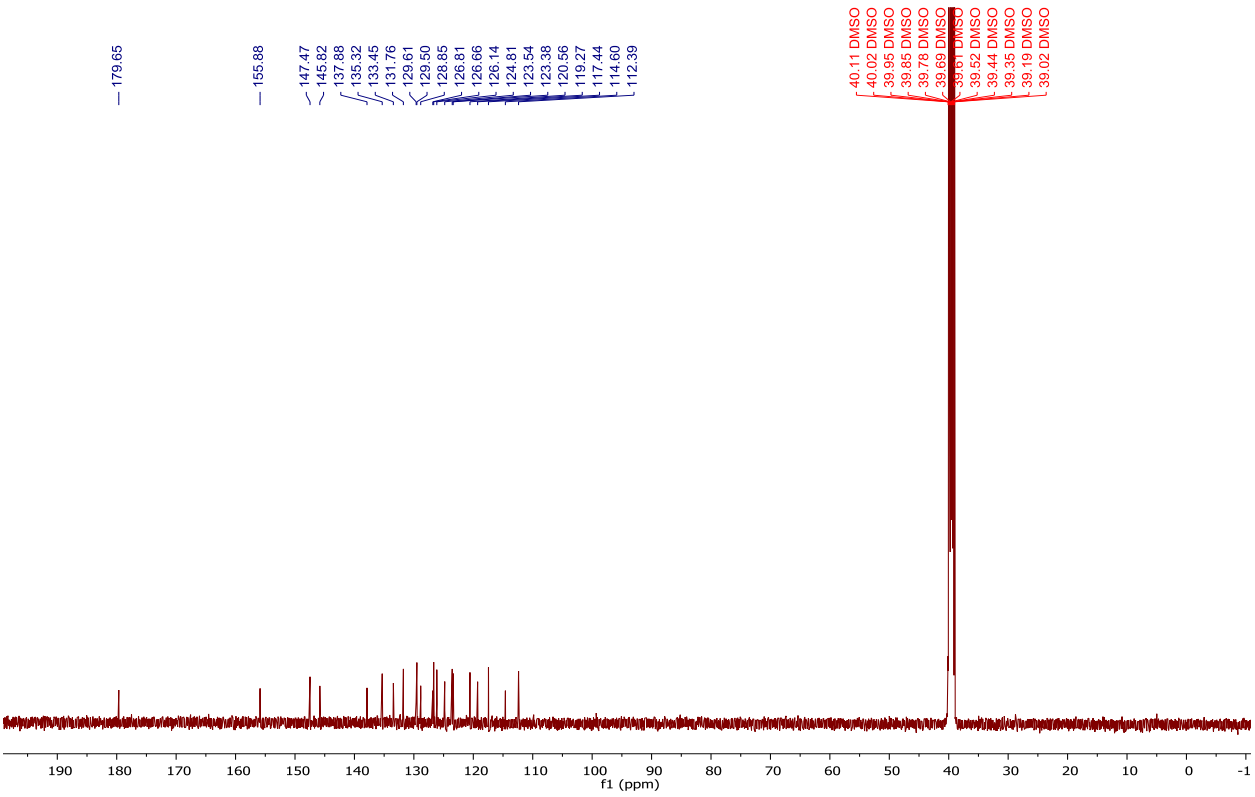
179.65 155.88 147.47 145.82 137.88 135.32 133.45 131.76 129.61 129.50 128.85 126.81 126.66 126.14 124.81 123.54 123.38 120.56 119.27 117.44 114.60 112.39
40.11 DMSO 40.02 DMSO 39.95 DMSO 39.85 DMSO 39.78 DMSO 39.69 DMSO 39.61 DMSO 39.52 DMSO 39.44 DMSO 39.35 DMSO 39.19 DMSO 39.02 DMSO
f1 (ppm)

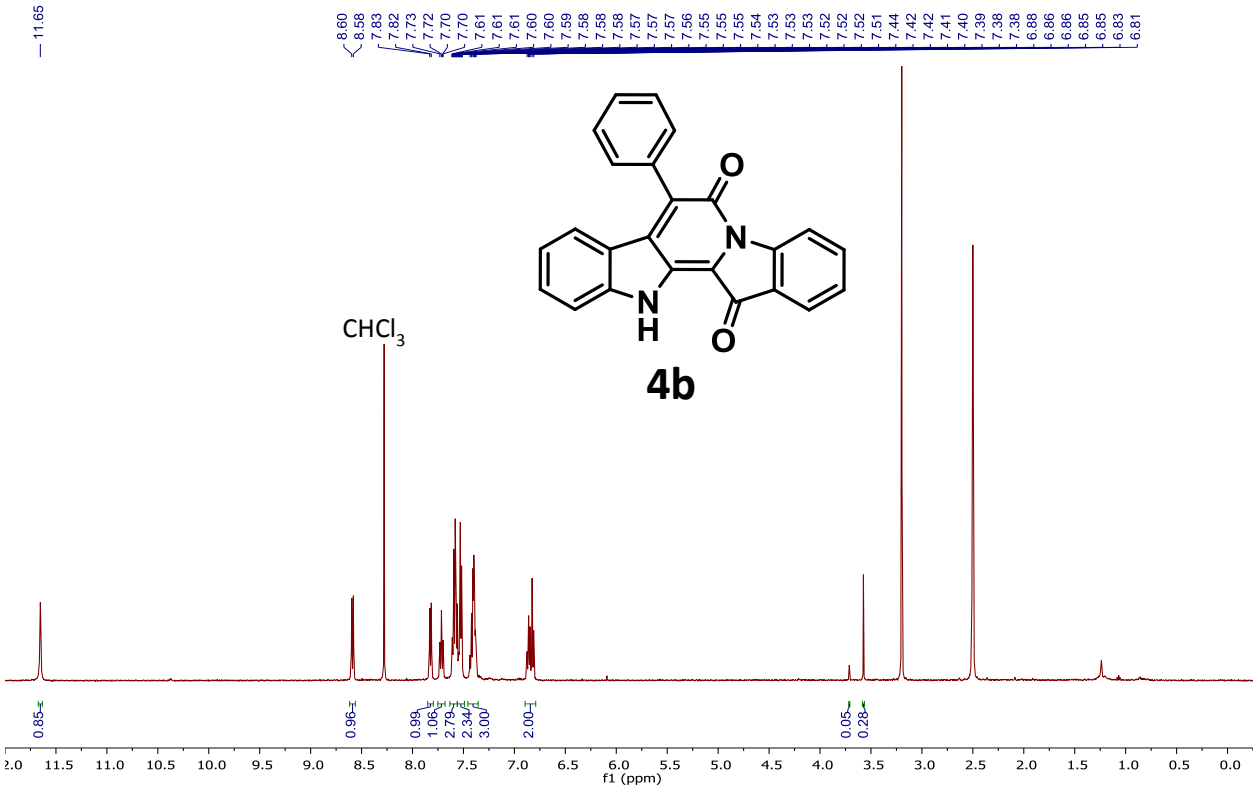
11.65
8.60
8.58
7.83
7.82
7.73
7.72
7.70
7.70
7.61
7.61
7.61
7.60
7.60
7.60
7.59
7.58
7.58
7.58
7.57
7.57
7.57
7.57
7.56
7.55
7.55
7.55
7.54
7.53
7.53
7.53
7.52
7.52
7.52
7.51
7.44
7.42
7.42
7.41
7.40
7.39
7.38
7.38
6.88
6.86
6.86
6.85
6.85
6.83
6.81
CHCl3
O
N
N
H
O
4b
0.85
0.96
0.99
1.06
2.79
2.34
3.00
2.00
0.05
0.28
f1 (ppm)

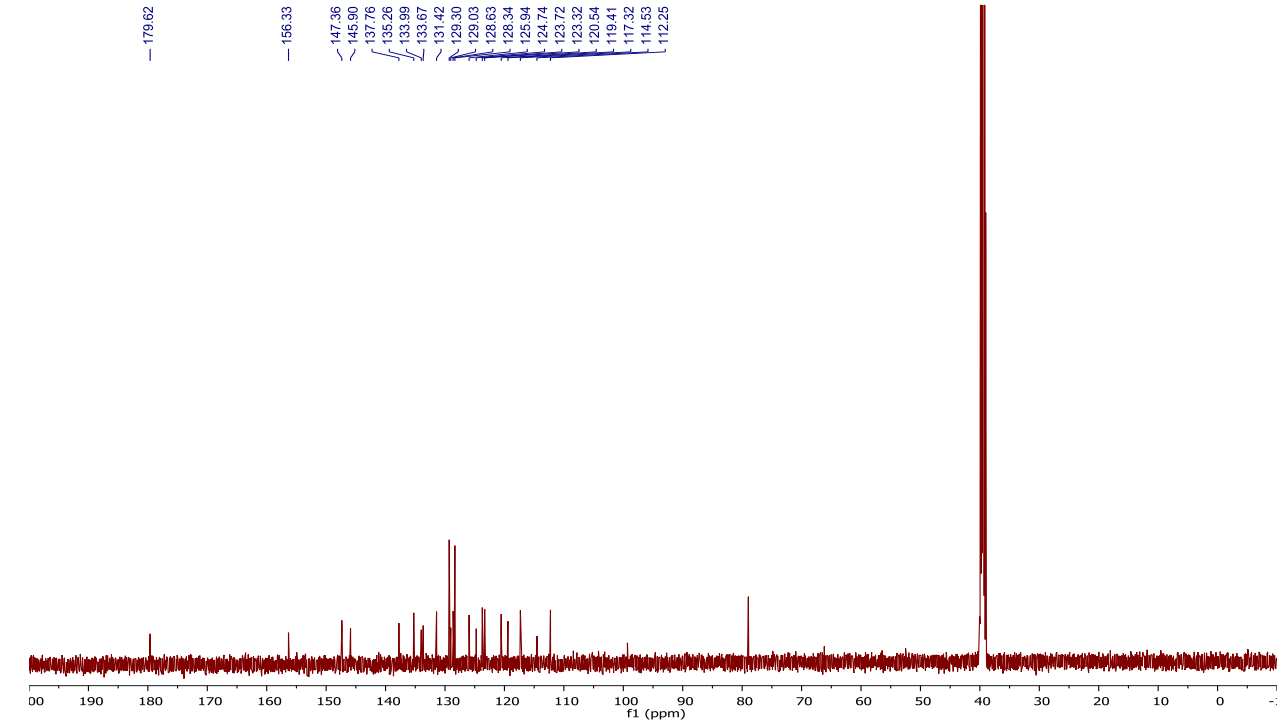
179.62
156.33
147.36
145.90
137.76
135.26
133.99
133.67
131.42
129.30
129.03
128.63
128.34
125.94
124.74
123.72
123.32
120.54
119.41
117.32
114.53
112.25
f1 (ppm)

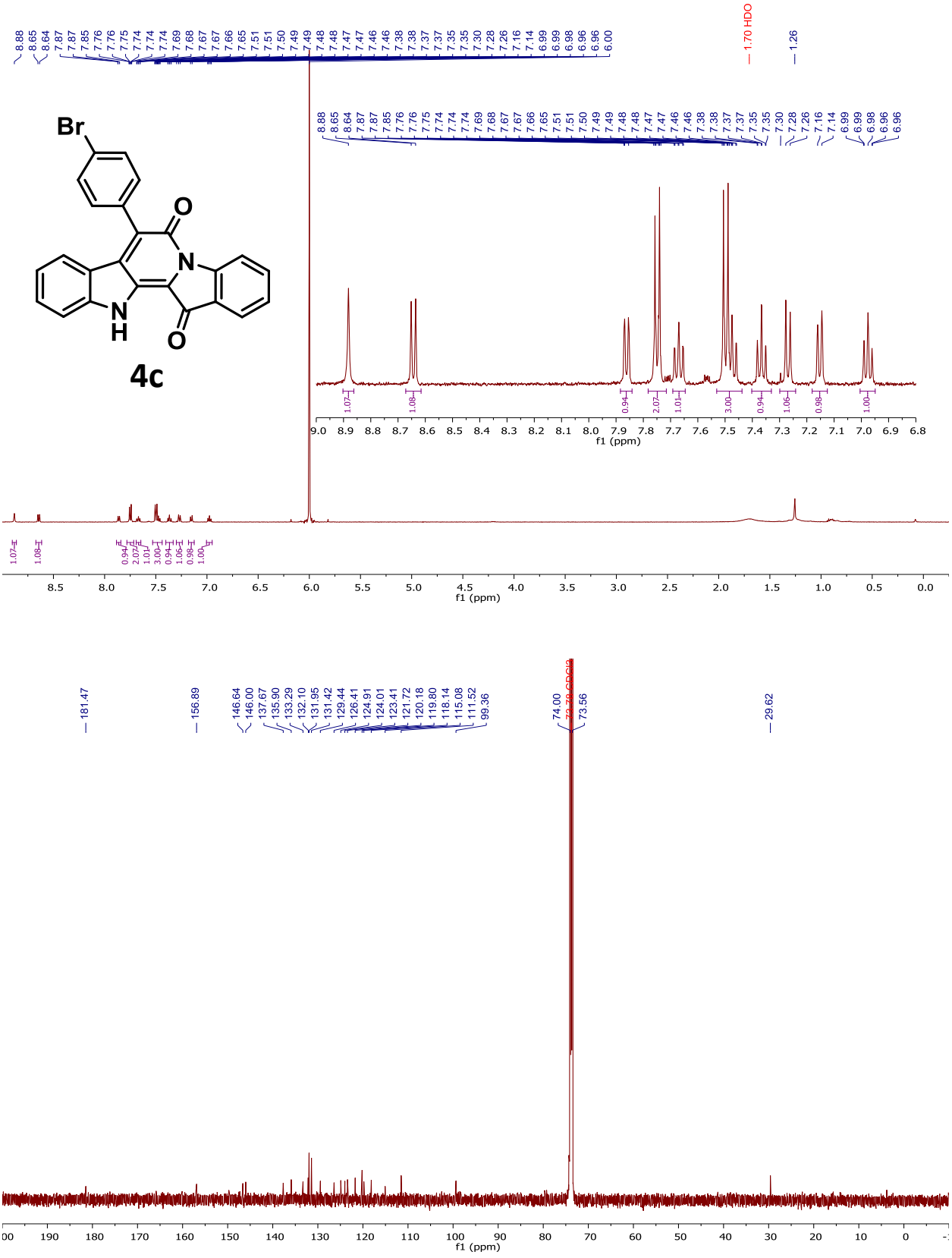
Br
O
N
N
H
O
4c
f1 (ppm)
f1 (ppm)

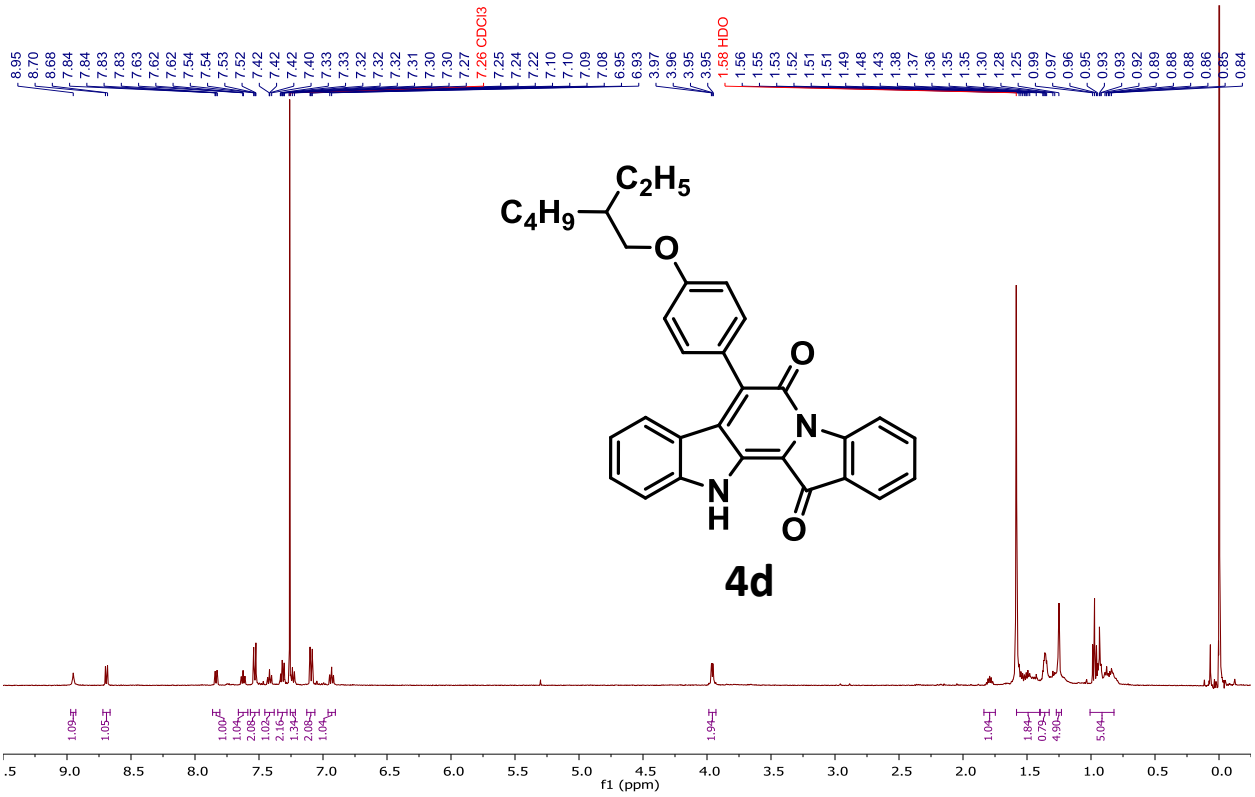
8.95 8.70 8.68 7.84 7.84 7.83 7.83 7.63 7.62 7.62 7.54 7.54 7.53 7.52 7.42 7.42 7.42 7.40 7.33 7.33 7.32 7.32 7.32 7.31 7.30 7.30 7.27 7.26 CDCl3 7.25 7.24 7.22 7.10 7.10 7.09 7.08 6.95 6.93 3.97 3.96 3.95 3.95 1.58 HDO 1.56 1.55 1.53 1.52 1.51 1.51 1.49 1.48 1.43 1.38 1.37 1.36 1.35 1.35 1.30 1.28 1.25 0.99 0.97 0.96 0.95 0.93 0.93 0.92 0.89 0.88 0.86 0.85 0.84
C2H5
C4H9
O
O
N
N
H
O
4d
1.09 1.05 1.00 1.04 2.08 1.02 2.16 1.34 2.08 1.04 1.94 1.04 1.84 0.79 4.90 5.04
f1 (ppm)

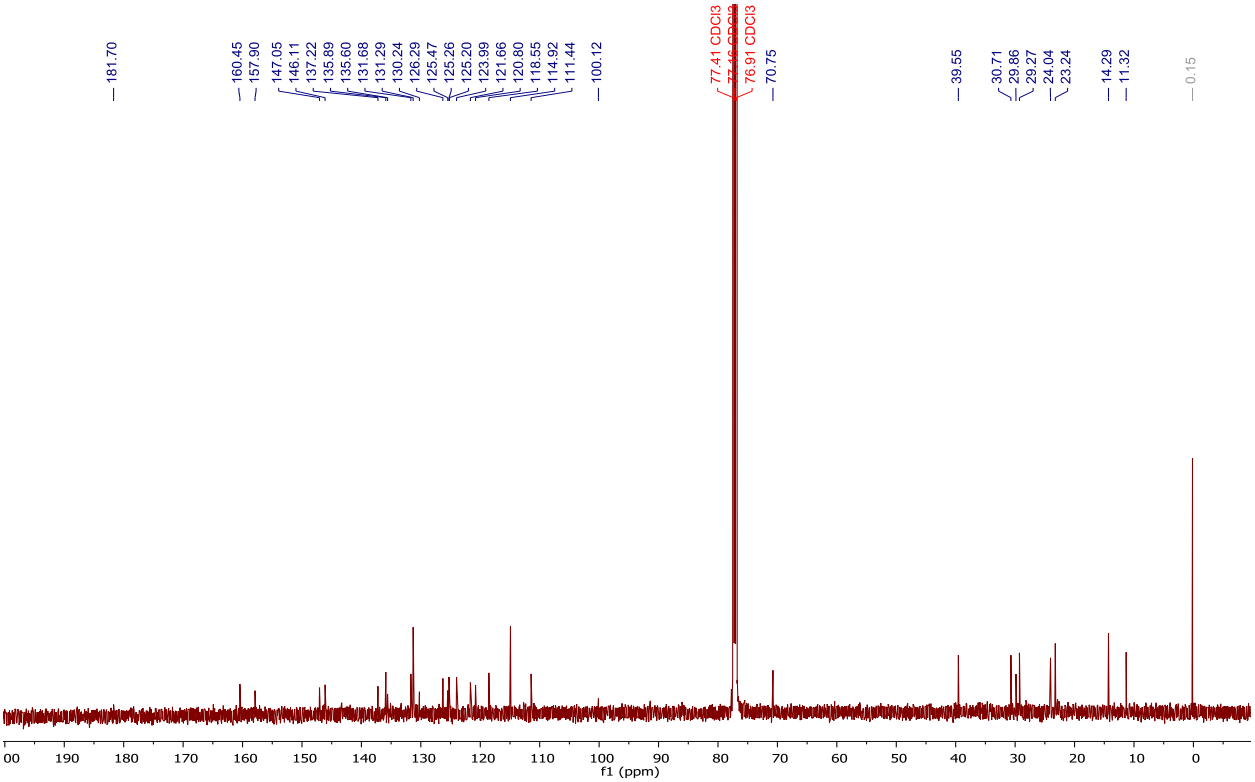
181.70
160.45 157.90 147.05 146.11 137.22 135.89 135.60 131.68 131.29 130.24 126.29 125.47 125.26 125.20 123.99 121.66 120.80 118.55 114.92 111.44 100.12
77.41 CDCl3 76.91 CDCl3 70.75
39.55 30.71 29.86 29.27 24.04 23.24 14.29 11.32 0.15
f1 (ppm)

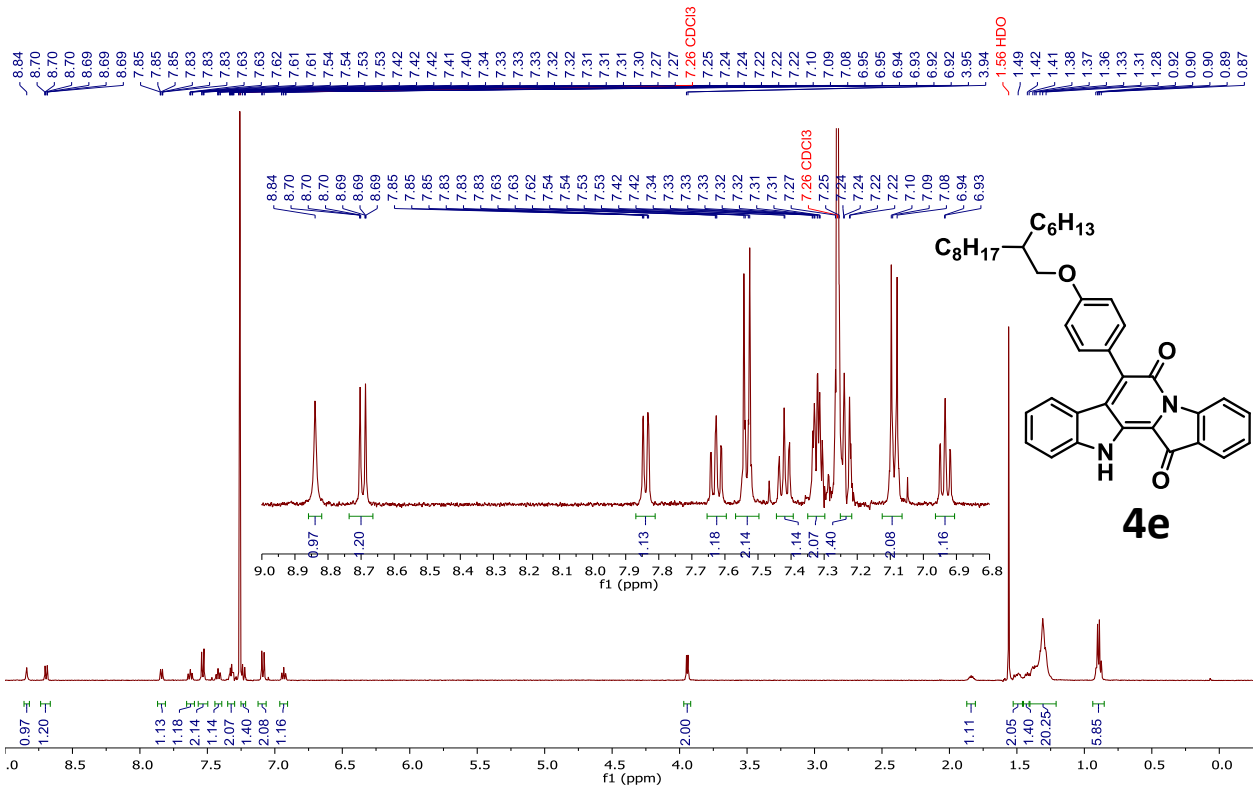
7.26 CDCl3
1.56 HDO
f1 (ppm)
4e

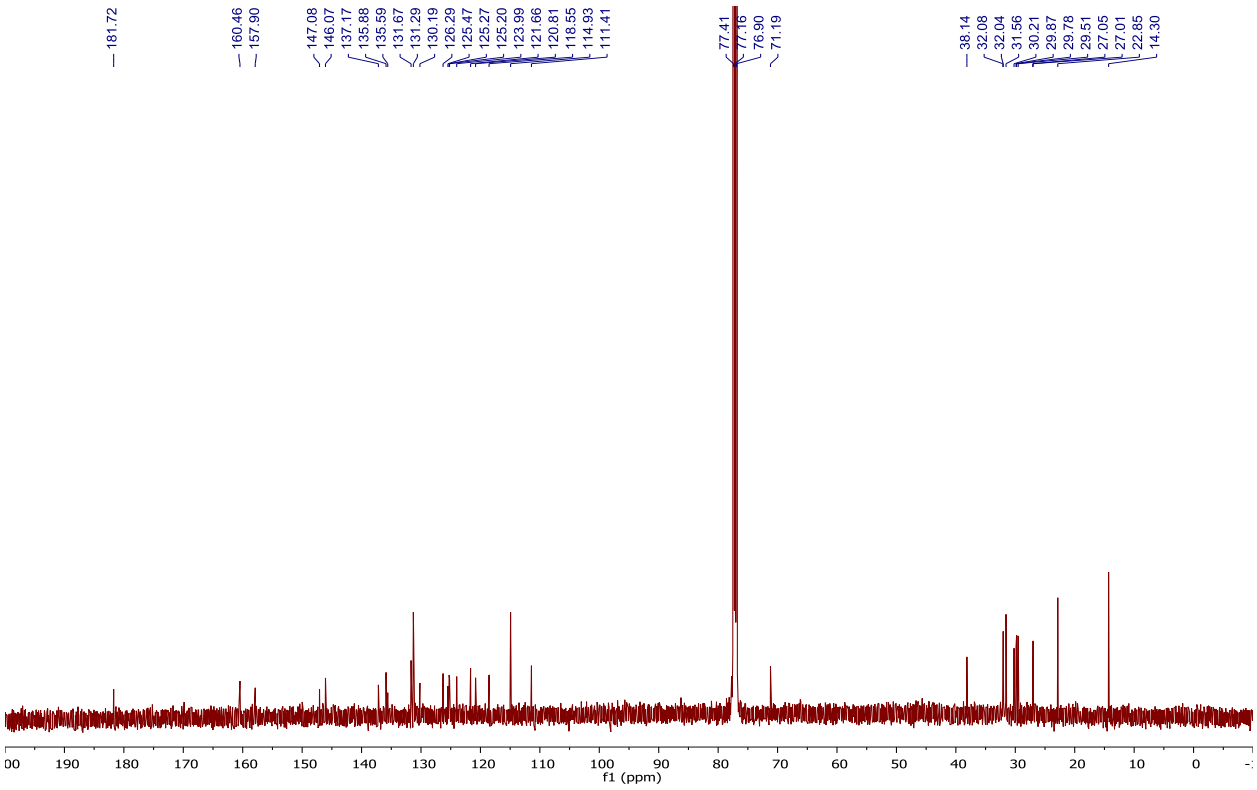
181.72
160.46
157.90
147.08
146.07
137.17
135.88
135.59
131.67
131.29
130.19
126.29
125.47
125.27
125.20
123.99
121.66
120.81
118.55
114.93
111.41
77.41
77.16
76.90
71.19
38.14
32.08
32.04
31.56
30.21
29.87
29.78
29.51
27.05
27.01
22.85
14.30
f1 (ppm)

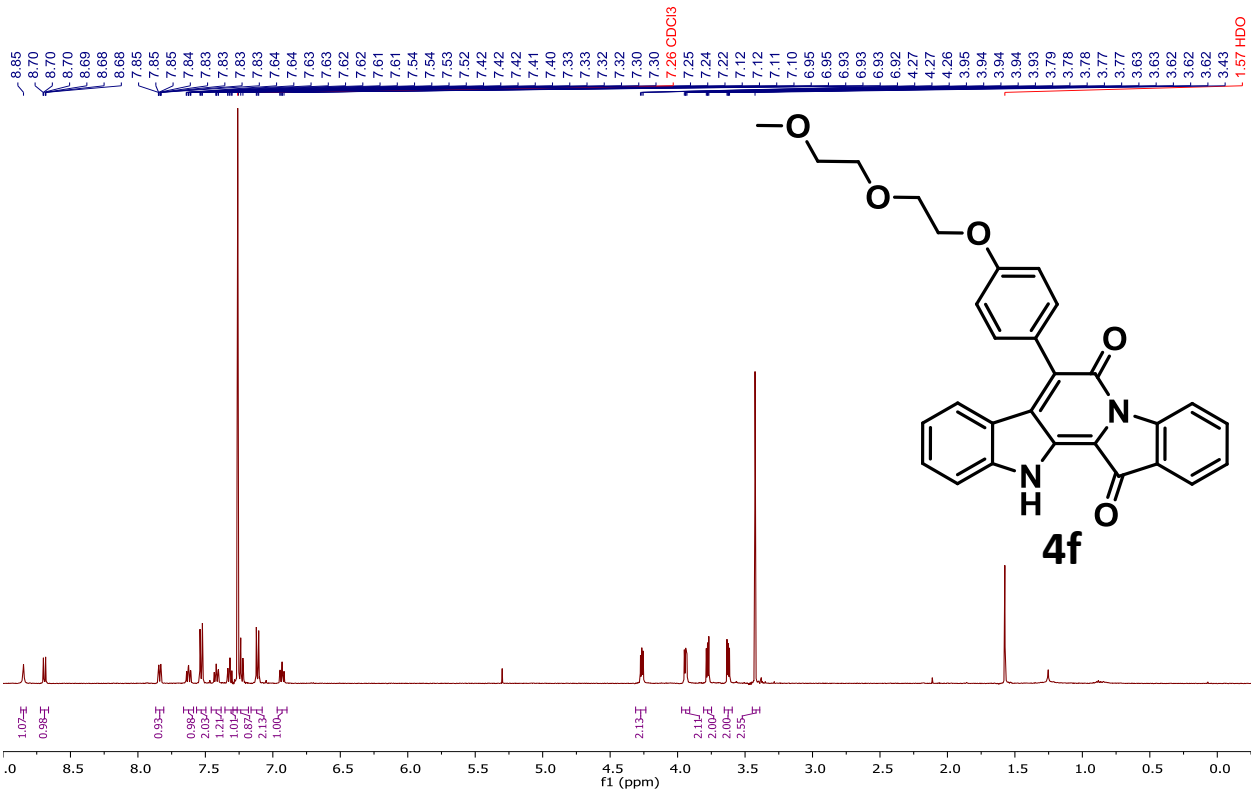
8.85 8.70 8.70 8.70 8.69 8.68 8.68 7.85 7.85 7.85 7.84 7.83 7.83 7.83 7.83 7.64 7.64 7.63 7.63 7.62 7.62 7.61 7.61 7.54 7.54 7.53 7.52 7.42 7.42 7.42 7.41 7.40 7.33 7.33 7.32 7.32 7.30 7.30 7.26 CDCl3 7.25 7.24 7.22 7.12 7.12 7.11 7.10 6.95 6.95 6.93 6.93 6.93 6.92 4.27 4.27 4.26 3.95 3.94 3.94 3.94 3.93 3.79 3.78 3.78 3.77 3.77 3.63 3.63 3.62 3.62 3.62 3.43 1.57 HDO
O
O
O
O
N
N
H
O
4f
1.07 0.98 0.93 0.98 2.03 1.21 1.01 0.87 2.13 1.00 2.13 2.11 2.00 2.00 2.55
f1 (ppm)

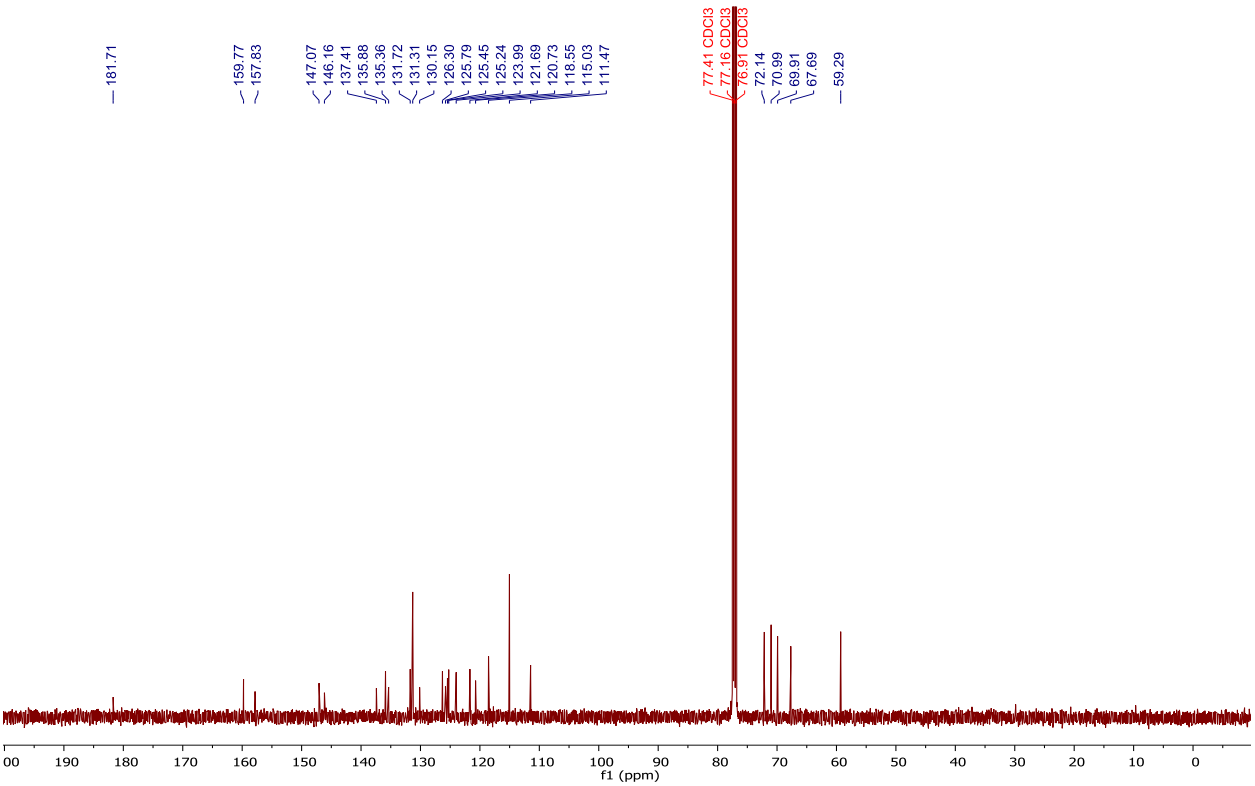
181.71
159.77
157.83
147.07
146.16
137.41
135.88
135.36
131.72
131.31
130.15
126.30
125.79
125.45
125.24
123.99
121.69
120.73
118.55
115.03
111.47
77.41 CDCl3
77.16 CDCl3
76.91 CDCl3
72.14
70.99
69.91
67.69
59.29
f1 (ppm)

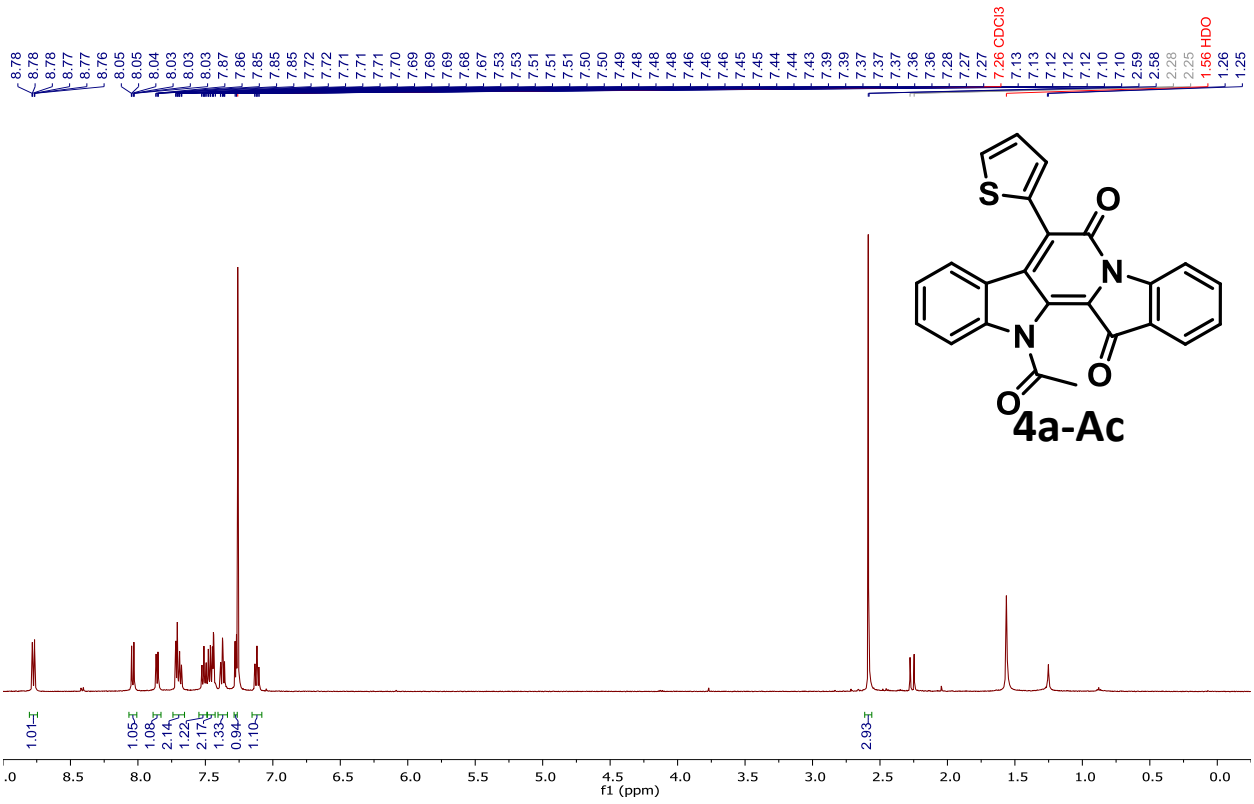
8.78 8.78 8.78 8.77 8.77 8.76 8.05 8.05 8.04 8.03 8.03 8.03 7.87 7.86 7.85 7.85 7.72 7.72 7.71 7.71 7.71 7.70 7.69 7.69 7.69 7.68 7.67 7.53 7.53 7.51 7.51 7.51 7.50 7.50 7.49 7.48 7.48 7.48 7.46 7.46 7.46 7.45 7.45 7.44 7.44 7.43 7.39 7.39 7.37 7.37 7.37 7.36 7.36 7.28 7.27 7.27 7.26 CDCl3 7.13 7.13 7.12 7.12 7.12 7.10 7.10 2.59 2.58 2.28 2.25 1.56 HDO 1.26 1.25
S
O
N
N
O
O
4a-Ac
1.01 1.05 1.08 2.14 1.22 2.17 1.33 0.94 1.10 2.93
.0 8.5 8.0 7.5 7.0 6.5 6.0 5.5 5.0 4.5 4.0 3.5 3.0 2.5 2.0 1.5 1.0 0.5 0.0
f1 (ppm)

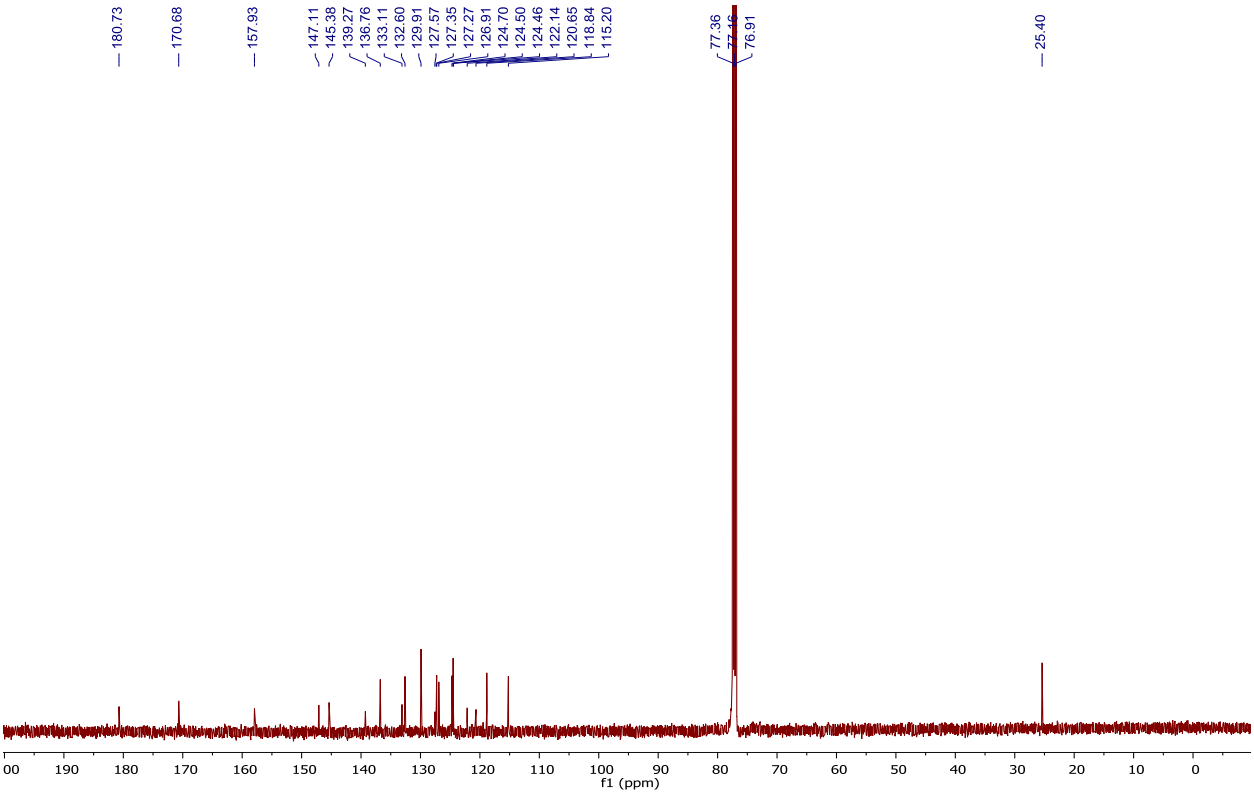
180.73 170.68 157.93 147.11 145.38 139.27 136.76 133.11 132.60 129.91 127.57 127.35 127.27 126.91 124.70 124.50 124.46 122.14 120.65 118.84 115.20 77.36 77.16 76.91 25.40
00 190 180 170 160 150 140 130 120 110 100 90 80 70 60 50 40 30 20 10 0
f1 (ppm)

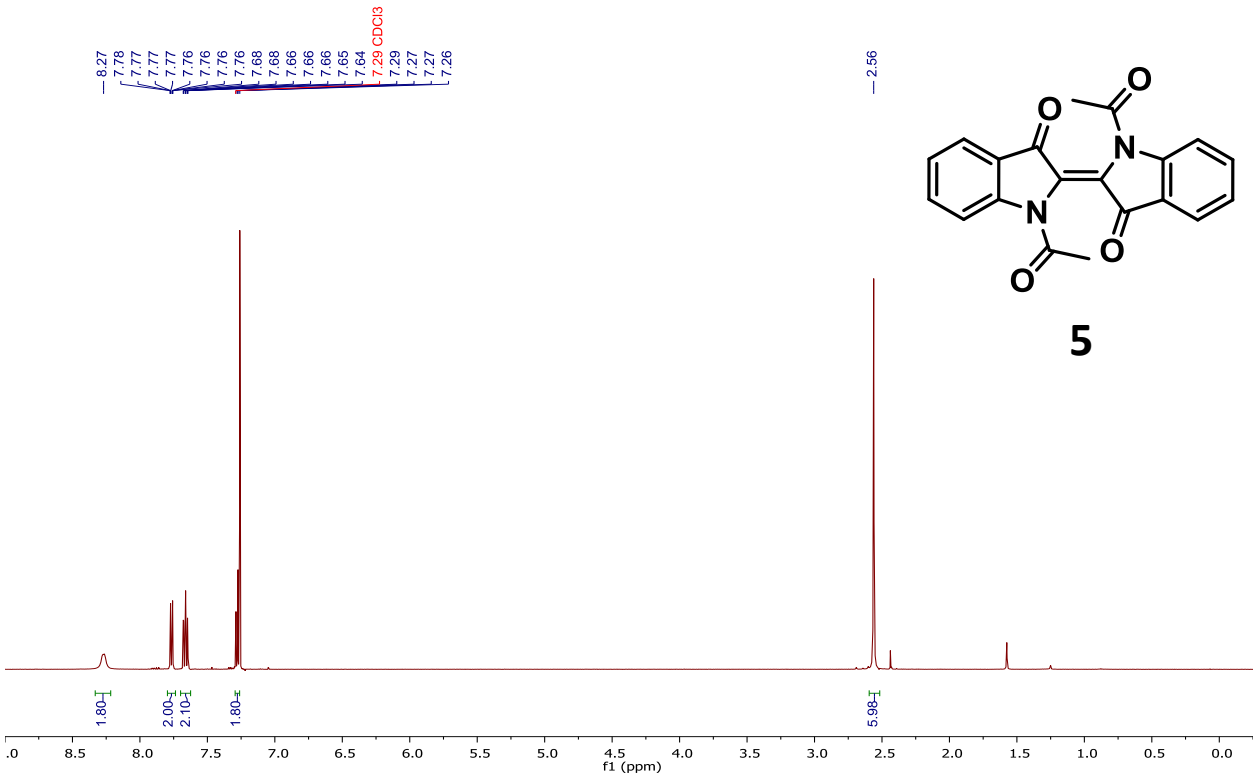
8.27
7.78
7.77
7.77
7.77
7.76
7.76
7.76
7.76
7.76
7.68
7.68
7.66
7.66
7.66
7.65
7.64
7.29 CDCl3
7.29
7.27
7.27
7.26
2.56
1.80
2.00
2.10
1.80
5.98
f1 (ppm)

5

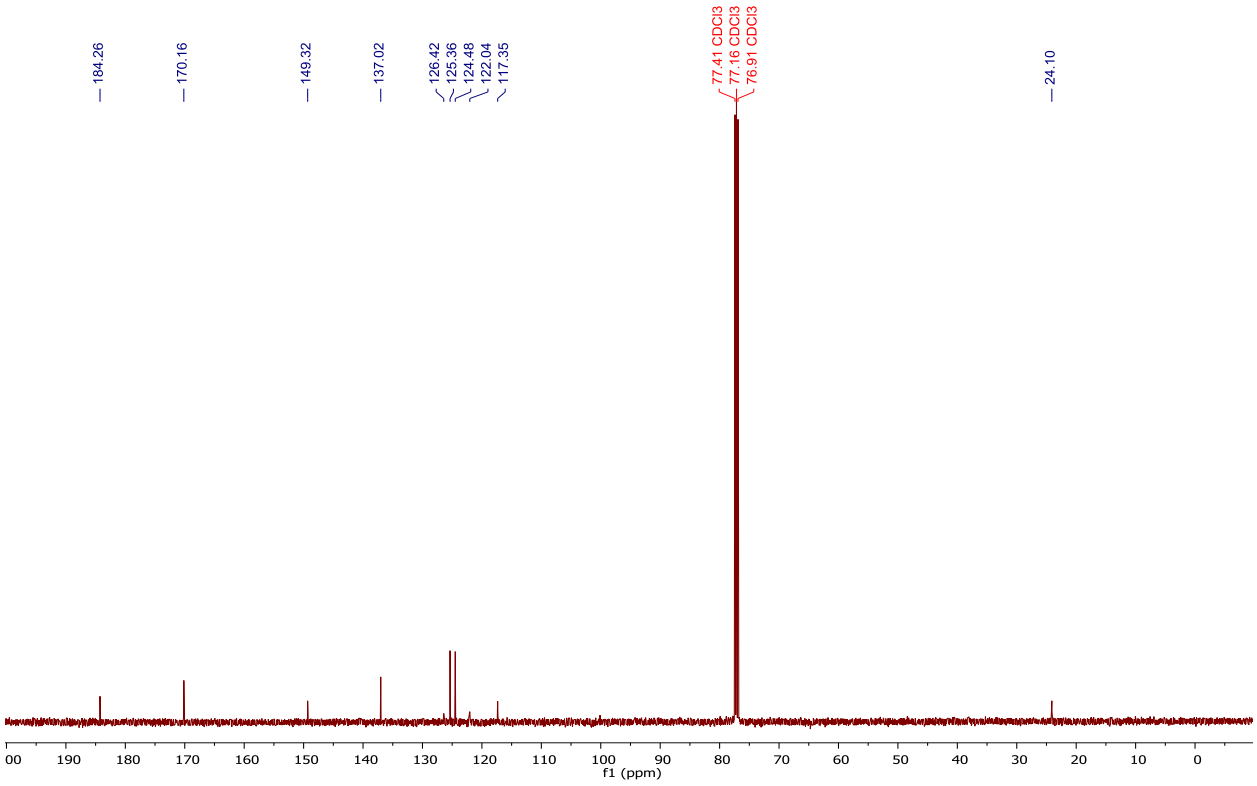
184.26
170.16
149.32
137.02
126.42
125.36
124.48
122.04
117.35
77.41 CDCl3
77.16 CDCl3
76.91 CDCl3
24.10
f1 (ppm)

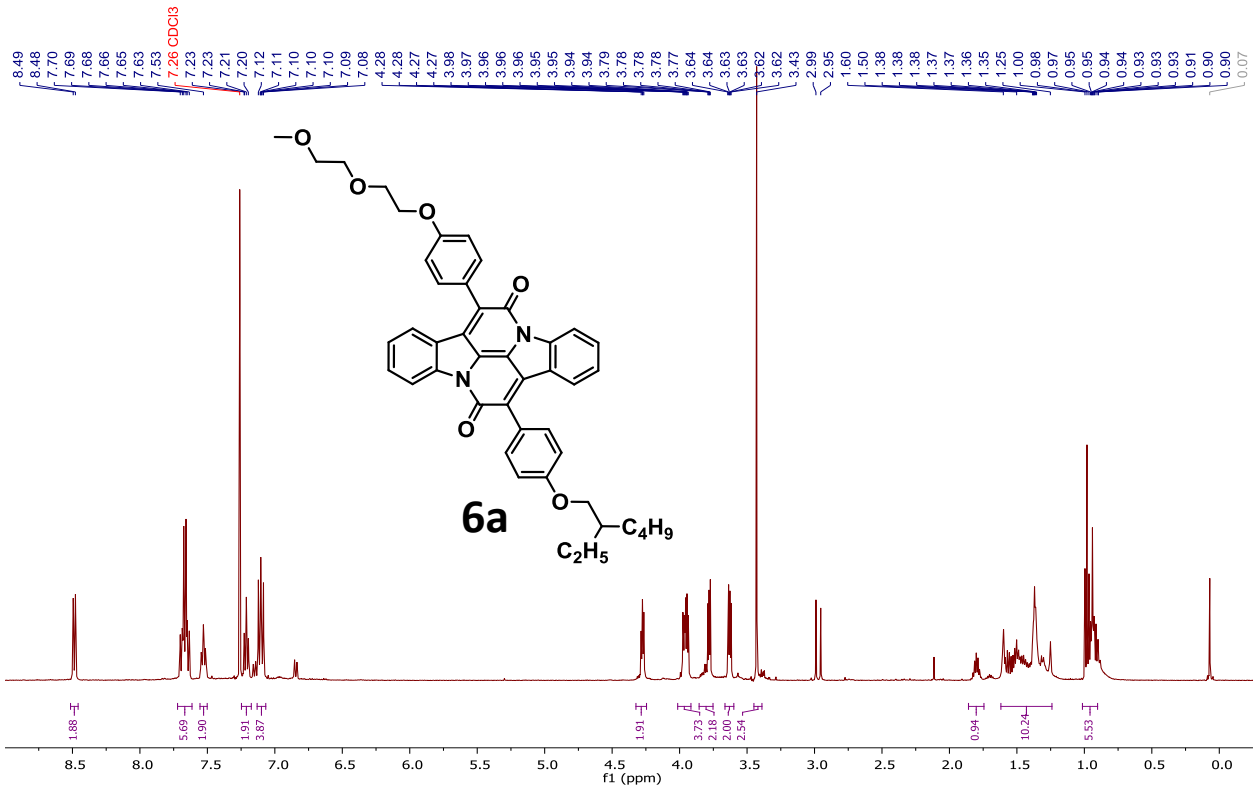
8.49 8.48 7.70 7.69 7.68 7.66 7.65 7.63 7.53 7.26 CDCl3 7.23 7.23 7.21 7.20 7.12 7.11 7.10 7.10 7.10 7.09 7.08 4.28 4.28 4.27 4.27 3.98 3.97 3.96 3.96 3.96 3.95 3.95 3.94 3.94 3.79 3.78 3.78 3.78 3.77 3.64 3.64 3.63 3.63 3.62 3.62 3.43 2.99 2.95 1.60 1.50 1.38 1.38 1.37 1.37 1.36 1.35 1.25 1.00 0.98 0.97 0.95 0.95 0.94 0.94 0.93 0.93 0.91 0.90 0.90 0.07
6a
1.88 5.69 1.90 1.91 3.87 1.91 3.73 2.18 2.00 2.54 0.94 10.24 5.53
f1 (ppm)

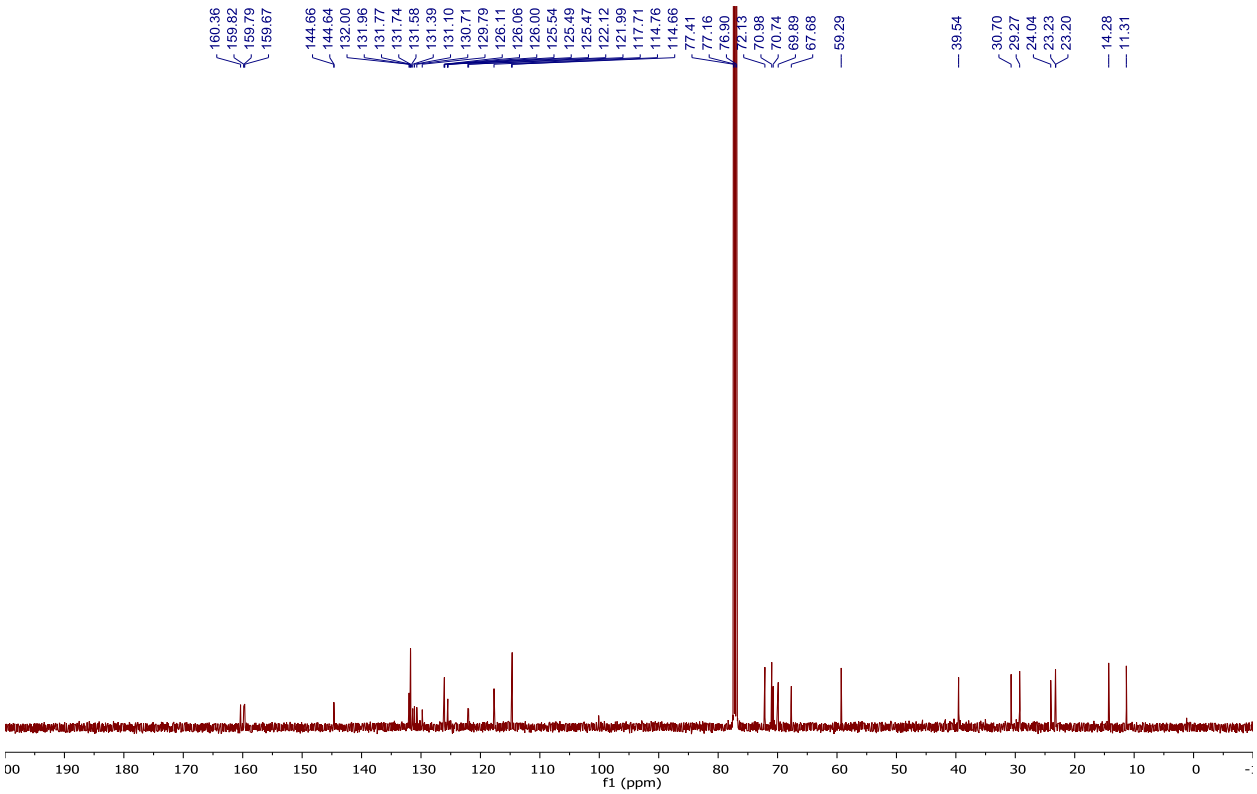
160.36 159.82 159.79 159.67 144.66 144.64 132.00 131.96 131.77 131.74 131.58 131.39 131.10 130.71 129.79 126.11 126.06 126.00 125.54 125.49 125.47 122.12 121.99 117.71 114.76 114.66 77.41 77.16 76.90 72.13 70.98 70.74 69.89 67.68 59.29 39.54 30.70 29.27 24.04 23.23 23.20 14.28 11.31
f1 (ppm)

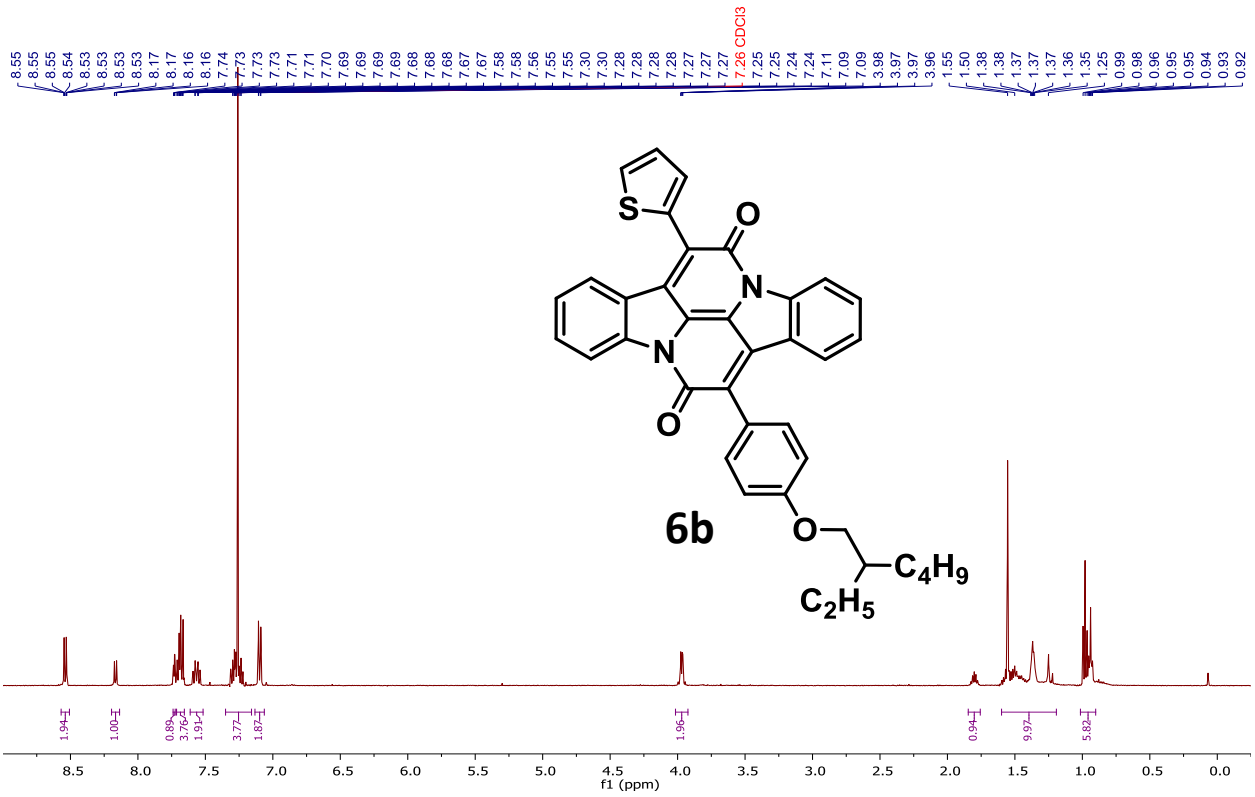
8.55 8.55 8.55 8.54 8.53 8.53 8.53 8.53 8.53 8.17 8.17 8.16 8.16 7.74 7.73 7.73 7.73 7.71 7.71 7.70 7.69 7.69 7.69 7.69 7.68 7.68 7.68 7.67 7.67 7.58 7.56 7.55 7.55 7.30 7.28 7.28 7.28 7.28 7.27 7.27 7.27 7.26 CDCl3 7.25 7.25 7.24 7.24 7.11 7.09 7.09 3.98 3.97 3.97 3.96 1.55 1.50 1.38 1.38 1.37 1.37 1.37 1.36 1.35 1.25 0.99 0.98 0.96 0.95 0.95 0.94 0.93 0.92
S
O
N
N
O
6b
O
C4H9
C2H5
1.94 1.00 0.89 3.76 1.91 3.77 1.87 1.96 0.94 9.97 5.82
8.5 8.0 7.5 7.0 6.5 6.0 5.5 5.0 4.5 4.0 3.5 3.0 2.5 2.0 1.5 1.0 0.5 0.0
f1 (ppm)

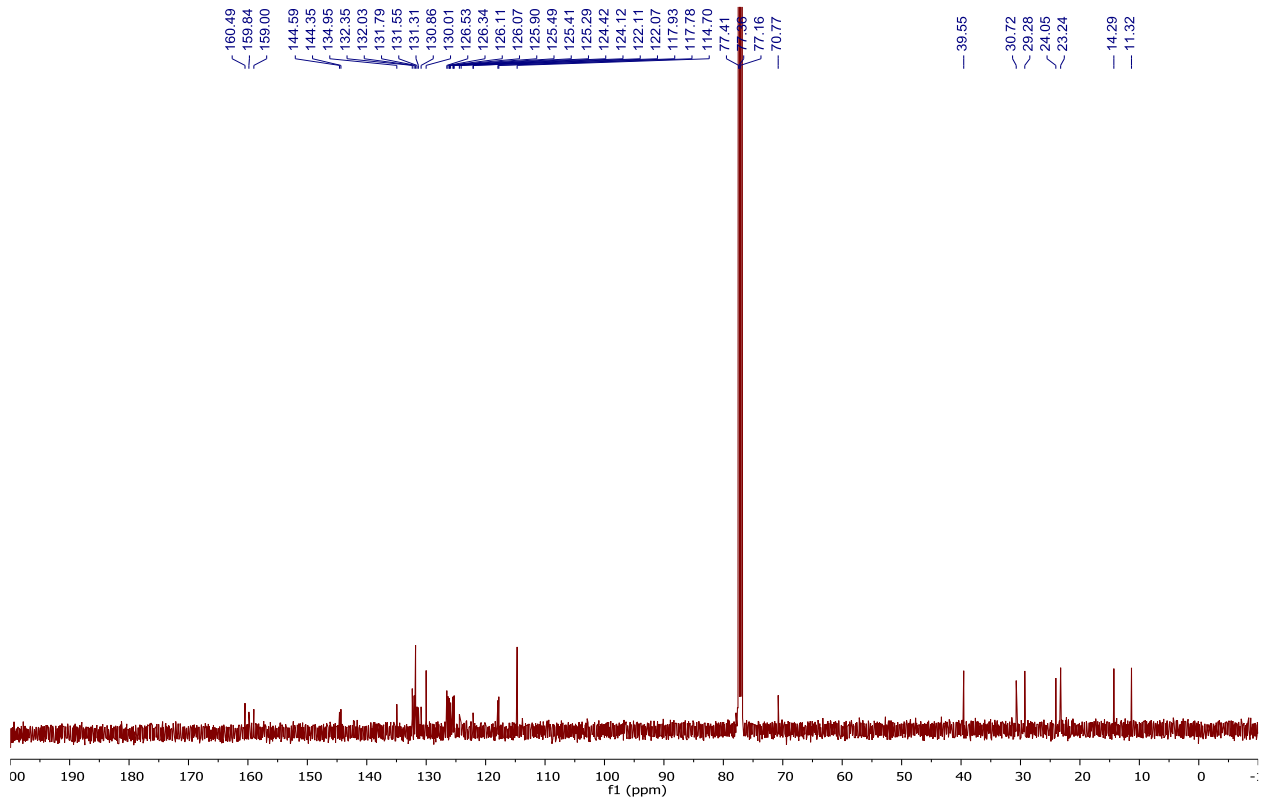
160.49 159.84 159.00 144.59 144.35 134.95 132.35 132.03 131.79 131.55 131.31 130.86 130.01 126.53 126.34 126.11 126.07 125.90 125.49 125.41 125.29 124.42 124.12 122.11 122.07 117.93 117.78 114.70 77.41 77.16 70.77 39.55 30.72 29.28 24.05 23.24 14.29 11.32
190 180 170 160 150 140 130 120 110 100 90 80 70 60 50 40 30 20 10 0
f1 (ppm)

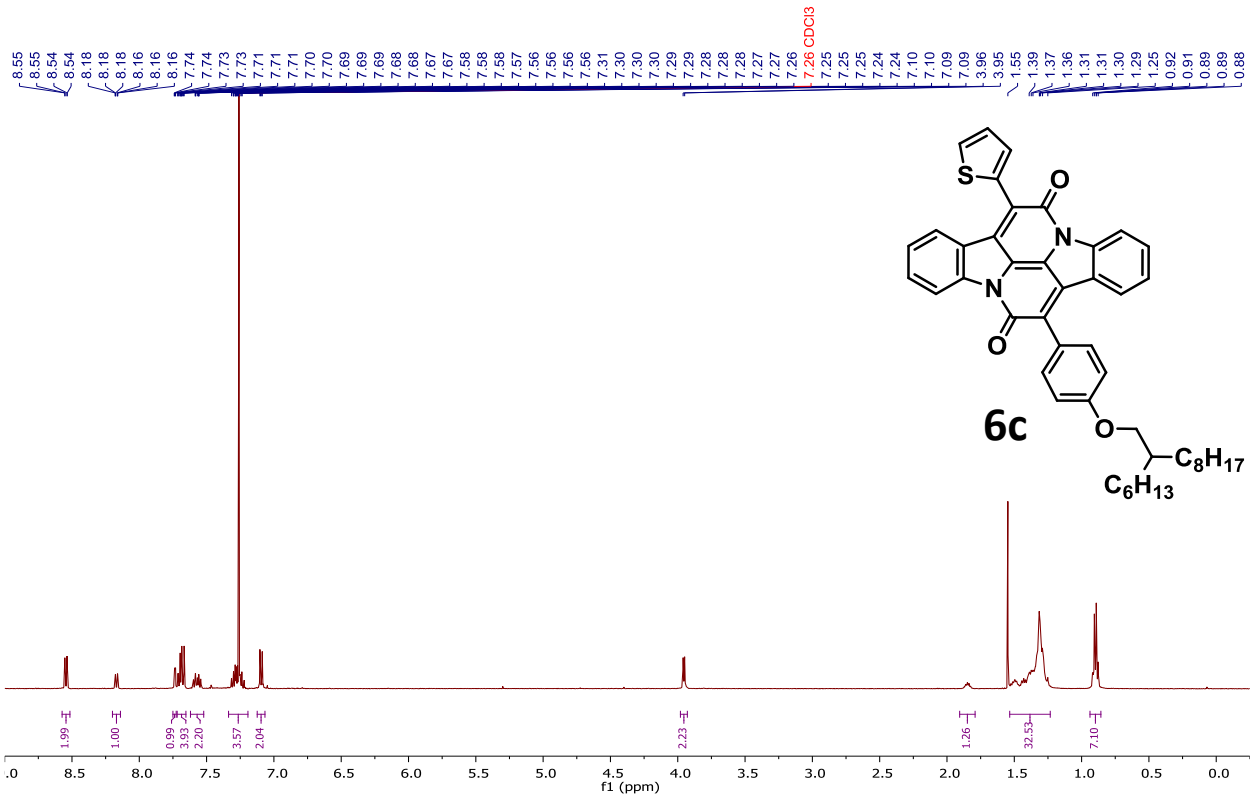
7.26 CDCl3
6c
f1 (ppm)

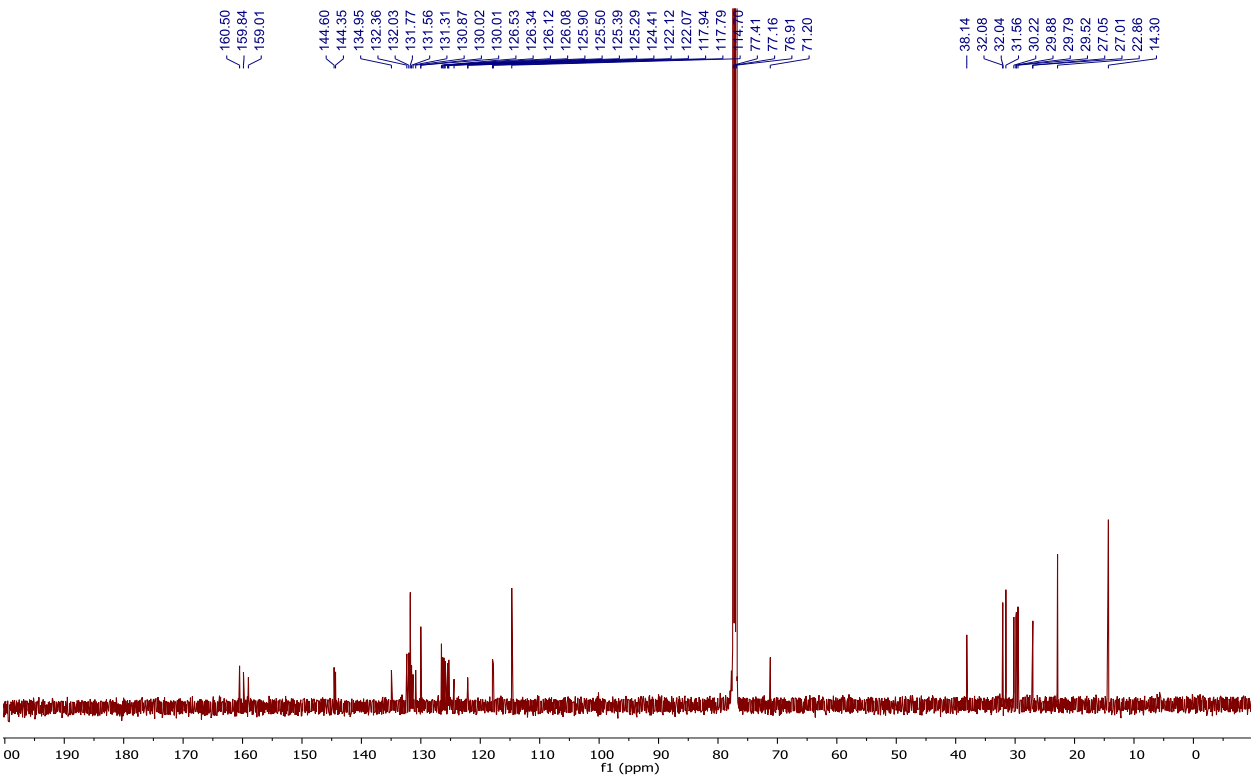
f1 (ppm)

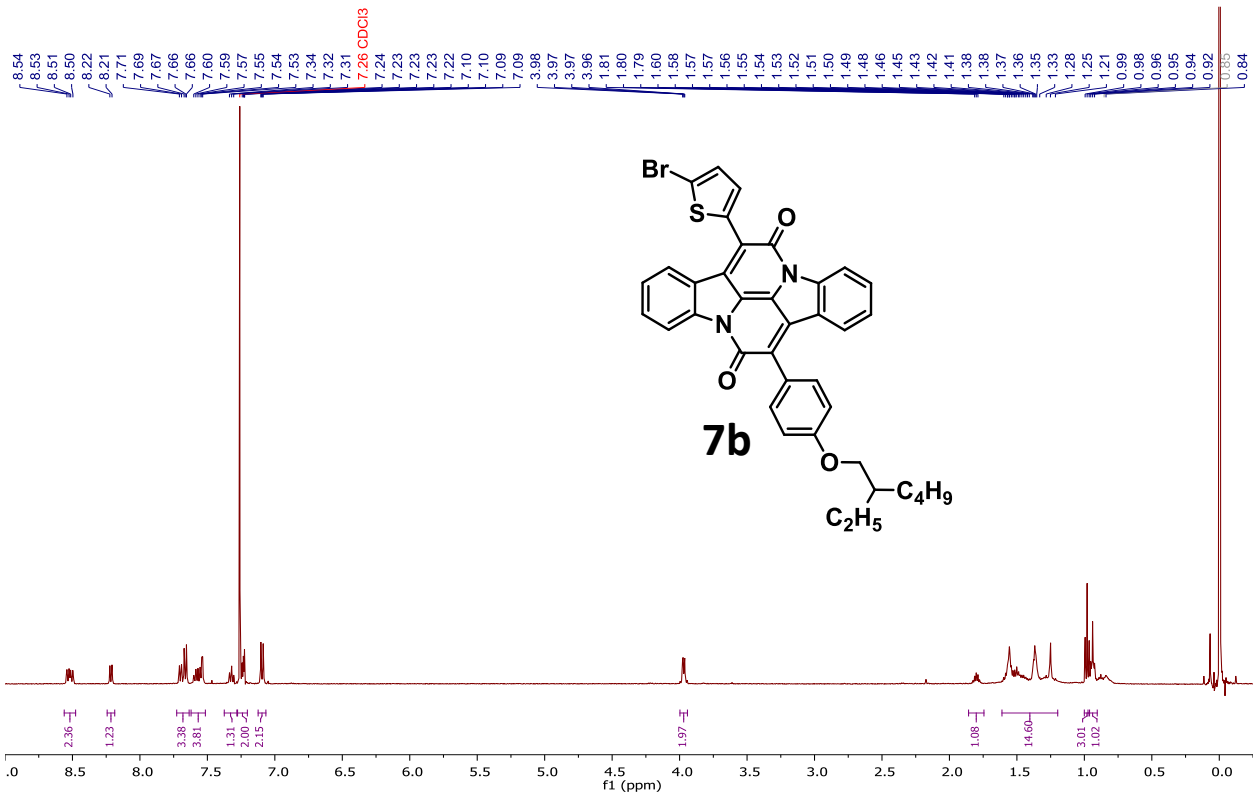
Br
S
O
N
N
O
7b
O
C_4H_9
C_2H_5
f1 (ppm)

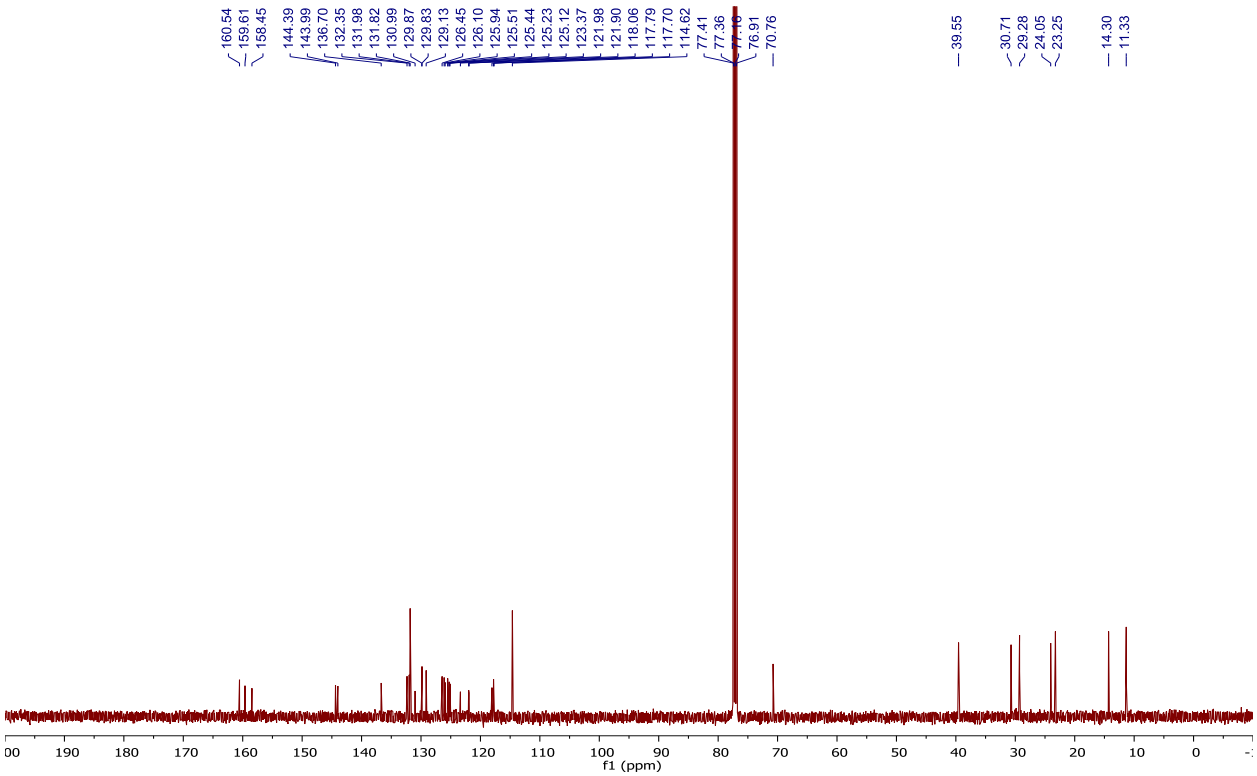
f1 (ppm)

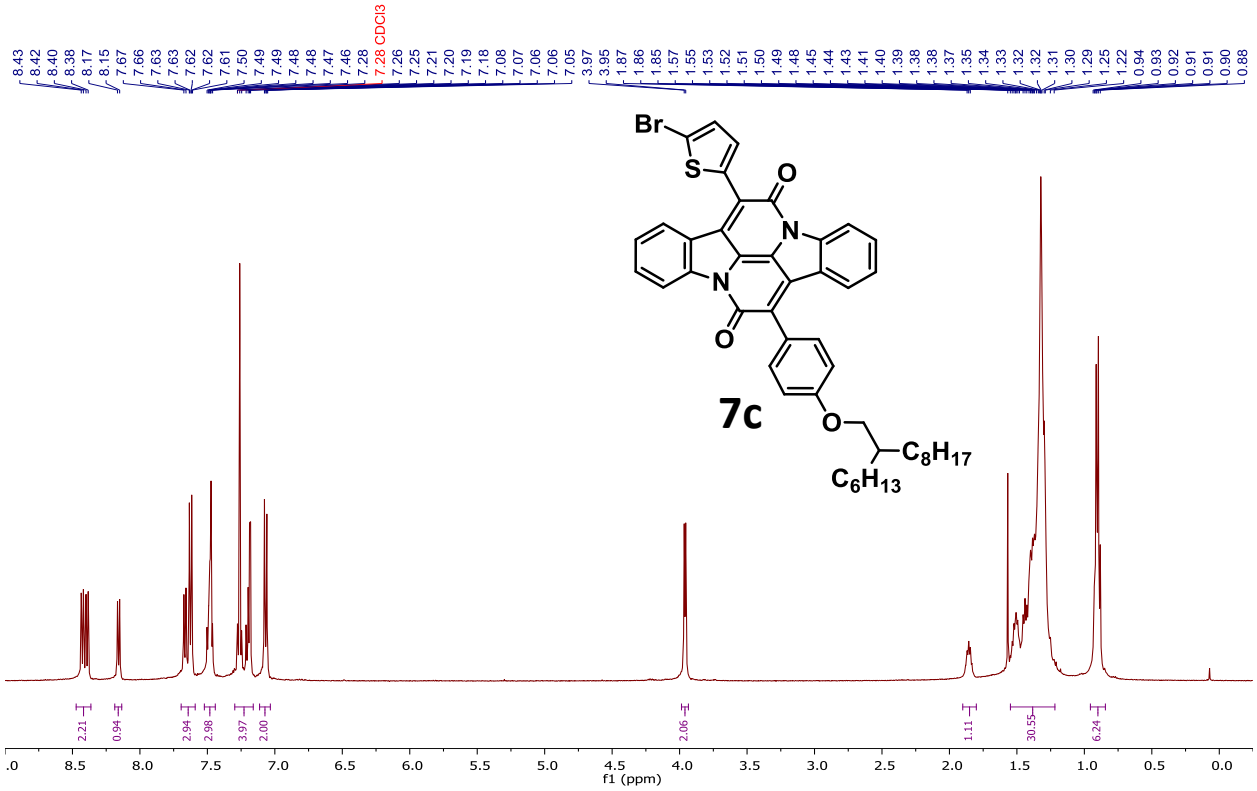
8.43 8.42 8.40 8.38 8.17 8.15 7.67 7.66 7.63 7.63 7.62 7.62 7.61 7.50 7.49 7.49 7.48 7.48 7.47 7.46 7.28 CDCl3 7.26 7.25 7.21 7.20 7.19 7.18 7.08 7.07 7.06 7.06 7.05 3.97 3.95 1.87 1.86 1.85 1.57 1.55 1.53 1.52 1.51 1.50 1.49 1.48 1.45 1.44 1.43 1.41 1.40 1.39 1.38 1.38 1.37 1.35 1.34 1.33 1.32 1.32 1.31 1.30 1.29 1.25 1.22 0.94 0.93 0.92 0.91 0.91 0.90 0.88
Br
S
O
N
N
O
7c
O
C8H17
C6H13
2.21 0.94 2.94 2.98 3.97 2.00 2.06 1.11 30.55 6.24
f1 (ppm)

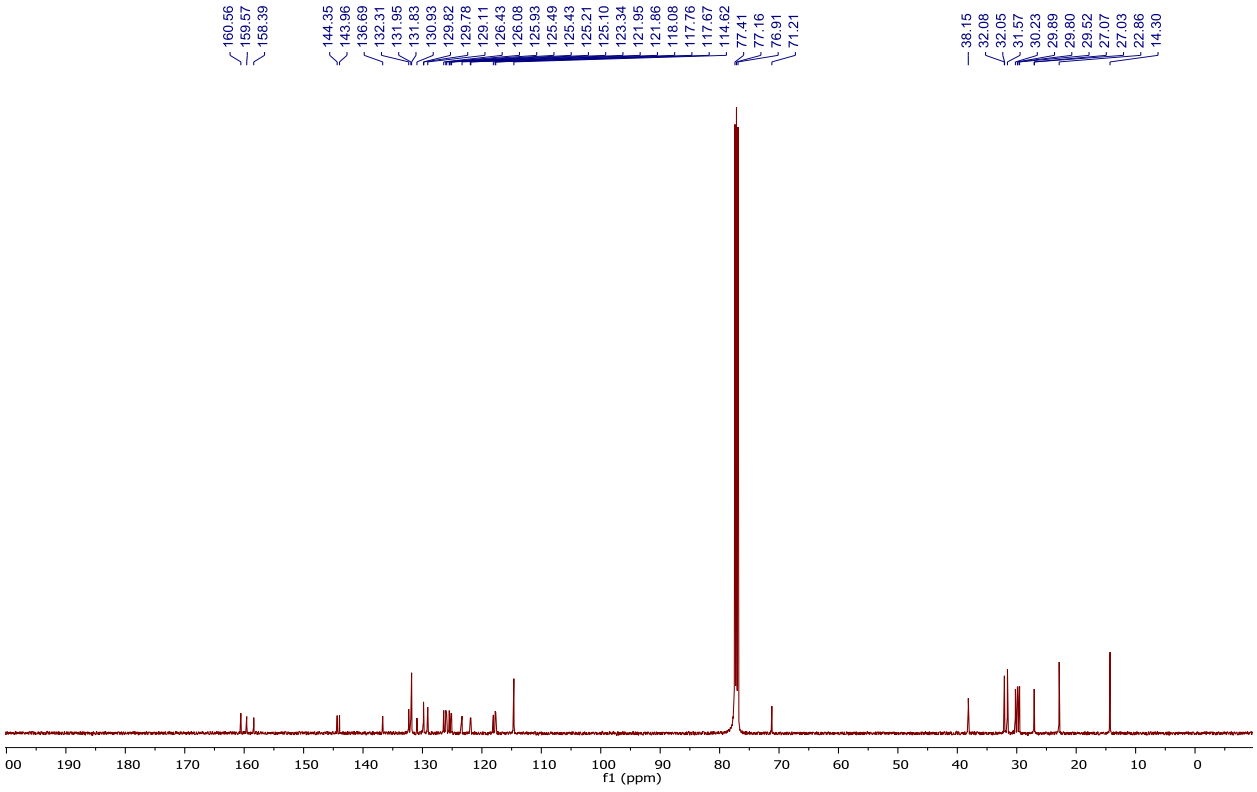
160.56 159.57 158.39 144.35 143.96 136.69 132.31 131.95 131.83 130.93 129.82 129.78 129.11 126.43 126.08 125.93 125.49 125.43 125.21 125.10 123.34 121.95 121.86 118.08 117.76 117.67 114.62 77.41 77.16 76.91 71.21 38.15 32.08 32.05 31.57 30.23 29.89 29.80 29.52 27.07 27.03 22.86 14.30
f1 (ppm)

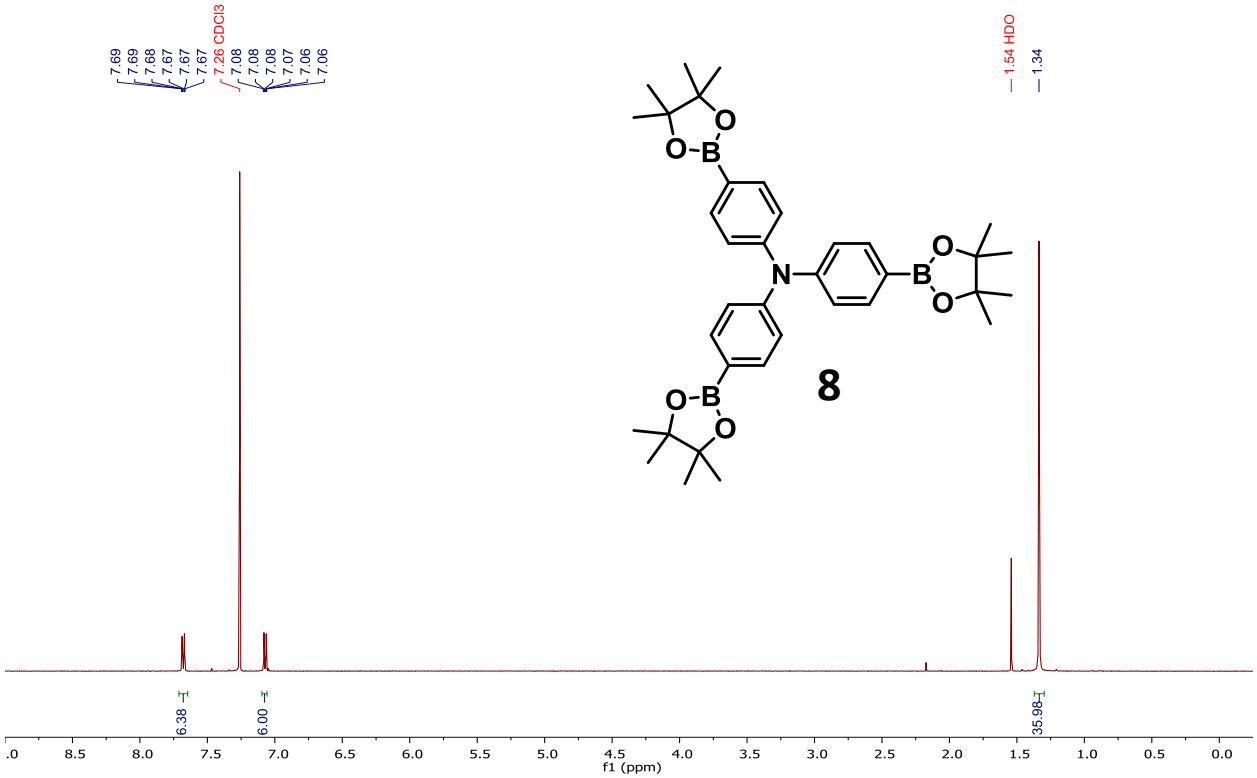
7.69
7.69
7.68
7.67
7.67
7.67
7.26 CDCl3
7.08
7.08
7.08
7.08
7.07
7.06
7.06
1.54 HDO
1.34
8
6.38
6.00
35.98
f1 (ppm)

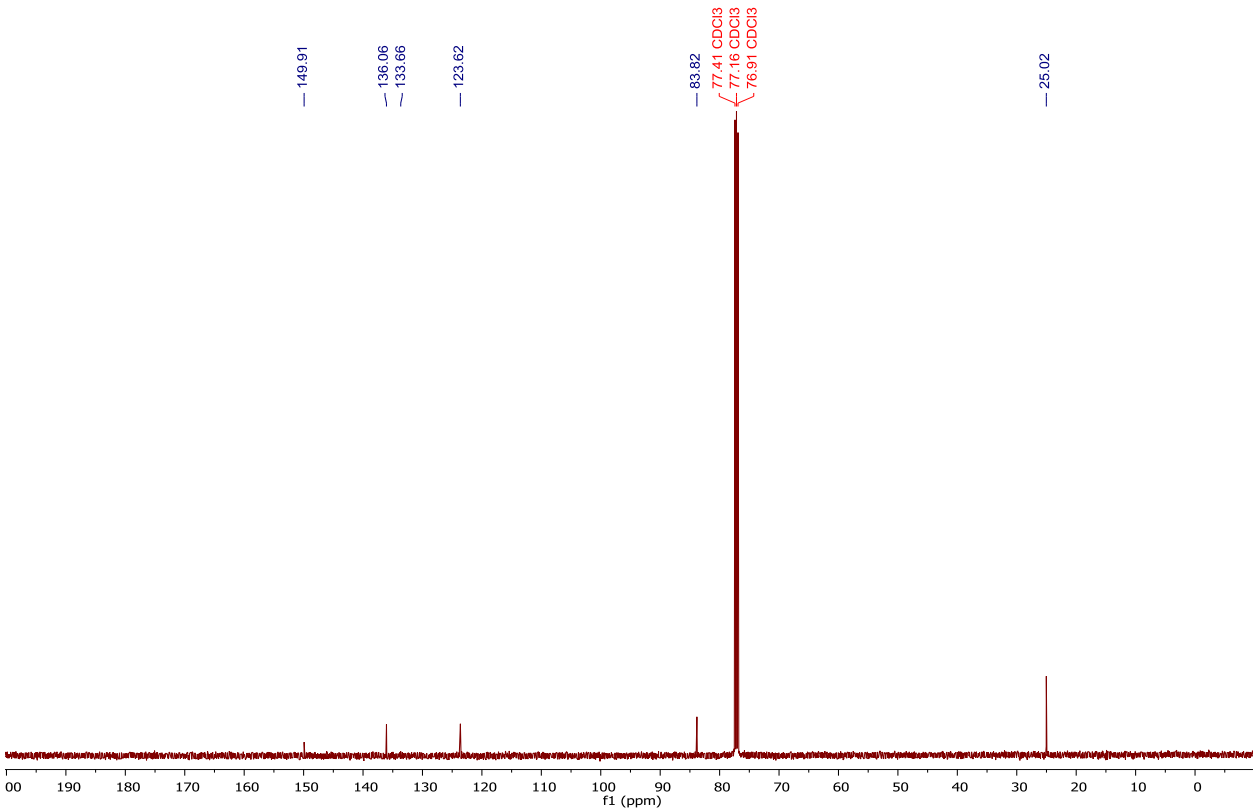
149.91
136.06
133.66
123.62
83.82
77.41 CDCl3
77.16 CDCl3
76.91 CDCl3
25.02
f1 (ppm)

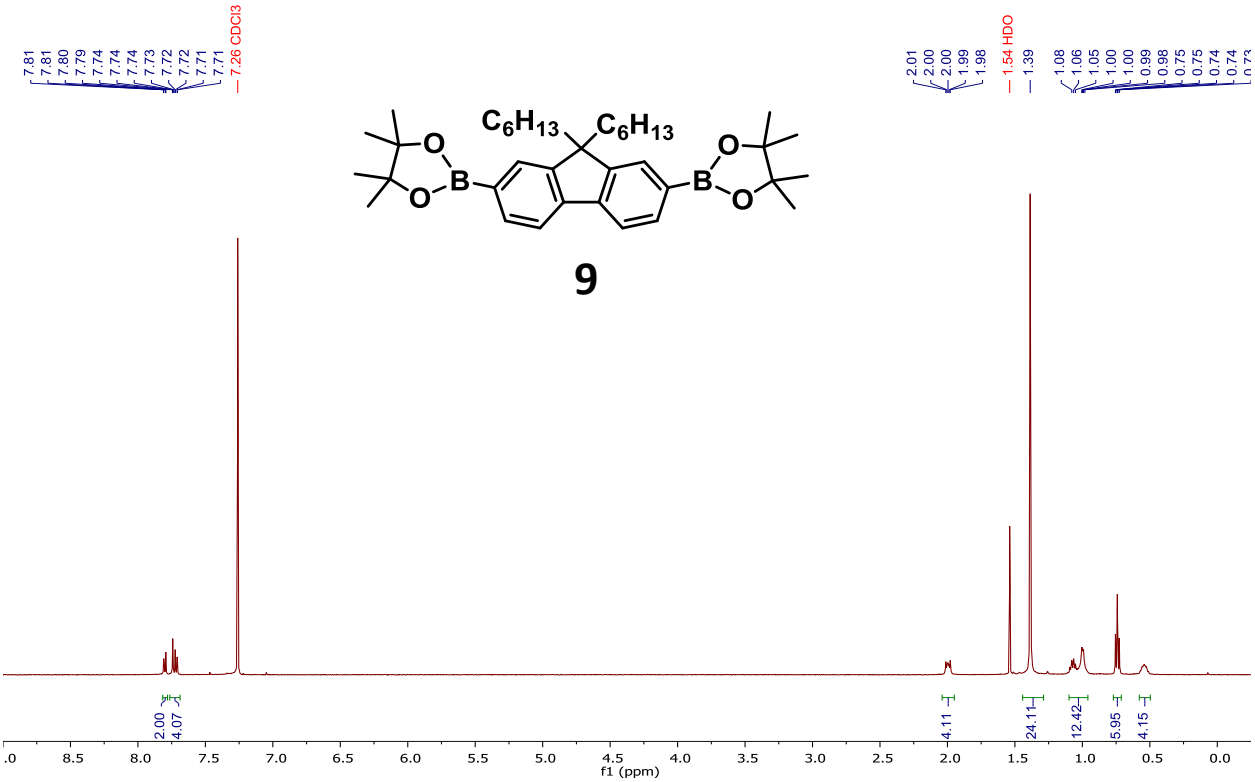
7.81
7.81
7.80
7.79
7.74
7.74
7.74
7.73
7.72
7.72
7.71
7.71
7.26 CDCl3
2.01
2.00
2.00
1.99
1.98
1.54 HDO
1.39
1.08
1.06
1.05
1.00
1.00
0.99
0.98
0.75
0.75
0.74
0.74
C6H13
C6H13
B
B
O
O
O
O
2.00
4.07
4.11
24.11
12.42
5.95
4.15
f1 (ppm)

9

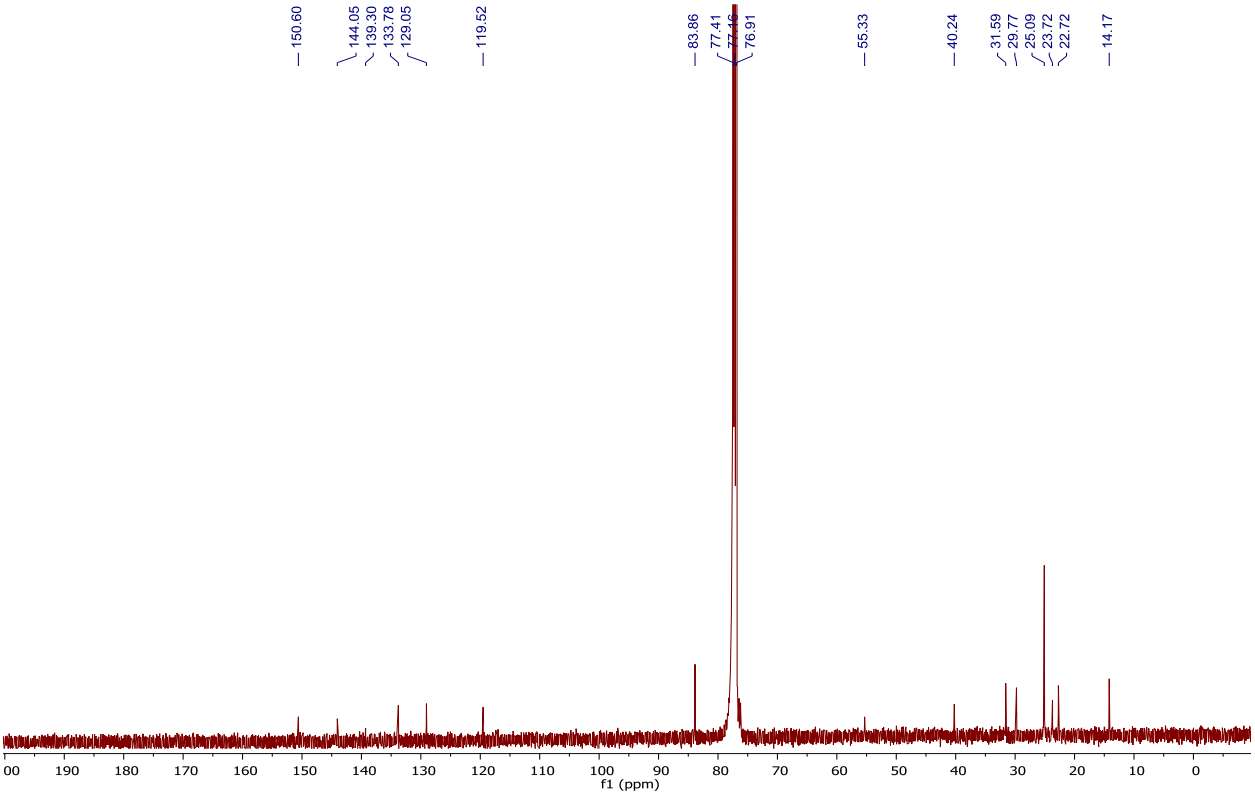
150.60
144.05
139.30
133.78
129.05
119.52
83.86
77.41
77.16
76.91
55.33
40.24
31.59
29.77
25.09
23.72
22.72
14.17
f1 (ppm)

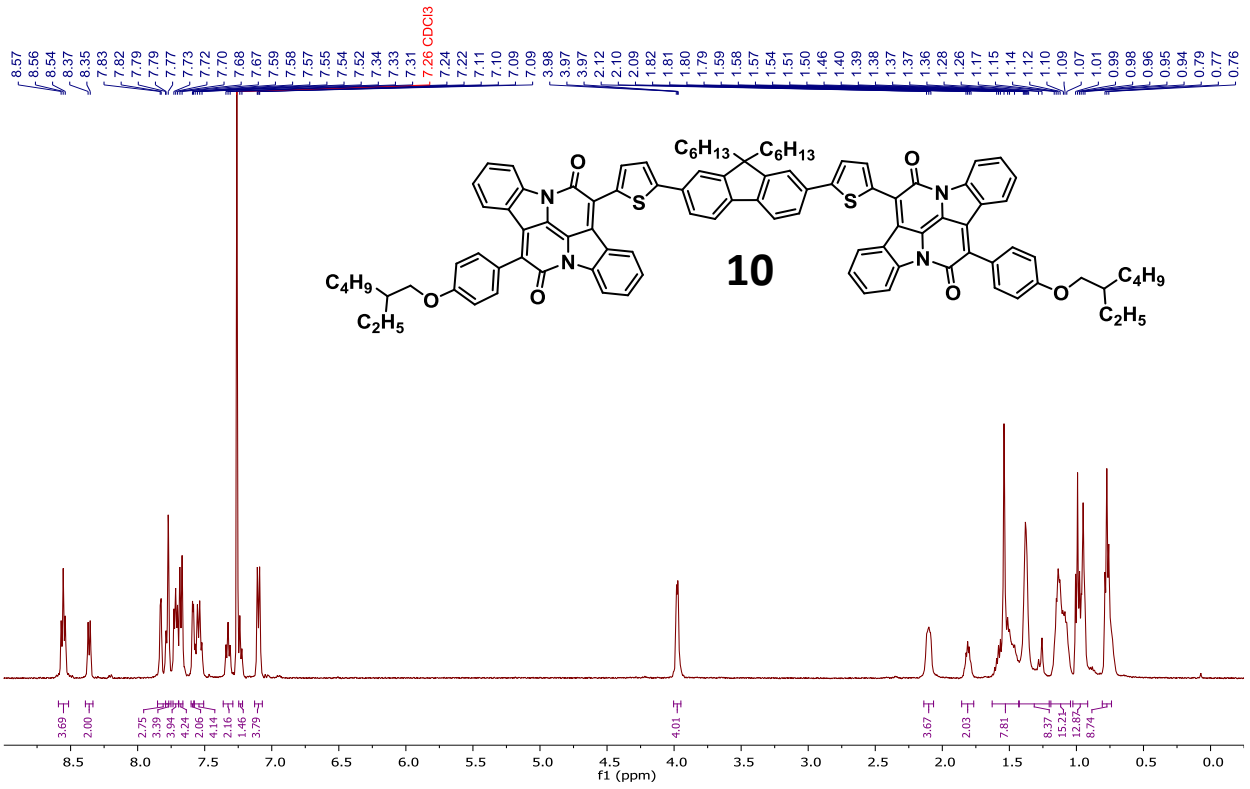
8.57 8.56 8.54 8.37 8.35 7.83 7.82 7.79 7.79 7.77 7.73 7.72 7.70 7.68 7.67 7.59 7.58 7.57 7.55 7.54 7.52 7.34 7.33 7.31 7.26 CDCl3 7.24 7.22 7.11 7.10 7.09 7.09 3.98 3.97 3.97 2.12 2.10 2.09 1.82 1.81 1.80 1.79 1.59 1.58 1.57 1.54 1.51 1.50 1.46 1.40 1.39 1.38 1.37 1.37 1.36 1.28 1.26 1.17 1.15 1.14 1.12 1.10 1.09 1.07 1.01 0.99 0.98 0.96 0.95 0.94 0.79 0.77 0.76
10
3.69 2.00 2.75 3.39 3.94 4.24 2.06 4.14 2.16 1.46 3.79 4.01 3.67 2.03 7.81 8.37 15.21 12.82 8.74
f1 (ppm)

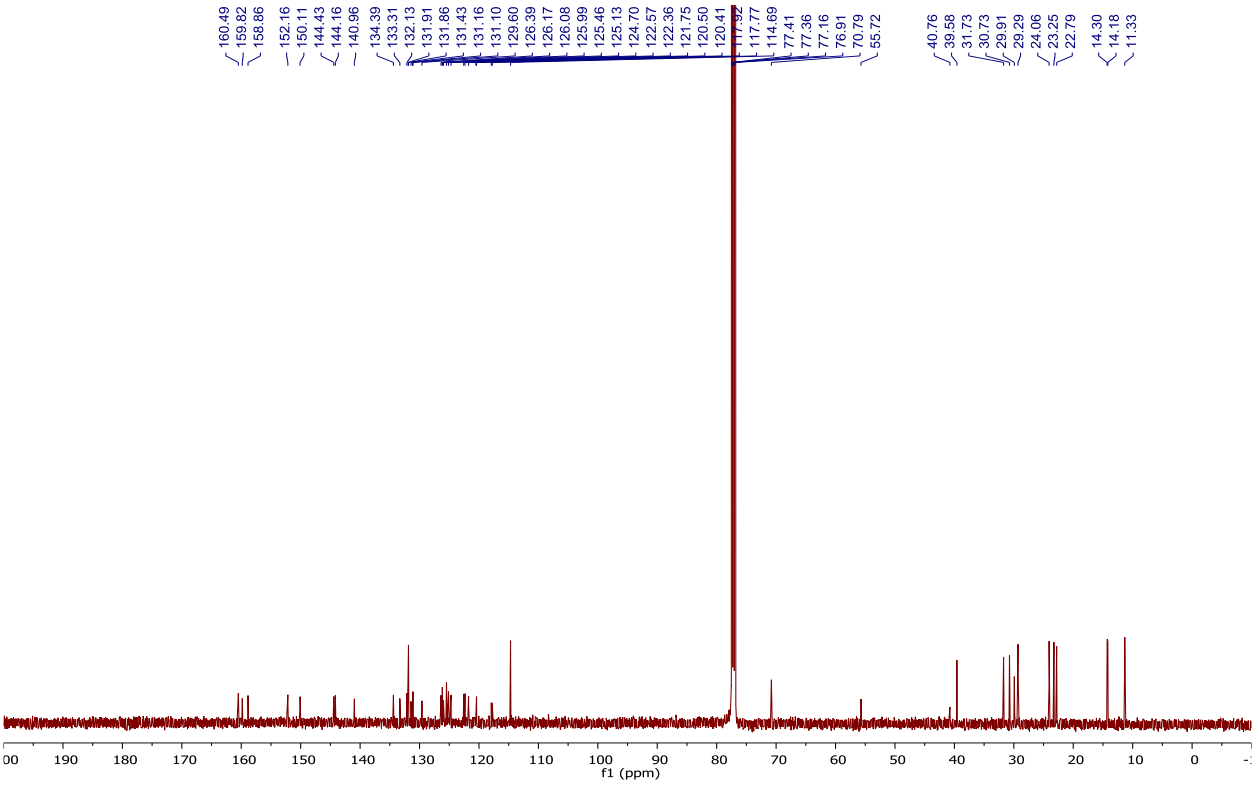
160.49 159.82 158.86 152.16 150.11 144.43 144.16 140.96 134.39 133.31 132.13 131.91 131.86 131.43 131.16 131.10 129.60 126.39 126.17 126.08 125.99 125.46 125.13 124.70 122.57 122.36 121.75 120.50 120.41 117.92 117.77 114.69 77.41 77.36 77.16 76.91 70.79 55.72 40.76 39.58 31.73 30.73 29.91 29.29 24.06 23.25 22.79 14.30 14.18 11.33
f1 (ppm)

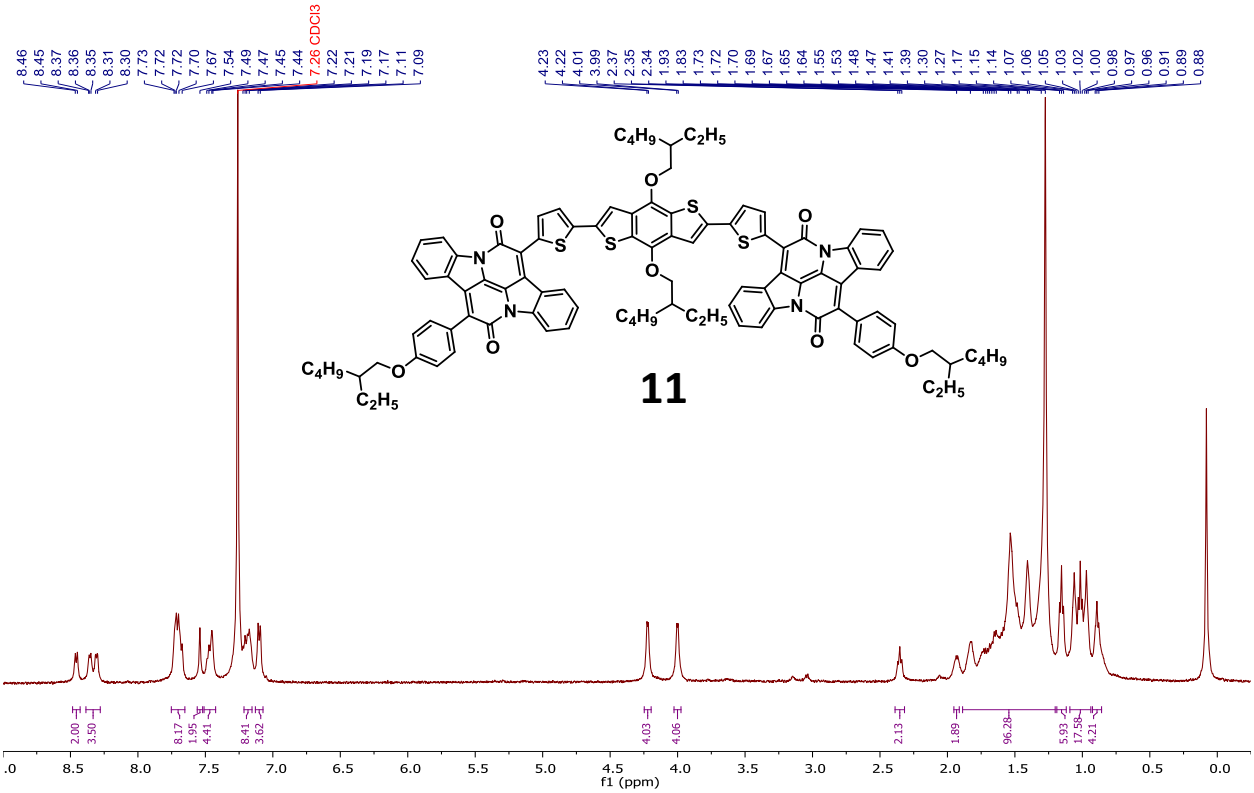

^{13}C prohibited by low solubility

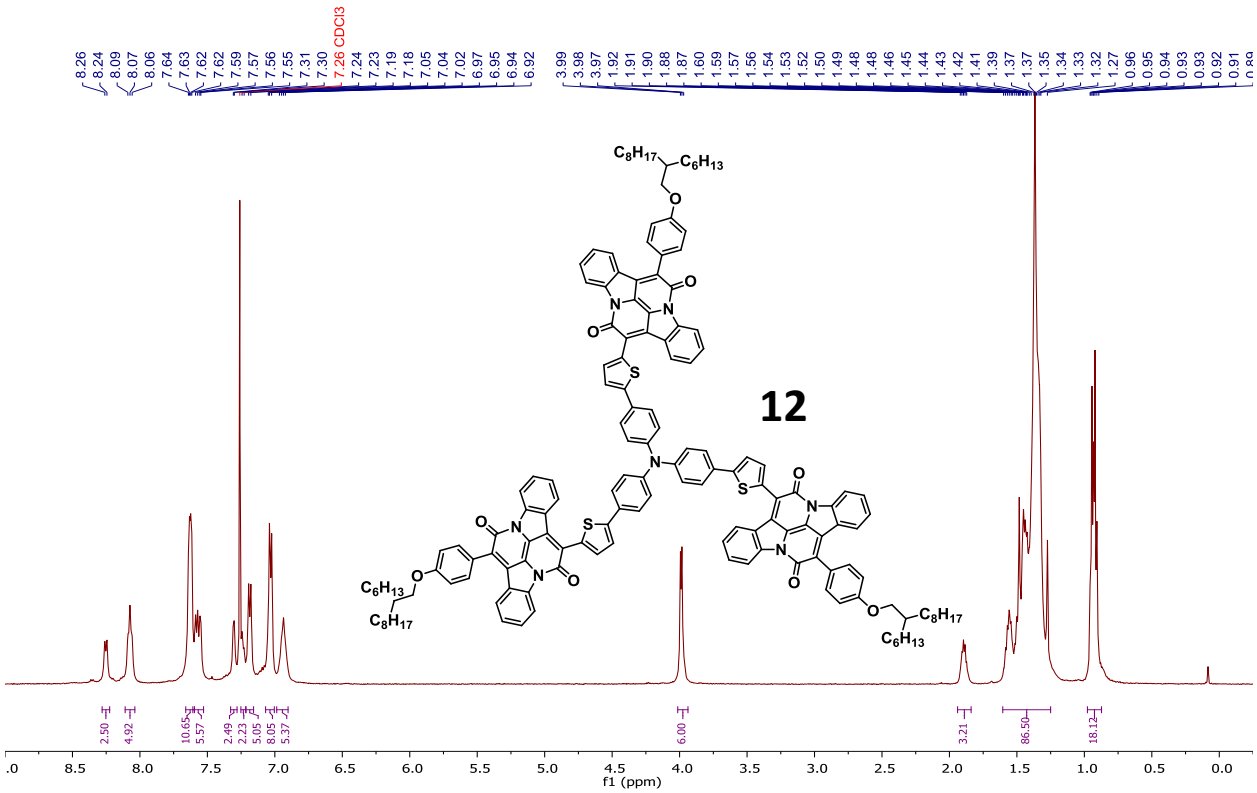
12
f1 (ppm)

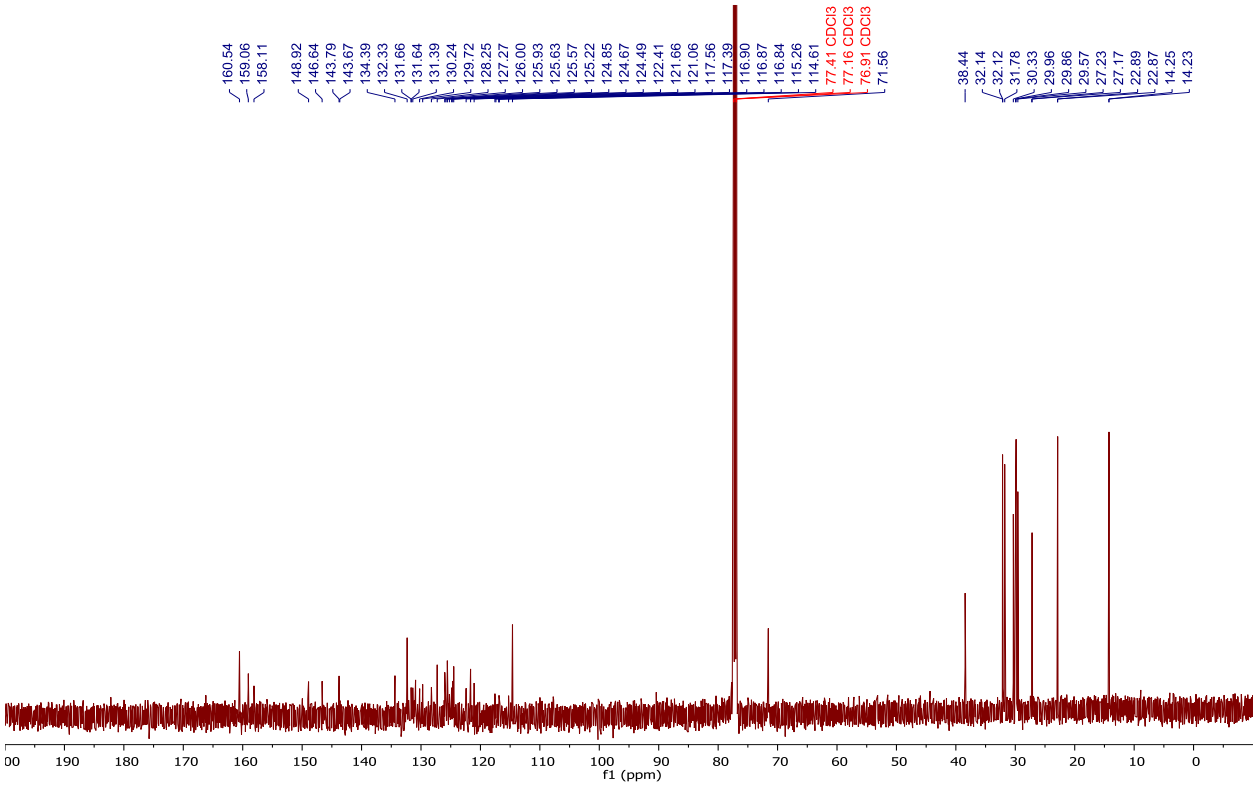
f1 (ppm)

Chapter 3. Double S_NAr Functionalization of 5,6-difluoro-1,2,5-benzothiadiazoles with 2-(1,3-dithiol-2-ylidene)malononitrile (DTM) to Improve *n*-type Carrier Transport

Abstract

The slow development of new electron deficient materials has long been a bottleneck for advancing organic semiconductors to the point of widespread commercialization. Increased research interest in non-fullerene acceptors (NFAs) underlies the demand for new strategies to improve acceptor ability. To this end, we propose the use of the 2-(1,3-dithiol-2-ylidene)malononitrile (DTM) as a functional group capable of modifying the electronic and physical properties of existing materials. Facile dithiolate salt formation and subsequent S_NAr reaction with aryl difluorides provide an efficient route for inserting DTM into conjugated systems. Because of the push-pull nature of this dithiolate, a strong withdrawing effect can be envisioned to act on these systems through a zwitterionic resonance effect.

Exchanging functionality in a 1,2,5-benzothiadiazole (BTD) model system allows for a direct comparison of DTM and other dithiolate groups to more common hydrogen, fluorine substituents. Polymers incorporating fluorine and DTM show similar withdrawing ability but DTM modified substrates boast broad light absorption, strong solvatochromic and thermochromic behavior, and improved crystallinity. As an extension of these enhanced properties, the DTM functionality imbues the modified polymer with ambipolar charge transport, where the fluorine analogue polymer is a unipolar hole transport material. This work validates DTM as a functional group capable of making meaningful improvements in both molecular and macroscopic properties of BTD acceptor materials.

3.1 Conceptualization

Advances in the performance of organic semiconductors are inextricably tied to improvements in molecular design. Over the past 20 years the greatest leaps in device efficiency have come from new electron deficient acceptor materials. There is a great need for novel functional group strategies in order to modulate the energy levels in acceptors. The lowest unoccupied molecular orbital (LUMO) energy is of particular importance since it is responsible for a host of properties, including the band gap and range of light absorption in donor-acceptor systems, V_{OC} for solar cells, and carrier type for OFETs.

The increasing library of available materials has pushed the boundaries of organic photovoltaics (OPV), organic light emitting diodes (OLEDs), and OFETs, but there is still significant room to grow. In particular, high performance electron conducting materials would allow organic compounds to be used in organic complementary logic circuits.[1] This would be particularly impactful as an alternative to Complementary Metal Oxide Semiconductor (CMOS) logic technology[2] which is used to make many essential electronic components such as integrated circuit chips, microprocessors, memory chips, and logic circuits. However, this technology requires both *n*-type and *p*-type materials, and there is a severe deficit of candidates for electron deficient organic semiconductors. To this end, one of the primary goals of this project is to develop new functionality which can improve the *n*-type conductivity of organic semiconductors.

A recent approach to improving *n*-type character is fluorination, which has become ubiquitous in acceptor molecules and polymers.[3] The high electronegativity of fluorine decreases the LUMO energy, which increases the stability with respect to reaction with water or oxygen.[4] Additionally, hydrogen bonding between fluorine and neighboring hydrogen atoms is strong enough to play a macroscopic role in the ordering of active layers, leading to more crystalline domains.[5] The use of fluorinated materials has serious drawbacks, however. Because of their stability, fluorinated compounds resist biological degradation, leading to bioaccumulation of persistent but biologically active molecules. This has led the United States Environmental Protection Agency (EPA) to list a number of perfluorinated compounds as emerging contaminants.[6] Although perfluorinated compounds are the worst actors,[7] fluorinated pharmaceuticals, herbacides, and insecticides also play an increasing role in biological contamination.[8] While fluorination is effective, alternative functional groups capable of the same withdrawing effect are highly sought after.

To this end, we propose the use of an alternative functional group 2-(1,3-dithiol-2-ylidene)malononitrile (DTM) (**Figure 1**). While fluorine provides an electron withdrawing effect through induction, the DTM group is proposed to provide an analogous effect through resonance. This can perhaps be best illustrated through a zwitterionic resonance form in which the anion is stabilized by two withdrawing groups and the cation is stabilized by neighboring electron rich thioethers.

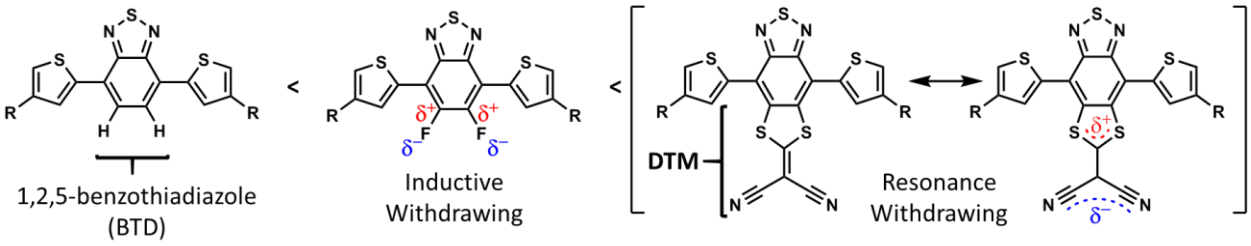

Figure 1: The electron withdrawing effect of fluorine by induction and the 2-(1,3-dithiol-2-ylidene)malononitrile (DTM) group by resonance.

This functional group has seen very limited use in organic semiconductors. However, when incorporated, the change in properties have been drastic. A double adduct in a benzoquinone system increases the electron affinity to the point of surpassing even chloranil.[9] Naphthalene diimide (NDI) derivatives have also been substituted with this functional group to vastly decrease LUMO levels compared to the parent NDI.[10] Despite these sporadic examples, the use of this functional group has only been limited in small molecules. DTM is cross conjugated, therefore, inserting it within a polymer chain would severely disrupt conjugation and harm the electronic properties.[11] This is inherently limiting of charge transport in conjugated polymers, which are highly dependent on streamlined conjugation pathways along the backbone.

In order to incorporate DTM into polymers, we propose placing the group tangential to the conjugation pathway. This would allow for the inclusion of the strong resonance effect, thereby increasing the electron deficient nature of acceptor monomers without disrupting conjugation. The primary way to add the DTM group is through nucleophilic aromatic substitution (S_NAr) of a dithiolate salt. The dithiolate group is highly nucleophilic due to the polarizable nature of the sulfur atoms. Crucially, the double sulfur addition locks the electron accepting subunit into a planar configuration with the rest of the molecule, enforcing strong orbital overlap and conjugation.

This precursor salt can be made simply from double addition of an activated methylene into carbon disulfide. Condensation has been accomplished with a number of acidic methylene groups, making it a highly versatile reaction. Dithiolate salts made from malononitrile,[12] 1,3-diketones,[13] and sulfones[14] have all been reported. Despite this, only malononitrile adducts have been added into organic semiconductors, which prompts us to explore the utilization of different activated methylene adducts other than malononitrile-based dithiolate for electron acceptors.

To implement this design, benzothiadiazole (BTD) was chosen as a model system due to its high performance and ubiquity among electron acceptors.[15] Benzothiadiazole is strongly withdrawing due to the electron deficient 1,2,5-thiadiazole functionality which locks the fused benzene into an orthoquinone configuration. Quinoidal species have long been shown to lower the bond length alternation in polymers, thus increasing charge mobilities and improving planarity.[16] There may be additional withdrawing capability from the thiadiazole adopting a hypervalent sulfur –N=S=N- linkage[17] or a three-center-four electron bond.[18]

There have been many efforts to supplement the withdrawing capability of BTD. The most common approach is 5,6-difluorination,[3, 19] but insertion of resonance withdrawing nitrile groups[20] has also been explored. Heteroannulation of benzothiadiazole has been a highly effective strategy to form infrared (IR) absorbing dyes such as thiadiazoloquinoxaline (TDQ)[21], benzobisthiadiazole (BBT)[22], and [1,2,5-]-thiadiazolo[3,4-f]benzotriazole (TZBTTT)[23]. Herein, we chose the common 5,6-difluorobenzothiadiazole unit as the electrophile for the S_NAr reaction given that the difluorination will effectively lower electron density on the BTD core to ensure high reactivity towards nucleophiles.

The work in this chapter sets out to determine if this functionality could be incorporated into polymers, rather than just small molecules, as an alternative withdrawing group to fluorine. Since only malononitrile based systems have been used in the literature, the scope was expanded to other activated methylene groups as well in an effort to explore the electronic effect of alternative withdrawing groups. The ultimate goal is to observe how changes in molecular functionality impact the materials properties on a macroscopic level, such as optical, aggregation, and charge transport properties in a polymeric system.

3.2 Synthesis of a Model System

To test the efficacy of this modification, the 5,6-difluorobenzothiadiazole model system was synthesized (**Scheme 1**). In an addition-aromatization reaction, commercially available 4,5-difluorobenzene-1,2-diamine **1**, is treated with two equivalents of thionyl chloride in the presence of triethylamine to produce the benzothiadiazole **2** with release of SO_2 gas. Iodination in concentrated sulfuric acid cleanly provides **3** which could undergo Stille coupling with **4a** or **4b** to provide the highly fluorescent compounds **5a** and **5b**.

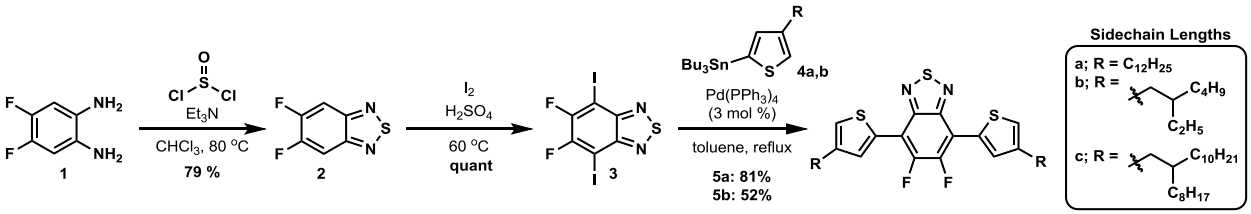

Scheme 1: Synthesis of 5,6-difluorobenzo[c][1,2,5]thiadiazole based substrates

To form the dithiolate salt, malononitrile is treated with sodium hydroxide before addition of carbon disulfide (**Scheme 2a**). The malononitrile dithiolate **salt-6** is isolated by filtration. After screening solvents, DMF is found to facilitate the desired S_NAr reaction to provide **6a** in 58% yield. The analogous salt formation could be accomplished with diethyl malonate **7** and acetylacetone **8**, affording **salt-7** and **salt-8**, respectively. The S_NAr reaction with the diethyl malonate dithiolate salt is effective, producing **7a** in 72% yield. Conversely, the acetylacetone dithiolate **salt-8** gives a low yield of **8a**, possibly due to low stability of the product. This establishes that nitrile, ester, and ketone functionality are all tolerated under the reaction conditions. The reaction of the **salt-6** with **5b** is lower yielding compared to the octyl alkylated **5a** (**Figure 3b**). However, reaction with brominated **9c** proceeds in excellent yield, selectively substituting leaving groups at the fluorinated positions over the less activated brominated positions.

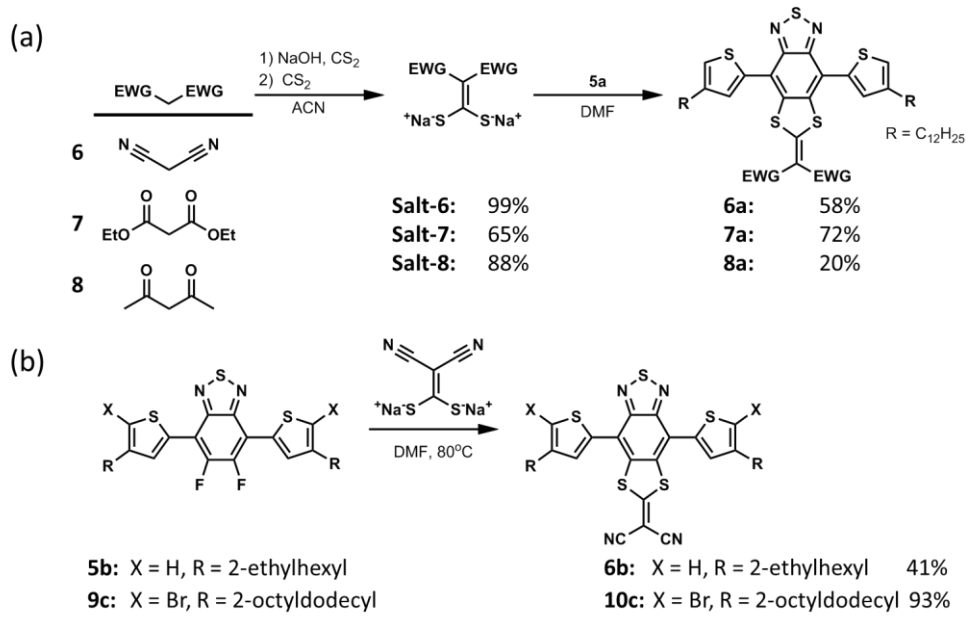

Scheme 2: S_NAr reaction with different (a) dithiolate salts and (b) alkyl chains

A one-pot reaction was attempted in order to avoid isolation of the hygroscopic dithiolate salts. It was believed that synthesizing the salt and executing the S_NAr reaction *in-situ* could simplify the reaction setup and reduce waste. By treating the activated methylene compounds with sodium *t*-butoxide and CS_2 in DMF before addition of **5a**, the above reactions are achieved. However, this produced lower reaction yields than in cases where the salt is isolated first. Despite the depressed yields, this route could be further optimized to be useful for applications where the dithiolate salt is non-isolable.

3.3 Characterization of the Model System

To assess the changes in electronic behavior due to functionalization, **5a** and **6a-c** are compared to the hydrogen substituted parent benzothiadiazole **S1** by UV-Vis and cyclic voltammetry (**Figure 2a**). The optical band gaps, determined from the absorption onset, are strikingly similar for all the model compounds (**Figure 2b**). This implies that any electronic changes due to functionalization affect both the HOMO and LUMO approximately equally. Interestingly, the dithiolate adducts introduce new absorption peaks, greatly enhancing the absorption around 400 nm. Compound **6a** has many additional peaks, providing both wider spectral coverage and a stronger extinction coefficient than difluoro substituted **5a**.

Cyclic voltammetry confirmed that the HOMO and LUMO levels are both lowered simultaneously. All substituted compounds **5a**-**8a** have lower lying HOMO and LUMO levels than the unsubstituted benzothiadiazole with hydrogen substituents **S1** (**Figure 2c**). While the reduction of compounds **S1**, **7a**, and **8a** are reversible, the remaining reduction and oxidation peaks are irreversible. Compound **6a** has the lowest HOMO level and a LUMO only slightly higher than that of **5a**, making it a compound of particular interest (**Figure 2d, Table 1**). Because of the superior extinction coefficient and low HOMO and LUMO levels **6a** was chosen as the most promising molecule to investigate further as an alternative to **5a**.

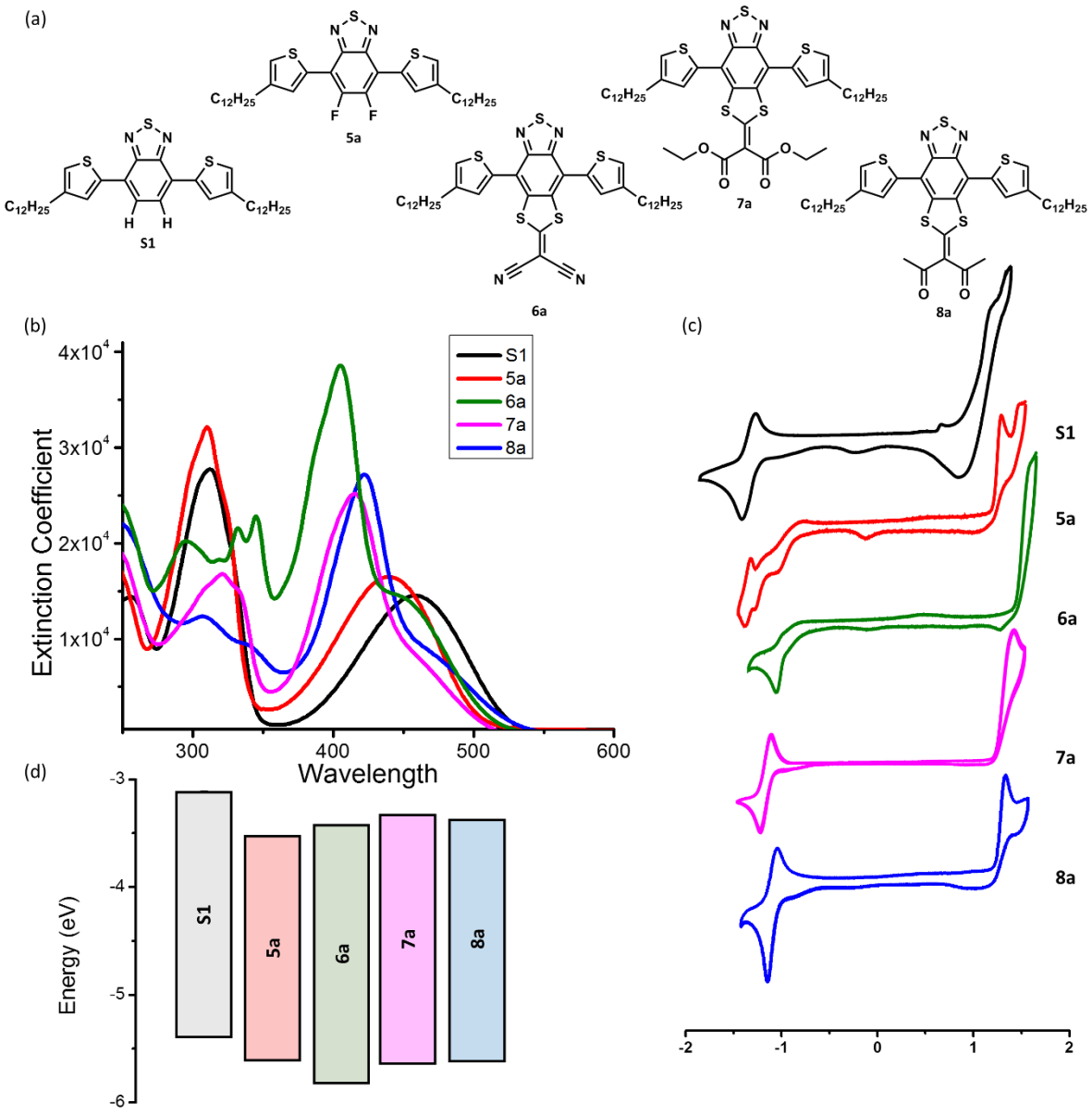

Figure 2: A comparison of the electronic properties of (a) substituted benzothadiazoles as tested by (b) UV-Vis spectroscopy and (c) cyclic voltammetry (with respect to Fc/Fc^{+}), with (d) a visual representation of the electrochemical band diagrams

Table 1: A Summary of Optoelectronic Properties of the BTD Based Small Molecules

Compd	UV-Vis				Cyclic Voltammetry		
	λ_{max} (nm)	ε_{max} (M^{-1} cm^{-1})	λ_{max} (/nm)	E_g^{opt} (eV)	E_{HOMO} (eV)	E_{LUMO} (eV)	E_g^{Elec} (eV)
S1	527	2.8E4	312	2.35	-5.40	-3.11	2.28
5a	503	3.3E4	310	2.46	-5.61	-3.52	2.08
6a	511	3.9E4	404	2.42	-5.83	-3.43	2.40
7a	530	2.5E4	415	2.34	-5.64	-3.32	2.31
8a	539	2.8E4	422	2.30	-5.62	-3.37	2.25

3.4 Polymeric Systems

With the model compounds **6a** & **6b** in hand, bromination with NBS is used pursed to provide a functional handle for cross coupling reactions (**Scheme 3a**). For the synthesis of organic semiconducting polymers, Stille coupling is preferred over Suzuki couplings as the former generally gives higher molecular weight polymers despite that it comes with the drawback of requiring toxic organotin reagents.

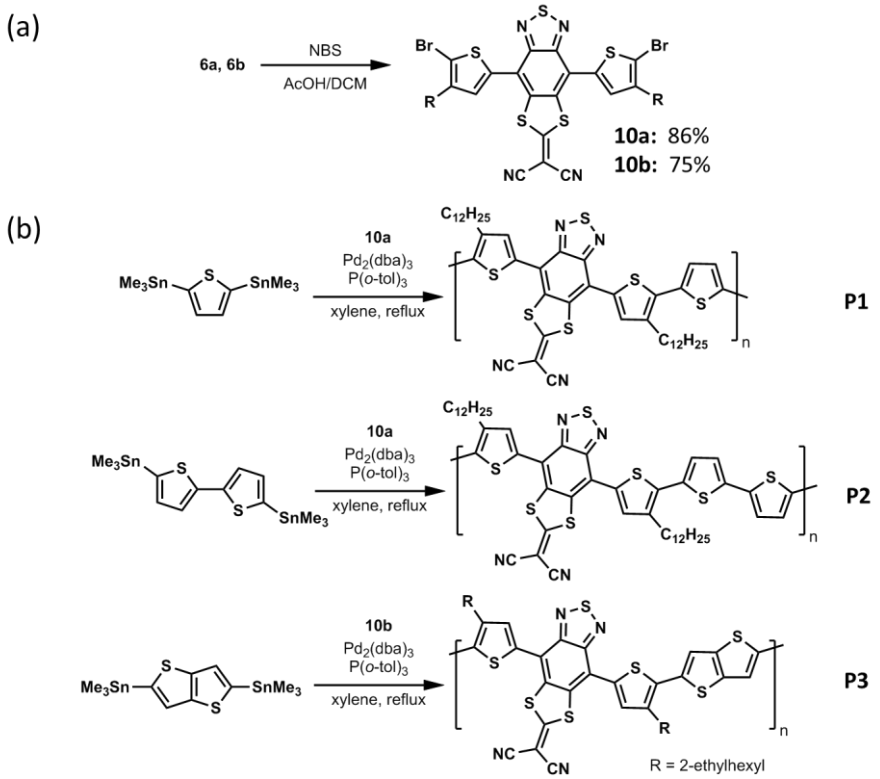

Scheme 3: (a) Monomer synthesis through bromination of **6a** and **6b** and (b) subsequent synthesis of polymers **P1-P3**

In order to lower the band gap, a donor-acceptor strategy has been employed, pairing the electron poor benzothiadiazole acceptor monomers with electron rich donor monomers.[24] Thiophene, bithiophene, and thienothiophene have been chosen as co-monomers due to their

electron rich character and stability. Monomer **6a** underwent Stille polymerization with thiophene and bithiophene to produce polymers **P1** and **P2** respectively (**Scheme 3b**). While the polymerization was successful, these polymers have very strong π stacking interactions between long polymer chains. This strong aggregation causes severely low solubility, which prevents the solution processability necessary to test them in electronic devices.

In order to improve solubility, branching 2-ethylhexyl alkyl chains are incorporated into the thiophene groups to sterically interrupt the backbone $\pi-\pi$ interactions. The resulting Stille polymerization with a thienothiophene monomer improves solubility, but only slightly. To further increase solubility, thiophene groups with pendant 2-octyldecyl chains **10c** are used for cross coupling with a prealkylated benzodithiophene (BDT) unit (**Figure 6a**). Because both monomers now have alkyl chains, solubility improved drastically (**Figure 6b**). As a control, the polymer **P4** has been made from the 5,6-difluorobenzothiadiazole based monomer **9c** (**Figure 6c**).

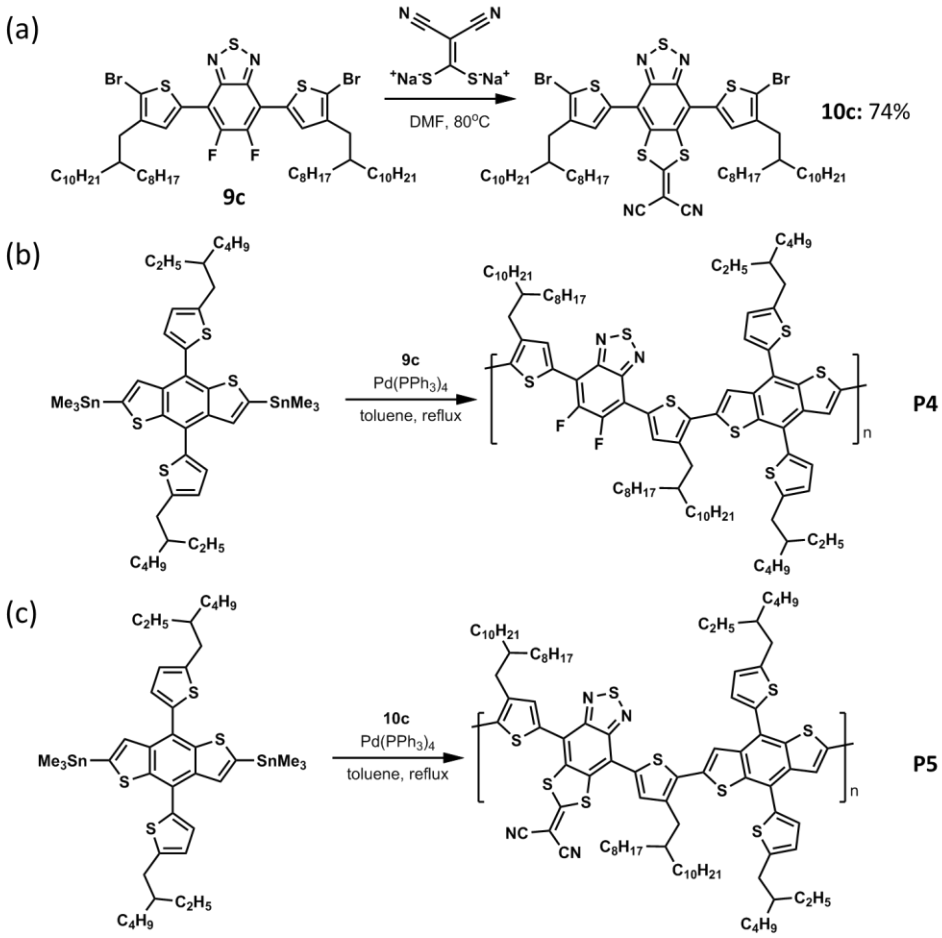

Scheme 4: (a) Monomer synthesis through S_NAr of prebrominated substrate **9c** and (b) subsequent synthesis of polymers **P4** and (c) **P5**

The effect of the sidechain length and branching is made even more apparent during purification. Because high molecular weight polymers tend to have better performance in transistors, it is common to separate polymers by molecular weight via Soxhlet extraction.[25] By

continuously extracting the precipitated polymer samples with increasingly polar solvents, the polymer chains can be separated by solubility. Intermolecular interactions increase with increasing chain length, which lowers solubility. This allows smaller molecular weight oligomers and polymer chains to be separated from longer ones. While polymers **P1-3** could be fractionated in this way, each gave only small amounts of soluble products with the remaining material almost completely insoluble. This also holds true in high boiling point solvents such as chlorobenzene and dichlorobenzene.

By increasing the size of the alkyl chains from 2-ethylhexyl to 2-hexyldecyl chains, the π-stacking can be partially disrupted due to increased steric interactions from the alkyl chains. The resulting polymers **P4** and **P5** are substantially more soluble. Unlike the insoluble **P1-P3**, **P4** has been fully extracted by hot hexanes, while **P5** has been fractionated into hexane and THF fractions. Once the polymers were purified, Size Exclusion Chromatography (SEC) was used to determine the molecular weight distribution of the polymer extracts. To overcome the aggregation in **P1-P3**, high temperature SEC was employed using heated trichlorobenzene as an eluent. Although too insoluble to be processed into devices, enough polymer could be sufficiently dissolved for SEC characterization (**Table 2, Figure A-1, Table A-1**). The insoluble Soxhlet fraction from **P1** has the highest molecular weight compared to the other tested polymers, while the low solubility of **P2** prevents characterization even in the high temperature system. The 2-ethylhexyl substituted **P3** provided low molecular weight oligomers, which is corroborated by low M_W and a narrow polydispersity of 1.1.

Table 2: High Temperature Gel Permeation Chromatography of Substituted Benzothiadiazole Polymers

Polymer	Soxhlet Fraction	M_W [a]	M_N [a]	polydispersity
P1	Insoluble	2.02E4	4.16E4	2.06
P2	Insoluble	-	-	-
P3	Insoluble	5.25E3	5.96E3	1.13
P4	Hexane	1.03E4	2.00E4	1.95
P5	Hexane	1.37E4	3.56E4	2.59
P5	THF	1.67E4	4.96E4	2.98

a Molecular weights in reference to polystyrene standards

The polymers **P4** and **P5** have substantially higher solubility and comparatively high molecular weights. Presumably the alkylated monomers prevent premature precipitation during the polymerization reaction, allowing for longer chain growth. The molecular weight distribution of **P4** was lower than either the hexane or THF Soxhlet extracts of **P5**. This clearly indicates that the DTM functionalization does not hinder polymerization.

It is notable that the high extinction coefficients and broad absorption profiles of these polymers interfere with light scattering detectors in standard analytical instruments. By calibrating the SEC with polystyrene of known molecular weights, this issue is compromised by using a viscometer based detector. Polystyrene equivalent molecular weights are not the exact molecular weights in the new polymeric system. Due to differences in shape and flow characteristics on the GPC column between polystyrene and **P1-P5**, direct calculations of

monomer units would not be accurate.[26] However, the measurements are still precise and can be used to reliably compare these structurally similar polymers.

3.5 Optoelectronic Properties of BTD Polymers

During the course of synthesizing and purifying **P1-P5** drastic shifts in polymer color were observed. This striking solvatochromic effect was characterized using UV-Vis spectroscopy, with the thiolate modified polymer **P5** displaying a large 105 nm shift in absorption onset by changing the solvent from chloroform to hexane (**Figure 3**). A deep green coloration of **P5** in hexane underwent a reversible color change to orange/brown when diluted in chloroform. The solvatochromic effect for **P4** is also present though less pronounced, showing a blue to purple color change under the same conditions.

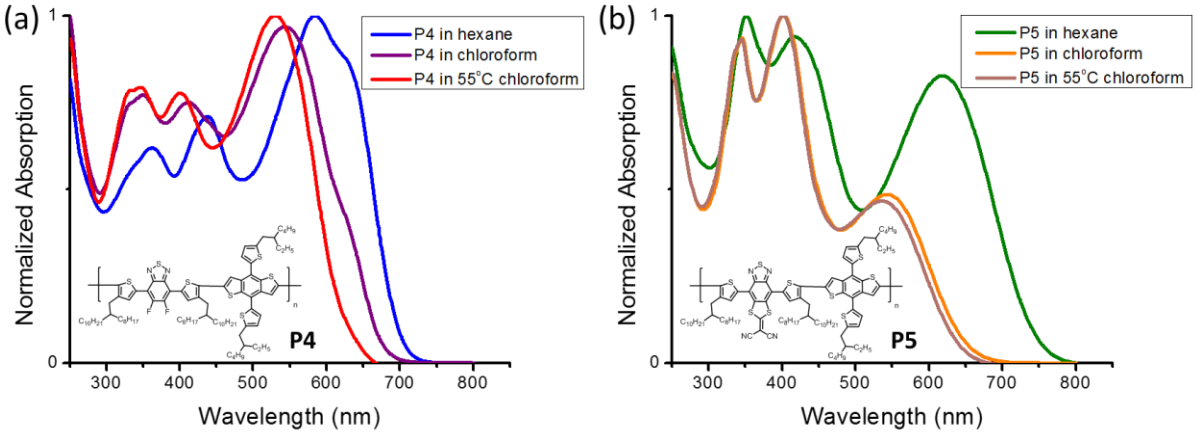

Figure 3: Solvatochromic behavior of (a) **P4** and (b) **P5** observed from solutions of hexane, chloroform and chloroform heated to 55°C

The analogous color change is observed for the remaining polymers **P1**-**P3** as well (**Figure 4a-c**). The largest blue shift is found in heated chloroform, although in the case of **P1** the hypsochromic shift is minor even at elevated temperatures. Conversely, a red shift was observed by decreasing the solvent polarity with a nonpolar 1:1 hexane/chloroform mixture, which was chosen over pure hexane to allow sufficient dissolution for the poorly soluble **P1**-**P3**. In the case of **P4** and **P5**, red shift was not as prominent in the 1:1 hexane chloroform mixture as was found for spectra in pure hexane (**Figure 4d,e**).

Perplexingly, the same redshift in absorption onset was also observed when chloroform is diluted with methanol, a more polar solvent. Positive solvatochromic materials red shift when solvent polarity is increased, while negative solvatochromic materials blue shift under the same conditions. This paradoxical trend of induced bathochromic shift when chloroform solutions are exposed to both more and less polar solvents is inconsistent with classical solvatochromic behavior.

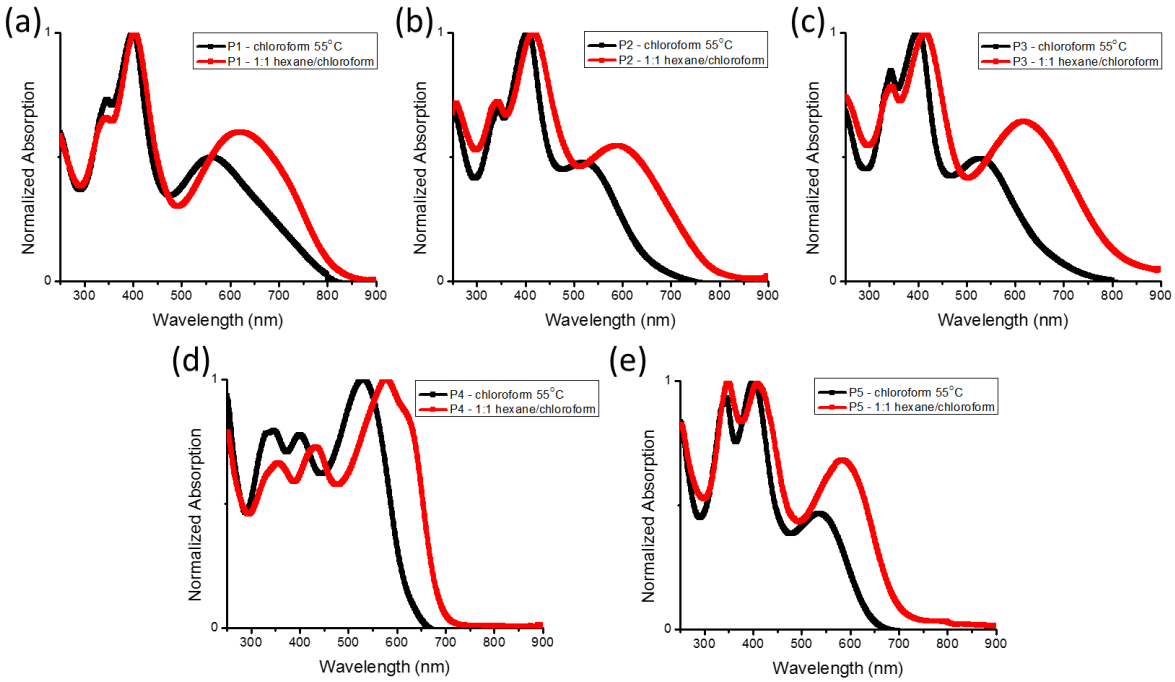

Figure 4: UV-Vis spectroscopy of **P1**-**P5** in solutions of 1:1 chloroform/hexane (red) and chloroform solution at 55 °C (black)

To understand these solvatochromic changes, a dilution experiment was undertaken. When **P5** is dissolved in chloroform a bright red solution is observed. Incrementally diluting the solution with methanol produces two distinct phases. From 0% to 50% methanol dilution, the absorption of **P5** drastically redshifts (**Figure 5a**). When additional methanol is added, the bathochromic shift ceases and the peak intensity decreases (**Figure 5b**).

To explain this phenomenon, an aggregation model is proposed. In chloroform the polymer backbone can be fully solvated, separating individual polymer chains. In non-polar hexane solvent, the interpolymeric π–π interactions are more stabilizing than interactions with solvent, inducing aggregation. This polymeric clustering is proposed to rigidify the polymers, increasing intermolecular π–π stacking and improving absorption in a process called *J*-aggregation. The dipole introduced through the DEM functional group would further favor polymer-polymer interactions, exaggerating the *J*-aggregation effect. Despite this aggregation, hexane is still able to interact strongly with the long alkyl chains, which maintains solubility. This is not the case for methanol which induces the same aggregation state, but after a 1:1 ratio of methanol in chloroform is attained the polymers reach a fully aggregated state that methanol is unable to solvate (**Figure 5**). This can explain why the intensity of light absorption decreases in methanol, since this highly polar solvent cannot dissolve the polymer aggregates which precipitate from solution.

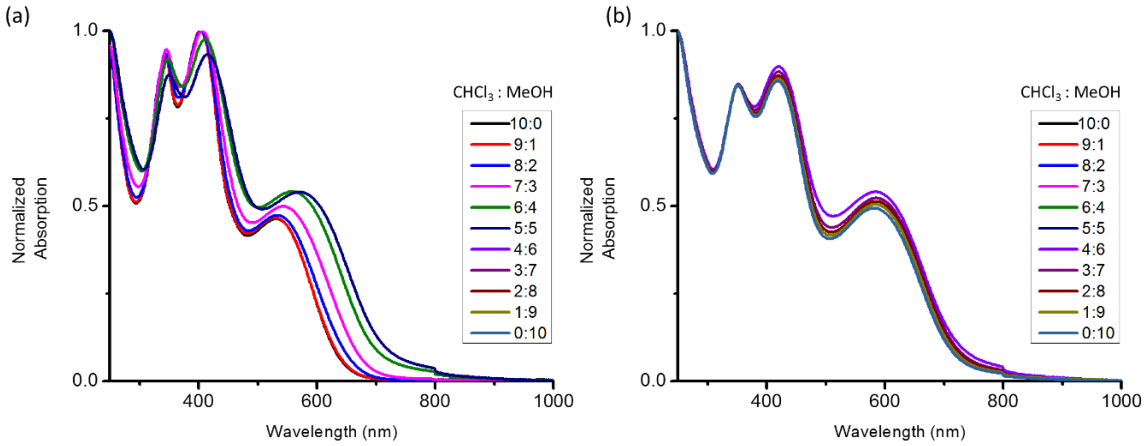

Figure 5: Solvatochromic behavior induced by diluting a chloroform solution of **P5** with methanol as an anti-solvent, showing a notable (a) aggregation regime and (b) precipitation regime

The same aggregation-disaggregation effect has also been observed thermally. Dissolving polymer **P2** in *o*-dichlorobenzene (ODCB) gives the proposed aggregated state (**Figure 6**). By increasing the temperature, the solvent would have the thermal energy necessary to break up aggregation and the resulting absorption onset is blue shifted by an outstanding 187 nm. An isosbestic point is observed around 600 nm, implying that transitioning from the aggregated to disaggregated states does not go through a third intermediate state.

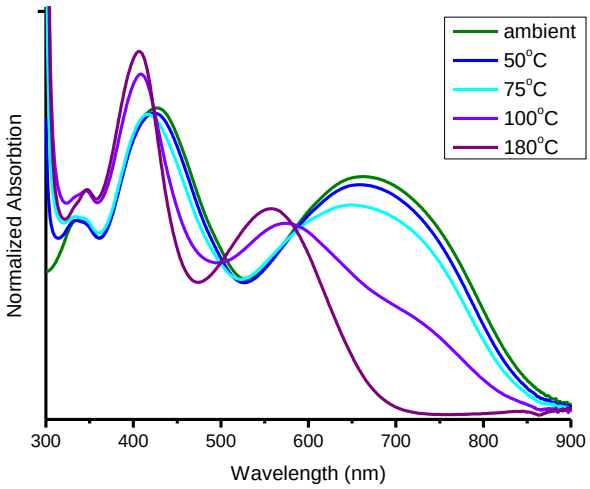

Figure 6: Thermochromatic behavior of **P2** heated in dichlorobenzene

The aggregation-based solvatochromism hypothesis is consistent with the absorption features observed in the solid state (**Figure 7**). When **P5** is cast as a thin film there is no solvent to break up potential aggregates. Accordingly, the absorption profile for the solid state very losely aligns with that of the hexane and methanol-$CHCl_3$ anti-solvent solution spectra, albeit with differing intensities.

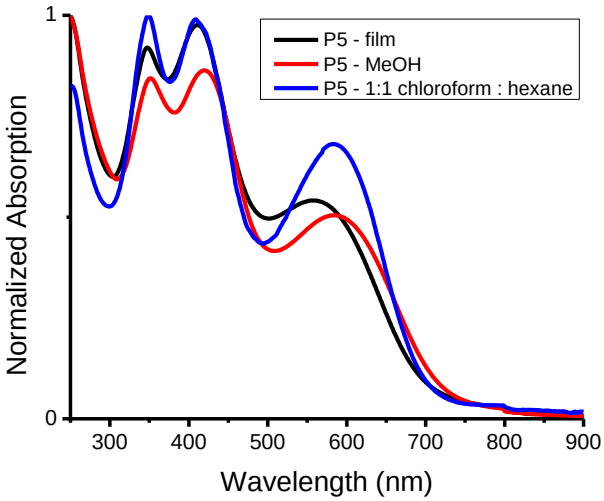

Figure 7: Comparison of the aggregated absorption profile for **P5** in the solid state, in methanol, and 1:1 hexane/chloroform solution

Cyclic voltammetry (CV) of polymer thin films show strong oxidation peaks, along with comparatively weak reductions. The electrochemical HOMO and LUMO levels follow the same trend as is observed in the monomeric system. The polymers **P4** and **P5** have similar LUMO levels of -3.66 eV and -3.59 eV respectively, and **P5** has a lower band gap overall (**Figure 8, Table 3**). These data show that the modification has a direct impact on the electronics of both monomeric and polymeric systems. Additionally, they confirm that the S_NAr modification provides a comparable withdrawing effect with the parent fluorinated compound, even within polymeric systems. It is also notable that the electrochemical band gaps match closely with optical band gap for the disaggregated polymers.

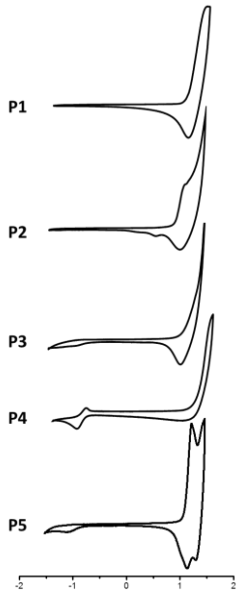

Figure 8: Cyclic voltammetry of polymers

Table 3: A Summary of Optoelectronic Properties of the Polymers

Compd	UV-Vis Aggregated		UV-Vis Disaggregated[a]		Cyclic Voltammetry		
	λ_{onset} /nm	E_g^{opt} /eV	λ_{onset} /nm	E_g^{opt} /eV	E_{HOMO} /eV	E_{LUMO} /eV	E_g^{Elec} /eV
P1	817[b]	1.52	800[d]	1.55[d]	-5.35	-3.61	1.74
P2	785[b]	1.58	662	1.87	-5.30	-3.40	1.90
P3	822[b]	1.51	682	1.82	-5.39	-3.54	1.85
P4	698[c]	1.77	616	2.01	-5.74	-3.66	2.08
P5	743[c]	1.66	639	1.94	-5.50	-3.59	1.92

a determined from 55°C chloroform solution. ***b*** determined from hexane solution, ***c*** determined from 1:1 hexane/chloroform solution ***d*** Not fully disaggregated, even at elevated temperatures

3.6 Morphological Studies

In order to understand how polymers **P4** and **P5** behave in the solid state, Grazing Incidence Wide Angle X-ray Scattering (GIWAXS) has been used to analyze polymer crystallinity (**Figure 9a-d**). The drastic changes in polymeric aggregation in the solution phase inspired investigation if similar changes could occur in the solid phase. Since heat has shown to cause disaggregation in solution, it is possible that changes in temperature could significantly alter the solid state crystallinity. To test this hypothesis, **P4** and **P5** thin films were prepared by spincasting from chloroform solution and analyzed by variable temperature GIWAXS in Ar-purged sample chamber with a heating stage.

Two parameters are particularly useful in understanding changes in crystallinity: *d*-spacing and crystallite size. The *d*-spacing describes the average distance between repeat units. Changes in the *d*-spacing correspond to changes in polymer structure such as the mean π–π stacking distance and lamellar stacking distance. The crystallite size τ describes the mean size of the crystalline domains. This parameter can be derived from peak broadening of a diffraction peak at full-width-half-maximum (FWHM) and is described using the Scherrer equation.[27] Derivation and calculations used to determine the *d*-spacing and crystallite size are provided in the appendix (**Figure A-2, Table A-2**).

The diffraction peaks for the initially prepared room temperature samples are rather broad, indicating small average crystallite sizes (**Figure 9a-d**). As the temperature is increased the polymers are given enough thermal energy to overcome local energetic minima, which allows them to reach more thermodynamically stable configurations, resulting in a more crystalline state and sharper peaks (**Figure 9e-f**). Unlike the reversible aggregation in solution, the changes in polymeric ordering remains set once the samples are recooled. This validates thermal annealing as an effective method to permanently alter the crystallinity of **P4** and **P5** in devices.

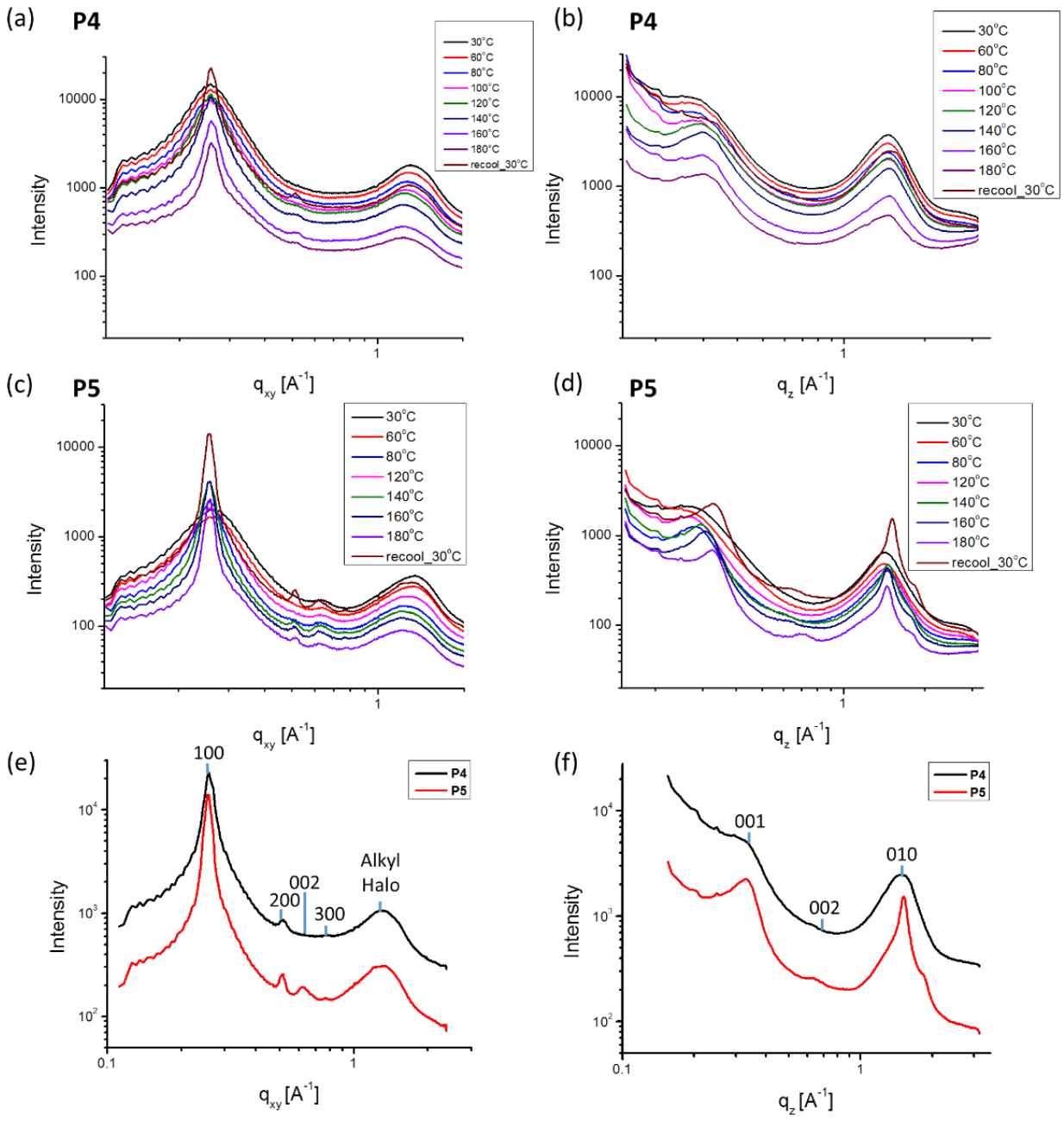

Figure 9: Variable temperature GIWAXS linecuts of **P4** in the (a) q_{xy} and (b) q_z planes and **P5** in the (c) q_{xy} and (d) q_z planes. For direct comparison, the initial and fully annealed scans of **P4** and **P5** are superimposed in the (e) in plane and (f) out of plane directions with labels for identified diffraction peaks

It was determined that both **P4** and **P5** prefer a face-on geometry, with the polymer π-surface lying parallel to the substrate, as indicated by prominent lamellar 100, 200, and even a 300 peak for **P5** in the q_{xy} plane and a strong π–π stacking 010 peak in the q_z direction.[28] Less prominent 001 and 002 peaks appear in both the q_{xy} and q_z directions, though there seems to be overlap between the q_{xy} 100 peak and 001 peak. Despite this, the q_{xy} 002 peak is clearly

identifiable both in-plane and out of plane. A diffraction from the alkyl groups, often called "alkyl halo" can be seen as a broad signal in the q_{xy} direction.

Comparing the crystallite sizes after annealing, it is clear that **P5** is more crystalline than **P4**. For **P4**, a lack of a 300 peak and 002 peaks are strong evidence for lower long-range order compared to **P5**. Calculating the mean crystallite size by Scherrer analysis confirms that **P5** has consistently higher crystallinity than **P4** for all analyzed peaks post-annealing (**Figure 10**). The rate of crystallite growth for **P4** increased nearly linearly with respect to temperature (**Figure 11a**,**c**,**e**). In contrast, **P5** follows a similar linear regime at low temperatures, but around 140 °C there is a large increase in crystallinity that can be observed in both the lamellar stacking 100 and π–π stacking 010 peaks (**Figure 11b,d**).

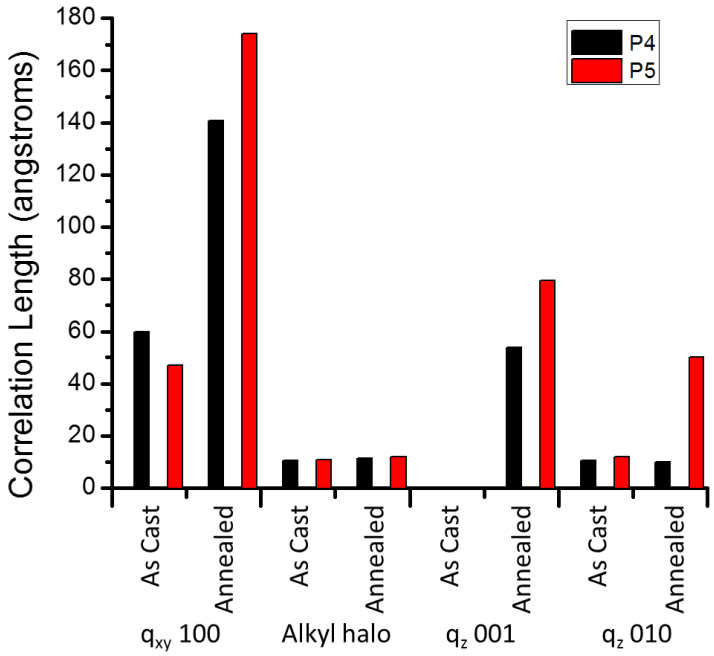

Figure 10: Comparison of the crystallinity of **P4** and **P5** pre- and post-annealing

Of particular interest are the 001 peaks, which correspond to the repeat units within the polymer backbone (**Figure 11e,f**). **P5** has almost double the monomers within linear stretches of the polymer backbone as **P4** with 4.4 repeat units compared to 2.6 repeat units (calculated monomer lengths in **Figure A-3**). This higher order within **P5** is highly beneficial for charge transport along the length of a polymer.

Changes in the *d*-spacing are also observed upon heating. The lamellar spacing for **P4** and **P5** are fairly consistent throughout heating, with the distance between lamella of 24 Å for **P5** post-heating (**Figure 11a,b**). In contrast, the out-of-plane 010 spacing for **P5** becomes much closer through the annealing, shrinking from 4.33 Å to 4.03 Å, indicative of strong π–π interactions (**Figure 11d**). Meanwhile, the 010 peak for **P4** remains constant at around 4.15 Å, outside the range of strong π-overlap between polymer chains (**Figure 11c**). The *d*-spacing for the 001 peaks decreases upon annealing for both polymers, although the decrease for **P5** is larger

(**Figure 11e,f**). Thermal annealing plays a significant role in the interpolymeric spacing for **P5**, whereas **P4** only experiences minor changes from heating.

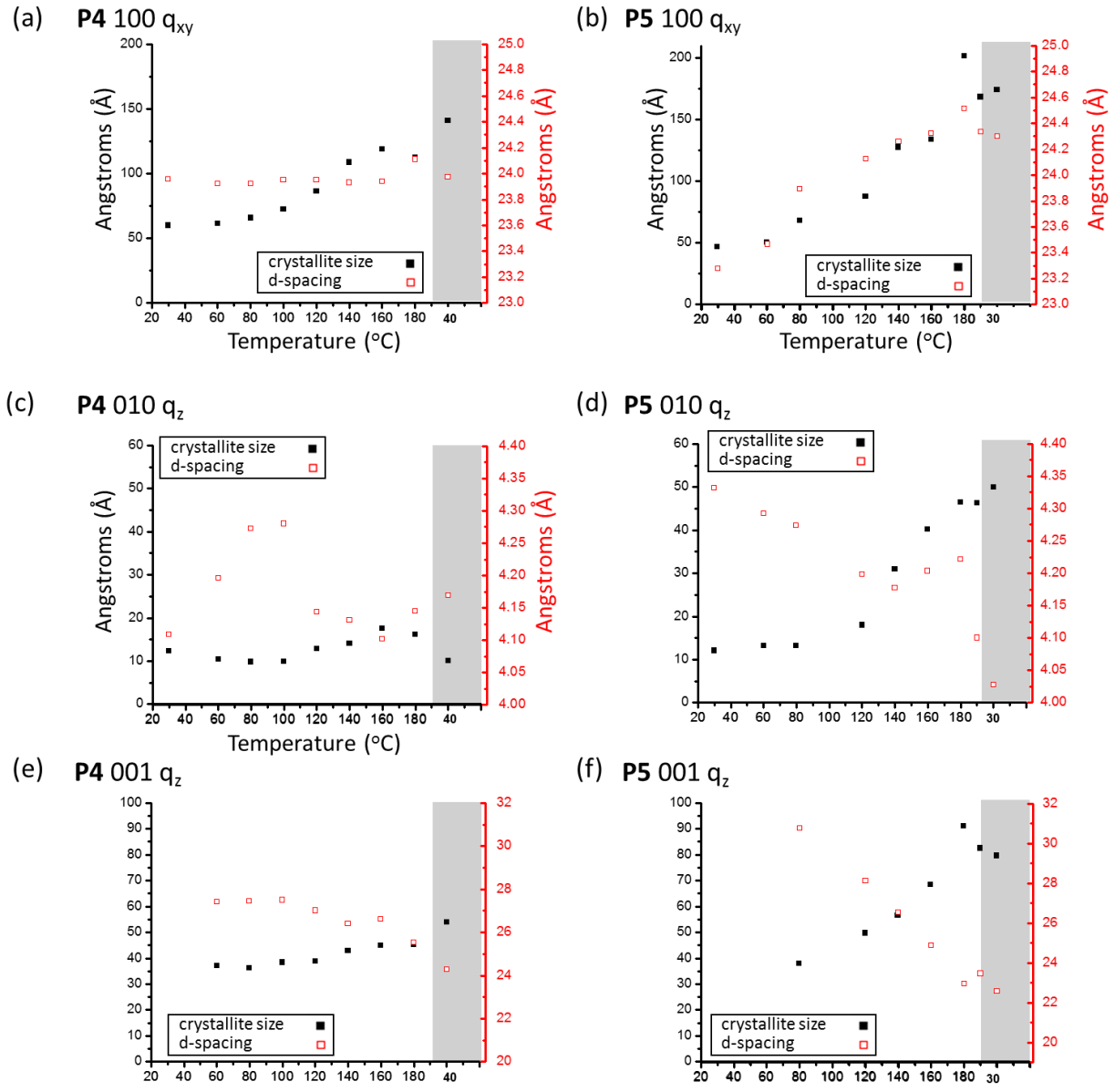

Figure 11: Plotting the changes in crystallite size (black squares) and d-spacing (red hollow squares) for notable peaks in the **P4** and **P5** spectra. The 100 q_{xy} lamellar stacking peak for (a) **P4** and (b) **P5**, the 010 q_z π–π stacking peak for (c) **P4** and (d) **P5**, and the 001 q_z polymer backbone peak (e) **P4** and (f) **P5** are analyzed

The high temperature stability shown in GIWAXS is confirmed through Thermogravimetric Analysis (TGA) (**Figure 12a**). The spectrum of **P5** shows insignificant weight loss up to 235 °C. Unlike what is observed in the variable temperature GIWAXS, the Differential Scanning

Calorimetry (DSC) does not show any clear transitions in **P5** when subjected to heating and cooling cycles (**Figure 16b**). This affirms the sensitivity of GIWAXS as a characterization method, which is able to detect subtle changes in crystallinity that are unobserved by bulk measurement techniques such as DSC.

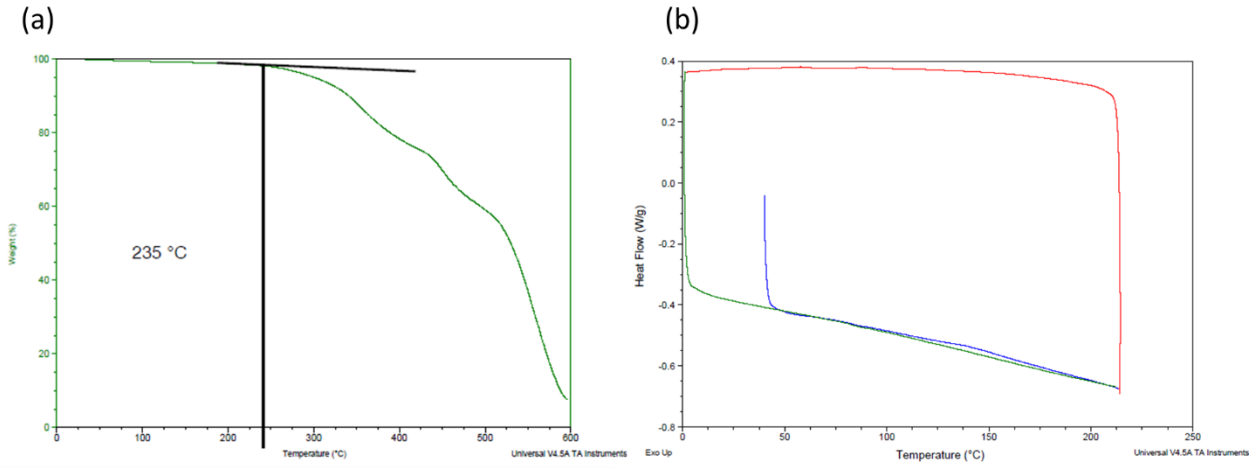

Figure 12: Thermal stability and heat capacity profile of **P5** as determined by (a) TGA and (b) DSC

3.7 Incorporation of P4 and P5 into Organic Field Effect Transistors (OFETs)

To examine how the functionalization with DTM effects macroscopic electronic properties, organic field effect transistors (OFETs) were prepared. Polymers similar to **P4** have been made into Organic Photovoltaic (OPV) devices[29], and Organic Field Effect Transistors (OFETs)[5c, 30] giving a clear point of reference. For simplicity, standard bottom-gate bottom-contact (BGBC) device structures are utilized, with a SiO_2 gate and either Al_2O_3 or octadecylsilyl (OTS)[30] dielectric layer. Despite having low LUMO levels, polymers incorporating 5,6-difluoro-1,2,5-benzothiadiazole monomers are known to only display *p*-type transport. Accordingly, **P4** does not display any electron conductivity, but does show hole mobilities up to 8.33E-3 $cm^2\ V^{-1}\ s^{-1}$ (**Figure 13, Table 4**). Deviation between the forward and reverse scans, or hysteresis, is severe for the BTBC devices (**Figure 13b**). This is likely due to defects and traps at the dielectric-polymer interface. [31]

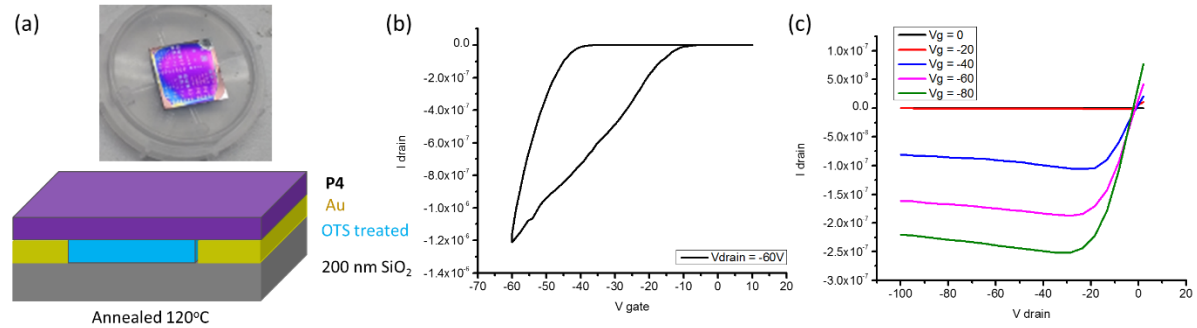

Figure 13: (a) BGBC device structure used to obtain OFET (b) transfer and (c) output curves for **P4**

While **P4** displays *p*-type transport, **P5** has a reversal in majority carriers from holes to electrons (**Figure 14, Table 4**). Despite the change in charge carrier, **P5** has the same hysteresis that is observed with **P4**. Observing the same hysteresis effect for both polymers despite different charge carriers could point to imperfections in the device assembly.

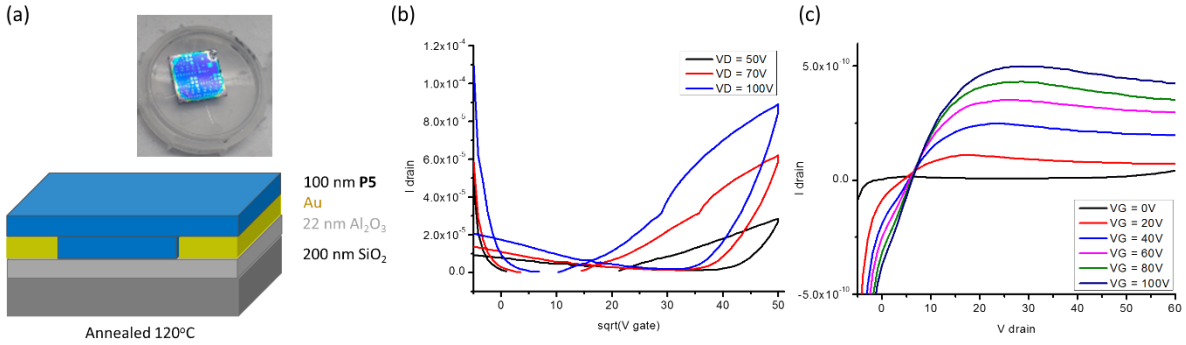

Figure 14: (a) BGBC device structure used to obtain OFET (b) transfer and (c) output curves for **P5**

Table 4: Bottom-Gate Bottom-Contact OFET Data for **P4** and **P5**

Polymer	Sweep Direction	Charge Carrier	Mobility /cm^2 V^{-1} s^{-1}	V_T /V	I_{on}/I_{off}
P4	Forward	Hole	2.72E-3	-5.9	
P4	Reverse	Hole	6.26E-3	-38.1	
P4	Average	Hole	4.90E-3	-22.0	4.6E5
P5	Forward	Electron	5.13E-6	19.4	
P5	Reverse	Electron	2.81E-5	40.6	
P5	Average	Electron	1.66E-5	30.0	1.5E3

This change in charge carrier for **P5** is consequential since *n*-type organic semiconductors have unique properties and are crucial for making the organic equivalent of Complementary Metal Oxide Semiconductor (CMOS) logic circuits. Electron conducting polymers are much less common than *p*-type (hole conducting) materials and have their own unique challenges.[2]

Since the excited state electrons necessary for *n*-type conductivity are highly energetic, these polymers are prone to react with ambient oxygen and water in addition to surrounding silicon and dielectric species. It has been proven that a LUMO energy of below -3.8 eV is required for stable electron transport under ambient conditions.[32] Otherwise, oxygen and surrounding species can act as traps, reacting with excited state electrons before they can be collected.

Another issue is that the most common choice of electrode material, unfunctionalized gold, has a work function of 5.1 eV that is much better suited for hole injection in *p*-type systems than electron injection into *n*-type materials. While gold has the advantage of high oxidative stability, the large contact resistance between gold and the *n*-type active layer can significantly lower measured electron mobilities in these systems. Metals such as aluminum, calcium, and barium have lower work functions that are more compatible with electron injection, but like the *n*-type polymers themselves, are easily oxidized. Alternatively, gold electrodes can be modified

to work in *n*-type systems by utilizing cesium salts as a hole blocking layer by lowering the electrode work function.[33]

Polymer **P5** has a LUMO of -3.6 eV, which is still energetically within the range of air oxidation and deleterious side reactions if not protected. In the initial devices, gold electrodes were used due to their stability, and a BGBC device architecture is used, leaving the active layer exposed to air. At best an electron mobility of 4.55E-5 cm^2 V^{-1} s^{-1} is obtained. Although unoptimized, these devices show drastic changes in electronic properties, solely due to the modification of the difluoride functionality by the DTM group, making it a better *n*-type material.

Because bottom-gate bottom-contact devices have the polymer film on the outermost layer of the device stack, it can be vulnerable to air exposure. An alternative top-gate bottom-contact (TGBC) architecture can relieve this issue. For these devices, the gate dielectric is deposited over the organic semiconductor, encapsulating it and protecting it from air and water. The TGBC devices tend to perform significantly better for *n*-type devices due to this shielding effect.[2]

To take advantage of an enclosed active layer, TGBC devices were made using PMMA as a dielectric layer which seals **P4** and **P5** from ambient conditions. For *p*-type devices, unfunctionalized gold was used for the electrodes, while for *n*-type devices Au-Cs_2CO_3 source-drain and Al gate electrodes were used to improve electron injection. Thin films of **P4** and **P5** were made by spincasting concentrated solutions of polymer in ODCB. Incorporating lessons learned from GIWAXS, the polymer films were annealed at 160^{o}C for 10 minutes in order to enlarge the crystalline domains and improve $\pi-\pi$ stacking.

In contrast with the BTBC devices, hysteresis is almost completely eliminated in the TGBC devices, which can be attributed to decreased traps (**Figure 19**). Polymer **P4** is confirmed to be a *p*-type semiconductor with a hole mobility of 1.3E-3 cm^2 V^{-1} s^{-1}, which is nearly identical to the mobility obtained for the BGBC OFETs (**Table 5**). Surprisingly, in addition to **P5** being electron conductive, the TGBC devices show that **P5** is also hole conductive, displaying ambipolar transport behavior! This ability to conduct electrons and holes is observed for devices made from **P5** with both hexane and THF Soxhlet fractions. Despite the **P5** THF fraction containing higher molecular weight polymers, both the electron and hole mobilities are slightly lower than the hexane fraction. This ambipolar charge transport is unique to **P5**, and solely linked to the addition of the new DTM functionality.

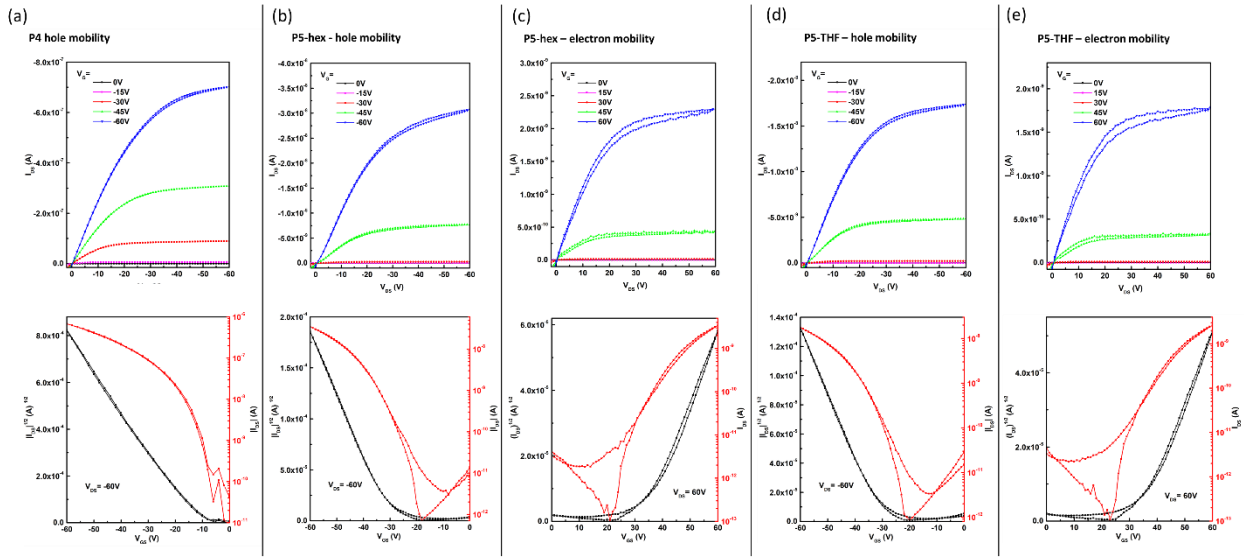

Figure 19: The output (above) and transfer (below) curves for TGBC device. Plots for (a) **P4** *p*-type carrier transport, the **P5**- hexane Soxhlet fraction (b) *p*-type and (c) *n*-type carrier transport, and **P5**- THF Soxhlet fraction (d) *p*-type and (e) *n*-type carrier transport are displayed.

Table 5: Top-Gate Bottom-Contact OFET Data for **P4** and **P5**

		Hole Transport				Electron Transport			
	Soxhlet Extract	$\mu_{average}$ /cm^2 V^{-1} s^{-1}	μ_{max} /cm^2 V^{-1} s^{-1}	V_T /V	I_{on}/I_{off}	$\mu_{average}$ /cm^2 V^{-1} s^{-1}	μ_{max} /cm^2 V^{-1} s^{-1}	V_T /V	I_{on}/I_{off}
P4	Hexane	1.9E-3	2.1E-3	-12	1E4	-	-	-	-
P5	Hexane	2.4E-4	2.6E-4	-30	1E4	3.0E-5	3.5E-5	33	1E4
P5	THF	1.3E-4	1.4E-4	-31	1E4	2.2E-5	2.6E-5	34	1E4

3.8 Small Molecule Acceptors

Another application of low LUMO materials is as electron acceptors for organic photovoltaics. Improving BTD withdrawing ability through the DTM modification could allow it to be an effective non-fullerene acceptor material. Similar BTD groups have been used effectively as molecular mediators,[34] and DTM modified small molecules could be interesting candidates for this application.

To tailor the BTD system for use in organic photovoltaic applications, additional electron withdrawing units are added to the thiophene positions. Dibromide **10c** is subjected to lithium-halogen exchange and reaction with DMF to produce dialdehyde **11** (**Scheme 5**). Compound **11** could be condensed with malononitrile to give **12**, or thiobarbituric acid to give **14**. A S_NAr reaction of these compounds with the malononitrile dithiolate **salt-6** provided **13** and **15** respectively, albeit in moderate yields.

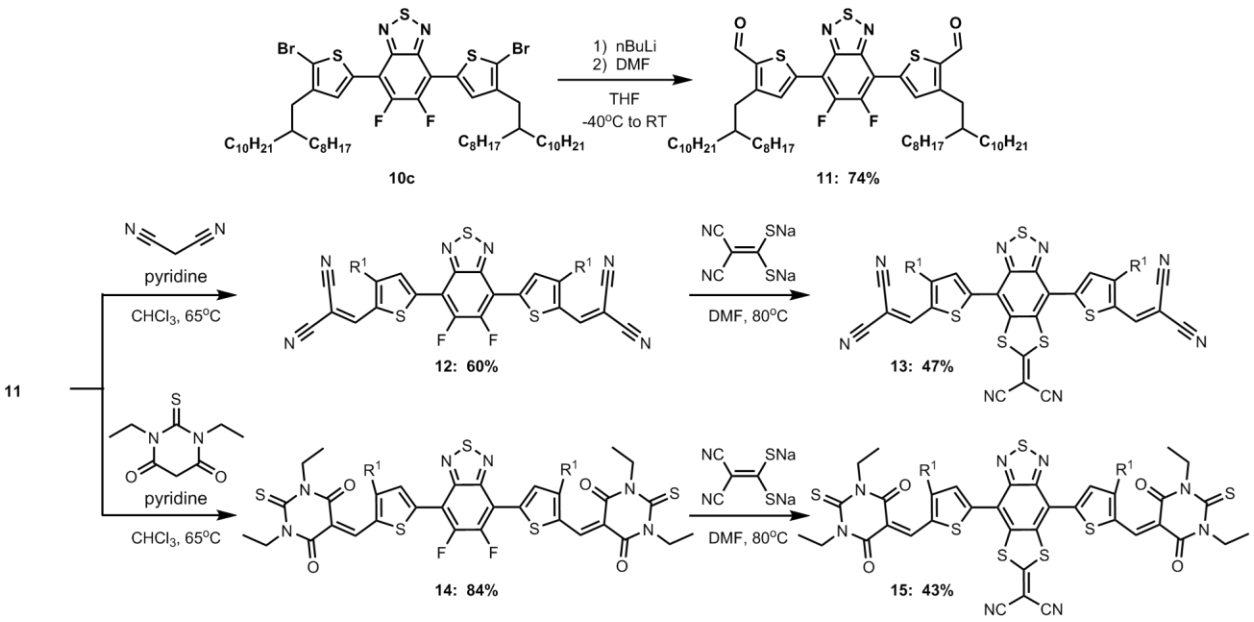

Scheme 5: Synthesis of malononitrile and thiobarbituric acid based non-fullerene acceptors

UV-Vis spectra of **12** and **13** both show a bathochromic shift of approximately 50 nm compared to the unfunctionalized **5a** (**Figure 20a**). The DTM adduct **13** has a similar absorption onset, but shows significantly improved spectral coverage in the visible region. This trend is continued for **14** and **15**, where **14** has a slightly lower bandgap while **15** absorbs light across a wider range of the visible spectrum (**Figure 20b**). This redshifted and broad absorption in the visible spectrum makes these molecules attractive candidates for further testing as non-fullerene acceptor materials.

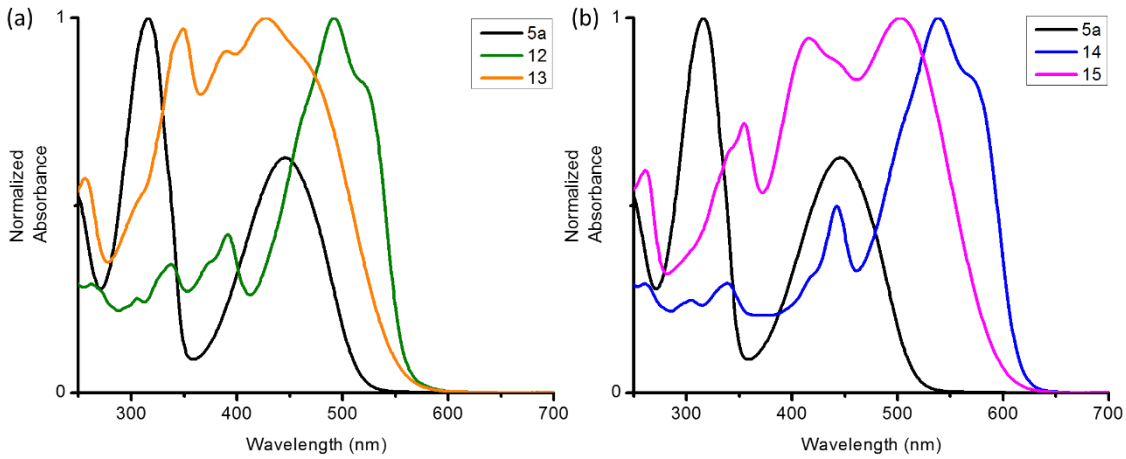

Figure 20: Optical absorption of the (a) malononitrile based system and (b) thiobarbituric acid system.

3.9 Conclusions

This work demonstrates that the modification of 1,2,5-benzothiadiazole (BTD) with 2-(1,3-dithiol-2-ylidene)malonitrile (DTM) *via* S_NAr reaction is an effective means of altering the physical and optoelectronic properties of acceptor materials. Furthermore, dithiolate salts based on acetylacetone and diethyl malonate have been successfully added into organic semiconductors for the first time, expanding the scope of this transformation. The modified BTD adducts have been endowed with new absorption peaks, broadening the overall absorption profile and improving extinction coefficients. The band gaps and low LUMO levels of these adducts are on par with 5,6-difluoro-1,2,5-benzothiadiazole **5a**, demonstrating that dithiolate functionalization can provide a comparable withdrawing effect to fluorine.

Polymers functionalized with DTM are imbued with an unusually strong aggregation effect. This manifests optically as reversible dramatic solvatochromic and thermochromic behavior with bathochromic shifts of up to nearly 200 nm in the aggregated state. Solid state order has been analyzed by variable temperature GIWAXS which confirms that the annealed DTM modified polymer is vastly more crystalline than the fluorinated counterpart, often a desirable quality for charge transport. Unlike in solution, heating in the solid state irreversibly modifies the aggregation, confirming that thermal annealing is an effective means of improving crystallinity in devices.

Organic field effect transistors with a DTM functionalized active layer display ambipolar charge transport, whereas the control fluorinated polymer is a unipolar hole transport material. Although the mobilities are modest, sidechain engineering and film optimization could potentially improve the morphology and increase performance. Potential non-fullerene acceptors for solar applications have also been synthesized using this methodology. By condensing additional electron deficient groups to the already electron poor DEM modified BTD, the withdrawing ability is strengthened even further.

Incorporation the DTM functional group into BTD polymers and small molecules is an effective way to lower the LUMO, modulate aggregation, and enhance optoelectronic properties. These changes, made on a molecular level, have a pronounced effect on macroscopic properties such as carrier type in OFETs and can be viewed as validation for future work to modulate electronic properties through DTM functionalization.

3.10 Materials and Methods

Reagents were used as purchased. Solvent was collected from an activated alumina column based solvent dispensing system (SDS). Reactions progress was monitored by thin layer chromatography (TLC) on precoated silica gel 60F on aluminum backing (Merck 5554). Proton (^{1}H) and carbon (^{13}C) NMR spectra were obtained on a Bruker Avance 500II spectrometer. Molecular weights were determined on a 4800 MALDI TOF/TOF analyzer from Applied Biosystems. Polymeric molecular weight distributions were determined by a Tosoh EcoSEC HT high temperature size exclusion chromatography (SEC) using heated trichlorobenzene as eluent. Optical measurements were carried out on a Cary 5000 UV-Vis-NIR spectrometer. Electrochemical measurements were obtained using 273A potentiostat (Princeton Applied Research), with a glassy carbon working electrode, a platinum coated aluminum counter electrode, and a silver wire as a pseudo-reference electrode. Samples were prepared in either acetonitrile or dichloromethane solutions with tetrabutylammonium hexafluorophosphate (0.1

M) as the electrolyte. Spectra were obtained with a scan rate of 100 mV s-1, using the ferrocene/ferrocenium (Fc/Fc+) redox couple as an internal standard. The HOMO and LUMO levels of compounds are calculated from the difference between the onset of first oxidation potential (E_{OX}) or reduction potential (E_{red}) of the compounds and the oxidation potential of ferrocene E_{HOMO} = -(4.8+E_{OX}) eV, E_{LUMO} = -(4.8+E_{RED}) eV.[35] Thermogravimetric Analysis (TGA) and Differential Scanning Calorimetry (DSC) were determined using a TA instruments TGA 5500 and DSC Q200 respectively.

Organic Field Effect Transistors were characterized under vacuum with a Lakeshore CPX-HF probe station and Agilent 4155C control box. Field effect mobility was calculated from the standard equation for saturation region in metal-dioxide-semiconductor field effect transistors: $I_{ds} = \mu(W/2L)C_i(V_g-V_t)^2$, where Ids is drain-source current, μ is field effect mobility, W and L are the channel width and length, C_i is the capacitance per unit area of the gate insulator (C_i = 10 nF/cm2), Vg is the gate voltage and Vt is the threshold voltage.[36]

Grazing Incidence Wide Angle X-ray Scattering (GIWAXS) experiments were conducted at the 7.3.3 Beamline of Advanced Light Source, Lawrence Berkeley National Laboratory.[37]

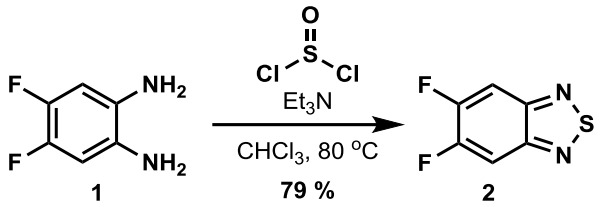

2 5,6-difluorobenzo[c][1,2,5]thiadiazole

1,2-difluoro-4,5-diaminobenzene (1.5 g, 10.4 mmol, 1 equiv.) added to an oven dried flask with a reflux condenser and backfilled with nitrogen. Chloroform (110 mL, 0.09 M) and triethylamine (5.9 mL, 42 mmol, 4.05 equiv.) added followed by a slow addition of thionyl chloride (1.53 mL, 21.0 mmol, 2.02 equiv). Reaction transferred to an 80°C bath and monitored by TLC. After completion (3.5 hrs) the reaction was quenched by the addition of enthanol, then water. The solution was extracted three times with DCM and washed with brine before drying with $MgSO_4$. The volatiles were removed under reduced pressure, and the residue was subjected to column chromatography (gradient elution 0 to 100% ethyl acetate in hexane) to give the title compound as a beige/white solid (1.41 g, 8.2 mmol, 79%). ^{1}H NMR (500 MHz, Chloroform-*d*) δ 7.60 (t, *J* = 8.7 Hz, 1H). ^{13}C NMR (500 MHz, Chloroform-*d*) δ 154.7 (d, *J* = 20.0 Hz), 152.6 (d, *J* = 20.0 Hz), 150.7, 77.2 (t, J = 31.8 Hz). HRMS for $C_6H_2F_2N_2S$ (MALDI): $[M+Na]^+$ Calcd: 194.9799, found 194.9704.

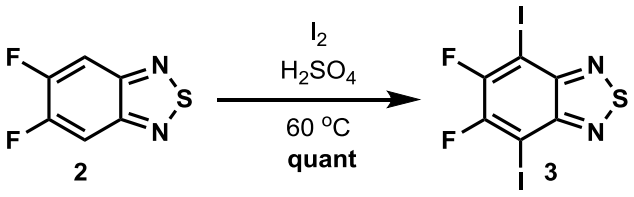

3 5,6-difluoro-4,7-diiodobenzo[c][1,2,5]thiadiazole

Fuming sulfuric acid (12 mL, 0.2M) added to a roundbottom flask followed by iodine (2.36 g, 9.29 mmol, 4 equiv.). Compound **2** (400 mg, 2.32 mmol) was added and a reflux condenser with nitrogen balloon was added before adding the reaction to a 60°C bath overnight. The following

day, the crude reaction mixture was poured onto ice and extracted with chloroform. The organic layer was washed three times with water, two times with 2M sodium hydroxide, once with sodium bicarbonate before drying with $MgSO_4$. The crude mixture was concentrated under reduced pressure and recrystallized from ethyl acetate to give off white crystals (2.31 g, 2.31 mmol, 100%). ^{13}C NMR (500 MHz, DMSO-*d6*) δ 153.3 (dd, 95, 1015 Hz) 150.1, 75.4 (dd, 45, 65 Hz). HRMS for $C_6F_2I_2N_2S$ (MALDI): $[M]^+$ calcd: 423.7840, found 423.8362.

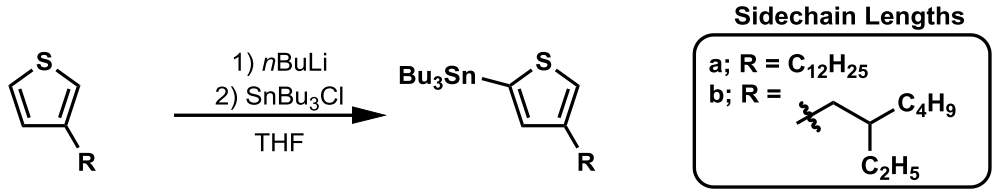

4a tributyl(4-dodecylthiophen-2-yl)stannane

3-dodecylthiophene (1.7 mL, 6 mmol) added to an oven dried flask under nitrogen. THF (15 mL, 0.4M) and tetramethylethylenediamine (TMEDA) (1.1 mL, 7.2 mmol, 1.2 equiv.) added and cooled to -78^{O}C, at which point a white slurry forms. A 1.6 M *n*-BuLi solution in hexane (4.5 mL, 7.2 mmol, 1.2 equiv) was then added dropwise. After 1 hr, the reaction was warmed to ambient temperature to dissolve the solid before recooling to -78^{O}C and adding tributyltin chloride (2 mL, 7.5 mmol, 1.25 equiv). The reaction was stirred for 30 minutes before rewarming to ambient temperature. Once complete by TLC (2 hrs), the reaction was concentrated and filtered through a fritted funnel. The crude reaction mixture was isolated as 3.219 g mixture of unreacted 3-dodecylthiophene, product (0.13:1) and minor tin impurities. Purification by silica gel column chromatography or by distillation was unsuccessful. The crude reaction mixture (a yellow tinted oil) was used without further purification.

4b tributyl(4-(2-ethylhexyl)thiophen-2-yl)stannane

3-(2-ethylhexyl)thiophene (1 g, 6 mmol) added to an oven dried flask under nitrogen. THF (15 mL, 0.4M) and tetramethylethylenediamine (TMEDA) (1.1 mL, 7.2 mmol, 1.2 equiv.) added and cooled to -78^{O}C. A 1.6 M *n*-BuLi solution in hexane (4.5 mL, 7.2 mmol, 1.2 equiv) was then added dropwise, at which point a tan cloudy solution forms. After 1 hr tributyltin chloride (2 mL, 7.5 mmol, 1.25 equiv) was added. The reaction was stirred for 30 minutes before rewarming to ambient temperature. Once complete by TLC (2 hrs), the reaction was concentrated and filtered through a fritted funnel. The crude reaction mixture was isolated as 2.929 g mixture of unreacted thiophene starting material, product (0.15:1) and minor tin impurities. The crude reaction mixture (a yellow tinted oil) was used without further purification.

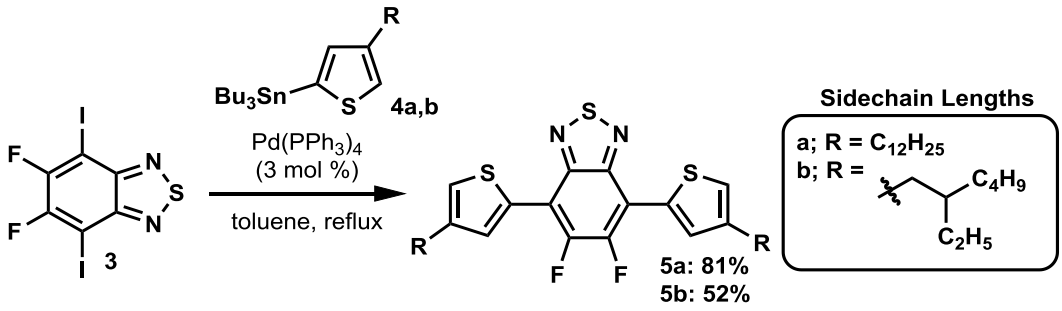

5a 4,7-bis(4-dodecylthiophen-2-yl)-5,6-difluorobenzo[c][1,2,5]thiadiazole[29]

Iodide **3** (1.86 g, 4.38 mmol) added to a flame dried roundbottom flask with condenser and backfilled with nitrogen. Xylene (50 mL, 0.09 M) was added via cannula, followed by tin reagent (88% purity) **4a** (4.61 g, 9.63 mmol, 2.2 equiv.). The reaction was sparged with nitrogen for 20 minutes. $Pd(PPh_3)_4$ (506 mg, 0.438 mmol, 0.1 equiv.) was added and the reaction was further sparged for 15 minutes before being placed in a 140°C bath overnight. The reaction was cooled to ambient temperature, diluted with DCM, washed with water and brine before drying over $MgSO_4$. The crude reaction mixture was concentrated under reduced pressure and purified by column chromatography (gradient elution 0 to 25% DCM in hexane) to give the title compound as a bright yellow solid (2.38 g, 3.54 mmol, 81%). ^{1}H NMR (500 MHz, Chloroform-*d*) δ 8.12 (d, *J* = 1.4 Hz, 1H), 7.20 (s, 1H), 2.71 (t, *J* = 7.7 Hz, 2H), 1.70 (t, *J* = 7.5 Hz, 2H), 1.44 – 1.32 (m, 4H), 1.34 – 1.24 (m, 14H), 0.87 (t, *J* = 6.9 Hz, 3H). ^{13}C NMR (126 MHz, Chloroform-*d*) δ 151.0 (d, *J* = 20.4 Hz), 149.56 – 148.51 (m), 143.9, 132.5 (t, *J* = 3.8 Hz), 131.4, 124.2, 112.2 – 111.2 (m), 32.2, 30.8, 30.7, 29.9, 29.9, 29.9, 29.8, 29.7, 29.6, 29.6, 22.9, 14.4. HRMS for $C_{38}H_{54}F_2N_2S_3$ (MALDI): $[M+H]^+$ Calcd: 673.3490, found 673.4219.

5b 4,7-bis(4-(2-ethylhexyl)thiophen-2-yl)-5,6-difluorobenzo[c][1,2,5]thiadiazole

Iodide **2** (1 g, 2.36 mmol) added to a flame dried roundbottom flask with condenser and backfilled with nitrogen. Xylene (40 mL, 0.06 M) was added via cannula, followed by tin reagent **4b** (87% purity) (2.90 g, 5.19 mmol, 2.2 equiv.). The reaction was sparged with nitrogen for 20 minutes. $Pd(PPh_3)_4$ (272 mg, 0.24 mmol, 0.1 equiv.) was added and the reaction was further sparged for 15 minutes before being placed in a 140°C bath overnight. The reaction was cooled to ambient temperature, diluted with $CHCl_3$, washed three times with water and brine before drying over $MgSO_4$. The crude reaction mixture was concentrated under reduced pressure and purified by column chromatography (hexane eluent) to give the title compound as a bright yellow solid (686 mg, 1.22 mmol, 52%). ^{1}H NMR (500 MHz, Chloroform-*d*) δ 8.07 (d, *J* = 1.4 Hz, 2H), 7.16 (d, *J* = 1.3 Hz, 2H), 2.65 (d, *J* = 6.9 Hz, 4H), 1.65 (p, *J* = 6.8, 6.3 Hz, 2H), 1.40 – 1.27 (m, 16H), 0.92 (t, *J* = 7.3 Hz, 12H). ^{13}C NMR (126 MHz, Chloroform-*d*) δ 150.9 (d, *J* = 20.5 Hz), 149.1 – 148.5 (m), 142.5, 132.9 (t, *J* = 3.9 Hz), 131.2, 125.0, 112.1 – 111.3 (m), 40.6, 34.6, 32.7, 29.1, 25.8, 23.3, 14.4, 11.1. HRMS for $C_{30}H_{38}F_2N_2S_3$ (MALDI): $[M]^+$ Calcd: 560.2165, found 560.2909.

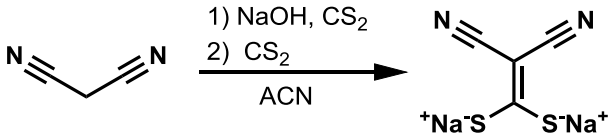

Salt-6

Salt-6 sodium 2,2-dicyanoethene-1,1-bis(thiolate)[38]

Pellets of sodium hydroxide (0.61 g, 15.14, 2 equiv.) were ground to a powder and added to a vial with a septa cap and stir bar. Acetonitrile (3.2 mL) was added and the mixture was cooled to 0°C followed by addition of malononitrile (0.5 g, 7.57 mmol, 1 equiv.) in acetonitrile. After stirring for 5 minutes, carbon disulfide (0.46 mL, 7.57 mmol, 1 equiv.) was added forming a brown slurry. The reaction was warmed to room temperature and stirred for 24 hours. The solids were filtered

and washed with acetonitrile to provide a white solid (1.408 g, 7.55 mmol, 99%) which was stored in a desiccator and used without further purification.

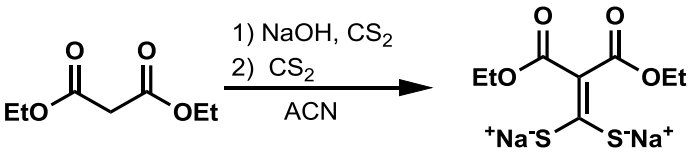

Salt-7

Salt-7 sodium 3-ethoxy-2-(ethoxycarbonyl)-3-oxoprop-1-ene-1,1-bis(thiolate)[38]

Pellets of sodium hydroxide (192 mg, 4.8 mmol, 2 equiv.) were ground to a powder and added to a vial with a septa cap and stir bar. Acetonitrile (1.5 mL) was added and the mixture was cooled to 0°C followed by addition of diethyl malonate (0.366 mL, 2.4 mmol, 1 equiv.) forming a white paste. After stirring for 5 minutes, carbon disulfide (0.145 mL, 2.4 mmol, 1 equiv.) was added forming an orange slurry. The reaction was warmed to room temperature and stirred for 24 hours. The solids were filtered and washed with acetonitrile to provide yellow solid (592 mg, 2.11 mmol, 88%) which was stored in a desiccator and used without further purification.

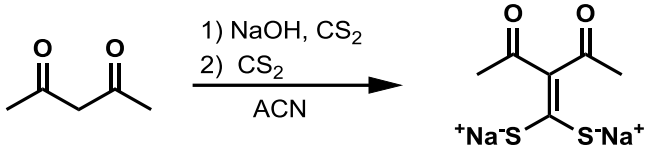

Salt-8

Salt-8 sodium 2-acetyl-3-oxobut-1-ene-1,1-bis(thiolate)[38]

Pellets of sodium hydroxide (192 mg, 4.8 mmol, 2 equiv.) were ground to a powder and added to a vial with a septa cap and stir bar. Acetonitrile (1.5 mL) was added and the mixture was cooled to 0°C followed by addition of acetyl acetone (0.25 mL, 2.4 mmol, 1 equiv.) forming a white paste. After stirring for 5 minutes, carbon disulfide (0.145 mL, 2.4 mmol, 1 equiv.) was added forming an orange slurry. The reaction was warmed to room temperature and stirred for 24 hours. The solids were filtered and washed with acetonitrile to provide a brown-orange solid (341 mg, 1.55 mmol, 65%) which was stored in a desiccator and used without further purification.

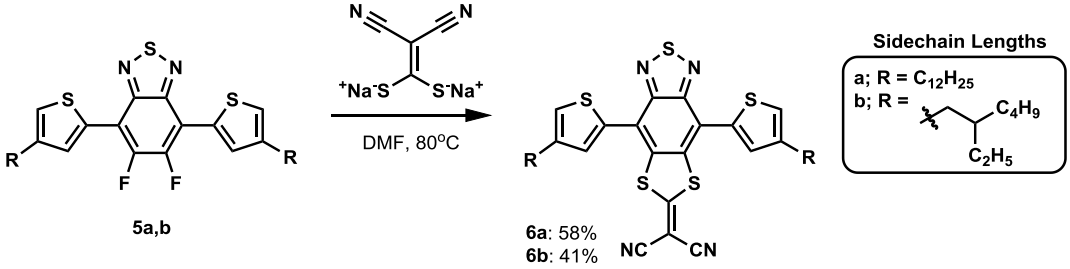

6a 2-(4,8-bis(4-dodecylthiophen-2-yl)-[1,3]dithiolo[4',5':4,5]benzo[1,2-c][1,2,5]thiadiazol-6-ylidene)malononitrile

Difluoride **5a** (25 mg, 0.04 mmol) and **salt-6** (10.3 mg, 0.056 mmol, 1.5 equiv.) added to a vial with septa cap and backfilled with nitrogen. DMF (2 mL, 0.02M) was added and the vial placed in a 140°C bath, quickly converting the yellow solution to brown. Once starting material was consumed by TLC the solution was diluted with DCM, washed with water then brine before drying over $MgSO_4$. The crude reaction mixture was concentrated under reduced pressure and purified by column chromatography (gradient elution 0 to 25% DCM in hexane) to give the title compound as a bright orange solid (18 mg, 0.023 mmol, 58%). ^{1}H NMR (500 MHz, Chloroform-*d*) δ 7.51 (s,

2H), 7.28 (s, 2H), 2.73 (t, *J* = 7.8 Hz, 4H), 1.70 (t, *J* = 7.6 Hz, 4H), 1.26 (m, 36H), 0.88 (t, *J* = 6.8 Hz, 6H). ^{13}C NMR (126 MHz, Chloroform-*d*) δ 177.4, 152.8, 144.5, 137.2, 135.0, 131.8, 124.7, 122.4, 112.4, 68.0, 32.1, 30.6, 30.6, 29.9, 29.9, 29.9, 29.8, 29.7, 29.6, 29.5, 22.9, 14.4. HRMS for $C_{42}H_{54}N_4S_5$ (MALDI): $[M]^+$ Calcd: 774.2952, found 774.3621.

6b 2-(4,8-bis(4-(2-ethylhexyl)thiophen-2-yl)-[1,3]dithiolo[4',5':4,5]benzo[1,2-c][1,2,5]thiadiazol-6-ylidene)malononitrile

Difluoride **5b** (509 mg, 0.91 mmol) and **salt-6** (253 mg, 1.36 mmol, 1.5 equiv.) added to a vial with septa cap and backfilled with nitrogen. DMF (50 mL, 0.018 M) was added and the vial placed in a 140°C bath, quickly converting the yellow solution to brown. After no further conversion by TLC (1.5 hrs) the solution was diluted with chloroform, washed with water then brine before drying over $MgSO_4$. The crude reaction mixture was concentrated under reduced pressure and purified by column chromatography (gradient elution 0 to 90% $CHCl_3$ in hexane) to give the title compound as a bright orange solid (249 mg, 0.376 mmol, 41%). ^{1}H NMR (500 MHz, Chloroform-*d*) δ 7.49 (d, *J* = 1.4 Hz, 2H), 7.26 (d, *J* = 1.3 Hz, 2H), 2.74 – 2.62 (m, 4H), 1.63 (q, *J* = 6.1 Hz, 2H), 1.44 – 1.28 (m, 16H), 0.98 – 0.87 (m, 12H). ^{13}C NMR (126 MHz, Chloroform-*d*) δ 177.2, 152.7, 143.0, 137.1, 134.9, 132.2, 125.6, 122.3, 112.3, 68.0, 40.6, 34.5, 32.7, 29.1, 25.7, 23.2, 14.4, 11.1. HRMS for $C_{34}H_{38}N_4S_5$ (MALDI): $[M]^+$ Calcd: 662.1700, found 662.2310.

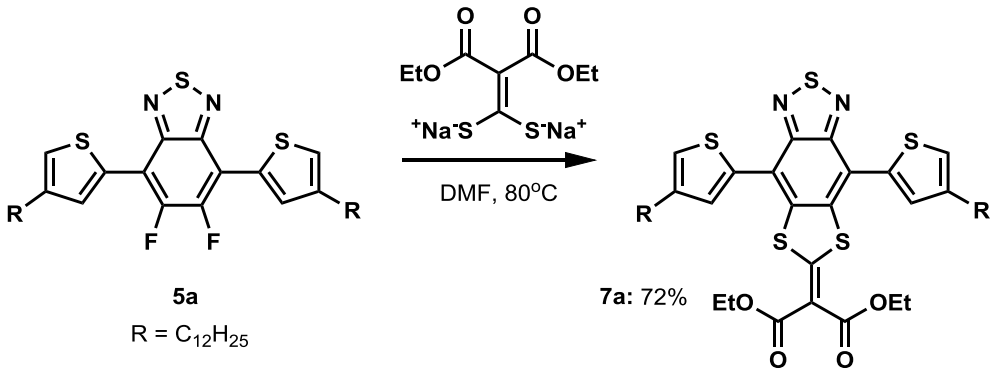

7a diethyl-2-(4,8-bis(4-dodecylthiophen-2-yl)-[1,3]dithiolo[4',5':4,5]benzo[1,2-c][1,2,5]thiadiazol-6-ylidene)malonate

Difluoride **5a** (25 mg, 0.037 mmol) and the **salt-7** (11.4 mg, 0.041 mmol, 1.1 equiv.) were added to a vial with a stir bar and septa cap. DMF (1 mL) was added and the solution as heated to 80°C. After 1 hour, an additional portion of the salt (6.8 mg, 0.024 mmol, 0.65 equiv.) was added. After 24 hours the reaction was quenched with 2N HCl, extracted with ethyl acetate, washed with brine and dried over $MgSO_4$. The crude reaction mixture was concentrated under reduced pressure and purified by column chromatography (gradient elution 25 to 100% $CHCl_3$ in hexane) to give the title compound as a bright orange solid (23 mg, 0.026 mmol, 72%). ^{1}H NMR (500 MHz, Chloroform-*d*) δ 7.58 (d, *J* = 1.4 Hz, 2H), 7.21 (s, 2H), 4.33 (q, *J* = 7.1 Hz, 4H), 2.72 (t, *J* = 7.7 Hz, 4H), 1.71 (p, *J* = 7.6 Hz, 4H), 1.45 – 1.21 (m, 42H), 0.87 (t, *J* = 6.9 Hz, 6H). ^{13}C NMR (126 MHz, Chloroform-*d*) δ 169.5, 165.4, 152.9, 143.9, 140.1, 135.6, 131.8, 123.5, 120.6, 108.6, 61.7, 32.1, 30.7, 30.7, 29.9, 29.9, 29.8, 29.7, 29.6, 29.6, 22.9, 14.4, 14.4. HRMS for $C_{46}H_{64}N_2O_4S_5$ (MALDI): $[M]^+$ Calcd: 868.3470, found 868.4719.

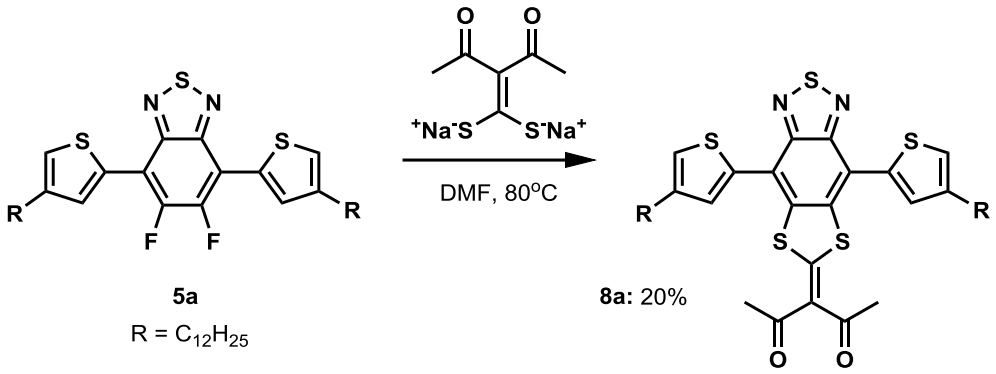

8a 3-(4,8-bis(4-dodecylthiophen-2-yl)-[1,3]dithiolo[4',5':4,5]benzo[1,2-c][1,2,5]thiadiazol-6-ylidene)pentane-2,4-dione

Difluoride **5a** (25 mg, 0.037 mmol) and **salt-8** (9 mg, 0.041 mmol, 1.1 equiv.) were added to a vial with a stir bar and septa cap. DMF (1 mL) was added and the solution as heated to 80°C. After 1 hour, an additional portion of the salt (9 mg, 0.041 mmol, 1.1 equiv.) was added. After an additional hour, a third portion of the salt (18 mg, 0.082 mmol, 2.2 equiv.) was added. After 24 hours the reaction was quenched with 2N HCl, extracted with ethyl acetate, washed with brine and dried over $MgSO_4$. The crude reaction mixture was concentrated under reduced pressure and purified by column chromatography (gradient elution 25 to 75% $CHCl_3$ in hexane) to give the title compound as a bright orange solid (6 mg, 0.007 mmol, 20%). ^{1}H NMR (500 MHz, Chloroform-*d*) δ 7.64 (s, 2H), 7.24 (s, 2H), 2.75 (t, *J* = 7.2 Hz, 4H), 2.62 (d, *J* = 2.1 Hz, 6H), 1.73 (p, *J* = 7.7 Hz, 4H), 1.47 – 1.16 (m, 40H), 0.87 (t, *J* = 7.0, 6H). ^{13}C NMR (126 MHz, Chloroform-*d*) δ 194.4, 172.5, 152.9, 144.0, 140.1, 135.5, 132.0, 131.1, 123.7, 121.2, 32.2, 31.3, 30.7, 30.7, 29.9, 29.9, 29.9, 29.7, 29.6, 29.6, 22.9, 14.4. HRMS for $C_{44}H_{60}N_2O_2S_5$ (MALDI): $[M]^+$ Calcd: 808.3258, found 808.4111.

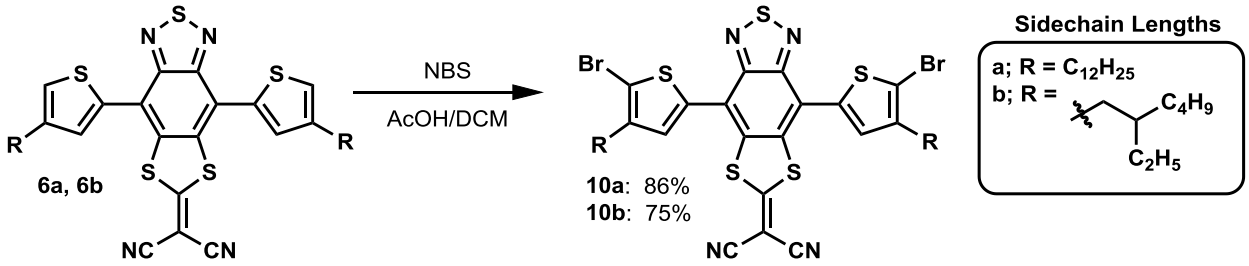

10a 2-(4,8-bis(5-bromo-4-dodecylthiophen-2-yl)-[1,3]dithiolo[4',5':4,5]benzo[1,2-c][1,2,5]thiadiazol-6-ylidene)malononitrile

Substrate **6a** (452 mg, 0.58 mmol) and N-bromosuccinimide (259 mg, 1.46 mmol, 2.5 equiv.) added to roundbottom flask and backfilled with nitrogen. DCM (24 mL, 0.024M) added followed by acetic acid (24 mL, 0.024M) and the reaction was stirred overnight after which there was no starting material remaining by TLC. The reaction was extracted 3x with DCM, washed with water (3x) and brine before drying over $MgSO_4$. The crude reaction mixture was concentrated under reduced pressure and purified by column chromatography (gradient elution 0 to 40% DCM in hexane) to give the title compound as a bright orange-red solid (465 mg, 0.50 mmol, 86%). ^{1}H NMR (500 MHz, Chloroform-*d*) δ 7.38 (s, 2H), 2.68 (t, *J* = 7.7 Hz, 4H), 1.65 (p, *J* = 7.9 Hz, 4H), 1.44 – 1.21 (m, 36H), 0.93 – 0.84 (m, 6H). ^{13}C NMR (126 MHz, Chloroform-*d*) δ 176.5, 152.4, 143.3,

137.0, 134.8, 131.2, 121.5, 115.1, 112.2, 68.7, 32.2, 29.9, 29.9, 29.8, 29.6, 29.6, 29.4, 22.9, 14.4. HRMS for $C_{42}H_{52}Br_2N_4S_5$ (MALDI): $[M]^+$ Calcd: 930.1162, found 930.2996.

10b 2-(4,8-bis(5-bromo-4-(2-ethylhexyl)thiophen-2-yl)-[1,3]dithiolo[4',5':4,5]benzo[1,2-c][1,2,5]thiadiazol-6-ylidene)malononitrile

Substrate **6b** (174 mg, 0.26 mmol) and N-bromosuccinimide (117 mg, 0.66 mmol, 2.5 equiv.) added to roundbottom flask and backfilled with nitrogen. DCM (5 mL, 0.05M) added followed by acetic acid (5 mL, 0.05M) and the reaction was stirred overnight after which there was no starting material remaining by TLC. The reaction was extracted 3x with DCM, washed with water (3x) and brine before drying over $MgSO_4$. The crude reaction mixture was concentrated under reduced pressure and purified by column chromatography (gradient elution 0 to 40% DCM in hexane) to give the title compound as a bright orange-red solid (160 mg, 0.195 mmol, 75%). ^{1}H NMR (500 MHz, Chloroform-*d*) δ 7.35 (s, 2H), 2.72 – 2.52 (m, 4H), 1.76 – 1.62 (m, 2H), 1.44 – 1.18 (m, 16H), 1.03 – 0.81 (m, 12H). ^{13}C NMR (126 MHz, Chloroform-*d*) δ 176.3, 152.4, 142.4, 136.9, 134.7, 131.8, 121.5, 115.7, 112.2, 68.7, 40.1, 34.0, 32.7, 29.0, 25.8, 23.3, 14.4, 11.0. HRMS for $C_{30}H_{36}Br_2F_2N_2S_3$ (MALDI): $[M+Na]^+$ Calcd: 739.0268, found 739.0882.

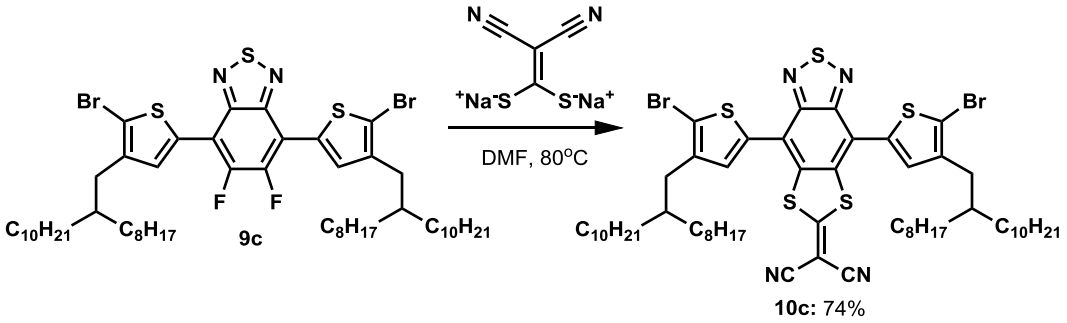

10c 2-(4,8-bis(5-bromo-4-(2-octyldodecyl)thiophen-2-yl)-[1,3]dithiolo[4',5':4,5]benzo[1,2-c][1,2,5]thiadiazol-6-ylidene)malononitrile

Difluoride **9c** (500 mg, 0.47 mmol) and **salt-6** (110 mg, 0.59 mmol, 1.25 equiv.) added to a vial with septa cap and backfilled with nitrogen. DMF (2 mL, 0.02M) was added and the vial placed in a 80°C bath, quickly converting the yellow solution to brown. Once starting material was consumed by TLC (1 hour) the solution was diluted with $CHCl_3$, washed with ammonium chloride (aq), water, and brine before drying over $MgSO_4$. The crude reaction mixture was concentrated under reduced pressure and purified by column chromatography (gradient elution 0 to 100% EtOAc in hexane) to give the title compound as a bright orange-red solid (506 mg, 0.44 mmol, 93%). ^{1}H NMR (500 MHz, Chloroform-*d*) δ 7.36 (s, 2H), 2.61 (d, *J* = 7.1 Hz, 4H), 1.77 – 1.69 (m, 2H), 1.39 – 1.16 (m, 64H), 0.87 (t, *J* = 6.8 Hz, 12H). ^{13}C NMR (126 MHz, Chloroform-*d*) δ 176.1, 152.3, 142.5, 136.8, 134.6, 131.9, 121.4, 115.6, 112.1, 68.7, 38.7, 34.4, 33.5, 32.1, 30.2, 30.2, 29.9, 29.9, 29.8, 29.6, 29.6, 26.7, 22.9, 14.4. HRMS for $C_{58}H_{84}Br_2N_4S_5$ (MALDI): $[M]^+$ Calcd: 1154.3666, found 1154.5504.

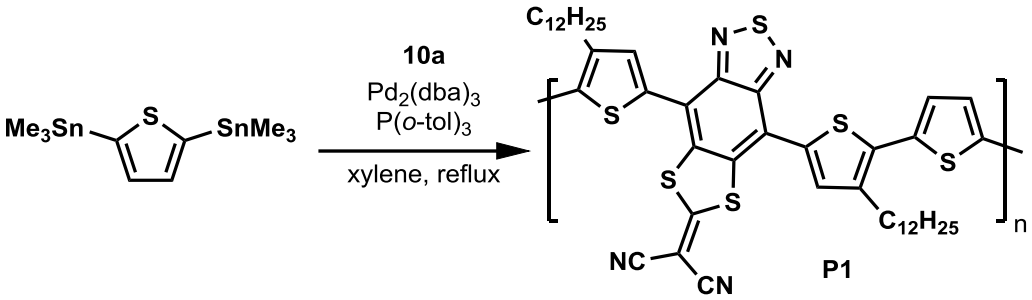

P1 Poly[2-(4,8-bis(4-dodecylthiophen-2-yl)-[1,3]dithiolo[4',5':4,5]benzo[1,2-c][1,2,5]thiadiazol-6-ylidene)malononitrile-*alt*-thiophene][39]

Compound **10a** (233.25 mg, 0.25 mmol, 1 equiv.), 2,5-bis(trimethylstannyl)thiophene (102.44 mg, 0.25 mmol, 1 equiv.), $Pd_2(dba)_3$ (4.8 mg, 0.00525 mmol, 0.021 equiv.), and tri(o-tolyl)phosphine (6.1 mg, 0.02 mmol, 0.08 equiv.) were added to an oven dried 50 mL 2-neck roundbottom flask with reflux condenser and stir bar. Nitrogen gas was allowed to flow through the headspace for 30 minutes. Dry xylene (11 mL, 0.023 M) was added and the reaction was heated to 150°C for 4 days, with an additional 5 mL xylene added after the first day due to solvent evaporation. Tributylstannyl thiophene (0.2 mL, 0.63 mmol) was added followed by 2-bromothiophene (0.2 mL, 0.63 mmol) after 4 hours. The following day, the reaction was concentrated and precipitated into methanol (100 mL). The polymer was purified via sequential soxhlet extraction with methanol, acetone, hexane, DCM, $CHCl_3$, and chlorobenzene.

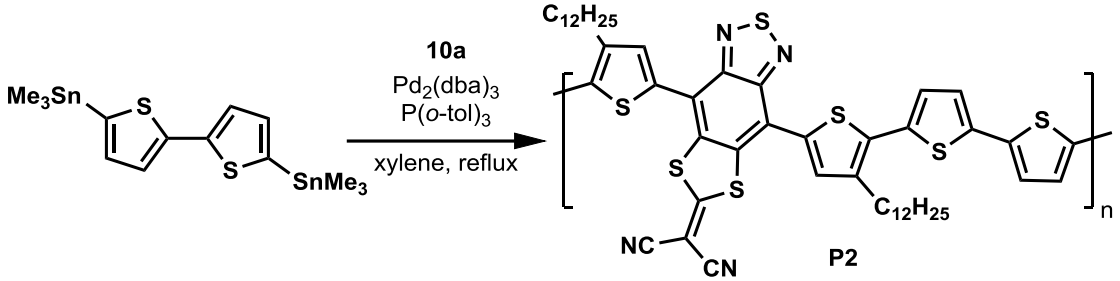

P2 Poly[2-(4,8-bis(4-dodecylthiophen-2-yl)-[1,3]dithiolo[4',5':4,5]benzo[1,2-c][1,2,5]thiadiazol-6-ylidene)malononitrile-*alt*-bithiophene]

Compound **10a** (100 mg, 0.107 mmol, 1 equiv.), 5,5'-bis(trimethylstannyl)-2,2'-bithiophene (52.7 mg, 0.107 mmol, 1 equiv.), $Pd_2(dba)_3$ (2.1 mg, 0.0022 mmol, 0.021 equiv.), and tri(o-tolyl)phosphine (2.6 mg, 0.0086 mmol, 0.08 equiv.) were added to a vial with septa cap. Nitrogen gas was allowed to flow through the headspace for 30 minutes. Dry xylene (2.14 mL, 0.05 M) was added and the reaction was heated to 150°C for 4 days, with an additional 2 mL xylene added after the second day due to solvent evaporation. Tributylstannyl thiophene (0.1 mL, 0.32 mmol) was added followed by 2-bromothiophene (0.1 mL, 0.32 mmol) after 4 hours. The following day, the reaction was concentrated and precipitated into methanol. The polymer was purified via sequential soxhlet extraction with methanol, acetone, hexane, DCM, $CHCl_3$, and chlorobenzene.

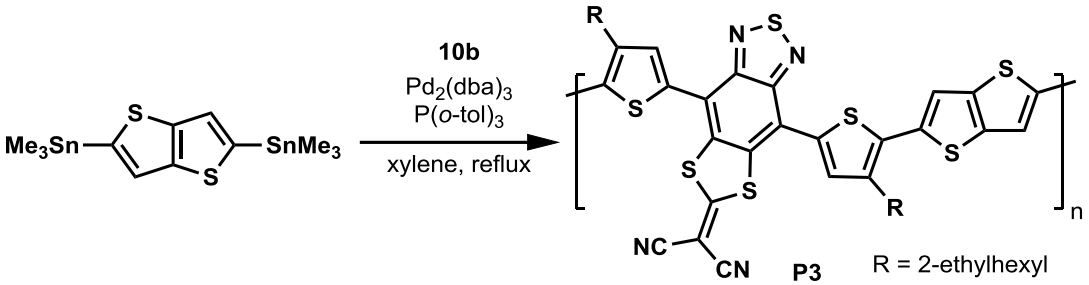

P3 Poly[2-(4,8-bis(4-(2-ethylhexyl)thiophen-2-yl)-[1,3]dithiolo[4',5':4,5]benzo[1,2-c][1,2,5]thiadiazol-6-ylidene)malononitrile-*alt*-thieno[3,2,b]thiophene]

Compound **10b** (76 mg, 0.163 mmol, 1 equiv.), 2,5-bis(trimethystannyl)thieno[3,2-b]thiophene (134mg, 0.163 mmol, 1 equiv.), $Pd_2(dba)_3$ (3.1 mg, 0.0034 mmol, 0.021 equiv.), and tri(o-tolyl)phosphine (3.97 mg, 0.013 mmol, 0.08 equiv.) were added to an oven dried 50 mL 2-neck roundbottom flask with reflux condenser and stir bar. Nitrogen gas was allowed to flow through the headspace for 30 minutes. Dry xylene (11 mL, 0.023 M) was added and the reaction was heated to 150°C for 4 days, with an additional 5 mL xylene added after the third day due to solvent evaporation. Tributylstannyl thiophene (0.2 mL, 0.63 mmol) was added followed by 2-bromothiophene (0.2 mL, 0.63 mmol) after 4 hours. The following day, the reaction was concentrated and precipitated into methanol (100 mL). The polymer was purified via sequential soxhlet extraction with methanol, acetone, hexane, DCM, $CHCl_3$, and chlorobenzene.

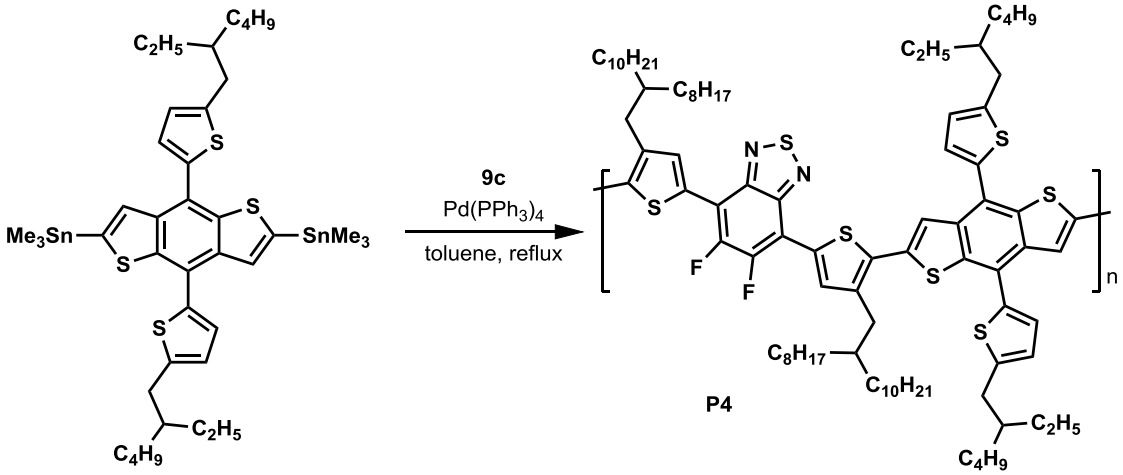

P4[29] Poly[5,6-difluoro-4,7-bis(4-(2-octyldodecyl)thiophen-2-yl)benzo[c][1,2,5]thiadiazole-*alt*-4,8-bis(5-(2-ethylhexyl)thiophen-2-yl)benzo[1,2-b:4,5-b']dithiophene]

Compound **9c** (183 mg, 0.173 mmol, 1 equiv.) and (4,8-bis(5-(2-ethylhexyl)thiophen-2-yl)benzo[1,2-b:4,5-b']dithiophene-2,6-diyl)bis(trimethylstannane) (156 mg, 0.173 mmol, 1 equiv.) were added to an oven dried 50 mL 2-neck roundbottom flask with reflux condenser and stir bar. The system was backfilled four times with nitrogen gas and dry toluene (12 mL, 0.014 M) was added. The solution was sparged with nitrogen for 15 minutes before $Pd(PPh_3)_4$ (15 mg, 0.013 mmol, 0.075 equiv.) was added. The solution was sparged with nitrogen for an additional 10 minutes before being placed in a 90°C bath. After 3 days the reaction was concentrated and precipitated into methanol. An attempt was made to purify the polymer via sequential soxhlet extraction but it was completely soluble in hot hexanes.

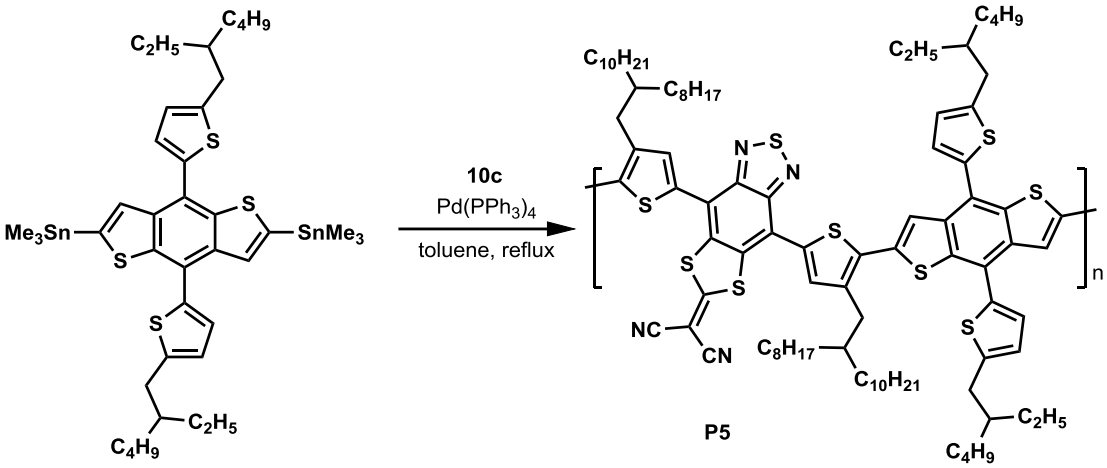

P5 Poly[2-(4,8-bis(4-(2-octyldodecyl)thiophen-2-yl)-[1,3]dithiolo[4',5':4,5]benzo[1,2-c][1,2,5]thiadiazol-6-ylidene)malononitrile-*alt*-4,8-bis(5-(2-ethylhexyl)thiophen-2-yl)benzo[1,2-b:4,5-b']dithiophene]

Compound **10c** (200 mg, 0.173 mmol, 1 equiv.) and (4,8-bis(5-(2-ethylhexyl)thiophen-2-yl)benzo[1,2-b:4,5-b']dithiophene-2,6-diyl)bis(trimethylstannane) (156 mg, 0.173 mmol, 1 equiv.) were added to an oven dried 50 mL 2-neck roundbottom flask with reflux condenser and stir bar. The system was backfilled four times with nitrogen gas and dry toluene (12 mL, 0.014 M) was added. The solution was sparged with nitrogen for 15 minutes before $Pd(PPh_3)_4$ (15 mg, 0.013 mmol, 0.075 equiv.) was added. The solution was sparged with nitrogen for an additional 10 minutes before being placed in a 90°C bath. After 3 days the reaction was concentrated and precipitated into methanol. The polymer via sequential soxhlet extraction with hexane and THF.

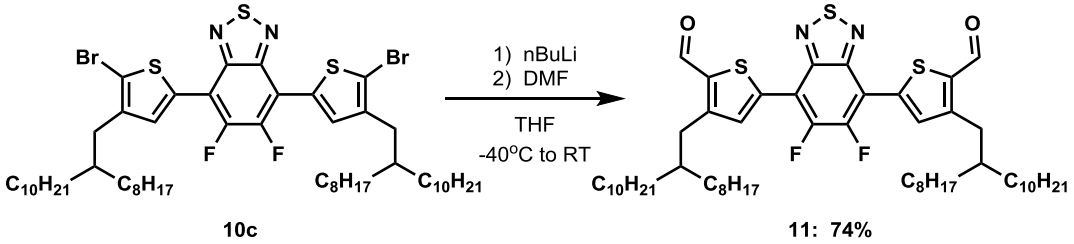

11 5,5'-(5,6-difluorobenzo[c][1,2,5]thiadiazole-4,7-diyl)bis(3-(2-octyldodecyl)thiophene-2-carbaldehyde)

Bromide **10c** (300 mg, 0.28 mmol) added to an ovendried flask and backfilled with nitrogen. THF (11 mL, 0.025M) was added and the solution was cooled to -40°C in a dry ice/acetonitrile bath. *n*-BuLi (1.6 M in THF) (0.54 mL, 0.86 mmol, 3.1 equiv) was added dropwise. After 30 minutes, DMF (0.5 mL, 1.4 mmol, 5 equiv.) was added dropwise and the solution turned from an orange to dark orange-red color. After complete by TLC the reaction was quenched with 1M HCl and extracted with EtOAc. The organic layer was washed with water and brine before drying over $MgSO_4$. The crude reaction mixture was concentrated under reduced pressure and purified by column chromatography (gradient elution 0 to 20% EtOAc in hexane) to give the title compound as a solid (196 mg, 0.21 mmol, 74%). ^{1}H NMR (500 MHz, Chloroform-*d*) δ 10.11 (s, 2H), 8.13 (s, 2H), 2.95 (d, *J* = 7.2 Hz, 4H), 1.79 – 1.68 (m, 2H), 1.28 – 1.20 (m, 64H), 0.85 (q, *J* = 7.8, 7.1 Hz, 12H). ^{13}C NMR (126 MHz, Chloroform-*d*) δ 182.7, 151.9 (d, *J* = 20.4 Hz), 151.5, 149.8 (d, *J* = 20.5 Hz), 148.6, 140.5, 138.7, 135.0, 112.3 (d, *J* = 8.7 Hz), 40.4, 33.5, 33.3, 32.1, 32.1, 30.2, 30.1, 30.1, 29.84,

29.8, 29.8, 29.5, 29.5, 26.7, 22.9, 22.8, 14.3. HRMS for $C_{56}H_{86}F_2N_2O_2S_3$ (MALDI): $[M]^+$ Calcd: 952.5819, found 952.7314.

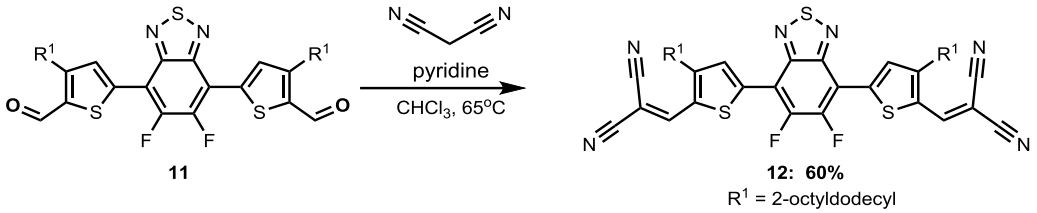

12 2,2'-(((5,6-difluorobenzo[c][1,2,5]thiadiazole-4,7-diyl)bis(3-(2-octyldodecyl)thiophene-5,2-diyl))bis(methanylylidene))dimalononitrile

Dialdehyde **11** (41 mg, 0.043 mmol) and malononitrile (17 mg, 0.258 mmol, 6 equiv.) added to a vial with septa cap and backfilled with nitrogen. Chloroform (2 mL, 0.02 M) was added followed by pyridine (70 μL, 0.86 mmol, 20 equiv.) and the reaction was stirred overnight. The reaction was quenched with 1M HCl and extracted with $CHCl_3$ and washed with brine before drying over $MgSO_4$. The crude reaction mixture was concentrated under reduced pressure and purified by column chromatography (gradient elution 25 to 100% EtOAc in hexane) to give the title compound as a red solid (27 mg, 0.025 mmol, 60%). ^{1}H NMR (500 MHz, Chloroform-*d*) δ 8.23 (s, 2H), 7.93 (s, 2H), 2.78 (d, *J* = 7.3 Hz, 4H), 1.71 (p, *J* = 6.8, 6.2 Hz, 2H), 1.43 – 1.18 (m, 64H), 0.86 (t, *J* = 6.7 Hz, 12H). ^{13}C NMR (126 MHz, Chloroform-*d*) δ 154.9, 151.1 (dd, *J* = 265.6, 20.2 Hz), 148.4, 148.3, 140.1, 134.3, 133.8, 114.6, 113.5, 112.3, 77.8, 40.5, 34.1, 33.5, 32.1, 32.1, 30.1, 29.9, 29.9, 29.8, 29.8, 29.6, 29.5, 26.7, 22.9, 22.9, 14.3. HRMS for $C_{62}H_{86}F_2N_6S_3$ (MALDI): $[M]^+$ Calcd: 1048.6044, found 1048.7506.

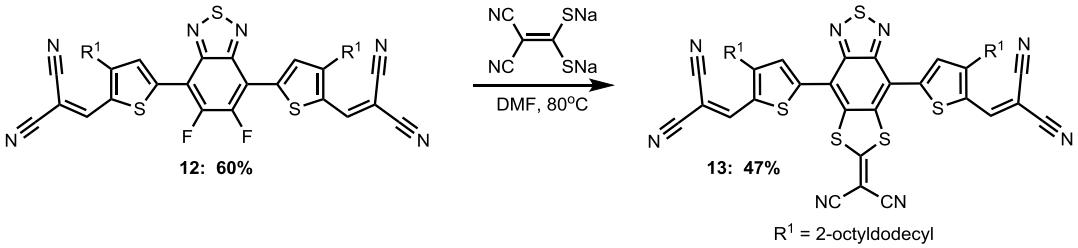

13 2,2'-(((6-(dicyanomethylene)-[1,3]dithiolo[4',5':4,5]benzo[1,2-c][1,2,5]thiadiazole-4,8-diyl)bis(3-(2-octyldodecyl)thiophene-5,2-diyl))bis(methanylylidene))dimalononitrile

Malononitrile adduct **12** (25 mg, 0.024 mmol) and **salt-6** (5.5 mg, 0.029 mmol, 1.25 equiv.) added to a vial with a septa cap and backfilled with nitrogen. DMF (2.5 mL, 0.01M) added and placed in 80°C bath. After 1 hour and additional **salt-6** (2 mg, 0.01 mmol, 0.45 equiv.) added. Once complete by TLC, the reaction was quenched with 1M HCl and extracted with EtOAc and washed with brine before drying over $MgSO_4$. The crude reaction mixture was concentrated under reduced pressure and purified by column chromatography (gradient elution 50 to 100% $CHCl_3$ in hexane) to give the title compound as a red solid (13 mg, 0.011 mmol, 47%). ^{1}H NMR (500 MHz, Chloroform-*d*) δ 7.98 (s, 2H), 7.59 (s, 2H), 2.82 (d, *J* = 7.1 Hz, 4H), 1.69 (s, 2H), 1.40 – 1.16 (m, 64H), 0.86 (t, *J* = 6.9 Hz, 12H). ^{13}C NMR (126 MHz, $CDCl_3$) δ 174.4, 155.0, 152.1, 148.1, 142.9, 138.3, 134.1, 133.1, 121.4, 114.1, 113.1, 111.7, 79.3, 70.3, 40.7, 34.3, 33.5, 32.1, 32.1, 30.1, 29.85,

29.8, 29.8, 29.6, 29.5, 26.7, 22.9, 22.9, 14.4. HRMS for $C_{66}H_{86}N_8S_5$ (MALDI): $[M+Na]^+$ Calcd: 1173.5471, found 1173.7117.

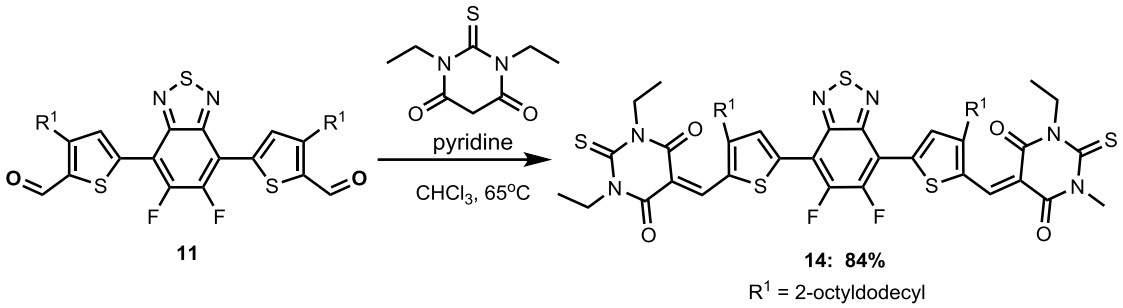

14 5,5'-(((5,6-difluorobenzo[c][1,2,5]thiadiazole-4,7-diyl)bis(3-(2-octyldodecyl)thiophene-5,2-diyl))bis(methanylylidene))bis(1,3-diethyl-2-thioxodihydropyrimidine-4,6(1H,5H)-dione)

Dialdehyde **11** (198 mg, 0.21 mmol) and 1,3-diethyl-2-thiobarbituric acid (891 mg, 4.45 mmol, 6 equiv.) added to a dried flask and backfilled with nitrogen. Chloroform (37 mL, 0.02 M) was added followed by pyridine (1.2 mL, 14.8 mmol, 20 equiv.) and the reaction was stirred overnight. The reaction was quenched with 1M HCl and extracted with $CHCl_3$ and washed with brine before drying over $MgSO_4$. The crude reaction mixture was concentrated under reduced pressure and purified by precipitation into MeOH from $CHCl_3$ to give the title compound as a purple solid (235 mg, 0.176 mmol, 84%). ^{1}H NMR (500 MHz, Chloroform-*d*) δ 8.86 (s, 2H), 8.28 (s, 2H), 4.64 (q, *J* = 7.0 Hz, 4H), 4.57 (q, *J* = 7.0 Hz, 4H), 2.98 (d, *J* = 7.1 Hz, 4H), 1.76 (q, *J* = 6.0 Hz, 2H), 1.39 (t, *J* = 7.0 Hz, 6H), 1.33 (t, *J* = 6.7 Hz, 6H), 1.24 (m, 64H), 0.85 (td, *J* = 7.0, 2.1 Hz, 12H). ^{13}C NMR (126 MHz, $CDCl_3$) δ 178.8, 161.2, 159.8, 159.0, 151.3 (m), 148.8, 146.0, 144.3, 135.5, 134.7, 113.0, 111.2, 44.3, 43.5, 41.1, 34.9, 33.5, 32.1, 30.2, 29.9, 29.9, 29.8, 29.6, 26.7, 22.9, 14.4, 12.8, 12.6. HRMS for $C_{72}H_{106}F_2N_6O_4S_5$ (MALDI): $[M]^+$ Calcd: 1316.6847, found 1316.8080.

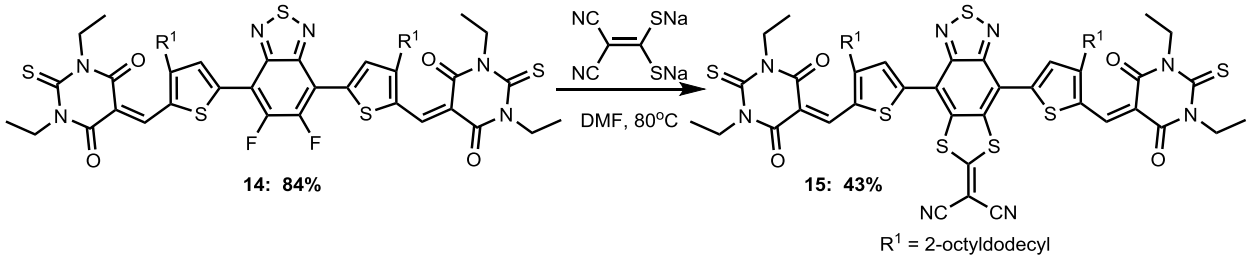

15 2-(4,8-bis(5-((1,3-diethyl-4,6-dioxo-2-thioxotetrahydropyrimidin-5(2H)-ylidene)methyl)-4-(2-octyldodecyl)thiophen-2-yl)-[1,3]dithiolo[4',5':4,5]benzo[1,2-c][1,2,5]thiadiazol-6-ylidene)malononitrile

TBTA adduct **14** (24 mg, 0.018 mmol) and **salt-6** (4.2 mg, 0.023 mmol, 1.25 equiv.) added to a vial with a septa cap and backfilled with nitrogen. DMF (2 mL, 0.01M) added and placed in 80°C bath. After 1 hour and additional **salt-6** (2 mg, 0.01 mmol, 0.55 equiv.) added. Once complete by TLC, the reaction was quenched with 1M HCl and extracted with EtOAc and washed with brine before drying over $MgSO_4$. The crude reaction mixture was concentrated under reduced pressure and purified by column chromatography (gradient elution 20 to 100% $CHCl_3$ in hexane) to give the title compound as a purple solid (11 mg, 0.008 mmol, 43%). ^{1}H NMR (500 MHz, Chloroform-*d*) δ

8.96 (s, 2H), 7.73 (s, 2H), 4.60 (q, *J* = 6.9 Hz, 8H), 3.03 (d, *J* = 7.2 Hz, 4H), 1.76 (p, *J* = 7.1, 6.4 Hz, 2H), 1.36 (dt, *J* = 14.0, 8.3 Hz, 12H), 1.30 – 1.18 (m, 64H), 0.86 (td, *J* = 6.8, 2.3 Hz, 12H). ^{13}C NMR (126 MHz, $CDCl_3$) δ 178.7, 175.6, 161.0, 160.0, 159.2, 152.4, 147.0, 145.9, 138.3, 135.3, 133.9, 122.2, 112.1, 112.0, 69.4, 44.4, 43.6, 41.2, 35.1, 33.6, 32.1, 30.2, 29.9, 29.9, 29.9, 29.8, 29.6, 29.6, 26.7, 22.9, 14.4, 12.7, 12.6. HRMS for $C_{76}H_{106}N_8O_4S_7$ (MALDI): $[M+H]^+$ Calcd: 1419.6455, found 1419.8638.

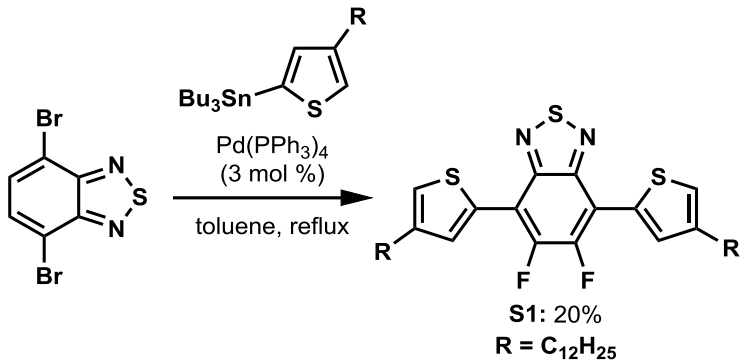

S1: 20%

R = $C_{12}H_{25}$

S1 4,7-bis(4-dodecylthiophen-2-yl)benzo[c][1,2,5]thiadiazole

4,7-dibromobenzo[c]-1,2,5-thiadiazole (49 mg, 0.168 mmol) and $Pd(PPh_3)_4$ (10 mg, 0.008 mmol, 0.05 equiv.) added to dried vial with septa cap and backfilled with nitrogen. **4a** (200 mg, 0.37 mmol, 2.2 equiv.) sparged with nitrogen and transferred to the vial with solids with toluene (2 mL, 0.084 M). The mixture was further sparged with nitrogen. The reaction was placed in a 110°C bath overnight. Once no further conversion was detected by TLC, the solution was diluted with EtOAc and washed with water and brine before drying over $MgSO_4$. The crude reaction mixture was concentrated under reduced pressure and purified by column chromatography (gradient elution 0 to 25% $CHCl_3$ in hexane) to give the title compound as a yellow solid (21 mg, 0.033 mmol, 20%). ^{1}H NMR (500 MHz, Chloroform-*d*) δ 7.97 (d, *J* = 1.4 Hz, 2H), 7.82 (s, 2H), 7.04 (d, *J* = 1.3 Hz, 2H), 2.69 (t, *J* = 7.7 Hz, 4H), 1.75 – 1.65 (m, 4H), 1.45 – 1.22 (m, 30H), 0.88 (t, *J* = 6.9 Hz, 6H). ^{13}C NMR (126 MHz, $CDCl_3$) δ 152.8, 144.6, 139.2, 129.2, 126.2, 125.8, 121.7, 32.2, 30.9, 30.7, 29.9, 29.9, 29.9, 29.7, 29.6, 29.6, 22.9, 14.4. HRMS for $C_{38}H_{56}N_2S_3$ (MALDI): $[M]^+$ Calcd: 636.3606, found 636.3769.

The 4-bromo-7-(4-dodecylthiophen-2-yl)benzo[c][1,2,5]thiadiazole byproduct was also isolated (30 mg, 0.064 mmol, 38%)

3.11 References

[1] a) H. Yoo, M. Ghittorelli, E. C. P. Smits, G. H. Gelinck, H.-K. Lee, F. Torricelli, J.-J. Kim, *Sci. Rep.* **2016**, *6*, 35585; b) T. T. Dao, H. Sakai, H. T. Nguyen, K. Ohkubo, S. Fukuzumi, H. Murata, *ACS Appl. Mater. Interfaces* **2016**, *8*, 18249-18255; c) A. Dathbun, S. Kim, S. Lee, D. K. Hwang, J. H. Cho, *Mol. Syst. Des. Eng.* **2019**, *4*, 484-490; d) H. Sun, M. Vagin, S. Wang, X. Crispin, R. Forchheimer, M. Berggren, S. Fabiano, *Adv. Mater.* **2018**, *30*, 1704916.

[2] J. T. E. Quinn, J. Zhu, X. Li, J. Wang, Y. Li, *J. Mater. Chem. C* **2017**, *5*, 8654-8681.

[3] R. Ragni, A. Punzi, F. Babudri, G. M. Farinola, *Eur. J. Org. Chem.* **2018**, *2018*, 3500-3519.

[4] a) N. Bauer, Q. Zhang, J. J. Rech, S. Dai, Z. Peng, H. Ade, J. Wang, X. Zhan, W. You, *Nano Research* **2019**, *12*, 2400-2405; b) M. Chen, D. Liu, W. Li, R. S. Gurney, D. Li, J. Cai, E. L. K. Spooner, R. C. Kilbride, J. D. McGettrick, T. M. Watson, Z. Li, R. A. L. Jones, D. G. Lidzey, T. Wang, *ACS Appl. Mater. Interfaces* **2019**, *11*, 26194-26203.

[5] a) T. Okamoto, K. Nakahara, A. Saeki, S. Seki, J. H. Oh, H. B. Akkerman, Z. Bao, Y. Matsuo, *Chem. Mater.* **2011**, *23*, 1646-1649; b) P. Panini, D. Chopra, in *Hydrogen Bonded Supramolecular Structures* (Eds.: Z.-T. Li, L.-Z. Wu), Springer Berlin Heidelberg, Berlin, Heidelberg, **2015**, pp. 37-67; c) X. Liang, W. Sun, Y. Chen, L. Tan, Z. Cai, Z. Liu, L. Wang, J. Li, W. Chen, L. Dong, *J. Mater. Chem. C* **2018**, *6*, 1774-1779; d) D. Wang, X. Qiao, G. Ouyang, H. Wu, H. Li, *Chem. Commun.* **2019**, *55*, 6253-6256.

[6] United States Environmental Protection Agency, National Service Center for Environmental Publications (NSCEP), **2014**.

[7] a) K. Steenland, T. Fletcher, A. Savitz David, *Environ. Health Perspect* **2010**, *118*, 1100-1108; b) B. J. Henry, J. P. Carlin, J. A. Hammerschmidt, R. C. Buck, L. W. Buxton, H. Fiedler, J. Seed, O. Hernandez, *Integr. Environ. Assess. Manag.* **2018**, *14*, 316-334.

[8] B. D. Key, R. D. Howell, C. S. Criddle, *Environ. Sci. Technol.* **1997**, *31*, 2445-2454.

[9] Y. Yamashita, T. Suzuki, G. Saito, T. Mukai, *ChemComm* **1986**, 1489-1491.

[10] X. Gao, C.-a. Di, Y. Hu, X. Yang, H. Fan, F. Zhang, Y. Liu, H. Li, D. Zhu, *J. Am. Chem. Soc.* **2010**, *132*, 3697-3699.

[11] a) P. A. Limacher, H. P. Lüthi, *Wiley Interdiscip. Rev. Comput. Mol. Sci.* **2011**, *1*, 477-486; b) N. F. Phelan, M. Orchin, *J. Chem. Educ.* **1968**, *45*, 633.

[12] W. O. Foye, *J. Chem. Educ.* **1969**, *46*, 841.

[13] Y. N. Mabkhot, F. D. Aldawsari, S. S. Al-Showiman, A. Barakat, S. M. Soliman, M. I. Choudhary, S. Yousuf, M. S. Mubarak, T. B. Hadda, *Chem. Cent. J.* **2015**, *9*, 24.

[14] M. L. Gorbaty, W. E. Truce, J. E. Tracy, *J. Org. Chem.* **1971**, *36*, 237-239.

[15] a) B. Nketia-Yawson, A. R. Jung, H. D. Nguyen, K.-K. Lee, B. Kim, Y.-Y. Noh, *ACS Appl. Mater. Interfaces* **2018**, *10*, 32492-32500; b) Q. Zhang, L. Yan, X. Jiao, Z. Peng, S. Liu, J. J. Rech, E. Klump, H. Ade, F. So, W. You, *Chem. Mater.* **2017**, *29*, 5990-6002; c) J. You, L. Dou, K. Yoshimura, T. Kato, K. Ohya, T. Moriarty, K. Emery, C.-C. Chen, J. Gao, G. Li, Y. Yang, *Nat. Commun.* **2013**, *4*, 1446.

[16] J. L. Brédas, *J. Chem. Phys* **1985**, *82*, 3808-3811.

[17] a) K. Ono, S. Tanaka, Y. Yamashita, *Angew. Chem.* **1994**, *33*, 1977-1979; b) M. Wang, Y. Sun, M. Tong, E. S. Chesnut, J. H. Seo, R. Kumar, F. Wudl, *J. Polym. Sci. Pol. Chem.* **2011**, *49*, 441-451; c) T. C. Parker, D. G. Patel, K. Moudgil, S. Barlow, C. Risko, J.-L. Brédas, J. R. Reynolds, S. R. Marder, *Mater. Horiz.* **2015**, *2*, 22-36.

[18] a) D. Leusser, J. Henn, N. Kocher, B. Engels, D. Stalke, *J. Am. Chem. Soc.* **2004**, *126*, 1781-1793; b) D. G. Patel, F. Feng, Y.-y. Ohnishi, K. A. Abboud, S. Hirata, K. S. Schanze, J. R. Reynolds, *J. Am. Chem. Soc.* **2012**, *134*, 2599-2612.

[19] J. Lee, M. Jang, S. M. Lee, D. Yoo, T. J. Shin, J. H. Oh, C. Yang, *ACS Appl. Mater. Interfaces* **2014**, *6*, 20390-20399.

[20] a) A. Casey, Y. Han, Z. Fei, A. J. P. White, T. D. Anthopoulos, M. Heeney, *J. Mater. Chem. C* **2015**, *3*, 265-275; b) S. Shi, P. Chen, Y. Chen, K. Feng, B. Liu, J. Chen, Q. Liao, B. Tu, J. Luo, M. Su, H. Guo, M.-G. Kim, A. Facchetti, X. Guo, *Adv. Mater.*, *0*, 1905161.

[21] a) M. L. Keshtov, S. A. Kuklin, N. A. Radychev, A. Y. Nikolaev, I. E. Ostapov, M. M. Krayushkin, I. O. Konstantinov, E. N. Koukaras, A. Sharma, G. D. Sharma, *Phys. Chem. Chem. Phys.* **2016**, *18*, 8389-8400; b) M. L. Keshtov, S. A. Kuklin, N. A. Radychev, A. Y. Nikolaev, E. N. Koukaras, A. Sharma, G. D. Sharma, *RSC Adv.* **2016**, *6*, 14893-14908.

[22] a) J. Qi, W. Qiao, Z. Y. Wang, *Chem Rec.* **2016**, *16*, 1531-1548; b) Y. Wang, T. Michinobu, *J. Mater. Chem. C* **2016**, *4*, 6200-6214.

[23] X. Hu, Y. Dong, F. Huang, X. Gong, Y. Cao, *J. Phys. Chem. C* **2013**, *117*, 6537-6543.
[24] X. Guo, M. Baumgarten, K. Müllen, *Prog. Polym. Sci.* **2013**, *38*, 1832-1908.
[25] H. Kang, M. A. Uddin, C. Lee, K.-H. Kim, T. L. Nguyen, W. Lee, Y. Li, C. Wang, H. Y. Woo, B. J. Kim, *J. Am. Chem. Soc.* **2015**, *137*, 2359-2365.
[26] M. Netopilík, P. Kratochvíl, *Polymer* **2003**, *44*, 3431-3436.
[27] D.-M. Smilgies, *J. Appl. Crystallogr* **2009**, *42*, 1030-1034.
[28] a) H. Lee, D. Lee, D. H. Sin, S. W. Kim, M. S. Jeong, K. Cho, *NPG Asia Mater.* **2018**, *10*, 469-481; b) S. Chae, K. H. Cho, S. Won, A. Yi, J. Choi, H. H. Lee, J.-H. Kim, H. J. Kim, *Adv. Mater. Interfaces* **2017**, *4*, 1701099.
[29] N. Wang, Z. Chen, W. Wei, Z. Jiang, *J. Am. Chem. Soc.* **2013**, *135*, 17060-17068.
[30] Z. Li, J. Lu, S.-C. Tse, J. Zhou, X. Du, Y. Tao, J. Ding, *J. Mater. Chem.* **2011**, *21*, 3226-3233.
[31] a) M. Egginger, S. Bauer, R. Schwödiauer, H. Neugebauer, N. S. Sariciftci, *Monatsh. Chem.* **2009**, *140*, 735-750; b) G. Paasch, S. Scheinert, A. Herasimovich, I. Hörselmann, T. Lindner, *Phys. Status Solidi* **2008**, *205*, 534-548.
[32] a) D. M. de Leeuw, M. M. J. Simenon, A. R. Brown, R. E. F. Einerhand, *Synth. Met.* **1997**, *87*, 53-59; b) J. Zaumseil, H. Sirringhaus, *Chem. Rev.* **2007**, *107*, 1296-1323.
[33] a) R. Kim, P. S. K. Amegadze, I. Kang, H.-J. Yun, Y.-Y. Noh, S.-K. Kwon, Y.-H. Kim, *Adv. Funct. Mater.* **2013**, *23*, 5719-5727; b) D. Khim, K.-J. Baeg, J. Kim, J.-S. Yeo, M. Kang, P. S. K. Amegadzea, M.-G. Kim, J. Cho, J. H. Lee, D.-Y. Kim, Y.-Y. Noh, *J. Mater. Chem.* **2012**, *22*, 16979-16985.
[34] Y. Ma, X. Zhou, D. Cai, Q. Tu, W. Ma, Q. Zheng, *Mater. Horiz.* **2019**.
[35] R. R. Gagne, C. A. Koval, G. C. Lisensky, *Inorganic Chemistry* **1980**, *19*, 2854-2855.
[36] X. Liu, B. He, A. Garzón-Ruiz, A. Navarro, T. L. Chen, M. A. Kolaczkowski, S. Feng, L. Zhang, C. A. Anderson, J. Chen, Y. Liu, *Adv. Funct. Mater.* **2018**, *28*, 1801874.
[37] A. Hexemer, W. Bras, J. Glossinger, E. Schaible, E. Gann, R. Kirian, A. MacDowell, M. Church, B. Rude, H. Padmore, *Journal of Physics: Conference Series* **2010**, *247*, 012007.
[38] W. R. Hatchard, *J. Org. Chem.* **1964**, *29*, 660-665.
[39] B. Fu, J. Baltazar, Z. Hu, A.-T. Chien, S. Kumar, C. L. Henderson, D. M. Collard, E. Reichmanis, *Chem. Mater.* **2012**, *24*, 4123-4133.

Appendix III. NMR Spectra for Compounds Discussed in Chapter 3

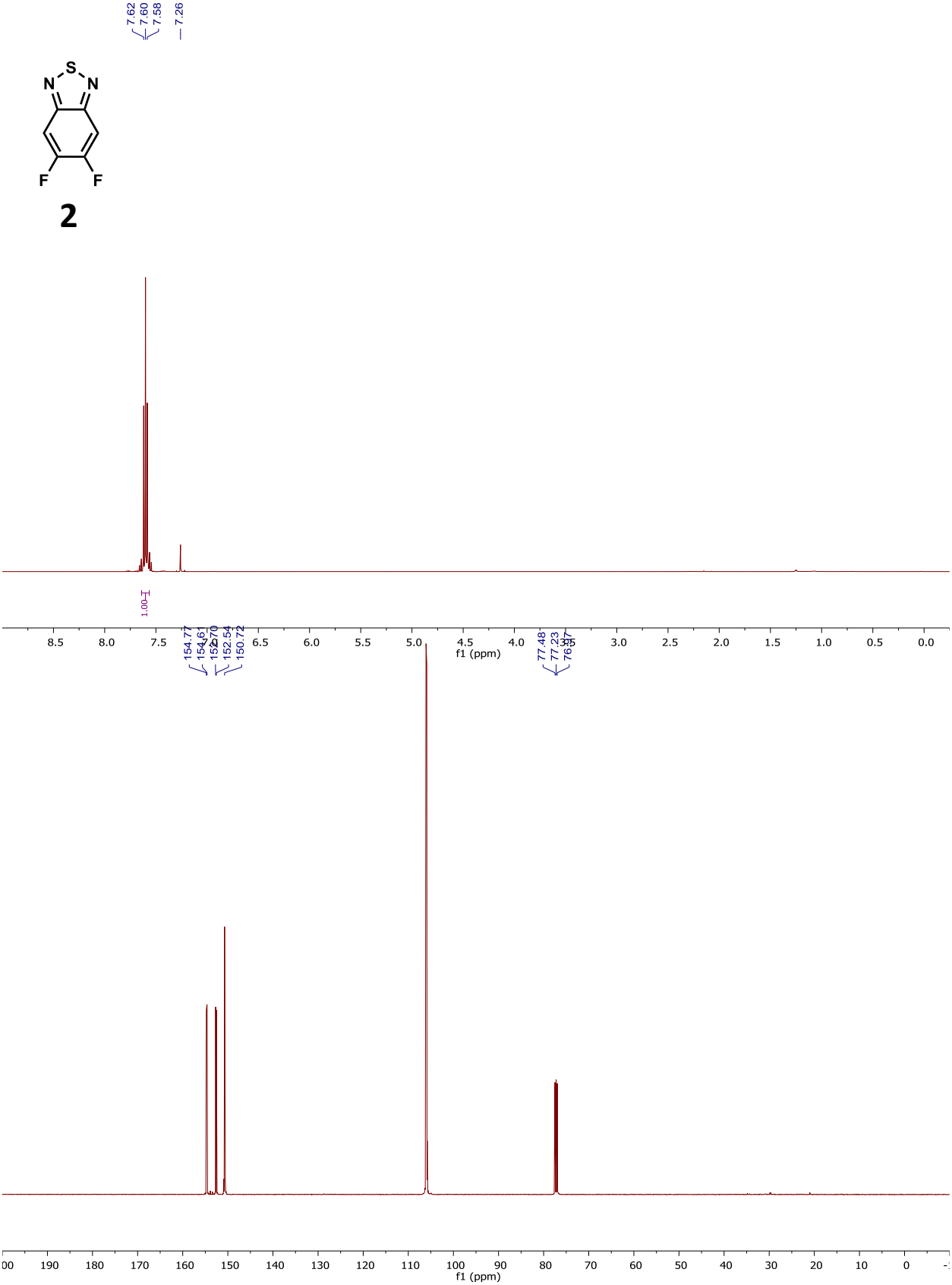

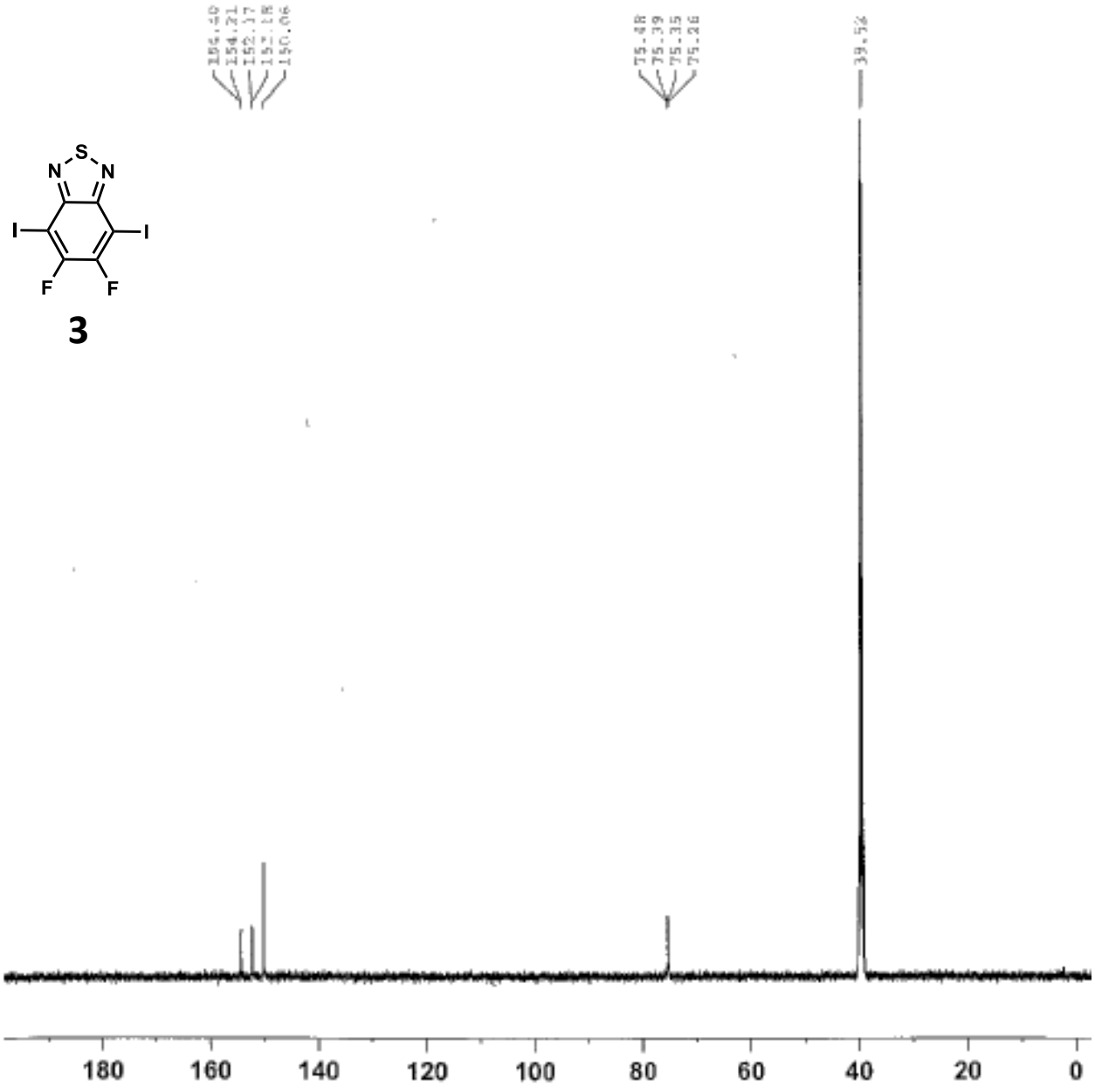
156.40
154.21
152.17
151.18
150.06
75.48
75.39
75.35
75.26
39.56
N
S
N
I
I
F
F
180
160
140
120
100
80
60
40
20
0

3

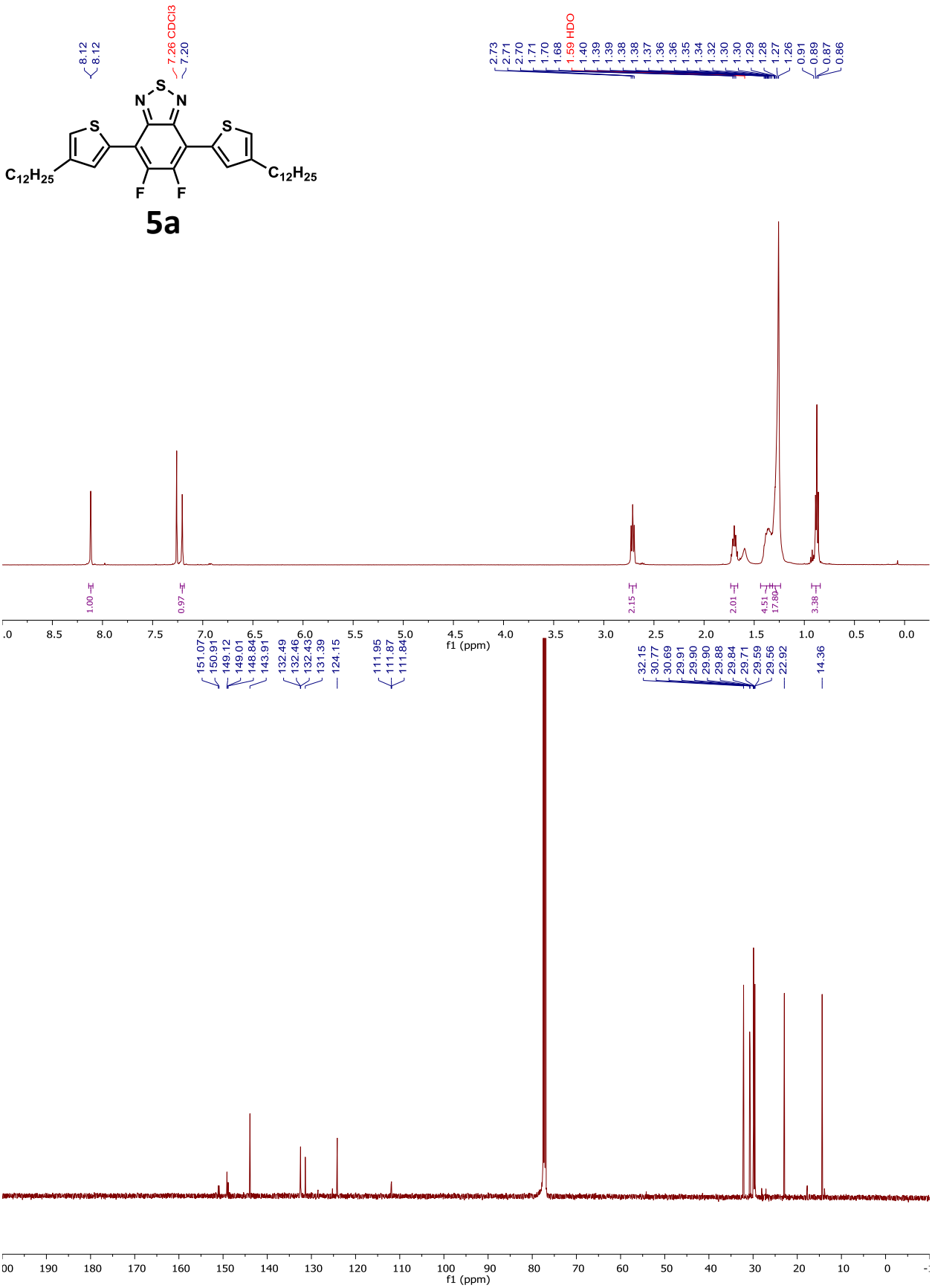
8.12
8.12
7.26 CDCl3
7.20
N
S
N
S
S
$C_{12}H_{25}$
$C_{12}H_{25}$
F
F
5a
2.73
2.71
2.70
1.71
1.70
1.68
1.59 HDO
1.40
1.39
1.39
1.38
1.38
1.37
1.36
1.36
1.35
1.34
1.32
1.30
1.30
1.29
1.28
1.27
1.26
0.91
0.89
0.87
0.86
1.00
0.97
2.15
2.01
4.51
17.80
3.38
f1 (ppm)
151.07
150.91
149.12
149.01
148.84
143.91
132.49
132.46
132.43
131.39
124.15
111.95
111.87
111.84
32.15
30.77
30.69
29.91
29.90
29.88
29.84
29.71
29.59
29.56
22.92
14.36
f1 (ppm)

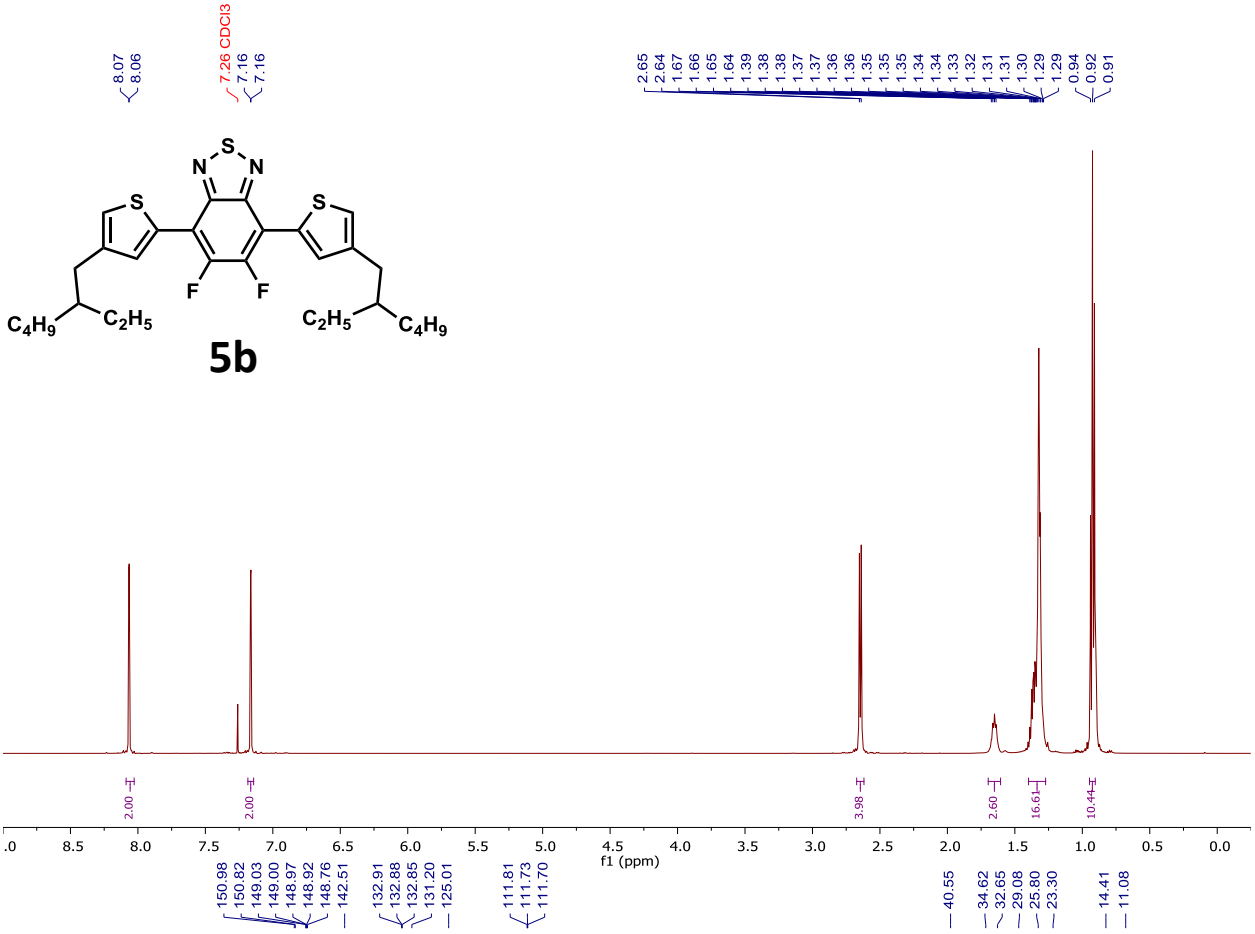
8.07
8.06
7.26 CDCl3
7.16
7.16
2.65
2.64
1.67
1.66
1.65
1.64
1.39
1.38
1.38
1.37
1.37
1.36
1.36
1.35
1.35
1.35
1.34
1.34
1.33
1.32
1.31
1.31
1.30
1.29
1.29
0.94
0.92
0.91
S
N
N
S
S
F
F
C4H9
C2H5
C2H5
C4H9
2.00
2.00
3.98
2.60
16.61
10.44
f1 (ppm)
150.98
150.82
149.03
149.00
148.97
148.92
148.76
142.51
132.91
132.88
132.85
131.20
125.01
111.81
111.73
111.70
40.55
34.62
32.65
29.08
25.80
23.30
14.41
11.08
f1 (ppm)

5b

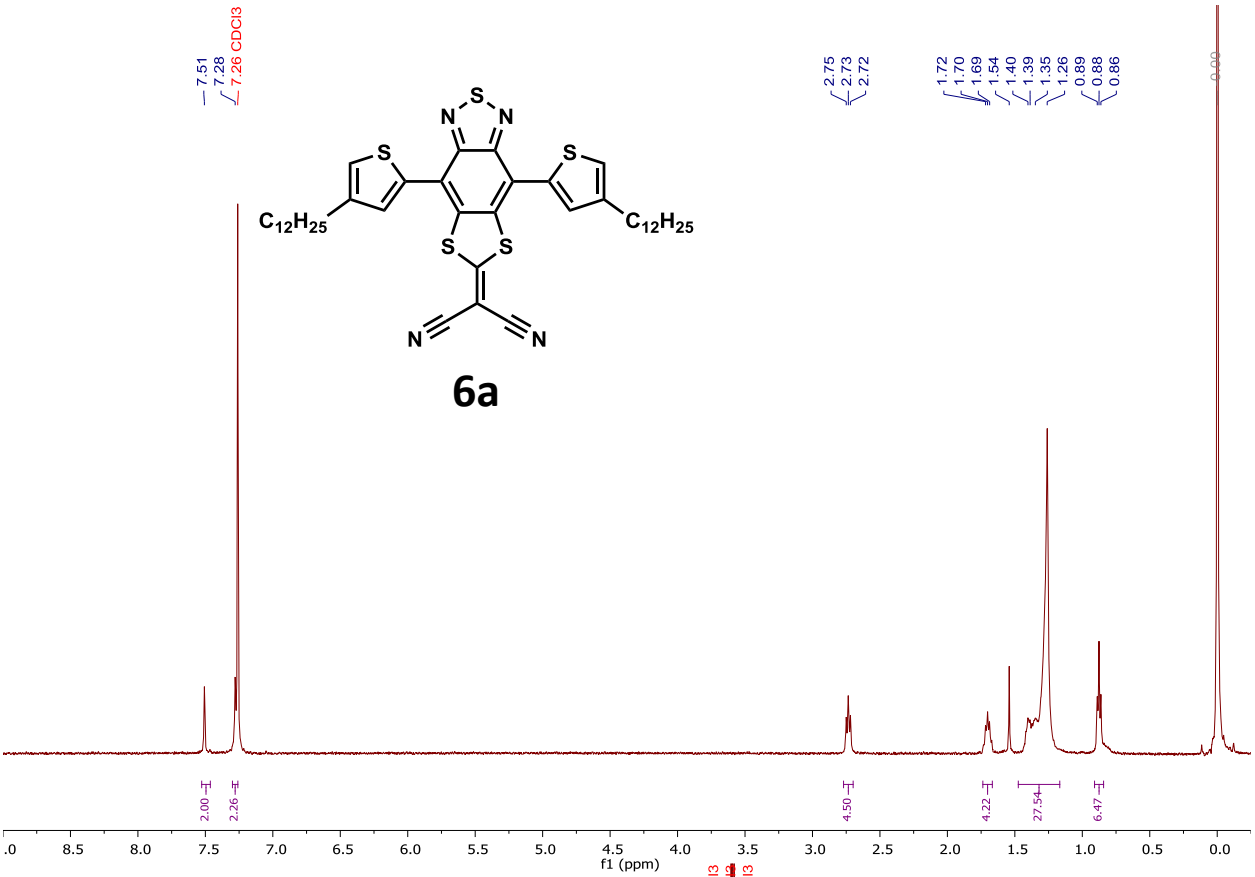
7.51
7.28
7.26 CDCl3
2.75
2.73
2.72
1.72
1.70
1.69
1.54
1.40
1.39
1.35
1.26
0.89
0.88
0.86
0.00
2.00
2.26
4.50
4.22
27.54
6.47
f1 (ppm)

S
N
S
N
S
S
S
$C_{12}H_{25}$
$C_{12}H_{25}$
S
S
N
N

6a

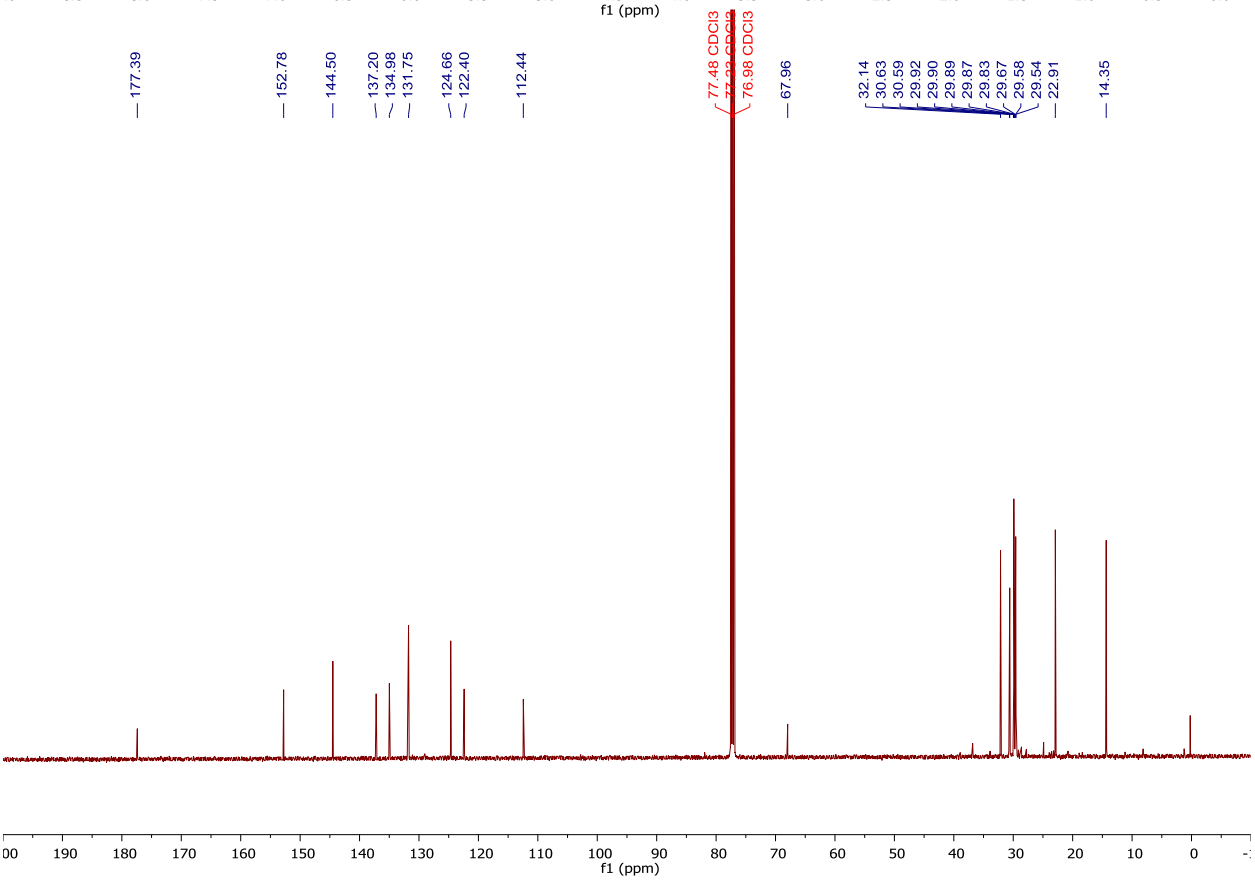
177.39
152.78
144.50
137.20
134.98
131.75
124.66
122.40
112.44
77.48 CDCl3
77.23 CDCl3
76.98 CDCl3
67.96
32.14
30.63
30.59
29.92
29.90
29.89
29.87
29.83
29.67
29.58
29.54
22.91
14.35
f1 (ppm)

S
N
N
S
S
S
S
C_4H_9
C_2H_5
C_2H_5
C_4H_9
N
N

6b

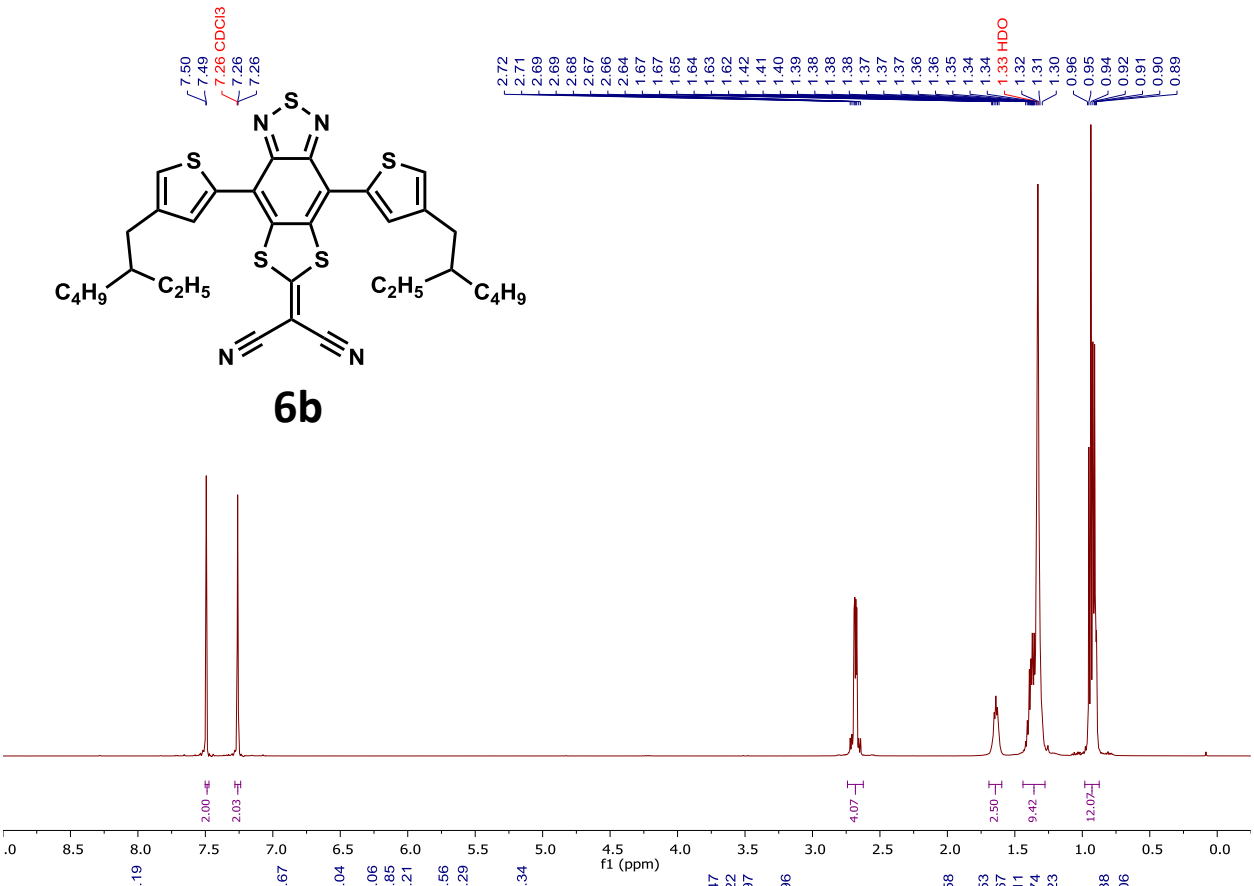
7.50
7.49
7.26 CDCl3
7.26
7.26
2.72
2.71
2.69
2.69
2.68
2.67
2.66
2.64
1.67
1.67
1.65
1.64
1.63
1.62
1.42
1.41
1.40
1.39
1.38
1.38
1.37
1.37
1.37
1.36
1.35
1.34
1.34
1.33 HDO
1.32
1.31
1.30
0.96
0.95
0.94
0.92
0.91
0.90
0.89
2.00
2.03
4.07
2.50
9.42
12.07
f1 (ppm)

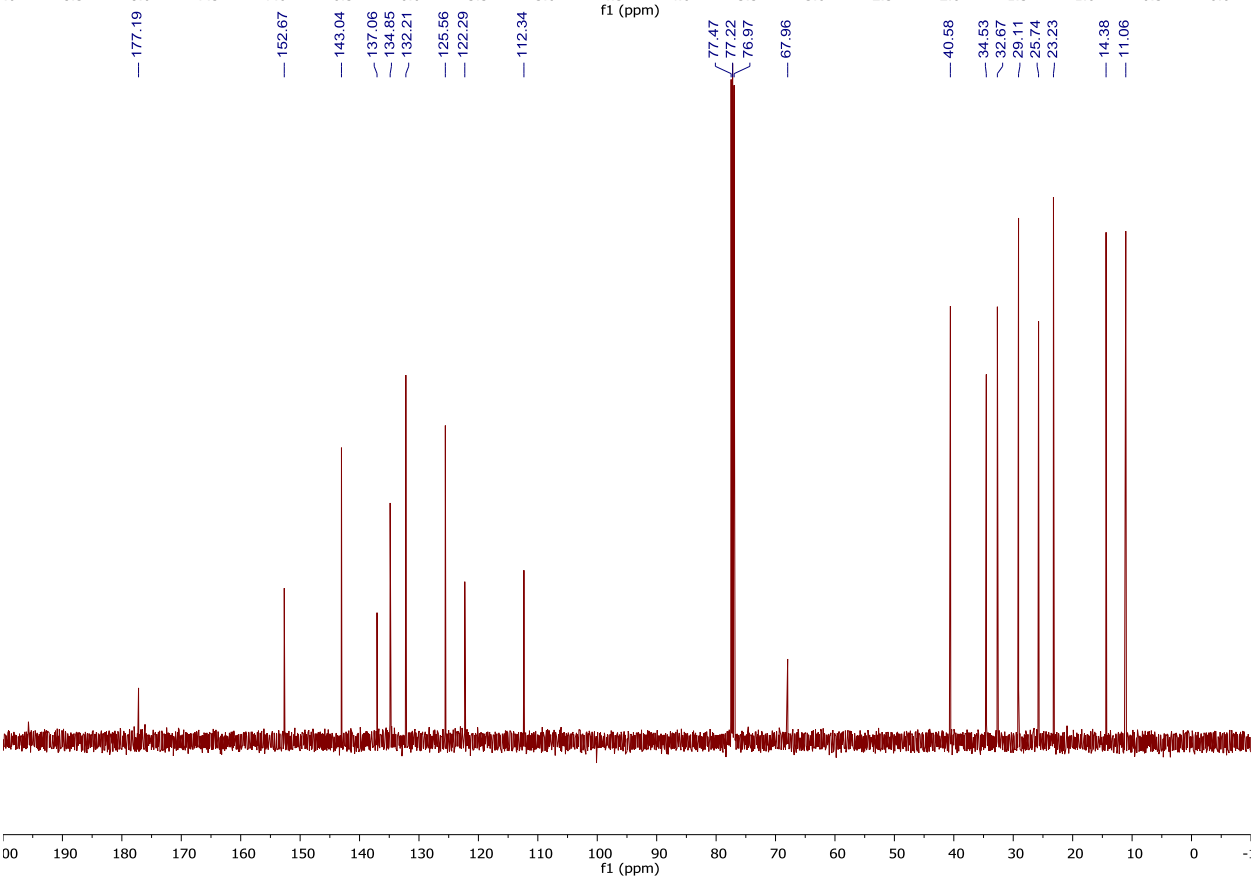
177.19
152.67
143.04
137.06
134.85
132.21
125.56
122.29
112.34
77.47
77.22
76.97
67.96
40.58
34.53
32.67
29.11
25.74
23.23
14.38
11.06
f1 (ppm)

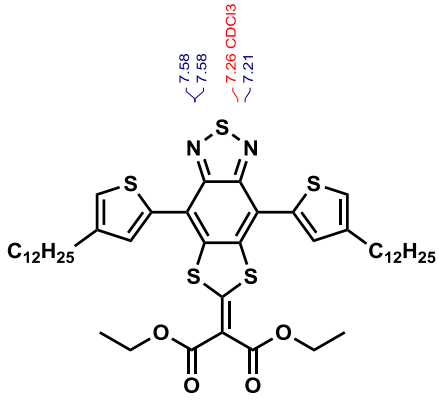
7.58
7.58
7.26 CDCl3
7.21
N
S
N
S
S
S
S
O
O
O
O
$C_{12}H_{25}$
$C_{12}H_{25}$

7a

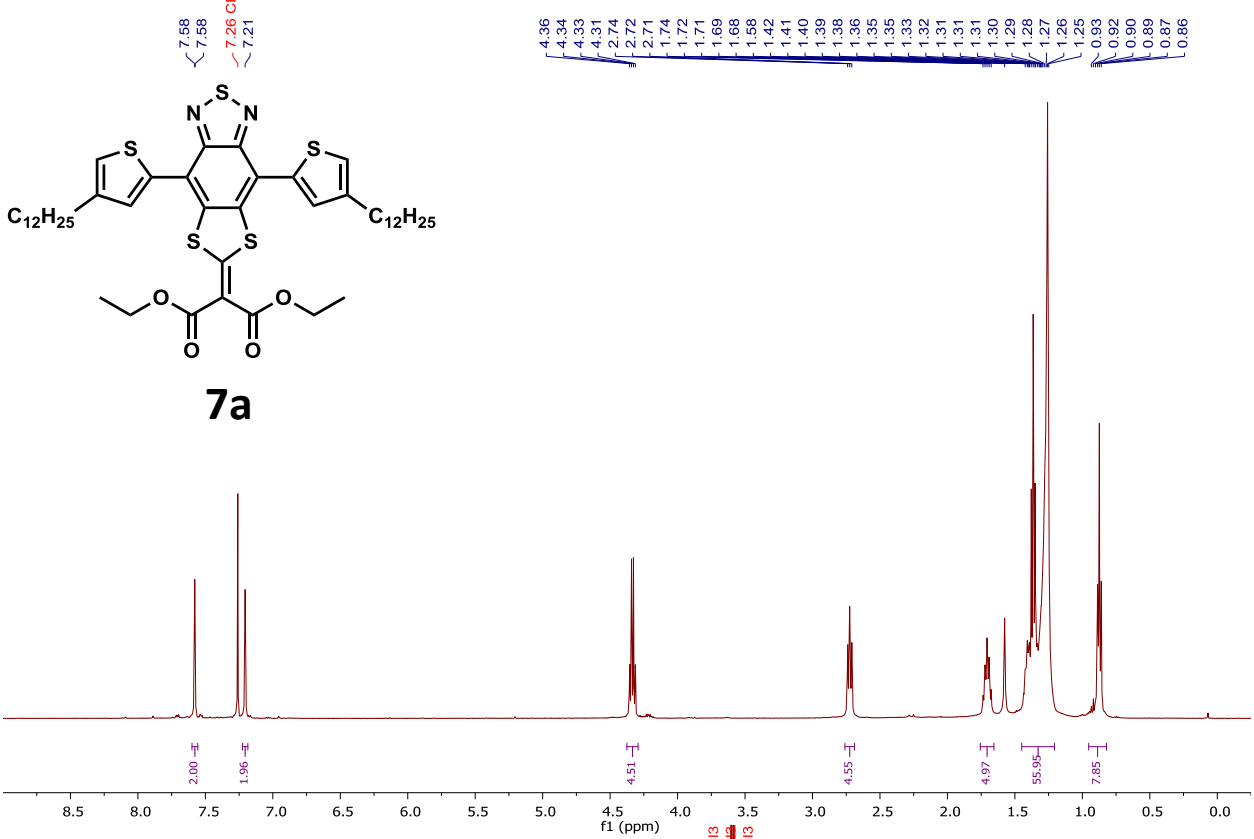
4.36
4.34
4.33
4.31
2.74
2.72
2.71
1.74
1.72
1.71
1.69
1.68
1.58
1.42
1.41
1.40
1.39
1.38
1.36
1.35
1.35
1.33
1.32
1.31
1.31
1.31
1.30
1.29
1.28
1.27
1.26
1.25
0.93
0.92
0.90
0.89
0.87
0.86
2.00
1.96
4.51
4.55
4.97
55.95
7.85
f1 (ppm)

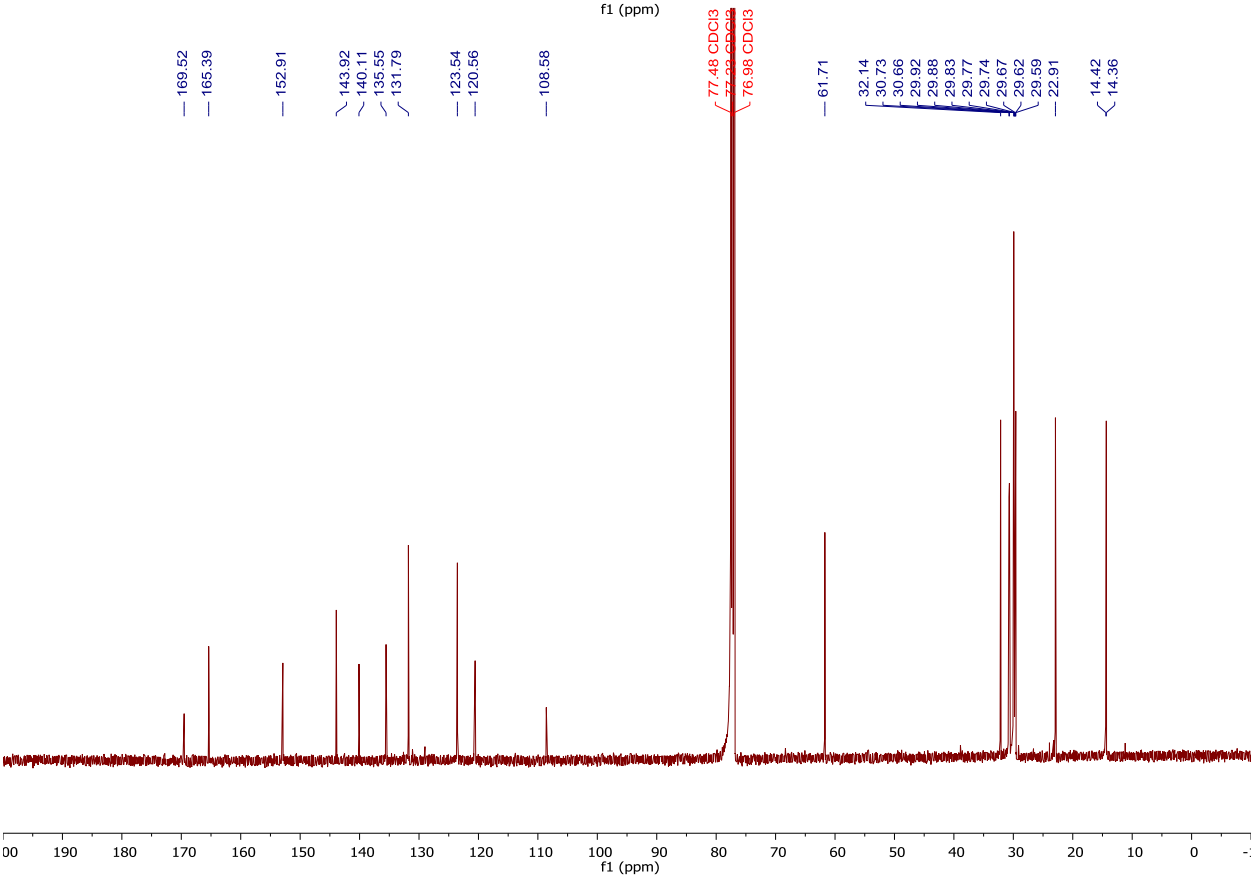
169.52
165.39
152.91
143.92
140.11
135.55
131.79
123.54
120.56
108.58
77.48 CDCl3
77.22 CDCl3
76.98 CDCl3
61.71
32.14
30.73
30.66
29.92
29.88
29.83
29.77
29.74
29.67
29.62
29.59
22.91
14.42
14.36
f1 (ppm)

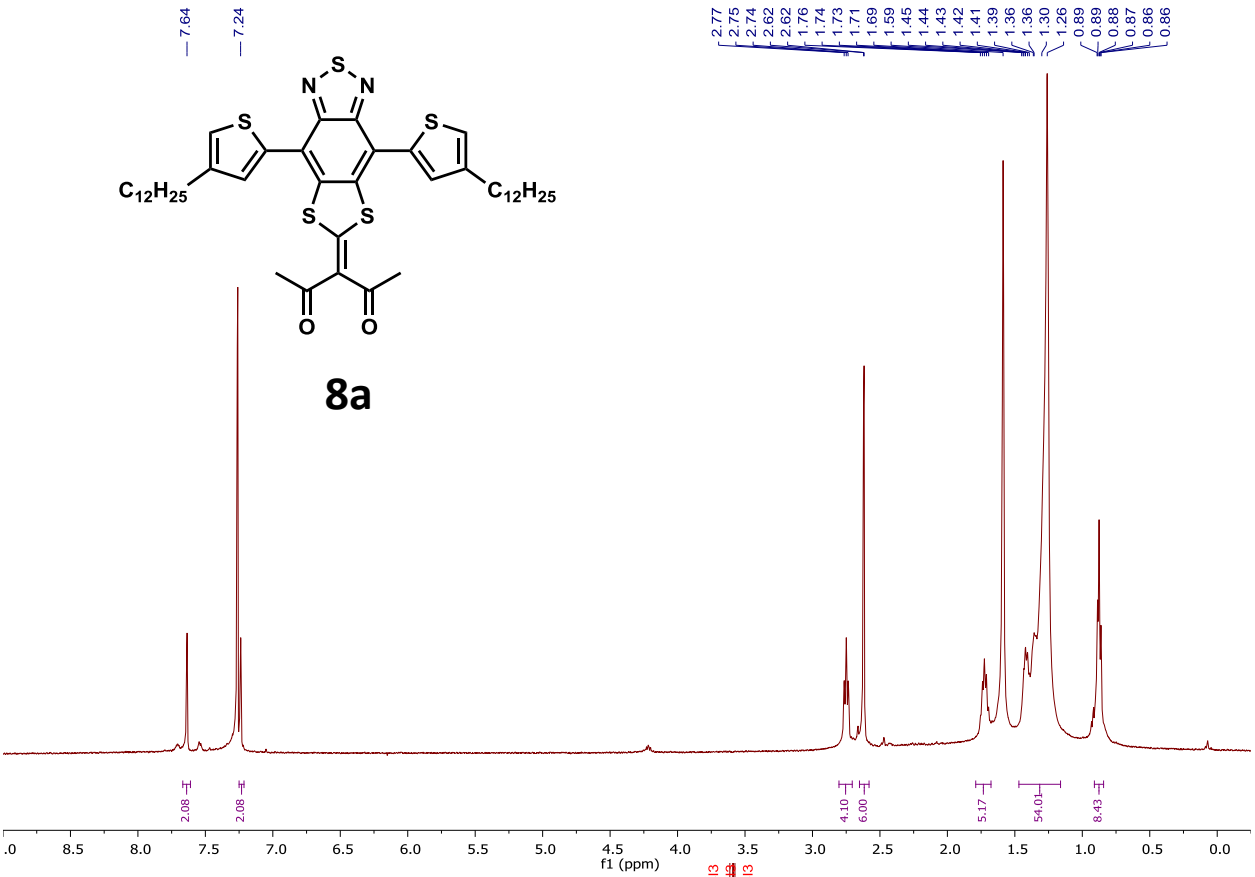
7.64
7.24
2.77
2.75
2.74
2.62
2.62
1.76
1.74
1.73
1.71
1.69
1.59
1.45
1.44
1.43
1.42
1.41
1.39
1.36
1.36
1.30
1.26
0.89
0.89
0.88
0.87
0.86
0.86
2.08
2.08
4.10
6.00
5.17
54.01
8.43
f1 (ppm)

8a

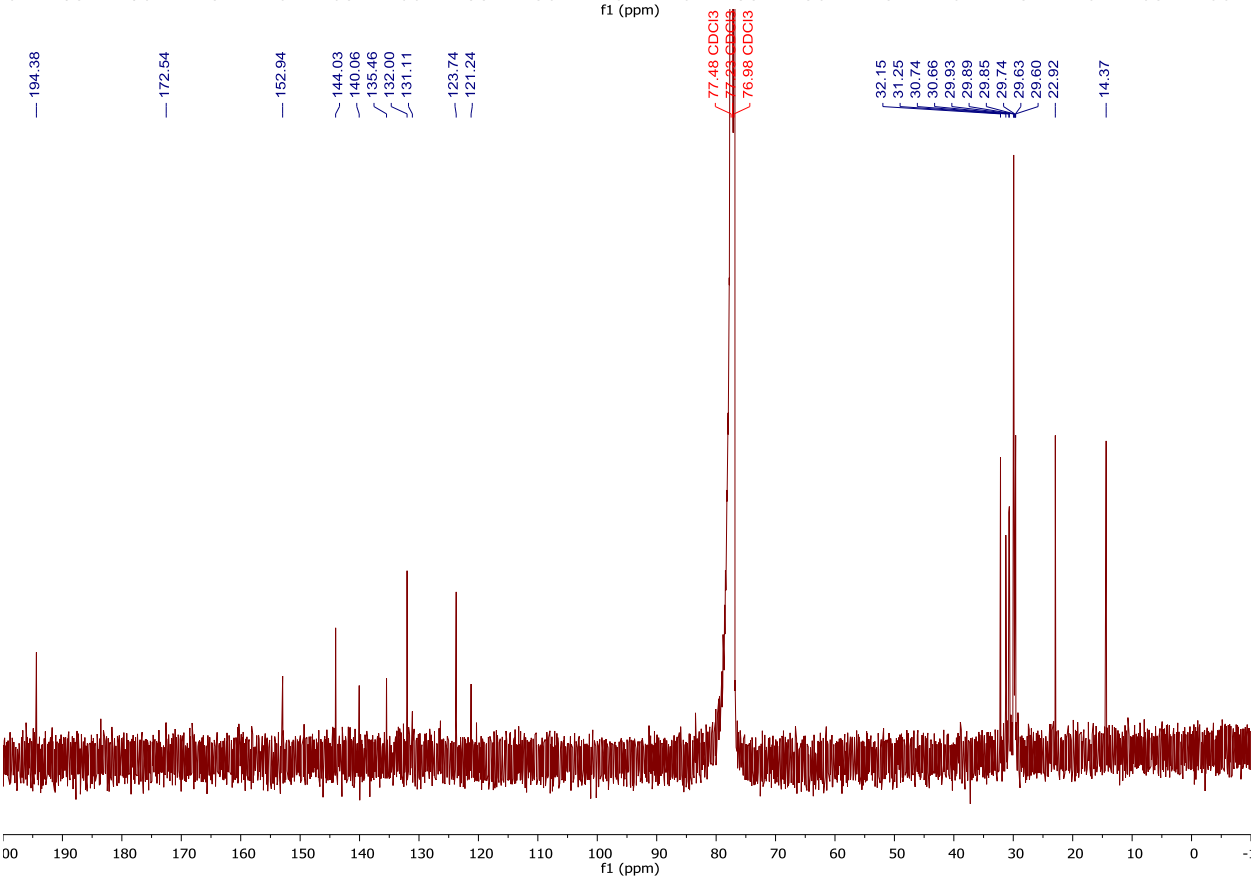
194.38
172.54
152.94
144.03
140.06
135.46
132.00
131.11
123.74
121.24
77.48 CDCl3
77.23 CDCl3
76.98 CDCl3
32.15
31.25
30.74
30.66
29.93
29.89
29.85
29.74
29.63
29.60
22.92
14.37
f1 (ppm)

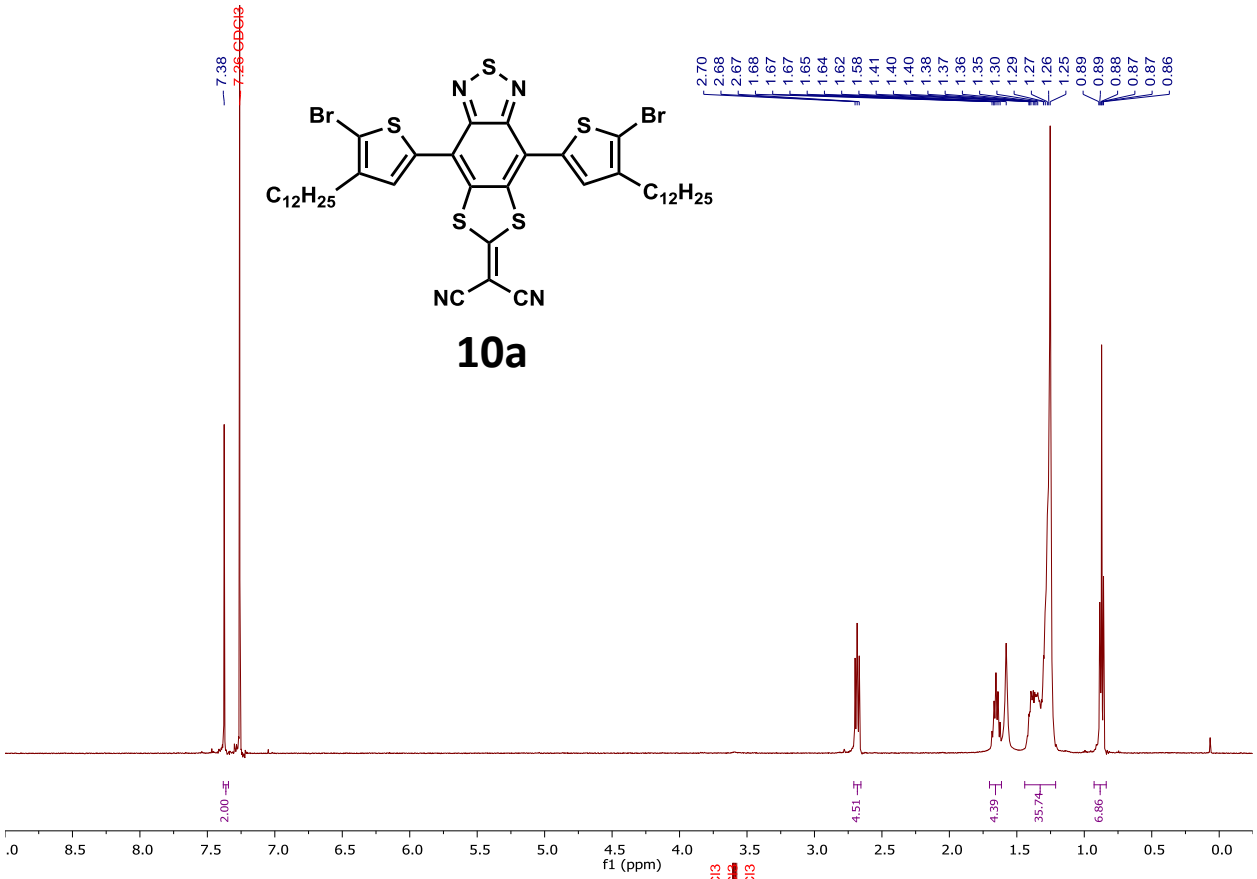
7.38
7.26 CDCl3
2.70
2.68
2.67
1.68
1.67
1.67
1.65
1.64
1.62
1.58
1.41
1.40
1.40
1.38
1.37
1.36
1.35
1.30
1.29
1.27
1.26
1.25
0.89
0.89
0.88
0.87
0.87
0.86
Br
S
N
S
N
Br
C12H25
C12H25
S
S
NC
CN
2.00
4.51
4.39
35.74
6.86
f1 (ppm)

10a

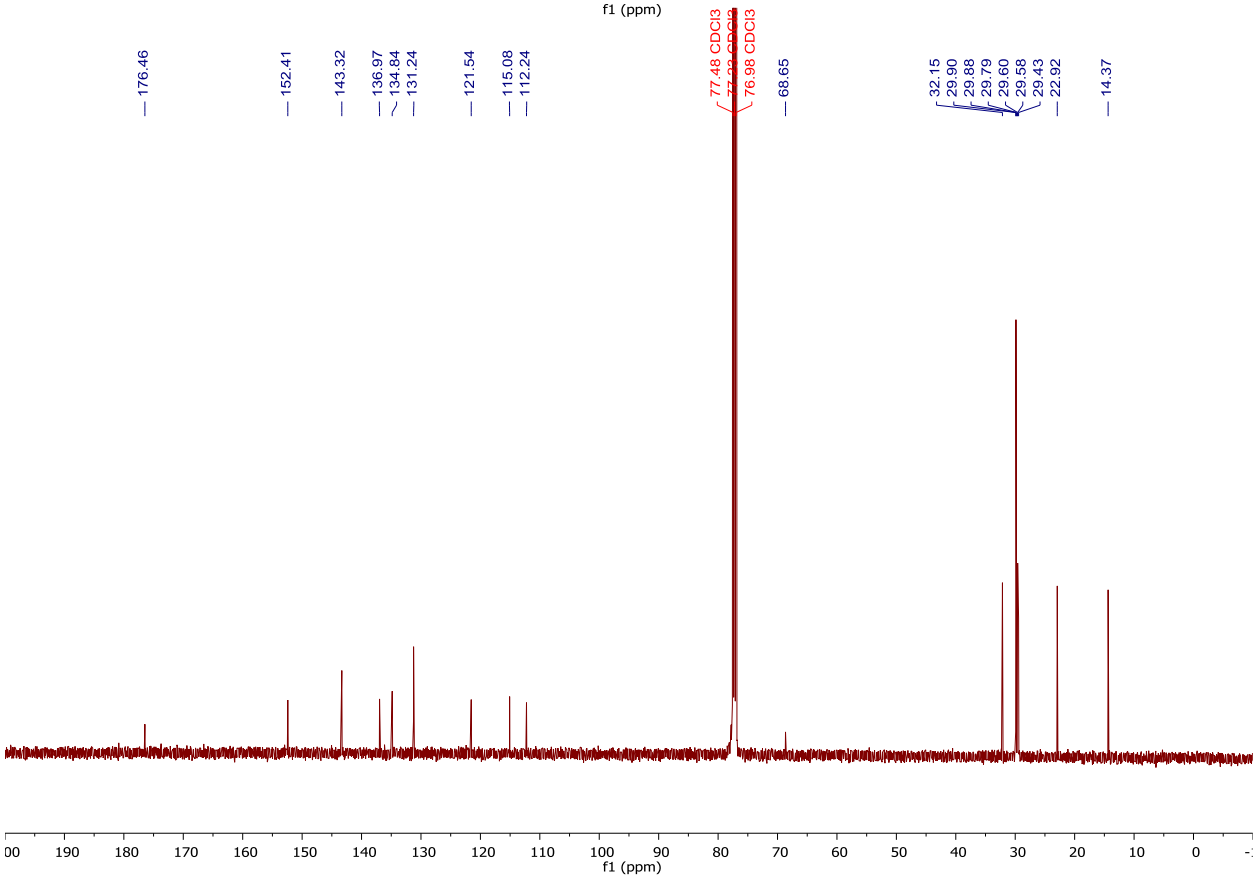
176.46
152.41
143.32
136.97
134.84
131.24
121.54
115.08
112.24
77.48 CDCl3
77.22 CDCl3
76.98 CDCl3
68.65
32.15
29.90
29.88
29.79
29.60
29.58
29.43
22.92
14.37
f1 (ppm)

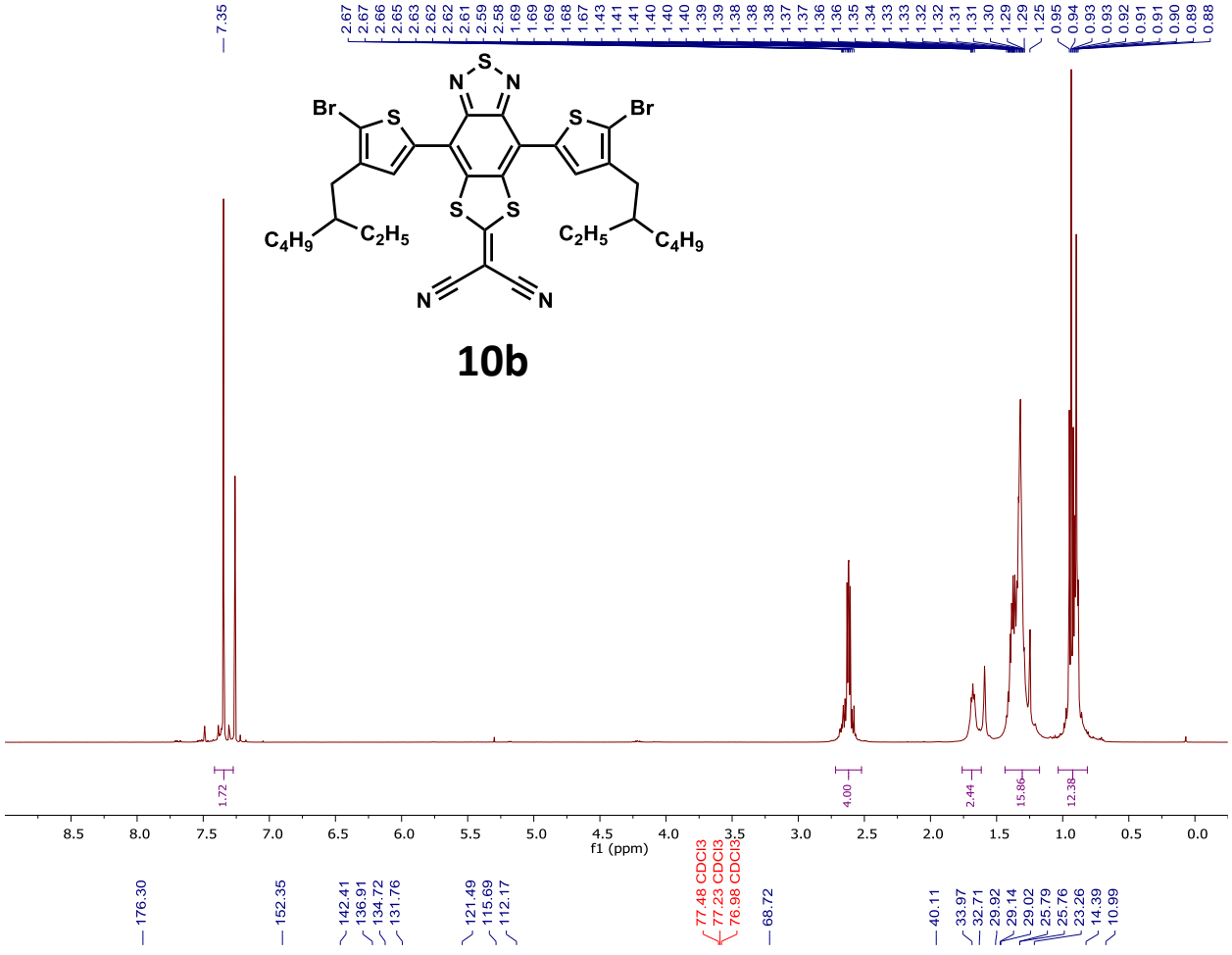
7.35
2.67 2.67 2.66 2.65 2.63 2.62 2.62 2.61 2.59 2.58 1.69 1.69 1.69 1.68 1.67 1.43 1.41 1.41 1.40 1.40 1.40 1.39 1.39 1.38 1.38 1.38 1.37 1.37 1.36 1.36 1.35 1.34 1.33 1.33 1.32 1.32 1.31 1.31 1.30 1.29 1.29 1.25 0.95 0.94 0.93 0.93 0.92 0.91 0.91 0.90 0.89 0.88
Br
S
N
S
N
S
Br
S
S
C4H9
C2H5
C2H5
C4H9
N
N
1.72
4.00
2.44
15.86
12.38
8.5 8.0 7.5 7.0 6.5 6.0 5.5 5.0 4.5 4.0 3.5 3.0 2.5 2.0 1.5 1.0 0.5 0.0
f1 (ppm)

10b

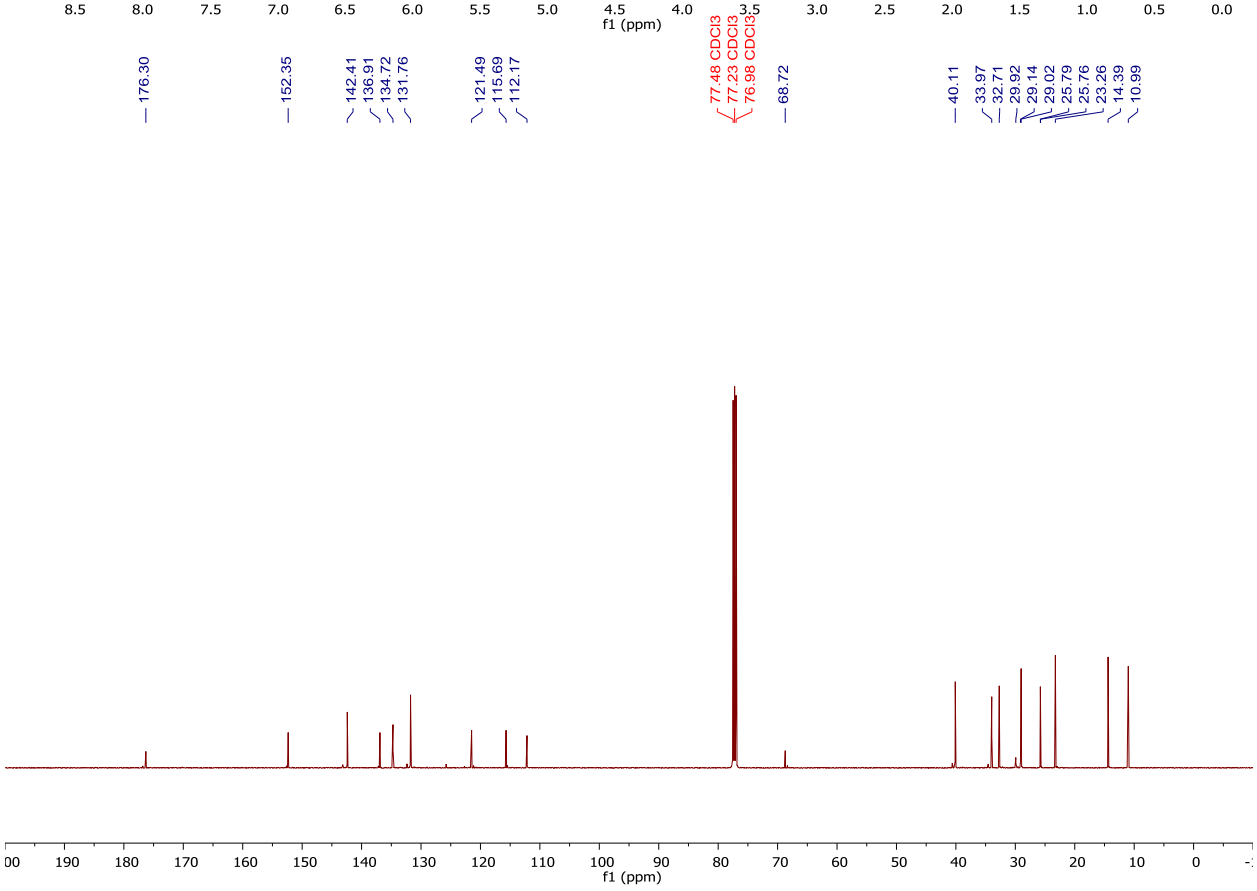
176.30
152.35
142.41
136.91
134.72
131.76
121.49
115.69
112.17
77.48 CDCl3
77.23 CDCl3
76.98 CDCl3
68.72
40.11
33.97
32.71
29.92
29.14
29.02
25.79
25.76
23.26
14.39
10.99
190 180 170 160 150 140 130 120 110 100 90 80 70 60 50 40 30 20 10 0
f1 (ppm)

Br
S
N
S
N
S
Br
S
S
$C_{10}H_{21}$
C_8H_{17}
C_8H_{17}
$C_{10}H_{21}$
NC
CN

10c

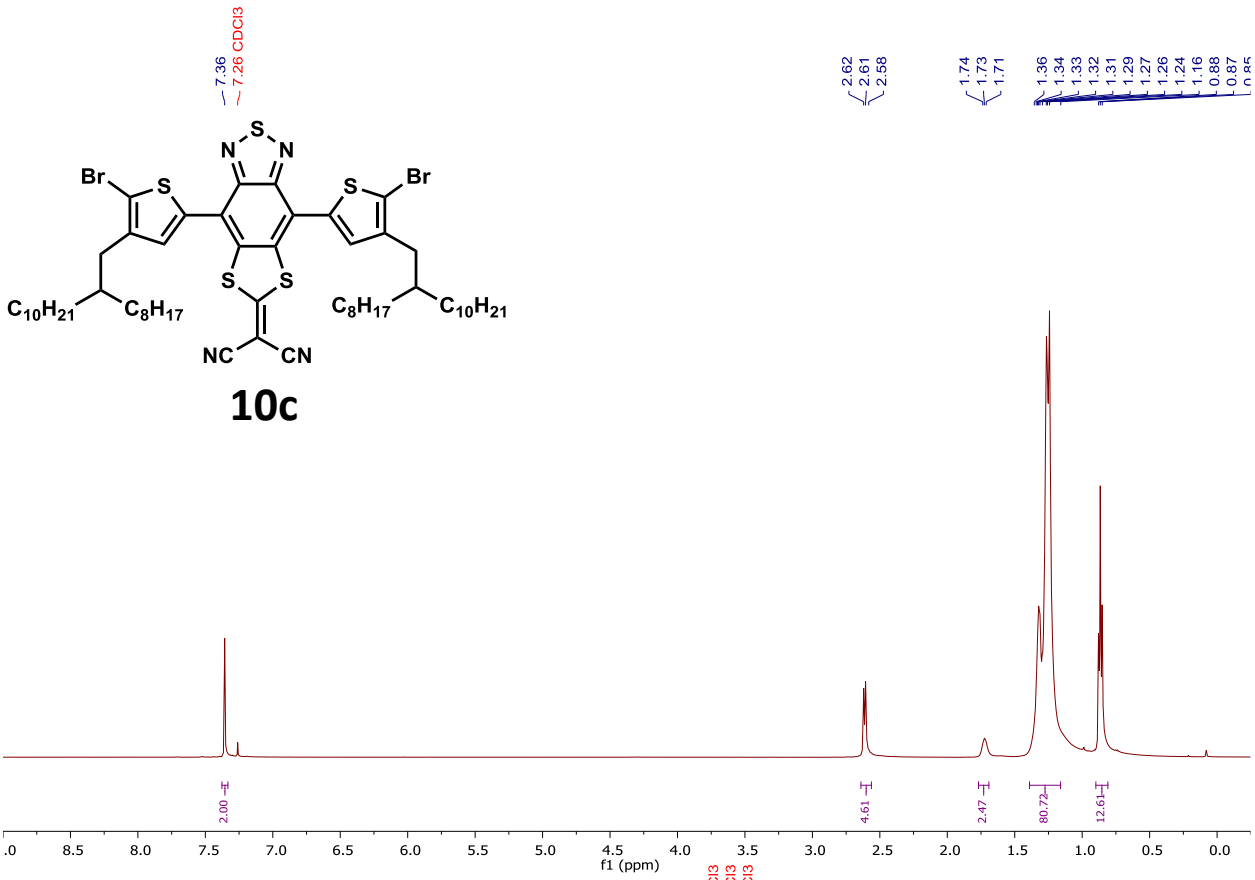
7.36
7.26 CDCl3
2.62
2.61
2.58
1.74
1.73
1.71
1.36
1.34
1.33
1.32
1.31
1.29
1.27
1.26
1.24
1.16
0.88
0.87
2.00
4.61
2.47
80.72
12.61
f1 (ppm)

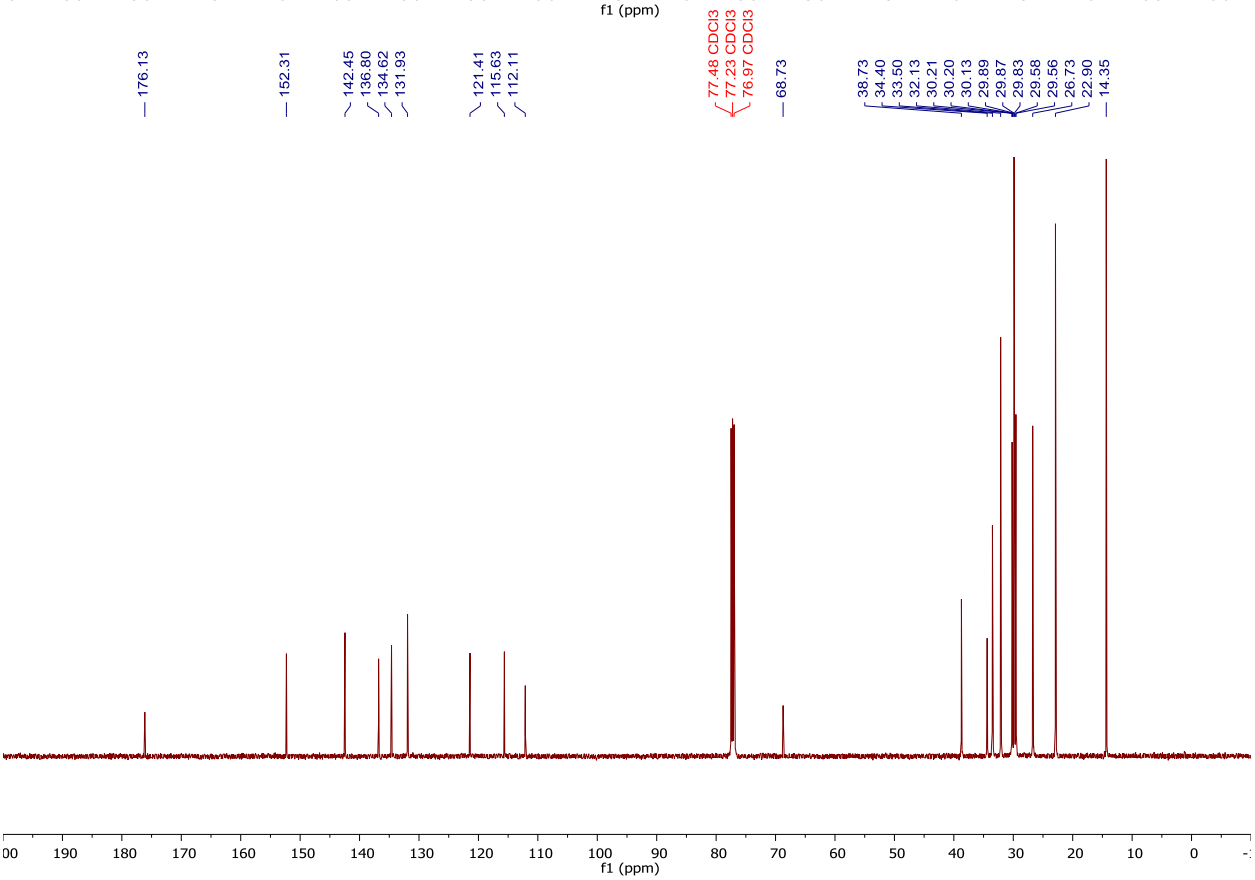
176.13
152.31
142.45
136.80
134.62
131.93
121.41
115.63
112.11
77.48 CDCl3
77.23 CDCl3
76.97 CDCl3
68.73
38.73
34.40
33.50
32.13
30.21
30.20
30.13
29.89
29.87
29.83
29.58
29.56
26.73
22.90
14.35
f1 (ppm)

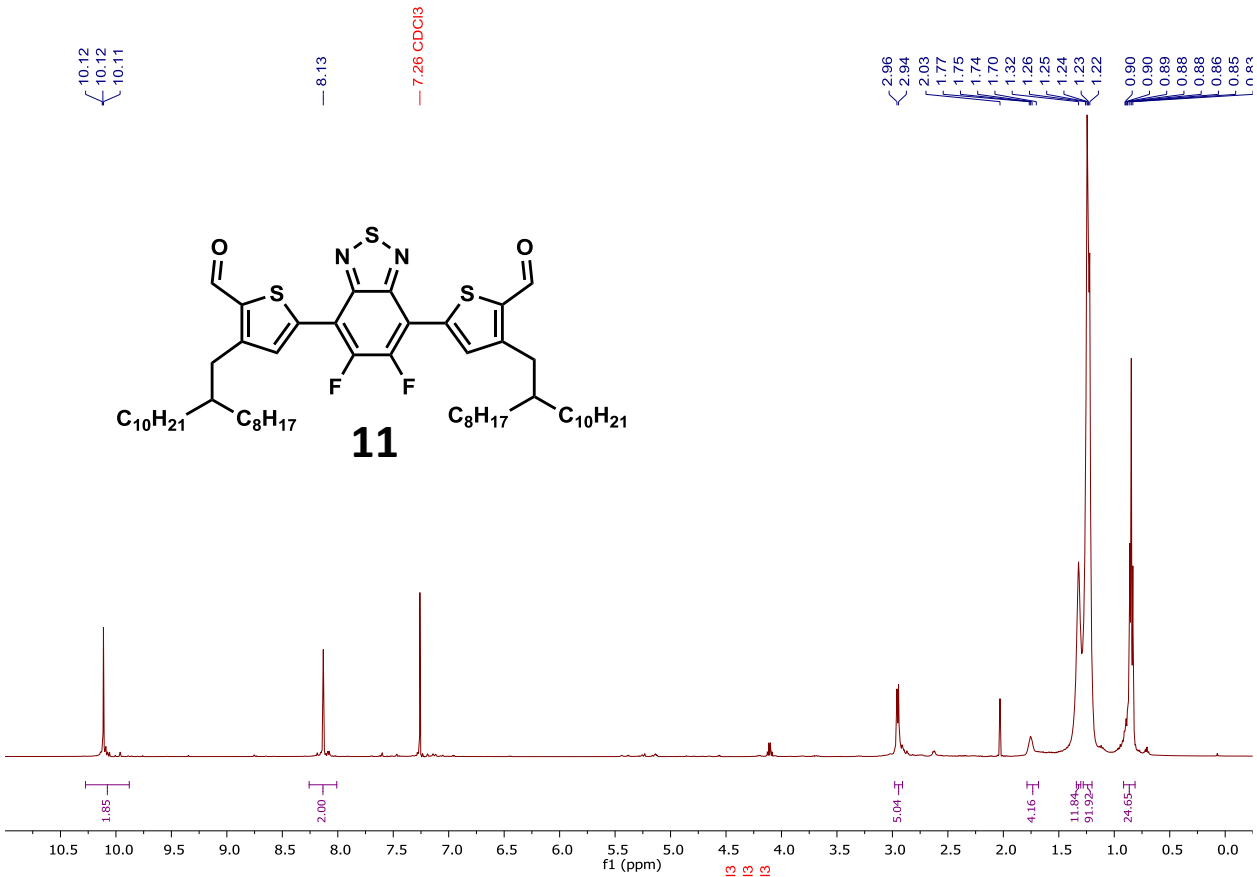
10.12
10.12
10.11
8.13
7.26 CDCl3
2.96
2.94
2.03
1.77
1.75
1.74
1.70
1.32
1.26
1.25
1.24
1.23
1.22
0.90
0.90
0.89
0.88
0.88
0.86
0.85
1.85
2.00
5.04
4.16
11.84
91.92
24.65
f1 (ppm)

O
S
N
S
N
O
S
S
F
F
C10H21
C8H17
C8H17
C10H21

11

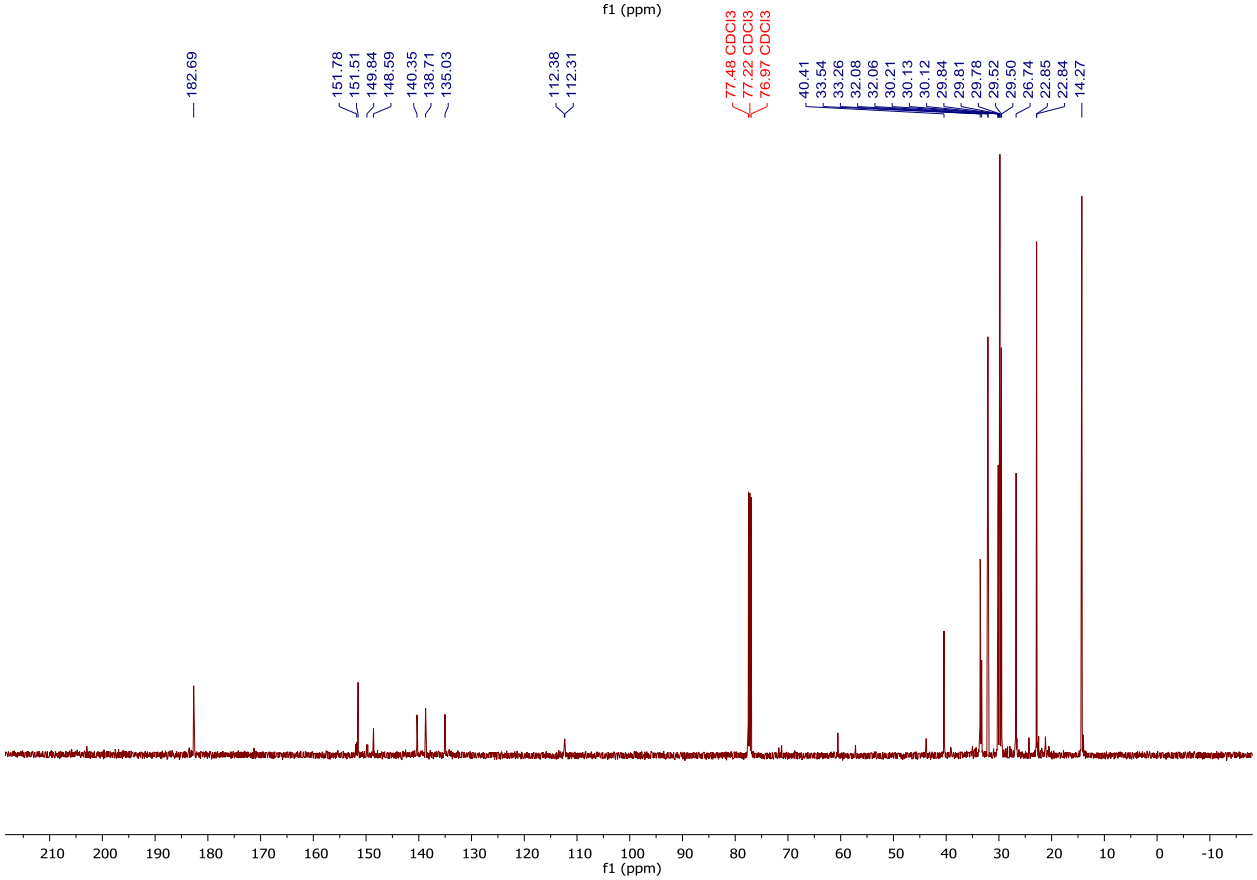
182.69
151.78
151.51
149.84
148.59
140.35
138.71
135.03
112.38
112.31
77.48 CDCl3
77.22 CDCl3
76.97 CDCl3
40.41
33.54
33.26
32.08
32.06
30.21
30.13
30.12
29.84
29.81
29.78
29.52
29.50
26.74
22.85
22.84
14.27
f1 (ppm)

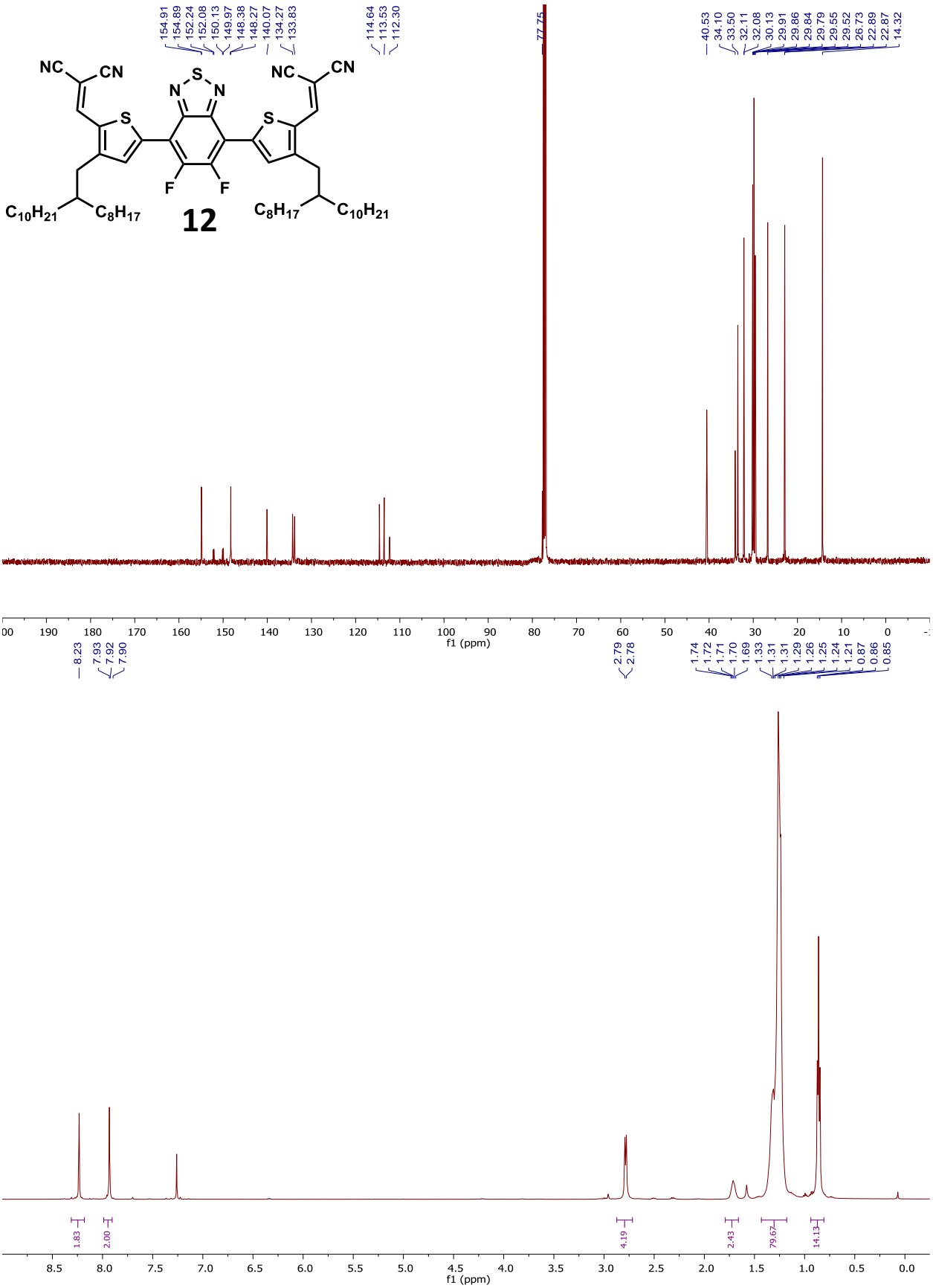
NC
CN
NC
CN
S
N
S
N
S
S
F
F
$C_{10}H_{21}$
C_8H_{17}
C_8H_{17}
$C_{10}H_{21}$
12
154.91
154.89
152.24
152.08
150.13
149.97
148.38
148.27
140.07
134.27
133.83
114.64
113.53
112.30
77.75
40.53
34.10
33.50
32.11
32.08
30.13
29.91
29.86
29.84
29.79
29.55
29.52
26.73
22.89
22.87
14.32
f1 (ppm)
8.23
7.93
7.92
7.90
2.79
2.78
1.74
1.72
1.71
1.70
1.69
1.33
1.31
1.31
1.29
1.26
1.25
1.24
1.21
0.87
0.86
0.85
1.83
2.00
4.19
2.43
79.67
14.13
f1 (ppm)

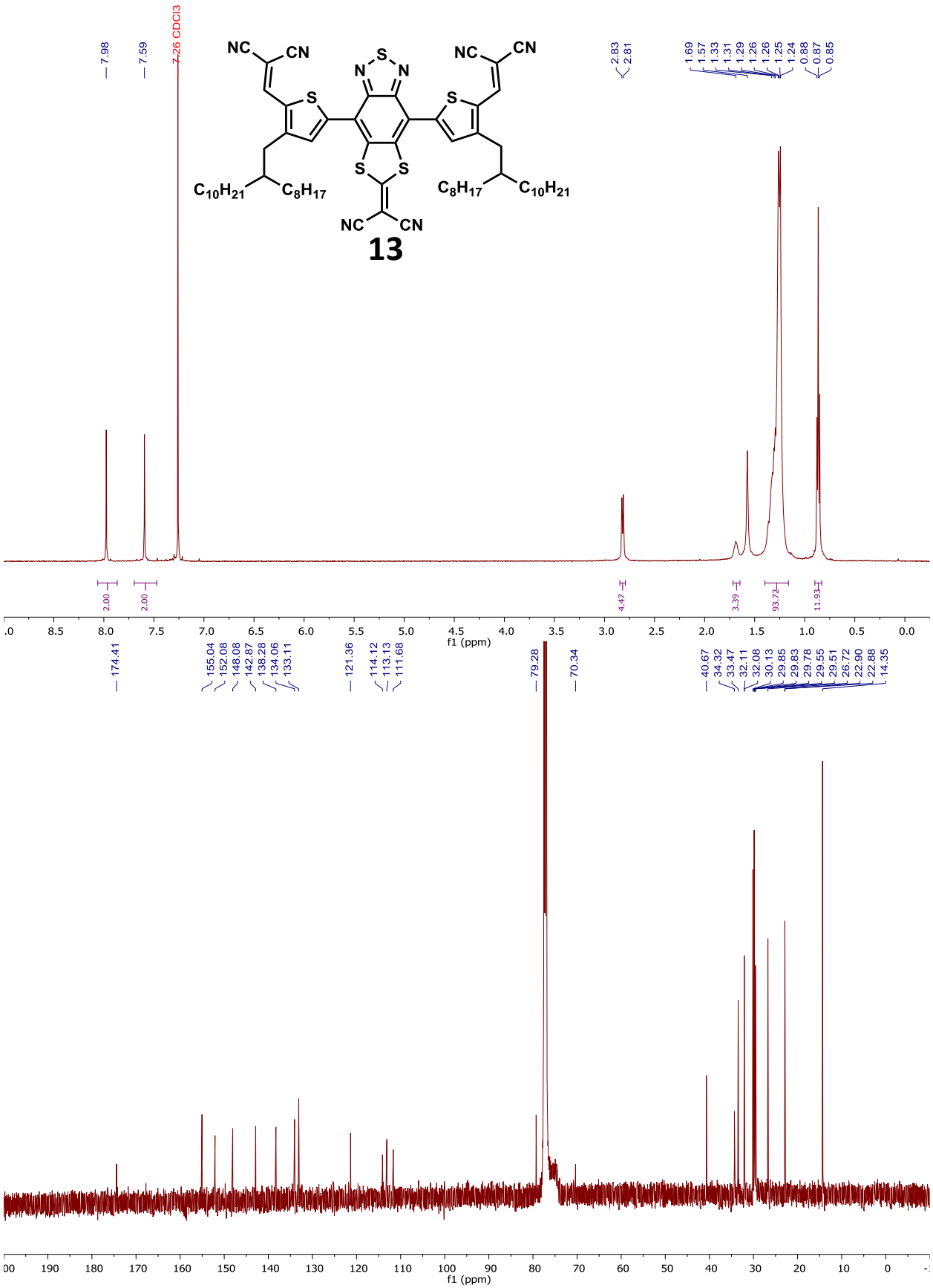
7.98
7.59
7.26 CDCl3
2.83
2.81
1.69
1.57
1.33
1.31
1.29
1.26
1.26
1.25
1.24
0.88
0.87
0.85
NC
CN
S
N
S
N
S
S
S
C10H21
C8H17
C8H17
C10H21
NC
CN
NC
CN
13
2.00
2.00
4.47
3.39
93.72
11.93
f1 (ppm)
174.41
155.04
152.08
148.08
142.87
138.28
134.06
133.11
121.36
114.12
113.13
111.68
79.28
70.34
40.67
34.32
33.47
32.11
32.08
30.13
29.85
29.83
29.78
29.55
29.51
26.72
22.90
22.88
14.35
f1 (ppm)

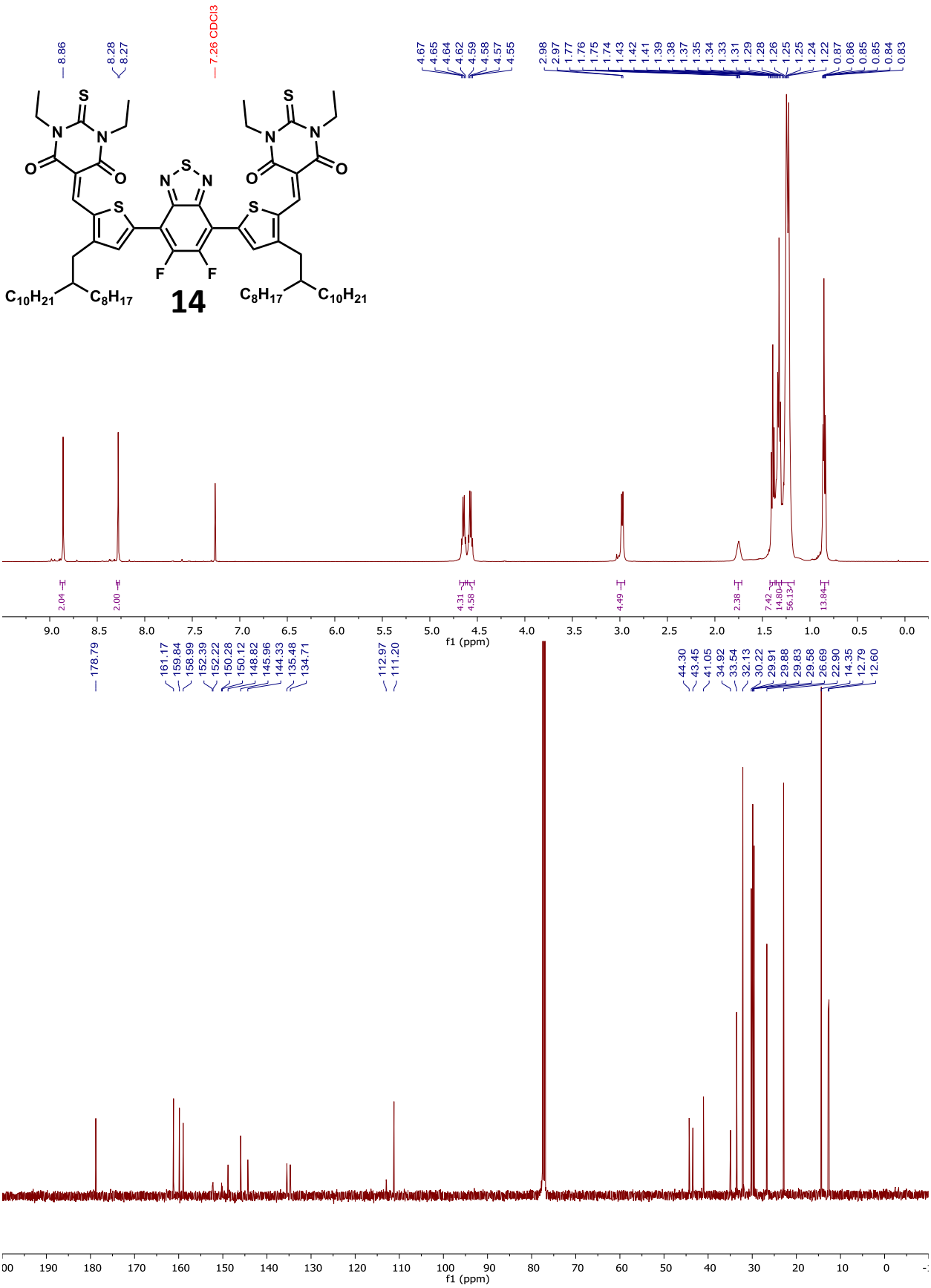
8.86
8.28
8.27
7.26 CDCl3
4.67
4.65
4.64
4.62
4.59
4.58
4.57
4.55
2.98
2.97
1.77
1.76
1.75
1.74
1.43
1.42
1.41
1.39
1.38
1.37
1.35
1.34
1.33
1.31
1.29
1.28
1.26
1.25
1.25
1.24
1.22
0.87
0.86
0.85
0.85
0.84
0.83
14
2.04
2.00
4.31
4.58
4.49
2.38
7.42
14.80
56.13
13.84
f1 (ppm)
178.79
161.17
159.84
158.99
152.39
152.22
150.28
150.12
148.82
145.96
144.33
135.48
134.71
112.97
111.20
44.30
43.45
41.05
34.92
33.54
32.13
30.22
29.91
29.88
29.83
29.58
26.69
22.90
14.35
12.79
12.60
f1 (ppm)

S
N
N
O
O
S
N
S
N
S
S
S
N
N
O
O
S
C10H21
C8H17
C8H17
C10H21
NC
CN

15

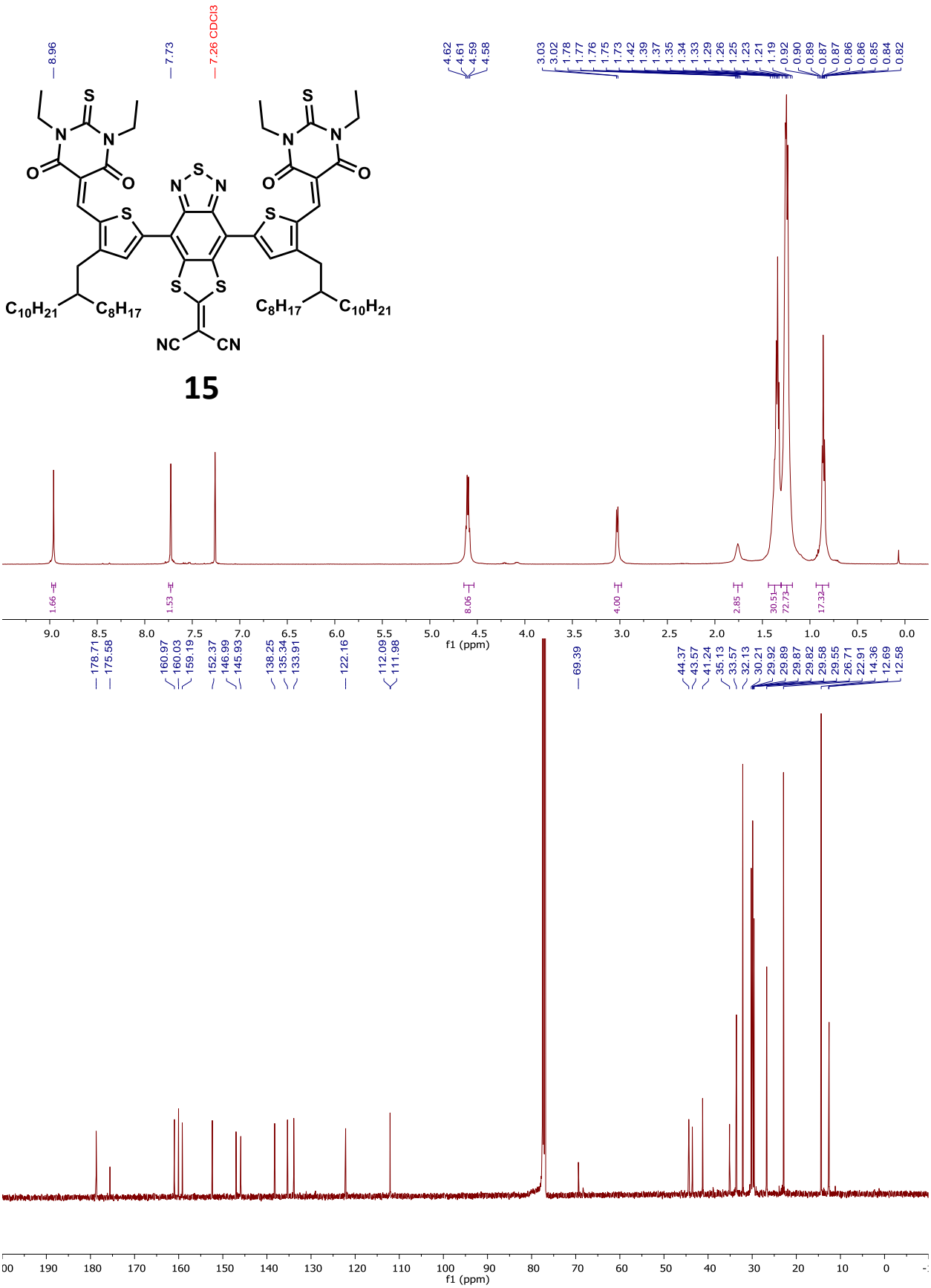
8.96
7.73
7.26 CDCl3
4.62
4.61
4.59
4.58
3.03
3.02
1.78
1.77
1.76
1.75
1.73
1.42
1.39
1.37
1.35
1.34
1.33
1.29
1.26
1.25
1.23
1.21
1.19
0.92
0.90
0.89
0.87
0.87
0.86
0.86
0.85
0.84
0.82
1.66
1.53
8.06
4.00
2.85
30.51
72.73
17.32
f1 (ppm)
178.71
175.58
160.97
160.03
159.19
152.37
146.99
145.93
138.25
135.34
133.91
122.16
112.09
111.98
69.39
44.37
43.57
41.24
35.13
33.57
32.13
30.21
29.92
29.89
29.87
29.82
29.58
29.55
26.71
22.91
14.36
12.69
12.58
f1 (ppm)

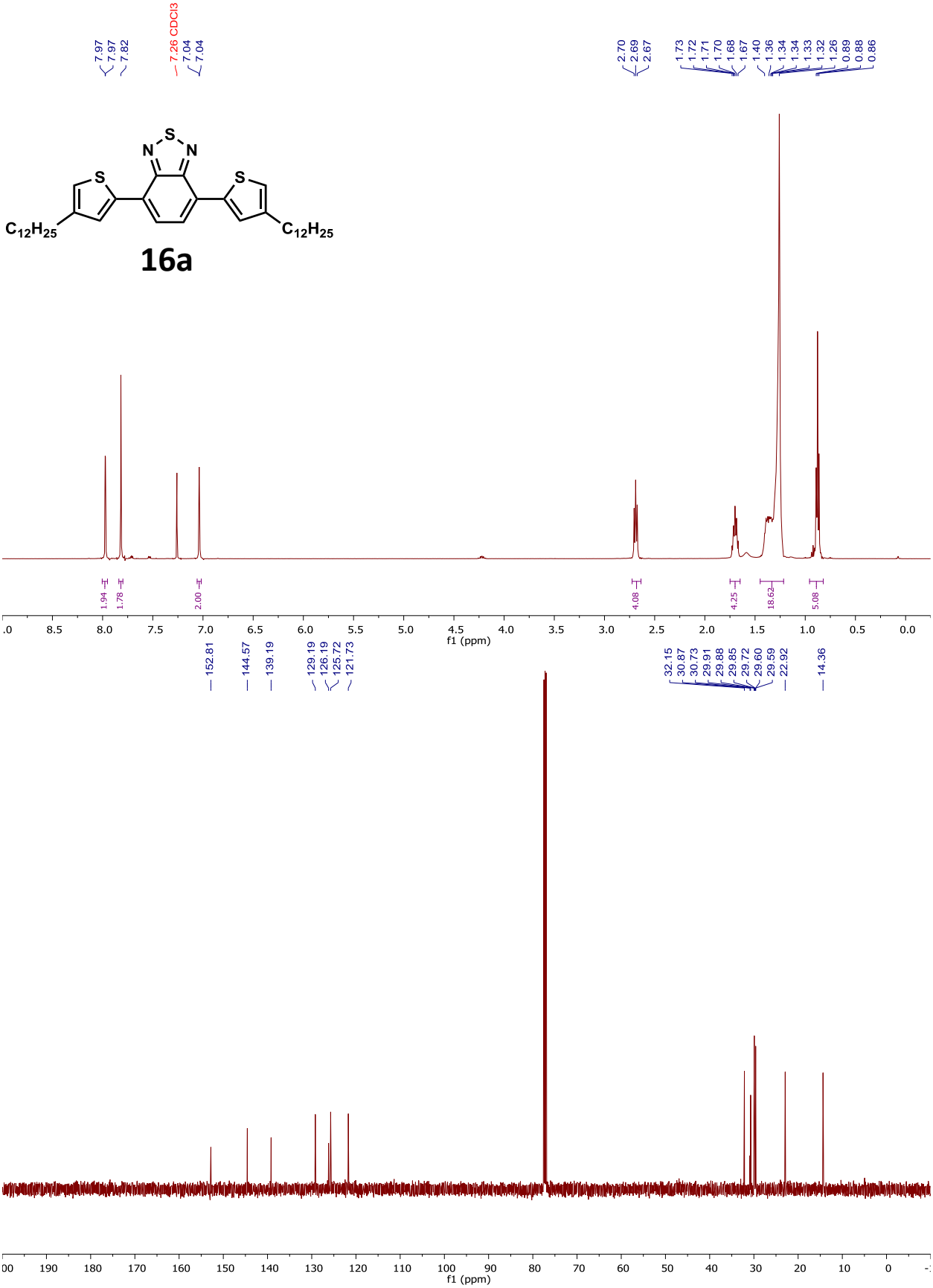
7.97
7.97
7.82
7.26 CDCl3
7.04
7.04
2.70
2.69
2.67
1.73
1.72
1.71
1.70
1.68
1.67
1.40
1.36
1.34
1.34
1.33
1.32
1.26
0.89
0.88
0.86
S
N
S
N
S
S
C12H25
C12H25
16a
1.94
1.78
2.00
4.08
4.25
18.62
5.08
f1 (ppm)
152.81
144.57
139.19
129.19
126.19
125.72
121.73
32.15
30.87
30.73
29.91
29.88
29.85
29.72
29.60
29.59
22.92
14.36
f1 (ppm)

Chapter 4. Morphological Study of High V_{OC} Non-Fullerene Acceptors with Thiobarbituric Acid End Groups

Abstract

Recent advances in non-fullerene acceptors have pushed the boundaries of organic solar cell performance. In our efforts to boost open circuit voltage (V_{OC}), we have designed a new non-fullerene acceptor based on thiobarbituric acid to increase the LUMO level. This improvement in V_{OC} has allowed the new acceptor to outperform the flagship ITIC acceptor. However, very little is known about how the end group substitution impacts solar cell performance.

To this end, a morphological study has been undertaken to develop these structure-property relationships. Thiobarbituric acid end groups are alkylated with linear, branched, and aromatic sidechains in an effort to understand their impact on intermolecular interactions. Because the alkyl groups have only minor effects on electronics, the intermolecular interactions and physical properties can be clearly analyzed with minimal complicating electronic factors.

The solar cell performance is highly dependent on these molecular modifications. To understand these effects, grazing incidence wide angle x-ray scattering (GIWAXS) is used to provide valuable insight into how intermolecular interactions within the active layer is moderated through the variations in the end groups. It was discovered that there is an ideal window of crystallinity that is permitted by medium length hydrocarbon chains such as ethyl and benzyl. Deviation to the shorter methyl group decreases performance by making the acceptor too crystalline to form proper domains, decreasing efficiency by 38%. Whereas longer and branched alkyl chains are too sterically bulky and hinder charge transport, decreasing power conversion efficiency (PCE) by 71%. This underlying fact reveals the complicated nature of thin film morphology and the need for these studies.

4.1 Introduction

Fullerene based acceptors have dominated the field of organic electronics for over two decades. The discovery of materials with high electron mobilities and depressed lowest unoccupied molecular orbital (LUMO) energy levels was a major breakthrough in the development organic photovoltaics (OPVs) (**Figure 1a**).[1] Solubilized fullerenes, such as $PC_{61}BM$ increased solar cell PCE from below 1% to as high as 10.1% (**Figure 1b**).[2] But for all their advantages, fullerene acceptors suffer from a number of inherent limitations. Poor light absorption in the visible region means they do not significantly contribute to photocurrent generation. The low LUMO energy pins the V_{OC} to unacceptably low levels and limits the scope of compatible donor materials. Because of the ubiquity of fullerene-based acceptors, development of new acceptor materials has lagged behind the progress of donor polymers.

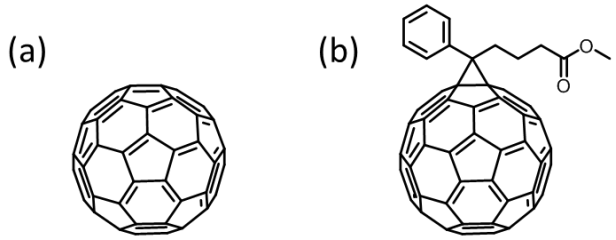

Figure 1: Fullerene based acceptors. (a) Unsubstituted fullerene and (b) a soluble fullerene derivative phenyl-C61-butyric acid methyl ester PC[61]BM

The disparity has spurred development of new design strategies for the next generation of acceptor materials. This research focus has given rise to entirely new non-fullerene acceptor (NFA) molecules that have far exceeded fullerene based materials. The flagship NFA is 2,2′-[[6,6,12,12-Tetrakis(4-hexylphenyl)-6,12-dihydrodithieno[2,3-*d*:2′,3′-*d*′]-s-indaceno[1,2-*b*:5,6-*b*′]dithiophene-2,8-diyl]bis[methylidyne(3-oxo-1*H*-indene-2,1(3*H*)-diylidene)]]bis[propanedinitrile] (ITIC) (**Scheme 1a**). ITIC is a symmetrical molecule that has three functional regions: 1) an electron rich IDTT core,[3] that is locked into planarity via 2) spirocenters with solubilizing groups, and capped with 3) electron withdrawing 1,1-dicyanomethylene-3-indanone (DCI) end groups.[4] Each of these areas can be functionalized independently, allowing for control over the electronic and physical properties (**Scheme 1b**).

The ITIC core is a highly electron rich ladderized polycyclic aromatic structure. Due to the inherent acceptor-donor-acceptor structure of ITIC, the HOMO level of the ITIC system is nearly completely controlled by the electron donating ability of the core. When the number of outer fused thiophenes decreases from the IDTT core **b**, the HOMO energy decreases, as can be seen for **a** (**Figure 2a**). [5] Likewise, the addition of fused thiophenes in **c** increases the HOMO independent of the LUMO.[6] This trend also continues if the central benzene **d** ring is replaced with other donors (**Figure 2b**). Altering weakly donating benzene groups with stronger thiophene groups, such as benzodithiophene[7] **e** and thienothiophene[8] **f** greatly increase the HOMO level, with only minor perturbations to the LUMO.

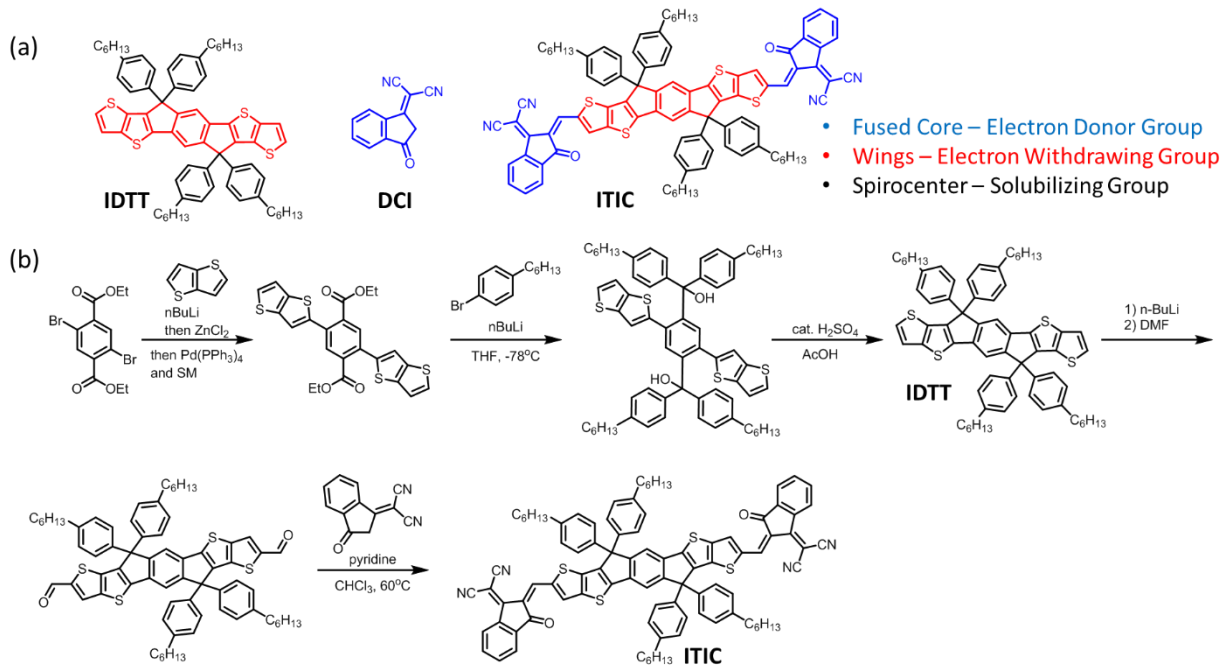

Scheme 1: (a) The structural components and (b) synthesis of ITIC, which demonstrates the modularity

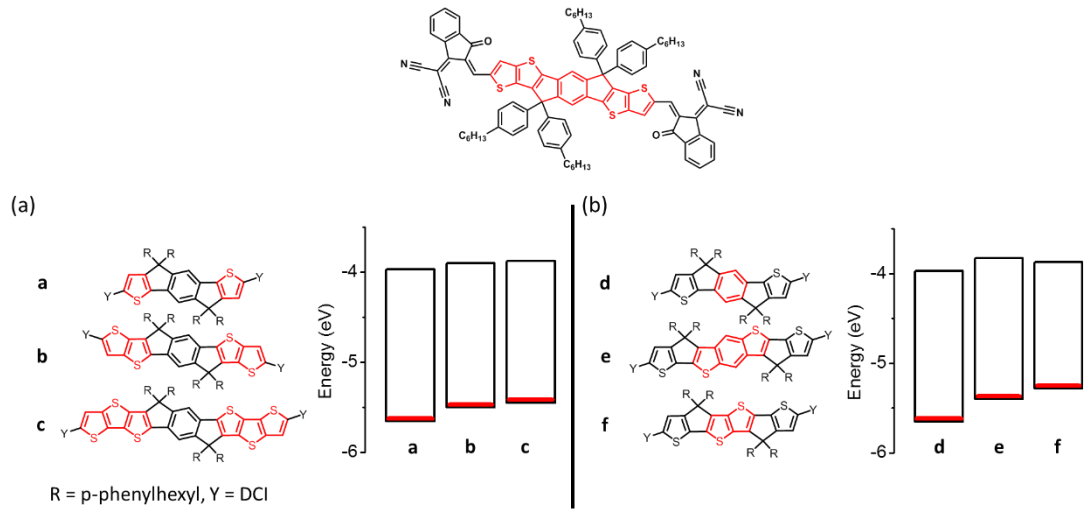

Figure 2: Energetic changes to the HOMO of the ITIC core (modifications highlighted in red) by changing (a) the number of fused thiophene units in the periphery and (b) the electron donor ability of central unit

The planar core is locked into planarity via multifunctional spirocenters. These quaternary carbon centers not only provided steric bulk to prevent self-aggregation,[3] but also increase solubility through the introduction of alkyl groups. These combined factors play a large role in moderating intermolecular interactions with donor polymers.[9] As such, small modifications to the aromatic group or alkyl chains can have a large impact on the overall order of the active layer (**Figure 3**).[9d, 10] Substituting the original p-phenylhexyl (**g**) with the isomeric meta isomer **h**, or with 2-hexylthienyl **i** both afforded improvement in solar cell performance. The purely alkyl spirocenters, exemplified by **j**, are less ridged and tend to give stronger aggregation than aromatic substituted spirocenters.

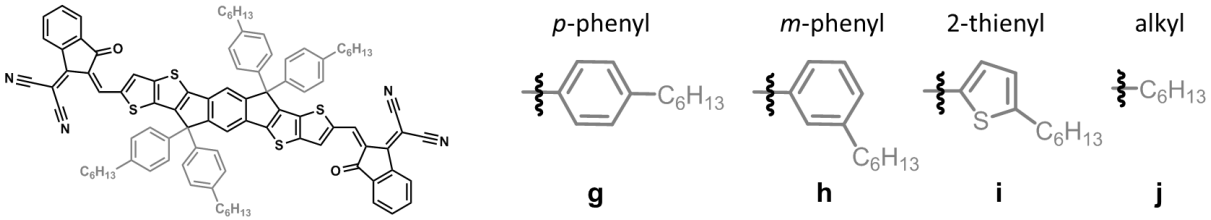

Figure 3: Common substitution groups on the spirocyclic center (highlighted in gray)

In order to make the ITIC acceptor molecule sufficiently electron poor, the fused core is flanked with two electron withdrawing units in an acceptor-donor-acceptor structure. Analogously to what was observed by altering the donor core, the electron withdrawing strength of the end groups allows the LUMO energy to be raised or lowered independently of the HOMO level (**Figure 3a**).[11] Fluorinating DCI such as with compound **k** has been showed to lower the LUMO level compared to the original DCI (**l)** through an electronegative inductive effect.

The acceptor LUMO is particularly important for determining a number of device properties. A common strategy to increase efficiency is to lower the acceptor LUMO energy in order to increase the short circuit current (J_{SC}) and absorption of lower energy light (**Figure 4**). Alternatively, increasing the acceptor LUMO can greatly improve V_{OC}, giving a boost in efficiency (**Figure 5a**). [12] The maximum V_{OC} for an active layer is equivalent to ΔE (**Figure 5b**). By increasing the LUMO of the acceptor and/or decreasing the HOMO of the donor, the V_{OC} can be maximized.

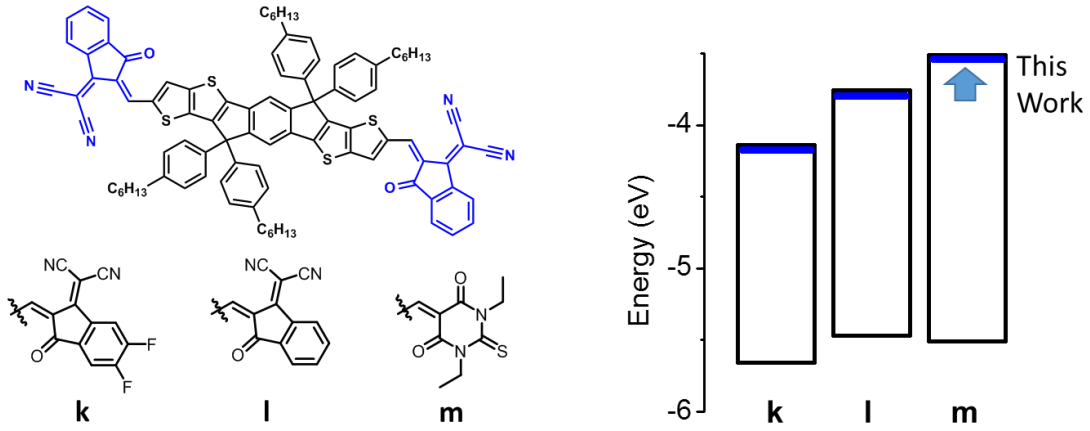

Figure 4: Energetic changes to the LUMO of ITIC by modifying the ITIC end groups (modifications highlighted in blue).

Utilizing the modular nature of the ITIC system, new withdrawing groups can be incorporated to raise the LUMO energy of the acceptor. To this end, thiobarbituric acid (TBTA) end groups have been chosen due to their weakly electron withdrawing monothioimide functionality **m** (**Figure 4**). The thiocarbonyl moiety is also highly polarizable, further improving the electron withdrawing ability.[13]

The TBTA group has been utilized in a fluorene based acceptor for organic solar cells to provide an exceptional V_{OC} of 1.15V.[14] However, the J_{SC} in this system is limited to 7.5 mA cm^{-2}, leaving significant room for improvement. Our research group has recently demonstrated a TBTA end-capped IDTT acceptor capable of achieving over 10% PCE in binary solar cells, which has increased the V_{OC} to 1.015 compared to ITIC with a V_{OC} of 0.825, without sacrifices in J_{SC} (**Figure 5c**).[12] Later, the Huang group has reported similar results based on the same acceptor design, confirming these results.[15] In addition, we have incorporated an IDT-based acceptor in a ternary system with PCEs up to 12.3%.[16]

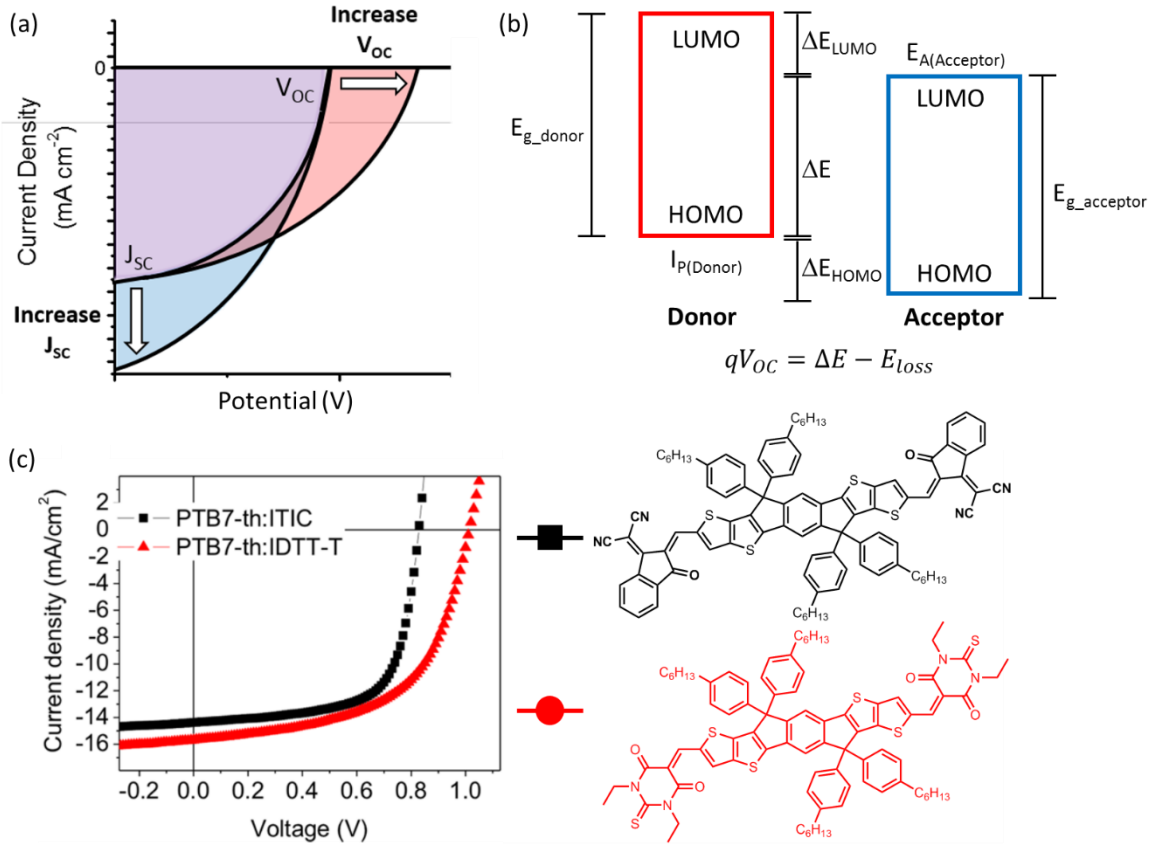

Figure 5: (a) The strategy to raise the V_{OC} to improve solar cell power output, with the original solar power output in purple, increase in power due to improved V_{OC} displayed in red, and increase in power due to improved J_{SC} in blue. Following is (b) the energetic derivation of V_{OC}, and (c) previous work in our group using this strategy with IDTT-TBTA to improve V_{OC} over ITIC. Reproduced with permission from reference [12], Copyright © 2018, American Chemical Society.

The end groups are postulated to be a location of significant π overlap between molecules which is necessary for electronic communication in the active layer and efficient charge transport.[11e] This makes intermolecular and steric interactions between end groups of critical importance. Despite this, prior to this work only ethyl chains have been explored for TBTA alkyl groups. The lack of understanding about end group composition warrants an in depth study of their effect on morphology. Alkyl chains can easily be appended to the TBTA core, which are expected to affect solubility and moderate these intermolecular interactions, and have a large impact on device performance. In this chapter, a series of thiobarbituric acids with varying alkyl chain lengths and types have been prepared, incorporated into IDTT based non-fullerene acceptors, and examined as active materials in organic solar cells.

4.2 Synthesis of TBTA Based Non-Fullerene Acceptors

In order to gain the most information from material analysis, a wide range of alkyl chain length and shapes have been chosen to study. Methyl, ethyl, and n-octyl chains are used in order to compare linear chain length effects on solubility and endgroup interactions. The 2-ethylhexyl chain is an isomer of the n-octyl chain, allowing for a direct comparison between linear and branched effects on steric interactions. To further test the hypothesis that the endgroups are responsible for intermolecular interactions, a benzyl substituted system has also been chosen as a way to increase the overall π-surface area.

The synthesis of thiobarbituric acid derivatives, and incorporation of alkyl groups began with thiourea formation (**Scheme 2a**). The first addition of amine to carbon disulfide proceeds smoothly under mild conditions to give the alkylcarbamodithioic acids (**Scheme 2b**). However, harsh conditions are necessary in order to eliminate H_2S to form the isothiocyanate group. Only then can the isothiocyanate group undergo a second addition of primary amine to form the respective dialkylthioureas. Because of the higher temperature conditions necessary for the second addition, mixed thiourea products can also hypothetically be formed using this method though it has not been pursued here.

Reaction of thioureas with diethyl malonate under basic conditions provides a functionalized TBTA in varying yields. This reaction requires harsh conditions over multiple days due to the weakly nucleophilic nature of the thiourea. Reaction times are also increased because the diethyl malonate is partially deprotonated under the basic reaction conditions, making it a less effective electrophile. Even under these forcing conditions the yields of **2d** and **2e** were depressed, likely due to the steric bulk of the pendant octyl and 2-ethylhexyl groups.

The condensation of ITIC-dialdehyde with TBTA groups **2a-e** is rapid and efficient, converting the bright yellow aldehyde to deep blue acceptors with strong absorption in the red portion of the spectrum. It was observed during purification on silica gel column that, the TBTA addition is at least slightly reversible (**Figure A-1**).[17] The effect on yields is minor, but may hint at possible material instability.

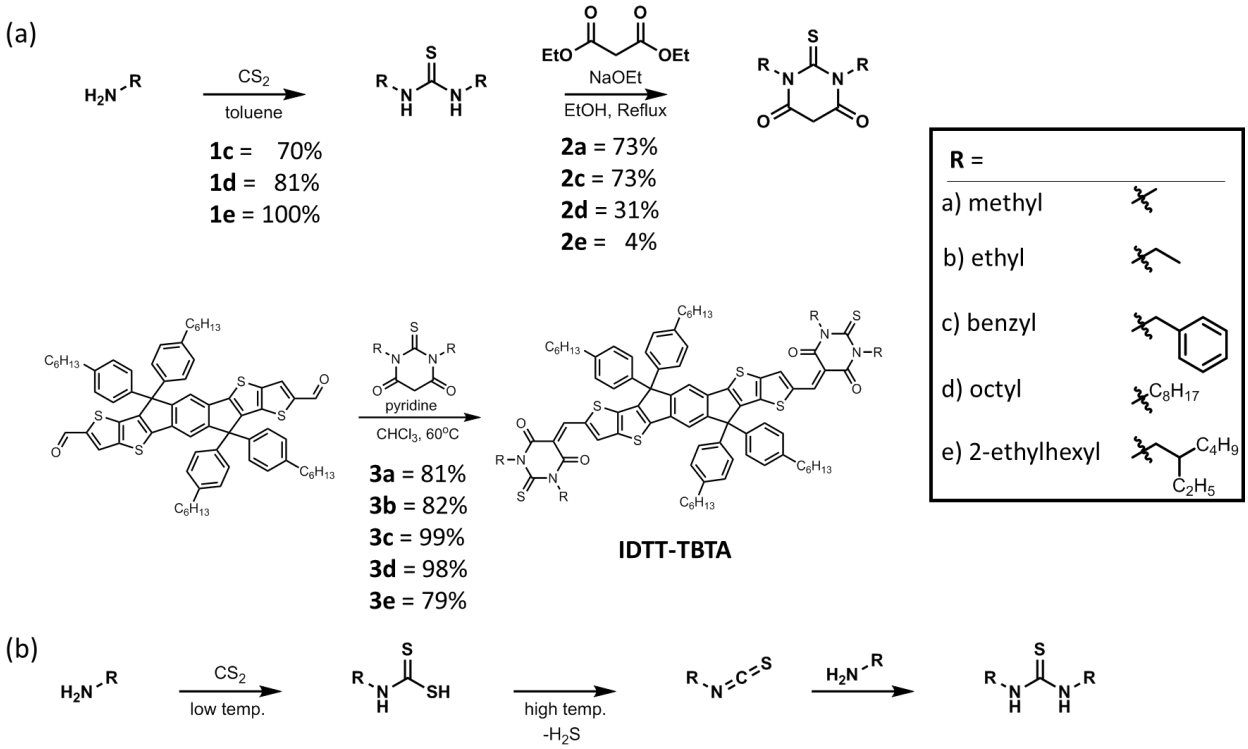

Scheme 2: Synthesis of (a) thiobarbituric acid withdrawing groups and addition to the donor core. A mechanistic look at (b) thiourea formation is also outlined.

4.3 Optoelectronic and Physical Properties

In order to mitigate electronic factors from the morphological study, the acceptor molecules **3a-e** are designed to be iso-energetic. Simple alkyl chains cannot donate electron density thorough resonance, and their donation through induction should be similar. Therefor the optoelectronic properties should be roughly equivalent. To confirm this, the optical and electronic properties have been characterized.

UV-Vis spectroscopy is utilized to find the optical band gap and absorption intensity for compounds **3a-e** (**Figure 6**). As predicted, the acceptors **3b, 3d** and **3e** have identical profiles. Interestingly, there is a slight red-shift present in the benzyl substituted **3c** species. This energetic shift may be occurring due to slight orbital overlap between the benzyl groups and the TBTA ring through homoconjugation.[18] Because the phenyl group is separated from the rest of the acceptor by a single non-conjugated methylene group, a small amount of energetic overlap can still occur.

The energy levels of the frontier molecular orbitals (FMOs) have been approximated through cyclic voltammetry (CV). All the acceptors have consistently reversible oxidation peaks at approximately -5.5 eV, while irreversible reduction occurs at -3.7 eV (**Figure 7a**). An energy

level diagram is provided which compares the IDTT-TBTA acceptors to the donor polymer PCE10 (**Figure 7b**).[19] This chart illustrates that although the FMOs of the acceptors are roughly equivalent, acceptors **3a** and **3b** have slightly lower HOMO and LUMO levels than the other molecules.

Because the HOMO of PCE10 is above that of the acceptors, hole transfer from the donor to acceptor should be efficient (**Table 1**).[20] The LUMO of the acceptors is energetically similar to that of PCE10, so the driving force for electron transfer is expected to be low. However, an energy offset as small as 0.12 eV has been shown to permit charge separation in bulk heterojunctions, making charge transfer still feasible.[21]

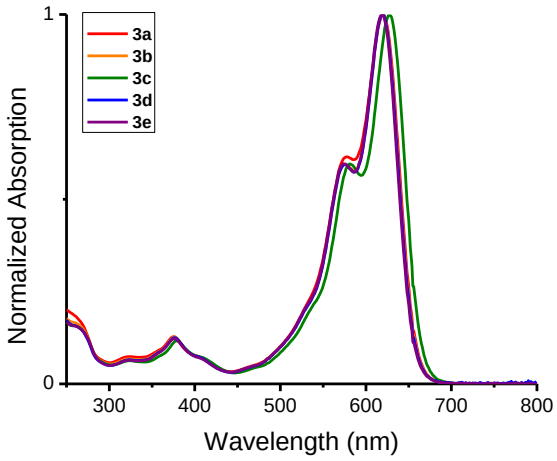

Figure 6: UV-Vis spectroscopy of NFA materials **3a**-**e**.

The potential electronic communication between the PCE10 donor and acceptors that is implied from CV is confirmed through photoluminescence (PL) spectroscopy (**Figure 8**). A decrease in the intensity of the PCE10 fluorescence spectrum upon mixing with acceptors **3a**, **3b**, and **3c** shows that efficient energy transfer is occurring. Fluorescence quenching by methyl and ethyl derivatives are nearly equivalent and more efficient than benzyl. This weaker quenching by **3c** could potentially be due to the energetically similar energy levels between this acceptor and PCE10, making charge transfer less favorable.

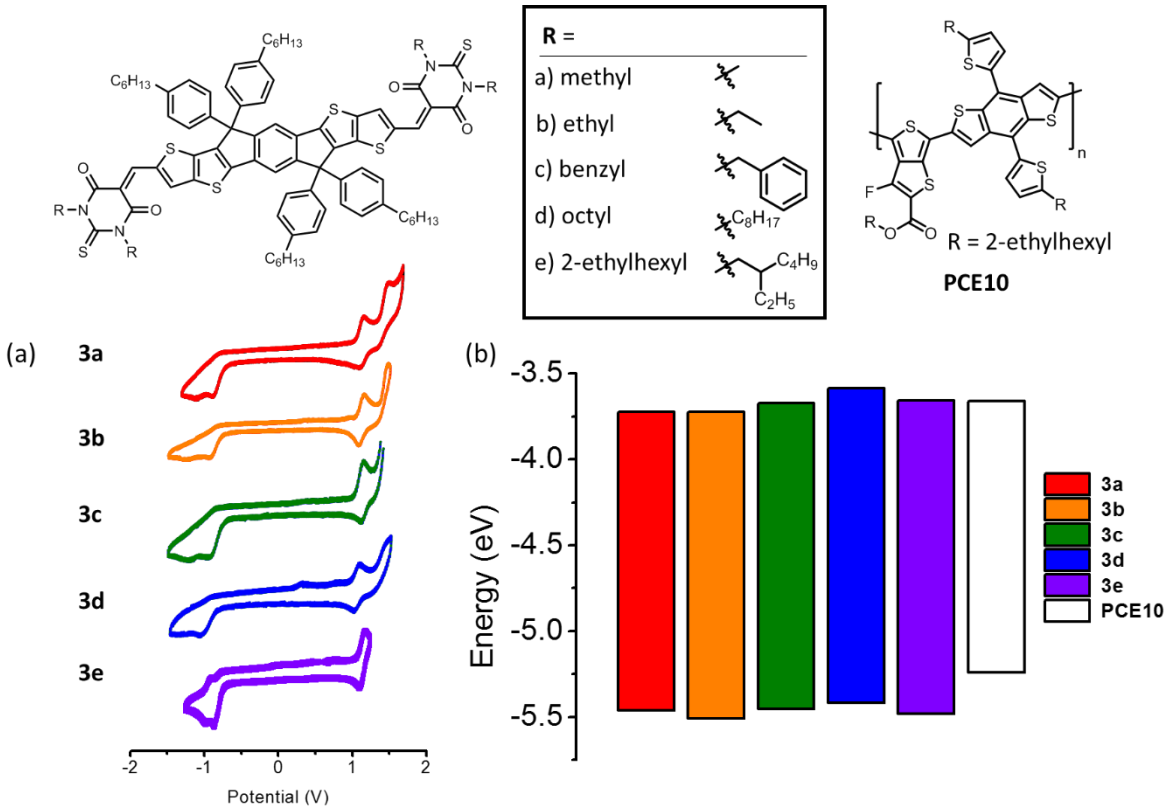

Figure 7: Cyclic voltammetry of (a) nonfullerene acceptors and (b) the energy alignment with PCE10 donor polymer.

Table 1: Frontier Molecular Orbital (FMO) data for NFA acceptors and PCE10

Compound	Solubilizing group	HOMO (eV)	LUMO (eV)	E_g^{Elec} (eV)	E_g^{Opt} (eV)
3a	Methyl	-5.46	-3.72	1.74	1.89
3b	Ethyl	-5.51	-3.72	1.78	1.89
3c	Benzyl	-5.45	-3.67	1.78	1.87
3d	Octyl	-5.42	-3.59	1.83	1.89
3e	2-ethylhexyl	-5.48	-3.65	1.83	1.89
PCE10[a]	2-ethylhexyl	-5.24	-3.66	1.58	1.58

a Cited form reference [20]

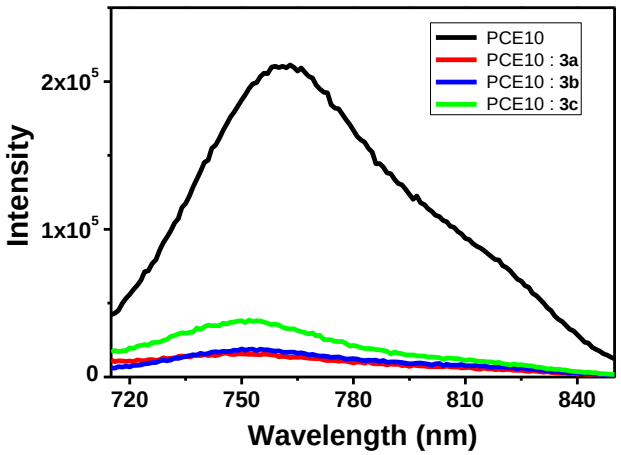

Figure 8: Photoluminescence of PCE10 and mixtures of PCE10 with **3a**, **3b**, and **3c**

4.4 Incorporating TBTA Based Acceptors into Organic Photovoltaic (OPV) Devices

With a confirmation of the energetic similarity between the acceptors, organic photovoltaic (OPV) devices were constructed. Due to the established electronic compatibility, the **3a**-**3e** non-fullerene acceptors were paired with PCE10 as the donor polymer. An inverted device stack with a structure of ITO/ZnO/active layer/MoOx/Ag was utilized which avoids exposing easily oxidized metals in contact with air, improving stability and performance. Indium tin oxide (ITO) is used as a transparent electrode with zinc oxide as an electron transport layer. The semiconductor active layer is protected from exposure to air by being sandwiched between the aforementioned ITO cathode layer on one side and a molybdenum oxide hole transport layer with outer silver electrode on the other.

OPV performance is evaluated by plotting the current generated when the device illuminated with respect to voltage applied in a so-called J-V curve (**Figure 8**). The effect of raising the LUMO level of the acceptors succeeded in significantly increasing the V_{OC} of acceptors **3a**, **3b**, and **3d** to 1.00 V (**Table 2**). This is a large improvement over that of ITIC, that has a V_{OC} of 0.825 V under these conditions (**Figure 5c**).[12] However, the V_{OC} for **3c** and **3e** are slightly depressed. Because the energy levels of the acceptors are roughly equivalent, the lower V_{OC} for **3c** and **3e** must be morphological in nature. A likely culprit for the potential loss is defects in the microcrystalline structure of the active layer, warranting further investigation.

While the V_{OC} is fairly consistent between acceptors, the short circuit current (J_{SC}) and fill factor (FF) are found to be highly dependent on the acceptor sidechain. The J_{SC} is a measure of the photocurrent that can be obtained from a device. Any factors that would decrease mobility or carrier density, such as poorly defined domains, small grain size, or high trap density, depress the current. These factors are all morphological in nature.[22] The J_{SC} is maximized with acceptors **3b** and **3c**, with significant drops in current for the acceptors with both shorter and longer alkyl chains. This Goldilocks zone implies that there is a balance of factors at play within the active layer.

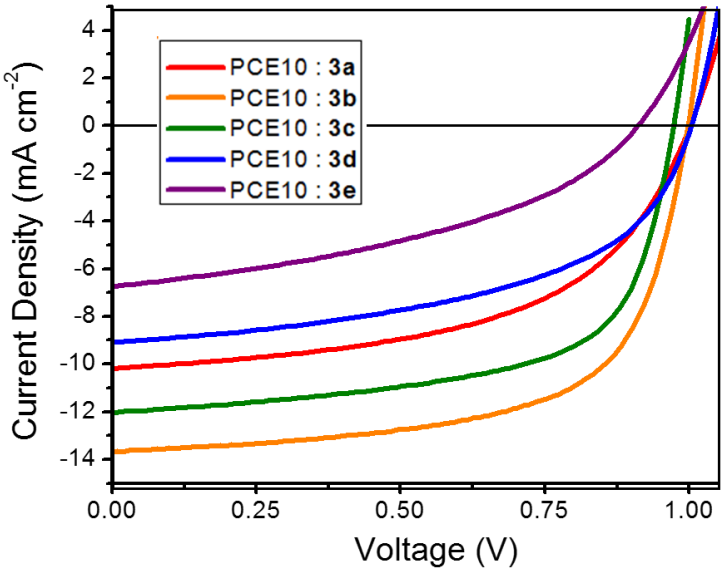

Figure 8: J-V curve for PCE10:NFA mixtures (1:1.5 ratio) under standard AM1.5 irradiation

Table 2: Frontier Molecular Orbital (FMO) data for NFA acceptors and PCE10

Compound	Solubilizing group	DIO (wt %)	J_{SC} (mA cm^{-2})	V_{OC} (V)	FF (%)	PCE (%)
3a	Methyl	0	10.19	1.00	53.3	5.44
3b	Ethyl	0	13.70	1.00	64.0	8.77
3c	Benzyl	0.5	12.04	0.97	63.2	7.41
3d	Octyl	0	9.10	1.01	51.3	4.69
3e	2-ethylhexyl	0	6.72	0.92	41.0	2.52

The fill factor precisely follows the same pattern as the J_{SC}. Because the FF is a measure of resistive factors within the cell, any factors that worsen morphology will likewise lower the FF. Since all the solar cells have the same structure, resistive effects from the contacts can be discounted, making the FF a gauge of active layer resistances.

Because of the similar V_{OC} between devices, the J_{SC} and FF are the most responsible metrics for the variations seen in efficiency. The highest performing device uses **3b** as an acceptor and shows an efficiency of almost 9%. Both decreasing and increasing the alkyl chain length decreases the overall efficiency, exclusively from decreases in the J_{SC} and FF.

Since the active layer characteristics are primarily responsible for efficiency decreases, attempts have been made to alter the film morphology. A solvent additive, 1,8-diiodooctane (DIO) is often used to attempt to selectively solvate one of the active layer materials to improve domain purity.[23] This has a negative impact on all active layers except the benzyl **3c** species, which presents a slight improvement (**Figure A-2b**).

To understand the wavelength dependence on current generation, the External Quantum Efficiency (EQE) has been determined for the best three devices (**Figure 9**). By examining the

ratio of charge carriers generated to the number of incident photons, a wavelength dependent conversion efficiency can be established (**Equation 1**).

$$EQE = \frac{charges\ generated\ at\ \lambda}{incident\ photons\ at\ \lambda} \quad (1)$$

The integrated current density in an EQE curve should be equivalent to the J_{SC} in a J-V plot, and is in good agreement with the J-V data (**Table 3**). The peak efficiency is between 500 and 700 nm, corresponding to the acceptor absorption profile. This confirms that the acceptor is a major contributor to current generation in this device.

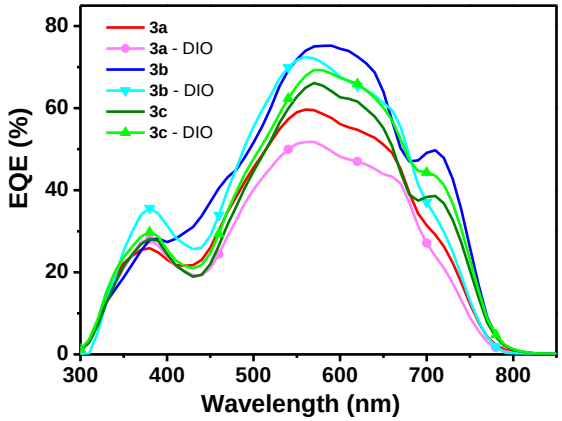

Figure 9: EQE curves for the active layers based on NFAs **3a**, **3b**, and **3c**

Table 3: Integrated Current Density of PCE10:NFA Devices

Compound	Solubilizing group	Without DIO	With DIO
3a	Methyl	10.08	8.99
3b	Ethyl	13.15	12.06
3c	Benzyl	11.01	11.46

To determine the charge carrier mobility, monopolar devices were produced. By choosing electrodes with the appropriate work functions, hole-only or electron-only monopolar devices can be produced (**Figure 10**). By fitting the current in the quadratic regime, a mobility can be calculated using the Mott-Gurney equation (**Equation 2**).[24]

$$J = \frac{9}{8}\mu\varepsilon_0\varepsilon_r\frac{V^2}{L^3} \quad (2)$$

In this equation, J is the measured current, μ is the charge carrier mobility, e_0 is the permittivity of free-space, e_r is the dielectric constant, V is the applied voltage, and L active layer thickness. In the space charge limited current (SCLC) regime, the inherent carrier concentration is negligible compared to the injected current which can be used to directly measure the mobility.

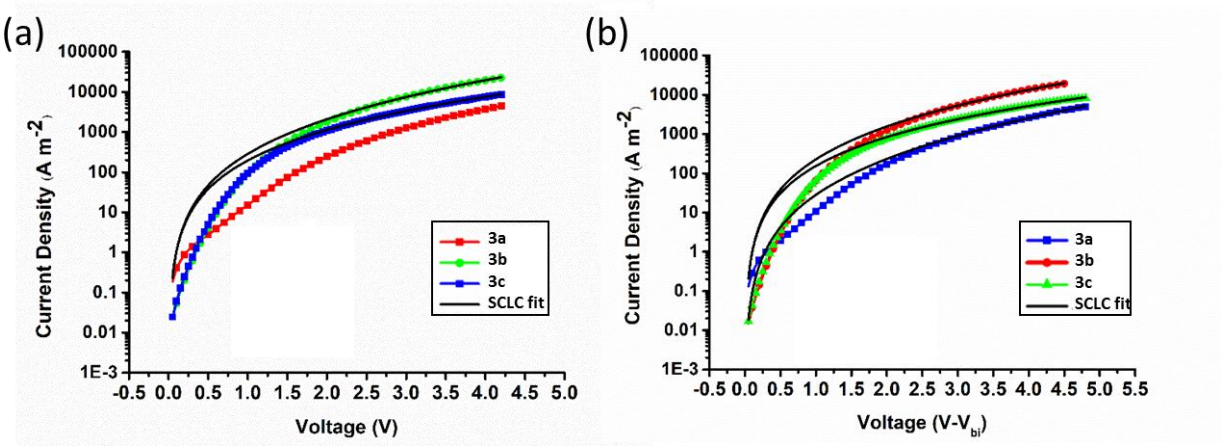

Figure 10: SCLC measured in (a) electron only ITO/ZnO/active layer/PFN-Br/Al and (b) hole only ITO/PEDOT:PSS/active layer/MoOx/Ag devices with PCE10 : **3a**, **3b**, and **3c** in a 1:1.5 ratio

Table 4: SCLC measured in electron-only and hole-only devices

Compound	Solubilizing group	μ_e ($cm^2\ V^{-1}\ s^{-1}$)	μ_h ($cm^2\ V^{-1}\ s^{-1}$)
3a	Methyl	4.35E-5	2.35E-4
3b	Ethyl	3.06E-4	1.25E-3
3c	Benzyl	2.16E-4	4.50E-4

In the case of the PCE10:IDTT-TBTA active layers, the mobilities of both electrons and holes are reasonably well matched, but with consistently higher hole mobilities. The best electron and hole mobilities are observed for IDTT-TBTA-Et **3b**, which are also consistent with the highest solar cell performance. High carrier mobility in a material means that there are fewer traps and there is a sufficient percolation pathway for charges to flow in a material. A high mobility allows charges to travel further, increasing the probability of collection. The electron and hole mobilities in the methyl alkylated **3a** are 7 and 5 times lower than then those observed for **3b**, supporting the hypothesis that defects in the active layer are responsible for decreased J_{SC}, FF, and PCE.

4.5 GIWAXS Characterization

The high variability in metrics such as FF, J_{SC}, and charge mobility demand a closer study of film characteristics. Grazing incidence wide-angle x-ray scattering (GIWAXS) is a highly effective technique for probing the crystallinity of thin film samples. It is particularly useful for providing information on crystallite size, spacing between repeating units (d-spacing), and orientation with respect to the substrate.

The acceptor and polymer samples both are observed to highly favor a face-on orientation. This is evident from a strong q_{xy} oriented 100 lamellar stacking peak and the 010 q_z π–π stacking peak (**Figure 11a,b** & **Figure 12a,b**). Face-on stacking is advantageous for solar cell performance since it allows for vertical charge transport within the device stack.[25] This is also advantageous since mixing donor and acceptor components with differing preferred orientation

can lower efficiencies.[26] The peak situated around 1.46 Å^{-1} in the q_{xy} plane is not associated with π–π stacking, but is instead assigned to diffraction from disordered alkyl chains.

To understand how the choice of alkyl chains affect film crystallinity, the d-spacing and crystallite size have been calculated. The 100 lamellar peak corresponds to horizontal edge-to-edge stacking (**Figure 11a,b**). By looking at the d-spacing for the acceptors **3a**-**3e** a pattern arises that is analogous to the pattern in device efficiency and carrier mobility (**Figure 11c**). The acceptors **3b** and **3c** have the smallest d-spacing, and yield the highest performing devices. The d-spacing is higher both for acceptors with longer alkyl chains such as **3e** and **3f**, as well as shorter alkyl substitution **3a**. These higher d-spacings also correspond to lower device performance. The pattern is overwhelmed by the polymeric contribution to the 100 peak in the mixed PCE10:acceptor systems. However, this can still potentially give information about how efficiently the acceptors can pack within the pure domains of the bulk heterojunction.

When looking at the crystallite size of the 100 peak, acceptor **3a** stands out with a correlation length between three to four times larger than the other acceptors (**Figure 11d**). However, unlike the other acceptors, when the methyl NFA is mixed with PCE10, the spectrum matches almost exactly with the neat **3a** (**Figure 11e**). This lack of change in d-spacing or crystallite size implies that there is minimal mixing between donor and acceptor domains which is a necessity for efficient charge separation.

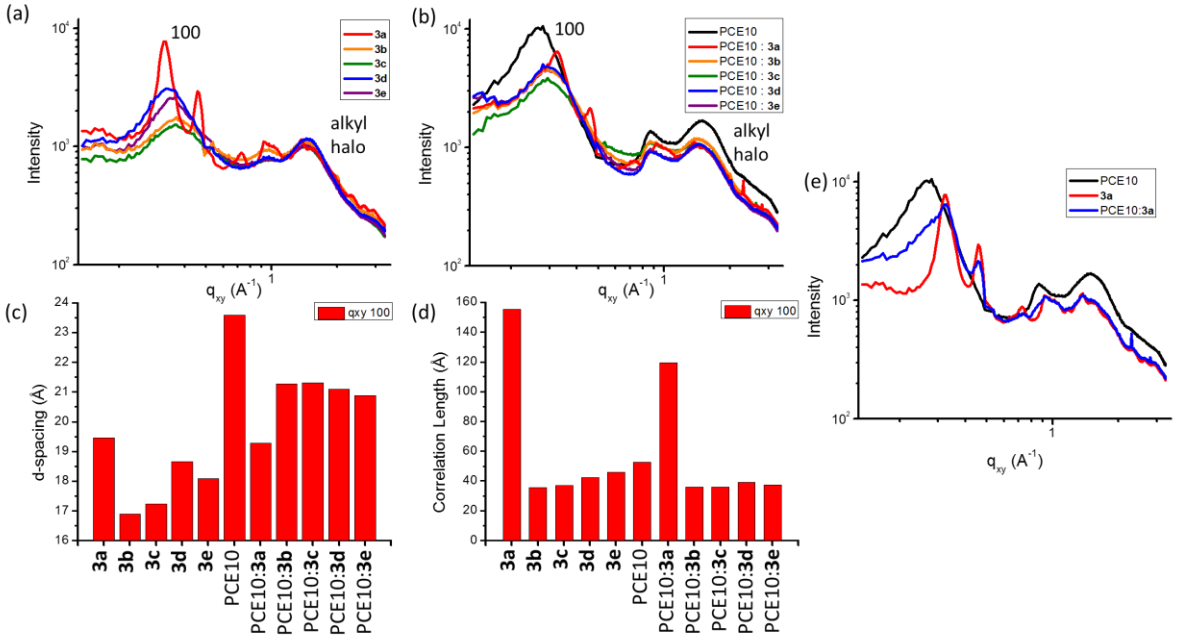

Figure 11: GIWAXS linecuts in the in-plane q_{xy} direction for (a) neat NFA acceptors **3a**-**3e**, and (b) mixtures of the acceptors with PCE10. Quantitative analysis of the (c) d-spacing and (d) crystallite size for the 100 q_{xy} peak for pure acceptors, PCE10 donor, and mixtures. (e) A superposition of q_{xy} linecuts PCE10, 3a, and the mixture is also provided

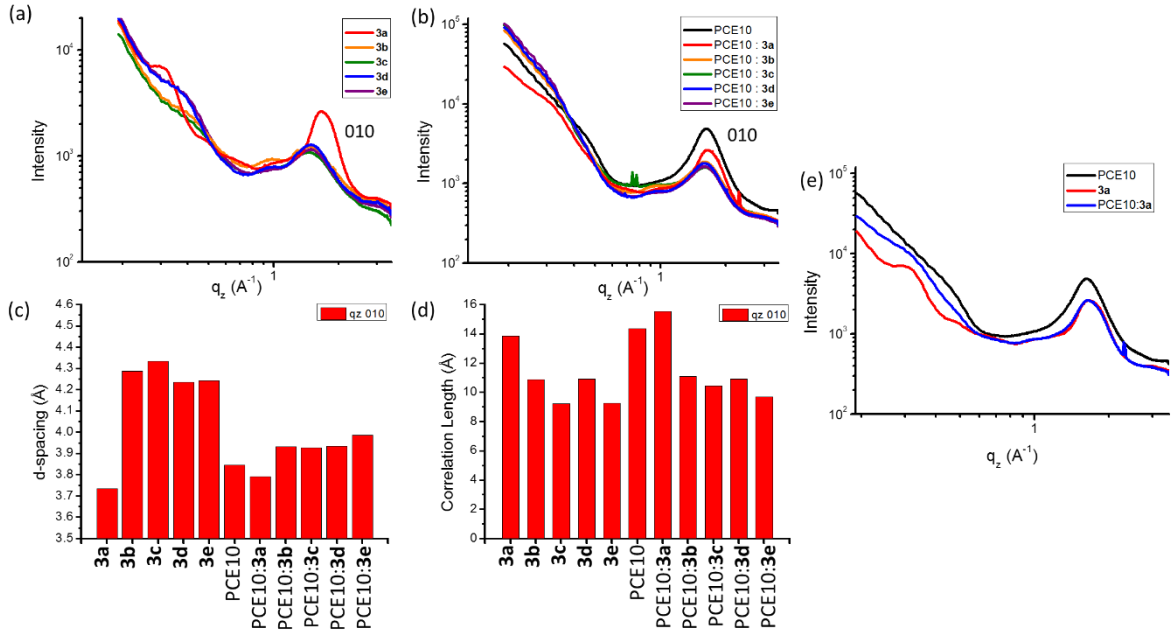

Figure 12: GIWAXS linecuts in the out-of-plane q_z direction for (a) neat NFA acceptors **3a**-**3e**, and (b) mixtures of the acceptors with PCE10. Quantitative analysis of the (c) d-spacing and (d) crystallite size for the 100 q_{xy} peak for pure acceptors, PCE10 donor, and mixtures. (e) A superposition of q_{xy} linecuts PCE10, 3a, and the mixture is also provided

The 010 q_z diffraction peak corresponds to repeating units participating in vertical π–π stacking (**Figure 12a,b**). Since an intermolecular distance below 4 Å is necessary to participate in π–π stacking, the neat **3a** and PCE10 films are considered to be truly π stacking (**Figure 12c**). While the acceptors **3b-3e** have wider d-spacings in the pure films, when mixed with the polymer donor, the d-spacing decreases to within the 4 Å cutoff. This also suggests that domain mixing is occurring. The decrease in d-spacing upon mixing is not observed for **3a**.

The crystallite size of the 010 peak can also illustrate some useful patterns (**Figure 12d**). The acceptors alkylated with linear ethyl (**3b**) and n-octyl (**3d**) are nearly identical, which may be due to similar steric conditions close to the TBTB unit.[27] However, the branched 2-ethylhexyl acceptor **3e** has a smaller crystallite size, potentially due to the larger steric effect of branching alkyl chains. NFA **3c** also has a larger steric cone due to the benzyl group, potentially hindering π–π stacking in the solid state, decreasing crystallite size. The pattern in crystallite size is consistent when mixed with PCE10, showing that the crystallinity of the acceptors does have an effect on the overall system. For **3a** the peak overlap, consistency of d-spacing, and crystallite size remains constant, similar to the behavior of the 100 peak. This further implies a lack of domain mixing (**Figure 12e**).

Looking at these data as a whole, a number of patterns arise that can help elucidate differences in device performance. Since the trend in lamellar 100 peaks matches well with device performance, it is possible that the narrower intermolecular distances seen for **3b** and **3c** could aid in charge transfer in the devices. Additionally, the wider π–π stacking d-spacing

distances seen for **3c** and **3e** could explain why they performed worse than their linear counterparts **3b** and **3d** respectively.

The methyl derivative **3a** is an outlier for having very sharp peaks and a number of side peaks not present in the other samples. This alone suggests very high crystallinity, which matches the shortest $\pi-\pi$ stacking distance and the largest crystallite sizes for the acceptors. However, unlike the other acceptors, there is no evidence for mixing between donor and acceptor domains, which is a necessity for efficient charge separation (**Figures 11e, 12e**). The result of insufficient domain mixing and hard grain boundaries is likely the cause of the low performance of the PCE10:**3a** active layer.[28] This could also explain the poor mobilities, as completely isolated donor and acceptor domains are less likely to form a percolation pathway to allow for the flow of charges.

The device and GIWAXS data paints a picture of how the alkyl chains interact on a molecular level to determine properties on a materials level. The methyl substitution provides highly crystalline materials, but so crystalline that there are insufficient mixed domains with the donor polymer. This provides low mobilities as well as depressed J_{SC}, FF, and PCE due to lower surface area for charge generation. At the other extreme, the octyl and 2-ethylhexyl substituted **3d** and **3e** are observed to have wider lamellar stacking distances and $\pi-\pi$ stacking distances when mixed with the donor polymer. This increased spacing between acceptor units and addition of additional insulating alkyl chains may be responsible for the low device performance. The acceptors **3b** and **3c** have crystallinity that straddles these two extremes, providing the optimal performance. The top performing acceptor **3b** has closer lamellar and $\pi-\pi$ stacking than **3c**, possibly allowing for the small boost in performance through better electronic communication.

4.6 Conclusions

Introducing TBTA end groups to the IDTT core successfully increases the LUMO energy of these non-fullerene acceptors, greatly improving the V_{OC}. By interchanging the alkyl chains on the TBTA unit, a controlled morphological study could be undertaken without altering the electronic properties. The resulting device and GIWAXS experiments shows that the ethyl and benzyl substituted acceptors **3b** and **3c** have superior performance. This could potentially be due to small lamellar stacking distances and good heterojunction formation in the crystalline state. The champion device has a high V_{OC} of 1.0V and a PCE of 8.77%.

Simply shortening the alkyl chains from ethyl to methyl groups in **3a** creates an acceptor that was too crystalline to form an ideal heterojunction and decreases PCE by 38%. Conversely, acceptors **3d** and **3e** with longer alkyl chains have larger intermolecular distances, which perhaps have led to a hampered ability to transfer charge. The TBTA with increased alkyl chain length from ethyl to n-octyl and 2-ethylhexyl results in a 46% and 71% decrease in efficiency respectively. This underlies the challenges associated with morphological control in materials design and the need for further study.

4.7 Materials and Methods

Reagents were used as purchased. Solvent was collected from an activated alumina column based solvent dispensing system (SDS). Reactions progress was monitored by thin layer chromatography (TLC) on precoated silica gel 60F on aluminum backing (Merck 5554). Proton (^{1}H) and carbon (^{13}C) NMR spectra were obtained on a Bruker Avance 500II spectrometer. Molecular

weights were determined on a 4800 MALDI TOF/TOF analyzer from Applied Biosystems. Optical measurements were carried out on a Cary 5000 UV-Vis-NIR spectrometer. Electrochemical measurements were obtained using 273A potentiostat (Princeton Applied Research), with a glassy carbon working electrode, a platinum coated aluminum counter electrode, and a silver wire as a pseudo-reference electrode. Samples were prepared in either acetonitrile or dichloromethane solutions with tetrabutylammonium hexafluorophosphate (0.1 M) as the electrolyte. Spectra were obtained with a scan rate of 100 mV s-1, using the ferrocene/ferrocenium (Fc/Fc+) redox couple as an internal standard. The HOMO and LUMO levels of compounds are calculated from the difference between the onset of first oxidation potential (E_{OX}) or reduction potential (E_{red}) of the compounds and the oxidation potential of ferrocene E_{HOMO} = -(4.8+E_{OX}) eV, E_{LUMO} = -(4.8+E_{RED}) eV.[29]

Grazing Incidence Wide Angle X-ray Scattering (GIWAXS) experiments were conducted at the 7.3.3 Beamline of Advanced Light Source, Lawrence Berkeley National Laboratory.[30]

Solar cells were fabricated with an inverted device a structure of ITO/ZnO/active layer/MoOx/Ag.[16] Where the ZnO electron transport layer was prepared through the sol-gel method[31] and a molybdenum oxide hole transport layer was deposited via thermal evaporation.[32] ITO coated glass substrates were cleaned prior to device fabrication by sonication in acetone, low concentration soap water, deionized water, and isopropyl alcohol and then dried in the oven. After treated in an ultraviolet-ozone chamber (Ultraviolet Ozone Cleaner, Jelight Company, USA) for 20 min, 15 nm of ultrathin zinc oxide nano particle (ZnO NP) layer was spin-casted on the ITO-coated glass substrates at 4000 rpm for 1 minute, the substrates were subsequently dried at 120 ℃ for 10 min in air and then transferred to a N2-glovebox. The active layer was deposited via spincoating. Finally, 10 nm molybdenum oxide (MoO3) and 100 nm aluminum (Al) were evaporated with a shadow mask as the top electrode.

PCEs were determined from J-V characteristics measured by a Keithley 2400 source-measurement unit under AM 1.5G spectrum from a solar simulator (Oriel model 91192).[33] The active area was defined by the mask area of 0.16 cm^2. Solar simulator illumination intensity was determined using a Newport calibrated monocrystal silicon reference cell with KG-5 visible color filter. External quantum efficiency (EQE) values of the encapsulated devices were measured by using an integrated system (QE-R Enlitech, Taiwan). Photoluminescence spectra were recorded on a Horiba Nanolog fluorescence spectrophotometer.

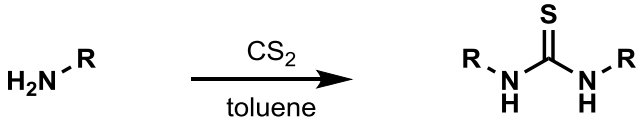

1c = 70%, R = benzyl
1d = 81%, R = octyl
1e = 100%, R = 2-ethylhexyl

1c 1,3-dibenzylthiourea

Benzylamine (0.87 mL, 8 mmol, 2 equiv.) added to an ovendried flask with stirbar and reflux condenser. Toluene (10 mL, 0.4 M) added and cooled to 0°C. Carbon disulfide (0.24 mL, 4 mmol, 1 equiv.) added and heated to 110°C. After 12 hours the solution was cooled to ambient temperature and solid precipitated out of solution. The solution was concentrated to approximately 5 mL and filtered to yield a white crystalline solid (780 mg, 3.04 mmol, 76%). ^{1}H

NMR (500 MHz, Chloroform-*d*) δ 7.37 – 7.21 (m, 10H), 6.01 (s, 2H), 4.63 (s, 4H). ^{13}C NMR (126 MHz, Chloroform-*d*) δ 182.0, 136.8, 129.1, 128.1, 127.7, 48.7. HRMS for $C_{15}H_{16}N_2S$ (MALDI): $[M]^+$ Calcd: 256.1034, found 256.7882.

1d 1,3-dioctylthiourea

Octylamine (6.62 mL, 40 mmol, 2 equiv.) added to an ovendried flask with stirbar and reflux condenser. Toluene (25 mL, 0.8 M) and carbon disulfide (1.2 mL, 20 mmol, 1 equiv.) added at room temperature and heated to 110°C. After 12 hours the solution was cooled to ambient temperature and was concentrated to approximately 10 mL. The solid product was collected by filtration and washed with hexane to yield a white crystalline solid (4.85 g, 16.15 mmol, 81%). ^{1}H NMR (500 MHz, Chloroform-*d*) δ 6.05 (s, 1H), 3.36 (s, 2H), 1.55 (p, *J* = 7.4, 7.0 Hz, 2H), 1.30 – 1.19 (m, 11H), 0.83 (t, *J* = 6.9 Hz, 3H). ^{13}C NMR (126 MHz, Chloroform-*d*) δ 181.2, 44.6, 31.9, 29.4, 29.3, 29.1, 27.0, 22.7, 14.2. HRMS for $C_{17}H_{36}N_2S$ (MALDI): $[M]^+$ Calcd: 300.2599, found 300.9851.

1e 1,3-bis(2-ethylhexyl)thiourea

2-ethylhexylamine (1.31 mL, 8 mmol, 2 equiv.) added to an ovendried flask with stirbar and reflux condenser. Toluene (5 mL, 0.8 M) added and cooled to 0°C. Carbon disulfide (0.24 mL, 4 mmol, 1 equiv.) added and heated to 110°C. After 12 hours the solution was cooled to ambient temperature concentrated to yield a yellow oil that was used without further purification (1.212 g, 4.0 mmol, 100%). ^{1}H NMR (500 MHz, Chloroform-*d*) δ 5.72 (s, 2H), 3.33 (s, 4H), 1.58 – 1.52 (m, 2H), 1.42 – 1.32 (m, 4H), 1.35 – 1.22 (m, 12H), 0.89 (td, *J* = 7.0, 4.1 Hz, 12H). ^{13}C NMR (126 MHz, Chloroform-*d*) δ 181.9, 47.7, 39.3, 31.3, 29.1, 24.6, 23.2, 14.3, 11.1. HRMS for $C_{17}H_{36}N_2S$ (MALDI): $[M+H]^+$ Calcd: 301.2672, found 301.2464.

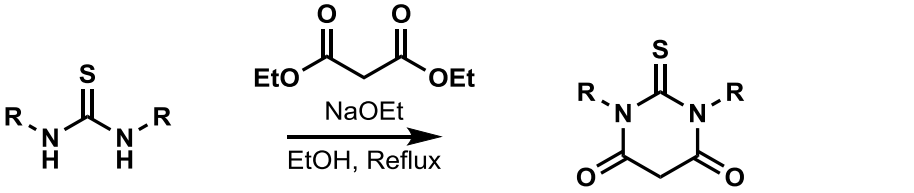

2a = 73%, R = methyl
2c = 73%, R = benzyl
2d = 31%, R = octyl
2e = 4%, R = 2-ethylhexyl

2a 1,3-dimethyl-2-thioxodihydropyrimidine-4,6(1H,5H)-dione[34]

Dimethyl thiourea (1 g, 9.6 mmol, 1 equiv.) added to microwave vial with septa cap and backfilled with nitrogen. 21 wt % sodium ethoxide in ethanol (14 mL, 37.5 mmol, 3.9 equiv.), and diethyl malonate (5.86 mL, 38.4 mmol, 4 equiv.) added sequentially and heated to reflux for 2 days. The crude reaction mixture was diluted with water and ethanol was removed via reduced pressure. The crude reaction mixture was acidified with 1M HCl, extracted with ethyl acetate, dried with $MgSO_4$ and the solvent was removed under reduced pressure. The crude solid was recrystallized from chloroform to yield **2a** as a white solid (1.21 g, 7.0 mmol, 73%), in an approximately 60:40 ratio of keto and enol forms. ^{1}H NMR (500 MHz, DMSO-d_6) δ 10.71 (s, 1H), 5.37 – 4.98 (m, 1H),

3.86 (s, 1H), 3.53 (s, 6H). ^{13}C NMR (126 MHz, DMSO-d_6) δ 182.4, 176.8, 164.8, 160.6, 82.2, 35.1. HRMS for $C_6H_8N_2O_2S$ (MALDI): $[M]^+$ Calcd: 172.0306, found 172.8449.

2c 1,3-dibenzyl-2-thioxodihydropyrimidine-4,6(1H,5H)-dione

Benzyl thiourea (1.7 g, 6.65 mmol, 1 equiv.) added to microwave vial with septa cap and backfilled with nitrogen. Ethanol (6.7 mL, 0.4 mL), 21 wt % sodium ethoxide in ethanol (9.93 mL, 26.6 mmol, 4 equiv.), and diethyl malonate (4.05 mL, 26.6 mmol, 4 equiv.) added sequentially and heated to reflux for 48 hours. The reaction was diluted with water and the ethanol was removed under reduced pressure and solids were removed by filtration. The filtrate was acidified with 1M HCl, extracted with ethyl acetate, dried with $MgSO_4$ and the solvent was removed under reduced pressure. The crude reaction mixture was purified by column chromatography (0 – 100% ethyl acetate in hexane) to yield a yellow viscous oil which crystallized over time (1.585 g, 4.89 mmol, 73%). ^{1}H NMR (500 MHz, Chloroform-*d*) δ 7.40 – 7.22 (m, 10H), 5.61 (s, 4H), 3.85 (s, 2H). ^{13}C NMR (126 MHz, Chloroform-*d*) δ 180.8, 163.6, 135.8, 128.5, 128.4, 127.9, 50.8, 40.7. HRMS for $C_{18}H_{16}N_2O_2S$ (MALDI): $[M+H]^+$ Calcd: 325.1005, found 325.1627.

2d 1,3-dioctyl-2-thioxodihydropyrimidine-4,6(1H,5H)-dione

Dioctyl thiourea (420 mg, 1.4 mmol, 1 equiv.) added to microwave vial with septa cap and backfilled with nitrogen. Ethanol (2 mL, 0.7 mL), 21 wt % sodium ethoxide in ethanol (2.24 mL, 6 mmol, 4 equiv.), and diethyl malonate (0.92 mL, 6 mmol, 4 equiv.) added sequentially and heated to reflux for 4 days. The crude reaction mixture was acidified with 1M HCl, extracted with ethyl acetate, dried with $MgSO_4$ and the solvent was removed under reduced pressure. The crude reaction mixture was purified by column chromatography (0 – 100% ethyl acetate in hexane) to yield a yellow viscous oil which crystallized over time (160 mg, 0.43 mmol, 31%). ^{1}H NMR (500 MHz, Chloroform-*d*) δ 4.36 – 4.27 (m, 4H), 3.71 (s, 2H), 1.67 – 1.60 (m, 4H), 1.38 – 1.20 (m, 20H), 0.88 (t, *J* = 6.8 Hz, 6H). ^{13}C NMR (126 MHz, Chloroform-*d*) δ 180.6, 163.5, 48.4, 40.8, 32.0, 29.4, 29.4, 27.1, 27.0, 22.9, 14.4. HRMS for $C_{20}H_{36}N_2O_2S$ (MALDI): $[M+H]^+$ Calcd: 369.2570, found 369.2687

.

2e 1,3-bis(2-ethylhexyl)-2-thioxodihydropyrimidine-4,6(1H,5H)-dione

1,3-bis(2-ethylhexyl)thiourea thiourea (2 g, 6.65 mmol, 1 equiv.) added to microwave vial with septa cap and backfilled with nitrogen. Ethanol (6.7 mL, 0.4 mL), 21 wt % sodium ethoxide in ethanol (9.93 mL, 26.6 mmol, 4 equiv.), and diethyl malonate (4.05 mL, 26.6 mmol, 4 equiv.) added sequentially and heated to reflux for 48 hours. The reaction was diluted with water and the ethanol was removed under reduced pressure and solids were removed by filtration. The filtrate was acidified with 1M HCl, extracted with ethyl acetate, dried with $MgSO_4$ and the solvent was removed under reduced pressure. The crude reaction mixture was purified by column chromatography (0 – 20% ethyl acetate in hexane) to yield a yellow viscous oil (100 mg, 0.26 mmol, 4%). ^{1}H NMR (500 MHz, Chloroform-*d*) δ 4.37 – 4.24 (m, 4H), 3.74 (s, 2H), 1.97 (dt, *J* = 13.2, 6.6 Hz, 2H), 1.26 (pd, *J* = 21.3, 17.3, 9.8 Hz, 16H), 0.88 (h, *J* = 91 Hz, 12H). ^{13}C NMR (126 MHz, Chloroform-*d*) δ 181.6, 164.1, 51.4, 41.0, 37.1, 30.7, 28.8, 24.1, 23.3, 14.3, 10.9. HRMS for $C_{20}H_{36}N_2O_2S$ (MALDI): $[M+H]^+$ Calcd: 369.2570, found 369.2670.

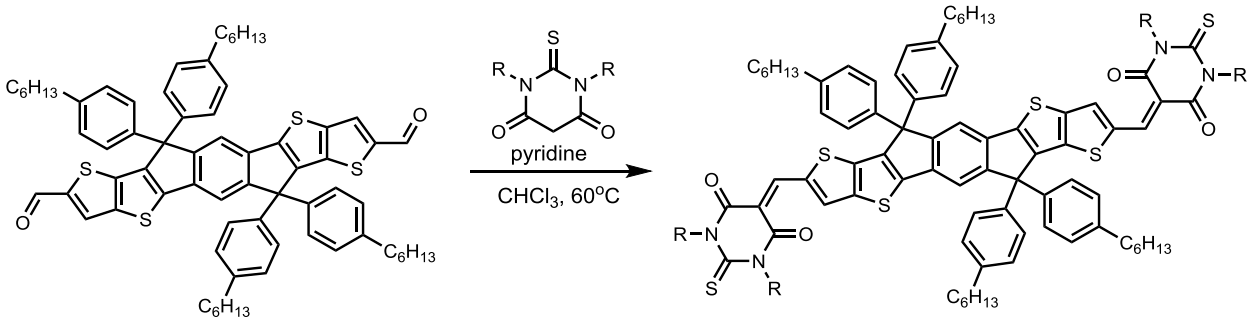

3a = 81%, R = methyl
3b = 82%, R = ethyl
3c = 99%, R = benzyl
3d = 98%, R = octyl
3e = 79%, R = 2-ethylhexyl

3a IDTT-TBTA-methyl

ITIC dialdehyde (100 mg, 0.093 mmol, 1 equiv.) and ethyl TBTA (96 mg, 0.56 mmol, 6 equiv.) added to an ovendried roundbottom flask with reflux condenser and stirbar. Chloroform (5 mL, 0.019 M) was added followed by pyridine (0.15 mL, 1.86 mmol, 20 equiv.) and heated to 60°C. After 24 hours the reaction was concentrated and purified by column chromatography (70 – 100% $CHCl_3$ in hexanes) to provide **3a** as a blue solid (125 mg, 0.09 mmol, 97%). ^{1}H NMR (500 MHz, Chloroform-*d*) δ 8.69 (s, 2H), 8.14 (s, 2H), 7.64 (s, 2H), 7.22 (d, *J* = 8.3 Hz, 8H), 7.14 (d, *J* = 8.4 Hz, 8H), 3.81 (s, 8H), 3.80 (s, 8H), 2.60 – 2.53 (m, 8H), 1.59 (ddd, *J* = 13.0, 8.3, 6.3 Hz, 8H), 1.39 – 1.22 (m, 24H), 0.87 (t, *J* = 7.0, 6.1 Hz, 12H). ^{13}C NMR (126 MHz, Chloroform-*d*) δ 180.1, 161.8, 160.4, 155.9, 153.3, 150.4, 148.5, 147.8, 143.6, 142.7, 140.0, 139.1, 138.8, 137.1, 129.0, 128.1, 118.8, 109.7, 63.5, 36.3, 35.8, 35.5, 31.9, 31.5, 29.4, 22.8, 14.3. HRMS for $C_{82}H_{86}N_4O_4S_6$ (MALDI): $[M]^+$ Calcd: 1383.5046, found 1383.7555.

3b IDTT-TBTA-ethyl[16]

ITIC dialdehyde (100 mg, 0.093 mmol, 1 equiv.) and ethyl TBTA (112 mg, 0.56 mmol, 6 equiv.) added to an ovendried roundbottom flask with reflux condenser and stirbar. Chloroform (5 mL, 0.019 M) was added followed by pyridine (0.15 mL, 1.86 mmol, 20 equiv.) and heated to 60°C. After 24 hours the reaction was concentrated and purified by columfn chromatography (50 – 100% $CHCl_3$ in hexanes) to provide **3b** as a blue solid (129 mg, 0.09 mmol, 96%). ^{1}H NMR (500 MHz, Chloroform-*d*) δ 8.67 (s, 2H), 8.16 (s, 2H), 7.67 (s, 2H), 7.26 (d, *J* = 8.3 Hz, 8H), 7.16 (d, *J* = 8.1 Hz, 8H), 4.60 (dq, *J* = 13.8, 6.9 Hz, 8H), 2.63 – 2.55 (m, 8H), 1.71 – 1.57 (m, 8H), 1.41 – 1.25 (m, 36H), 0.91 – 0.85 (m, 12H). ^{13}C NMR (126 MHz, Chloroform-*d*) δ 178.7, 161.2, 159.8, 155.7, 153.0, 149.8, 148.1, 147.7, 143.5, 142.6, 140.0, 139.2, 138.4, 137.0, 129.0, 128.1, 118.7, 110.2, 63.5, 44.2, 43.3, 35.8, 31.9, 31.4, 29.4, 22.8, 14.3, 12.7, 12.6. HRMS for $C_{86}H_{94}N_4O_4S_6$ (MALDI): $[M]^+$ Calcd: 1438.5599, found 1438.7133.

3c IDTT-TBTA-Benzyl

ITIC dialdehyde (100 mg, 0.093 mmol, 1 equiv.) and benzyl TBTA (181 mg, 0.56 mmol, 6 equiv.) added to an ovendried roundbottom flask with reflux condenser and stirbar. Chloroform (5 mL, 0.02 M) was added followed by pyridine (0.15 mL, 1.86 mmol, 20 equiv.) and heated to 60°C. After 24 hours the reaction was concentrated and purified by column chromatography (20 – 100%

$CHCl_3$ in hexanes) to provide **3c** as a blue solid (141mg, 0.084, 90%). ^{1}H NMR (500 MHz, Chloroform-*d*) δ 8.73 (s, 2H), 8.13 (s, 2H), 7.72 (s, 2H), 7.48 – 7.39 (m, 8H), 7.38 – 7.27 (m, 20H), 7.18 (d, *J* = 8.1 Hz, 8H), 5.85 (s, 4H), 5.80 (s, 4H), 2.62 (t, *J* = 7.9 Hz, 8H), 1.64 (p, *J* = 7.9, 7.3 Hz, 8H), 1.42 – 1.32 (m, 24H), 0.95 – 0.90 (m, 12H). ^{13}C NMR (126 MHz, Chloroform-*d*) δ 179.4, 161.6, 160.2, 155.8, 153.3, 150.5, 148.5, 147.7, 143.7, 142.6, 140.1, 139.1, 138.7, 137.1, 136.6, 136.6, 129.0, 128.5, 128.5, 128.1, 128.0, 128.0, 127.5, 127.4, 118.8, 109.6, 63.4, 51.6, 50.6, 35.8, 31.9, 31.4, 29.4, 22.8, 14.3. HRMS for $C_{106}H_{102}N_4O_4S_6$ (MALDI): $[M]^+$ Calcd: 1686.6225, found 1686.9984.

3d IDTT-TBTA-octyl

ITIC dialdehyde (78 mg, 0.07 mmol, 1 equiv.) and octyl TBTA (160 mg, 0.43 mmol, 6 equiv.) added to an ovendried roundbottom flask with reflux condenser and stirbar. Chloroform (4 mL, 0.018 M) was added followed by pyridine (0.11 mL, 1.4 mmol, 20 equiv.) and heated to 60°C. After 24 hours the reaction was concentrated and purified by columfn chromatography (0 – 100% $CHCl_3$ in hexanes) to provide **3d** as a blue solid (125 mg, 0.07 mmol, 100%). ^{1}H NMR (500 MHz, Chloroform-*d*) δ 8.63 (s, 2H), 8.16 (s, 2H), 7.63 (s, 2H), 7.22 (d, *J* = 8.3 Hz, 8H), 7.13 (d, *J* = 8.3 Hz, 7H), 4.46 (dt, *J* = 10.7, 5.9 Hz, 8H), 2.60 – 2.53 (m, 8H), 1.75 – 1.69 (m, 10H), 1.62 – 1.56 (m, 4H), 1.45 – 1.22 (m, 64H), 0.92 – 0.82 (m, 24H). ^{13}C NMR (126 MHz, Chloroform-*d*) δ 179.1, 161.4, 160.0, 155.7, 152.9, 149.8, 148.1, 147.7, 143.6, 142.7, 140.1, 139.3, 138.2, 137.0, 129.0, 128.1, 118.7, 110.4, 63.5, 48.9, 48.1, 35.8, 32.1, 32.0, 31.9, 31.5, 29.5, 29.5, 29.5, 29.4, 27.2, 27.2, 27.1, 22.9, 22.9, 22.8, 14.4, 14.3, 14.3. HRMS for $C_{110}H_{142}N_4O_4S_6$ (MALDI): $[M+H]^+$ Calcd: 1775.9428, found 1775.1682.

3e IDTT-TBTA-(2-ethylhexyl)

ITIC dialdehyde (44 mg, 0.045 mmol, 1 equiv.) and benzyl TBTA (100 mg, 0.27 mmol, 6 equiv.) added to an ovendried roundbottom flask with reflux condenser and stirbar. Chloroform (2.25 mL, 0.02 M) was added followed by pyridine (73 μL, 0.9 mmol, 20 equiv.) and heated to 60°C. After 24 hours the reaction was concentrated and purified by column chromatography (20 – 100% $CHCl_3$ in hexanes) to provide **3e** as a blue solid (63 mg, 0.035 mmol, 79%). ^{1}H NMR (500 MHz, Chloroform-*d*) δ 8.67 (s, 2H), 8.13 (s, 2H), 7.66 (s, 2H), 7.24 (dt, *J* = 8.9, 4.6 Hz, 9H), 7.14 (dd, *J* = 8.3, 3.3 Hz, 8H), 4.58 – 4.45 (m, 8H), 2.57 (td, *J* = 7.9, 1.9 Hz, 8H), 2.09 (ddd, *J* = 13.3, 6.5 Hz, 4H), 1.60 (dt, *J* = 33.4, 7.5, 6.9 Hz, 8H), 1.41 – 1.22 (m, 56H), 0.95 – 0.83 (m, 36H). ^{13}C NMR (126 MHz, Chloroform-*d*) δ 179.9, 179.9, 162.1, 160.6, 155.7, 152.7, 150.0, 148.1, 147.6, 143.4, 142.6, 142.6, 140.2, 139.3, 139.2, 138.1, 137.0, 129.0, 129.0, 128.1, 128.1, 118.7, 110.2, 63.4, 51.9, 50.8, 37.32, 37.3, 37.1, 35.8, 31.9, 31.5, 30.8, 30.7, 29.4, 29.4, 28.9, 28.8, 24.2, 24.0, 23.3, 22.8, 14.3, 11.0, 10.9. HRMS for $C_{110}H_{142}N_4O_4S_6$ (MALDI): $[M]^+$ Calcd: 1774.9355, found 1774.1312.

4.8 References

[1] a) Y. Liu, J. Zhao, Z. Li, C. Mu, W. Ma, H. Hu, K. Jiang, H. Lin, H. Ade, H. Yan, *Nat. Commun.* **2014**, *5*, 5293; b) J. Zhao, Y. Li, G. Yang, K. Jiang, H. Lin, H. Ade, W. Ma, H. Yan, *Nature Energy* **2016**, *1*, 15027; c) I. Etxebarria, J. Ajuria, R. Pacios, *J. Photonics Energy* **2015**, *5*, 1-25, 25.

[2] J.-D. Chen, C. Cui, Y.-Q. Li, L. Zhou, Q.-D. Ou, C. Li, Y. Li, J.-X. Tang, *Adv. Mater.* **2015**, *27*, 1035-1041.

[3] K.-T. Wong, T.-C. Chao, L.-C. Chi, Y.-Y. Chu, A. Balaiah, S.-F. Chiu, Y.-H. Liu, Y. Wang, *Org. Lett.* **2006**, *8*, 5033-5036.

[4] a) Y. Lin, T. Li, F. Zhao, L. Han, Z. Wang, Y. Wu, Q. He, J. Wang, L. Huo, Y. Sun, C. Wang, W. Ma, X. Zhan, *Adv. Energy Mater.* **2016**, *6*, 1600854; b) Y. Lin, J. Wang, Z.-G. Zhang, H. Bai, Y. Li, D. Zhu, X. Zhan, *Adv. Mater.* **2015**, *27*, 1170-1174.

[5] Y. Lin, F. Zhao, Y. Wu, K. Chen, Y. Xia, G. Li, S. K. K. Prasad, J. Zhu, L. Huo, H. Bin, Z.-G. Zhang, X. Guo, M. Zhang, Y. Sun, F. Gao, Z. Wei, W. Ma, C. Wang, J. Hodgkiss, Z. Bo, O. Inganäs, Y. Li, X. Zhan, *Adv. Mater.* **2017**, *29*, 1604155.

[6] S. Dai, F. Zhao, Q. Zhang, T.-K. Lau, T. Li, K. Liu, Q. Ling, C. Wang, X. Lu, W. You, X. Zhan, *J. Am. Chem. Soc.* **2017**, *139*, 1336-1343.

[7] B. Kan, H. Feng, X. Wan, F. Liu, X. Ke, Y. Wang, Y. Wang, H. Zhang, C. Li, J. Hou, Y. Chen, *J. Am. Chem. Soc.* **2017**, *139*, 4929-4934.

[8] X. Shi, L. Zuo, S. B. Jo, K. Gao, F. Lin, F. Liu, A. K. Y. Jen, *Chem. Mater.* **2017**, *29*, 8369-8376.

[9] a) Z. Li, K. Jiang, G. Yang, J. Y. L. Lai, T. Ma, J. Zhao, W. Ma, H. Yan, *Nat. Commun.* **2016**, *7*, 13094; b) Y. Lin, Q. He, F. Zhao, L. Huo, J. Mai, X. Lu, C.-J. Su, T. Li, J. Wang, J. Zhu, Y. Sun, C. Wang, X. Zhan, *J. Am. Chem. Soc.* **2016**, *138*, 2973-2976; c) Y. Lin, F. Zhao, Q. He, L. Huo, Y. Wu, T. C. Parker, W. Ma, Y. Sun, C. Wang, D. Zhu, A. J. Heeger, S. R. Marder, X. Zhan, *J. Am. Chem. Soc.* **2016**, *138*, 4955-4961; d) Y. Yang, Z.-G. Zhang, H. Bin, S. Chen, L. Gao, L. Xue, C. Yang, Y. Li, *J. Am. Chem. Soc.* **2016**, *138*, 15011-15018; e) C. e. Zhang, S. Feng, Y. Liu, R. Hou, Z. Zhang, X. Xu, Y. Wu, Z. Bo, *ACS Appl. Mater. Interfaces* **2017**, *9*, 33906-33912; f) Z. Zhang, L. Feng, S. Xu, Y. Liu, H. Peng, Z.-G. Zhang, Y. Li, Y. Zou, *Adv. Sci.* **2017**, *4*, 1700152; g) F. Zhao, S. Dai, Y. Wu, Q. Zhang, J. Wang, L. Jiang, Q. Ling, Z. Wei, W. Ma, W. You, C. Wang, X. Zhan, *Adv. Mater.* **2017**, *29*, 1700144.

[10] H. Bin, L. Zhong, Y. Yang, L. Gao, H. Huang, C. Sun, X. Li, L. Xue, Z.-G. Zhang, Z. Zhang, Y. Li, *Adv. Energy Mater.* **2017**, *7*, 1700746.

[11] a) H. Bai, Y. Wu, Y. Wang, Y. Wu, R. Li, P. Cheng, M. Zhang, J. Wang, W. Ma, X. Zhan, *J. Mater. Chem. A* **2015**, *3*, 20758-20766; b) H. Bin, L. Gao, Z.-G. Zhang, Y. Yang, Y. Zhang, C. Zhang, S. Chen, L. Xue, C. Yang, M. Xiao, Y. Li, *Nat. Commun.* **2016**, *7*, 13651; c) S. Li, L. Ye, W. Zhao, S. Zhang, S. Mukherjee, H. Ade, J. Hou, *Adv. Mater.* **2016**, *28*, 9423-9429; d) D. Xie, T. Liu, W. Gao, C. Zhong, L. Huo, Z. Luo, K. Wu, W. Xiong, F. Liu, Y. Sun, C. Yang, *Solar RRL* **2017**, *1*, 1700044; e) H. Yao, L. Ye, J. Hou, B. Jang, G. Han, Y. Cui, G. M. Su, C. Wang, B. Gao, R. Yu, H. Zhang, Y. Yi, H. Y. Woo, H. Ade, J. Hou, *Adv. Mater.* **2017**, *29*, 1700254; f) W. Zhao, S. Li, H. Yao, S. Zhang, Y. Zhang, B. Yang, J. Hou, *J. Am. Chem. Soc.* **2017**, *139*, 7148-7151; g) W. Zhao, S. Li, S. Zhang, X. Liu, J. Hou, *Adv. Mater.* **2017**, *29*, 1604059.

[12] B. He, B. Yang, M. A. Kolaczkowski, C. A. Anderson, L. M. Klivansky, T. L. Chen, M. A. Brady, Y. Liu, *ACS Energy Lett.* **2018**, *3*, 1028-1035.

[13] Suman, S. P. Singh, *J. Mater. Chem. A* **2019**, *7*, 22701-22729.

[14] W. Ni, M. Li, B. Kan, F. Liu, X. Wan, Q. Zhang, H. Zhang, T. P. Russell, Y. Chen, *Chem. Commun.* **2016**, *52*, 465-468.

[15] Y. Gong, Z. Kan, W. Xu, Y. Wang, S. H. AlShammari, F. Laquai, W.-Y. Lai, W. Huang, *Solar RRL* **2018**, *2*, 1800120.

[16] L. Xiao, B. He, Q. Hu, L. Maserati, Y. Zhao, B. Yang, M. A. Kolaczkowski, C. L. Anderson, N. J. Borys, L. M. Klivansky, T. L. Chen, A. M. Schwartzberg, T. P. Russell, Y. Cao, X. Peng, Y. Liu, *Joule* **2018**, *2*, 2154-2166.
[17] S. Park, H. J. Son, *J. Mater. Chem. A* **2019**.
[18] V. Mancini, O. Piovesana, S. Santini, *Z. Naturforsch. B Chem. Sci* **1974**, *29*, 815.
[19] S. Zhang, L. Ye, W. Zhao, D. Liu, H. Yao, J. Hou, *Macromolecules* **2014**, *47*, 4653-4659.
[20] M. A. Alamoudi, J. I. Khan, Y. Firdaus, K. Wang, D. Andrienko, P. M. Beaujuge, F. Laquai, *ACS Energy Lett.* **2018**, *3*, 802-811.
[21] X. Gong, M. Tong, F. G. Brunetti, J. Seo, Y. Sun, D. Moses, F. Wudl, A. J. Heeger, *Adv. Mater.* **2011**, *23*, 2272-2277.
[22] D. Credgington, J. R. Durrant, *J. Phys. Chem. Lett.* **2012**, *3*, 1465-1478.
[23] J. K. Lee, W. L. Ma, C. J. Brabec, J. Yuen, J. S. Moon, J. Y. Kim, K. Lee, G. C. Bazan, A. J. Heeger, *J. Am. Chem. Soc.* **2008**, *130*, 3619-3623.
[24] a) J. A. Röhr, D. Moia, S. A. Haque, T. Kirchartz, J. Nelson, *J. Phys. Condens. Matter* **2018**, *30*, 105901; b) J. Dacuña, A. Salleo, *Phys. Rev. B* **2011**, *84*, 195209.
[25] a) R. Hou, M. Li, J. Wang, Z. Bi, S. Feng, X. Xu, W. Ma, Z. Bo, *Journal of Materials Chemistry C* **2019**, *7*, 3335-3341; b) J. R. Tumbleston, B. A. Collins, L. Yang, A. C. Stuart, E. Gann, W. Ma, W. You, H. Ade, *Nat. Photonics* **2014**, *8*, 385; c) V. Vohra, K. Kawashima, T. Kakara, T. Koganezawa, I. Osaka, K. Takimiya, H. Murata, *Nat. Photonics* **2015**, *9*, 403.
[26] a) Y. Yang, W. Chen, L. Dou, W.-H. Chang, H.-S. Duan, B. Bob, G. Li, Y. Yang, *Nat. Photonics* **2015**, *9*, 190; b) A. Salleo, *Mater. Today* **2007**, *10*, 38-45.
[27] a) K. C. Harper, E. N. Bess, M. S. Sigman, *Nature Chemistry* **2012**, *4*, 366; b) D. Datta, D. Majumdar, *J. Phys. Org. Chem.* **1991**, *4*, 611-617.
[28] a) I. Botiz, N. Stingelin, *Materials (Basel, Switzerland)* **2014**, *7*, 2273-2300; b) A. J. Bourque, S. Engmann, A. Fuster, C. R. Snyder, L. J. Richter, P. B. Geraghty, D. J. Jones, *J. Mater. Chem. A* **2019**, *7*, 16458-16471; c) A. J. Moulé, K. Meerholz, *Adv. Mater.* **2008**, *20*, 240-245.
[29] R. R. Gagne, C. A. Koval, G. C. Lisensky, *Inorganic Chemistry* **1980**, *19*, 2854-2855.
[30] A. Hexemer, W. Bras, J. Glossinger, E. Schaible, E. Gann, R. Kirian, A. MacDowell, M. Church, B. Rude, H. Padmore, *Journal of Physics: Conference Series* **2010**, *247*, 012007.
[31] a) K.-L. Ou, R. Ehamparam, G. MacDonald, T. Stubhan, X. Wu, R. C. Shallcross, R. Richards, C. J. Brabec, S. S. Saavedra, N. R. Armstrong, *ACS Appl. Mater. Interfaces* **2016**, *8*, 19787-19798; b) I. Ullah, S. K. Shah, S. Wali, K. Hayat, S. A. Khattak, A. Khan, *Materials Research Express* **2017**, *4*, 125505.
[32] D. Y. Kim, J. Subbiah, G. Sarasqueta, F. So, H. Ding, Irfan, Y. Gao, *Appl. Phys. Lett.* **2009**, *95*, 093304.
[33] C. A. Gueymard, D. Myers, K. Emery, *Solar Energy* **2002**, *73*, 443-467.
[34] M. Klikar, V. Jelínková, Z. Růžičková, T. Mikysek, O. Pytela, M. Ludwig, F. Bureš, *Eur. J. Org. Chem.* **2017**, *2017*, 2764-2779.

Appendix IV. NMR Spectra for Compounds Discussed in Chapter 4

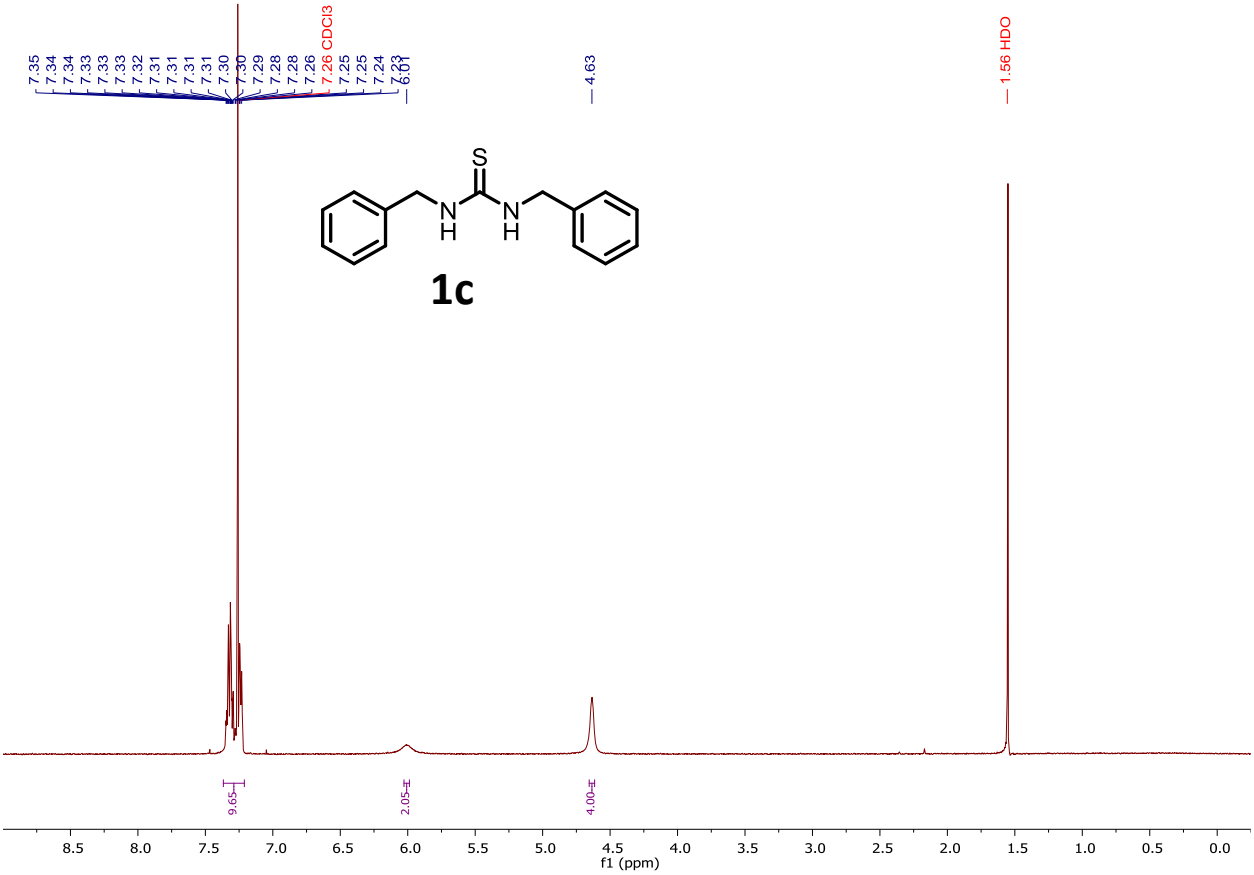

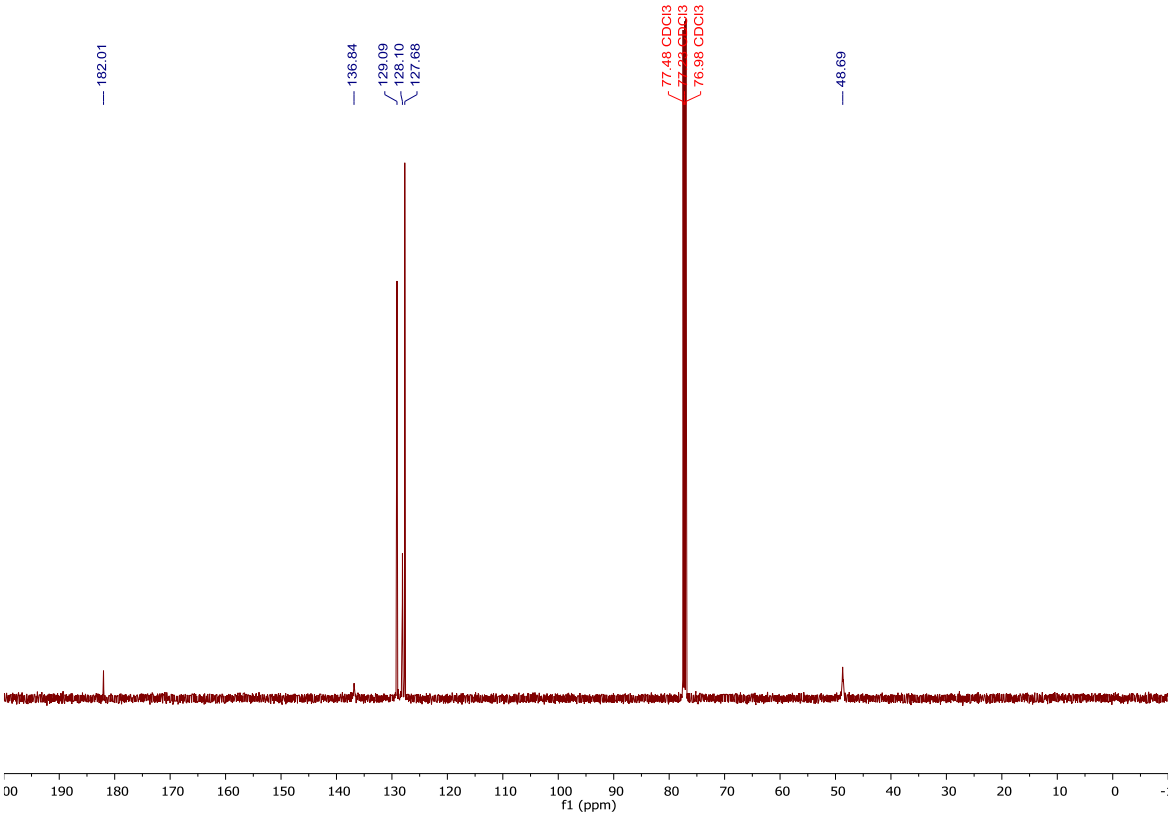

S
C8H17
N
H
N
H
C8H17

1d

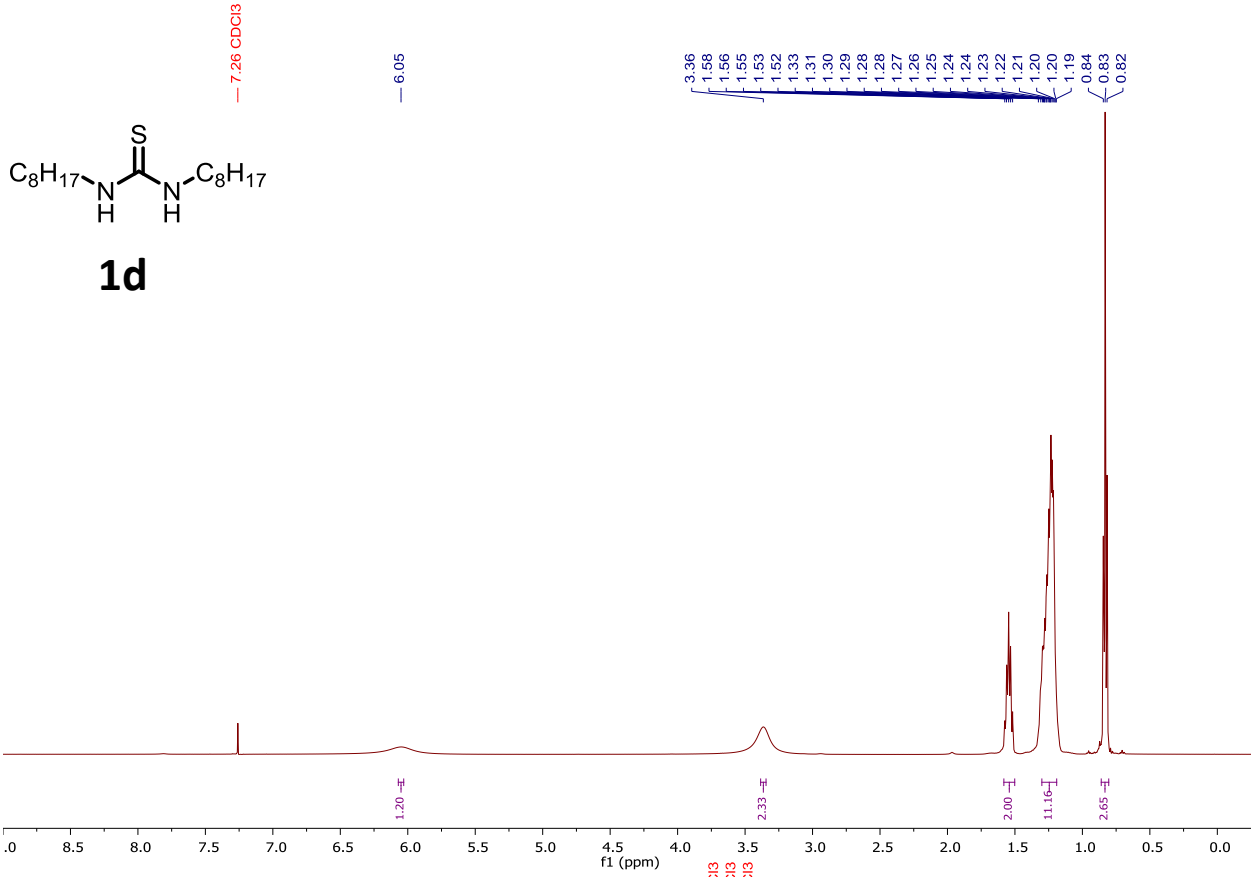
7.26 CDCl3
6.05
3.36
1.58
1.56
1.55
1.53
1.52
1.33
1.31
1.30
1.29
1.28
1.28
1.27
1.26
1.25
1.24
1.24
1.23
1.22
1.21
1.20
1.20
1.19
0.84
0.83
0.82
1.20
2.33
2.00
11.16
2.65
f1 (ppm)

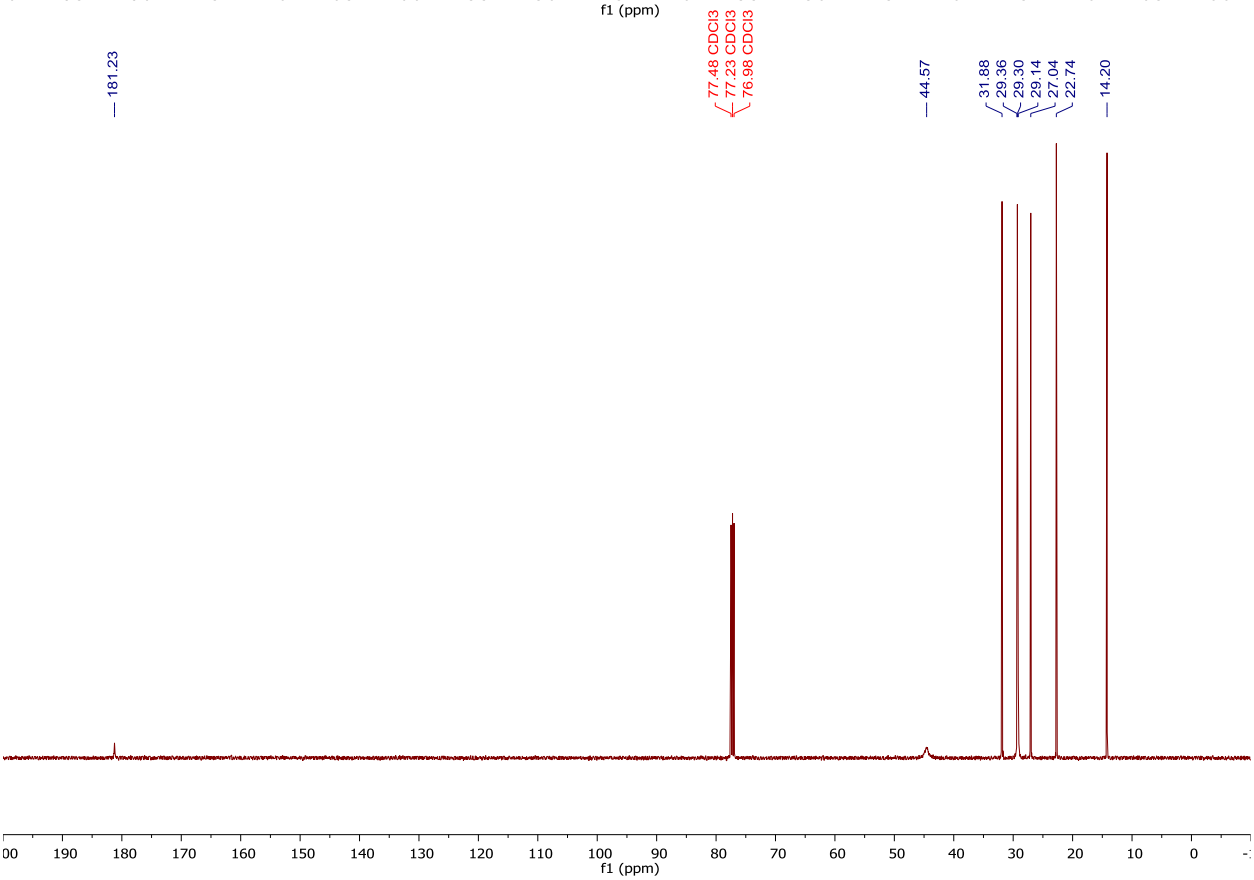
181.23
77.48 CDCl3
77.23 CDCl3
76.98 CDCl3
44.57
31.88
29.36
29.30
29.14
27.04
22.74
14.20
f1 (ppm)

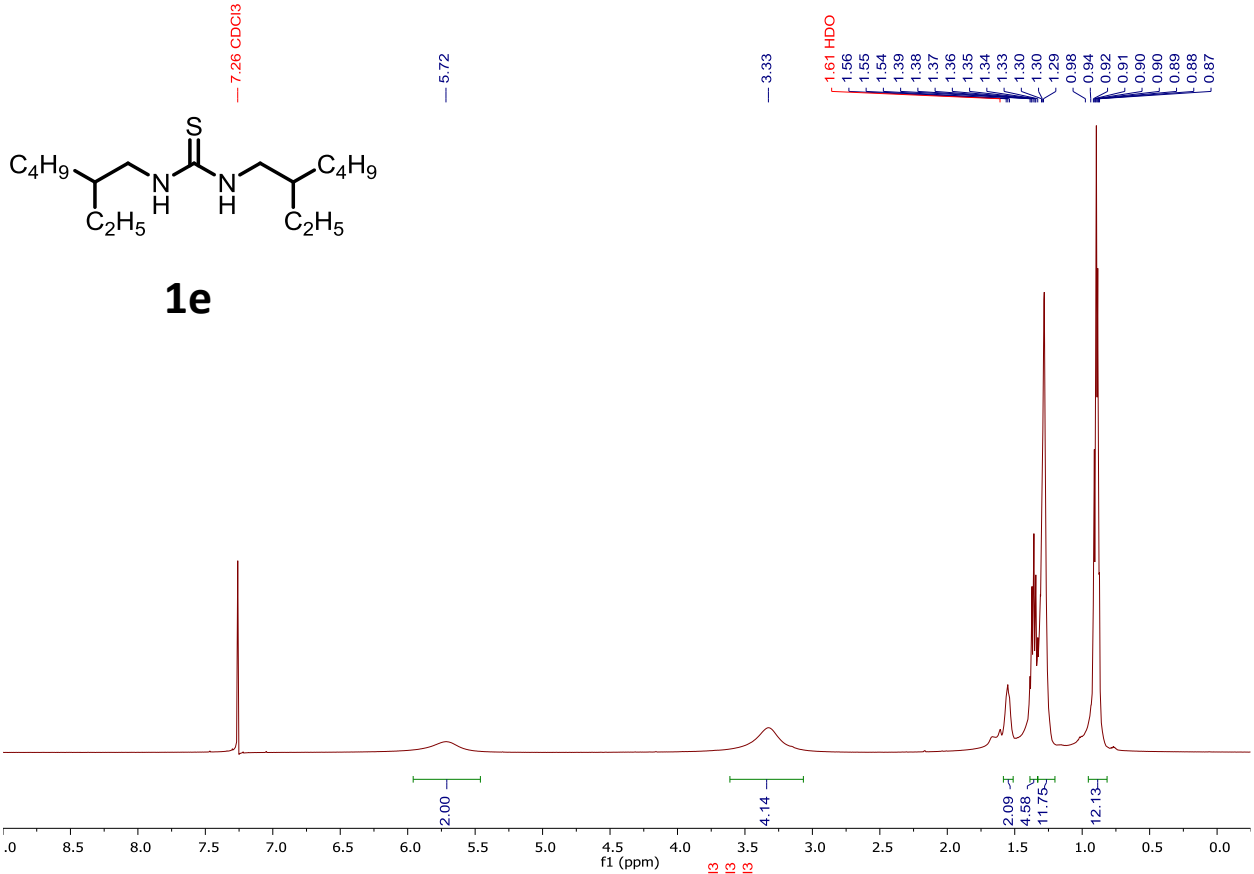
7.26 CDCl3
5.72
3.33
1.61 HDO
1.56
1.55
1.54
1.39
1.38
1.37
1.36
1.35
1.34
1.33
1.30
1.30
1.29
0.98
0.94
0.92
0.91
0.90
0.90
0.89
0.88
0.87
S
C4H9
N
H
N
H
C4H9
C2H5
C2H5
1e
2.00
4.14
2.09
4.58
11.75
12.13
f1 (ppm)

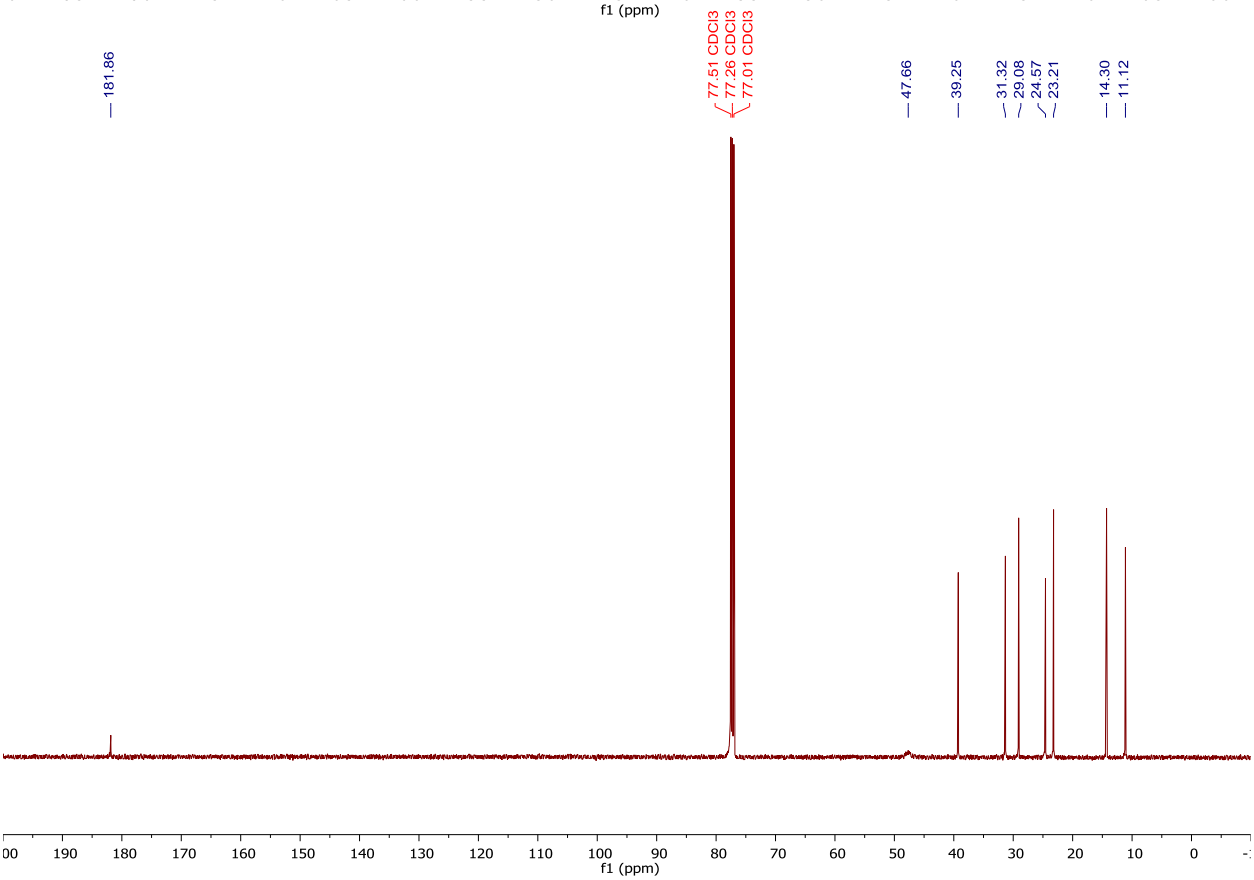
181.86
77.51 CDCl3
77.26 CDCl3
77.01 CDCl3
47.66
39.25
31.32
29.08
24.57
23.21
14.30
11.12
f1 (ppm)

2a

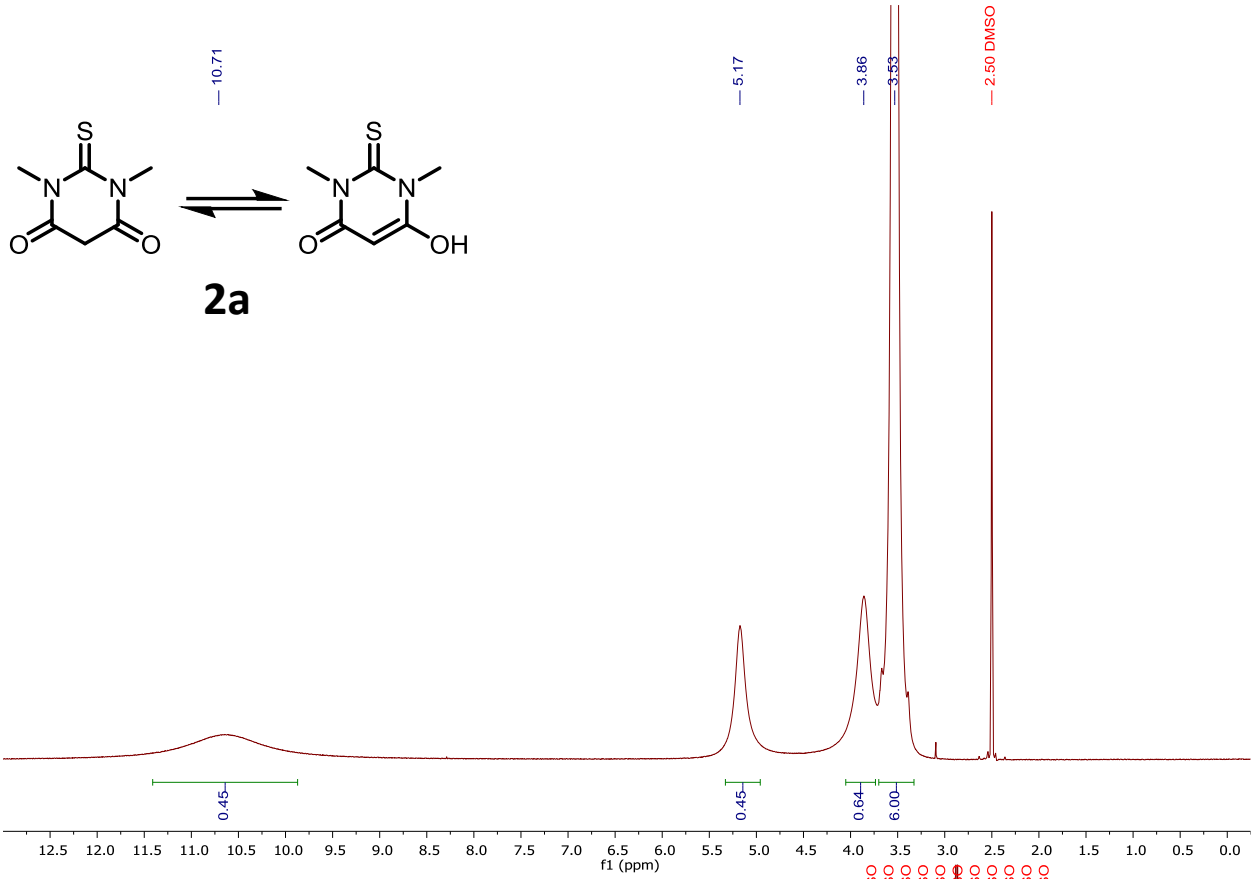
10.71
5.17
3.86
3.53
2.50 DMSO
0.45
0.45
0.64
6.00
f1 (ppm)

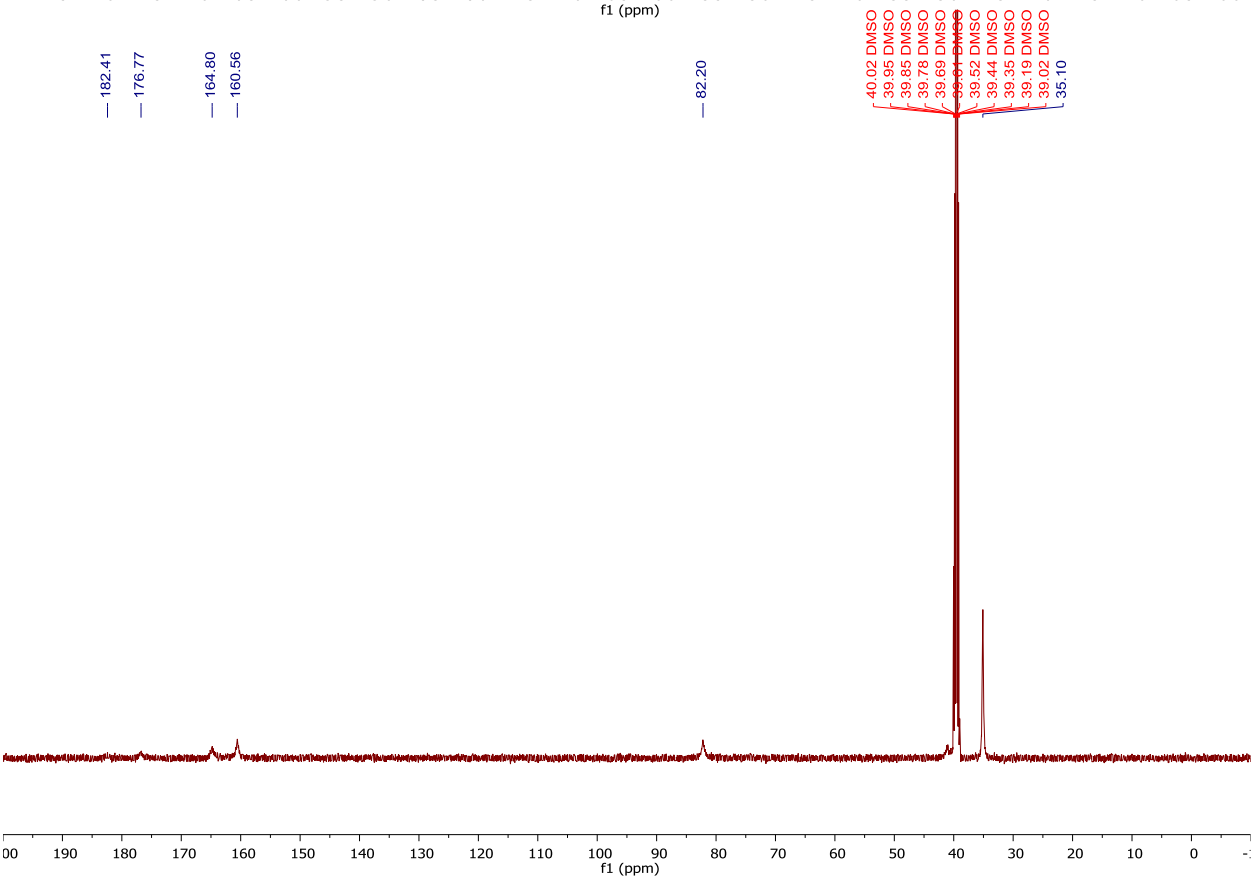
182.41
176.77
164.80
160.56
82.20
40.02 DMSO
39.95 DMSO
39.85 DMSO
39.78 DMSO
39.69 DMSO
39.52 DMSO
39.44 DMSO
39.35 DMSO
39.19 DMSO
39.02 DMSO
35.10
f1 (ppm)

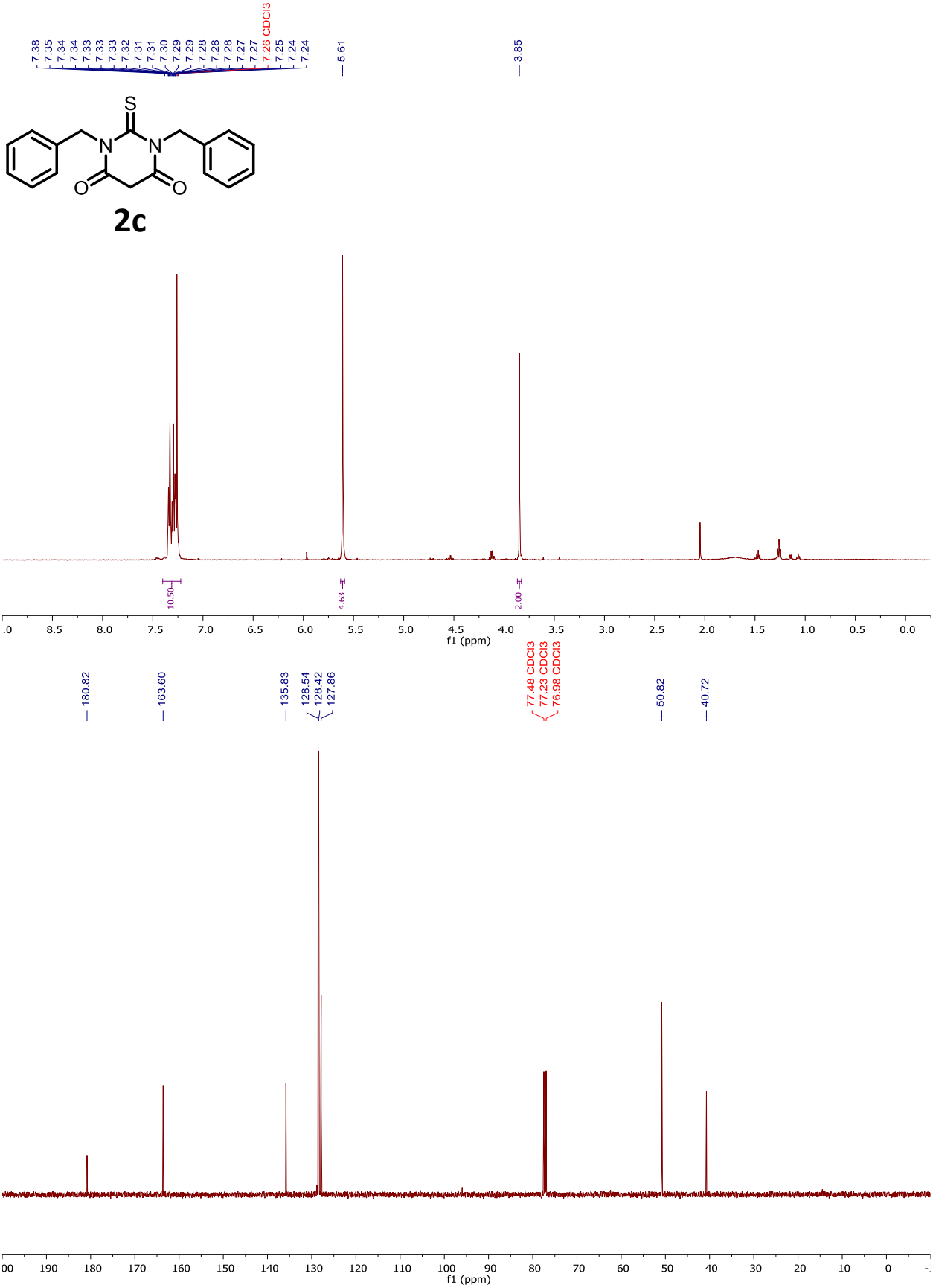
7.38
7.35
7.34
7.34
7.33
7.33
7.33
7.32
7.31
7.31
7.30
7.29
7.29
7.28
7.28
7.28
7.27
7.27
7.26 CDCl3
7.25
7.24
7.24
5.61
3.85
S
N
N
O
O
2c
10.50
4.63
2.00
f1 (ppm)
180.82
163.60
135.83
128.54
128.42
127.86
77.48 CDCl3
77.23 CDCl3
76.98 CDCl3
50.82
40.72
f1 (ppm)

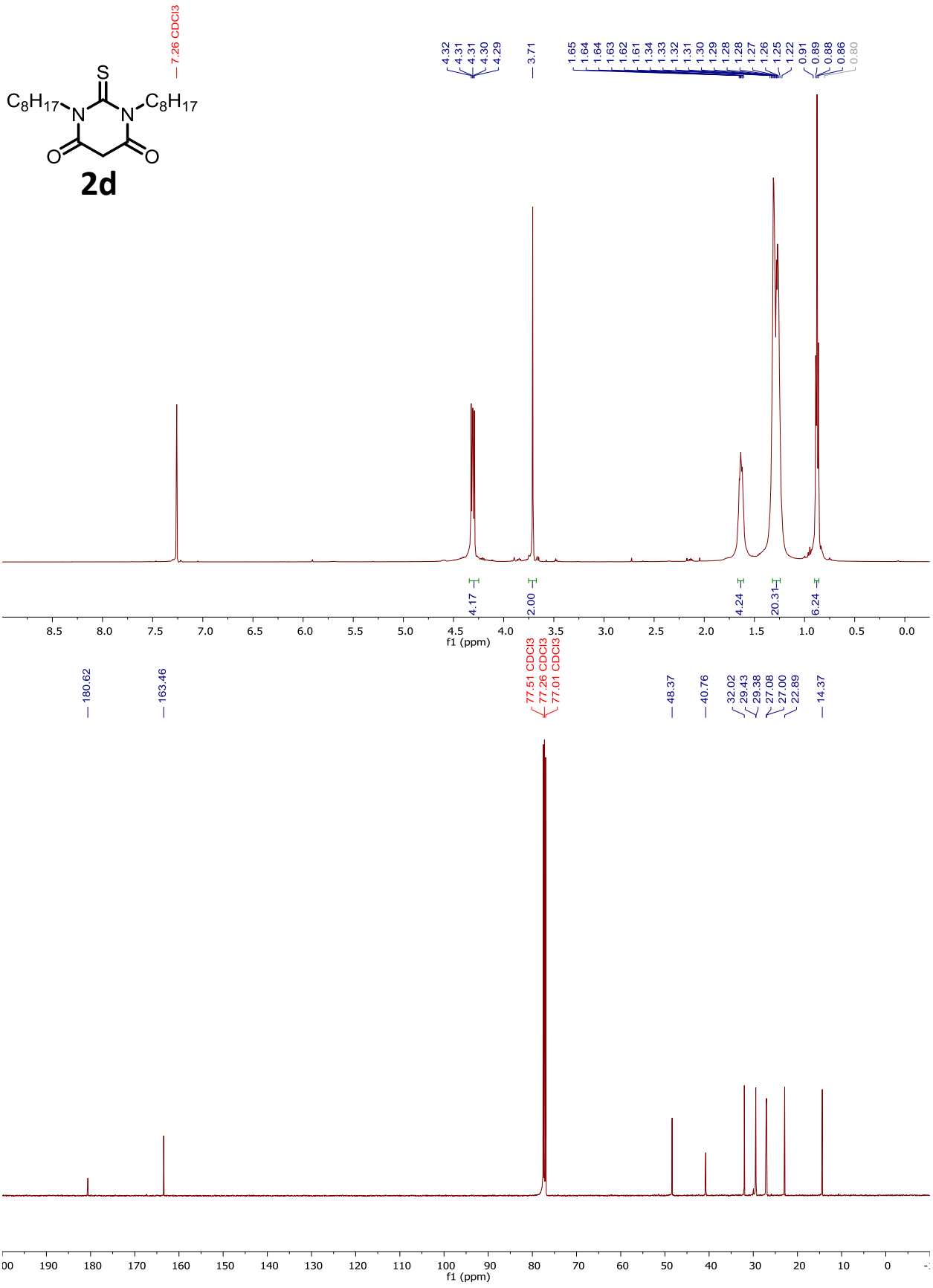
7.26 CDCl3
S
C8H17
N
N
C8H17
O
O
2d
4.32
4.31
4.31
4.30
4.29
3.71
1.65
1.64
1.64
1.63
1.62
1.61
1.34
1.33
1.32
1.31
1.30
1.29
1.28
1.28
1.27
1.26
1.25
1.22
0.91
0.89
0.88
0.86
0.80
4.17
2.00
4.24
20.31
6.24
f1 (ppm)
180.62
163.46
77.51 CDCl3
77.26 CDCl3
77.01 CDCl3
48.37
40.76
32.02
29.43
29.38
27.08
27.00
22.89
14.37
f1 (ppm)

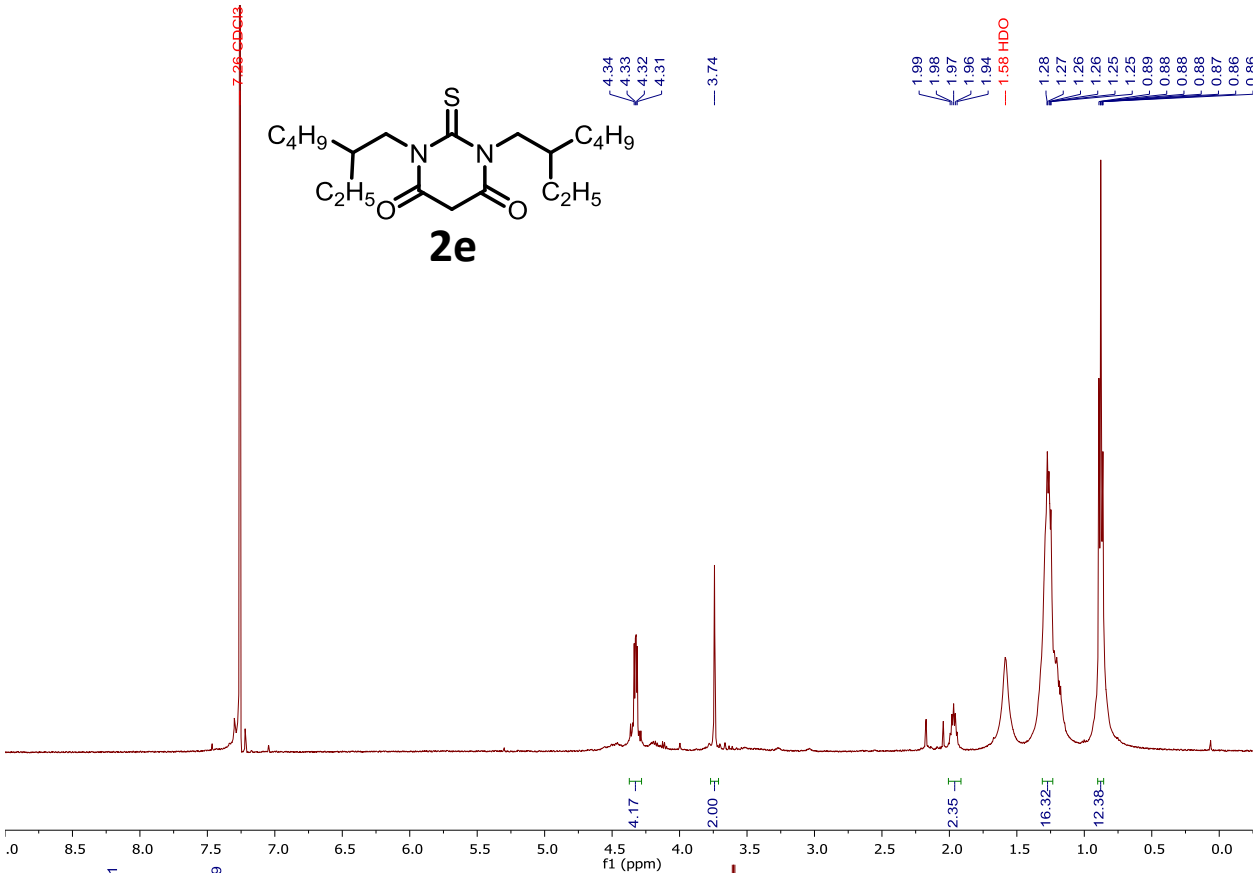
7.26 CDCl3
4.34
4.33
4.32
4.31
3.74
1.99
1.98
1.97
1.96
1.94
1.58 HDO
1.28
1.27
1.26
1.26
1.25
1.25
0.89
0.88
0.88
0.88
0.87
0.86
4.17
2.00
2.35
16.32
12.38
f1 (ppm)

2e

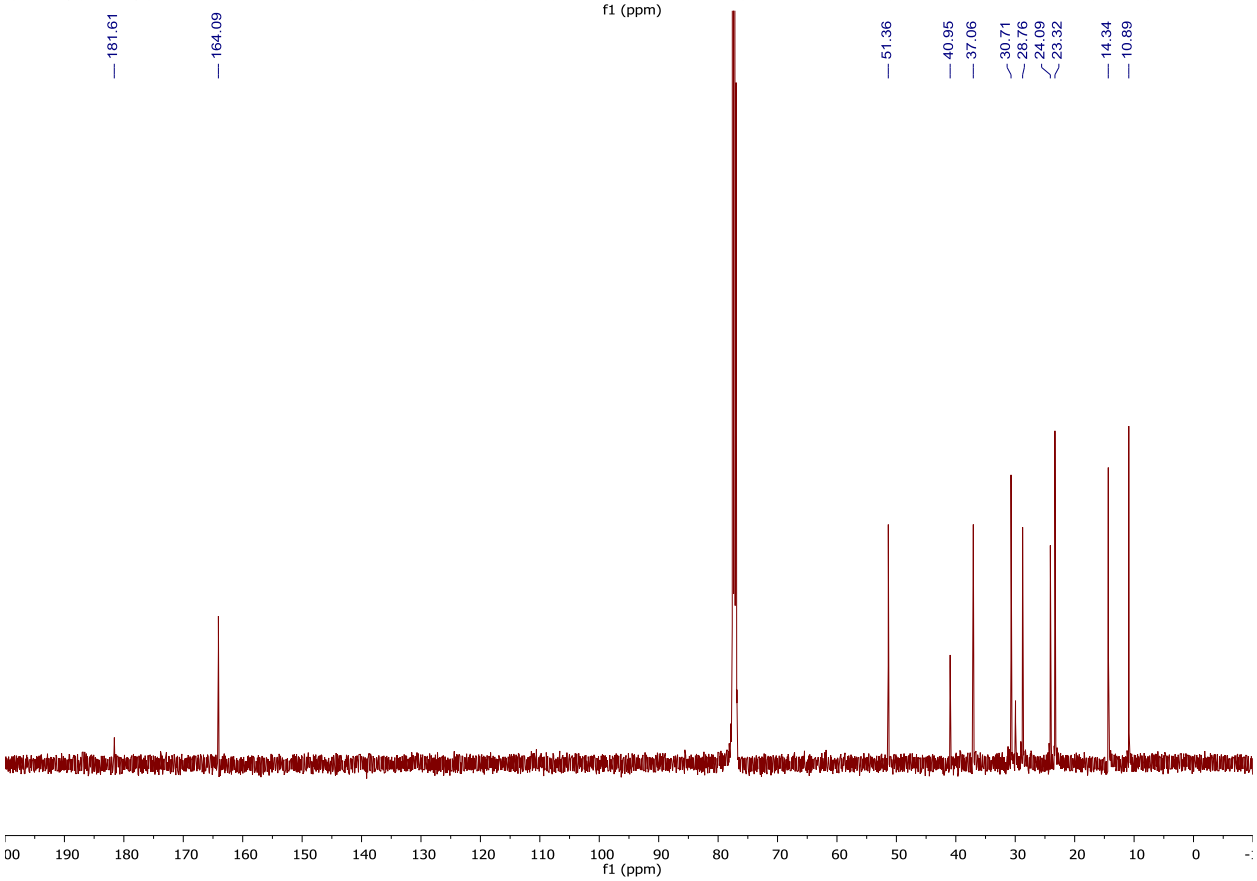
181.61
164.09
51.36
40.95
37.06
30.71
28.76
24.09
23.32
14.34
10.89
f1 (ppm)

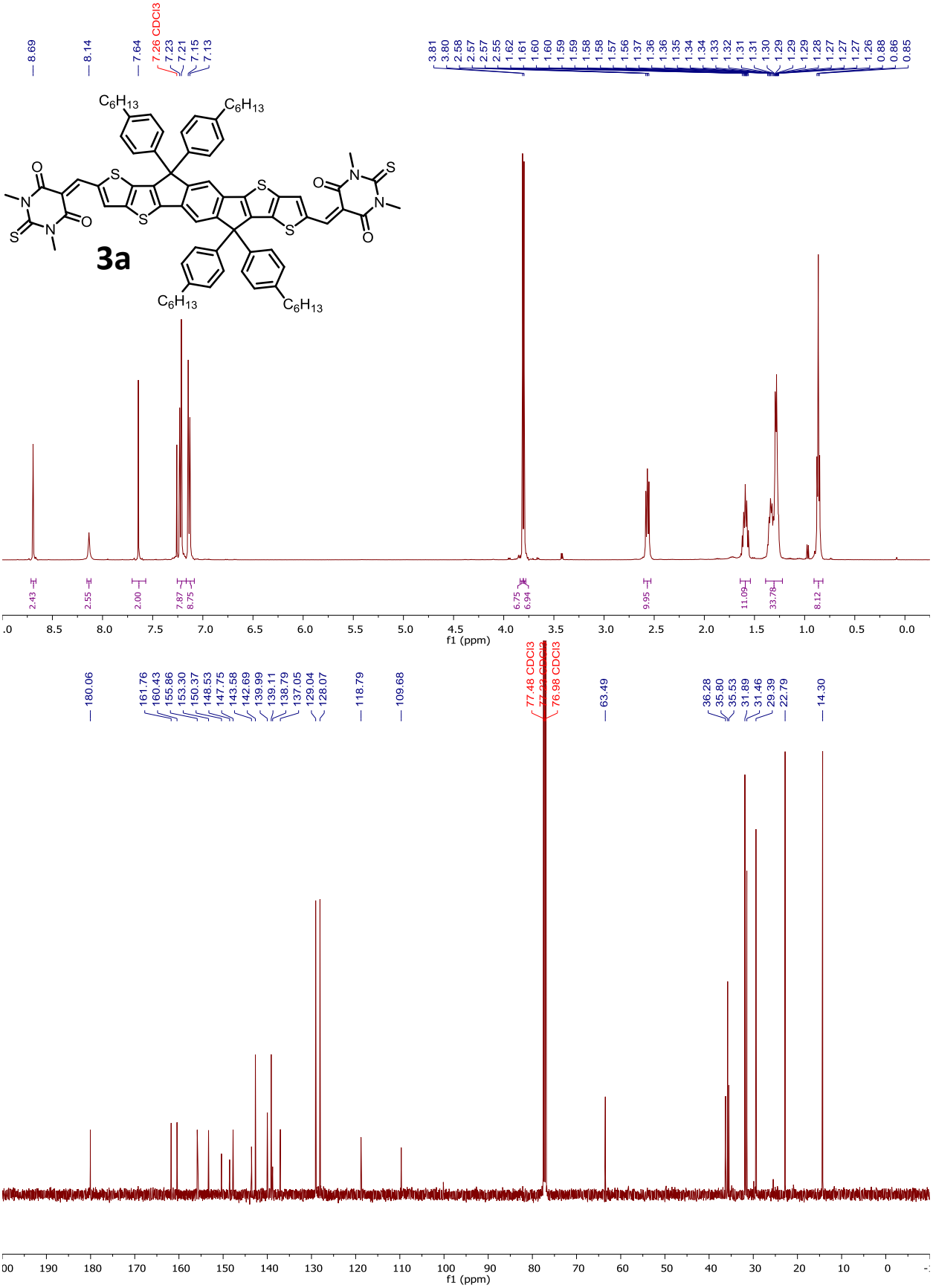
8.69
8.14
7.64
7.26 CDCl3
7.23
7.21
7.15
7.13
3.81
3.80
2.58
2.57
2.57
2.55
1.62
1.61
1.60
1.60
1.59
1.59
1.58
1.58
1.57
1.56
1.37
1.36
1.36
1.35
1.34
1.34
1.33
1.32
1.31
1.31
1.30
1.29
1.29
1.29
1.28
1.27
1.27
1.27
1.26
0.88
0.86
0.85
C6H13
C6H13
C6H13
C6H13
3a
2.43
2.55
2.00
7.87
8.75
6.75
6.94
9.95
11.09
33.78
8.12
f1 (ppm)
180.06
161.76
160.43
155.86
153.30
150.37
148.53
147.75
143.58
142.69
139.99
139.11
138.79
137.05
129.04
128.07
118.79
109.68
77.48 CDCl3
77.23 CDCl3
76.98 CDCl3
63.49
36.28
35.80
35.53
31.89
31.46
29.39
22.79
14.30
f1 (ppm)

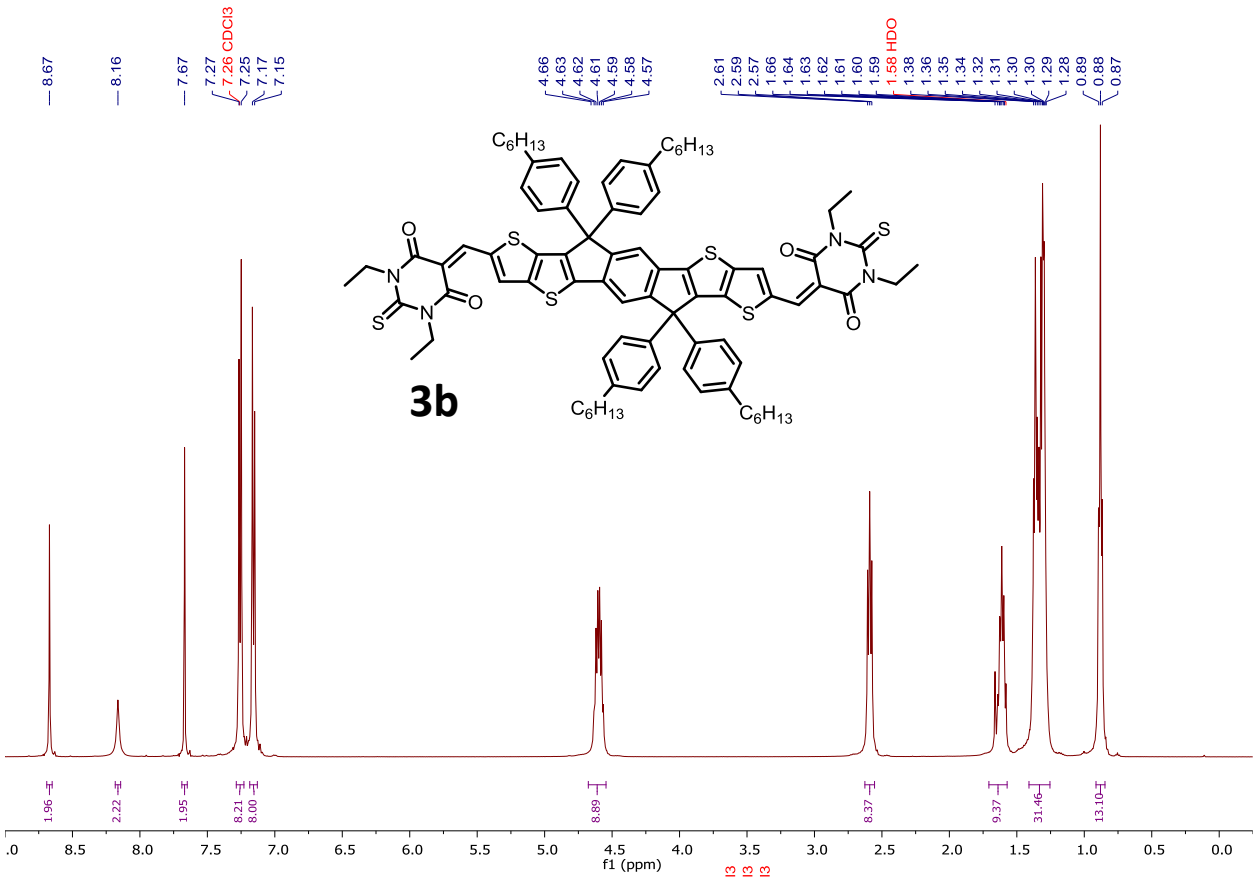
8.67
8.16
7.67
7.27
7.26 CDCl3
7.25
7.17
7.15
4.66
4.63
4.62
4.61
4.59
4.58
4.57
2.61
2.59
2.57
1.66
1.64
1.63
1.62
1.61
1.60
1.59
1.58 HDO
1.38
1.36
1.35
1.34
1.32
1.31
1.30
1.30
1.29
1.28
0.89
0.88
0.87
3b
1.96
2.22
1.95
8.21
8.00
8.89
8.37
9.37
31.46
13.10
f1 (ppm)

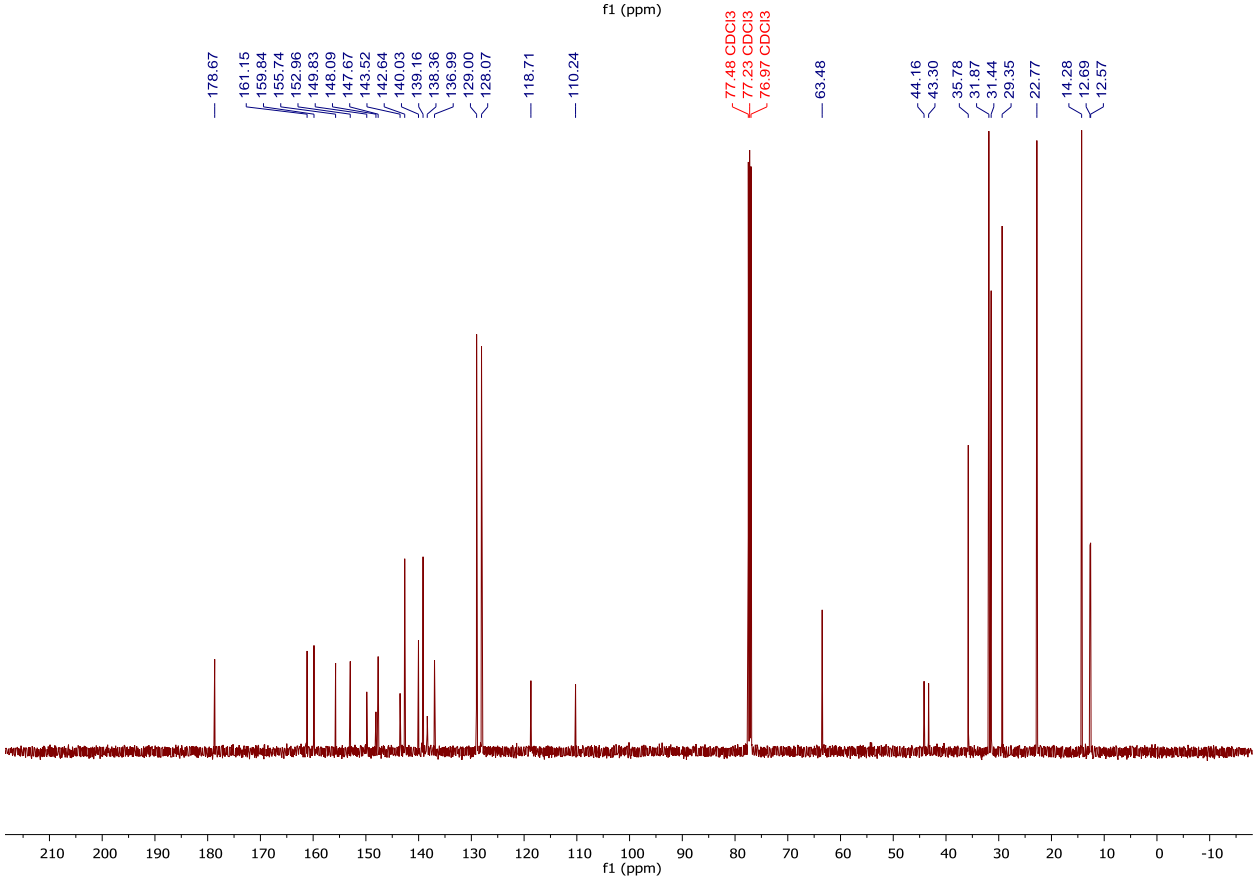
178.67
161.15
159.84
155.74
152.96
149.83
148.09
147.67
143.52
142.64
140.03
139.16
138.36
136.99
129.00
128.07
118.71
110.24
77.48 CDCl3
77.23 CDCl3
76.97 CDCl3
63.48
44.16
43.30
35.78
31.87
31.44
29.35
22.77
14.28
12.69
12.57
f1 (ppm)

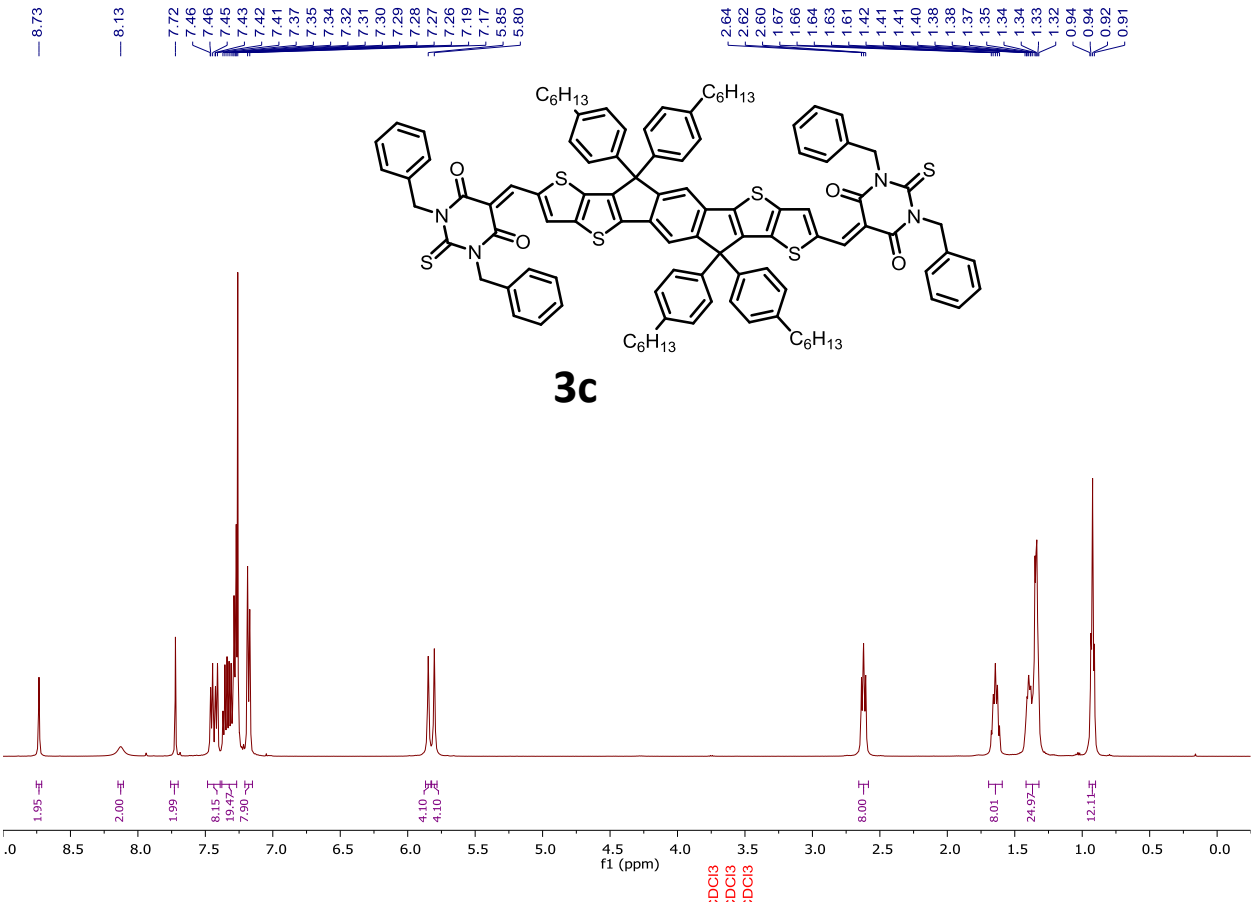
8.73
8.13
7.72
7.46
7.46
7.45
7.43
7.42
7.41
7.37
7.35
7.34
7.32
7.31
7.30
7.29
7.28
7.27
7.26
7.19
7.17
5.85
5.80
2.64
2.62
2.60
1.67
1.66
1.64
1.63
1.61
1.42
1.41
1.41
1.40
1.38
1.38
1.37
1.35
1.34
1.34
1.33
1.32
0.94
0.94
0.92
0.91
C6H13
C6H13
C6H13
C6H13
1.95
2.00
1.99
8.15
19.42
7.90
4.10
4.10
8.00
8.01
24.97
12.11
f1 (ppm)

3c

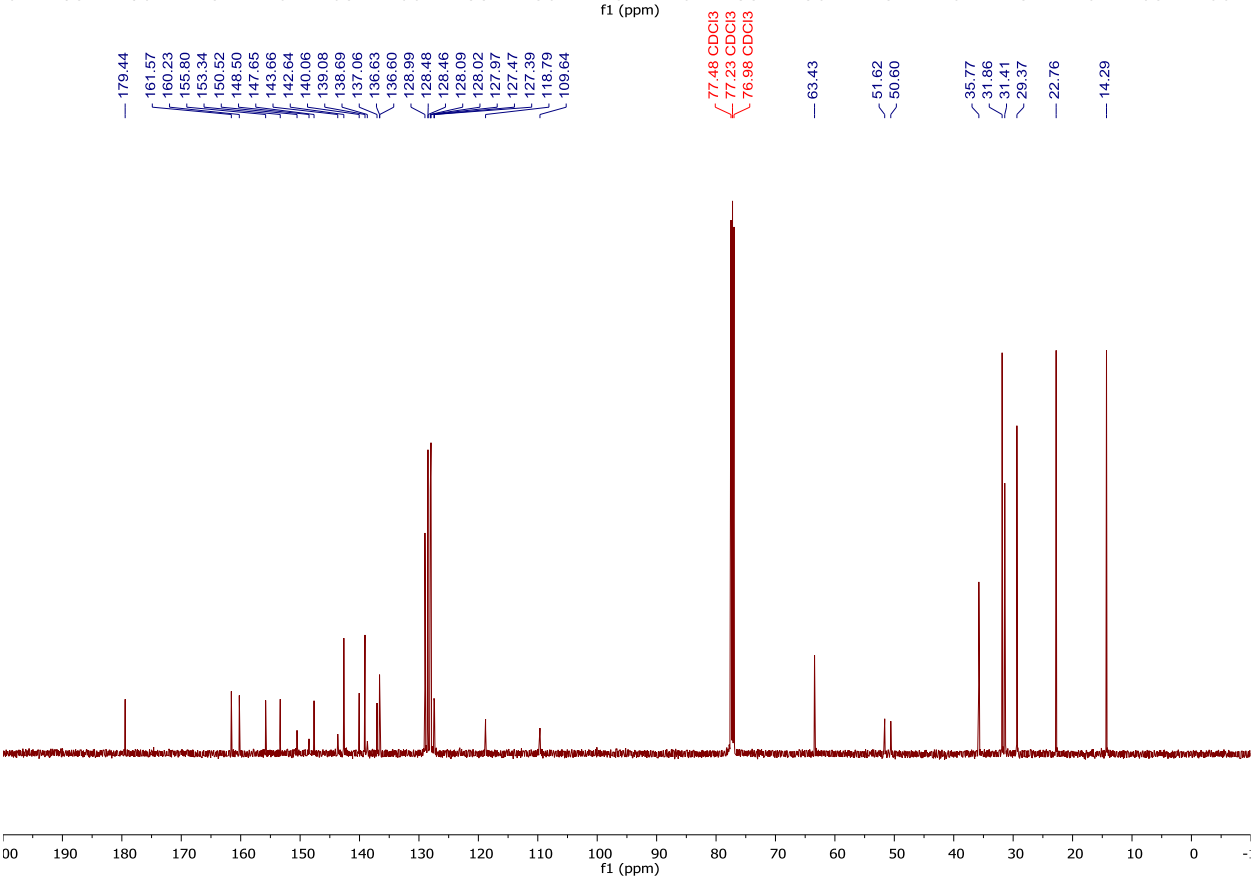
179.44
161.57
160.23
155.80
153.34
150.52
148.50
147.65
143.66
142.64
140.06
139.08
138.69
137.06
136.63
136.60
128.99
128.48
128.46
128.09
128.02
127.97
127.47
127.39
118.79
109.64
77.48 CDCl3
77.23 CDCl3
76.98 CDCl3
63.43
51.62
50.60
35.77
31.86
31.41
29.37
22.76
14.29
f1 (ppm)

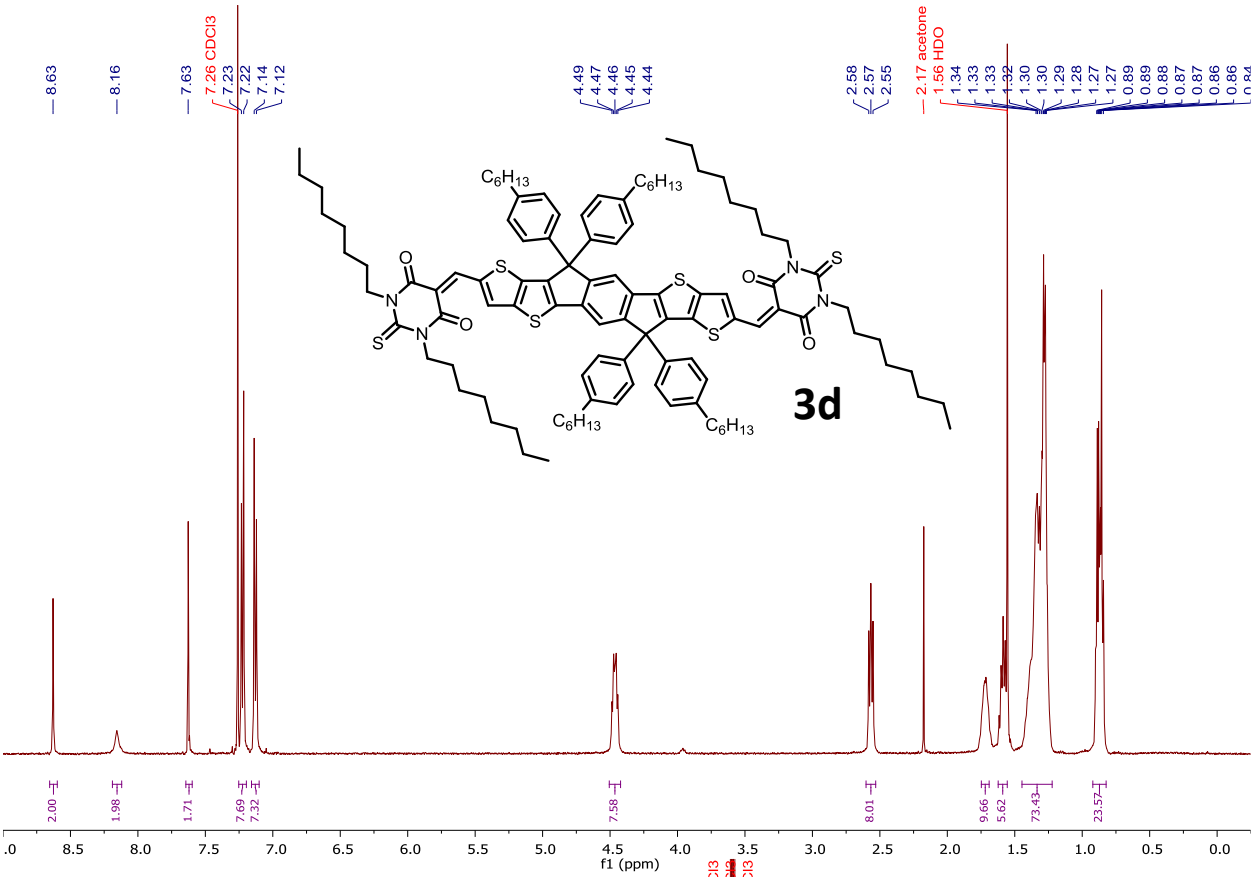
8.63
8.16
7.63
7.26 CDCl3
7.23
7.22
7.14
7.12
4.49
4.47
4.46
4.45
4.44
2.58
2.57
2.55
2.17 acetone
1.56 HDO
1.34
1.33
1.33
1.32
1.30
1.30
1.29
1.28
1.27
1.27
0.89
0.89
0.88
0.87
0.87
0.86
0.86
2.00
1.98
1.71
7.69
7.32
7.58
8.01
9.66
5.62
73.43
23.57
f1 (ppm)
3d

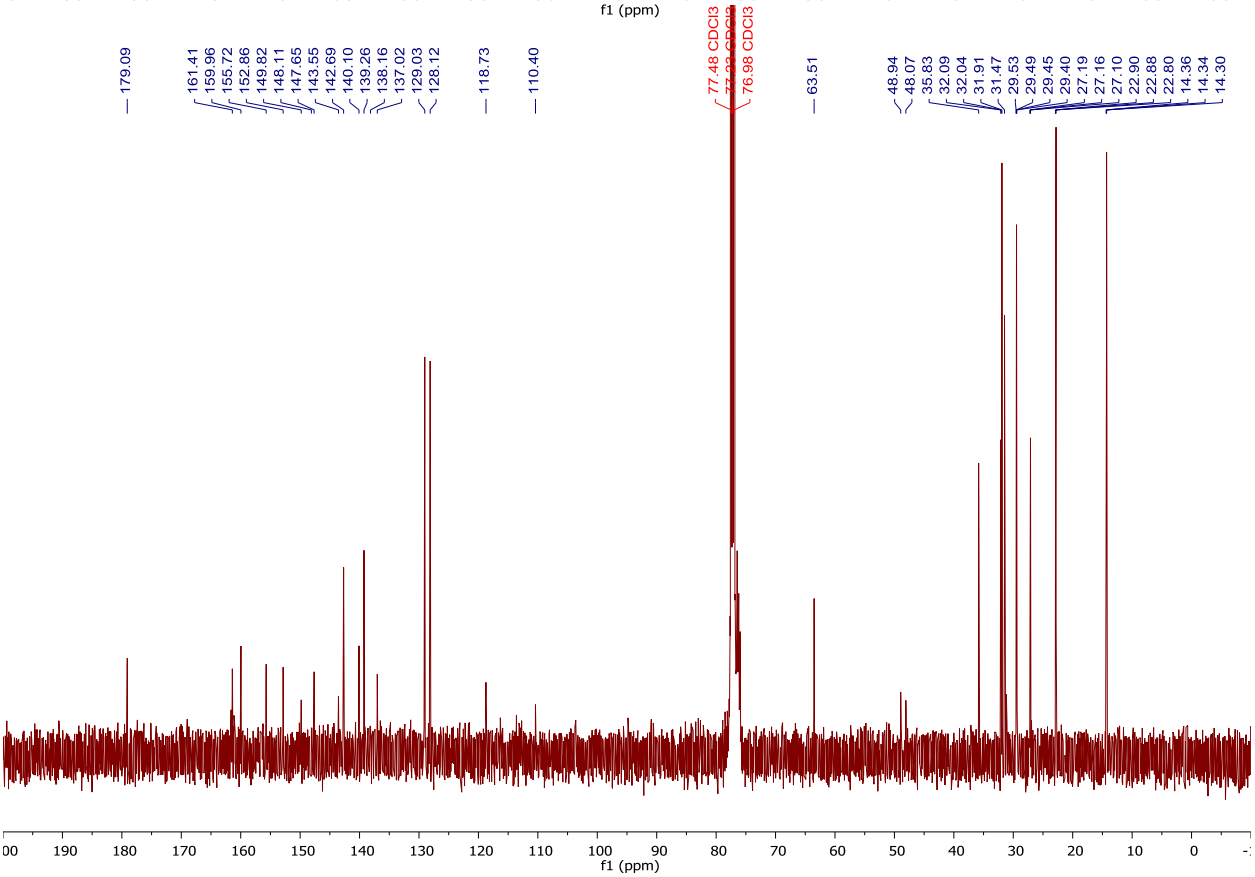
179.09
161.41
159.96
155.72
152.86
149.82
148.11
147.65
143.55
142.69
140.10
139.26
138.16
137.02
129.03
128.12
118.73
110.40
77.48 CDCl3
77.02 CDCl3
76.98 CDCl3
63.51
48.94
48.07
35.83
32.09
32.04
31.91
31.47
29.53
29.49
29.45
29.40
27.19
27.16
27.10
22.90
22.88
22.80
14.36
14.34
14.30
f1 (ppm)

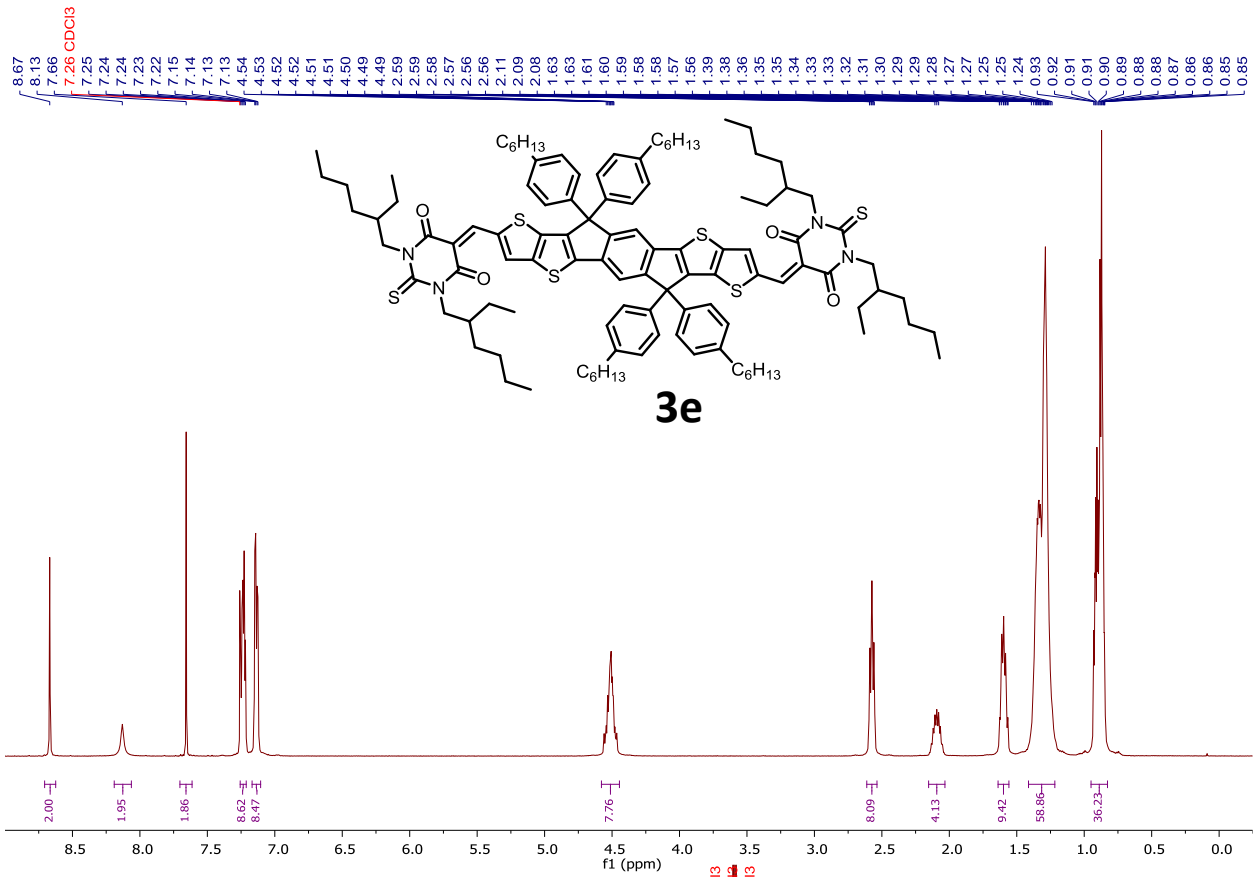
8.67 8.13 7.66 7.26 CDCl3 7.25 7.24 7.24 7.23 7.22 7.15 7.14 7.13 7.13 4.54 4.53 4.52 4.52 4.51 4.51 4.50 4.49 4.49 2.59 2.59 2.58 2.57 2.56 2.56 2.11 2.09 2.08 1.63 1.63 1.61 1.60 1.59 1.58 1.58 1.57 1.56 1.39 1.38 1.36 1.35 1.35 1.34 1.33 1.33 1.32 1.31 1.30 1.29 1.29 1.28 1.27 1.27 1.25 1.25 1.24 0.93 0.92 0.91 0.91 0.90 0.89 0.88 0.88 0.87 0.86 0.86 0.85 0.85
C6H13
3e
2.00 1.95 1.86 8.62 8.47 7.76 8.09 4.13 9.42 58.86 36.23
f1 (ppm)

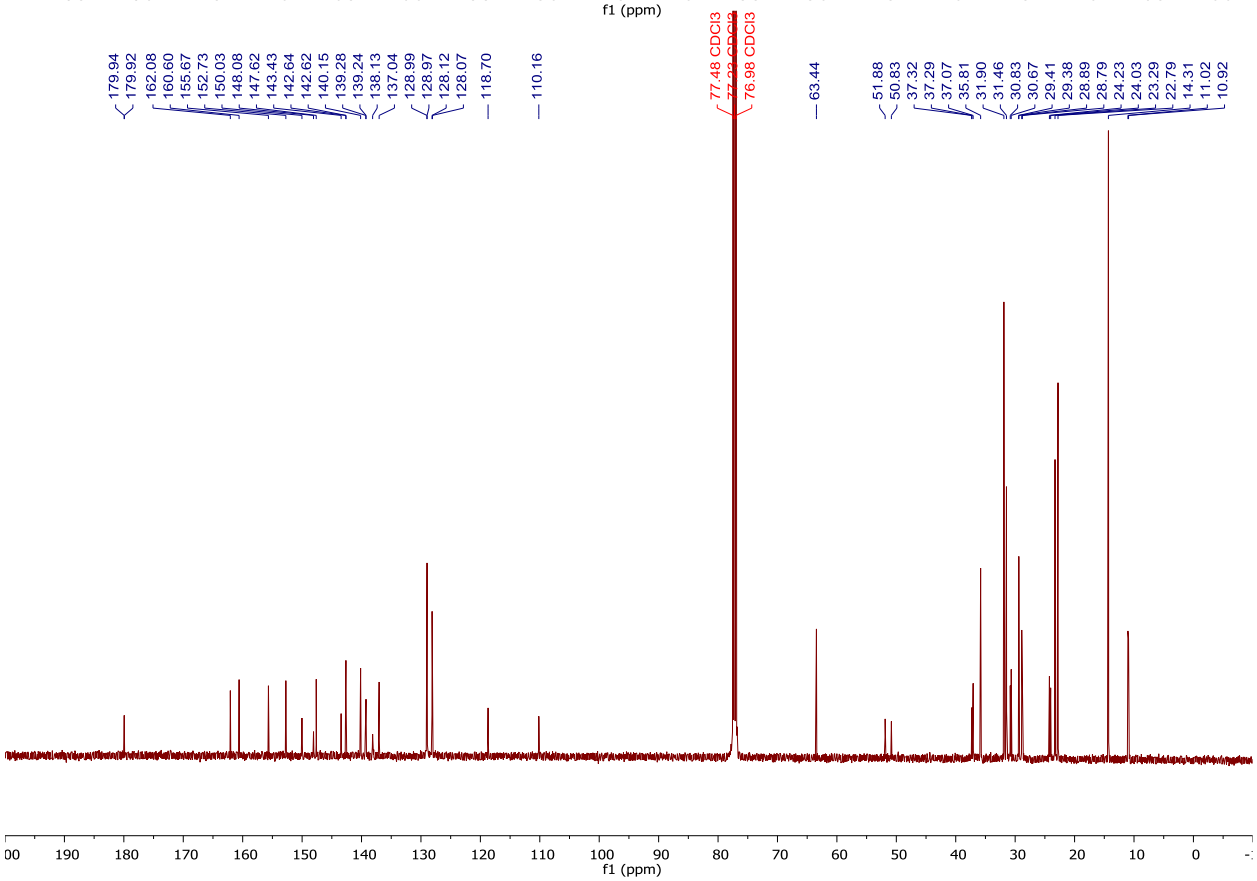
179.94 179.92 162.08 160.60 155.67 152.73 150.03 148.08 147.62 143.43 142.64 142.62 140.15 139.28 139.24 138.13 137.04 128.99 128.97 128.12 128.07 118.70 110.16
77.48 CDCl3 77.23 CDCl3 76.98 CDCl3
63.44
51.88 50.83 37.32 37.29 37.07 35.81 31.90 31.46 30.83 30.67 29.41 29.38 28.89 28.79 24.23 24.03 23.29 22.79 14.31 11.02 10.92
f1 (ppm)